Materials Based on the Polymer of Intrinsic Microporosity PIM-1 for Hydrogen Storage Applications

Holyfield, Leighton

Award date:
2018

Awarding institution:
University of Bath

Materials Based on the Polymer of Intrinsic Microporosity PIM-1 for Hydrogen Storage Applications

Leighton Thomas Holyfield

Supervisors:

Prof. Tim Mays, Department of Chemical Engineering (Lead)

Prof. Andy Burrows, Department of Chemistry

A thesis submitted for the degree of Doctor of Philosophy

University of Bath

Centre for Sustainable Chemical Technologies

Department of Chemical Engineering

February 2018

COPYRIGHT

Signed:

Date: 06/02/2018

AUTHORSHIP DECLARATION

The presented PhD was funded through the Doctoral Training Centre for Sustainable Chemical Technologies, by the UK Engineering and Physical Sciences Research Council.

The work presented in this thesis, except where otherwise noted, was done by the author with supervision and guidance from his academic supervisor, Dr Timothy J Mays, Head of Department in the Department of Chemical Engineering at the University of Bath.

Some of the work reported in this thesis has been published in journal articles and presented at conferences, as indicated in the dissemination section.

Abstract

In response to the ever-increasing global energy demand and the need to move away from non-renewable and CO_2-emitting fossil fuels as the primary energy production method, renewable energy sources have become more and more viable as energy production methods. However, given the unreliable and instantaneous nature of these energy sources, reliable, renewable energy storage methods are required. Hydrogen is an excellent candidate as a chemical energy store, as it is highly abundant, relatively easily produced as diatomic hydrogen (including from water electrolysis), and only produces water upon its complete combustion. Hydrogen also has the highest gravimetric energy density of any known chemical fuel, meaning that not very much of it is required relative to other chemical fuels. However, hydrogen gas is incredibly sparse, and therefore hydrogen has a very low volumetric energy density, making storage of the material a key challenge in the development of the so-called "hydrogen economy". Most commonly, hydrogen is stored by compressing it to 70 MPa. However, this technique has a number of flaws, including the high expense of strong tanks (and in the case of light duty vehicles, lightweight materials are also required), and the inherent safety risks that high pressure, highly flammable gas poses.

One of the alternatives to compression is to store hydrogen by adsorption, which uses high surface area materials to densify hydrogen via the formation of weak physical bonds. This research line is well developed, and a number of different materials has been created that show good potential as hydrogen storage materials, such as activated carbons and metal organic frameworks. However, the vast majority of materials developed for this purpose are tailored only with the hydrogen uptake in mind, which can cause issues as the focus of development shifts from small scale tests to full tank scale. One adsorptive that shows a number of highly useful engineering properties on the large scale, such as good thermal resistance and solution processability, is the polymer of intrinsic microporosity PIM-1. This material can be processed into a number of morphologies without losing porosity, and shows good thermal and mechanical resistance. However, its adsorption capacity is rather limited, with the BET surface area generally reported in the 700 – 800 $m^2 g^{-1}$ range, and hydrogen uptake of 1.45 wt% at 77 K and 1 MPa.

This thesis presents two separate studies on attempting to improve the hydrogen uptake of PIM-1 without adversely affecting the material properties that make it attractive. The first of these was the creation of mixed-matrix-membrane style composite films solution cast from PIM-1 and the metal organic framework MIL-101. PIM-1 proved slightly difficult to synthesise consistently with high molecular weight, but MIL-101 is an easy hydrothermal synthesis. Film casting was successfully performed, producing flat, homogeneous films that maintained the MOF crystallinity. These materials were tested for their thermal properties – thermal decompositions proceeded according to the rule of mixtures of the two starting materials, whilst an increasing concentration of MOF was shown to decrease the specific heat capacity.

Both PIM-1 and MIL-101 were shown to adsorb nitrogen as previously reported. The composites showed increasing uptake with MIL-101 content, but at a lower rate than the rule of mixtures. This was a common theme for the N_2 (77 K), CO_2 (293 K) and low pressure H_2 isotherms performed. High pressure isotherms up to 17 MPa were performed on PIM-1 for the first time, showing a maximum excess uptake of 1.8 wt% on the powder and 1.6 wt% on the film, both at 77 K. The composites showed improved uptake with increasing MIL-101, but the maximum uptakes did not meet the rule of mixtures. The uptakes at the highest pressure did, however. Multiple temperature isotherm sets were performed on the PIM-1 film and powder, as well as the 30 wt%

composite. These data sets were hampered largely by machine faults, but contained sufficient valuable data to be able to proceed with parameter fitting. The sensitivity of the isotherms produced in this study to the value of skeletal density is also examined closely.

The second theme of improved H_2 uptake in PIM-1 was to carbonise the material. TGA studies on PIM-1 showed good thermal stability in anoxic conditions, and TGA twinned with mass spectroscopy was able to confirm a previously proposed mechanism of thermal decomposition. Carbonised and activated PIM-1 film samples, and a carbonised powder, were produced using physical activation methods. The adsorption performance of the carbons was disappointing, as the uptakes of N_2 and H_2 (< 0.1 MPa) were reduced post-carbonisation, with little recovery in the activated film. CO_2 uptakes were improved, however. High pressure H_2 isotherms on both the carbonised and activated films showed unusual 'stepping' behaviour in the adsorption curve, but maximum uptakes for both (1.0 – 1.3 wt%) were less than that seen for PIM-1 alone.

Parameter fitting was performed on all of the high pressure H_2 isotherms performed in this study, using a method previously proposed by the Mays group. The parameter fits all showed effective hydrogen densification in the adsorbate layer, although the repeatability of parameter values, and the smoothness of the parameters as a function of temperature were undermined by the low quality of some of the isotherms. Using the parameters acquired, it was possible to calculate the isosteric enthalpy of adsorption for PIM-1 powder (-9.5 kJ mol^{-1}), film (- 8.0 kJ mol^{-1}) and the 30 wt% composite (-9.3 kJ mol^{-1}). The stored and deliverable hydrogen contained within tanks featuring the tested materials were estimated, although only the MIL-101 powder on its own competes with other hydrogen storage adsorbents currently reported.

Acknowledgements

My goodness, it appears we have reached the end. The past four years have been a deeply enriching experience for me, and I have learnt lessons over the course of the last four years that I will never forget.

First and foremost, I must thank my lead supervisor, Prof. Tim Mays. Tim's enthusiasm for science, engineering and the development of young people are evident when you speak to him, and I found his enthusiasm for these subjects infectious! Despite his heavy workload as the Head of Department for Chemical Engineering throughout the entirety of my time at Bath, he has found time for me whenever I've needed it, never failed to provide the resources I needed to get the job done, and always came to our meetings with an abundance of new ideas. Tim also facilitated me in travelling the world for conferences and internships alike, which is a series of experiences that I will forever be grateful for.

Thanks also to my second supervisor Prof. Andy Burrows, whom I admittedly did not consult all that much as my PhD went on, but was always prompt and enthusiastic whenever I needed something of him. Thanks also to Dr. Valeska Ting, who whilst not officially associated with my project, continually acted as a pseudo-supervisor for my project, and I am very grateful for all her help and support, including facilitating my DSC time at the University of Bristol following her move there.

I would never have been able to enjoy these experiences in the first place without the support of the Doctoral Training Centre (DTC) for Sustainable Chemical Technologies, the wider Centre for Sustainable Chemical Technologies (CSCT), the University of Bath and the Engineering and Physical Sciences Research Council (EPSRC), both financially and in terms of other resources. Thank you specifically to Prof. Matthew Davidson, Dr. Janet Scott, Tim, Dr. Marc Hutchby and everyone at the CSCT for giving me this opportunity, and for continuing to drive this excellent institution forward. Happy retirement also to Sheila Apps, who served the CSCT as administrator with a smile, friendly words and a relentless ability to solve the CSCT's problems, no matter how small.

As part of my CSCT experience I was lucky enough to be able to spend 2 months at General Motors' Global Research and Development Centre in Warren, MI. For this, I must say a big thank you to Dr. Anne Dailly, who took me on and supervised my time there, and to Dr. Thomas Yersak, with whom I shared an office and who spared no effort to make me more comfortable in the U.S. Whilst it was a shame I did not perform any work in that time that was relevant to this thesis, I am very grateful to them both for the effort they went to to facilitate my request to work in their facilities, and how comfortable they made my time in the U.S.

In less glamorous times, I have a number of people to thank for facilitating my experimental work in Bath. Thank you to the Chemical Engineering technical team, led first by Dr. Daniel Lou-Hing and later by Dr. Brigite Nunes Simoes Rodrigues, for supporting the laboratories professionally and with friendly faces. In particular, thanks to Fernando Acosta, who served as the technician for Lab 1.04, and always provided help with the adsorption machines when needed – which was more often than we'd have liked! Thank you also to Dr. John Mitchels, Ursula Potter, Dr. Philip Fletcher and Diana Lednitzky from the Microscopy and Analysis Suite for their help acquiring SEM images, Dr Gabriele Kociok-Köhn and Alan Carver for facilitating the acquisition of PXRD samples, and to Dr. Rémi Castaing, who operated a number of pieces of equipment within the CSCT's Chemical Characterisation and Analysis Facility (CCAF), and was ceaselessly helpful in acquiring

data for this thesis. Thanks also to Dr. Paul McKeown, a fellow member of the DTC, who performed some of my GPC analysis. I also had to perform a number of techniques outside of Bath, so I need to thank Ian Gent and the ACCIS lab at the University of Bristol for allowing me to use their DSC, and Stephen Boyer at London Metropolitan University, who performed the CHN analysis.

It could be argued that your research group is one of, if not the biggest, factor affecting your research work, and I am therefore incredibly grateful to have shared laboratory space with some awesome people. When I arrived in Bath, Dr. Nuno Bimbo, Dr. Antonio Noguera-Díaz, and Andrew Physick were the people who were my early support from within Tim's and Valeska's groups, and I am hugely grateful to them all for having patience with me as I messed everything up whilst learning the ropes! Since then, Dr. Mi Tian has joined us, and she also has been a constant source of support and knowledge in my time in the lab. I am grateful to Mi for performing the Raman spectroscopy for this study. In addition, Dr. Rob Dawson, and later Dr. Sébastien Rochat have both been very helpful and friendly postdocs in Chemistry, and both sought to support me in my synthetic adventures without hesitation. I am also grateful to Dr. Katarzyna Polak-Kraśna, a postdoc in Mechanical Engineering, who has participated in the greater research project to which I contributed in the latter part of my PhD, and she has also been nothing if not a pleasure to work with. Thank you all, and I wish you the very best in your continuing careers.

This PhD experience would have been nothing like the experience I had if it had not been for my CSCT cohort. As well as helping me with some of the chemical analyses of my samples (thanks to Helena for her help with both GPC and FTIR!), the 12 others that made up the 2013 cohort have been nothing but wonderful friends and colleagues, with whom I have shared some excellent experiences, and I will always consider each of them friends. To Jemma, Jon, James, Oli, Emma S, Helena, Emma L, Bill, Tami, Tristan, Matt and James James, thank you very much. I love you all.

However, of all the relationships I have cultivated in my four years in Bath, one person has really stood out, becoming my closest ally both in the lab and the social circle. To Jemma Rowlandson, thank you so much for being my partner in crime throughout our time here. Thanks for putting up with me day after day, and for tolerating entire weeks of my presence on our conference trips. I really missed your presence when you followed Valeska to Bristol, and yet still you were able to both facilitate my work and be a great friend. From the bottom of my heart, thank you.

No man is an island, and I must thank my family for continuously supporting me through this adventure. Thank you to my in-laws, Jonathan and Janet Hales, who have provided support and sage wisdom when I've needed it (also for proof reading parts of this thesis, thank you!). To my brother Daniel, thanks for being at my side all this time, and continuing to do so. And to my Mum and Dad, Richard and Katrina Holyfield, thank you for all of your boundless love and support throughout my life. It is my honour to be the first Holyfield to be a doctor.

Last, but by no means least, thank you to Mrs. Robin Anna Holyfield. You are the love of my life, and life is so, so greatly augmented by having you in it. You inspire me to be a better man, and I look forward to sharing my life with you, and growing together with you, for the rest of our days.

Contents

List of Figures

List of Tables

Abbreviations

Abbreviation	Meaning
ASAP	Accelerated Surface Area and Porosimetry
bdc	Benzene Dicarboxylate
BET	Brunauer-Emmett-Teller
BJH	Barrett, Joyna and Helenda
CCD	Charge Coupled Device
CCS	Carbon Capture and Storage
CFRP	Carbon Fibre Reinforced Polymer
CHN	Carbon, Hydrogen and Nitrogen (analysis)
CMP	Conjugated Microporous Polymer
COD	Coefficient of Determination
COF	Covalent Organic Framework
C-SEM	Channel Secondary Electron Multiplier
DA	Dubinin-Astakov (model)
DEF	Diethylformamide
DFT	Density Functional Theory
DMF	Dimethylformamide
DOE	Department of Energy
DR	Dubinin-Radushkevich (model)
DSC	Differential Scanning Calorimetry
DTG	Differential Thermogravimetric (analysis)
EDX	Energy Dispersive X-Ray Spectroscopy
ENG	Expanded Natural Graphite
FTIR	Fourier Transform Infrared Spectroscopy
GPC	Gel Permeation Chromatography
HCP	Hyper Crosslinked Polymer
HK	Horvarth-Kawazoe
HSECOE	Hydrogen Storage Engineering Centre of Excellence
HTP	High Temperature and Pressure
IRMOF	Isoreticular Metal Organic Framework
IUPAC	International Union of Pure and Applied Chemistry
LH_2	Liquid Hydrogen
LHV	Lower Heating Value
LN_2	Liquid Nitrogen
MDSC	Modulated Differential Scanning Calorimetry
MIL	Material d'Institute Lavoisier
MMM	Mixed Matrix Membrane
MOF	Metal Organic Framework
MS	Mass Spectroscopy
NIST	National Institute of Standards and Technology
NLDFT	Non-Localised Density Functional Theory

OEM	Original Equipment Manufacturer
PAF	Porous Aromatic Framework
PALS	Positron Annihilation Lifetime Spectroscopy
PDI	Polydispersity Index
PEM	Proton Exchange Membrane
PIM	Polymer of Intrinsic Microporosity
PPN	Porous Polymer Network
PSD	Pore Size Distribution
PTFE	Poly(tetrafluoroethylene)
PXRD	Powder X-Ray Diffraction
RBF	Round Bottomed Flask
RI	Refractive Index
SEM	Scanning Electron Microscopy
SMR	Steam Methane Reforming
SRNL	Savannah River National Laboratory
TGA	Thermogravimetric Analysis
TG-MS	Thermogravimetric Analysis with Mass Spectroscopy
THF	Tetrahydrofuran
UM	University of Michigan
UQTR	Université du Québec à Troís-Riviéres
UV	Ultraviolet
XPS	X-ray photoelectric spectroscopy
XRD	X-Ray Diffraction
ZIF	Zeolitic Imidazolate Framework

Nomenclature

Symbol	Unit	Designation
a	$g\ mol^{-1}$	BET plot gradient
A	-	Area under Gaussian curve
A_{BET}	$m^2\ g^{-1}$	BET surface area
A_{HF}	$J\ s^{-1}$	Sinusoidal heat flow amplitude
A_{HR}	$°C\ s^{-1}$	Sinusoidal heating rate amplitude
A_{mol}	m^2	Surface area covered by a molecule
b	$g\ mol^{-1}$	BET plot intercept
b	MPa^{-1}	Affinity constant
b_0	MPa^{-1}	Entropic parameter
C		BET Parameter
c	-	Tóth heterogeneity parameter
C_p	$J\ g^{-1}\ K^{-1}$	Specific heat capacity
$C_{p,r}$	$J\ g^{-1}\ K^{-1}$	Reversible specific heat capacity
D	nm	Intermolecular lattice spacing
D	nm	Pore diameter
D_{max}	nm	Maximum pore diameter (considered)
D_{min}	nm	Minimum pore diameter (considered)
$E(Y_i)$	-	Calculated value of dependent variable
E_1	$kJ\ mol^{-1}$	Energy of adsorption on solid surface
E_L	$kJ\ mol^{-1}$	Energy of liquefaction of adsorptive
E_o	$J\ mol^{-1}$	Adsorption Potential Energy
f	-	Filling ratio
m_A	wt%	Adsorbed phase mass
m_B	wt%	Bulk phase mass
m_E	wt%	Excess mass
M_H	kg	Total mass of hydrogen
M_n	$g\ mol^{-1}$	Number-averaged molar mass
M_r	$g\ mol^{-1}$	Molar mass
M_s	kg	(Skeletal) mass of adsorbent
m_T	wt%	Total mass

M_w	g mol^{-1}	Weight averaged molar mass
N	-	Dubinin-Astakov exponent
N	-	Number of items
N	-	Integer multiplier
N	mol	Amount
n_A	mol	Amount of gas adsorbed
N_A	mol^{-1}	Avogadro's number
$n_{A,DFT}$	mol	Amount adsorbed in a DFT kernel
n_{ex}	-	Number of data points
n_m	mol g^{-1}	Specific monolayer capacity
n_{para}	-	Number of parameters
P	MPa	Pressure
P_0	MPa	Vapour pressure
Q	J g^{-1} s^{-1}	Heat flow
Q	kJ mol^{-1}	Differential isosteric enthalpy of adsorption
q	MPa^{-1}	Compressibility fit parameter
Q_b	kJ mol^{-1}	Characteristic adsorption enthalpy
R	J mol^{-1} K^{-1}	Molar gas constant
r	MPa^{-2}	Compressibility fit parameter
R^2	-	Coefficient of Determination
s	MPa^{-1}	Compressibility fit parameter
T	K	Temperature
t	MPa^{-2}	Compressibility fit parameter
t	s	Time
T_f	°C	Finish temperature
T_f	K	Final temperature
T_g	°C	Glass transition temperature
T_i	K	Initial temperature
T_o	°C	Onset temperature
V	cm^3 g^{-1}	Micropore volume
$\dot{V}$	m^3 mol^{-1}	Molar volume
v_A	cm^3 g^{-1}	Adsorbed phase specific volume
V_A	m^3	Volume of adsorbed phase

v_B	$cm^3\ g^{-1}$	Bulk phase specific volume
V_B	m^3	Volume of bulk phase
V_{BP}	m^3	Volume of bulk gas in pores
V_C	m^3	Total volume
V_c	cm^3	Sample chamber volume
V_D	m^3	Displaced volume
V_F	m^3	Volume full of adsorbent
V_I	m^3	Interstitial volume
V_m	cm^3	Manifold volume
v_o	$cm^3\ g^{-1}$	Limiting micropore volume
V_p	m^3	Total pore volume
v_p	$cm^3\ g^{-1}$	Pore volume
V_s	m^3	Skeletal volume
V_T	m^3	Total volume displaced by particles
V_U	m^3	Ullage volume
W	-	Gaussian curve width
w_i	-	Weighting parameter
X	-	Packing ratio
X	-	Independent variable (Gaussian fit)
x_c	-	Centre point of Gaussian curve
Y	-	Dependent variable (Gaussian Fit)
y0	-	Translation variable (Gaussian Fit)
Y_i	-	Inputted dependent variable
Z	-	Compressibility
β	-	Dubinin-Astakov affinity constant
Δh	$kJ\ mol^{-1}$	Change in molar enthalpy
Θ	-	Fractional filling ratio
θ	°	Angle
λ	nm	Wavelength
ρ_A	$kg\ m^{-3}$	Adsorbed phase density
ρ_B	$kg\ m^{-3}$	Bulk phase density
ρ_s	$g\ cm^{-3}$	Skeletal density
χ^2	-	Reduced chi squared

Dissemination

Publications

The author has been involved in the preparation and publication of four research articles during his PhD time, and will be a co-author on a fifth upcoming publication. These publications contain previously disseminated information contained within this thesis (as well as other work within the research group to which the author has contributed); in particular, entry 3 details the PIM-1 (2) N_2 and high pressure H_2 studies as detailed in Chapter 4, and entry 5 will present many of the adsorptive studies on PIM-1/MIL-101 composites detailed in Chapters 4 and 6. These studies are listed in chronological order below.

1. Bimbo, N.; Physick, A.J.; Noguera-Díaz, A.; Pugsley, A.; Holyfield, L.T.; Ting, V.P.; and Mays, T.J. (2015) *High volumetric and energy densities of methane stored in nanoporous materials at ambient temperatures and moderate pressures*. Chemical Engineering Journal, 272 pp. 38-47
2. Noguera-Díaz, A.; Bimbo, N.; Holyfield, L.T.; Ahmet, I.Y; Ting, V.P.; and Mays, T.J. (2016). *Structure-property relationships in metal-organic frameworks for hydrogen storage*. Colloids and Surfaces A., 496 pp. 77-85
3. Polak-Kraśna, K.; Dawson, R.; Holyfield, L.T.; Bowen, C.R.; Burrows, A.D.; and Mays, T.J. (2016) *Mechanical Characterisation of polymer of intrinsic microporosity PIM-1 for hydrogen storage applications*. Journal of Materials Science, 52 (7) pp. 3862-3875
4. Rochat, S.; Polak-Kraśna, K.; Tian, M.; Holyfield, L.T.; Mays, T.J.; Bowen, C.R.; and Burrows, A.D. (2017) *Hydrogen storage in polymer-based processable microporous composites*. Journal of Materials Chemistry A., 5 pp. 18752-18761
5. Tian, M.; Holyfield, L.T.; Rochat, S.; Polak-Kraśna, K.; Burrows, A.D.; Bowen, C.R. & Mays, T.J., *Polymer-based composites for enhanced hydrogen storage: A comparison between activated carbon, MOF and PAF as porous fillers*. International Journal of Hydrogen Energy (To be submitted)

Oral Presentations

Throughout his PhD time, the author was afforded the opportunity to disseminate both the work presented in his thesis, and other work undertaken during this time, to both national and international audiences. A list of such presentations is given in chronological order below.

1. Holyfield, L.T.; Dawson, R.; Noguera-Diaz, A.; Bennet, J.; Weatherby, N.; Burrows, A.D. & Mays, T.J.; *PIM-MOF Composites for Use in Hybrid Hydrogen Storage Tanks*. Hydrogen & Fuel Cell SUPERGEN Researcher Conference, Bath, UK, 14th-16th December 2015
2. Holyfield, L.T.; Dawson, R.; Weatherby, N.; Burrows, A.D. & Mays, T.J.; *Novel Hydrogen Storage Solutions for Road Transport Applications*. U4C Colloquium, Campinas, Brazil, 16th – 19th November 2016
3. Holyfield, L.T.; Weatherby, N.; Burrows, A.D. & Mays, T.J.; *Towards a novel hybrid hydrogen storage system featuring a PIM-1/MIL-101 adsorbent composite*. Hydrogen & Fuel Cell SUPERGEN Researcher Conference, Belfast, UK, 12th-14th December 2016
4. Holyfield, L.T.; Weatherby, N.; Burrows, A.D. & Mays, T.J.; *Towards a novel hybrid hydrogen storage system featuring a PIM-1/MIL-101 adsorbent composite*. EPSRC Project

"Integrated Safety Strategies for Onboard Hydrogen Storage Systems" Workshop, Bath, UK, 26th-27th April 2017

Poster Presentations

In addition to the oral presentations indicated above, the author has disseminated the presented work (as well as other efforts to research within the group) via a number of poster presentations at national and international conferences. The poster presentations given by the author are listed chronologically below:

1. Holyfield, L.T.; Bimbo, N.; Ting, V.P.; Burrows, A.D.; & Mays, T.J.; *Evaluation of an Activated Carbon as an Adsorbent in Hybrid High Pressure Hydrogen Storage Tanks.* Hydrogen & Fuel Cell SUPERGEN Researcher Conference, Birmingham, UK, 15th-17th December 2014
2. Holyfield, L.T.; Bimbo, N.; Ting, V.P.; Burrows, A.D.; & Mays, T.J.; *Evaluation of an Activated Carbon as an Adsorbent in Hybrid High Pressure Hydrogen Storage Tanks*. Seventh International Workshop on Characterisation of Porous Materials: From Ångstroms to Millimeters (CPM-7), Delray Beach, FL, USA, 3rd-6th May 2015
3. Holyfield, L.T.; Dawson, R.; Noguera-Diaz, A.; Bennet, J.; Weatherby, N.; Burrows, A.D. & Mays, T.J.; *PIM-MOF Composites for Use in Hybrid Hydrogen Storage Tanks*. Ninth International Symposium of Surface Heterogeneity Effects in Adsorption and Catalysis on Solids (ISSHAC-9), Wrocław, Poland, 17th-23rd July 2015
4. Holyfield, L.T.; Dawson, R.; Weatherby, N.; Burrows, A.D. & Mays, T.J.; *PIM-MOF Composites for Use in Hybrid Hydrogen Storage Tanks.* ChemEngDay UK 2016, Bath, UK, 31st March-1st April 2016
5. Holyfield, L.T.; Weatherby, N.; Burrows, A.D. & Mays, T.J.; *Evaluation of PIM-1/MIL-101 Composites for Use in a Hybrid High Pressure Hydrogen Storage System*. 11th International Symposium on the Characterization of Porous Materials (COPS-XI), Avignon, France, 14th-17th May 2017

1. Introduction

1.1. Scope and Motivation

Energy is fundamental to the modern way of living, and demand for energy is rising globally as both the human population and the average quality of life increases. Whilst providing ever increasing amounts of energy is challenging enough, this issue is further exacerbated by the fact that the majority of global energy (and particularly electricity) is generated via the burning of fossil fuels. This act releases very large quantities of carbon dioxide into the earth's atmosphere, which increases the greenhouse effect generated by the atmosphere, and contributes to the global warming that currently concerns many climate scientists. Whilst alternative, renewable sources of energy have been found and can be used for generation, such as solar and wind, these energy sources are unpredictable and fleeting, and require reliable, large-scale storage solutions in order to help meet demand.

Electricity is the primary method of energy transfer, and electricity generation is well understood and widely practised. However, direct electricity storage (via batteries or other means) is difficult to perform on a large scale, and therefore chemical energy stores are attractive means by which to achieve this large scale storage. Hydrogen is particularly attractive, as it is a colourless, odourless gas that can be produced by the electrolysis of water (providing a direct electrical-chemical energy conversion), and produces only water when combusted. Traditionally, hydrogen has been stored either by compression to 70 MPa (as is common in most hydrogen vehicles), or as a liquid at 20 K. Alternatives to these well-known storage options are cryocompression, in which the gas is both cooled and pressurised to a higher density; chemisorption, in which the hydrogen is chemically bound into a storage material; or physisorption (henceforth known as adsorption), in which the diatomic hydrogen molecules form weak physical bonds with high surface area materials.

A number of different materials, such as activated carbons, metal organics frameworks (MOFs) and porous polymers, has been developed in order to more effectively adsorb gases, including hydrogen. However, efforts to develop adsorptive gas storage materials have focussed on the uptake of the material, and very little else. In considering these materials when the development moves from the lab scale to the engineered tank scale, other material properties come into greater focus. The aim of this thesis is to investigate whether PIM-1, a well-known porous polymer that has a number of highly beneficial chemical, thermal and mechanical properties for engineering design, can be tailored such that it shows a combination of these beneficial properties as well as a high hydrogen uptake.

In this study, PIMs have been tailored to increase their hydrogen uptake using two separate methods: by combining with MIL-101 (a chromium-based MOF) to form a composite material in the form of a mixed matrix membrane, and by carbonising the material to form an activated carbon. The chemical and thermal properties of these materials are investigated, as is the adsorption performance. High pressure hydrogen isotherms are fitted to a model previously reported by the Mays group in order to find a number of important parameters about the material, which are then used to model their performance in high pressure, large scale systems.

1.2. Thesis Structure

After this introduction, Chapter 2 will discuss the background information to the thesis by further investigating into the motivation as discussed above, and by analysing the current state of the literature around both hydrogen storage and the use of PIM-1. This chapter terminates by setting out the aims and objectives of the thesis. Chapter 3 will present the methods and materials used in this study, detailing the source of all the materials used, detailing the synthetic methods used in full and discussing how the automated analytical methods work and the principle behind them. Chapter 4 sees the discussion of all of the experimental results relating to the PIM-1/MIL-101 composites, including the results of the syntheses, and the chemical, thermal and adsorptive properties of the base materials (PIM-1 powder and film morphologies, MIL-101 powder, and the composites made therefrom). Chapter 5 presents the results of the PIM-1 carbonisation study, focussing on the thermal performance of PIM-1 and the carbonisation process, before examining the same properties of the carbons as discussed in Chapter 4. Chapter 6 details all of the modelling work performed in this thesis, providing a background on the model and the theory used, and presenting and discussing the parameters found for each of the high pressure H_2 isotherms. This chapter also features isosteric enthalpy of adsorption calculations, and an analysis of the expected system-level performance of the materials. Chapter 7 presents the main conclusions of the study, and suggests future work based on the determined conclusions.

2. *Background*

2.1. Sustainability

Since the industrial revolution in the 1760s, the quality of life for people throughout the world has increased at an immense rate. In that time, the availability of inexpensive food and ever-improving healthcare has resulted in a huge population boom. United Nations estimates put the world population at 7.55 billion as of June 2017, and medium-term projections foresee a rise up to 9.77 billion by 2050 [1].

The rise in both population and quality of life (and hence overall wealth) increases the demand for the Earth's natural resources. As more and more people demand ever more food, water, shelter and other items required to maintain the expected quality of life, more of the planet's finite resources are consumed. This picture becomes particularly acute when taking into account the greater growth rate in both population and gross domestic product (and hence average quality of life) [2] of the less economically developed nations of the world, and thus the exponentially greater demand on resources that these people will provide. In response, humanity must find a way to manage the available land, water, fuels and other commodities so as to avoid a shortfall in resources that would force a reduction in quality of life for the planet's population.

2.2. Energy

Energy is one of the key resources that humanity must control to avoid a drop in quality of life. The modern way of life is highly dependent upon the consumption of energy, and this is likely to continue; the United States' Energy Information Agency estimates that total global primary energy consumption will rise from 607 EJ (10^{18} J) in 2015 to 776 EJ in 2040, based on both the population and quality of life rises discussed above [3]. However, it has been noted by the International Energy Agency that energy efficiency gains are slowing the rate at which energy use increases, with energy efficiency (i.e. the energy use per unit of economic growth) increasing at an average of 2.1 % y^{-1} between 2010 and 2016 [4].

The major issue with this rise in energy demand is that the main sources from which energy is currently supplied are regarded as unsustainable. Fossil fuels (which comprise coal, crude oil and natural gas) are all hydrocarbon-based, naturally occurring materials that are found in great abundance within the earth's crust, and have been used for well over a century as a highly energy dense and relatively easy to access source of fuel. As a result, their proliferation has been widespread. Fossil fuels provided 81.7% of the total primary energy supply in 2015 [5], a decrease of just 0.3 percentage points from 2012 [6]. The major issues with fossil fuels are twofold: the first is that whilst fossil fuels are naturally occurring, they require millions of years to form, and are therefore considered non-renewable. British Petroleum (BP), in its 2014 statistical review of world energy, defined a global reserves to production ratio (the ratio of estimated reserves to rate of production that provides a crude estimate for the amount of oil left) of 53.3 years, despite an increase in known reserves from 2012 to 2013 [7].

The other issue is that the combustion of these hydrocarbon fuels results in the emission of carbon dioxide, a well-established greenhouse gas. 32.3 billion tonnes of CO_2 was emitted to the atmosphere in 2015 from fossil fuel combustion alone [5]. As a result of the emergence of this key finding of climate science, there has been an ever-growing political push to shift away from fossil

fuel-based energy and into low carbon options; the latest global accord on CO_2 emissions, known as the 2015 Paris Agreement, aimed to bind the nations of the world into a < 2 °C increase in global warming, with < 1.5 °C being preferred, primarily through the reduction of CO_2 emissions [8].

Clearly, one of the great challenges for humanity is to replace the use of fossil fuels with zero carbon, sustainable alternatives. One of the most well established alternative sources of energy is nuclear, which produced 4.8% of the world's primary energy in 2012 [6]. The process of nuclear fission produces no CO_2, which makes this technology an appealing option, but the process does produce highly radioactive nuclear waste, which must be appropriately sealed and stored away for millennia (some isotopes in nuclear waste have half-lives as long as 17.7 million years [9]). The waste can also sometimes be utilised to produce nuclear weaponry [10]. The uranium feedstock for the fission reaction is also a non-renewable resource, like fossil fuels, although Jewell [10] estimates that there is enough uranium in the Earth's crust for over a century of nuclear power, even with a large increase in use.

The other alternatives are all classified as renewable sources of energy. These take the form of a wide array of techniques from an equally diverse set of energy sources, including solar photovoltaics, concentration solar thermal, wind, geothermal and biofuels. These sources accounted for 24.5% of global electricity production by the end of 2016, as shown in Figure 2.1 [8]. All of these fuel sources are very attractive, as they produce electricity and heat with zero carbon dioxide emissions (except biofuels, which are carbon neutral), and their energy sources are naturally occurring, so there is zero associated fuel cost. However, many of these energy sources are both variable and diffuse, requiring a large number of devices in order to collect sufficient energy, and energy storage is required to be able to meet demand when supply is low. These devices are also expensive on a per unit energy basis compared to traditional energy sources. However, renewable energy is being invested in and deployed at an ever faster rate, and the price of renewably generated electricity is falling as a consequence, a breakthrough that is allowing less economically developed nations, such as India, to undergo their own 'renewable revolutions'[8].

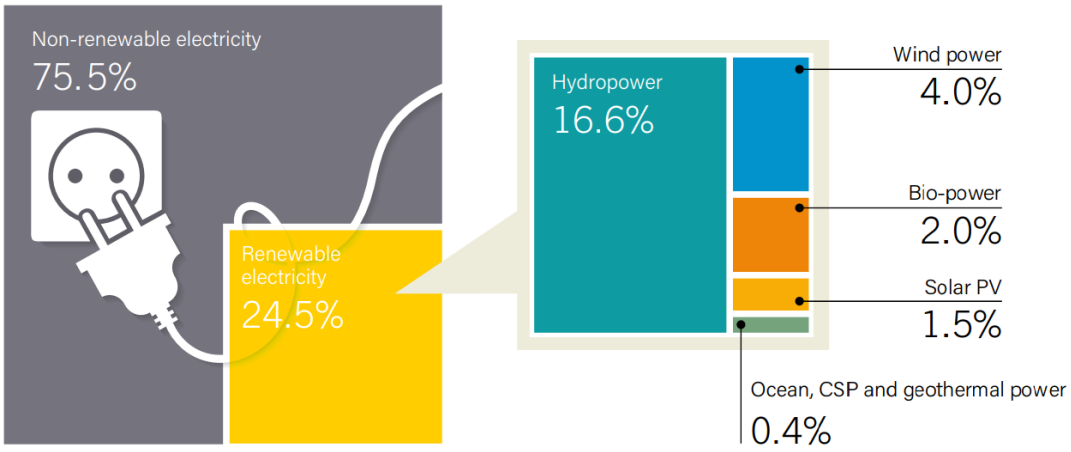

Figure 2.1 - Global Electricity Production by Fuel Type, End of 2016 [11]**.**

2.3. Hydrogen

As society transitions away from fossil fuels, finding alternative, renewable sources of energy storage, as well as energy production, is critical. Fossil fuels are commonly seen as sources of energy, as in the timescale in which humans have known about these fuels, they have solely been extracted out of the earth and burnt. Conversely, in reality they are energy vectors, storing solar energy that fell upon the earth millions of years ago. Likewise, in order to make the transition to renewable energy sources, which are inherently intermittent and require smoothing of the power delivery to ensure effective use of this energy, energy vectors must be used to store excess energy when it is not required, and to release it when required.

There are three main categories into which the alternatives are combined: heat, electricity, and chemical energy storage [12]. Heat is easy to generate and there is a large number of candidate materials that can be used to store it, but it is only really applicable for short term time scales [13]. Electricity is an attractive proposition as it is well understood, and the majority of nations around the world already have an infrastructure to transport electricity over long distances. However, devices to store electrical energy, such as batteries, flywheels and capacitors, often suffer from low power densities and high cost [13, 14]. Chemical energy stores, and hydrogen in particular, can be used to mitigate many of these issues.

Hydrogen is a very light, colourless, odourless, non-toxic diatomic gas in its elemental form under standard conditions. It is the lightest element in the periodic table, and is the most abundant element in the known universe. On earth it is generally found in various compounds, and was discovered in 1766, when Henry Cavendish reported his discovery of “inflammable air”. It was named “hydrogen” by Antoine Lavoisier in 1787 [15]. Hydrogen is a popular industrial feedstock, used in processes such as the catalytic cracking of petrochemicals and ammonia production in the Haber-Bosch process [16].

Hydrogen has been generating great interest as a sustainable energy vector for decades. This attention has been gained through a combination of hydrogen’s relative abundance on earth, the ability to both produce elemental hydrogen and recover the energy (with no CO_2 emissions) through well understood processes. As a long term energy vector, hydrogen has potential applications in both storage of intermittent renewable energy for grid purposes and as a transport fuel [17]. However, despite all this interest, there is a number of technical challenges that must be overcome in order for hydrogen-based technologies to enter the commercial marketplace.

2.3.1. Production

The first of these challenges is the production of hydrogen. Hydrogen is not found in its elemental form on earth, and must therefore be extracted from compounds. Traditionally, hydrogen has been extracted from hydrocarbons; 96% of industrial hydrogen is derived from a hydrocarbon feedstock [18]. Most (50%) of this hydrogen comes via steam methane reforming (SMR); SMR is responsible for as much as 70-80% of hydrogen production in North America, where supplies of natural gas are abundant and inexpensive [19]. The stripping of hydrocarbons of their hydrogen leaves carbon, however, and the vast majority of this carbon is emitted as carbon dioxide. This therefore means that SMR contributes to global warming and climate change in the same manner as burning the natural gas directly, and thus new, sustainable sources of hydrogen must be found.

Investigation is taking place into a number of alternative processes. The most promising of these is electrolysis, an electrochemical process by which water is split using electrical energy in order

to produce hydrogen. This shows promise as a cornerstone for a zero carbon economy, assuming zero carbon, renewable sources of energy such as wind or solar power are used to provide the electricity. Electrolytically produced hydrogen currently represents 4% of global hydrogen production [18]. Most of these electrolysers will use an alkaline ion transfer medium, which causes corrosion to the electrodes in the long term [20]. Alternative technologies, such as proton exchange membrane (PEM) electrolysers, are being developed as a more durable alternative to alkaline electrolysers [21].

Other processes being investigated include (but are not limited to): biomass gasification; aqueous phase reforming; photolysis and thermolysis, all of which are at varying stages of commercialisation [18]. SMR is also being investigated in combination with carbon capture and sequestration, although this is currently technologically challenging and comes at high cost [22].

2.3.2. Utilisation

The second great challenge of the hydrogen economy is how to utilise hydrogen efficiently. The solution is split into two avenues: combustion and electrochemical reaction. Hydrogen is a highly flammable gas, with a flammability range in air of between 4 - 74% [23]. Therefore the combustion of hydrogen was the first approach taken, with some success. Internal combustion engines were quickly developed that can utilise hydrogen as a fuel, such as BMW's Hydrogen 7 [24].

However, internal combustion engines are limited by Carnot efficiency – hydrocarbon combustion engines are thermodynamically limited to 60% efficiency, and in practice may achieve a maximum of 30 % [25]. In light of this, electrochemical methods of hydrogen energy release have become the new industrial standard. The device used for such a conversion is a fuel cell, a device very much like an electrolyser, but instead of electricity being fed into the system to start a decomposition, the energy output of a fuel cell is driven by the recombination of elemental hydrogen and oxygen into water molecules, allowing electrons to flow through a connecting circuit (and therefore do work). Fuel cells are very attractive because of their high exergetic (2^{nd} law) efficiency, which minimises irreversibility losses throughout the system [15].

Fuel cells were first reported in 1839 [15], and since then an array of fuel cell technologies has emerged, varying mainly upon the material used as the electrolyte and the temperature of operation. Six major classes of fuel cell exist, five of which use hydrogen as the primary fuel: PEM, alkaline, phosphoric acid, molten carbonate, and solid oxide. The sixth, direct methanol fuel cells, use methanol as the feedstock [26]. The most popular fuel cell type within the light duty vehicle industry is the PEM fuel cell, due to its solid electrolyte (Nafion polymer) and low operating temperature [26]. The current commercially available hydrogen vehicles, the Toyota Mirai, Hyundai iX-35 FCEV, and Honda FCX Clarity all run on PEM fuel cells [27–29].

2.4. Hydrogen Storage

The third great challenge to the hydrogen economy is the storage of hydrogen. Despite hydrogen having the highest gravimetric density of any known chemical fuel, its very low mass density means that it shows very poor volumetric energy density. For example, hydrogen's lower heating value (LHV) of 118.8 MJ kg^{-1} is three times that of gasoline (43.2 MJ kg^{-1}), but the volumetric energy density is 0.03% of gasoline's under normal temperature and pressure (0.101 MJ L^{-1} and 31.7 MJ L^{-1} respectively) [30]. Figure 2.2 shows how hydrogen, under both standard atmospheric

and densified conditions, compares in these metrics to other forms of energy storage. Because of this very low volumetric density, finding methods to increase the density of hydrogen is an important research challenge. A key factor to be considered in this challenge is the nature of the system used to store the hydrogen. The materials that compose the storage vessel and the surrounding equipment all have their own mass and volume, and as such decrease the efficiency of the storage system. In order to aid the development of efficient storage systems, the United States Department of Energy (DOE) has released a series of targets for research scientists and engineers to use to judge their progress. The targets, last revised in 2017, are specifically set for the light duty passenger vehicle application, and currently state a system gravimetric target of 5.5 wt% in 2020, and 7.5 wt% ultimate, and volumetric targets of 1.3 and 2.3 kWh L^{-1} for the 2020 and ultimate targets, respectively [30]. The standard also specifies that a storage system must deliver a minimum of 5.6 kg with a single fill, which is sufficient for a 500 km range [30]. Targets have been set by other institutions around the world, such as the Japanese institution NEDO (New Energy and Industrial Technology Development Organisation), which has published a series of hydrogen technology roadmaps [31], the most recent of which is due out sometime in Spring 2018 [32]. The development of hydrogen storage towards these targets has led to four major themes being identified: compression, liquefaction, chemisorption and physisorption.

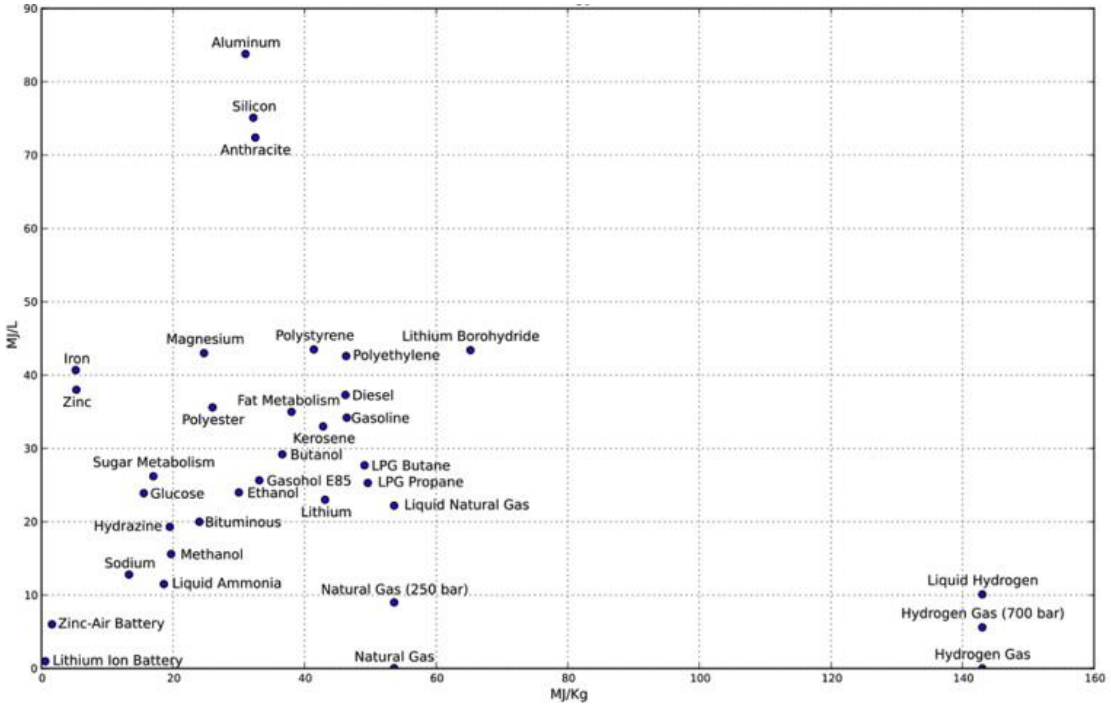

Figure 2.2 - Comparison of gravimetric and volumetric energy densities for a number of energy stores. Reproduced from [33] **with kind permission from Elsevier.**

2.4.1. Compression

Compressive hydrogen storage is the most well-developed of the hydrogen storage techniques, due largely to its simplicity and the well-established technologies for pressurising gases. Compression storage involves pressurising hydrogen up to 70 MPa inside a high tensile strength material tank. This compression greatly increases the density of the gas; hydrogen at 25 °C and 70 MPa has a density of 39.3 kg m^{-3}, meaning the volume required to store the requisite amount of hydrogen is reduced by 99.8% [34]. The work required to compress hydrogen to this pressure can vary, from 8.8 MJ kg^{-1} for isothermal compression to 24.7 MJ kg^{-1} for adiabatic compression, although these represent the ideal extremes, and the actual energy required for compression will

likely fall between the two. These values also assume a hydrogen inlet at atmospheric pressure, although many sources of hydrogen (such as electrolysers) provide H_2 at 15 - 35 bar, which could significantly reduce the compression work required [35].

In recent years, compressed hydrogen tanks have typically been made from carbon fibre reinforced polymer (CFRP) containing either an aluminium or a polymer liner (typically high density polyethylene). These tank designs have been designated the labels type III and type IV respectively [36]. This material choice has become very popular as CFRP is a low density material with high tensile strength, whilst both aluminium and polymer liners effectively resist hydrogen embrittlement [33]. This design choice has resulted in a system gravimetric density of 4.2 wt% and a volumetric density of 26.3 g L^{-1} (0.876 kWh L^{-1}) [37], which both ultimately fall short of the 2020 DOE target. It appears unlikely that this approach will ever satisfy the targets, although some attempts can be made to better engineer the system; Toyota attempted to use alternative carbon fibre winding strategies and a polyamine-based liner to improve the mass of their tanks in the Mirai, which resulted in a tank gravimetric density of 5.7 wt% [38–40]. This value is based on the tank only (i.e. the mass of stored gas and the tank materials), and does not include the rest of the balance of plant equipment provided [41]. Interestingly, the comprehensive study of Hua et al. [37] suggested that 35 MPa systems (which had been popular with earlier hydrogen vehicles) actually outperformed 70 MPa tanks in gravimetric performance and in every cost metric, but the reduced size of the 70 MPa tank and the higher volumetric density it produced has come to be weighted much more heavily by motor manufacturers due to the limited space available in vehicles [42].

Compressive hydrogen tanks can also be filled in the ~ 3 minute time frame expected for the refilling of gasoline cars, although this requires pre-cooling of the hydrogen (to -40 °C, to avoid overheating of the CFRP [33, 43]) and communication between the filling station and the vehicle [44]. The energy requirement for this precooling is relatively modest (41.7 kJ kg^{-1}) [43]. Because the system is constantly under positive pressure, no energy is required to recover the hydrogen [35].

On top of these somewhat disappointing densities and energy penalties, compressed hydrogen tanks are expensive (Hua et al. [37] estimated a 70 MPa system costs US$3500) and present inherent safety issues [43, 45]; hydrogen tank safety is an entire research field in its own right [46]. Despite these issues, 70 MPa technology is by far the most common hydrogen storage technique amongst vehicle manufacturers today. A comprehensive review of the hydrogen storage systems featured in hydrogen-fuelled vehicles produced by major original equipment manufacturers (OEMs) can be found in the supplementary information (SI-1).

Although bulk scale carbon fibre tanks are by far the most common method of storing compressed hydrogen, other techniques have also been explored. One alternative is pressurised gas storage in quartz capillaries/microspheres, in which hydrogen gas is pressured into small glass capillaries and sealed with a melted alloy, which is then remelted to release the hydrogen again [47]. This technique has a number of possible benefits, namely the modularity of the system (so can easily be tailored to size, and avoids containing large amounts of hydrogen in a single unit), lack of refilling infrastructure required (as the capillaries are refilled at a specialist facility) [33], and high gravimetric and volumetric densities (10.2 wt% and 48.3 g L^{-1} for capillaries loaded to 168.5 MPa) [47]. However, this system requires very high pressures, and lacks the long-term durability required for a consumer-operated system [33]. There has been an attempt at commercialising this technology, primarily by C.En, a Swiss company that first patented designs

based on glass microspheres in 2008 [48]. The company has since focussed on capillary technology [49, 50], demonstrating a number of projects, such as a hydrogen bike, mobile power packs and mobile traffic lights [51].

2.4.2. Liquefaction

Liquefaction is a technique that takes advantage of the higher volumetric density of liquid hydrogen for better storage. In this technique, hydrogen is cooled to 20 K (below its critical temperature of 33 K) and handled as a cryogenic liquid. The density of liquid hydrogen is 70.8 g L^{-1} at 20 K [52], nearly twice the density achievable via compression to 70 MPa [53]. Because liquid hydrogen (LH_2) systems only typically require pressure resistance to 0.6 MPa [53], far less material is required to contain the material, resulting in both excellent gravimetric and volumetric energy densities of the tank.

However, liquid hydrogen has a very high energy penalty. The theoretical energy demand for hydrogen liquefaction is 14.1 MJ kg^{-1}, which seems reasonable when compared to compression, although achieving this in reality is very difficult, and it is typical to see this process require 40 – 45 % of the LHV of hydrogen (47.5 – 53.5 MJ kg^{-1}) [35, 43]. Larger plants may be able to achieve liquefaction with 21 % of LHV (24.9 MJ kg^{-1}) [35].

The other major issue with LH_2 storage is boil off. Although attempts to engineer highly insulated cryogenic vessels have produced heat flows as low as 1 W into a 5 kg tank, ultimately the tank still warms, and if left dormant for a sufficiently long time, the pressure in the tank will rise to the point that some gas must be vented off. This phenomenon creates an issue of dormancy, namely that the fuel in the tank must be used within a particular period of time (dormancy period) before the system will begin to eject hydrogen itself, and will eventually self-empty [54]. A dormant vehicle stands to lose between 0.3-3% of its contained liquid hydrogen per day, given current cryogenic technology [53]. Boil off also typically requires an ullage of 5-15% of the tank volume to be designed in to lengthen the dormancy period [52].

Due to both the very high energy penalty and inescapable issues of boil off, vehicular liquid hydrogen has largely been abandoned; the last OEM-manufactured vehicle to feature a LH_2 tank was the BMW Hydrogen 7, first unveiled in 2006 [24].

2.4.3. Cryocompression

The idea of using cryogenic storage was not dismissed fully however, given the benefits of very high hydrogen density and the low cost and relative ease of operating a LH_2-based refuelling system [53]. The solution, first proposed by Aceves et al. [54], was to develop an insulated vessel that could withstand much higher pressures than standard LH_2 tanks, and then to fill them with LH_2. What would result as the gas expanded was high pressure, cryogenic, supercritical hydrogen, commonly known as cryocompressed hydrogen. Of the major OEMs, it is BMW who have focussed on this technology, as they have been developing their own cryocompression tanks since 2008 [55], and in 2015 showcased two fuel cell vehicles, based on the 5 series Gran Turismo and the i8 models, that featured cryocompressed hydrogen storage tanks [56, 57].

The primary benefit of cryocompressive hydrogen storage is the very high density of hydrogen. Although the ultimate storage density will alter slightly based on the exact pressure and temperature used, recent cryocompression tanks have been designed towards 35 MPa and 42 K being the ‘ultimate’ storage condition; such a condition yields a hydrogen density of 81 g L^{-1}, a

significant increase over liquid hydrogen density. This in turn leads to high gravimetric and volumetric energy densities; the aforementioned BMW tanks store 7.1 kg hydrogen at 4.4 wt% and 30.2 g L^{-1} [56, 58], which whilst both are short of the DOE targets, does again show the OEM preference for low volume, high capacity storage solutions. Aceves et al. [59] at Lawrence Livermore National Laboratory have also developed a number of cryocompressed tanks, the best of which stored 10.7 kg at 7.38 wt% and 45.5 g L^{-1}, which meets the 2020 DOE targets for both mass and volume of the storage system, something neither of the more traditional physical storage approaches have been able to achieve.

Raising the maximum allowable pressure in a cryogenic vessel from 0.6 MPa to 35 MPa not only increases the density of the stored hydrogen, but vastly increases the dormancy of the vehicle (particularly when the vehicle is used periodically), and also eliminates the possibility of complete boil off [52, 53]. At least 35% of the stored hydrogen will remain under conditions in which total boil off would occur in a LH_2 system [60], because the final equilibration temperature is atmospheric temperature, meaning the cryocompression vessel then simply behaves as a standard compression tank under these conditions [58]. This behaviour as a standard compression tank also allows for standard compressed hydrogen refuelling, which can be advantageous if multiple short trips are required [54].

Cryocompressed systems are also self-cooling, as the heat absorbed by the evaporating hydrogen serves to supress the temperature of the system [60]. These systems are also safer than either of the other options, due to the surprisingly low mechanical energy release of cryocompressed hydrogen suddenly exposed to atmospheric conditions [54].

There are some challenges remaining before cryocompression becomes as viable as room temperature compressed tanks for hydrogen storage. Cost is a large impediment to wide scale implementation of this technology [44]. The fuelling infrastructure, whilst a problem for all hydrogen vehicle progression, is currently focussed heavily on providing for compression tanks, and a different refuelling infrastructure is required for cryogenic storage, although BMW and Total have partnered to begin to address this issue [61]. Long term durability of these tanks has not received much attention and requires further work, and the energy penalty of liquefying hydrogen provides a hard thermodynamic limit of the round trip efficiency of this technology [44].

2.4.4. Chemisorption

Chemisorption is a chemical technique which uses the chemical dissociation and bonding of hydrogen in materials to densify the gas. This is a widely researched theme in hydrogen storage, and a large number of different materials have emerged. Chemisorption is attractive as a hydrogen storage option as it can store hydrogen at densities greater than liquid hydrogen [36], resulting in excellent volumetric energy densities. Materials containing hydrogen gravimetric densities as high as 19.8% have been reported [62]. However, most usable materials have a much lower accessible hydrogen content than this, and the extra volumetric density comes at the cost of material weight [45]. Hydrides often need heating to several hundreds of degrees in order to release the hydrogen; the heat required to decompose MgH_2 is 25 % higher than the lower heating value of the hydrogen released [45]. All of these factors contribute to a very low system gravimetric density, and it has been the challenge to researchers in this field to develop materials of high gravimetric density and low release temperature.

Perhaps the simplest of these materials are the metallic hydrides. These materials are typically ionic materials formed by the dissociation of hydrogen and its subsequent diffusion into metallic

lattices of either a Group I or II (of the periodic table) metal [63]. Of these binary hydrides, MgH_2 has generated much interest; the material has been known to show gravimetric hydrogen uptake as high as 7.7 wt%, although this is typically closer to 5 % [64]. LiH is another interesting candidate; this materials shows 12.1 wt% H_2 uptake [62]. However, these simple hydrides are often either too stable or too unstable to be used in a suitable pressure and temperature range within a vehicular system [63]. Nevertheless, the strong energy densities and inexpensiveness of these materials is attractive, and much research has focussed on attempting to alter the thermodynamic and kinetic behaviour of these materials (e.g. through microstructure alteration) [65].

One potential solution to the enthalpy issue in hydrides is to create interstitial hydrides featuring two or more metals. These so-called 'AB' or 'intermetallic' hydrides, mix high- and low-enthalpy metals to create a moderate material that still shows good energy density but can be operated in a more reasonable pressure and temperature window [63]. A good example of this is $LaNi_5H_6$, which releases hydrogen at a temperature similar to the operating conditions of a PEM fuel cell (0.1 – 1 MPa, 25 – 100 °C), although this particular system only stores 1.4 wt% hydrogen [62]. These low temperatures and pressures would give the added benefits of less expensive containing materials and shape conformability.

Alternatively, there exists a series of complex hydrides which feature hydrogen bound either ionically or covalently into the material bulk, rather than dissociated hydrogen ions diffusing into a metallic lattice [63]. The most popular groups of materials investigated for this purpose are the analates, borohydrates, amides and imides [65]. Perhaps the best studied of the complex hydrides is sodium alanate ($NaAlH_4$), which when doped with Ti becomes an effective chemical hydrogen store, with an uptake of 5.5 wt%, spread over 2 decomposition steps, possible in a realistic system [33, 65]. Issues with this material are the high charging and discharging temperatures, and difficulties with reversibility [65]. This material has been investigated in a 1 kg (H_2) tank design [66]. The borohydrides of lithium ($LiBH_4$) and sodium ($NaBH_4$) have been consistently attractive due to their high gravimetric energy densities (up to 18 wt%), but require very high decomposition temperatures and the effort to destabilise this material has been great [33, 64], although $NaBH_4$ can irreversibly dehydrogenate when reacted with water [33].

Whilst the term chemisorption has traditionally been applied to solid state and metallic materials, there is a growing research field in organic and inorganic hydrides that can occupy multiple states of matter. The best performing of these is ammonia borohydrate (NH_3BH_3), which can irreversibly desorb 19.8 wt% H_2 [62], and has been the focus of University College London spin-out company Cella Energy's efforts to produce commercial, lightweight, solid-state hydrogen storage [67]. Ammonia (NH_3) has attracted much attention as a relatively high density and inexpensive liquid hydrogen store (17.7 wt% H_2), although issues overcoming the thermodynamics of the decomposition reaction have limited this line of research [33]. Liquid organic hydrogen carriers, such as *N*-ethylcarbozole (5.8 wt%) and gaseous phase clathrates (4.0 wt% in a H_2O/0.15% THF hydride) have also been investigated for this purpose [64].

Ultimately, chemisorptive materials have found little success in on-board applications, but have seen use in alternative applications, such as large scale hydrogen stores for renewable energy and/or chemical facilities [68], as thermal energy stores in concentrated solar plants and as hydrogen compressors [69].

2.5. Adsorption

2.5.1. Theory

Physisorption (commonly referred to as adsorption) is a process involving weak physical interactions between a solid surface area and gas molecules in order to store hydrogen. As gas molecules approach the surface of a material, they are attracted to the molecules in the solid surface through van der Waals' dipole-dipole interactions, and a weak physical bond is formed (with an interaction strength of the order of 10s of kJ mol^{-1}, compared with 100s of kJ mol^{-1} for chemical bonds). This process works particularly well with nanoporous materials with high surface areas. The size and shape of the pores within a material can also have a very strong effect on the amount of adsorptive adsorbed, even when the surface areas and chemistries are very similar [70].

Like chemisorption, adsorption can raise the density of hydrogen above that of liquid hydrogen, but unlike in chemisorption, the bonds are weak and therefore the hydrogen is released easily. Physisorption also allows the maintenance of the gas molecule identity, allowing simple recovery through desorption [71]. The major issue with adsorption is the low uptake at ambient temperatures; adsorption is an exothermic process, and thus cryogenic conditions are required in order to improve the amount stored [72]. The storage of hydrogen in adsorbent materials is particularly difficult, given that hydrogen is a supercritical fluid above 33 K, and typically only forms a monolayer when adsorbed, due to the heat of adsorption for hydrogen multilayers being very similar to that of the evaporation enthalpy of hydrogen [73].

Nanoporous materials, which are classified as any materials featuring pores with a diameter at the opening smaller than 100 nm, are classified by IUPAC into three groups: micropores, with a pore size smaller than 2 nm; mesopores, with a pore size between 2 and 50 nm, and macropores, with a pore size greater than 50 nm [74]. The adsorption behaviour of a material can depend strongly on how the pore size distribution (PSD) fits into these categories. These behaviours can often be typical, so much so that the IUPAC standard for reporting adsorption science has created a series of standard 'types' of isotherm [74]. The original set, published in 1985, contained 6 types; the 2015 edition now shows 8 types of isotherm, which are illustrated in Figure 2.3.

Of particular interest to hydrogen adsorption is type I, which is indicative of a highly microporous material. This is due to a number of reasons; highly microporous materials have the largest surface areas (as determined by the BET method), which provides more space for the hydrogen monolayer, and hydrogen adsorption is strongly favoured at lower pore sizes, as the steric constriction of molecules entering the pore results in a significant increase in enthalpy of adsorption, largely due to the additive nature of molecular interactions [71]. The optimum pore size for hydrogen is believed to be 0.7 nm. This is because the walls in this size of micropore are far enough apart that a monolayer of hydrogen can comfortably form on either side of the pore, but close enough that the force fields of these monolayers overlap, resulting in stronger interactions within the pore [70, 75].

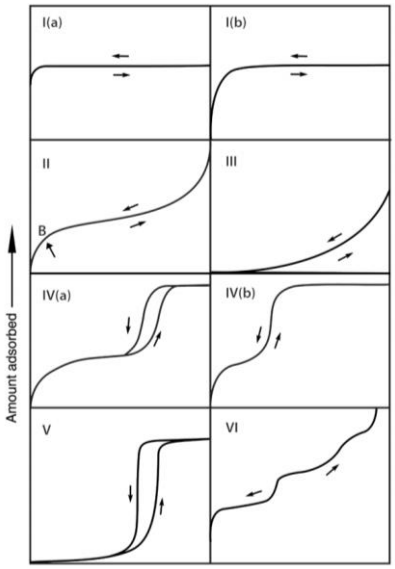

Figure 2.3 – 2015 IUPAC classification of isotherms [74] **© 2015 IUPAC & De Gruyter**

For adsorptive hydrogen storage, which will often be operated at high pressures in order to maximise the amount adsorbed, it is important to understand the thermodynamic definitions of adsorption, particularly the terms 'excess' and 'absolute' as defined by Gibbs in 1928 [76]. As an adsorptive (the gas molecules) is dosed into a pore within the adsorbent (the solid material), they will begin to adsorb, and condense into a liquid-like layer on the pore surface, known as the adsorbate. The total amount of gas in the adsorbate (i.e. in the condensed phase) is known as the absolute amount of gas adsorbed. The excess is a term which marks the increase in total density of the gas in the pore as a result of the interaction with the adsorbent surface. Formally, it is defined as the amount of gas present in the pore over what would be present if there was no such interaction with the wall.

For much adsorption testing, such as the very common nitrogen (N_2) isotherm at 77 K (the boiling point of N_2 at atmospheric pressure), the density of bulk gas under these conditions is very low, and the difference between excess and absolute can be safely neglected. However, under the high pressure, low temperature conditions in which hydrogen adsorption is most effective, the density of the bulk gas is significantly increased, and therefore the difference between the excess and absolute amounts becomes non-negligible. This delineation is important when reporting high pressure isotherms as it can be easy to state the incorrect uptake value for a given system, which may greatly affect any understanding of the effectiveness of an adsorbent, or worse, provide the incorrect values for a modelling approach. Throughout this study, the excess adsorption has been stated for uptake values from isotherms unless stated otherwise.

An important aspect of the adsorption process to consider is the differential enthalpy of adsorption, which is defined as the change in heat produced when an infinitesimal amount of adsorptive adsorbs onto a surface given a constant pressure, temperature and surface area [76]. This value is measured indirectly, either by measuring the differential energy of adsorption via calorimetric studies, or by the isosteric method, in which isotherms at multiple temperatures are used to derive the enthalpy graphically [76]. The value of the enthalpy ('heat') of adsorption is exothermic, explaining the preference for the adsorption process at cryogenic temperatures. The magnitude of this value (typically between 0 – 7 kJ (mol H_2)$^{-1}$ [75]) determines the readiness of this bond formation, which in turn determines the uptake of the gas under given pressure and temperature conditions; higher enthalpies of adsorption will result in greater uptake at lower pressures and higher temperatures.

For most materials, the enthalpy of adsorption has been shown to be surface area dependent, becoming less exothermic as the surface coverage increases. This drop can be greater in some materials than others, as is illustrated by the comparison of AX-21-33 (an activated carbon) and MOF-177 (a zinc-based MOF linked by benzenetribenzoate linkers [77]) in Figure 2.4. This drop can greatly affect how a material performs, particularly when considering not just hydrogen storage, but delivery. As a positive delivery pressure must be maintained in order to supply a fuel cell with sufficient hydrogen, the hydrogen stored in the material below the delivery pressure is 'dormant' and unusable. Clearly, the nature of the change in enthalpy of adsorption has a significant effect on the ability of a material to deliver hydrogen, as Figure 2.4 demonstrates. AX-21-33, a material with a large enthalpy of adsorption at low coverage but with a steep decline as the surface becomes covered, adsorbs a large quantity of hydrogen at low pressures, but at higher pressures the total hydrogen uptake plateaus. This combination of lower storage at high pressures, and greater storage at lower pressures, will result in a much lower deliverable hydrogen capacity from a tank containing this material than the MOF-177 (3.5 and 5.6 wt%, respectively for isothermal delivery to 0.2 MPa at 77 K [78]), which despite having a consistently lower enthalpy of adsorption (and therefore a more gradual increase in uptake with pressure), will be able to deliver more hydrogen to a fuel cell.

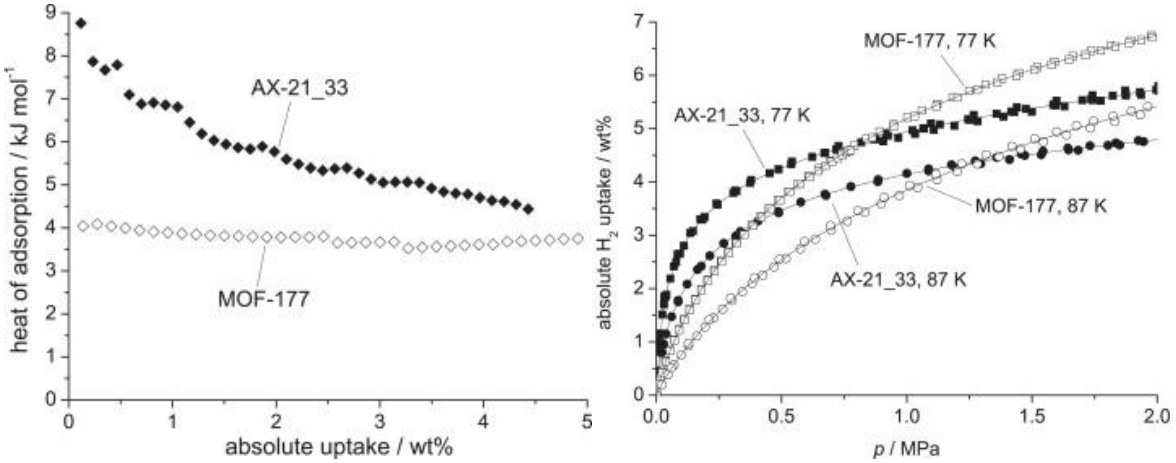

Figure 2.4 - Isosteric enthalpies of adsorption and total hydrogen uptake isotherms for the activated carbon AX-21-33 and the MOF MIL-177. Reproduced from [78] **with kind permission from Elsevier.**

A number of different materials have shown sufficient surface area and microporosity to be able to store large amounts of hydrogen in the adsorbed phase. Some of the common material classes are presented in section 2.5.2.

2.5.2. Materials

2.5.2.1. Carbons

Carbonaceous materials have been known to be good adsorbents for millennia; they are documented to have been used by the ancient Egyptians [79]. A number of different carbon morphologies have proved to form useful adsorbents, and carbonaceous materials are popular due to their low cost and effectiveness as adsorbents. However, many carbons feature complex surfaces and pore structures, and current carbon adsorbent preparation techniques do not produce specific and predictable properties in this regard [80].

By far the most common form of carbon used for adsorptive purposes is activated carbon. Activated carbons were first industrially produced in the early 20th century [79], and since then

have gone on to be widely used in many industrial adsorption processes. They are network polymers of graphitic sheets, which tend to have a wide array of pore sizes within the nanopore range [81]. Activated carbons can take on a number of morphologies, such as powders, cloths, fibres and monoliths.

Activated carbons are fundamentally created by carbonising (heating in a chemically inert environment) a carbon-based precursor to drive off any other elements present, before creating porosity in the material via activation. This process is illustrated in Figure 2.5. The conditions under which these processes are performed vary in their exact method, but most activations fall under two categories: physical, and chemical. Physical activations are performed by first heating the carbonaceous precursor to 700 – 1000 °C under a flowing inert gas, such as N_2 or Ar. This stage is followed by an oxidative activation, in which CO_2 or steam are used to gently oxidise and combust some of the material, resulting in the formation of voids within the carbon, although the exact mechanism is oxidising gas and temperature dependent [82]. Chemical activation first impregnates the material with an ionic activation agent before carbonisation. The carbonisation and activation steps then occur concurrently, as the pregnant material is heated to 300 – 800 °C to both carbonise the material and activate the ions inside, which intercalate in the material and create porosity by physical force. Activating agents can be acidic, basic or a neutral salt (H_3PO_4, NaOH and $ZnCl_2$ have all been used for this purpose), but the exact mechanism is again method-dependent [82].

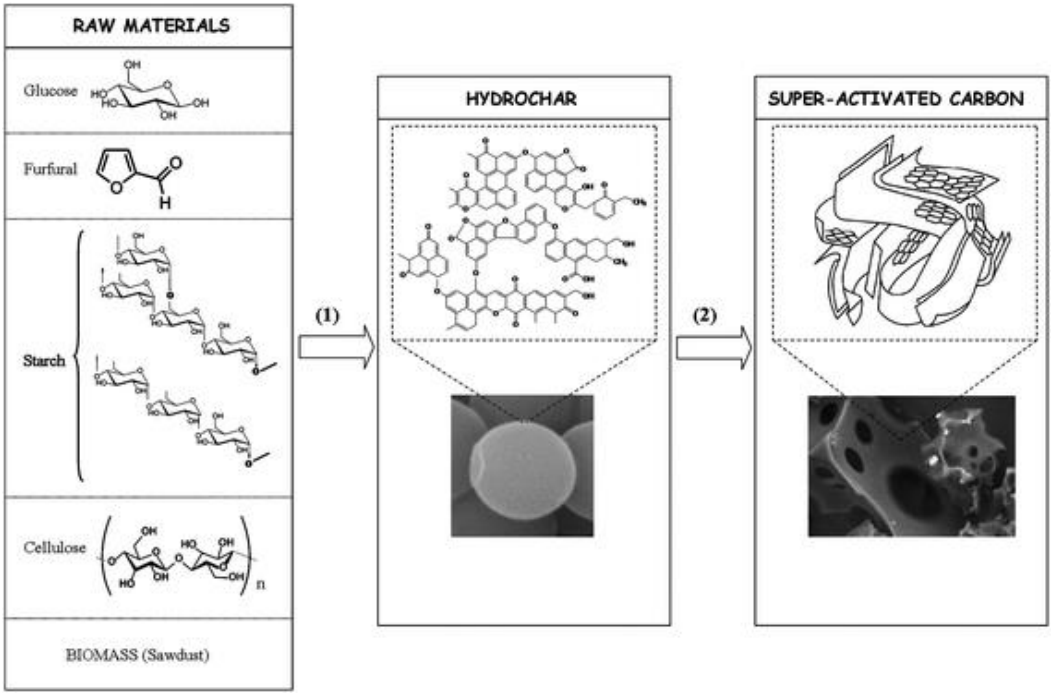

Figure 2.5 - The synthesis method for the activated carbons from biomass-sourced precursors studied by Sevilla, Fuertes and Mokoya [83]**. (1) represents hydrothermal carbonisation of saccharides, and (2) represents activation with KOH. Reproduced from** [83] **with kind permission from The Royal Society of Chemistry.**

Traditionally, these materials are produced from petroleum-based precursors, in particular the carbonaceous residues left after the incomplete combustion of petroleum (adsorbents such as carbon black and AX-21 fall into this category). However, with the widespread concerns about petroleum and the general drive towards more sustainable processes, biomaterials are being widely investigated as activated carbon precursors [79, 84–87]. Carbide derived carbons, zeolite-templated carbons and polymers have also been activated to produce high porosity materials [88].

One of the trailblazing carbons for high adsorption performance was the superactivated carbon AX-21. First developed by AMOCO in the 1970s [79, 89], AX-21 has repeatedly shown BET surface areas > 3000 $m^2 g^{-1}$, which is 2 – 3 times higher than most activated carbons [89]. The pore volume has also been reported to be ~ 1.3 $cm^3 g^{-1}$ [90], the vast majority of which is in the form of micropores [91]. The excess hydrogen uptake of the material is 5.1 wt% at 77 K and 3 MPa [90, 91]. The high pressure isosteric enthalpy of H_2 on AX-21 is between -6 - -8 kJ mol^{-1} at zero coverage [92].

Although AX-21 was an early leader in this field, many activated carbons produced since have been able to match or even surpass the hydrogen storage of this material. This is clearly illustrated by the study of Jordá-Beneyto et al. [93], who compared a number of activated carbons of both commercial (e.g. AX-21) and research lab (e.g. KUA5) origin, as well as a number of activated carbon fibre and carbon nanotube materials, for their properties as adsorbents. All of the activated carbons showed surface areas above 1000 $m^2 g^{-1}$ as determined by N_2 adsorption at 77 K, and micropore volumes ranged from 0.5 – 1.27 $cm^3 g^{-1}$, with the lab-synthesised KUA6 topping out at 3808 $m^2 g^{-1}$ and 1.27 $cm^3 g^{-1}$. However, KUA5 and AX-21 were the best hydrogen adsorbents, showing uptake of ~ 1.2 wt% at 298 K and 20 MPa, illustrating that surface area and pore volume are not completely correlated with hydrogen uptake. Nonetheless, this study illustrates the wide variety of activated carbons available, and their high storage capacities.

More recent studies have focussed on using renewable carbon precursors to develop high capacity carbonaceous adsorbents. A selection of the highest performing biomass-derived activated carbons for hydrogen storage is shown in Table 2.1 below.

Table 2.1 – Comparison of activated carbons made from biomass precursors for hydrogen storage. Activation ratios are stated as (mass of carbon):(mass of KOH). All BET surface areas (S.A.) are calculated from N_2 isotherms at 77 K, and all H_2 storage values quoted are for 77 K.

Author	Precursor	Carbonisation method	Activation method	BET S.A. / $m^2 g^{-1}$	Max H_2 Pressure / MPa	Max H_2 uptake / wt%	Ref.
Cheng et al.	Hydrolysed sawdust	650 °C, 1 h, N_2	CO_2/H_2O, 850 °C, 1h	2850	1.0	4.82	[94]
		750 °C, 1 h, Ar	KOH (1:1)	3100	1.0	5.05	
Sevilla, Fuertes and Mokoya	Cellulose	700 °C, 1 h, N_2	KOH (1:4)	2370	2.0	5.60	[83]
	Cellulose carbon	700 °C, 1 h, N_2	KOH (1:4)	2722	2.0	6.40	
Akasaka et al.	Waste coffee beans	500 °C, 1 h, H_2O	KOH (1:5)	2070	4.0	4.00	[95]
Yang et al.	Hemp	500 °C, 2 h, N_2	KOH (1:4.5), 800 °C, 3.5 h	3241	0.1	3.28	[96]
Bader and Ouederni	Olive stones	800 °C, 2 h, N_2	KOH (1:4)	1269	20.9	6.11	[97]

Other morphologies of carbon have also proven to be popular adsorbents. A related material to activated carbons, structured graphitic materials have gained much attention since the isolation of graphene in 2004 [98], and many studies have been performed investigating the potential of

graphene-based materials as hydrogen adsorbents, based on the inherent surface area of a graphene sheet (~2600 m^2 g^{-1}) [99]. Amongst the most successful hydrogen storage materials developed using this methodology are: a glucose-reduced graphene oxide that showed 2.7 wt% H_2 uptake at 298 K and 2.5 MPa, as reported by Yuan, Li and Li [100], and the hierarchical graphene materials of Guo, Wang and Li [101], which showed 4.0 wt% uptake at 77 K and 0.1 MPa. Graphene-based adsorbents generally appear highly suited to hydrogen adsorption, with a number of studies elucidating a much higher hydrogen uptake and enthalpy of adsorption for a given surface area for these materials over standard activated carbons [99].

Carbon nanotubes were one of the first morphologies of carbon to generate real excitement within the modern research community; this was particularly after the early study of Dillon et al. [102], who reported a very high excess hydrogen uptake between 5 - 10 wt% at 273 K. However, further research determined this very large uptake to be incorrect; Züttel et al. [103] determined a 0.6 wt% uptake experimentally, although molecular simulation appeared to show a maximum potential uptake of 3.3 wt%. This group also determined a maximum H_2 content of 6 wt% based on the assumption of hydrogen condensation in a 2.2 nm nanotube, although full condensation is unlikely given the critical temperature of hydrogen is 33 K. Experimental H_2 adsorption on carbon nanotubes by other groups have generally shown uptake of 0.15 – 0.63 wt% at room temperature, although there has generally been a struggle to replicate many of the studies of adsorption on this material [93, 104]. Nanotubes, in addition to other modern carbonaceous adsorbents such as molecular sieves and aerogels, can be produced to feature much more uniform properties than activated carbons, and thus show good potential for further research [80].

2.5.2.2. Zeolites

Zeolites are a collection of crystalline aluminosilicate materials whose chemical bonding is such that regular, well defined pores emerge within their atomic structure. Since the elucidation of their structures in the 1950s, zeolites have been used widely as molecular sieves [105], but recently they have generated interest as adsorbents for gas storage. In particular, the presence of cations within the structure (due to the substitution of electron-rich aluminium in place of silicon at certain points in the framework requiring a balance of electrostatic charge) means that non-polar adsorptives interact strongly with zeolites [105]. Zeolites have been looked at for hydrogen storage, as many of the zeolitic polymorphs show pore sizes in the optimal region for hydrogen adsorption. One reasonably well performing example is that of Na-LEV, which was shown by Dong et al. [106] to uptake 2.01 wt% of H_2 at 77 K and 1.6 MPa. However, the most promising zeolite to date is ITQ-33, which has a micropore volume of 0.30 cm^3 g^{-1}. If these pores were filled with hydrogen at the density of LH_2, this would only equate to an adsorbed excess of 2.5%, which is a long way behind the performance of other adsorbents [73]. Zeolites have been used for alternative approaches to adsorptive hydrogen storage, with techniques used ranging from the use of 13X as a template for activated carbons [107] to the entrapment of hydrogen within the pores of ZSM-5 using a disilane [108].

2.5.2.3. Metal Organic Frameworks (MOFs)

Metal Organic Frameworks (MOFs) are a subclass of coordination polymer (extended molecules consisting of repeating units of metallic and organic moieties), that form three dimensional, permanently porous structures [109]. These materials feature multivalent, labile metallic nodes and rigid multidentate organic linkers that self-assemble into rigid 3D networks [109]. They are

typically synthesised through one-pot solvothermal methods, often under quite mild conditions, although alternative methods include microwave and electrochemical synthetic methods [110]. MOFs are not always rigid, however. In particular cases, the crystalline framework can universally deform in so-called 'breathing' MOFs, depending on environmental factors, such as temperature and the presence of guest molecules [111, 112].

MOFs have gained a large amount of attention as adsorbents in recent years due to their very large BET surface areas and hydrogen uptakes relative to other adsorbent materials. The two breakthrough stable MOF materials, HKUST-1 and MOF-5 (the latter of which is discussed in greater detail in section 2.5.2.5 below) have been repeatedly reported to have surface areas of 1500 – 2100 $m^2 g^{-1}$ and ~ 3000 $m^2 g^{-1}$ respectively [113, 114]. Many MOFs synthesised since have shown this trend for high surface area [113, 115, 116], and some have shown extraordinary surface areas; the highest BET surface area ever seen for a MOF is 7140 $m^2 g^{-1}$, as reported for NU-110 by Farha et al. [115]. Additionally, Farha et al.'s study showed that theoretically, MOFs with surface areas as high as 14600 $m^2 g^{-1}$ could be possible [115].

As a natural result of the fixed free volume and high available surface area, MOFs have gained a large amount of attention as hydrogen storage materials [117]. This potential has largely been realised, as MOFs have consistently shown much higher hydrogen uptake than other adsorbent materials; maximum uptakes of 3 wt% and up are common (as seen in Table 2.2 below). The highest hydrogen uptake MOF known to the author is NU-100, which in 2010 was shown to have excess H_2 uptake of 9.95 wt% at 77 K and ~ 6 MPa [118]. However, the enormous gravimetric adsorption capacity of these materials has been shown to be sub-optimal; Goldsmith et al. [119] performed an extensive study modelling both the gravimetric and volumetric hydrogen storage density in a wide range of MOFs. They determined that in order to meet the DOE targets, the optimal MOF had a surface area of 3100 – 4800 $m^2 g^{-1}$, as materials in this region showed both gravimetric uptake of > 5.5 wt% and volumetric uptake > 40 g L^{-1}, albeit the volumetric densities are based only on the crystal volumes of the MOFs, and not the powder densities. Instead, the group recommends focussing on MOF materials that show moderate porosity and mass density, and on other properties, such as thermal and chemical stability. Clearly, how the MOF is implemented in such a storage system is also a question of research, as issues such as low crystal density and low thermal conductivity in these materials have to be considered [120].

In addition to hydrogen storage, MOF materials have also shown some the highest natural gas storage capacities yet seen [121]. Beyond gas adsorption, MOFs have been investigated for a number of purposes, such as gas sensing [122], light emitting diodes, magnets, and drug delivery [110].

Table 2.2 - Maximum excess H_2 uptake at 77 K for a variety of MOFs [123, 124]

MOF	Pressure / MPa	H_2 Uptake / wt%	MOF	Pressure / MPa	H_2 Uptake / wt%
IRMOF-1	4.01	5.93	ZIF-7	4.12	1.43
IRMOF-3	4.07	5.02	ZIF-8	3.22	3.46
IRMOF-6	4.53	4.85	ZIF-9	3.86	1.37
IRMOF-8	6.15	3.68	ZIF-11	5.15	2.53
IRMOF-9	4.12	2.41	ZIF-12	5.15	2.63
IRMOF-11	3.37	3.52	ZIF-CoNIm	3.23	2.18
IRMOF-20	7.76	6.67	MIL-101(Cr)	3.20	4.38
IRMOF-62	3.90	4.84	NH_2-MIL-101 (Cr)	2.59	3.25
MOF-74	4.99	2.26	NH_2-MIL-101 (Al)	4.08	3.82
MOF-177	6.85	7.52	UiO-66	2.59	2.60
MOF-324	3.30	3.34	UiO-67	3.23	3.84
HKUST-1	2.60	2.38			

Another reason MOFs are generating interest as adsorbents is the 'building block' approach they offer [117]; by changing the nodes and/or linkers used, the properties of the material, such as pore size, can be tailored. As a result, an enormous number of MOFs have been created and analysed; the Cambridge Structure Database held information on ~ 22,700 different MOFs as of 2013 [119]. These different MOF creations have not only come as a result of changing the nodes and linkers of these materials, but also by synthetic strategy. An extension of this customisability is not only changing the chemical components of the MOF material, but also how the material comes together. Rowsell and Yaghi [125] proposed a number of different strategies for improving H_2 storage in MOFs, including by impregnation (incorporating smaller particles into the free volume within the MOF to raise the available surface area for adsorption), catenation (linking or interweaving MOF structures together to provide a higher number of smaller voids), and the use of open metal sites, amongst other techniques. The ability to tune the chemistry of these materials to fit a very particular purpose has made MOF materials the subject of a very broad range of research studies [110, 126–128].

Because MOFs have been demonstrated to be such effective materials for a wide variety of applications, the transition of their synthesis and use from the lab up to industrial scale has recently become a topic of focus. Although this is a niche market currently, Kaskel [129] lists ten separate suppliers of such materials, on scales ranging from grams to tens of kilograms. However, research is very much ongoing into the scale up of MOF synthesis. One recent study of interest is that of DeSantis et al. [130], who investigated a number of synthetic methods for four of the most interesting MOFs from an industrial perspective (HKUST-1, MOF-5, and the Ni- and Mg- variations of MOF-74). They determined that liquid assisted grinding could produce 2.5 Tg y^{-1} of Mg-MOF-74 for 82.5 % less expense than the traditional solvothermal methods at current yields ($12.50 vs $71.44 kg^{-1}). This reduces if the yields are optimised to 92 % (75.5 % difference in cost), and sensitivity analysis showed that the cost of production could be as low as $8.23 kg^{-1} given favourable circumstances.

2.5.2.4. MIL-101

MIL-101 is a MOF material first reported by Gérard Férey and his group at the Lavoisier Institute at the University of Versailles in 2005 [131]. Since then, MIL-101 has become a highly popular choice of research material in a number of applications, due to its thermal and chemical stability, large pore volume and ease of functionality [132]. It is not currently produced commercially.

The fundamental building blocks of this MOF are trimers of chromium (III) tetrahedra, which share a μ_3-O vertex, connected by carboxylate groups, and 1,4-benzenedicarboxylate (bdc) linkers. These materials immediately form into small 'super-tetrahedra', in which four trimers are connected together by the bdc linkers, which in themselves contain microporous cavities with an inner free diameter of 0.7 nm [133]. These supertetrahedra are then further linked by bdc units into a mesoporous zeolite-like structure (highly similar to the mobil thirty-nine, or MTN, zeolitic topology) that features two different cage structures [134]. The smaller cages, made up of 20 tetrahedra, form pentagonal windows with an aperture of ~ 1.2 nm and a 2.9 nm internal diameter. The larger cages, made up of 28 super tetrahedra, feature both the same pentagonal and hexagonal (~ 1.47 x 1.6 nm) openings to an inner volume of diameter 3.4 nm [132, 133]. Such a structure results in a MOF with very large internal free volume, which has possibilities for a number of applications [132]. All of these structures are illustrated in Figure 2.6 below.

MIL-101 is traditionally synthesised in a solvothermal process, like most MOFs. The process involves stirring a stoichiometric combination of a chromium (III)-containing salt, such as chromium (III) nitrate ($Cr(NO_3)_3$) with terephthalic acid in deionised (DI) water as the solvent [132, 135]. An acid, often HF, is added as a crystallising agent for the MIL-101 crystals [135]. This solution is then typically heated to 493 K for 8 h under autonomous pressure in a hydrothermal reactor. Leaving this reaction longer will result in the formation of a Cr(III)-based MIL-53 structure [136]. Microwave-based synthesis is also relatively common for MIL-101 synthesis, and a dry-gel conversion method has also been published [132].

The reaction mixture is then purified via filtration, solvent treatments with water and ethanol, and a fluoride-anion exchange in an aqueous ammonium fluoride solution [132, 136]. This final step allows for the removal of terephthalate ions that are coordinated to the exposed chromium sites within the MOF and that act as inhibitors for gas adsorption; the BET surface area can increase sizeably using these purification steps [136, 137].

However, HF is well known for being a highly toxic and corrosive substance, and many attempts have been made to eliminate its use from MIL-101 synthesis. Approaches for doing this have ranged from attempting to substitute in other acids as crystallising agents (acetic and perfluorobenzoic [135], stearic, 4-methoxybenzoic,benzoic and 4-nitrobenzoic acids [138]) to attempting syntheses free of crystallising agents [135, 138, 139]. Attempts have also been made to synthesise MIL-101 in alkaline solutions of tetramethlyammonium hydroxide [132].

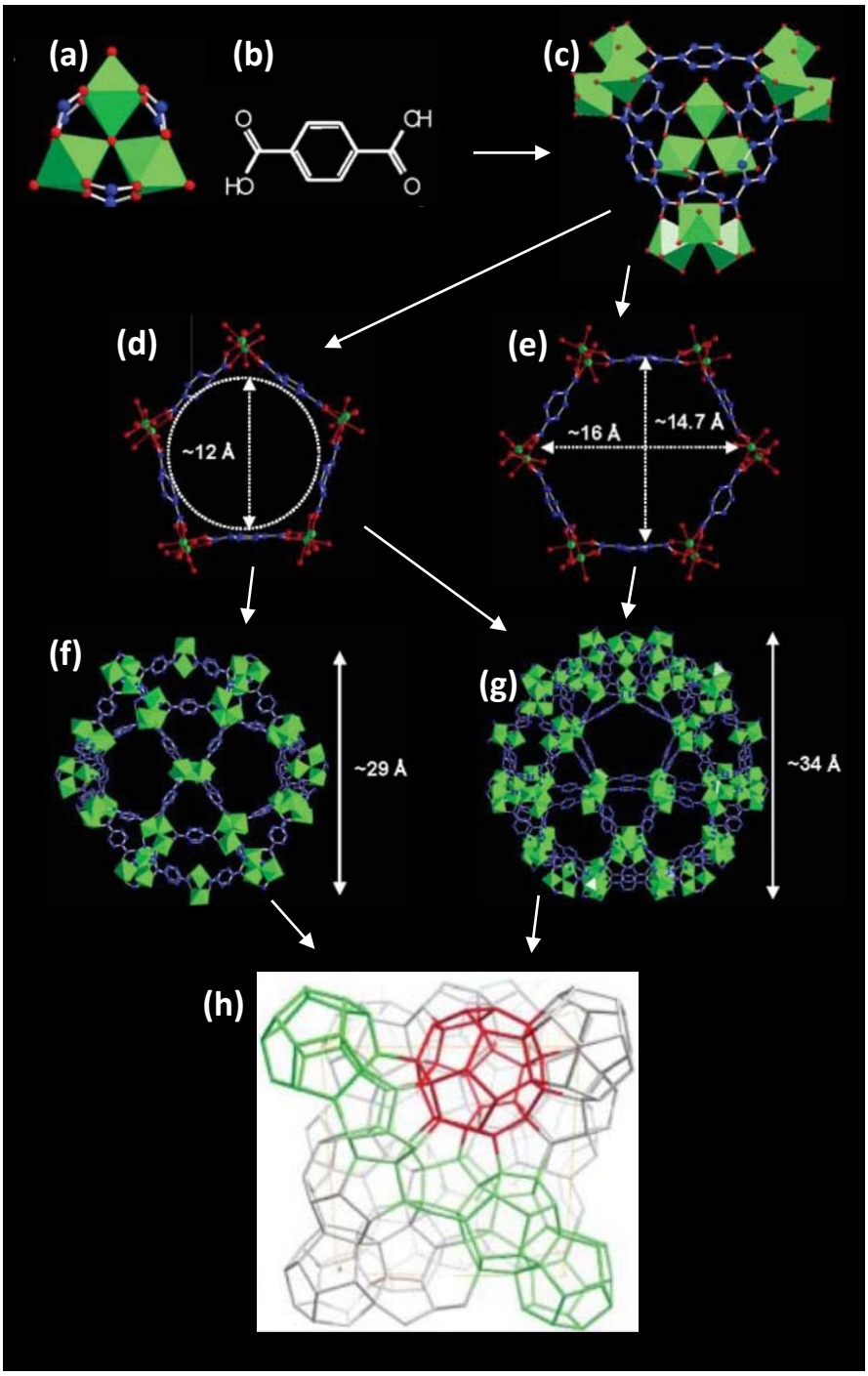

Figure 2.6 - Illustration of how the structure of MIL-101 is formed. Trimers of chromium octahedra (a) and 1,4-benzenedicarboxylate linkers (b) combine to form super tetrahedra (c), which are further linked by bdc units to form pentagonal (d) and hexagonal (e) apertures. These 2D shapes then arrange themselves into pentagonal only (f) and pentagonal and hexagonal (g) structures containing mesoporous voids. The green shapes represent the chromium tetrahedra, whilst the blue and red spheres seen represent carbon, oxygen and fluorine respectively. These structures then link together into the MTN-type zeolitic topology, as shown in (h), where the green edges represent the smaller structures shown in (f), and the red edges illustrate a larger cage (g). This figure is adapted from [131] **with kind permission from The American Association for the Advancement of Science.**

Unlike many MOF materials, MIL-101 has shown excellent chemical and thermal stability. Thermogravimetric (TGA) analysis by multiple groups has repeatedly shown thermal stability up to 275 °C, with the TGA trace showing two major mass losses: one at 20 - 100 °C as the guest adsorbates (such as water) are driven off, and the other at 275 – 400 °C, as the –OH and –F groups coordinated to the chromium are driven off and the structure collapses [136]. There is few data

with regards to other thermal properties of this MOF, such as specific heat capacity or thermal conductivity, which have been determined for other MOFs, such as MOF-5 [140, 141]. MIL-101's hydrolytic stability is also very good. As well as retaining its crystal structure when stored in air over many months (which other MOFs, such as MOF-5 or MOF-177 are incapable of), MIL-101 is also resistant to submersion in boiling water over 7 days, showing virtually identical N_2 adsorption behaviour following such exposure [136].

MIL-101 has been widely tested as an adsorbent for gas storage purposes, owing to its large surface area, pore volume and gas uptake. The initial reporting of MIL-101 by Férey et al. [131] reported MIL-101 as having a BET surface area of 4100 $m^2 g^{-1}$ and a micropore volume of ~ 2.0 g cm^{-3}. These values are relatively high for such a material, although later studies have reported a range of values for MIL-101 between 846 – 4200 $m^2 g^{-1}$ for the BET surface area, and 1.50 – 2.77 $cm^3 g^{-1}$ for the pore volume, although these values come from a number of samples with different methods of preparation [132]. The nitrogen isotherm of MIL-101 at 77 K is IUPAC type I, although it shows two sharp uptakes at P/P_0 = 0.1 and P/P_0 = 0.2; these 'secondary' uptakes are illustrative of the two types of microporous window within the MIL-101 structure [131, 136].

The values produced by the isotherm can be highly dependent on the method of activation of the MOF; the standard synthesis often leaves traces of recrystallized terephthalic acid in the large pores of the MOF, and much more can be coordinated to the exposed Cr(III) sites, resulting in a steric blocking of potential adsorption sites [142]. Latroche et al. [142] demonstrated this by testing two MIL-101 samples, one of which was solely activated through the use of heat and vacuum pressure (MIL-101a), and the other being subjected to separate solvent treatments with ethanol and water before undergoing the same heat activation (MIL-101b). They then demonstrated that the both the surface area and the hydrogen adsorption isotherms at 77 and 298 K were all significantly enhanced in MIL-101b. The density (assumed to be skeletal, although this is not confirmed in the paper) is determined to be 2.26 g cm^{-3} for MIL-101a, and 1.74 g cm^{-3} for MIL-101b, further demonstrating the presence of coordinated terephthalate, which will add mass to and occupy volume within the MOF structure.

A similar study was performed by Llewellyn et al. [137] on the adsorption of both CO_2 and CH_4 on MIL-101. This study determined the uptakes of both gases for three different MIL-101 samples, differing only in how much post-synthesis activation was performed: the first was activated solely by heating under vacuum, the second by hot ethanol treatment and the third sample had an additional treatment in aqueous ammonium fluoride. This study, like that of Latroche et al. [142], showed that both the BET surface area (2800 – 4230 $m^2 g^{-1}$) and the pore volume (1.37 – 2.15 $cm^3 g^{-1}$) increased with the additional activation. Whilst this greater porosity was a function of the loss of adsorbed terephthalic acid in the pores, infrared spectroscopy studies still showed an unusually high ratio of Cr-C complexes, thus illustrating that adsorbed terephthalic acid could not be completely eliminated even with the advanced activation process. The CO_2 isotherms on these samples did show a noticeable change in uptake, although experiments performed on different apparatuses for isotherm measurement in different laboratories showed good agreement, so clearly demonstrating that the difference is due to the samples. CO_2 was also fully recoverable from the samples by vacuum treatment at 303 K, so showing the MOF's potential as a carbon capture material. Interestingly however, there was no significant difference in CH_4 uptake.

This variability of gas uptake illustrates that the main site for hydrogen adsorption in MIL-101 is not the metal sites, as was originally suggested, and as is the case for the sister MOF MIL-100 [142]. Instead, MIL-101's abnormally large hydrogen uptake (despite its generally large pore size)

is actually due to adsorption within the super tetrahedra – these cavities, at 0.7 nm in diameter, are the perfect size for hydrogen adsorption (as discussed in section 2.5.1 above), and therefore are the main site of hydrogen adsorption [70, 75, 133]. In particular, H_2 molecules may collate in the corners of the supertetrahedra, close to the chromium trimers [142].

There have been relatively few detailed discussions on the adsorption sites of hydrogen in MIL-101, but one of the leading studies is that of Ardelean et al. [143]. Using the adsorption sites in MOF-5 proposed by Rowsell et al. [144] as a guide, the Romanian group attempted to explain the loss of uptake in densified MIL-101 pellets by identifying the adsorption sites in MIL-101. Their endeavour proposed four main sites: the uncoordinated chromium sites (labelled 'cus'); the α site, deemed "perpendicular to the centre of the Cr_3O unit" (analogous to a site over the triangular faces of the Zn_4O octahedra in MOF-5); the γ site "on the axis passing from Cr through the middle of each O-O distance of the carboxyl oxygen" (analogous to over the edges of MOF-5's Zn_4O octahedra); and the δ site, which is in and around the aromatic link in the bdc linker [143, 144].

Ardelean et al. [143] believe that these sites provide as many as 23 separate binding sites per Cr_3O trimer within MIL-101; this is equivalent to approximately 500 and 700 cm^3 (STP) g^{-1} of gaseous uptake. This is then proven through the location of two inflection points at roughly these uptakes in the nitrogen isotherm of MIL-101. The group then states that the hydrogen isotherm provided by Streppel and Hirsher [133] also shows inflexion points at these same uptakes, illustrating that hydrogen will also occupy these same adsorption sites, although the δ site is not fully occupied by hydrogen due to the low enthalpy of interaction between the aromatic ring and the hydrogen molecules [143].

Whilst this study is an excellent attempt to describe the adsorption of hydrogen within MIL-101, it leaves much to be desired – the model is entirely based on the work of Rowsell et al. [144] on MOF-5, who conducted specific X-ray crystallography experiments under a number of chemical environment and temperature conditions to determine the adsorption sites in MOF-5. This work attempts to piece together a similar theory by examining adsorption isotherms, some of which are very low resolution for such a precise discussion. The description of the locations around the trimer is also poor, which no diagrams made available to aid the reader.

MIL-101 shows very good hydrogen uptake. The original study of Latroche et al. [142] determined that MIL-101a had a maximum uptake of 4.5 wt% H_2 at 77 K and 8 MPa, which rose to 6.1 wt% for the MIL-101b sample. Since then, many studies have been performed on the hydrogen uptake of MIL-101 (and many derivatives thereof), with varying values: these are listed in the Table 2.3 below. The variation in hydrogen uptake is very likely caused by the activation method used.

Table 2.3 - Maximum hydrogen (excess) uptake on MIL-101 at various temperatures, as reported by different studies

Study	Pressure (MPa)	Temperature (K)	Uptake (wt%)	Reference
Latroche et al. (MIL-101a)	8	77	4.5	[142]
	8.6	298	0.36	
Latroche et al. (MIL-101b)	8	77	6.1	
	8	298	0.43	
Schmitz et al.	2	77	4.5	[145]
	2	298	0.1	
Oh et al.	5.8	77	5.82	[146]
Bimbo et al.	4.07	77	4.8	[92]
	8.51	130	2.6	
Ardelean et al.	6	77	5.8	[143]
Klyamkin et al.	4.07	81	4.49	[147]
	5.43	298	0.18	

Hydrogen adsorption by MIL-101 has also been investigated at liquid hydrogen temperatures (19.5 K). These studies, namely those of Streppel and Hirscher [133] and Oh et al. [146], ran hydrogen isotherms with reasonable detail at 19.5 K (at which the vapour pressure of hydrogen is 0.776 bar [34]), which allow not only for surface area determination with the BET or Langmuir theories, but also a study of how the pores of an adsorbent fill, allowing for an interesting insight into how hydrogen interacts with the material. As expected, both studies show the standard isotherm to be both fully reversible and of IUPAC type I(a) shape, which are typical of microporous hydrogen adsorption [133], without the sharp rises at P/P_0 = 0.1 and P/P_0 = 0.2 seen in nitrogen isotherms at 77 K [131].

Whilst the absolute amount of hydrogen these samples take up is not the same (Streppel and Hirscher [133] reported a maximum uptake of 10.7 wt%, Oh et al.'s [146] maximum was 11.9 wt%), both illustrate the same two step uptake when the isotherm was plotted – this isotherm can be seen in Figure 2.7. The first step, between $P/P_0 = 0 – 10^{-3}$, is attributed to adsorption on the pore surface, particularly within the microporous super tetrahedra, although the resolution of the isotherms given is too low to resolve a step between adsorption in the super tetrahedra and that in the larger pores [133]. Streppel and Hirscher [133] estimate that the super tetrahedra will take up 22% of the hydrogen in this step based on the ratios of surface area attributable to each of the pore types within the MOF. However, this calculation is purely geometric, and assumes all three pore sizes are spherical, which limit its utility. The second rise, between $P/P_0 = 10^{-2} – 1$, is attributed to the condensation of hydrogen into the larger pores at the sub-critical temperature – Oh et al estimate that this condensation could provide as much as 75% more hydrogen under these conditions than through surface adsorption alone [146].

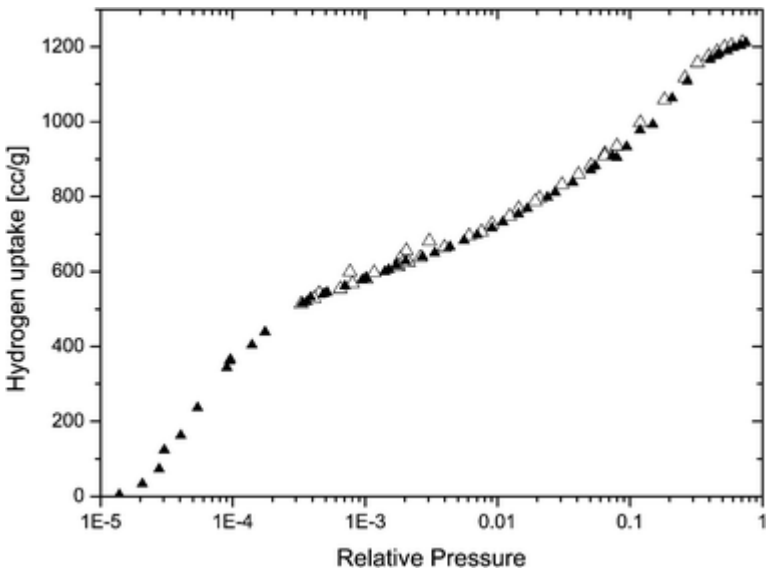

Figure 2.7 - Hydrogen isotherm on MIL-101 at 20 K (P_0 = 76 kPa), plotted on a logarithmic pressure axis to demonstrate the two-stage uptake. Reproduced from [133] **with kind permission from the PCCP Owner Societies.**

The isosteric enthalpy of hydrogen adsorption on MIL-101 has also been well studied. This value was first reported to be in the range of -9.3 - -10.0 kJ mol^{-1} by Latroche et al. [142], who performed this study on their MIL-101b sample, although there is no mention of the method of calculation of this range of values, and it appears that the only isotherms used were at 77 and 300 K, so lacking the rigour of an in-depth enthalpy analysis. Nevertheless, this was one of the highest enthalpies of hydrogen adsorption determined for a MOF at the time.

A more rigorous study was put forth by Schmitz et al [145], who calculated the isosteric enthalpy of hydrogen adsorption on two activated carbons and four MOF samples. This group used hydrogen isotherms between 0 – 2 MPa at 77, 87, 97, 112, 127 and 296 K in order to capture a wide range of surface coverages. Whilst their methodology is not clearly explained, it appears that they use the isotherms, normalised to the maximum uptake for the adsorbent, to draw linear isosteres on a graph of ln P vs 1/T. The result is a detailed graph showing how the isosteric enthalpy varies with surface coverage, in which MIL-101 drops from -4.5 kJ mol^{-1} at 10% coverage to -4.1 kJ mol^{-1} at 65%. An average value of -4.3 kJ mol^{-1} is quoted, which was quoted by Bhattacharjee, Chen and Ahn [132] in their summary of adsorption characteristics of MIL-101. Schmitz et al's [145] study also makes an attempt to correlate their determined isosteric enthalpies with pore size and dimension, drawing a direct (negative) correlation between pore diameter and the enthalpy, although MIL-101 is not included in this part of the study due to the uncertainty in location of the hydrogen adsorption sites in the MOF (due to the multiple pore sizes) at the time.

There has also been work done in this field at the University of Bath. Bimbo et al. [92] determined the isosteric enthalpy of MIL-101 and AX-21 activated carbon using the Clausius, Clausisus-Clapeyron and the Virial theories. The isotherms used were between 0 – 12 MPa, at temperatures of 77, 90, 100, 110, 120 and 130 K. The Clausius-Clapeyron and Virial analyses featuring two different numbers of parameters all produced results consistent with one another, with a relatively linear decrease in enthalpy from -6 kJ mol^{-1} at 0 coverage to -2 kJ mol^{-1}. The result produced by the thermodynamically more accurate Clapeyron equation has a sharper drop (-6.2 - -1.5 kJ mol^{-1} over 0.5 – 6 wt%). This sharp increase is a result of the chemical heterogeneity of the material, as the high affinity sites become occupied first. This is a thorough study that closely looks at the isosteric enthalpy of H_2 on MIL-101, using multiple approximation methods and the

thermodynamically true equation to provide reasonable confidence that the correct value has been calculated for both materials studied.

2.5.2.5. MOF-5

MOF-5, also known as isoreticular MOF 1 (IRMOF-1), was one of the very first MOFs to be reported, and along with HKUST-1, was of importance to the emergence of MOF chemistry, due to their permanently porous three dimensional structures [148]. MOF-5 is constructed from Zn_4O metallic clusters, linked by bdc linkers into a cubic structure of isoreticular topology. MOF-5 was the first isoreticular MOF, with a number of homologues featuring longer or more complicated linkers, but all featuring the same Zn_4O metallic clusters, linear dicarboxylate linkers and isoreticular topology; these are all identified by the IRMOF label [117, 149]. MOF-5/IRMOF-1 is also known by the BASF brand name Basolite Z100H [150].

A unit cell of MOF-5 is illustrated in Figure 2.8. It shows free space of approximately spherical shape with an apparent diameter of 1.5 nm, more than double that of the ideal pore width for hydrogen storage [125]. Approximately 55-61% of the volume of the crystals are open to guest molecules, which is equivalent to a specific pore volume (v_p) of 1.04 $cm^3\ g^{-1}$, as measured by nitrogen adsorption at 77 K [151]. Nevertheless, the adsorption performance of MOF-5 is very good: BET surface areas are reported as high as 3800 $m^2\ g^{-1}$, but typically in the range of 3000 $m^2\ g^{-1}$ [114]. Hydrogen adsorption performance is also promising; Rosi et al. [149] were the first to publish hydrogen adsorption data on a MOF when they announced a hydrogen uptake of 4.5 wt% at 0.7 bar and 78 K. Maximum excess uptakes as high as 7.1 wt% (at 4 MPa and 77 K) have since been published [114].

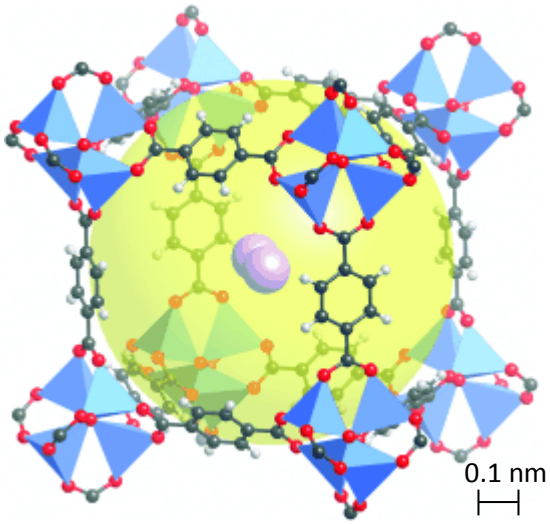

Figure 2.8 - Unit cell of MOF-5, illustrating the free volume of the pore (yellow) in relation to the kinetic diameter of a hydrogen molecule (lilac). Framework atoms are carbon (black), oxygen (red), hydrogen (white) and zinc (blue tetrahedra). Reproduced from [125] **with kind permission from John Wiley and Sons.**

Whilst it shows great promise, MOF-5 also presents a number of challenges. The enthalpy of adsorption is estimated to be -3.8 kJ mol^{-1} [148]. This value is low, particularly for a MOF, and results in very poor hydrogen uptakes at atmospheric conditions. MOF-5 has a very low thermal conductivity of 0.32 W $m^{-2}\ K^{-1}$ at 300 K, a very low value based on the low atom density of the MOF (2.46 x 10^{28} atoms m^{-3}). This value is low even for microporous materials, which tend to have low thermal conductivities [141]. This low atom count also contributes to a crystal density of 0.59 g cm^{-3}, one of the lowest known at the time of MOF-5's discovery [151], and an extremely low

bulk powder density of 0.19 g cm^{-3} [150]. All of these low densities present significant engineering challenges when working on the vehicle scale.

The greatest challenge with using MOF-5, however, is its hydrolytic instability. Zinc has a high affinity for binding with water, and therefore when water is present, it is believed that the Zn-O bond connecting the metal clusters to the bdc ligands are displaced by similar bonds Zn makes to the water molecules [152, 153]. This results in a change of phase from $Zn_4O(BTC)_3$ to one of a number of zinc carboxylate complexes, including the structure of MOF-63c ($Zn_3(OH)_2(BTC)_2$), depending on the concentration of water and the temperature [153]. These alternative structures have much lower porosity than MOF-5, with either greatly reduced or complete loss of N_2 or H_2 adsorption frequently experienced in the presence of water [114, 154]. MOF-5 is unstable in the presence of air consisting of ≥ 4 wt% water vapour, although distortion of the framework by the displacement of Zn-O bonds or by the hydrogen bonding of water to the framework structure can be in water vapour concentrations as low as 2.3 wt% [152]. Hausdorf et al [153] showed that MOF-5 (with pores still full of diethylformamide (DEF), the solvent in which MOF-5 synthesis is typically performed) in a saturated water environment took less than an hour to convert to the MOF-69c structure. However, the stability of MOF-5 is a function of both relative humidity and time: samples kept at 45% humidity show only a minor drop in H_2 uptake even after 24 h, but in 61% humidity 2 h is long enough to have a significant effect [155].

Nevertheless, MOF-5 has attracted serious industrial attention. Currently, BASF, Ford and the University of Michigan (UM) are jointly developing vehicle-scale engineering systems featuring MOF-5 [156]. This group have identified MOF-5 as a well-known MOF showing good gravimetric and volumetric hydrogen storage densities [119], and are thus pursuing it on a larger scale, ramping up production to a space-time-yield of 299 kg m^{-3} d^{-1} [150], whilst preserving particle size (7% change), BET surface area (1% change) and hydrogen uptake (negligible change) [156]. This work fits into a larger, DOE-funded research effort in the United States, known as the Hydrogen Storage Engineering Center of Excellence (HSECOE) [156].

2.5.2.6. Porous Polymers

It has long been known that polymeric materials always contain an element of free volume due to incomplete packing of the polymer chains. However, recently a concerted effort has been made to create and maintain useful free volume within polymers as a method of porous material creation. Porous polymers offer many of the benefits of traditional porous materials, such as high surface area and pore volume, but can be synthesised via a number of routes (many of which are reasonably simple) and are often much easier to process than traditional adsorbents, either because the polymers can be synthesised directly in the desired morphology by direct templating, or because the polymer is soluble in a particular range of solvents and can be solution processed [157]. A number of different approaches towards porous materials via polymer synthesis are discussed below.

Hyper crosslinked polymers (HCPs) were first developed in 1969 [158], but the potential of these materials for practical uses was not uncovered until the early 2000s [159]. The concept of hyper crosslinked polymers is that by cross-connecting polymer chains at regular intervals with sufficiently large linkers, the material begins to exert free volume that the chains cannot collapse into, leaving a large surface area for gas adsorption [160]. Early attempts at hypercrosslinking polystyrene resulted in surface areas as large as 1000 m^2 g^{-1} [158], although later attempts have reported BET surface areas as high as 2090 m^2 g^{-1} [161]. This latter attempt, a crosslinking of

poly(vinylbenzyl chloride) with dichloroethane and a Lewis base to form diethane bridges connecting the aromatic groups from different chains, was also shown to have promising hydrogen uptake, adsorbing 3.04 wt% H_2 at 77 K and 1.5 MPa. Other examples of HCPs include the polysilane-based 'element organic frameworks' and polyamines reacted with boron trihalides, which have seen BET surface areas as high as 1046 and 1364 $m^2 g^{-1}$ respectively [159].

A similar class of porous polymers are the conjugated microporous polymers (CMPs), which are synthesised and behave in a similar manner to HCPs but are defined by the carbon-carbon or aromatic linkers that form the vast majority of the network [159]. The first CMPs were reported by Jiang et al. [162] in 2007, who coupled di- and tri-ethylyne substituted aromatics with similar di- and tri-halogenated aromatic compounds. The resulting powders showed BET surface areas of 522 – 834 $m^2 g^{-1}$ and total pore volumes of 0.26 – 0.49 $cm^3 g^{-1}$. Since then, an enormous array of CMPs has been synthesised and tested, with many displaying BET surface areas of 200 – 1200 $m^2 g^{-1}$ [159, 163], with some exceptions, such as the thiophene-based polymers of Palma-Cando, Brunklaus and Scherf [164], who reported a maximum BET surface area of 2020 $m^2 g^{-1}$ and a hydrogen uptake of 1.81 wt% at 77 K (no pressure quoted). Hydrogen uptake in CMPs has generally been in the < 1.5 wt% range, with the exceptions of the stereocontorted polymers of Yuan et al. [165], which showed 3.7 wt% uptake (77 K, 6 MPa) despite a relatively modest surface area (1043 $m^2 g^{-1}$), and the Li^+-doped CMP of Li et al. [166] that uptook 6.1 wt% at 77 K and 0.1 MPa (up from 1.6 wt% without the metal ions). In addition to gas adsorption, CMPs have been investigated for use in organic electronics such as diodes and solar cells, and for a variety of photocatalytic applications, such as hydrogen evolution [159, 163].

Despite the relatively modest hydrogen storage performance of most microporous polymers, a small subcategory of these materials has stood out significantly. The first series were the poly-aromatic frameworks (PAFs), first published in 2009 by Ben et al. [167]. This series of diamond-like structures of aromatic rings connected by aliphatic linkers was first optimised for the number of aromatic units between carbon centres via molecular dynamics, before the material was synthesised by the Yamamoto cross-coupling of tetrakis(4-bromophenyl)methane. Characterisation of the produced structure showed exceptional gas adsorption, with a BET surface area of 5600 $m^2 g^{-1}$ from N_2 (77 K) studies, and a maximum excess H_2 uptake of 7.0 wt% at 77 K and 4.8 MPa. Both of these values were higher than any MOF synthesised at the time. PAF-1 was also shown to be thermally stable to 520 °C by anoxic TGA, and resisted boiling water for 7 days.

Later attempts at PAF synthesis and design changed the tetra-bonded molecule that link the tetra(bromophenyl) precursors (Si for PAF-3, Ge for PAF-4) and coupled them in a similar manner [168]. Whilst the new materials did not produce the very high gas uptakes of the original material (5.5 wt% H_2 for PAF-3, 4.2 wt% for PAF-4), these altered materials did show raised isosteric enthalpies of adsorption of hydrogen, from 5.4 kJ mol^{-1} (PAF-1) to 6.6 kJ mol^{-1} (PAF-3) over the 0 – 0.1 MPa range. Both PAF-3 and PAF-4 showed similar chemical and thermal stability to PAF-1.

Inspired by PAFs, Lu et al. [169] set out to imitate the structure seen in PAF-1 but with alternative chemistry, naming their series of polymers 'porous polymer networks' (PPNs). The first attempts at PPNs were synthesised by the cross-coupling of tetraphenylmethane with ethynyl groups for PPN-1 (rather than PAF-1 which featured bromide groups) and both ethynylated- and brominated, versions of a tetraphenyladamantane precursor (PPN-2 and PPN-3 respectively). These polymers all showed thermal stability to 320 °C, and adsorption testing showed consecutively higher uptakes, with PAF-3 showing the highest BET surface area of 5323 $m^2 g^{-1}$ (N_2, 77 K) and a maximum excess H_2 uptake of 4.28 wt% at 77 K and 4.2 MPa.

The group then followed the example of Ben et al. by using silicon and germanium-based versions of the PPN-3 monomer in an attempt to increase the isosteric enthalpy of adsorption [170]. What resulted was the highest hydrogen uptake ever reported for a porous polymer, as (the Si-centred) PPN-4 reported a BET surface area of 6461 $m^2 g^{-1}$ (N_2, 77 K) and a maximum H_2 excess uptake of 8.34 wt% at 77 K and 5.5 MPa. Both PPN-4 and PPN-5 showed good thermal and hydrolytic stability. However, like all of the PAFs and PPNs previously reported, this material was not soluble in any common solvents [168, 170], which limits the processability of these materials.

Another approach to porous polymers was to treat their synthesis in the same auto-assembly manner as MOFs, which would show all of the same benefits of fixed porosity as the metal-based variants, but would only consist of lower mass elements and could therefore be made to be very low density [171, 172]. The result were covalent organic frameworks (COF) which, unlike all the other materials described in this section, are crystalline organic porous materials [173]. The first COF was synthesised by the group of Omar Yaghi (one of the principal discoverers of MOFs) in 2005; this study condensed boronic acid into boroxine anhydride to form the node, which were then cross-linked with diboronic acid to form COF-1 [172]. N_2 adsorption studies at 77 K demonstrated that this material had a BET surface area of 711 $m^2 g^{-1}$.

The experimental hydrogen storage capabilities of pure COFs were all largely reported by Furukawa and Yaghi [172], who synthesised a large number of COFs (of both 2D and 3D topographies) and tested their H_2 adsorption performance. From their results, they were able to categorise the materials into three categories: group 1, which were 2D materials with small pores; group 2, which consisted of 2D materials with large pores; and group 3, consisting of the 3D COFs. These groups of COFs, during high pressure hydrogen isotherms at 77 K, showed maximum excess uptakes of 1 – 2.5 wt%, 3 – 4 wt% and ~ 7 wt% respectively, and the isosteric enthalpies of H_2 on these groups of materials were also shown to be near identical within the group, with higher uptake groups showing smaller enthalpies.

More recent studies of hydrogen storage in COFs has been largely dominated by theoretical modelling, and by the use of metallic ions to raise the isosteric enthalpy of COFs for better storage performance at room temperature [174]. This includes the Li^+-doped COF-105 of Cao et al. [175], which showed uptake of 6.84 wt% at 298 K and 10 MPa. It has been theorised that very high hydrogen storage could also be performed in native COF materials that have had their organic linkers modified: Klontzas, Tylianakis and Froudakis [176] published such a work changing the single aromatic ring in COF-122 into numerous multi-ring entities, the best of which showed 25 wt% total hydrogen uptake (adsorbed and bulk gas in the pore) at 77 K, and 6.5 wt% at 300 K, both at 10 MPa.

An extension of the synthetic approach to porous materials is the creation of single macromolecules that contain intrinsic porosity. Such molecules can take on a number of topographies, namely bowls (calixarenes and other macrocycles) and single cages (cavitands, cryptophanes, carcerands, metal phthalocyanine crystals, etc.). There is a number of extrinsically porous materials also; such molecules are not intrinsically porous, but misalign in the crystalline formation such that free volume is left between the molecules [177]. Porous molecules have been determined to have 600 – 1000 $m^2 g^{-1}$ [177]. Such an approach has also resulted in the development of 'permanently porous liquids', which can either take the form of a liquid made up of the hollow macroporous molecules themselves, or can be empty 'cage' molecules within a solvent, the molecules of which are sterically prevented from entering the cages [178, 179]. Quantification of the porosity of such molecules has not yet been widely determined however,

and it is unlikely that they will be competitive for adsorptive gas storage purposes, although they may have value as gas separation materials [179].

2.5.2.7. Polymers of Intrinsic Microporosity (PIMs)

Polymers of intrinsic microporosity (PIMs) are polymeric porous materials that were discovered in 2004 [180]. Typically, these polymers feature a regularly occurring contorting site (either a spiro-centre or a covalent bond around which rotation is limited) within the chain, which when combined with a sufficiently rigid co-monomer, produces a polymer chain with high rigidity and a large number of distortions [180]. This combination of inflexible chains and distortions results in the chains displaying inefficient space packing, as any voids in the structure produced by the distortions cannot be made up for by the flexibility of the polymer [180]. This 'forced' free volume created by the steric frustration of the polymer results in an intrinsic microporosity. The microporous structure of PIMs is much like the amorphous chains that constitute the structure of activated carbons, although the chemistry of the chains is well defined [81]. Non-network PIMs are typically soluble in polar aprotic solvents, such as tetrahydrofuran (THF), chloroform and dichloromethane, which allows the formation of thin films [181]. This has allowed this class of PIMs to be considered for applications such as gas separation membranes, as they are easily processable into various shapes, such as films.

PIMs were primarily synthesised through the formation of benzodioxin, which typically involve a double aromatic nucleophilic substitution, which readily, consistently and simultaneously forms two separate covalent ether linkages [182]. This allows the creation of fused rings and thus propagation to a high weight, rigid polymer. This reaction is particularly readily performed if the halogen leaving group on the co-monomer is activated by the presence of another electron withdrawing group, such as a cyano- or fluoro- group [182]. The long chain molecules formed are typically soluble in polar aprotic solvents, such as tetrahydrofuran (THF), chloroform and dichloromethane, which allows the formation of thin films [181]. This has allowed non-network PIMs to be considered for applications such as gas separation membranes, as they are easily processable into various shapes, such as films. More recent developments in PIM synthesis techniques has allowed the formation of new PIMs, primarily through the use of Tröger's base (e.g. in the production of the popular PIM PIM-EA-TB [183]), and through polyimide formation (e.g. for the series of PIM-PI materials) [184].

PIMs have attracted attention as adsorbents due to this processability and microporosity. PIMs have BET surface areas up to 1990 $m^2 g^{-1}$, which results in hydrogen uptakes of up to 1.92 wt% at 0.1 MPa and 77 K, rising to 3.94 wt% at 1 MPa [173]. However, most of the higher porosity PIMs, such as TRIP-PIM (based on triptycene linkers) and Porph-PIM (based on porphyrin linkers), do not share the solution processability of the simpler linear PIMs (such as PIM-1 and PIM-7) [185]. Ultimately, their uptakes have largely been too low to consider them seriously as materials for industrial hydrogen storage use, given how far below the DOE targets they fall. Studies on hydrogen adsorption in unmodified PIM materials were last seen in 2012 [173].

Nevertheless, PIMs have found a wide range of applications, primarily as gas separation materials (a subject discussed in more detail in sections 2.5.2.8 – 2.5.2.11 below), but also as catalyst supports and liquid contaminant removal materials [173]. 2015 also saw the first commercial use for PIMs; PIM-1 was used in an organic vapour sensor developed by 3M [184, 186].

2.5.2.8. PIM-1

PIM-1 was the first PIM ever reported, first presented in a communication by Budd et al. in 2004 [180]. PIM-1 is synthesised from the reaction of 3,3,3',3'-tetramethyl-1,1''-spirobisindane-5,5',6,6'-tetrol and 2,3,5,6-tetrafluoroterephthalanitrile to form a linear polymer featuring a recurring spiro-centre. A 3D model of the contorted polymer chain is illustrated in Figure 2.9. The polymer is bright yellow in colour, and is fully soluble in polar aprotic solvents, with chloroform and THF being the most commonly used in the literature.

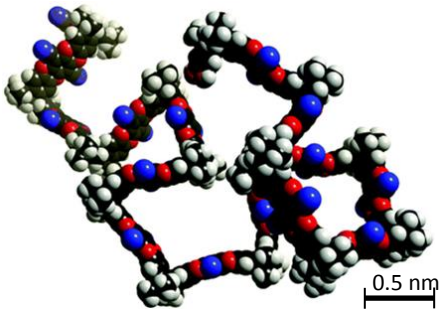

Figure 2.9 - 3D visualisation of a PIM-1 chain. Chain atoms are carbon (black), hydrogen (white), oxygen (red) and nitrogen (blue). Reproduced from [81] **with kind permission from The Royal Society of Chemistry.**

The synthesis, as with most PIMs, is a dinucleophilic substitution in which the fluoride groups of the tetrafluoroterephthalonitrile are attached by the hydroxyl groups on the spirobisindane. This is typically performed in solution; the original method of Budd et al. [180, 187] combined the reagents in an equimolar ratio, and a twofold excess of dry potassium carbonate, in a dimethylformaide (DMF) solvent, and left at 65 °C for 72 h. The reaction can typically performed to high product molar mass, with M_n (number-averaged molar mass) values of 270,000 g mol^{-1} achievable [187]. However, multiple groups reported issues with this synthesis, in particular stating that a much lower M_n was actually achieved (typically < 18,000 g mol^{-1}) due to the cyclisation and cross-linking that can occur due to the multiple reactive sites (and orientations in which they can combine) on the reagents [188–190]. A number of groups suggested alternatives for this low temperature method, most notably Song et al. [190], who tested a number of variables within the polycondensation, and determined that the best result came from a 55 °C experiment run for 23 h under the same ratios as Budd et al. had determined; this study produced a soluble polymer of M_n = 101400 g mol^{-1} and PDI = 3.33.

Alternatively, Du et al. [189] proposed a high temperature solvent method, in which toluene was added as a dehydrating agent, and a small amount of water added to improve salt solubility. The 155 °C synthesis was performed for 8 minutes with a threefold excess of K_2CO_3. After 8 minutes, the polymer produced showed a M_n of 102000 g mol^{-1}, and a PDI of 2.5, an impressive synthesis given the short time required, although this synthesis does require more solvent and greater temperature than the otherwise already solvent-heavy low temperature method.

It has been also shown that PIM-1 can be synthesised with mechanochemistry. Zhang et al. [191] combined 2 mmol of each of the reagents with 1.2 g of K_2CO_3 in a 300 W, 1200 rpm vibrating ball mill, and the powders were ground together for 15 minutes. This produced a fully soluble polymer of M_n = 337000 g mol^{-1} and PDI = 1.4, all without the use of a solvent, so potentially indicating a more environmentally friendly production method of this material. The milling-produced PIM-1 was shown to be chemically identical via FTIR and NMR studies, although the BET surface area was somewhat lower than expected by solvent-based production methods.

PIM-1 is a low density material, as expected due to the low mass of the constituent atoms (namely C, N, O and H) and the presence of free volume. The powder skeletal density has been determined to be 1.4 g cm^{-3}, as measured by helium pycnometry [192, 193], although it is unclear as to how this value was achieved, particularly relating to the method of pycnometry testing, and number of runs performed (see section 3.10 below). The powder density has been calculated to be 0.94 g cm^{-3} [194]. The bulk density of a solvent-cast PIM film (as determined by mass measurements in air and a fluorocarbon) is 1.06 – 1.09 g cm^{-3}, depending on the age and thickness of the film [193].

Due to its high rigidity and lack of ability to rotate within the chain, PIM-1 is a glassy polymer at room temperature. This has been determined by both differential scanning calorimetry (DSC), which showed no evidence of phase change (therefore no glass transition temperature (T_g)) before 370 °C [187], and Dynamic Mechanical Analysis shows no major change in the elastic modulus between 25 - 350 °C, which indicates no change from a glassy state in this temperature range [180]. Zhang et al. [191] later reported that the T_g for PIM-1 occurs at -89 °C, although there is no other evidence (to the author's knowledge) to support this claim, and investigation of the DSC curves in their supplementary information does not show the endothermic shoulder typical of a glass transition at this temperature. Similarly, Staiger et al. [195] seem to indicate that a T_g is seen at 436 °C, based on a large endothermic transition seen in their DSC curve. Although it would make more sense for the material to show a T_g at this temperature (given rubbery behaviour is initiated in most polymers by having room in which parts of the chain can rotate freely), the data presented in this study are unconvincing given that very little data are shown after this transition, and given that this temperature is above the previously reported charring temperature. There is also no evidence of a glass transition in the DMTA curves reported by Polak-Kraśna et al. [196], which run from – 150 °C to 350 °C. It is determined by both of these DMTA studies that the sample begins to thermally decompose at about 350 °C.

Thermogravimetric analysis (TGA) allows for a much more detailed look at the thermal decomposition of the material (in both anoxic and oxidising environments), and disagreement is shown with the DMTA studies. A large selection of studies have published TGA results of PIM-1 in inert environments [195, 197–200], all of which largely agree that the material is stable until at least 450 °C, with a large drop in the mass of the sample seen in the ~ 500 °C. It is generally agreed that 60 % of the original mass of the sample is present at 800 °C. The heating rate of these studies is variable from 3 – 10 °C min^{-1}, if they are reported at all. The mechanochemically synthesised PIM-1 was less stable, showing a ~10 % decrease in weight at 400 °C before a larger drop reminiscent of other samples reported [191].

The only oxidising TGA study known to the author is that of Hao, Liao and Chung [201], who heated a PIM-1 sample under purified air at 10 °C min^{-1} to 800 °C. The mass of this sample was stable to ~ 350 °C, before a steady decline in mass, combusting completely just after 650 °C.

Mechanically, PIM-1 is fairly robust, as it makes flexible films when cast from solution [180, 190]. Quantitative data on the mechanical properties of the films are difficult to come by however; Song et al [190] give a stress-strain curve demonstrating a tensile strength of 47.8 MPa at an extension of 10 %. However, there is very little detail on the sample size and shape, sample preparation or device used to measure this curve, and as such it should be viewed with caution. A much more comprehensive study was performed within our group in Bath [196]; repeated tensile tests indicate a breaking stress of 30.9 ± 5.4 MPa, and a breaking strain of 4.4 ± 2.0 %. The reduction is suggested to be due to inhomogeneities within the sample as a result of faster than

ideal evaporation of chloroform during film production. Nevertheless, these values are still much higher than the 0.4 – 1.9 % failure strain estimated for carbon fibres, so suggesting that this material would not mechanically fail within a hydrogen tank. The 1.26 GPa Young's modulus shows reasonable agreement with the DMTA studies of both Budd et al. [187] and Polak-Kraśna et al. [196], which indicate storage moduli of ~ 1 GPa and 967.2 ± 37.6 MPa respectively.

The N_2 isotherm for PIM-1 powder at 77 K is well documented [185, 187], and shows elements of both type I(a) and type IV(a) isotherm behaviour. An example is shown in Figure 2.10 below. This is indicative of the presence of both micropores (from the high performance at low pressures) and mesopores (continued increase in uptake through the higher pressures). The hysteresis present has previously been explained by two mechanisms: constrictions in the free volume ('throats' through which the movement of nitrogen molecules into and out of the cavities are limited), and adsorbent swelling, which is induced by the presence of the adsorbate [185, 192]. However, this latter theory has largely been dismissed by the work of Jeromenok and Weber [202], who showed by macroscopic soaking of PIM-1 in liquid argon that the pores in this material do not swell significantly in the presence of gaseous adsorbates. They argue that the hysteresis loop is largely a function of solvation pressure in the narrow restrictions, which further narrow the pore diameter and create a thermodynamic pseudoequilibrium in the mesopores that is not disturbed until the low P/P_0 pressures are reached. They also attribute the linearly rising uptake in the mesoporous range, "which is phenomenological[ly] similar to a solution effect (Henry-type behaviour)", to this effect [202].

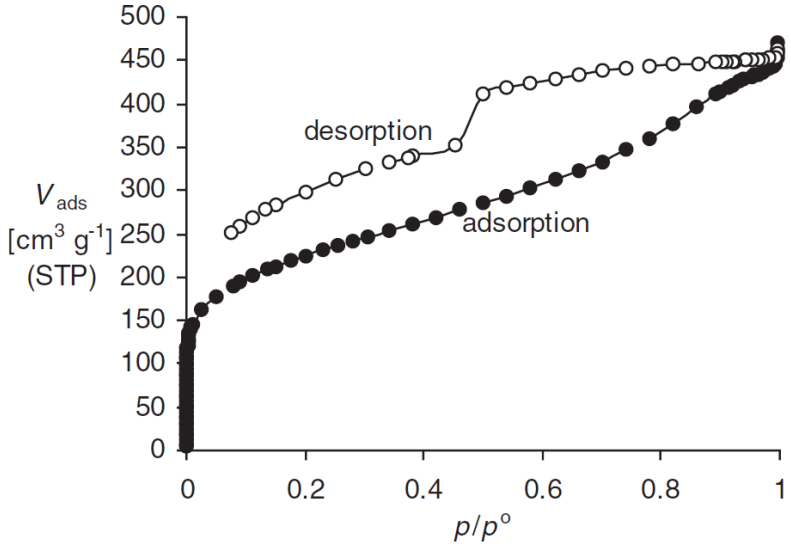

Figure 2.10 - N_2 isotherm of PIM-1 at 77 K, as reported by Budd et al. [187]**. Reproduced from** [187] **with kind permission from John Wiley and Sons.**

The BET surface area of PIM powder is determined to be anywhere in the range 750 – 860 $m^2 g^{-1}$, based on the sample [185, 187]. When cast into a film, this measured surface area then drops to ~ 600 $m^2 g^{-1}$ [180, 187]. The maintenance of surface area when the polymer is recast is due to the inability of the rigid, contorted chains to relax into the free volume present, as discussed above. However, the reduction seen is due to the loss of mesoporosity seen within the PIM powder, which is dependent on the form of the polymer, and may change from sample to sample [180].

The pore size distribution for PIM-1 powder has been determined by a number of different studies. By far the most common method used to calculate the PIM-1 PSD is the Horvath-Kawazoe method, which is a well-established theoretical method for the calculation of micropores (see section 3.11.5.2). This PSD has been reported multiple times, mostly from within the groups of

Budd and McKeown, but all of them consistently show a PSD with a high intensity of micropores generally starting at 0.6 nm, which decays as the pore size increases, but generally without going to zero as it passes 2 nm (the lower limit for mesopores) [193, 203–206]. There is often a small shoulder peak at 0.7 nm. This PSD highlights the microporous nature of this material, with a much greater total free volume present in the microporous region of the distributions. It is also highly repeatable, given the large number of studies that have given the same PSD, so illustrating the consistently of the free volume left within the material by the inability of the chains to relax fully.

PSDs have also been calculated by other methods. Both Chaukura [205] and Tedds [206] used multiple different theories (including the Barrett-Joyna-Helenda, density functional theory and Dubinin-Astakhov theories discussed in sections 3.11.5 and 3.11.4.2 below. All other theories tested showed the presence of microporosity, although at times in different manners (such as the greater intensity of larger micropores shown by Chaukura's BJH and DFT results). The theories tested by Tedds generally showed a good match to the HK distribution he calculated. All of these results reinforce the general idea of PIM-1 showing good microporosity, at least for the powder form (there is little discussion about the differences between the distributions between powder and film morphologies of this material, possibly to difficulties in running nitrogen isotherms on film samples [205]).

Positron annihilation lifetime spectroscopy (PALS) has also been commonly used to determine the pore size distribution and free volume present in PIM-1. This technique, which calculates the free volume within a material from the amount of time a positronium (a bound positron-electron particle) spends within the material before annihilating with an electron (and therefore finding the limit of the void in which it lies), has the advantage of resolving down to 0.106 nm (the size of a positronium), whilst providing all of the information on pore volume and PSD that traditional adsorption experiments can [207]. Whilst some high free volume polymers can exhibit two separate positronium lifetimes that can ultimately deliver a bimodal pore distribution, this is unlikely to actually be the case given the lack of support for such a model from other sources [182]. When compared, numerous sources have produced fairly similar average pore sizes for PIM-1: Staiger et al. [195] published comparative PALS-derived PSDs for PIM-1 powder and for a film sample, with peaks centred on 0.49 and 0.57 nm for the powder and film samples respectively; Lima de Miranda et al. [208] reported an average size of 0.48 nm for their film sample (although this appeared to decrease above 110 °C, possibly due to chain contraction); and Alentiev et al. [209] measured a 0.517 nm average free volume in their PIM films materials. These values all correspond reasonably well with the highest intensity of pores in the HK PSD distribution published by Budd and McKeown's groups. It is also interesting to note that both Staiger et al. and Alentiev et al. reported slightly higher average pore sizes for PIM-1 film materials, despite this morphology's lower surface area as determined by N_2 adsorption. It has been theorised that the accessible microporosity is greater in the powder, but that the change into a film creates larger pores [195].

The estimated pore volume for PIM-1 powder shows less certainty. Early experimental values (calculated by the Gurvich method) have ranged from 0.68 $cm^3\ g^{-1}$ [187] to 0.78 $cm^3\ g^{-1}$ [180] for the powder sample. Later attempts reported by Swaidan et al. [210] and Patel and Yavuz [211] reported lower pore volumes of 0.70 and 0.57 $cm^3\ g^{-1}$, respectively. Calculated values for v_p from molecular simulations are much lower, ranging from 0.194 – 0.3495 $cm^3\ g^{-1}$ [194, 212], which may perhaps be indicative of the micropore volume in PIM films, when the mesoporosity has been removed. However, this is countered by the study of Jue et al. [213], who reported a pore volume of 0.42 $cm^3\ g^{-1}$ for their PIM-1 films.

To add to this uncertainty, it has been proven in multiple studies that PIM-1 swells in the presence of particular organic solvents. This was first seen by Budd et al. [214], who used methanol soaking to improve the apparent free volume of PIM-1 films for use as gas separation membranes. This study found that following an overnight soak in methanol and drying increased the average free volume radius as determined by PALS from 0.522 to 0.575 nm, and the permeability of PIM-1 films to oxygen increases twofold post-treatment. There is mention of methanol soaking by Lima de Miranda et al. [208] a year earlier, although there are no references provided and no further mention of the action of methanol outside of the experimental methodology.

While the ability of methanol to increase the free volume has been widely acknowledged in the literature, few studies have taken a close look at the reasons for this swelling. The most comprehensive study to address this issue is that of Jue et al. [213], who address a number of non-solvent induced phenomena such as swelling and plasticisation. The team, based across Georgia Institute of Technology and Exxon Mobil, demonstrated that methanol was a highly effective solvent for the regeneration of PIM-1 due to its high vapour pressure, strong swelling induction and weak polymer-penetrant interaction (methanol soaked films are proved by TGA to be much drier than more strongly interacting penetrants, such as dimethylformamide (DMF)). Unlike methanol, DMF plasticises PIM-1 (makes the behaviour of the polymer more rubbery), and the strong interactions with PIM-1 can actually lead to a decrease in surface area and free volume if left in the pores for a sufficient period of time (as illustrated in Figure 2.11). Jue et al.'s study clearly indicates the variability that processing (particularly with solvents) can have on the material, and it is therefore important to understand the idea that PIMs can show highly variable porous behaviour depending on the thermal and solvated history of the material.

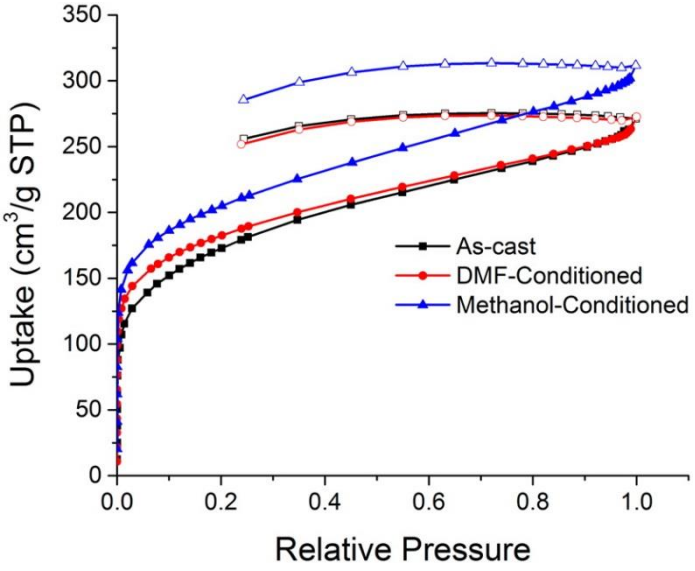

Figure 2.11 - N_2 isotherms at 77 K for PIM-1 films as cast (black), and soaked in dimethylformamide (red) and methanol (blue). Reproduced from [213] **with kind permission from the American Chemical Society.**

Another manner in which the porosity of PIM-1 changes over time is through aging. All glassy materials (including glassy polymers) are by definition out of equilibrium, as they take on glassy properties when the molecules in the glass cannot keep up with changes in the thermodynamic environment surrounding them [215]. This results in glassy materials slowly trending towards a thermodynamic equilibrium over time. In the case of PIM-1, this results in the polymer chains slowly relaxing further into one another and eliminating the free volume within the material [210, 216]. This therefore reduces any free volume within glassy polymers, and ultimately reduces the

benefits of using PIM-1 for said volume. This effect is exacerbated when solvents are used to eradicate the thermal history of the polymer; methanol-soaked PIM films experience a rapid aging process over the first 15 days of life, before reverting to a slower, more intrinsic thermodynamic equilibration [210].

This aging in PIM-1 has been quantified: Lau et al. [217] determined that CO_2 permeability decreased by 62% in a pure PIM-1 film sample aged for 240 days, and the same group in a later study saw drops of ~ 90% for both H_2 and N_2 permeability [216]. Staiger et al. [195] reported a visible drop in the average free volume radius for their PIM-1 films after permeability testing, as well as direct drops in the permeability of several gases, ranging from 20 % (He) to 40 % (CO_2). Du et al. [218] also demonstrated permeability reductions of 60 % and 40 % for CO_2 and CH_4 respectively over 120 days. Aside from the abundant permeation characterisation of aged PIM-1, there are little data on how the adsorbent properties change over time. The lone exception to this is the recent study of Bernardo et al. [219], who performed CO_2 adsorption experiments alongside the more common permeability experiments. It was determined that CO_2 solubility in PIM-1 films does not appear to change with age, as the isotherms stay constant with different heat treatment temperatures (simulating different ages), but there is a noticeable difference in the kinetics of the adsorption experiments, with older (hotter treated) films showing slower uptake kinetics, and therefore lower diffusion constants with time.

This phenomenon appears to be relatively large for PIM-1, largely thanks to the intrachain rigidity and high free volume for which it has gained its notoriety. Physical aging is known to be faster for PIM-1 than for lower fractional free volume polymers [219, 220]. The high intrachain rigidity, originally thought to allow the polymer to be resistant to physical aging, is shown to be culpable for both aging and plasticisation of the polymer; Swaidan et al. [221] demonstrated this by comparing the aging of PIM-1 films to membranes of a self-synthesised 'TPIM', which showed greater chain rigidity, higher BET surface area and greater permeability when freshly synthesised, but appeared to age faster than the original PIM.

By far the most common proposed use for PIM-1 is for use as a gas separation membrane material. Membrane technology shows promise as an energy-efficient and highly practical method of separation, and suitable materials for a wide variety of separations are highly sought after. One field of membrane technology is that of gas separations, as processes such as nitrogen purification (N_2/O_2) and natural gas sweetening (CH_4/CO_2) require high efficiency separation (therefore high selectivity of one gas over another is desired) at a high gas throughput (therefore high permeability of the separated gas is also required). However, finding materials that meet both of these requirements for a given gas pair is difficult, with high permeability materials showing low selectivity and vice versa. This fact was established by Robeson [222] in 1991, who performed a comprehensive literature review of gas separation membranes at the time, and established the Robeson upper bound for a number of gas pairs, which defined an upper limit of the combination of selectivity and permeability that very few membranes were shown to breach.

In investigating the potential of their newly reported PIM materials as gas separation membranes, Budd et al. [203] reported that both PIM-1 and PIM-7 films showed permeability and selectivity of O_2/ N_2 and CO_2/CH_4 mixtures above that of the Robeson upper bound. Combining this with the ease with which these polymers could be formed into thin films, and it was quickly concluded that this material showed incredible potential to advance the science of membrane separations. Since this study, an enormous array of studies has been published evaluating the gas separation performance of PIM-1 films and derivatives thereof. This exceptional performance has been

acknowledged by Robeson himself, who revised the upper bound in 2008 to take into account the advancement in materials that had occurred since the initial limits were published [223].

PIM-1 has been investigated for hydrogen storage, initially because its apparent H_2 solubility coefficient was the highest known for a polymer at the time of testing [185]. The hydrogen uptake of PIM-1 powder at 77 K is 1.45 wt% at 0.1 MPa [185], which while promising for a polymeric material, is disappointing if used solely as an adsorbent. Despite PIMs in general receiving much attention for hydrogen storage purposes [173], the studies on PIM-1 alone in the published literature ended with the study of McKeown, Budd and Book [185]. Due to the relatively low surface area and hydrogen uptake relative to other adsorbents, gas storage is not considered one of the main applications of PIM-1 [182], although some research still continues in the unpublished domains, evidenced by the PhD theses of Chaukura [205] and Tedds [206].

Due to its reasonably low hydrogen uptake, there has been little interest in the isosteric enthalpy of adsorption for hydrogen on PIM-1. The only study of this type known to the author was performed by Tedds [206], who used both the Clausius-Clapeyron and Virial methods for determining the isosteric enthalpy of PIM-1 powder from 0 - 20 bar H_2 isotherms at 77 K. The values for these varied from 9.3 – 13.4 kJ mol^{-1} at zero coverage to 6.5 – 6.7 kJ mol^{-1} at 0.8 wt% absolute uptake. This is a rather high value, and appears to show that hydrogen has a high affinity for the PIM surface, although the ~ 50% decrease in enthalpy (for the lower estimates at zero coverage) bode less well for the amount of hydrogen that the material could deliver from a working system.

2.5.2.9. Thermal treatment of PIM-1

As a polymer structure based around aromatic and cyclic aliphatic units, and a material that shows free volume in its unprocessed state, PIM-1 has attracted attention as a precursor for activated carbon materials.

The gentlest method of thermal PIM-1 modification is thermal crosslinking. This was first reported by Yun Li et al. [224], who heated PIM-1 films under vacuum to 250 – 300 °C between 0.5 – 2 days in order to induce crosslinking. The materials emerged as either a dark brown or black colour, and the study suggests that the reaction has formed a triazide from the nitrile groups of three chains in order to create the crosslink (from both FTIR and XPS studies). This results in a more thermally stable material (TGA) that shows ever increasing ideal selectivity coefficients for H_2/N_2, H_2/CH_4, O_2/N_2, CO_2/CH_4 and CO_2/N_2 separations with increasing heating time. The permeability for these materials also increases with increasing heating time. No adsorption data are presented for these materials.

Following this, Song et al. [225] also synthesised thermally cross linked PIM-1 films, heated at 385 °C under a 1 mbar vacuum for 24 h. This material was shown to have higher elastic modulus than the original film, but was also more brittle. Nitrogen adsorption in the thermally cross-linked (TOX) PIM-1 showed very low uptake until P/P_0 = 0.5, followed by a very sharp rise; this phenomenon is attributed to a gate-opening mechanism connecting the free volume elements in the TOX-PIM, albeit this theory is not thoroughly expanded upon. Low (1 bar) and high (35 bar) isotherms show very similar behaviour between the standard and TOX-PIM samples for CH_4, N_2, O_2 and H_2, but consistently higher uptake in regular PIM-1 for CO_2. TOX-PIM-1 was also shown to improve the selectivity of CO_2/CH_4 six fold over traditional PIM-1 films, and CO_2/N_2 twofold, although this reduced with increasing CO_2 fugacity.

This study was also very interesting as it featured results of a TGA study coupled with an in-situ FTIR analyser (under pure Ar flow), which determined that decomposition of the ether linkages was the primary method of PIM-1 chain decomposition. From this, Song et al. refute the crosslinking theory proposed by Yun Li et al. [224], instead suggesting that the broken ether linkages initiate a free radical chain reaction that creates hydroxyl radicals at the ether termini, which can then go on to react with other ether linkages, the methyl groups on the spirobisindane or the spiro-carbon itself.

One of the most comprehensive studies on the full carbonisation of PIM-1 was done by Salinas et al. [197], who sought to create an ethene/ethane separation membrane by carbonising a PIM-1 film. The films, manufactured from a 3 wt% solution in THF, were dried, methanol soaked for 12 h and then thermally annealed under vacuum at 250 °C for 24 h. These films then underwent carbonisation under N_2 flow by first holding the films at 400 °C for 30 minutes (to cross-link the polymer), and then a further 30 minutes at either 600 or 800 °C, depending on sample. The group performed CO_2 isotherms on these materials, determining surface areas via non-linear density functional theory (NLDFT) applied across the whole isotherm, and determined that the available surface area of these materials increased with increasing severity of carbonisation conditions, rising from 513 $m^2 g^{-1}$ in the original annealed films to 700 $m^2 g^{-1}$ in the films carbonised at 800 °C. This report also provides PSDs for the materials showing an increase in the ultramicroporous intensity with increasingly carbonised materials. The use of CO_2 isotherms up to 1 bar for this purpose naturally restricts the pore size range that is tested (CO_2 at 0 °C and 1 bar is only at P/P_0 = 0.03), and thus both the surface areas and PSDs are not representative of the full nanoporosity of the materials, but solely of the ultramicroporosity in these materials.

However, Salinas et al. [197] present a thorough analysis of the thermal decomposition of PIM-1, including a proposed hypothesis of the mechanism of thermolysis. This is primarily done through the use of thermogravimetric analysis twinned with a mass spectrometer (TG-MS), in which the sample is heated under an anoxic gas flow, and the off-gas from the reaction channelled into the mass spectrometer for analysis. To the author's knowledge, this is the only study of its kind for this material, and provides a unique insight into the carbonisation of PIM-1. Starting with the theory of partial dioxane splitting first proposed by Song et al. [225], the group then suggest that full dioxane splitting then occurs at ~ 500 °C, followed by a dehydrogenation step at ~ 750 °C. The TG-MS data (shown in Figure 2.12) finish at 800 °C, but present sufficient evidence to make a case for this mechanism, supported by Fourier transform infrared spectroscopy (FT-IR) and Raman spectra.

Carbonaceous PIM-1 films were also studied by Kim et al. [198] for the purposes of water filtration. Following PIM-1 film synthesis from a chloroform solution, carbonisation in this study was performed under a N_2/H_2 mix (in a 95%:5% ratio) at temperatures between 1100 and 1300 °C and carbonisation times up to 6 h. This variety of carbonisation conditions produced a variety of mass burn offs (between 35 – 60 %), and it was demonstrated via both X-ray photoelectron spectroscopy (XPS) and Raman spectroscopy that the high mass loss films had very little amorphous carbon content, therefore containing a higher proportion of graphitic carbon. The BET surface area of the films decreased after carbonisation (from 819 to 643 $m^2 g^{-1}$ for the 40% burn off film); although the median pore size was also shown to decrease, indicating a shift in the structure towards microporosity. This decrease is due to the film solely being carbonised; if an activation step were also performed, this would be expected to increase the available surface area and any adsorptive uptake.

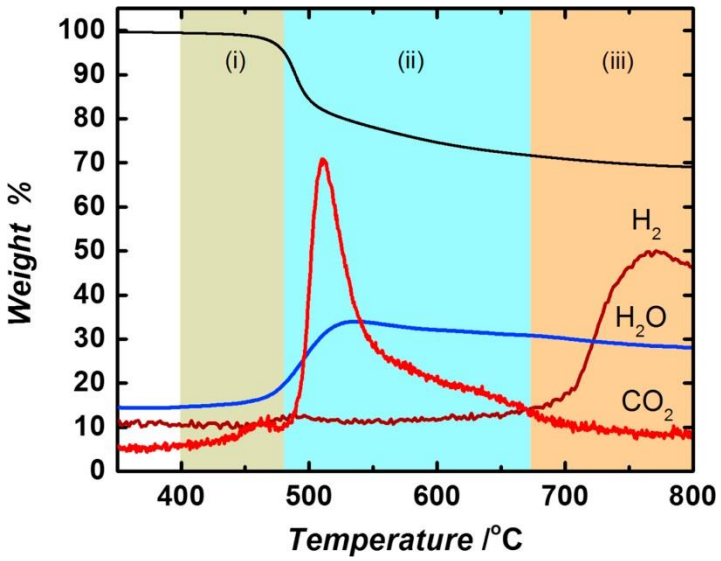

Figure 2.12 - TG-MS study of PIM-1 as presented by Salinas et al. [197]**. Reproduced from** [197] **with kind permission from Elsevier.**

Bonso et al. [199] created activated carbon fibres from PIM-1 for use as an electrochemical double layer capacitor. Electrospun PIM-1 fibres were carbonised at 1000 °C (ramped at 5 °C min^{-1}) for 1 hour, before activation with steam at 800 °C for 1 h. The fibrous material was then annealed under N_2 flow at 900 °C, before characterisation. The fibres are stated to have retained flexibility and mechanical strength after activation, and show a BET surface area of 546 $m^2 g^{-1}$ for the carbonised fibres, as determined by N_2 adsorption. This increases to 1162 $m^2 g^{-1}$ following activation, and the pore size distribution saw an increase in larger micropores (1 – 2 nm) and mesopores (2 – 6 nm). Given the main purpose of this study was to examine the electrical capacitance and energy transfer rates of these materials, the study is comprehensive in terms of its analysis of the porosity of the materials. However, the surface areas and pore distributions for the original PIM-1 (either in unprocessed or electrospun fibre format) are not given, which eliminates the possibility of tracking how the fibres compared pre- and post-processing.

The only other study of carbonisation of PIM-1 known to the author is that of Son et al. [226], who carbonised a spun-coated layer of PIM-1 to serve as a graphitic electrode for organic solar cells. The carbonisation was performed by a ramp at 5 °C min^{-1} up to 1200 °C under a mixture of hydrogen and argon gases, although the composition and flow rate of this carrier gas is unknown. The carbon is determined to have very high carbon content (typically > 93 %) by XPS, and the burnoff is determined to be as high as 94.3 % at 1200 °C. However, there is no further analysis on the carbon in terms of the change of porosity, as the layers are supported on quartz, and are immediately built into the solar cells, which are then characterised for electrochemical performance.

2.5.2.10. Modified PIM-1

PIM-1 generated a lot of interest as a result of its ease of processing, high porosity and excellent combination of permeability and selectivity towards particular gases. However, it was immediately seen that modifying PIM-1, whether by cross linking to increase microporosity, or by changing the functional groups on the aromatic rings from the terephthalonitrile, could lead to incremental changes towards the microstructure desired for the given application. A selection of these studies is presented below, although this discussion is by no means exhaustive.

An alternative method for PIM-1 cross linking (to the thermal means presented above) is by exposure to ultraviolet (UV) radiation. Such an idea was first presented in a U.S. patent by Liu, Wilson and Lesch [227], who proposed the irradiation of a number of PIM materials (with a focus on PIM-1) with UV radiation for 30 minutes in order to improve the selectivity for the separation of a number of gas pairs. This treatment increased selectivity for CO_2 over CH_4 by 267% and H_2 over CH_4 1909% over standard PIM-1 films (at 50 °C), albeit with reduced permeabilities. The UV-treated films were also shown to have selectivity coefficients of 22.2, 2.26 and 5.62 for CO_2/N_2, propylene/propane and O_2/N_2 respectively. The patent demonstrates a number of functional reagents that would be suitable for such a treatment, but do not provide any further characterisation of these materials, nor provide any information on the chemical alteration the UV irradiation performs.

UV irradiation of PIM-1 was also studied by Yun Li et al. [228]. PIM-1 films are irradiated up to 4 hours, and the porosity and gas separation properties carefully studied. This study proposes that as a result of the formation of a hydrogen free radical due to the UV irradiation, the material undergoes a series of 1,2-migrations that result in the formation of a cyclohexyl ring out of one of the cyclopentyl rings that shared the spiro-centre carbon, which is consequentially eliminated (the reaction mechanism is presented in Figure 2.13 below). The result is a modified PIM-1 that packs more closely, which increases the microporosity within the material; this is determined both by PXRD and PALS studies. The study shows a 30 minute irradiation produces an optimal CO_2/CH_4 selectivity of 31.3 and O_2/N_2 of 6.8, but a 4 hour irradiation results in a H_2/N_2 selectivity of 166 and a H_2/CO_2 of 7.3, all of which are shown to exceed the 2008 Robeson upper bound. No adsorption characterisation of these materials is presented.

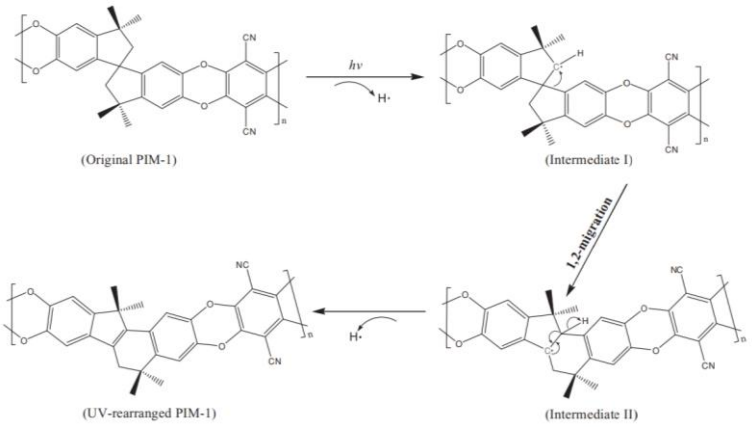

Figure 2.13 - Reaction mechanism for the UV-induced rearrangement of PIM-1, as presented by Yun Li et al. [228]**. Reproduced from** [228] **with kind permission from John Wiley and Sons.**

One of the earliest attempts to chemically modify PIM-1 was the carboxylation experiments performed by Du et al. [229]. This study modified PIM-1 films by soaking them in a 20 % solution of NaOH at temperatures between 25 - 120 °C, and times between 0.5 – 72 h, following by boiling in a pH 4 - 5 solution for 3 - 4 hours. This carboxylated the nitrile groups on the PIM-1 chains, instead replacing them with carboxylate groups. This adjusted material had lower thermal resistance, mechanical strength and permeability, but showed greater selectivity for a number of gas pairs. This alteration generally did not get PIM-1 closer to the 2008 Robeson upper bound than the previously reported values for the original material. The group published a follow up study in 2011 [230] which provided an extensive examination of the porosity of this material, with N_2 and CO_2 isotherms showing lower uptake than the original PIM-1 material. The N_2 isotherms showed similar behaviour to the thermally crosslinked films of Song et al. [225], showing very

little adsorption uptake until P/P_0 = 0.6, before rapidly rising; this is again allocated to a potential swelling/throttling mechanism within the polymer. The pore volumes are calculated by NLDFT from the CO_2 isotherms (so only taking into account ultramicroporosity), and are shown to reduce from 0.195 $cm^3\ g^{-1}$ for the original material to 0.155 $cm^3\ g^{-1}$ for the 120 °C, 5 h carboxylated polymer.

An extension of this carboxylation work was presented by Liao, Lai and Chung [231], who used the electron rich carboxylate groups to facilitate PIM-1 cross linking using metallic ions. The group partially hydrolysed PIM-1 (typically replacing one –CN group with a –COOH), and then cross-linked the polymer using either Zn^{2+}, Mg^{2+} or Ag^{2+} ions. PALS determined that the metallic cross-linked polymers all showed a reduction in fractional free volume and positronium lifetime distribution, as well as a four- to fivefold increase in the selectivity of ethene from ethane, whilst showing higher permeability than the carboxylated PIM alone. No adsorption study is presented in this publication.

The same group then performed an alternative study using the same carboxylated PIM, instead incorporating a number of boron-based cross-linking agents and carbonising the films in order to create an effective ethene/ethane separation membrane [232]. Mildly carbonised PIM-1 was synthesised, redissolved and then stirred with the boronic cross-linking agent at 80 °C for 3 days. These films, as well as the original carboxylated PIM, were then carbonised under vacuum at temperatures between 500 – 900 °C. The 700 °C carbonised PIM was shown to have the best performance for C_2H_4/C_2H_6 separation, so this temperature was focussed on for the boron-containing polymers. Carbonised films synthesised using 9,9-dihexylfluorene-2,7-diboronic acid (by far the largest cross-linking agent used) produced the largest average free volume (by PALS), as well as the highest permeability and selectivity of ethene over ethane.

Patel and Yavuz [211] created an amidoxime-functionalised PIM-1 (AO-PIM-1) in order to increase the capacity of PIM-1 to adsorb CO_2. After refluxing with hydroxyl amine in order to substitute the cyano- groups with amidoxime groups, the polymer was tested for N_2 and CO_2 adsorption, as well as FTIR for functional group determination. The AO-PIM-1 was shown to have much lower N_2 uptake, although the large hysteresis loop was all but eliminated, suggesting that AO-PIM-1 shows fewer mesopores, but maintains an open micropore network that allow for rapid mass transfer of adsorptives. CO_2 uptake is increased 17 % in the AO-PIM-1. Although multiple surface areas, pore volumes and isosteric enthalpies are quoted, no pore size distribution is presented, only quoting the 'calculated average pore size' (no method is given). Swaidan et al. [210] also synthesised AO-PIM-1, with the intent of examining its gas separation properties. This group repeats the experiments of Patel and Yavuz, and shows the PSD for the material. Gas permeation studies show AO-PIM-1 has twice the selectivity for CO_2/CH_4, and better maintains this electivity over a greater range of CO_2 partial pressures.

Larsen, Hart and Colina [233] tested the porosity, adsorption potential and permeabilities of a number of PIM-1 variations in-silico. Alongside the original material, the variations tested include swapping the twin methyl groups on the spirobisindane for carbonyl groups (PIM-1c), swapping the terephthalonitrile aromatic ring for a pyridine ring with a single cyano- group (PIM-1n) and swapping the CH_3 groups for CF_3 (PIM-1f). The 1n and 1f variations improved both surface area and pore volume, but the 1c variation showed much greater CO_2 uptake on both gravimetric and volumetric bases. Only 1f showed great deviation from the original in terms of O_2 and N_2 adsorption, showing much lower uptake, although the spread across all of the samples increased when plotted on a volumetric basis. PIM-1c showed the greatest solubility values for all four gases

tested (CO_2, CH_4, O_2, N_2), but the only had the highest selectivity for CO_2/CH_4 and CO_2/N_2 pairs. The study also presents comparisons with experimental results, acknowledging the ideality of the calculations performed and deviations from experiment due to physical effects (such as pore swelling) that are not encountered in their simulations.

Zhang et al. [234] performed an intriguing study into the value of the flexibility of the spiro-centre in PIM-1 by 'locking' it via the formation of an ether bond across the spirobisindane. Creating this locked polymer appeared to give a much lower distribution in the end-to-end distance of a repeating unit in the polymer (as determined by molecular simulation), so confirming the extra rigidity of this polymer. As with the functional group modifications above, no solubility of the polymer was lost. Curiously, the locked PIM-1 showed both greater permeability and greater selectivity than unmodified PIM-1 for a number of gases, making the modified PIM highly competitive with insoluble PIMs, albeit at the cost of much greater synthetic complexity. There is no study performed to measure the available pore volume in the locked PIM.

There have also been attempts to synthesise co-polymers of PIM-1. One example of this is the work of Du et al. [235], who created co-polymers of PIM-1/PIM-4 and PIM-1/TOT-PIM-100. Although some synthetic steps were required to prepare the reagents for the co-polymers, the polycondensation was very similar to that of the high temperature method previously proposed by the group [189], but for 120 mins. The polymers produced ranged in M_n from 14,000 to 65,000 and PDIs from 1.6 – 3.1, albeit it is determined that a number of cyclic polymers are produced. The co-polymers are all determined to be less thermally and mechanically stable, and have lower BET surface areas and pore volumes. The co-polymers with PIM-4 are shown to be competitive with original PIM-1 in terms of O_2/N_2 separation.

2.5.2.11. Adsorbent Composites

Creating composites from well-known adsorbent materials is a growing field, largely because of the desire to enhance positive characteristics of materials whilst minimising any unwanted properties. One simple way to do this is to blend two or more materials together that have properties that compensate for one another.

Adsorbent composites have been reported as early as 2001, when Biloe, Goetz and Mauran [236] compressed together PX-21 activated carbon (pre-treated with a polymer binder) and expanded natural graphite (ENG) to create a porous composite of higher gravimetric density (and thus higher methane storage densities) and better heat transfer, to lose the heat generated by the exothermic adsorption process. This process was relatively successful, having a relatively minor effect on the pore size distribution (reducing the intensity of the micropore response, but ultimately retaining the same profile) whilst increasing the thermal conductivity between 10 – 40 fold, depending on the ratio of PX-21 to ENG.

This work is very similar to that being done within the Ford/BASF/UM consortium on MOF-5 storage. One of the approaches the group has taken to overcome the issue of low thermal conductivity in the MOF is to create a densified composite material with ENG, citing the use of ENG for the raising of thermal conductivities in metal hydride systems [237]. Their first generation composite, formed by mixing, milling, and then compressing the two solids into cylindrical shapes, was a homogeneous dispersion of ENG 'worms' throughout the compacted MOF pellet. Similar to the results of Biloe, Goetz and Mauran [236], they found that hydrogen uptake decreased both with increasing ENG content and increasing pellet density, although they noticed that for low density pellets, the addition of 1 – 10 wt% ENG either increased or did not greatly affect the

measured BET surface area. The thermal conductivity in the high ENG, high density pellets was as much as 12 times as high as the low density pellets of MOF-5 alone.

However, further studies on this pellet morphology showed that a tendency for the ENG to reorient itself perpendicular to the direction of compression resulted in a pellet with a highly anisotropic thermal conductivity [140]. Thus a second generation design was created in which MOF-5 and ENG were layered; this produced an increase in the thermal conductivity parallel to the ENG layers up to 20 times larger than MOF-5 alone. Since then, further engineering studies have been performed, using aluminium pins to improve the thermal conductivity perpendicular to the ENG layers, and also experimenting with graphene as the conductive material, which was found to better coat the MOF-5 particles and thus reduce the anisotropy of a homogeneously distributed material [238].

PIM-1 has also been the subject of intense focus for composite synthesis. The polymer is very attractive for gas separation membrane applications for a number of reasons: it can be very easily processed into suitable shapes (due to its solubility); the material exhibits gas selectivities and permeabilities that exceed Robeson's upper bound [203]; and these properties can be further enhanced by altering the chain packing [239]. As a result, a large number of mixed matrix membranes (MMM) have been made with PIM-1 as the composite matrix. Forming mixed matrix membranes from PIM-1 has become such a popular approach for increasing the effectiveness of this material that a review paper detailing the wide range of organic and inorganic fillers used to created MMMs has recently been released [240]. Fillers for PIM-1 based MMMs have been highly diverse featuring: nanomaterials, such as fumed silica nanoparticles [239] and graphene sheets [241, 242]; porous carbon materials, such as carbon nanotubes [243]; zeolites (silicate [244]); and porous polymers, including but not limited to CC3 organic nanocages [245], PAF-1 [216, 217] and COFs [246]. Possibly the most popular filler for PIM-1 based MMMs are metal organic frameworks; a wide variety of MOFs have been tried in PIM-1 in order to boost the selectivity whilst maintaining the permeability of the membranes. A selection of some of the most interesting and/or relevant publications to this study on this subject are presented below.

Whilst MOFs had been embedded into polymeric materials for MMM purposes since 2008, the first instance of a PIM-MOF composite was reported by Bushell et al. [247], who created a composite of PIM-1 and ZIF-8 nanoparticles. The composite was made by combining ZIF-8 particles (suspended in chloroform) into a PIM-1 solution (dissolved in chloroform), and solvent casting in the same manner as a PIM film is manufactured. A number of ratios of PIM-1:ZIF-8 was tried; anything higher than 1:0.1 resulted in excessively brittle films, although most were sufficiently robust to test.

Whilst most of the analysis performed relates to the membrane properties, some CO_2 isotherms for each of the composites are given. At 25 °C and between 0 – 8 bar, the CO_2 uptake for each of the composites lies between those of pure PIM-1 and ZIF-8, with the ZIF-8-heavy composites showing behaviour more like that of pure ZIF-8. This behaviour potentially indicates a relationship between the composite composition and adsorption behaviour that is not strongly explored in this communication. However, Bushell et al. [247] do mention potential effects that the composite may show that two separate materials may not; namely, if the wetting in such a composite is good, then the external surface area of the MOF particles is not available, but if it is poor, then adsorption would be possible at the interface between MOF and polymer. Swelling effects may also be possible. Free volume studies by PALS showed an increase in both free volume and free volume connectivity over pure PIM-1.

A very interesting extension of this study was performed by Semino et al. [248], who performed a molecular simulation of the PIM-1/ZIF-8 MMM in order to further understand the interactions at the interface of these materials. The main conclusions of this study appear to be threefold. Firstly, the PIM-1 chains (which are free to move around the ZIF-8 crystal) orient themselves either so that there is a favourable interaction between the –CN group on the polymer and the NH of the imidazole linker on the ZIF-8 (the dominant interaction between the two materials), or the kinked shape of the polymer rests into the 'zigzag' surface presented by the crystal, so orienting a methyl group towards the same NH group. These phenomena are illustrated in Figure 2.14 below. Secondly, the rigidity of the polymer chains at the interface appears to be higher than those in the bulk, due to a different conformation of the polymer at the interface. Thirdly, the polymer appears to arrange into two phases: the interfacial region, which is of lower density and exhibits pore sizes of 0.6 – 0.7 nm, and a bulk-like phase, which starts ~ 1.3 nm from the interface and shows pores of 0.4 – 0.6 nm, albeit at a density still lower than experimentally determined. Although the results of this study are interesting, there is little in the way of how this change in conformation affects the macro-scale behaviour in the material, although this is acknowledged in the study as a course of future work.

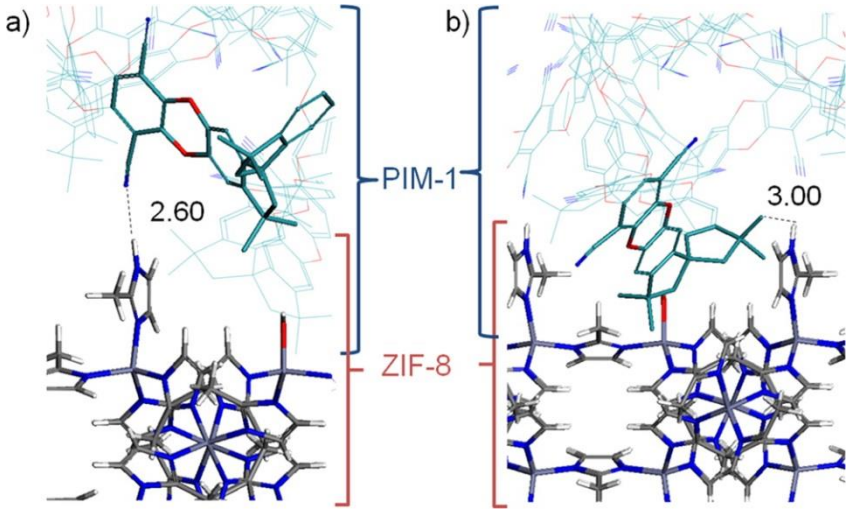

Figure 2.14 - Visualisation of the interaction between the (a) $(NH)_{ZIF-8}$ and N_{PIM-1}, (b) $(NH)_{ZIF-8}$ and (CH_3)PIM-1 at the interface between PIM-1 matrix and ZIF-8 crystals in a MMM. The numbers refer to intermolecular distance, measured in Å. Reproduced from [248] **with kind permission from the American Chemical Society.**

Smith et al. [249] compared zirconium-based UiO-66 and its titanium-substituted analogue Ti-UiO-66 in PIM-1 based MMMs, based on the smaller pore size and higher adsorption of the Ti version. Both MOFs increase not only free volume (as determined by membrane casting solution viscosity and CO_2 permeability) but thermal stability also (as determined by DSC). In both cases, the Ti-based MOF shows further property improvement than the Zr-MOFs, particularly for permeability. No comment is made on a change in the nature of the free volume.

Khdhayyer et al. [250] extended this study by investigating different variations of UiO-66(Zr) using bdc linkers with different functionalities (namely, the original bdc, 2-amino(bdc) and 1,2,4,5-benzenetetracarboxylic acid) embedded in a PIM-1 matrix. All three of the UiO-66 varieties tested improved the permeability of the MMMs, although only the $–NH_2$ variety maintained the selectivity of CO_2/CH_4 shown by neat PIM-1 at these higher permeabilities. Each of the MOF varieties also showed a maximum in CO_2 permeability with respect to MOF loading, typically showing optimal performance in the 10 – 20 wt% range. Although the BET surface areas for the MOFs themselves are reported, there is no further characterisation of the porosity either of the MOFs or the MMMs made therefrom.

Similarly, Hao, Liao and Chung created three composites of ZIF-71 in PIM-1, at concentrations of 10, 20 and 30 wt% ZIF respectively [201]. The free volume is determined to increase by PALS, although UV irradiation of the composites leaves a thin dense layer on the polymer with a smaller free volume. Permeability of N_2, CH_4, O_2 and CO_2 are all increased as the ZIF-71 content increased, but the selectivities are not greatly affected, demonstrating good compatibility between PIM and ZIF due to a lack of non-selective voids within the composite. A similar finding was made by Bushell et al in their PIM-1/ZIF-8 MMMs [247].

Perhaps the study of greatest interest to this work is that of Alentiev et al. [209], who published a study focussed on a PIM-1/MIL-101 MMM. This study featured a single composite, which contained 33 wt% MIL-101. This study, whilst limited in its scope, presented a detailed analysis of the results generated, including a full breakdown of the FT-IR spectra generated for both PIM-1 and MIL-101. This study also suggests that the two materials show an element of chemical interaction rather than just coexisting as a physical mixture, due to the broadening of the peaks in the IR spectra for the composite. Whilst this communication did not present adsorption studies, it did show by PALS that free volume had increased within the polymer, as the free volume elements has increased from 0.245 and 0.517 to 0.273 and 0.551 nm respectively. It was also shown that the permeability and selectivity of O_2/N_2 and CO_2/N_2 were both greatly improved by the presence of the MIL-101. No adsorption studies are presented.

This is not the only study to consider MIL-101 as an MMM filler. Naseri et al. [251] synthesised and characterised an MMM in which MIL-101 was embedded into Matrimid in 10, 15, 20 and 30 wt% concentrations. Extensive characterisation is performed on the MIL-101 alone in order to test its suitability as an MMM filler (which it is deemed to be, particularly based on its performance as an adsorbent), but the composites are only tested for gas permeability. The 10 wt% composite is deemed to be the most suitable for this application, showing higher permeability than the original Matrimid membranes, whilst showing higher CO_2/CH_4 and CO_2/N_2 selectivity than the higher MOF content membranes. No evidence is provided to demonstrate how the porosity and/or free volume of the membrane changes with MIL-101 content.

A variation of MIL-101 was also used to create a three phase MMM. Ma et al. [252] introduced a task-specific ionic liquid into the pores of NH_2-MIL-101 (a variation of MIL-101 in which 2-amino(bdc) is used as the linker), which were then suspended in a PIM-1 matrix. The structure of the MOF was confirmed not to change (following the introduction of the ionic liquid in the pores) with XRD, and both gas separation and N_2 and CO_2 isotherms are performed on all samples. The introduction of NH_2-MIL-101 into PIM-1 improved permeability of CO_2 with increasing concentration, but CO_2/N_2 selectivity gradually decreased, accelerating as the concentration of the MOF increased. With the introduction of the ionic liquid, the permeability is largely unaffected from the PIM-MOF composite, but the selectivity is much higher and peaks for the 5 wt% composite, indicating that the ionic liquid plays a role in selecting for CO_2. This was confirmed by adsorption studies on the filled and unfilled MOFs, as both N_2 (77 K) and CO_2 (293 K) uptake were reduced by the presence of the ionic liquid, but nearly twice as much (in relative terms) for N_2, resulting in a much higher theoretical selectivity. No adsorption experiments are performed upon the membranes themselves. As a relatively recent paper (published Apr 2016), this paper also presents a comparison between their own study and a number of other MMMs, which is shown in Figure 2.15 below. This comparison features the PIM-1 MMMs of ZIF-8, Ti-UiO-66, and ZIF-71 discussed above [201, 247, 249] , as well as composites featuring PAF-1 particles [216] and CC3 organic cages [245].

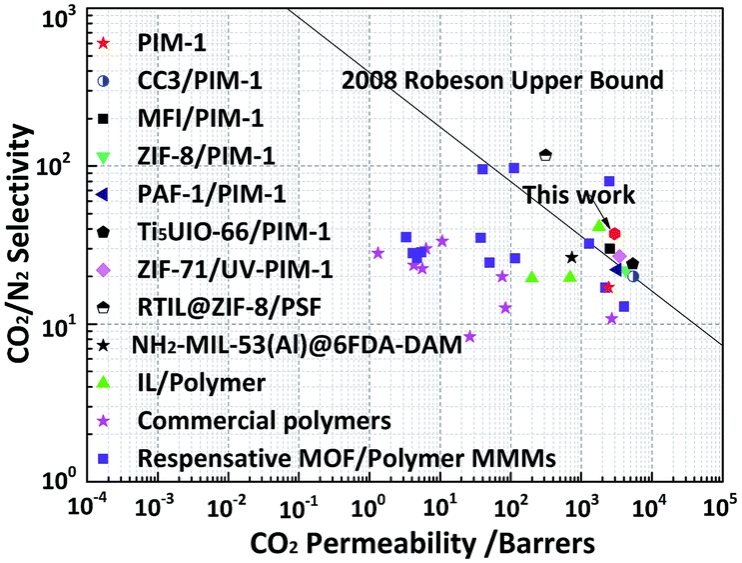

Figure 2.15 – CO_2/N_2 permeability and selectivity for a wide variety of mixed matrix membranes. Reproduced from [252] **with kind permission from The Royal Society of Chemistry.**

MIL-101 has commonly been altered in order to tailor it towards a specific purpose. This is certainly so with the application of hydrogen storage in mind; a number of modifications have been tried in order improve the uptake of MIL-101, particularly at higher temperatures [132]. Primarily, this has come in the form of using spillover, whereby a metal nanoparticle, which can chemisorb to hydrogen and disassociate it, before the H^+ ion migrates onto a more porous adsorbent on which the proton adsorbs.

The earliest study on MIL-101-based spillover adsorbents was performed by Li and Yang [251], who immobilised a Pt/activated carbon catalyst onto MIL-101, via the carbonisation of sucrose to form a continuous carbon bridge. By doing so, the hydrogen uptake at 10 MPa and 298 K is improved by a factor of 2.6, from 0.45 wt% to 1.45 wt%. The isosteric enthalpy of this system is also calculated, with the value for Pt/AC@MIL-101 calculated at -21 kJ mol^{-1} at zero coverage, descending to -12 kJ mol^{-1} at 0.014 wt%.

Later attempts at H_2 spillover storage in MIL-101 have included: the improved results of Liu et al. [253], who also used Pt/AC on MIL-101 to achieve 1.14 wt% H_2 uptake at 50 MPa and 293 K compared to 0.75 wt% for a carbon-bridgeless material under the same conditions; the palladium-based spillover material of Lin et al. [254], which uptook 0.45 wt% H_2 at 3.2 MPa and 298 K (again showing a twofold increase over a bridge-less material); and the Li-ion doping studies of Xiang et al. [255], who raised the H_2 capacity of MIL-101 at 0.1 MPa and 77 K from 2.41 wt% to 3.5 wt%.

MIL-101 has also been popular for particle encapsulation within its large cage structures in order to improve its adsorption performance. One such example of this is the impregnation of MIL-101 with particles of the superactivated carbon AX-21 by Rallapalli et al. [256]. As AX-21 is a highly porous, high hydrogen uptake material in its own right, the idea was to try and combine the uptakes of these two materials by synthesising the MOF around small particles of the carbon. This worked to an optimum: four different loadings of AX-21 were tried, and only the highest loading showed lower BET surface area and hydrogen uptake than the original MOF. The peak was reached by the lowest carbon loading (10 mg AX-21 in a 10 mmol MIL-101 reaction), which showed a BET surface area of 3556 $m^2 g^{-1}$ and a hydrogen uptake of 10.1 wt% at 6 MPa and 77 K, although from the shapes of the curves, this appears to be absolute uptake. PSDs are also attempted, although they are patched together from a mixture of N_2 and CO_2 isotherms, and show relatively little difference between the MIL-101 and the AX-21 loaded sample.

A similar attempt at carbon loading into MIL-101 was performed by Musyoka et al. [90], who loaded a self-synthesised zeolite-templated carbon into MIL-101 in order to increase its hydrogen storage uptake. The group loaded 150 mg of carbon into a 10 mmol synthesis of the MOF, and saw a rise both in BET surface area (as determined by N_2 adsorption at 77 K) and hydrogen uptake, particularly over MIL-101. However, the performance of most of the important metrics was very similar to that of the carbon (2577 m^2 g^{-1} and 2.39 H_2 wt% at 0.1 MPa and 77 K for the carbon, 2957 m^2 g^{-1} and 2.55 wt% for the loaded MOF), so the value of loading this carbon material into MIL-101 is questionable. The hydrogen testing is also performed to 1 bar only, which is very difficult to extrapolate into the kind of pressure ranges in which such a storage system would be used in industry.

An alternative example of encapsulation is the study of Klyamkin et al. [147], who encapsulated large ionic particles (namely $[Re_4S_4F_{12}]^{4-}$ and $[SiW_{11}O_{39}]^{7-}$) within MIL-101, with the aim of tailoring the pore volume within the MOF to be more suitable for hydrogen adsorption, and to increase the number of active sites on which hydrogen can adsorb. Indeed, both the BET surface area and pore volume were reduced as a result of ion impregnation, although the higher density of the modified materials meant that the gravimetric hydrogen uptake was not improved at cryogenic temperatures (maximum excess uptakes of 4.5 wt% for the original MIL-101, versus 2.1 wt% for the $[Re_4S_4F_{12}]^{4-}$–doped and 2.2wt% for the $[SiW_{11}O_{39}]^{7-}$–doped materials). At 298 K however, the materials were highly competitive gravimetrically, and on a volumetric basis, the doped materials outperformed the original (the volumetric density of hydrogen in the sample holder volume was 0.012, 0.030 and 0.016 g cm^{-3} respectively), albeit the exact volume over which this is calculated is unclear. The introduction of ionic adsorption sites, particularly the presence of electronegative fluoride ions in the material induced strong dipoles in hydrogen, raising the enthalpy of adsorption and therefore the higher temperature performance. This paper is also highly interesting due to the very high pressures (190 MPa) that the hydrogen isotherms are performed to, illustrating clearly the delineation between excess and absolute uptake.

2.6. Modelling of Adsorptive Hydrogen Storage Systems

In order to step up from laboratory scale hydrogen adsorption to industrial scale tanks, there must first be a process of understanding the engineering challenges that such a system poses. One way of tackling this is to model systems to estimate storage performance, as well as other parameters that are less important in the laboratory, such as heat transfer and hydrogen equilibration rates.

The seminal early work on modelling adsorptive hydrogen storage was that of Bhatia and Myers [257], who used theoretical thermodynamic analysis to provide optimal thermodynamic properties for an adsorbent-based gas storage system. For hydrogen, assuming a storage pressure of 30 bar and a delivery pressure of 1.5 bar, the optimal isosteric enthalpy was determined to be – 15.1 kJ mol^{-1} for delivery at 298 K, substantially higher than most adsorbents reported, and deemed essentially unattainable in carbon materials. Alternatively, it was determined that for an activated carbon with an isosteric enthalpy of -5.8 kJ mol^{-1} (the average value for such a material at the time), the optimal temperature for storage is 114.4 K, confirming that a cryogenic approach needs to be taken for adsorptive storage to be effective. These values are further reinforced through Monte Carlo simulations of graphitic slit pores (representing activated carbon materials) and atomistic models of carbon nanotubes to recreate these values.

One useful approach to system performance modelling is to parameterise experimental isotherms, and to then use a mass balance approach to simulate static system performance. This approach was led by Richard et al. [72], who fitted a modified Dubinin-Astakhov (DA) model to their 77 K hydrogen isotherms on a tank of Maxsorb MSC-30 activated carbon (~3000 m^2 g^{-1}). These parameters were then fed back into a tank-scale mass balance equation to determine hydrogen storage, and a series of net storage values (of deliverable hydrogen) were created. As shown in Figure 2.16 below, they determined that a 150 L tank of MSC-30 could store the 5 kg required for a vehicular system, but conditions of 80 K and 7.8 MPa were required to better the break even curve, which represents compressed gas at the same temperature and pressure.

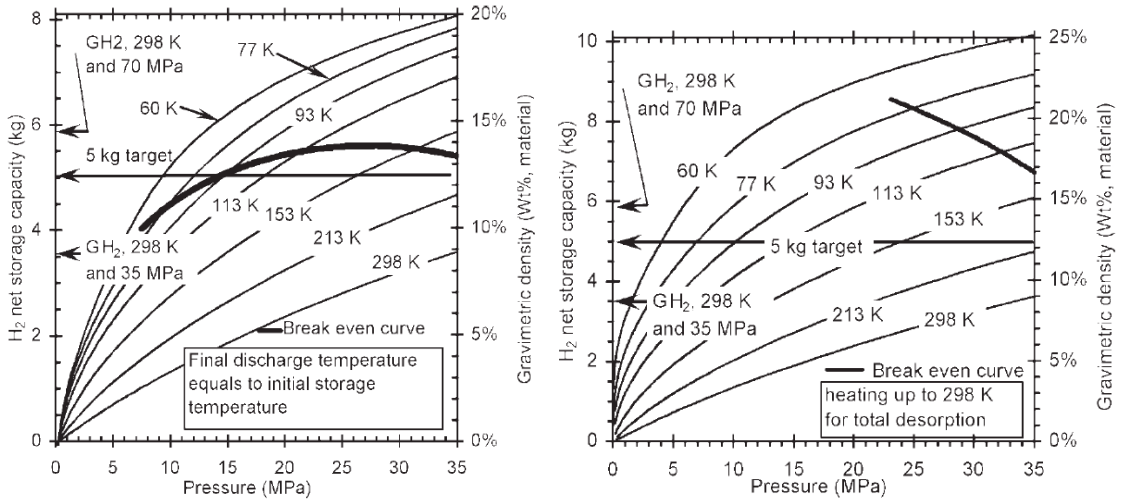

Figure 2.16 - Deliverable hydrogen capacity in a 150 L tank for isothermal delivery (left) and delivery with raising temperature (right). Reproduced from [72] **with kind permission from John Wiley and Sons.**

However, the hydrogen stored and available from a tank is not the only information required, and dynamic modelling must be performed. One of the most prolific researchers in this field is Jinsheng Xiao at the Wuhon University of Technology (China) (and later of Université du Québec à Troís-Riviéres (UQTR)), who in the space of a year released a number of articles discussing dynamic simulations of heat transfer and hydrogen charge/discharge on tanks filled with both activated carbon and MOF materials [258–261]. These works detail a wide array of engineering properties, including mass stored, gas velocity and temperature distributions, typically through the use of finite element analysis, although computational fluid dynamics are required for finer detailed properties, such as mass, heat and momentum transfer [261]. The modified DA equation is used as the adsorption model, regardless of adsorbent.

More recent work within this group focuses on the dynamics of hydrogen flow and storage within a MOF-5 based system, almost certainly in support of the work occurring in the HSECOE. In particular, these studies have focussed on cooling during adsorption via flow-through cooling [262] and endothermic para-ortho conversion [263] (compared with experimental results from the 2.5 L system discussed in section 2.7 below), as well as scaling up the model to a 20 m^3 system, and investigating charge-discharge dynamics [264].

Similar dynamic modelling work has been performed at General Motors. Kumar, Raju and Senthil Kumar [265] used a linear driving force model of AX-21 carbon adsorption kinetics twinned with real world drive cycle data to produce an elaborate model of how pressure, temperature and mass of hydrogen change within a cryo-adsorption tank during the drive cycle. They also did the same with a sodium analate-based tank. Senthil Kumar, Raghunathan and Kumar have also

considered the pressure and temperature response to system dormancy in a MOF-5 filled tank, using a lumped-parameter model [266].

2.7. Experimental Adsorptive Hydrogen Storage Systems

Despite the diverse array of materials available and the promise shown by system modelling, there has been very little experimental work on tanks filled with adsorbent materials [44]. The first prominent example of an experimental adsorbent tank was reported by Richard et al. [72] at UQTR, who filled a 2.5 L tank with 670 g of Maxsorb MSC-30 to validate their models of thermal performance (heat leaks, dormancy etc.). The tank was a stainless steel unit with a working pressure of 10 MPa, and was submerged in a liquid nitrogen (LN_2) Dewar fitted with 8 thermocouples to measure the rate of boil-off. This work demonstrated a number of important engineering considerations, such as the energy requirement to get hydrogen fuel into the right condition in the tank, and the heat input required to release sufficient hydrogen, given that desorption is an endothermic process. This 2.5 L unit has also been used to validate the MOF-5 model of Xiao et al. [259], and to test new designs for MOF-5 compaction as part of the on-going work in the HSECOE [267]. This unit was also the empirical basis for Ubaid et al.'s studies on ortho/para conversion [263] and flow-through cooling [262].

An alternative design has been used by Paggiaro et al [268], again to validate heat and mass transfer calculations during the filling process. This design featured seven 1 m long x 80 mm diameter stainless steel tubes arranged in a hexagonal pattern, connected to a single hydrogen inlet by a manifold. The tubes were filled with a coconut shell-derived activated carbon (10 kg), and submerged in an LN_2 Dewar, with any large void space filled with copper wool to smooth out any thermal effects. A hydrogen 'flow-through' recooling system is used in which non-adsorbed hydrogen that has been heated by the adsorption of other hydrogen molecules is flowed out, and replaced by pre-cooled hydrogen. This allows the hydrogen to act as a cooling mechanism. This report detailed a number of experiments related to the use of both hydrogen and external LN_2 as the cooling source, and the pressure and temperature responses to these changes.

Another recently reported vessel is that built by Schlemminger, Næss and Bünger [269, 270], who developed a pilot-study vessel for their studies on thermal effects within a bed of Fe-BTC MOF. They produced a 1.59 L stainless steel vessel with a helical aluminium tube around the outside of the sample holder, through which liquid nitrogen flows to cool not only the H_2-dosed solid within the inner enclosure, but hydrogen gas that is simultaneously dosed into an empty concentric space between the outside of the "storage enclosure" and the enclosure that held the adsorbent. Separate hydrogen inlets were provided for the inner and outer enclosures. The whole unit was then submersed in liquid nitrogen for the course of the experiments. 876 g of the tested Fe-BTC MOF was always included within the inner enclosure, occupying 1.35 L, which expanded to 1.45 L with the inclusion of an aluminium foam heat transfer agent. The vessel was rated up to 4 MPa.

This unit was used for two published studies. The first showed that the altering composition of ortho- and para-hydrogen during cryogenic adsorption changed the reported values of specific heat capacity and thermal conductivity within the bed by 3.6 % and 21 % respectively [270]. This confirms multiple studies which have concluded by cryogenic adsorption of hydrogen catalyses the conversion from ortho-H_2 to para-H_2. The model used for both studies used the Sips equation to estimate the adsorption thermodynamics; the parameters found for this study are shown to fit conventional adsorption isotherms well [270].

The second study [269] investigated the potential of inserting an aluminium foam into the Fe-BTC bed. The same amount of MOF was used for both the control (MOF alone) and Al foam cases, resulting in a bed volume 7.4 % larger in the enhanced case, but the model showed that the temperature distribution in this large bed was significantly more uniform than the control, that the foam vastly decreased the time in which the temperature stopped increasing post-hydrogen introduction (80 s vs. 260 s), and the enhanced cooling the foam provided allowed for the bed to be fully charged with H_2 within 400 s, compared to 80 % charged in the unmodified system.

The most advanced work of this nature was presented at the DOE's Hydrogen and Fuel Cells Annual Merit Review meeting in 2016 by Anton and Motyka of the Savannah River National Laboratory (SRNL), who presented a facility for testing a 2 L vessel filled with MOF-5 [271, 272]. This work, in collaboration with Oregon State University as part of the HSECOE, featured a flanged stainless steel vessel, complete with a heat exchanger in which metallic plates are sandwiched between densified 'pucks' of MOF-5 (0.4 g_{MOF} cm^{-3}). The presentation also featured a collaboration between SRNL and UQTR, which used another 2 L vessel, this time fitted with an aluminium 'Hex-cell' heat exchanger (a honeycomb structure into which the MOF powder is loaded at 0.19 g_{MOF} cm^{-3}). This design also featured a 'flow-through' cooling system.

The work performed with this unit included heat transfer analysis (coupled with 2D thermal modelling) for the HexCell design, and multiple charge-discharge cycle testing for both systems, primarily to investigate the storage capacity after multiple high pressure cycles (very little loss in either system over the test duration). Perhaps the most interesting finding from this study is the comparison of deliverable hydrogen from these systems compared to standard compression hydrogen storage, the details of which are in Table 2.4 below. Both systems, using the tank material and balance of plant equipment estimates that are well documented by the HSECOE, estimate that the system gravimetric and volumetric capacities compete with a standard compression tank, and in the case of the MOF-5 pucks, exceed it, albeit they do not meet up to the DOE 2020 targets.

Table 2.4 - Gravimetric and volumetric storage capacities of the experimental MOF-5 hydrogen storage systems developed by the HSECOE, and projections for larger scale uptakes on a tank internal volume and full system basis. The calculated values for a 70 MPa compression tank are provided for comparison [271, 272]

	MOF-5 Pucks	MOF-5 HexCell	Compressed Gas
Measured (2 L Prototype)			
Start conditions	84.5 K, 10 MPa	90 K, 8 MPa	-
End conditions	83.7 K, 0.11 MPa	85 K, 0.17 MPa	-
Gravimetric Capacity	9.2 wt%	11.2 wt%	-
Volumetric Capacity	37.2 g L^{-1}	23.6 g L^{-1}	-
Full scale system (material and heat exchanger)			
Start conditions	80 K, 10 MPa	80 K, 10 MPa	-
End conditions	160 K, 0.5 MPa	160 K, 0.5 MPa	-
Gravimetric Capacity	10.0 wt%	12.5 wt%	-
Volumetric Capacity	44.4 g L^{-1}	32.9 g L^{-1}	-
Full scale (full system with balance of plant)			
Start conditions	80 K, 10 MPa	80 K, 10 MPa	293 K, 70 MPa
End conditions	160 K, 0.5 MPa	160 K, 0.5 MPa	293 K, 0.5 MPa
Gravimetric Capacity	3.1 wt%	3.2 wt%	2.6 wt%
Volumetric Capacity	21.0 g L^{-1}	18.9 g L^{-1}	20.1 g L^{-1}

There is little evidence to suggest that industrial light duty vehicle OEMs are pursuing adsorbent-based systems currently. Howewer, a number of chemisorptive systems comprised the storage method for a number of vehicle prototypes in the early 1990s [273] (see SI-1 for more information). Although the details of many of these tanks remain guarded due to commercial confidentiality, in 2011 Mori and Hirose [36], of the Toyota Motor Company, reported filling a 180 L, type III tank (shown in Figure 2.17) with a $Ti_{1.1}CrMn$ hydride capable of 1.9wt% uptake. Although there was mention of a metal hydride tank by Hirose in 2012 [274], it is not known if this system was ever installed in a vehicle.

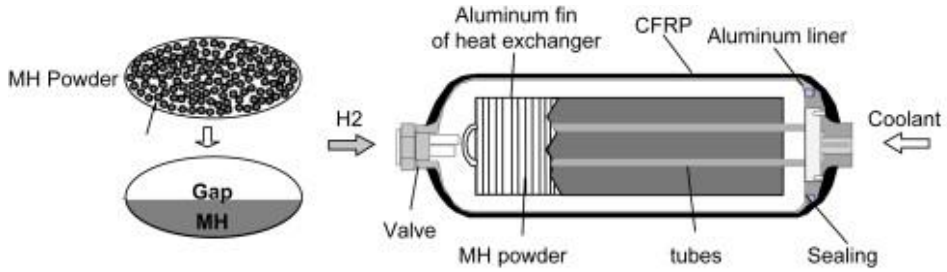

Figure 2.17 - Design of a 180 L, type III tank featuring a Ti1.1MnCr hydride as proposed by Mori and Hirose of Toyota. Reproduced from [36] **with kind permission from Elsevier.**

2.8. Aims and Objectives

The main aims of this PhD project are: (a) to determine whether a material based on the polymer of intrinsic porosity PIM-1 can be an effective hydrogen adsorbent; (b) to determine whether such a material retains the thermal and mechanical properties required to be effectively used in a large scale hydrogen tank; and (c) to design such a tank featuring this material.

The objectives to achieve these aims are:

1. Synthesise PIM-1 and any fillers separately.
2. Synthesise a series of composite films.
3. Carbonise and activate PIM-1 films.
4. Characterise the pure and modified materials for a number of properties, including:
    a. Adsorption properties (including BET surface area, pore volume, H_2 amount adsorbed).
    b. Mechanical properties (including tensile strength, Young's modulus).
    c. Thermal properties (including thermogravimetric analysis, thermal conductivity, enthalpy of adsorption).
5. Develop and use models of the hydrogen adsorption isotherms of these materials to determine parameters such as adsorbate density and pore volume.
6. Design and model a tank suitable for light duty vehicle applications featuring the materials in question.

3. Materials and Methods

3.1. Syntheses

The chemicals listed in Table 3.1 were used for the syntheses described. All commercial products were used as received.

Table 3.1 - Reagents used during the syntheses described in sections 4.1.2-4.1.4

Name	Grade	Supplier
5,5',6,6'-Tetrahydroxy-3,3,3',3'-tetramethyl-1,1'-spirobisindane	97%	Alfa Aesar
Chloroform	ReagentPlus, 99.8%, 0.5 - 1.0% ethanol as stabiliser	Sigma Aldrich
Methanol	CHROMASOLV® for HPLC, ≥ 99.9%	Sigma Aldrich
N,N-Dimethylformamide	Anhydrous, 99.8 %	Sigma Aldrich
Potassium carbonate	Anhydrous, Reagents ACS	Acros Organics
Potassium carbonate	Anhydrous, free-flowing, Redi-Dri™, ACS Reagent, 99%	Sigma Aldrich
Tetrafluoroterephthalonitrile	98%	Alfa Aesar
Chromium nitrate nonahydrate	99%	Sigma Aldrich
Terephthalic Acid	98%	Sigma Aldrich

3.1.1. Materials

3.1.2. PIM-1 Synthesis

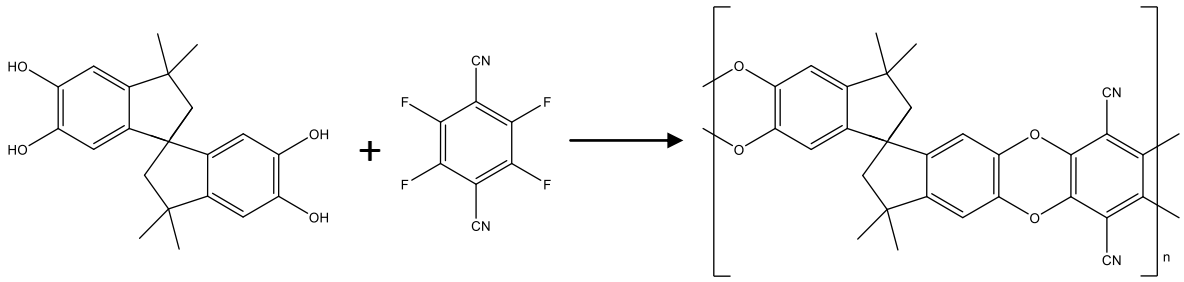

Figure 3.1 - Basic reaction scheme for the synthesis of PIM-1

Two separate methods were used to synthesise PIM-1. The first was based on the optimal reaction conditions determined by Song et al. [190]: 30 mmol (6.003 g) of 5,5',6,6'-tetrahydroxy-3,3,3',3'-tetramethyl-1,1'-spirobisindane, 30 mmol (10.213 g) of tetrafluoroterephthalonitrile and 60 mmol (8.292 g) of potassium carbonate were combined in a 500 mL dual necked round-bottomed flask (RBF). This flask was then clamped into place over a heating stirrer plate, and a water cooled condenser fixed into the vertical neck of the RBF. The other neck was plugged with a rubber subaseal. A gas feeder was fixed into the top of the condenser, which was connected to a Schlenk line. The RBF was then evacuated and backfilled with N_2 three times to ensure full removal of air. 200 mL of anhydrous dimethylformamide (DMF) was then added through the subaseal via a long double-ended needle, using a nitrogen flow into the bottle to ensure no water

absorption by the solvent. With the solvent in place, the reaction mixture was then left to stir for 20 minutes. Following this stirring, the RBF and condenser setup was lowered into an oil bath at 55 °C and the stirring rate set to 810 rpm. The reaction was left for 23 h to complete.

After allowing the reaction mixture to cool, it was poured into 300 mL distilled water. A bright yellow precipitate formed, which was then vacuum filtered off using Buchner apparatus. A Buchner flask collected the clear filtrate, containing the underreacted reagents and low molecular weight product. Following an extended filtration to dry off the polymer, the bright yellow cake was then redissolved in as little chloroform as possible (typically 100 – 150 mL), stirring overnight to ensure complete dissolution. The polymer solution was then filtered through filter paper and deposited into a 250 mL separating funnel, which was fixed over a 1 L conical flask containing 800 mL methanol which was stirred vigorously. The polymer solution was slowly dripped into the stirred methanol to reprecipitate the PIM-1. Once all the polymer solution had dripped into the 1 L flask, the yellow precipitate was again vacuum filtered until dry. This reprecipitation procedure was followed twice more to ensure complete removal of any low molecular weight product. Using this method, 5.4984 g of PIM-1 was collected at 39.7 % yield.

The second method was based on that of Budd et al [187]. The process was very similar to that described above, with the main differences being the temperature and length of reaction (65 °C, 72 h) respectively, and the use of a fresh batch of K_2CO_3 powder (from Sigma Aldrich) to help reduce water content. This reaction produced ~13 g of PIM-1. Three different batches of PIM-1 made by this method were used in this project; the first of these was labelled PIM-1 (2), which was synthesised by Dr. Rob Dawson, a postdoctoral researcher in the Department of Chemistry at the time. Approximately 2 g of PIM-1 (2) was kindly donated to this project. I synthesised the other batches, named PIM-1 (3), PIM-1 (4), and PIM-1 (5), although the production of PIM-1 (5) was aided by Dr. Sébastien Rochat, also in the Department of Chemistry. All of these batches used half the reagent (15 mmol) of the reaction described above.

PIM-1 films were manufactured through a solvent casting method first proposed by Budd et al. [187]. A 2 wt% solution of PIM-1 (0.1582 g) in chloroform (5 mL) was prepared, and cast in a 6 cm diameter glass petri dish. This was left with the dish lid on for 72 h whilst the chloroform slowly evaporated, leaving a smooth yellow film of PIM-1. Later attempts at film casting used an 8 cm deep evaporating dish topped with a 12 cm watch glass in order to further slow the evaporation rate. Following casting, the films were then cured at 70 °C for 48 h to enhance mechanical strength and to remove any excess solvent remaining.

3.1.3. MIL-101 Synthesis

The method for MIL-101 synthesis was that of Sharpe et al. [275], which in turn was adapted from Jiang et al. [138]. 0.8 g (2 mmol) of chromium nitrate nonahydrate, 0.33 g (2 mmol) of terephthalic acid and 10 ml of deionised water were combined in a 25 ml poly(tetrafluoroethylene) (PTFE) hydrothermal reactor liner, and allowed to stir for 1 hour. The stirrer bar was then removed, and the liner sealed into a hydrothermal reactor. This mixture was then heated in an oven at 180 °C for 8 h, and allowed to cool slowly in the oven. The mixture was vacuum filtered through grade 1 (11 μm pores) filter paper, allowing the removal of any recrystallized terephthalic acid. The filtrate was washed with more deionised water (approximately 10 - 20 ml). The blue-green permeate was then centrifuged at 8500 rpm for 10 minutes, in which a green solid settled, and a blue liquid was poured off. The centrifuge tube was then refilled with 30 ml of deionised water, and the centrifugation repeated. The solid was then

washed and centrifuged for a third and final time, before being dried under vacuum at 40 °C for 21 h. The MOF was then activated under vacuum at 180 °C for 24 h.

3.1.4. MOF-5 Synthesis

All MOF-5 used in this project was synthesised for the 2015 undergraduate MEng project of Jack Bennet, overseen by PhD student Antonio Noguera-Diaz. The synthesis was based on Method 3 in the IRMOF-1 Examples (paragraph 0134) in Yaghi et al [276]. 0.3570 g (1.20 mmol) of zinc nitrate hexahydrate and 0.066 g (0.20 mmol) terephthalic acid were placed into a 25 mL hydrothermal reactor liner and dissolved in 10 mL of diethylformamide (DEF) at a stirring rate of 200 rpm. The stirrer bar was removed from the liner, which was then sealed into a hydrothermal reactor, and heated in an oven at a fixed rate of 2 °C min^{-1} up to 105 °C, at which the temperature is held for 20 h. Following cooling to room temperature, the yellow crystals were gravity filtered and washed with three separate 5 mL doses of DEF. The material was then stored under DEF (in a desiccator) until required.

3.1.5. Composite Synthesis

The method used for creating PIM-MOF composites was based on that of Bushell et al. [247].

For the PIM-1/MOF-5 composites, one batch of MOF-5 crystals (0.0607 g) was used to minimise handling in air. The MOF-5 crystals were solvent exchanged from diethylformamide (DEF) to chloroform over 48 h, replacing the solvent every 24 h. A 5 wt% solution of PIM-1 (0.5463 g) in chloroform (7 mL) was prepared. Both the PIM and MOF mixtures were then sonicated separately for 15 mins, and then mixed. This mixture was left stirring overnight under an atmosphere of N_2. The mixture was then sonicated for a further 15 minutes. During this time, a small desiccator fitted with a gas feeder was evacuated and backfilled with N_2 three times. The solution was poured into a 6 cm diameter glass petri dish, the lid placed on top, and the dish lowered into the desiccator, which continued to receive a N_2 flow to ensure an anhydrous environment. This was left for 72 h to completely dry out, before being cured in an oven at 70 °C for 48 h.

For the PIM-1/MIL-101 composites, 0.2 g of PIM-1 was always used, and the amount of MIL-101 used was calculated to make up either 10 wt% (0.0222 g), 20 wt% (0.05 g) or 30 wt% (0.0857 g) of the entire film. The MIL-101 was then suspended in 3 mL of chloroform (regardless of amount of MOF used) in a small glass vial, and the PIM-1 dissolved into 5 mL of chloroform in a large glass vial. Both solutions were left to stir overnight, before being sonicated for 15 minutes. The MIL-101 suspension was then transferred to the large vial, using 1 mL of chloroform to ensure no solid matter was left in the smaller vial, and left to stir overnight once more. The combined solution was cast into a 6 cm diameter glass petri dish, and the lid placed on. The solution was then left to evaporate for 48 h. The composites were removed from the dishes using a small amount of water, replaced in the petri dishes and cured at 70 °C for 24 h.

A second attempt at manufacturing PIM-1/MIL-101 composites was made. The method for this was identical as that described in the previous paragraph, until after the overnight stirring of the combined solution. After this, the second attempt then involved sonicating the solution for a further 15 minutes, before being cast in a 6 cm diameter PTFE evaporating dish, left within an 8 cm diameter glass evaporating basin topped with a 12 cm diameter watch glass, in order to slow the evaporation. This was left for 48 h, before the composite films were removed from the evaporating dishes, placed on a 20 cm glass petri dish, and cured at 70 °C for 24 h.

3.2. Gel Permeation Chromatography (GPC)

For this project, determination of the molar mass of synthesised PIM-1 was performed by gel permeation chromatography. This was undertaken on a Polymer Laboratories PL-GPC 50 Integrated GPC, controlled by Cirris software. All the runs were completed at 35 °C using THF as the solvent. The system is calibrated to polystyrene standards. The runs themselves were performed either by Dr. Rob Dawson (PIM-1 (2)) or PhD students Paul McKeown and Helena Quilter (all other PIM-1 samples) on ~ 1 mg mL^{-1} solutions of PIM-1 in THF.

Gel permeation chromatography, a particular variation of liquid chromatography, is a technique that determines the molar mass of a polymer sample based on the hydrodynamic volume of the molecules present [277]. This is done through the use of a porous medium to provide sites in which small molecules will interact and therefore take longer to elute than larger ones. Typically, a column packed with silica has a solvent passed through it at a known flow rate, and the polymer sample, which has already been pre-dissolved in the same solvent, in then pulsed in at the bottom of the column. The sample molecules then transport through the free volume in the column, with larger molecules passing through without interacting with the solid medium (usually due to being too large to fit in the pores of the silica), meaning they pass out the other end of the column and are therefore detected first. Medium sized molecules that have parts that can fit within the pores of the material take slightly longer due to these interactions with the pores, and the smallest molecules, which can fit entirely into the pores of the silica gel, frequently interact with these pores and therefore take the longest time to emerge from the column. A detector, typically a refractive index (RI) or ultraviolet detector, senses the concentration of foreign material in the flow at the end of the column and logs how much of the sample is present at a given time.

The PL-GPC 50 is fitted with an RI detector, which uses changes in the refractive index of the flowing solvent to determine polymer concentration. This works as the greater the concentration of polymer in the solution passing the detector, the greater the change in the refraction constant of the fluid, and therefore the angle at which light will refract through the solution will change [278]. An RI detector uses a small glass case in which the sample-containing solution and the pure solvent are passed close to one another, and a light beam passed through. A light detector then tracks the beams and notes any changes in the angle of incidence into the detector, and therefore the change in refractive index in the sample. RI detectors are popular for measurement devices such as GPCs and high pressure liquid chromatographs due to their universality – they can measure a large number of different solutes in a wide array of different solvents. However, they do generally lack the precision of detectors such as infrared or ultraviolet detectors, and should be combined with other techniques to achieve a highly accurate measurement [278].

Comparing the volume of sample detected after a given time, for a given solvent flow rate, to the calibration curve (typically performed with polystyrene) allows for an estimate of the molecular weight of the polymer – doing this for every point the detector collects allows a distribution to be determined, and both the number averaged molecular mass (M_n) and the weight averaged molecular mass (M_w) to be determined. These are calculated using the following formulae [279]:

$$M_n = \frac{\sum_{i=1}^{\infty}(M_i N_i)}{\sum_{i=1}^{\infty} N_i} \qquad (\mathbf{3.1})$$

$$M_w = \frac{\sum_{i=1}^{\infty}\left(M_i{}^2 N_i\right)}{\sum_{i=1}^{\infty}(M_i N_i)} \qquad (\mathbf{3.2})$$

where i is the sample point, M_i is the molar mass recorded at point i, and N_i is the number of molecules (concentration) detected at point i [279]. As M_w is impacted far more by the presence of larger molecules, the two values are rarely the same. Taking a ratio of the two gives the polydispersity index (PDI), which provides a convenient measure of the breath of the distribution. A PDI of 1 indicates a perfectly uniform distribution, whilst increasingly larger PDI values indicate wider distributions of molecular masses.

Because the molecular weight distribution is relative to a standard polymer, and is not precisely determined for each separate polymer, there is an element of inaccuracy in the absolute value of molecular weight produced, and therefore the molar mass distribution generated. However, as long as the relative polymer is stated, M_n, M_w and PDI values determined by GPC have good value as a tool for the comparison of different polymer samples, particularly of the same chemical composition.

3.3. Powder X-Ray Diffraction (PXRD)

Powder X-ray diffraction (PXRD) is a useful technique for analysing the crystal structures of highly ordered materials. PXRD was used in this project to confirm the crystal structure of MIL-101 (and therefore confirm that the MOF had been successfully synthesised), and also to evaluate the crystallinity of the composite films. PXRD was performed on a Bruker D8 Advance machine fitted with a Cu Kα (wavelength λ = 0.154 nm) X-ray source. In the case of PXRD, a sample is defined as a 'powder' for the numerous regions of crystalline material within the sample, not necessarily for a finely divided solid material [280].

X ray diffraction works by firing a beam of X-rays at a target sample. X-rays have a wavelength in the range of 10 – 10^{-3} nm, which is very similar to the interatomic spacing in crystalline solids [281]. The X-rays interact with the atoms in the sample, striking the electrons in the shells and deflecting. The X-rays detected by the PXRD are near exclusively those that undergo elastic collisions (so called Thomson scattering), and thus maintain their energy and wavelength. Depending on the spacing of the atoms in the structure of the sample, X-rays deflected at the same angle and in phase will positively interfere with one another, and produce high intensity diffraction patterns that can be detected. The spacing between the atoms and the angles at which the characteristic XRD peaks are seen are related by Bragg's law [280]:

$$2d \sin\theta = n\lambda \qquad (\mathbf{3.3})$$

where d is the spacing between the atoms in the lattice, ϑ is the angle of incidence of the beam, n is any integer value and λ is the wavelength of the X-ray. All of these parameters are illustrated in Figure 3.2. The beam is slowly rotated around the sample in order to change the angle at which the X-rays interact with the sample, and so a distribution of diffraction angle against received signal intensity can be plotted. Highly crystalline samples will produce PXRD traces that contain a number of sharp, high intensity peaks due to the very clear and regular intermolecular spacing in these morphologies; amorphous materials will show very few if any clear signals in their PXRD traces. As the angles at which high intensity peaks can be clearly defined by PXRD experimentation, it is possible to calculate the lattice spacing within a material and therefore use the technique as a method for calculating the crystal structure of a material.

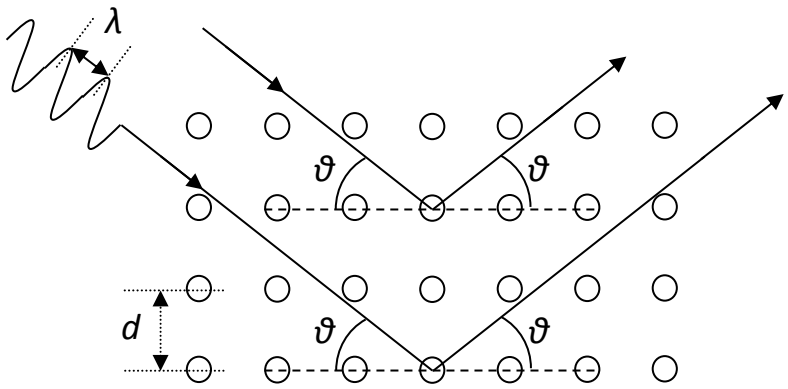

Figure 3.2 - Illustration of Bragg's law [280, 281]

The X-ray source in the D8 advance is a Cu Kα X-ray tube. When the source is switched on, electrons are fired from a cathodic source towards an anodic copper plate. The high energy electrons strike the copper atoms, ejecting an electron in one of the lower (K) electron shells. The hole is the lower shell is quickly filled by an electron from an outer shell; this process releases a photon of energy with a frequency in the X-ray range. In the case of the copper atoms in the anode, these photons are typically of a characteristic energy (Kα) which corresponds to a wavelength of 0.154 nm. Whilst other wavelengths of photons are produced by the electron beam hitting the anode, these are largely filtered out, leaving a monochromatic stream of X-rays that can be easily detected [281].

The Bruker D8 also uses a NaI scintillation counter as a detector [281]. Scintillation is the basic principle that molecules that interact with high energy photons generally undergo an excitement or ionisation process, which is then reversed through the release of another photon when the atom is reformed or the excited electron returns to a lower energy state. X-rays interact with the NaI crystals in the detector and excite the atoms, which then emit photons of light as a result. These photons strike a photocathodic material, which emits electrons as a result. As this emission of electrons is very small, they pass into a vacuum tube that contains a number of anodic metal or semiconductor plates, which attract the electrons. When an electron strikes the anode, a number of secondary electrons are released, which in turn are attracted to the next anodic plate in the tube. The flow of electrons that hit the final anode (with the highest potential difference from the photocathode) constitute an electric signal that can then be processed by software into a signal intensity [282].

3.4. Fourier Transform Infrared Spectroscopy (FTIR)

Fourier Transform Infrared Spectroscopy (FTIR) is a chemical analysis technique that identifies particular types of chemical bonding within a sample. The basic principle of infrared spectroscopy is that the bonds between atoms will adsorb the energy from particular wavelengths of infrared radiation, normally transferring this into increased vibration within the bond. As a result, a spectrum of infrared radiation that is passed through a sample has a set of frequencies removed from the spectrum that provide a characteristic chemical fingerprint for the sample being tested. FTIR is the most popular of these spectrometers, providing fast and easy-to-operate results.

Every FTIR at its heart is based on a Michelson interferometer, which is made up of a beam source, a fixed mirror, a moveable mirror, and a beam splitter. As the beam from the source passes through the beam splitter, it is separated into two separate beams, which reflect off the mirrors, recombine at the beam splitter and then pass out of the interferometer and towards the

sample. The power of this approach comes from the moveable mirror, as the changing path length of the beam that hits the moving mirror causes a variable interference pattern in the recombined beam, creating a interferogram [283, 284]. These functions of interferometer output with time can be quite complicated for spectra of radiation rather than a single frequency [283]. This output beam is then passed through the sample, where the wavelengths of infrared of corresponding energy to the amount required to excite the bonds within the material are absorbed, and finally the signal reaches an infrared detector [284]. The interferogram produced after passing through the sample is compared to a blank interferogram and the background removed, and the electrical signal is then acted upon by the controlling software, which using a Fourier Transform-based algorithm to convert the time-based corrected interferogram into a function of wavenumber (a unit of frequency), which is far more recognisable [283, 284].

Using a Michelson interferometer allows for direct measurement of multiple frequencies instantaneously, and does not require the use of finely tuned prisms or gratings, which cause severe issues when using multiple frequencies of radiation. This allows for much faster and more sensitive measurement, despite the need for coding and uncoding of the frequency information by the interferometer and the computer [285].

All FTIR experiments performed for this study were done on a Perkin-Elmer Spectrum 100 unit. Each run consisted of 4 scans at a resolution of 2 cm^{-1}.

3.5. Scanning Electron Microscopy (SEM)

Scanning Electron Microscopy (SEM) is an imaging technique used for creating highly magnified images of the surface of materials down to the micrometre scale. For the interests of this study, SEM was used for visual inspection of the materials in the expectation that some information may be gained from a magnified view, mainly to determine the particle size of the MIL-101 powder, and to inspect the interaction between the PIM matrix and MOF particles within the composites. All SEM studies were performed on a JEOL JSM-6480LV scanning electron microscope.

A scanning electron microscope works by isolating a sample in a vacuum, and then generating an electron beam that is fired at the sample. The electron source is a tungsten filament that has sufficient current passed through to thermoionise the material and release a stream of electrons. The vacuum, which is required to be 2 x 10^{-4} mbar before the electron beam is switched on for the JSM-6480LV, is required to both protect the filament from oxidation and to eliminate the possibility of foreign molecules in the column interacting with the electron beam. The generated electrons are attracted down the SEM column by an anode plate, accelerating the electrons and allowing some to miss the plate completely and travel down the column as an electron beam [286]. These highly accelerated electrons are then focussed into a beam by either two or three electromagnetic focussing lenses, and finally directed onto the sample surface by a scanning coil. The beam itself can be varied by voltage (typically somewhere between 5 and 30 kV) and beam diameter (20 μm – 2.5 nm, depending on the microscope used) [287]. The electron beam then hits the sample surface, either reflecting off the surface of the sample (backscattering), or burying into the surface of the sample, and displacing another (secondary) electron, which is then emitted. The emitted electrons are then detected, converted to an electronic signal, amplified, and then fed into a computer display, which shows the image. The beam is moved across the sample at high speed in order to generate a full 2D image of the sample surface at a given frame rate, meaning any movement of the beam across the sample surface can be ‘watched’ via the display [288]. The magnification the SEM generates is determined by the size of the area that the

beam scans at any given time. Any image displayed on the monitor can be captured by the computer software for later analysis.

The primary electron signal used for SEM imaging is secondary electrons. When the electron beam hits the sample, many electrons will collide inelastically with the sample atoms, displacing one of the electrons in an atom in the surface. This displaced electron is then ejected (typically at a wide angle) at an energy less than 50 eV. They are attracted to a positively charged detector, which gathers the electrons and relays this information as an image. As the number of electrons emitted this way is proportional to the brightness of the image, secondary electron SEM images are useful for studying surface topography, and produce clear images [286, 287]. Secondary electrons also emit photons that contain inherent information about the atom from which they came (typically due to the energy of the photon being characteristic of the shift of an electron between energy levels, and therefore carrying a particular wavelength), and therefore they can be used to study surface chemistry, with techniques such as energy dispersive x-ray spectroscopy [289].

The other main electron signal in the SEM is that from backscattered electrons, which are electrons that have undergone elastic collisions with the atoms on, or close to, the surface on the sample and as a result retain most of the energy gained from its journey down the column. Backscattered electrons typically have energies greater than 50 eV, and have small angle deflections from the sample, meaning they are detected by a toroidal detector fitted just beneath the objective lens [288]. Backscattered electrons reflect in a straight line from the surface they interacted with, and therefore require a wide area of detection. As a result, images generated with backscattered electrons typically show greater topological detail and contrast, although the signal is noisy due to the presence of secondary electrons that are not attracted away as the positive bias is switched off for backscatter detection [286, 287].

One effect of the electron beam interacting with the sample surface is that of charge build up. A sample must be electrically conducting in order to transfer charge gained through the interaction of the beam electrons with the sample, or else the images produced in the SEM become overly bright [288]. All samples in the SEM are loaded onto a metallic stub, and attached with graphitic tape, both of which are electrically conducting. However, as all of the samples tested in this project are electrically non-conducting, they must first be coated with a fine film (typically a few nanometres thick) of electrically conductive material in order to avoid this electron build up on the sample. For this project, this was achieved by coating all samples with gold in an Edwards Sputter Coater S150B, in which the sample was exposed to low vacuum and flushed with argon 3 times before sputtering with Au for 3 minutes. No charging issues were reported.

3.6. CHN Elemental Analysis

CHN elemental analysis is a technique that, as the name implies, allows for the quantitative determination of the quantities of carbon, hydrogen and nitrogen in a sample. This technique works by combusting a small amount of the sample material in a high temperature, oxygen-rich environment in order to fully combust the sample into carbon dioxide, water, and nitrogenous oxides. These gases then pass through a column of adsorptive, which adsorbs any impurities that may be present in the effluent, and then into a column of copper, which reduces the nitrogen oxides into diatomic nitrogen (N_2). Finally, the gases are passed into the detector, which is typically a gas chromatography column (to separate the gases) and then a thermal conductivity detector, which quantifies the amount of each gas present [290].

Elemental analyses for PIM-1 (5) and its carbonised products were performed by Stephen Boyer in the Science Centre, London Metropolitan University on a ThermoScientific (Carlo Erba) Flash 2000 Elemental Analyser, configured for %CHN. Two runs were performed on each sample.

3.7. Raman Spectroscopy

Raman Spectroscopy is another chemical characterisation technique that has gained much popularity in recent years. Raman spectroscopy is based on the idea that a monochromatic beam of photons that is fired at a material will exert a spectrum, based on the fact that some the photons will lose energy equivalent to that needed to raise the vibrational energy level of a molecular bond. The emission of these lower energy photons is known as Raman scattering. Although the number of Raman scattered electrons from the sample is far less than those that are Rayleigh scattered (emitted with exactly the same energy as the incident beam), the frequency difference between the Rayleigh and Raman scattered electrons can be detected, and the spectrum plotted as a function of wavenumber, from which characteristic information about the chemical nature of the sample can be determined [291].

A Raman spectrometer is primarily made up of four parts: the radiation source (laser); the sample excitation and emissions collections system; the wavelength selector; and the detector [292]. The choice of laser wavelength can be reasonably important, as shorter wavelengths lasers will produce more sensitive and better spatially resolve signals, but are more prone to photoluminescence; longer wavelength near infrared lasers are less prone to this phenomenon [293]. The beam then requires optical focus before hitting the sample, and the scattered signal that emerges must be passed through collecting and focussing lenses in order to concentrate the beam once more. The Rayleigh scattered electrons are then filtered out of the beam using a holographic notch filter, which is manufactured to have a very strong, sharp absorption band at the wavelength of the laser, but transmits all other frequencies [294].

The detector is a charge-coupled device (CCD), which is a 1- or 2-D array of silicon-based semiconductor pixels that generate electrical charge when stimulated by the presence of photons. The charge on each pixel is stored and built up until the charge is measured and documented by an analogue-to digital converter, which then send the signal to the controlling computer to store. Reading the pixels in order, given that the Raman signal is scattered such that the low wavenumber photons hit one end of the CCD and high wavenumber photons are directed towards the other end, gives the spectrum [292].

Raman Spectroscopy was performed on PIM-1 (5) samples, in both powder and film morphologies, and all of the carbonised and activated samples manufactured therefrom. The spectra were performed by Dr. Mi Tian on a Renishaw InVia Raman Microscope. The PIM-1 powder and film were measured with a 785 nm (near infrared) laser. The carbonaceous samples were measured with a 532 nm (green) laser. The laser power was set to 10% of maximum (~ 1.0 mW).

3.8. Thermogravimetric Analysis (TGA)

Thermogravimetric analysis (TGA) is a technique used to determine the thermal stability of materials under varying temperature and atmospheric conditions. Ultimately, the technique involves heating a material in a specific chemical environment at a particular heating rate, and using a fine microbalance to measure the mass of the sample in real time – as the sample heats up, it will eventually undergo a reaction, either combusting with oxygen in the atmosphere, or thermally degrading if the environment is anoxic. In both occurrences, this is usually seen by the TGA as a mass loss. Following the experiment, the system produces data for the mass and the temperature over time, which can then be processed (if the heating rate is a continuous function) into a mass against temperature graph. This graph then demonstrates how much mass the sample lost, and the temperatures at which these mass losses occur. This allows for determination of safe operating temperatures for samples (particularly in preparation for the degassing step of adsorption experiments, as detailed below).

An additional analysis that may be performed based on this technique is differential thermal gravimetry (DTG). This analysis is performed by differentiating the mass loss curve with respect to time. With correct mathematical transformation, this differential curve can then be plotted against temperature to reveal the same information as seen in the TGA curve, but with new, more visible cues.

It should be noted that toxic cyanate ions are present when PIM-1 is thermally decomposed, as demonstrated in section 5.1.2 below. This health and safety risk is mitigated in this study by channelling the outlet gases from the TGA into a well ventilated, inaccessible area.

3.8.1. Standard TGA

The TGA used for the experiments in this report was the Setaram TG-92 (Caluire-et-Cuire, France), connected to a computer installed with SetSoft 2000 software. It is a gravimetric device, using a 100 µL alumina crucible to hold the sample, which is held in a metallic bracket at the end of a long wire. This wire is connected to an electronically operated null balance system, in which two photodiodes operate as detectors. In a fully equilibrated system, these photodiodes receive an equal amount of light. As the sample loses mass as the experiment goes on, the central beam begins to pivot and cuts the beam of light entering one of the photodiodes, so indicating an imbalance. Upon detecting this imbalance, the system activates a motor, which acts to apply force on the beam and rebalance it. The current that is sent to the motor in order to perform this rebalance is recorded, and is transformed into a mass change value by the software.

The bracket also contains an identical, clean alumina crucible that is used as a reference for heat flow measurements. The system is heated by two graphitic plates (capable of heating to 1750 °C), which are protected from combustion by flowing argon (1.8 L h^{-1}) as a protector gas. The system is cooled by flowing water (1.4 L min^{-1}) around the outside of the plates, with graphitic felt used as an insulator between them. The sample atmosphere gas, typically either N_2 or air, is flowed through the sample chamber at 1.8 L h^{-1}, and the sample and reference temperatures in the chamber are measured by a Pt/Pt-Rh thermocouple pair protruding from the bottom of the chamber. The system is fitted with 20 MPa cylinders of argon (BOC UN 1006, 99.998%), nitrogen (BOC UN 1066, oxygen-free) and air (BOC compressed air).

The experiments performed for this project have focussed on the thermal stability of PIM-1, MIL-101 and composites thereof. In particular, PIM-1 was carefully studied using TGA in order to

provide information on how the material might behave during carbonisation. The samples used between 10 - 20 mg for each run. N_2 was first used as the carrier gas, to simulate the anoxic conditions present in a degassing process; this was set at a flow rate of 1.5 L min^{-1}. Firstly, a clean, blank crucible was tested to correct for buoyancy effects. This was then followed by at least three runs of the sample under the same conditions, cleaning the crucible out after each process. This procedure was also performed under air, which determines the combustion point of the tested materials. All experiments were performed using a temperature ramp of 10 °C min^{-1} from 20 – 1000 °C. Differentiation of the TG curves (DTG analysis) was performed in the SetSoft software.

3.8.2. TGA with Mass Spectroscopy (TG-MS)

TGA coupled to mass spectroscopy was run on a Setaram SetSys Evolution TGA 16/18 machine, the gas outlet of which was fed into a Pfeiffer Vacuum Omnistar GSM 320 mass spectrometer. Both of these machines are connected to a computer loaded with Setaram Calisto (TGA) and Quadera (SEM) software. The use of the mass spectrometer allows for chemical analysis of the gases that are exhausted from the TGA experiment. By capturing these gases, it is possible to chemically analyse them and therefore begin to determine what chemical changes might be occurring during the heating process.

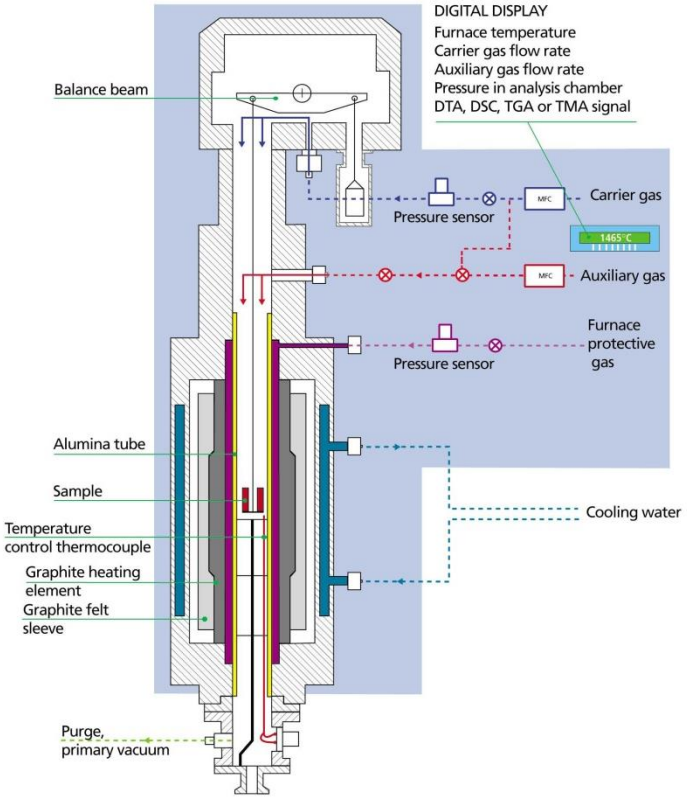

Figure 3.3 - Cut-through schematic of the Setaram SetSys TGA used for TG-MS experiments. The TG-92 looks very similar to this. Reproduced from [295] **with kind permission from Setaram.**

The TGA works on the same principle as described above, although the SetSys is a newer model than the TG-92; the layout of this is shown in Figure 3.3. It only features a hanging sample container however; this is a 170 µL alumina crucible with a platinum wire, which is hung directly onto the platinum wire attached the balance. Unlike the TG-92, there is no bracket nor a reference crucible, so heat flow data are not available from this machine. The mass is measured to ± 0.0001 mg, compared to the ± 0.01 mg the TG-92 is capable of. As the successor to the TG-92,

the SetSys still features graphite heating plates and a Pt-Pt/Rh thermocouple for sample measurement.

The outgas line from this TGA is attached to a mass spectrometer. Mass spectrometry (or mass spectrometer, MS) is a chemical analysis technique that uses the relative mass to charge ratio (m/z) of species that have undergone ionisation within the MS to identify chemical species present within a sample. In practice, it is a method of identifying chemical species within a sample by its molecular mass, as the charge is usually created within the MS. An MS system is primarily made up of three stages: ionisation; the mass analyser and the detector.

When a sample is introduced into the MS, the molecules are vaporised (if not already in a gaseous state), and then passed into the ionisation chamber, which uses the principle of electron ionisation. Electron ionisation uses a stream of electrons that pass through the chamber and collide with the travelling sample molecules. In the Omnistar GSM 320, the electron stream is produced by heating a tungsten filament. If a sample molecule is hit by an electron with energy greater than the molecule's ionisation energy, then the collision will emit an electron from the molecule and create a cation. Most molecules will undergo this process only once, although it is possible for a single molecule to be double- or triple-charged on its path through the ionisation chamber [296]. Electron ionisation is a hard method of ionisation, meaning it has a high success rate of creating ions from molecules, but excess energy from the impact can result in the molecule fracturing; this can leave either free radical ions or carbocations, depending on the nature of the molecule and the fragment. These fragments, if charged, can successfully be detected and can aid in the determination of the species entered into the MS [297].

The ions produced are then accelerated and focussed into a beam by anodic plates at the end of the ionisation chamber. From here they pass into the mass analysis chamber, which may utilise a number of different technologies to separate the ions by their m/z, such as time of flight (in which lighter or more heavily charged ions pass through a straight column to the detector faster) [296], and magnetic deflection (in which lighter and more charged ions are deflected more by a magnetic field in a curved chamber) [297]. The Omnistar GSM 320 uses a linear quadrapole analyser, which uses a sinusoidal electric field to separate ions by their m/z.

A quadrapole analyser is made up of four long cylindrical or hyperbolic tubes arranged in a quadrilateral formation, with opposite poles having the same part AC (sinusoidal), part DC (static) electric potential applied. These tubes either attract or repel the incoming ions for a short time, before applying the opposite force, due to the application of the sinusoidal AC potential. This results in a path for the ion that wanders in 3D space, although the inhomogeneous periodic electric field applies a net force on the ions in the direction parallel to the tubes. If an ion locates the correct position within the analyser (namely, a location equidistant between opposing polarity tubes), the ion will safely travel through the analyser without hitting the tubes. The ions that can successfully do this can be tuned for by altering the strength of the static and periodic potentials applied to the tubes in the analyser, as well as the period of the sinusoid [296].

At the end of the chamber is an electronic detector that identifies the rate at which ions successfully reach the end of the chamber, and these data are electronically logged. In the Omnistar, there is a choice between using a Faraday cup, or a channel secondary electron multiplier (C-SEM), detector. A Faraday cup is a relatively simple detector in which the ions hit an electrode and transfer their charge, which results in a measurable voltage passing over a connected resistor of high impedance. However, secondary electron multipliers are far more common in modern MS systems due to the much higher gain that these sensors produce. A C-

SEM detector works by directing the ions into a continuous tube made of either a metal to a semiconductor, both of which emit secondary electrons when struck by a charged particle. A positive voltage applied to one size of the tube then accelerates these electrons, which strike the other side of the tube and further release more secondary electrons. This cascade of secondary electrons causes a current large enough to be detected by a pre-amplifier after 12-18 cycles, which is then relayed as the signal. Continuous detectors vary from standard secondary electron multipliers by using a continuous material rather than separate plates, often curved to increase signal stability at high gains [296].

Traditionally, mass spectrometers are used to identify a single sample loaded into it, resulting in a two dimensional output of the intensity of a signal against the m/z for which that signal was received, typically plotted as a bar chart. However, as the composition of the gas from the TGMS changes with time, a third variable is introduced. Therefore, the intensity of signal for a given m/z is tracked over time by scanning MS; this cycles the m/z value that the system detects after a given time period over the time of the experiment. This then allows the intensity vs. time graph to be plotted for each individual m/z, either as a series of two dimensional line graphs, or as a three dimensional plot.

For the experiments performed in this project, TGMS runs were performed on both PIM-1 (powder) and MIL-101 separately. The runs performed were simple heat ramps from 30 – 1000 °C at 3 °C min^{-1} under an argon flow of 20 mL min^{-1}. These runs were preceded by a 30 minute period in which the protective gas was allowed to flow over the sample in order to remove air, in order to avoid contamination of the outgas. The slow ramp rate provided confirmation that the thermal effects seen for the standard TGA runs were a function of temperature and not time, and also to allow the scanning SEM to capture the emitted gases in high resolution. All TG runs were corrected by subtracting the values for a blank run, so correcting for buoyancy. All DTG curves were calculated by the Calisto software following buoyancy correction. Scanning mass spectrometry was performed with a time period for each m/z scan of 50 ms over the range m/z = 1 - 200, so each cycle lasted 40 s (unless otherwise stated). This cycling time is sufficient for adequate sampling of the gas, but also results in an intensity vs. time graph of excellent resolution over the course of the 6.5 hour experiment.

3.9. Differential Scanning Calorimetry (DSC)

Differential scanning calorimetry (DSC) is a thermal technique that measures the heat flow into or out of a material that is undergoing a constant temperature change. This information can reveal much information about a material, from melting and glass transitions temperatures of polymeric materials, which are seen in a DSC trace as peaks and shoulders, to the specific heat capacity of the material when carefully compared to a well-defined standard.

DSC works by heating up two aluminium pans, one containing the sample and an empty reference pan, at a specific rate of temperature change. The furnace in which the pans are contained heats up at the predetermined rate, and the temperature of each pan is measured by small thermocouples contained within the platforms on which they sit. As a result of the greater thermal inertia of the sample-containing pan, a temperature difference begins to emerge, with samples of greater specific heat capacities or undergoing endothermic phase changes heating up less quickly than the reference. This type of DSC is known as a heat-flux DSC [298]. The heat flow into the sample reference is then calculated by the controlling software by taking into account the temperatures of the furnace and the sample pans, as well as the thermal resistances and heat

capacities of the sensors [299]. If the sample is undergoing a change in physical state, such as melting, a peak will be seen in the heat flow with respect to time as the energy change associated with the phase change (i.e. the absorption of extra heat to satisfy the latent heat of fusion for melting) must take effect before the temperature of the sample is changed further. These peaks are characteristic of the material being tested.

DSC is also a quick and easy method for determining the specific heat capacity of materials, as the system fundamentally measures heat flow into a material as it increases in temperature. By comparing the heat flow vs. temperature curve to that of a well-known reference material, typically sapphire, the specific heat capacity can be calculated. This procedure normally requires 3 separate runs: a blank sample pan; the sapphire standard; and the sample [300]. Once the heat flow attributable to the sample is known, the heat flow to the sample can be calculated using equation 3.4 below, where Q is the heat flow (J g^{-1} s^{-1}), t is time (s), C_p is the isobaric specific heat capacity (J g^{-1} °C^{-1}), and T is temperature (°C):

$$\frac{dQ}{dt} = C_p \frac{dT}{dt} \tag{3.4}$$

However, this simple method for specific heat capacity determination does not take into account that the total heat flow into the material can be explained both by reversible heat flow (i.e. the heat required simply to warm up the sample, which is fully recovered when the sample is cooled) and non-reversible heat flow, which is based on kinetics (which are heavily affected by changes in crystallinity of the polymer) and is a function of absolute temperature and time, and not on the heat capacity of the material [301]. To overcome this issue and produce a more accurate value for the specific heat capacity of the material, a more advanced form of DSC, known as modulated DSC (MDSC), can be used.

MDSC works by applying a compound heating rate to the sample, typically a combination of a linear ramp (as used in standard DSC) and an oscillating modulation. The heat flow response to such a heating rate is an oscillating increase in heat flow with respect to time; this response is mathematically identical to superimposing the heat flow responses from both the linear and modulating heating rates. As the compound response can be time averaged over periods equivalent to the period of the sinusoidal heating rate to produce a curve that is nearly identical to that produced purely by the linear rate, the time-averaged curve can be subtracted from the total linear response in order to give the heat flow response to just a sinusoidal change in heating rate that shows no increase in temperature over time. Using Fourier transform analysis, the amplitude and period of the heat flow response (which will be sinusoidal) can be determined. The reversible heat capacity $C_{p,r}$ (J g^{-1} °C^{-1}) (i.e. the specific heat capacity of the material) can then be determined using equation 3.5, where A_{HF} is the calculated amplitude of the sinusoidal heat flow (J s^{-1}), and A_{HR} is the amplitude of the oscillating heating rate (°C s^{-1}) [302]:

$$C_{p,r} = \frac{A_{HF}}{A_{HR}} \tag{3.5}$$

The non-reversible part of the heat capacity can be calculated by subtracting the reversible heat capacity from the time averaged total heat flow divided by the linear heating rate.

DSC/MDSC runs for this study were performed on a TA Instruments Q200 Calorimeter fitted with an RSC 90 cooler in the engineering laboratories at the University of Bristol. MSDC was performed to accurately determine the specific heat capacity of PIM-1, MIL-101 and their composites. Runs were performed between – 50 and 200 °C, allowing the sample to first equilibrate at -50 and then linearly ramping at 3 °C min^{-1}. The modulation was performed with a period of 100 s and an

amplitude of ± 0.8 °C. Calibration was performed with a 25.4 mg sapphire standard under the same conditions.

3.10. Helium Pycnometry

Helium pycnometry is a technique for determining the skeletal density of a porous material. The skeletal density is defined as the mass of the sample divided by the skeletal volume of the sample, which is the total inaccessible volume to external molecules (meaning the solid material and any closed pores contained within it). This is an important property to know for volumetric measurements as any volumetric displacement by the material during these experiments can be accounted for accurately. Helium is used for this technique as it is a very small molecule, and can therefore penetrate even the smallest pores in the sample, and is assumed not to adsorb to the material, meaning that changes in the pressure recorded can accurately be translated to volume measurements. However, this assumption is questionable, given the available evidence suggesting helium does adsorb to porous materials of varying pore size and chemical composition [303]. However, under conditions close to atmospheric pressure, this adsorption is typically of the order of 10^{-2} - 10^{-3} mmol g^{-1}, making it a relatively minor issue for the pycnometry performed in this study. The helium pycnometer used for this project was a Micromeritics AccuPyc 1330 (Norcross, GA, USA) equipped with a BOC UN1046 20 MPa helium cylinder.

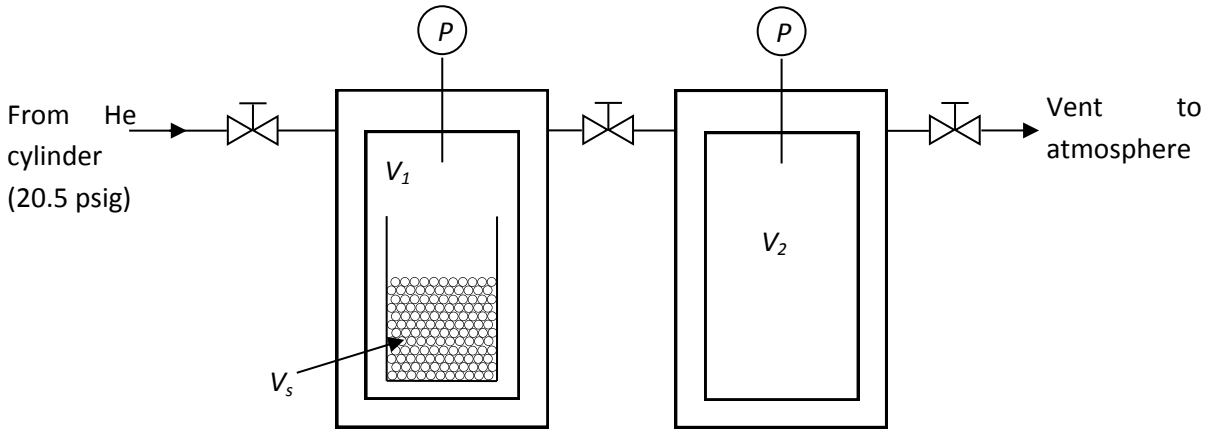

Figure 3.4 – Basic schematic of a helium pycnometer, illustrating the main volumes considered

The technique works on the basic principle of a gas expanding proportionally to the volume made available to it. As illustrated in Figure 3.4, a pycnometer is made up of two chambers, each of a fixed and known volume: the sample chamber, and the expansion chamber. When a pycnometry run is started, helium is dosed into the sample chamber until a target pressure (in this case a target pressure of 19.5 psig) is reached. The He supply line is then closed, and the pressure allowed to equilibrate to an initial pressure P_1:

$$P_1(V_1 - V_s) = n_1 RT \tag{3.6}$$

where V_1 is the sample chamber volume, V_s is the absolute skeletal volume of the sample, n is the amount of gas in the chamber, R is the molar gas constant and T is the temperature of operation. This assumes ideal gas behaviour. The reference volume starts with an equilibrated pressure of helium, typically atmospheric, which can be represented by P_2:

$$P_2 V_2 = n_2 RT \tag{3.7}$$

Following the equilibration of the starting pressures, the valve connecting the sample and expansion chambers is opened, and the pressure is again allowed to equilibrate. Assuming the

volume of the pipes connecting the two chambers is negligible, the pressure equilibrates to a medium pressure P_3, and the total gas in the system determined by:

$$P_3(V_1 - V_s + V_2) = (n_1 + n_2)RT \quad (3.8)$$

Summing equations 3.4 and 3.5 and equilibrating them to equation 3.6 results in

$$P_1(V_1 - V_s) + P_2V_2 = P_3(V_1 - V_s + V_2) \quad (3.9)$$

which cancels to:

$$V_s = V_1 + \frac{(P_2 - P_3)}{(P_1 - P_3)}V_2 \quad (3.10)$$

Whilst this equation sums the volumes of the sample chamber and a factored reference chamber volume, it is worth noting that $P_1>P_3>P_2$, resulting in the factored reference volume always being subtracted from the sample chamber volume to give the skeletal volume of the sample. The skeletal density is then calculated from the sample mass (which is measured separately beforehand) divided by the skeletal volume.

The skeletal densities of the bulk PIM-1 powder and MIL-101 were evaluated using the helium pycnometer. PIM-1 films were also attempted, albeit unsuccessfully, as discussed in section 4.7 below. The pycnometer was prepared for measurements by calibration using a 6.3222 cm^3 reference material (steel balls). The sample holder (a large steel cup with a plastic lid that fits into the sample chamber) is weighed and then filled as much as possible with sample, and is then degassed in a vacuum oven at 180 °C for 4 hours in order to remove any adsorbed material. Following the degas, the holder is immediately weighed again in order to get a dry weight of sample, and left in a desiccator for one hour to cool to room temperature. Once cool, the sample is loaded in air into the pycnometer, which is then sealed. The pycnometer is then programmed to perform 10 purges (a sequence of dosing helium to 19.500 psig (0.134 MPag), and then reducing the pressure back to atmospheric by venting), which further cleans the sample. The pycnometer then performs 20 recorded runs as discussed above. All pressure equilibrations were ensured to be within a tolerance of ± 0.005 psig (34.4 Pag) min^{-1}. This sequence of calibration, degas, weight, purge and run was repeated at least twice more to ensure accuracy of the data.

3.11. Adsorption

Adsorption studies are naturally critical to the science of hydrogen storage, and to the wider field of porous materials. The amount of gas that can be stored under various pressure conditions within an isotherm can unveil a large amount of information about the surface area and pore size distribution of a material, and ultimately hydrogen storage isotherms inform of exactly what a hydrogen storage system featuring these materials can do.

3.11.1. Low Pressure (≤ 0.1 MPa)

Two separate machines were used for low pressure isotherm analyses: the Accelerated Surface Area and Porosimetry Analyser (ASAP) 2020; and the 3-Flex; both are manufactured by Micromeritics (Norcross, GA, USA). Both machines were equipped with 20 MPa cylinders of helium (BOC UN 1046), nitrogen (UN 1066, oxygen-free), carbon dioxide (BOC UN 1013), and hydrogen (Air Products Ultra Pure Plus X47S), and a computer each with the respective operating software (Microactive for the ASAP, 3-flex software for the 3-flex) installed. Both sets of software are capable of calculating many important parameters related to porous materials, such as

surface area, pore size distributions and pore volumes, the methods for which are discussed in sections 3.11.3 - 3.11.5 below.

Both the ASAP and the 3-flex are high precision Sieverts' type apparatuses (described in further detail below) capable of performing adsorption isotherms between 0 – 0.1 MPa. The 3-flex, the newer model, is capable of performing up to three samples at once. Two of the ports are equipped with pressure transducers capable of measurement down to 10 mmHg (1.33 kPa), and the third equipped with a 0.1 mmHg (13 Pa) transducer, so making capable adsorption isotherms with great detail in the pressure region in which micropore interactions dominate the isotherm. All three samples are connected to a high vacuum line capable of pressures as low as 10^{-9} mmHg, as well as the aforementioned gases. The ASAP only features one sample port, although this transducer is rated down to 0.1 mmHg (13 Pa).

A Sieverts' type apparatus is a manometric technique for measuring gas adsorption. The technique works on a similar premise to that of the helium pycnometer, namely that it uses a change in pressure following the expansion of a known amount of gas to measure how much of the gas is adsorbed and therefore removed from the gaseous phase. The manometric approach first works by dosing the adsorptive gas into a known reference volume, which easily allows the total amount of gas to be calculated using the ideal gas law. A valve separating this reference manifold from the volume containing the sample is then opened, and the gas expands to fill the entire volume. As the porous material within the sample chamber begins to adsorb the gas, the pressure drops further than it would if the gas simply expanded into the available volume, and the difference between this expected pressure and the actual equilibrated pressure is the amount of gas in the adsorbed phase at that equilibrated pressure. Adsorption isotherms are built up stepwise, meaning that when one equilibrated point is taken, the manifold volume than then be dosed with the next set pressure of the adsorptive gas, and by mass balancing the amounts of gas in the manifold and sample volumes before and after equilibration, the amount of gas adsorbed at the next pressure up is calculated. This is also true for desorption isotherms, but the set amount of gas in the manifold is lower than the previous step.

It is important to note that both the volume in the sample holder (which will be slightly variable between flasks) and the skeletal volume of the sample must be known in order to correctly calculate the uptake. This is done by performing a 'free space' analysis with helium, which is essentially a helium pycnometry measurement. Doing this *in-situ* also allows for determination of the 'cold' freespace, which is the volume within the sample flask that is always submerged in cold Dewar fluid (either submerged fully or wicked up by the isothermal jacket on the tube), and the warm freespace, which is the volume above the isothermal jacket but below the equilibration valve. Having accurate values for both these parameters is very important for an accurate determination of gas adsorption. Both machines will perform this calculation, although a separate freespace analysis must be performed on the ASAP; it is performed *in-situ* by the 3-flex.

Samples for the ASAP are prepared by fitting a sample holder (a long glass tube) with a seal frit and weighed. The sample (typically ~100 mg) is then placed in the bottom of the tube (of known volume), and weighed again to determine the wet weight of the sample in the tube. The sample vessel is fit into one of the two available degassing ports, which are supported by a vacuum line independent of the analysis vacuum, meaning sample preparation can be performed simultaneously with an analysis. The corresponding heater is then fit onto the bulb of the sample tube and held in place with a metal clip. The experiment file is prepared, although only the degassing instructions are required at this point. The degas is then run automatically using the

sample file. Once the tube has cooled following the degas, it is removed from the port and reweighed in order to get the dry mass of sample in the tube. The sample vessel is then fitted with an isothermal jacket and fitted to the analysis port on the ASAP. The sample is manually evacuated, as per machine protocol. The experiment file is finalised, and once the correct level of vacuum is achieved (7 μmHg), the analysis is allowed to start. The sample on the analysis port is held at a fixed temperature by a Dewar (containing either LN_2 or a water-ice slurry, depending on the adsorptive used), which is raised by an automatic platform. The pressure in the ASAP is limited to 0.1 MPa. In order to perform a freespace analysis on the ASAP, the tube must be fully degassed again, and an experiment file that executes a single adsorption point (typically nitrogen at P/P_0 = 0.01) after measuring the freespace, as the Microactive software does not include a feature that allows for freespace measurement after the analysis, an issue raised due to the knowledge that helium is not the non-adsorptive gas it was once believed [303].

Figure 3.5 - *In-situ* degassing setup for the Micromeritics 3-flex

Samples for the 3-flex are prepared in the same way as for the ASAP, until the point at which the samples are fitted to the machine itself. On the 3-flex, before the samples are degassed, the tubes are fitted with isothermal jackets which are intentionally left high on the tube to avoid melting and burning on the heating mantle. The tubes are fed through the foam Dewar cover, and fixed in place. The entire experiment file (preparation, sample testing and analysis) is then prepared and run – this starts the *in-situ* degas, albeit there is a paused screen upon starting a sample run that allows for the fitting of the degassing mantle, as illustrated in Figure 3.5. This is a large, flat device with the heating element in the bottom that is pushed up until it is flush with the flat bottoms of the 3-flex tubes, and is held in place by a metal platform that has fixed into a vertical rail on the machine by a tightening screw. A fabric lid for the mantle is fixed on with Velcro tabs, to help retain heat around the powder/film samples themselves and protect the isothermal jackets. Once

the degas is finished and the tubes have cooled to 40 °C, the software pauses and invites the user to remove all of the degassing hardware, lower the isothermal jackets, swing the saturation pressure tube in with the sample tubes and load the dewar containing the temperature regulation fluid onto the automatically operated platform in order to continue the experiment. Upon manual acknowledgement of the completion of these tasks, the 3-flex automatically starts the analysis, and runs both the analysis and free space measurement before completion.

The ASAP was used to determine BET surface areas, pore size distributions and pore volumes for PIM-1, both in the powder and film morphologies. Before analysis, all PIM samples were degassed at 180 °C under high vacuum (7 μmHg, or 9.3 Pa) for 12 h. Analysis was generally done by 87 point isotherms covering the range P/P_0 = 0 – 1 at 77 K, using N_2 as the adsorptive and LN_2 as the temperature control medium in the dewar (the level of which is checked using a metallic level meter). Isothermal jackets were used to ensure constant warm and cold free spaces.

The 3-flex was used for BET surface areas and pore size distribution experiments with N_2 at 77 K, as well as all of the reported 0 – 0.1 MPa H_2 (77 K) and CO_2 (273 K) experiments. An ice-water slurry was used as the temperature control fluid for CO_2 experiments. All samples were loaded as described above, degassed at 180 °C under high vacuum (10^{-7} mmHg), and run. All H_2 runs were also leak tested between degassing and analysis to ensure no detected adsorption is from any gases other than hydrogen.

3.11.2. High Pressure (≤ 20 MPa)

For high pressure hydrogen isotherms, the Hiden Isochema High Temperature and Pressure 1 (HTP-1, henceforth known as HTP) device (Warrington, UK) was used fitted with 20 MPa cylinders of helium (BOC UN1046) and hydrogen (Air Products BIP PLUS). The HTP is capable of dosing pressures up to 20 MPa, and as such can capture a much wider range of pressures than the ASAP. It, like the ASAP and 3-flex described in section 3.11.1 above, is a Sieverts' apparatus-type machine and uses a manometric approach to determine the gas uptake.

The HTP has two reactor spaces, which are illustrated in Figure 3.6: one integral to the unit, which has a built in heater and a feed line for LN_2 such that the reactor temperature can be set anywhere between 77 and 773 K. All experiments performed at temperatures higher than 77 K were done in this unit. The other is a 'hang down' reactor for use with Dewars, which has an external electrical furnace for degassing. The degassing furnace uses 2 thermocouples embedded in the bed to relay temperature data back to the controlling software. The hangdown reactor was used exclusively for experiments at 77 K (using LN_2 as the temperature control fluid). The HTP is connected to a computer with IMIwin software installed.

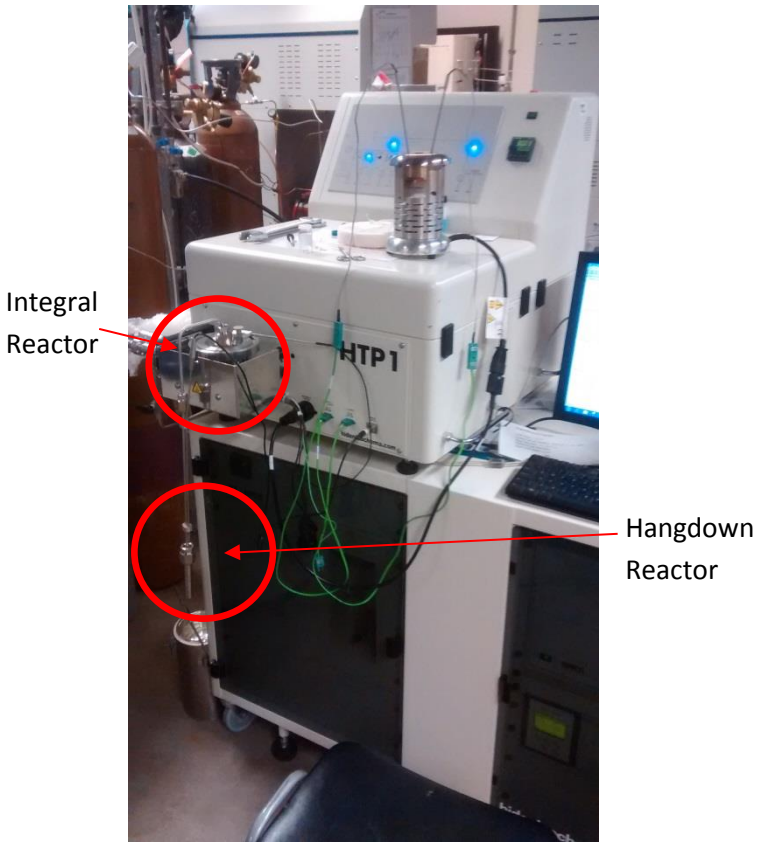

Figure 3.6 - The Hiden Isochema HTP 1, with the integral and hangdown reactors identified.

The HTP was used to acquire high pressure hydrogen adsorption data up to 17 MPa at 77 K. The sample vessel (a small metal cylinder) is washed with acetone and weighed, and then loaded with ~ 100 mg of sample. This is then placed in a vacuum oven at 180 °C for a minimum of 2 hours to drive off any adsorbents, and then reweighed to get an accurate measurement of the dry weight of the sample. This is then left to cool to room temperature, and ~ 20 mg of glass wool (which stops powders being drawn into the vacuum line) is added. The sample vessel is sealed, inserted into the sample chamber, either in the hangdown (77 K) or integral (all other temperatures) reactor. The vessel chamber is then sealed using a silver gasket to ensure a gas-tight seal. The integrity of the seal is checked by leak testing; this is done by dosing hydrogen at room temperature until the pressure in the chamber is 17 MPa, and the gas supply then closed off. Following the opening of the valve connecting the sample and manifold volumes, the pressure, temperature and molar uptake are monitored closely, ensuring that pressure and temperature trends match, and that the molar uptake does not change more than ± 1 µmol min^{-1}. Once these criteria are satisfied, the sample is degassed at 180 °C for 8 h under high vacuum (10^{-6} mbar, or 10^{-4} Pa). The skeletal volume of the sample in the vessel is then determined at room temperature by helium pycnometry – this is the 'freespace' measurement for the HTP, and is recorded by the IMISwin software. At this point, isotherm analysis may begin.

The logistics for running an isotherm change slightly depending on the reactor used. On the hangdown reactor (the more commonly used reactor for this project), degassing is performed by raising the external heater around the sample chamber, identifying within the software that this is the method of temperature control desired, and then running a pre-programmed temperature sequence from within the software. Following cooling and removal of the furnace, a small Dewar is filled with LN_2 and lifted around the sample chamber, and left to precool the sample for 15 mins. In this time, the larger reactor Dewar is filled to a very precise level indicated using a metallic level tool. After precooling, the small Dewar is removed and the large Dewar put in place,

and left for a further 5 minutes. The liquid Dewar is then identified in the software as the temperature control mechanism, and the isotherm is then initiated.

In the integral reactor, all of the temperature control is built in, and a single temperature control unit is identified in the software. Degasses can then be performed solely by executing the temperature sequence in the software, with no further action necessary. In order to operate an experiment below room temperature, the hose responsible for drawing LN_2 into the system must be immersed into a large Dewar before the isotherm is started, but once that is complete, the system will automatically set the temperature and adjust the flow of LN_2 through the cooling system in order to meet the desired temperature. Because both heating and cooling can be performed by the same temperature control unit, it is possible to program the HTP to perform multiple isotherms sequentially, degassing between each isotherm, although this is limited by the volume of the Dewar from which the system is drawing LN_2; in practice, it is limited to 2 or 3 isotherms at a time.

3.11.3. Brunauer-Emmett Teller (BET) Theory

One of the traditionally key pieces of information to collect regarding a porous material is its apparent surface area. Surface area data have long been used as a method of comparison for porous materials, based on the principle that materials featuring a higher apparent surface area has greater utility for various applications, such as a larger number of adsorption sites for gas storage (and/or separation) and an ability for greater catalyst loading for use as a catalyst support material. The most common protocol for determining the surface area of a porous material from adsorption data is the theory of Brunauer, Emmett and Teller, more commonly known as BET theory.

BET theory was first developed in the 1930s as a way of extending the Langmuir theory of monolayer adsorption on a homogeneous surface in order to take into account multilayer adsorption. What resulted was a theory that successfully matched the Type II isotherms Brunaeur et al. had generated with a number of different adsorptives for Fe-Al_2O_3 catalysts [304]. Using this theory, they then proceeded to calculate the apparent surface area at a number of different points along the type II isotherm, assuming close-packed monolayer coverage. What they discovered was that at the point at which the Type II isotherms became linear (the so called 'knee' of the isotherm) showed the closest match in surface area value between the various adsorptives. This finding was also backed by other findings, for example that the differential energy of adsorption substantially changed at the same point, indicating that gas adsorption was no longer occurring on the solid surface of the porous material but was instead building up in multilayers [304]. Brunauer et al. therefore determined that this knee in the isotherm was the point at which a monolayer covered the entire surface of the adsorbent, and the surface area could therefore be calculated using this assumption and knowledge of the size and packing density of the gaseous molecules on the surface.

Calculating the adsorbate surface area using BET theory follows a graphical protocol. The first step is to plot the isotherm as a linearised form of the BET equation, which reads [305]:

$$\frac{\frac{P}{P_0}}{n_A\left(1-\frac{P}{P_0}\right)} = \frac{1}{n_m C} + \frac{C-1}{n_m C}\cdot\frac{P}{P_0} \qquad (\mathbf{3.11})$$

Where P is the absolute pressure, P_0 is the vapour pressure of the gas at the isotherm temperature, n_A is the amount adsorbed, n_m is the specific monolayer capacity, and C is the BET

constant. If $\frac{\frac{P}{P_0}}{n_A\left(1-\frac{P}{P_0}\right)}$ vs P/P_0 is plotted, a linear plot should be produced (assuming the correct P/P_0 range is chosen – this is discussed further below). The parameters n_m and C can be then be calculated from taking the gradient (a) and the y-intercept (b) of the plot. This is done using the following equations:

$$C = \frac{b}{a} + 1 \tag{3.12}$$

$$n_m = \frac{1}{a+b} \tag{3.13}$$

Once the monolayer capacity has calculated, that can be then be converted into a surface area by:

$$A_{BET} = n_m A_{mol} N_A \tag{3.14}$$

Where A_{BET}, A_{mol} and N_A are the BET surface area, molecular cross-sectional area and the Avogadro constant respectively.

The BET parameter C, whilst not ultimately used in the calculation of surface area, is an important result of the BET theory, as it gives a strong indication of the thermodynamics of the adsorption process. According to the derivation of the BET equation, it is defined as function of the net energy of adsorption (the difference between the energy of adsorption on the surface E_1 and the liquefaction energy of the adsorptive E_L) [304]:

$$C \approx e^{\left(\frac{E_1 - E_L}{RT}\right)} \tag{3.15}$$

Traditionally, the P/P_0 range over which the BET plot should be considered is 0.05 – 0.3, as recommended by the international standard for surface area determination ISO 9277-2010 [305].This range was recommended by Brunaeur et al. because it produces a linear relationship for the BET plot for the mesoporous adsorbents upon which their work was based [306]. However, many adsorbents don't show this behaviour, or are not linear over the entire range, and therefore great care must be taken in selecting the range over which the BET equation is plotted, and therefore the values of n_m and C that the plot produces [307].

The validity of the BET model has been questioned particularly critically in relation to microporous adsorbents, based mainly on the fact that most of the adsorptive work of micropores is done at pressures lower than P/P_0 = 0.1 [305]. In this case, applying the traditional P/P_0 range for the BET method will result in errors, as micropore filling happens before this pressure, and as such the region in which Brunauer et al. deemed the 'correct' region for the application of the BET equation will generally be too high for microporous adsorbents [307]. In order to better apply BET theory to microporous solids, Rouquerol et al. [307] suggested the following steps to ensure the correct linear region is chosen:

1. *The straight portion of the BET plot should have a positive value of C.*
2. *The term $n_A(1-P/P_0)$ should continuously increase with P/P_0 in the region selected.*

In addition, it is possible to further check the validity of this range by calculating the P/P_0 value at which the monolayer has formed. This can be done by changing P/P_0 in equation 3.9 to $\left(\frac{P}{P_0}\right)_{n_m}$ (the relative pressure at which the monolayer is completed) and n_A to n_m [307]; this then cancels down to the following equation [306]:

$$\left(\frac{P}{P_0}\right)_{n_m} = \frac{1}{1+\sqrt{C}} \quad (3.16)$$

As long as $\left(\frac{P}{P_0}\right)_{n_m}$ falls within the range of pressure used for BET surface area determination, then the value acquired is valid. Indeed, the 2015 IUPAC report on the study of physisorption on porous solids suggests this check as a third criterion for ensuring the P/P_0 range selected is suitable [74].

A further factor that must be considered is the meaning of the number that the BET theory produces, and what exactly this represents. Although use of the BET surface area is highly commonplace in the study of porous materials, little consideration is given to what the number actually means. The 2015 IUPAC report begins to better define which surface areas are actually considered, as illustrated in Figure 3.7 [74]. The figure demonstrates three main surface areas that may be described: the Van der Waals surface area, outlined in green, is characterised by the exposed area of the Van der Waals spheres that represent atoms in the surface, and whilst this is closest to the true surface area of the material, this is very difficult to quantify. The surface shown in blue is the 'Connolly' surface area, and represents the actual surface area that gas molecules interacting with the surface can show (i.e., it is the area traced out if a spherical probe molecule is rolled across the Van der Waals surface). The red surface area is the r-distance surface area, and is the loci plane that is r distance from the Connolly surface area [74].

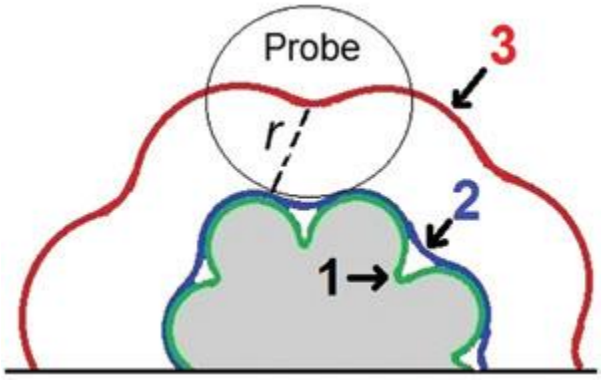

Figure 3.7 - Illustration of the various surface areas discussed by the 2015 IUPAC Report [74]**. © 2015 IUPAC & De Gruyter**

The BET surface area is actually most representative of this r-distance area, due to the mathematics involved. The BET theory assumes monolayer coverage across the entire surface, and the surface area is then calculated as multiplying the number of molecules in that monolayer by the cross-sectional area of the adsorptive molecule. As BET theory assumes the probe molecule to be Van der Waals spheres, the cross sectional area of each molecule is then assumed to be equivalent to a circle with the same kinetic diameter. These molecular cross-sectional areas are then projected onto the surface, rather than truly reflecting the surface beneath. The distance from which they are projected is the diameter of the probe molecule, hence the value of the r-distance area. The more accurate surface areas may be impossible to measure, as even with improved mathematical models, the adsorptive molecules will exert steric exclusion on one another, ensuring that any surface topology smaller than the curvature of the adsorptive molecules and/or closer than a probe molecule diameter cannot be captured by the physisorption process.

This issue becomes even worse with microporous adsorbents, as the assumption of monolayer coverage is highly questionable, largely due to the very different mechanisms at play on an open surface (for which BET was developed) and in highly constrained conditions (micropore filling) [306]. As such, it is recommended that the BET surface areas generated from microporous adsorbents are viewed as effective surface areas, and not as true representations of the available surface area of the adsorbent [307]. Nevertheless, the BET surface area is a highly useful tool when considering microporous materials, as it can be seen to be an "indicator of adsorbent 'activity'" [306], and is a very useful tool for comparing materials, particularly because the BET value is so widely quoted by porous materials scientists.

For this study, the BET surface area is determined by Micromeritics' software. The software presents the data as a raw isotherm, as the BET plot and in the form $n_A(1-P/P_0)$ vs. P/P_0 (titled 'Rouquerol BET'), all of which are equipped with sliders which allow the inclusion (or otherwise) of a range of data. The software is automatically set to include points between 0.05 – 0.3 for BET calculations, or to include every available point if only a very small range of points are taken. This range is adjusted manually within the software, using the slider on the Rouquerol BET plot until every point in the active range of selection continually goes up, and the first point larger than the range selected has a lower $n_A(1-P/P_0)$ value than the point before it. The system immediately recalculates the BET surface area and the various coefficients as the slider is moved, so it is easy to check whether C is still positive given the selected range. If both are correct, the value of $\left(\frac{P}{P_0}\right)_{n_m}$ is then manually calculated to check that this value is in the range of selected. If so, the calculated BET value is deemed to be valid for the microporous adsorbent and is therefore quoted as the Rouquerol BET surface area for the adsorbent in question.

3.11.4. Pore Volume Calculations

Calculating the total available free volume within a material is an important parameter in adsorption science, and is particularly useful when trying to consider the material in an adsorption-based storage system in which the bulk gas will not only occupy the space around the adsorbent, but will occupy the pores also. The volume of free space within the materials is determined using two main methods in this project: the Gurvich volume; and Dubinin-Radushkevich theory.

3.11.4.1. Gurvich

The total pore volume in the material is calculated from the point closest to $P/P_0 = 1$, in which the total porosity of the material is assumed to be full of nitrogen at the density of LN_2. The measured uptake at this point is then divided by this density to give the total pore volume.

This method is based on that proposed by Gurvich in 1915 for the total mesopore volume in mesoporous materials [308]. In his experiments, Gurvich noticed that many mesoporous adsorbents produced a vertical plateau perpendicular to the P/P_0 axis, which would represent the complete filling of the micropores. He therefore suggested if the adsorbate filled the pores completely, then the volume of the pores in question could be calculated by dividing the mass of adsorbate in the pore by the density of the liquid adsorptive at the temperature of the isotherm, given the liquid state in which adsorbed gases form when pore filling. This proved to be a successful method, generally providing mesopore volumes within ± 5%, regardless of the adsorptive used [308].

Although the rule Gurvich proposed was only for mesoporous adsorbents that showed strong Type IV behaviour, the general rule has been adapted for use with all adsorbents, moving the point at which the pores are assumed to be full from the vertical rise in a type IV isotherm to a point on an isotherm close to the vapour pressure of the adsorptive, in order to come as close to the ideal of the total porosity of an adsorbent being filled with liquid adsorbate as possible. It is clear that using this simple rule for total pore volume is a 'rough and ready' approach, which is susceptible to large error, and must therefore be viewed with caution. However, because of its ease of calculation, it is a convenient starting point for any discussion about the total pore volume in an adsorbent, and can be corroborated with other pore volume measurement techniques to provide a more certain value of the pore volume.

3.11.4.2. Dubinin-Radushkevich (DR) Model

An alternative pore volume of interest is the micropore volume. As micropores tend to be filled by hydrogen during the adsorption process, which mesopores and macropores do not, the volume of micropores available is a strong indicator of the potential hydrogen storage capacity of the material.

The classical theory for the determination of micropore volume in a porous adsorbent is that of Dubinin, who applied the concept of micropore filling to the Polanyi potential theory [304]. Polanyi's theory dictated that a temperature independent 'characteristic curve' could be drawn for any adsorptive-adsorbent combination, and in the process, define the 'adsorption potential' *E* (which is now better understood to be representative of the change in chemical potential in the system) [304]. Dubinin took Polayni's theory, and adapted it for micropore filling in activated carbons. His empirical approach derived the Dubinin-Radushkevich equation:

$$\ln v = \ln v_0 - \left(\frac{RT \ln\left(\frac{P}{P_0}\right)}{\beta E_0} \right)^2 \qquad (3.17)$$

Where *v* is the amount adsorbed, v_o is the limiting micropore uptake, *R* is the molar gas constant, and *T* is the temperature. E_o is the characteristic adsorption potential energy, which is the adsorption energy of a reference adsorptive (for Dubinin, this was benzene) on the adsorbent [309]. It has been suggested that E_o is inversely proportional to the pore size of the material, although it is likely that this relationship is unique for each adsorbent-adsorptive pair, depending heavily on pore geometry and surface chemistry [309]. β is the affinity constant, defined as the ratio of the adsorption energy of the adsorptive used in the experiment to that of the reference adsorptive (such that $E = \beta E_0$) [310]. Applying this equation to the isotherm data of a microporous material results in a straight line section on a graph of $\ln(P/P_0)^2$ vs. *v*, from which βE_0 and v_0 can be determined from the gradient and y-intercept respectively. As v_0 represents the maximum amount of adsorbate stored in the micropores, the micropore volume can then be determined if the adsorbate density is known [309].

However, it was later found that the power of 2 did not suit many microporous adsorbents, because either the linear section of the characteristic plot was very small, shifted into the very low pressure region, or the curve simply didn't show linearity at any point [304, 310]. Therefore the theory was revised, and the Dubinin-Astakov equation was proposed [309]:

$$\ln v = \ln v_0 - \left(\frac{RT \ln\left(\frac{P}{P_0}\right)}{\beta E_0} \right)^n \quad (3.18)$$

For the DA equation, *n* is a tunable exponent which allows greater statistical freedom to fit a straight line to the plot, although it comes at a cost of being less well defined as a physical parameter [309]. Dubinin reported that the value of *n* typically lies in the region of 2 – 6 [304]. Values of *n* in this region are typical of adsorbents with very narrow micropore distributions, such as unactivated or slightly activated carbons. However, values of $n < 2$ are still possible, and is often the case for materials with a broad micropore distribution [310]. The value of *n* is believed to be dependent on the pressure range and temperature the isotherm was performed at [304].

The method of determining the adsorption potential and micropore volume from the DA equation are exactly the same as for the DR, except the value of *n* must be adjusted to give the best linear plot. For this study, Microactive has the ability to optimise this value for a given data set by iterating through a least-squares regression study of the values of $\log_{10}(v)$ and $(\log_{10}(P/P_0))^n$, selecting the value of *n* that produces the smallest standard error of the y intercept [311]. Following this, the micropore volume is calculated by dividing v_0 by the density of the liquid adsorbate at the isotherm temperature, the data for which is pre-loaded into the software.

3.11.5. Pore Size Distribution (PSD) Calculations

From a full isotherm, it is also possible to determine the specific pore volume and the pore size distribution of a nanoporous material. Having an idea of the pore diameters in a nanoporous material can aid analysis of the adsorption performance of these materials, and help to direct materials towards suitable applications. In general, a PSD is calculated by applying a suitable model to the empirical data in order to generate a distribution. Both the MicroActive and 3-flex software packages supplied by Micromeritics feature an ability to apply a number of different models to generate PSDs. The Barrett, Joyna and Helenda (BJH), Horvath-Kawazoe (HK) and density functional theory (DFT) models are all popular choices that can be processed by these programmes, and all are discussed in sections 3.11.5.1 - 3.11.5.3 below. Deciding which model best fits the material is a choice that must be made studiously, taking into account the varying strengths and weaknesses of each model. Choosing an incorrect model may result in a highly erroneous PSD, whilst using multiple models can help clarify the common pore sizes.

3.11.5.1. Barrett-Joyna-Helenda (BJH) Model

One of the oldest theories for PSD calculation still in use today is that of Barrett, Joyna and Helenda (BJH), a relatively old (1951) model but still commonly used for the characterisation of mesopores and large macropores. The model is based on the application of the Kelvin equation in a cylindrical pore, adjusted to allow for multilayer adsorption [312]. The model works by assuming the pore is full of the liquid adsorbent (typically nitrogen), and works through the isotherm in decreasing steps [311].

Fundamentally, the BJH theory works by splitting a pore into three distinct regions: the evaporating core; the adsorbate thickness; and the pore walls. The pore is assumed to be full of liquid nitrogen, and the amount present is determined by a Gurvich pore volume approach. The nitrogen present is either physically bonded into the adsorbate within the adsorbate thickness range, or else it is condensed within the core. As the 'desorption' occurs, the amount of nitrogen

that is fixed in the adsorbate decreases, and therefore the adsorbate thickness decreases. This thickness is determined by a particular expression; in Micromeritics' software, this is done using either the Halsey or Harkens-Jura equations [311]. As a result of the thickness decrease, the diameter of the core will increase, and if this diameter increases to the point that the relative pressure difference is greater than the equilibrium pressure difference for that meniscus diameter determined by the Kelvin equation, then the core will evaporate and leave only the adsorbed nitrogen [311, 313].

Practically, this results in progressing through the pressure intervals in the isotherm, starting at the full pore and steadily emptying it, even in the case of the adsorption isotherm. The pore sizes are determined by calculating the change in adsorbate thickness, and then comparing the nitrogen lost to that lost in the isotherm: if the isotherm shows a higher loss of nitrogen, then new pores have reached the critical pressure and the cores have evaporated; in this case, the critical core diameter is added to twice the thickness loss, and the pore size corresponding to that loss is determined. If the nitrogen loss is less in the isotherm, then the adsorbate thickness is adjusted accordingly, but no new pores are accounted for, as no new cores have evaporated. This is done for each pressure interval between the upper and lower pressures, which is either the limits of the isotherm, or can be adjusted within Micromeritics' software. The surface area of the pores can also be determined using BJH theory but the area of the bottom of the pore is not accounted for [311].

The fact that BJH is still widely used more than 60 years after it was first published is a testament to the success of a first principles-based theory that did not assume a distribution shape [313]. However, it comes with an inherent flaw. As the theory is based on the Kelvin equation, which in turn is based on macroscopic thermodynamic principles, the theory diverges from the actual thermodynamic behaviour as the pores get smaller; estimates of pore sizes below 10 nm can underestimate the pore size by as much as 20% [74]. In these smaller pores, BJH can provide a rough guide to the PSD; more accurate measures can be provided by either of the PSD models detailed below.

3.11.5.2. Horvath-Kawazoe (HK) Model

The Horvath-Kawazoe (HK) method was first developed by Géza Horváth and Kunitario Kawazoe in 1983, and is a PSD calculation model built from first principles of thermodynamics and molecular potential theory [314]. The HK principle is to select a series of values for the pore width L (the lowest of which must be higher than the combined diameters of the adsorbent molecule and the atom on the absorbent surface) and iteratively solve for the value of P/P_0 that fills pores of this size. This is then done for steadily increasing values of L, finding the corresponding relative pressure for each pore width [311]. The cumulative pore size distribution is then found by matching the amount adsorbed at a given P/P_0 with the value of L found for that pressure; the differential PSD can be determined by finding the difference in amount adsorbed between the last value of L and the current one [314].

The equation used for the matching of L to P/P_0 depends on the pore size and adsorbent surface atoms chosen. In their original study, Horváth and Kawazoe chose a slit-shaped graphitic carbon pore, deriving the relationship from the potential function of a gas molecule over a graphite surface and their thermodynamic proof of the relationship between the differential heat of adsorption and the relative pressure [314]. However, the same principle can be applied to

different geometries, such as the cylindrical pore (Saito-Foley model) and the spherical pore (Cheng-Yang model), each of which use a different relationship to relate *L* and P/P_0.

HK theory has been established as a reliable method for PSD calculation, particularly providing a strong estimation of micropore distributions [312]. It has been viewed favourably both because it is built from first principles and therefore has a realistic description of the adsorption potential in the pore, as well as being pore shape and adsorbent specific [315]. However, as the technique has aged, it has been shown to underestimate the size of pores in the distribution due to the assumptions of homogeneous adsorbent surfaces and the adsorbate phase being liquid-like. Nonetheless, it still proves a worthwhile method to use for comparison of microporous distributions, and has distinction as the first attempt to provide a universal theoretical model for micropore filling [316].

3.11.5.3. Density Functional Theory Models

Density functional theory (DFT) and non-linear density functional theory (NLDFT) have emerged in recent years as an accurate method of determining PSDs throughout the nanopore range. Both methods use a statistical thermodynamic approach to solving the general adsorption equation and create a pore size distribution that matches the empirical isotherm to the 'kernel' that represents the adsorptive gas molecules, the adsorbent surface chemistry and the pore geometry [311].

At its core, DFT calculates the grand potential functional as a function of the density distribution of the adsorptive/adsorbate within the pore. In the grand canonical ensemble on which these calculations are performed, the chemical potential, volume and temperature of the system are held constant and the free energy is minimised in order to find the equilibrium state. The grand Helmholtz free energy can be split into the intrinsic Helmholtz free energy and an external interaction energy function; the intrinsic Helmholtz energy can be further split into an ideal gas term and the fluid-fluid molecule interactions. In older, standard DFT application, mean field theory is used to approximate the long distance interactions, but this falls apart when considering the interaction between adsorptive molecules and the pore walls. To correct this, NLDFT was developed, which uses a smoothing approximation in the short range to correct for this inaccuracy in the calculation [308].

The result of this statistical thermodynamic calculation is a kernel function. A kernel function is a composite of ideal isotherms for the interaction of a given adsorptive with a given pore shape, geometry and surface chemistry, but with different pore sizes [74, 308]. Kernels with multiple pore geometries are possible, but difficult to calculate, as are kernels that can account for pore blocking or cavitation effects [308, 315]. Because kernel functions are highly computationally intensive, a limited collection is provided by the Micromeritics software. In order to make the calculated PSD as accurate as possible, the kernel selected for the deconvolution must be as representative of the physical system as possible; for nitrogen on highly graphitic carbons, this may be relatively simple, given that the adsorption of nitrogen in carbon slit pores was the first system considered for this calculation [308]; more modern materials such as MOFs and PIMs may not be accurately represented by this kernel, and therefore some error can be expected in the final result [74].

PSDs are calculated using kernel functions through application of the general adsorption equation [317]:

$$n_A\left(\frac{P}{P_0}\right) = \int_{D_{min}}^{D_{max}} n_{A,DFT}\left(\frac{P}{P_0}, D\right) f(D)\,.\,dD \qquad (3.19)$$

Where $n_A(P/P_0)$ is the empirical isotherm, $n_{A,DFT}(P/P_0,D)$ is the kernel function, D_{min} and D_{max} are the minimum and maximum pore sizes specified in the kernel, and $f(D)$ is the pore size distribution. This integral is an ill-posed problem, meaning there are an infinite number of functional combinations within the integral that will result in a successful calculation [311]. However, with the application of a suitable regularization algorithm (such as the discrete Tikhonov method combined with a non-negative least squares algorithm), the integral can be solved numerically [317]. The implementation of DFT in the Microactive software allows for alteration of the regularization value; a greater numerical value serves to smooth out the calculated PSD and avoid over-fitting to noisy data, but at the cost of induced error of fit. Evidently, minimising both the roughness of the distribution and the error is advisable.

Because statistical thermodynamic models such as DFT and NLDFT provide detailed information about the fluid structure close to the pore walls, they are accurate in the micropore range. They also provide excellent information about the fluid-fluid interactions that may be occurring in a wider pore, meaning the accuracy of these models for mesoporous adsorbents is also good [74]. As a result, they have become a new standard for calculating the pore size distributions of porous materials. However, NLDFT is not a perfect model. Because NLDFT works on the assumption that the adsorbent surface is molecularly smooth, and predicts distinct layering steps in its kernels, a smooth isotherm can result in a large number of artefacts in the PSD. This is particularly common for amorphous carbons, which often show a pronounced artefacts at 1 nm [315]. Alternative approaches such as quenched solid density functional theory (QSDFT) have been developed [317], but these advanced approaches are beyond the capabilities of the Microactive/3-flex software, and were therefore not considered for this project.

4. PIM-1/MIL-101 Composites

4.1. Synthesis

4.1.1. PIM-1

Synthesis of PIM-1 was first attempted using the optimised method of Song et al. [190]. The first attempt at a batch of PIM-1 using this method produced small, hard lumps of a yellow solid as seen in Figure 4.1(a). 5.50 g of the material was produced (dry weight post-vacuum drying) at a yield of 39.7 %. This was originally deemed a success, as a material with the visual properties of PIM-1 was produced, and it dissolved into both chloroform and THF readily. A dilute chloroform solution showed a luminescent green colour that has previously been noted of PIM-1 [182]. However, when it was attempted to make thin films via solution casting, the films produced would be cracked and very brittle, unlike the full, flexible films described by Song et al. [190]. This solution casting process was tried a number of times, with different starting concentrations, but the same result occurred each time. The brittle shards are shown in Figure 4.1(b), with no extra mechanical breakdown performed during transfer from petri dish to vial.

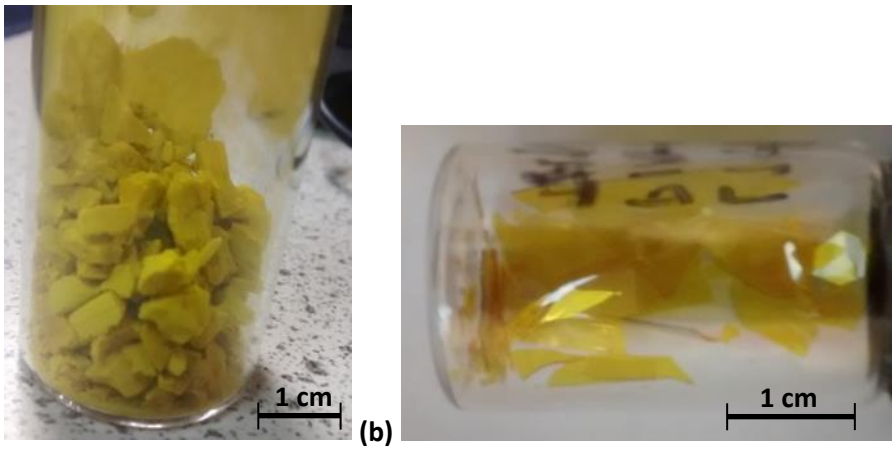

Figure 4.1 - PIM-1 as synthesised by the method of Song et al. [190] **in the form of (a) powder and (b) film**

Gel permeation chromatography (GPC) analysis performed on this polymer determined a number average molar mass (M_n) of 9,765 g mol^{-1}, and a polydispersity index (PDI) of 2.66, relative to polystyrene standards. This was a very disappointing figure, given the M_n of 101,400 g mol^{-1} reported for the same reaction conditions by Song et al. [190]. It was determined that the low molecular weight was ultimately the barrier to progress from this synthesis, as a material capable of forming robust films is required if a composite containing crystalline MOF is possible. Within the research group, Dr. Rob Dawson, a postdoctoral research associate at the time, repeated the synthesis a number of times, each time attempting to ensure the stoichiometry and water content of the reaction mixture was as carefully controlled as possible, but the results were always the same; a low molecular weight polymer that formed cracked and brittle films. A number of potential reasons for the low molecular weights were identified: poor reagent purity; water (vapour) present in the reaction mixture (either from the glassware, reagents, or imperfect seals in the reaction set up); or poor quality of base. Each of these was to be isolated and corrected. A new batch of K_2CO_3 was purchased, and substantive work was planned for the other two, although this work was dropped when method 2 was tried.

PIM-1 synthesis by the method of Budd et al. [187] was performed, and using this higher temperature method twinned with fresh K_2CO_3 powder produced a finer PIM-1 powder that produced flexible films upon solvent casting. GPC analysis of this powder determined a M_n = 76261 g mol^{-1}, and a PDI of 2.53. 2 g of this material were kindly donated to this project by Dr. Dawson; this is henceforth designated PIM-1(2).

All the subsequent syntheses of PIM-1, PIM-1 (2) included, produced a reasonably fine yellow powder, as illustrated in Figure 4.2. These small, irregular shapes were clearly a result of the reprecipitation step, as they always very close to the typical size of the drops that were allowed to fall into the stirred methanol. These high molecular weight solutions precipitated instantly, fixing the shape of the drop, which was conserved through the filtration and drying processes. Upon reflection, it is unknown why the early attempts at PIM-1 synthesis resulted in these large chunks; it is possible that due to the low molecular weight of these samples, not very much of the long chain polymer actually precipitated out when the solution was dropped in methanol, resulting in a much finer PIM-1 particle suspension in the methanol, which then agglomerated when filtered. Certainly, a much more dense cake was formed on the filter paper in these early attempts, which cracked into large chunks as it dried, and this morphology was kept when the material was dried.

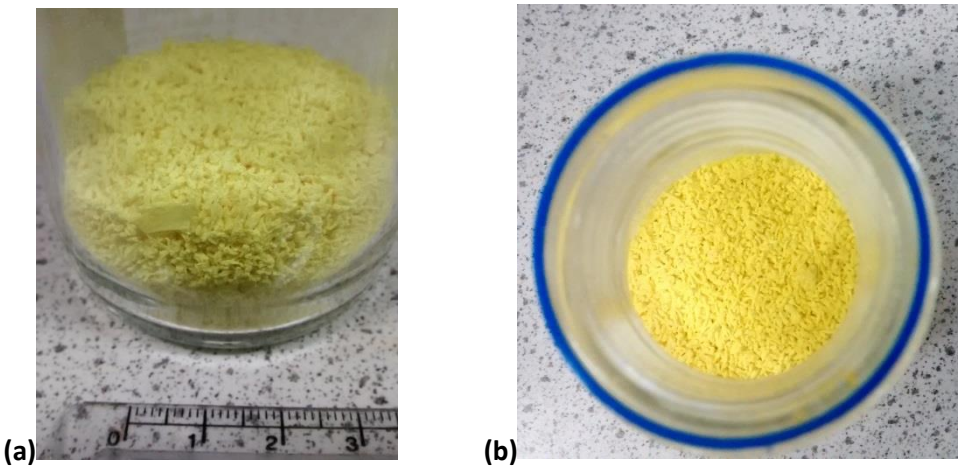

Figure 4.2 - PIM-1 powder sample (as synthesised by the method of Budd et al. [187]**, viewed from the (a) side and (b) top**

Synthesis of PIM-1 was continued from this point, as 2 g was insufficient to perform all the experiments required. A final batch was attempted with the oversight of Dr. Dawson, but PIM-1 (3), although again apparently successful as the bright yellow irregular powder dissolved in both chloroform and THF comfortably and formed an iridescent green solution, this batch again failed to form coherent films, despite attempts from multiple concentrations. 6.8 g of this batch was recovered, an apparent yield of 98.7 % (the amount of reagent used had been halved for this experiment). The results of one attempt can be seen in Figure 4.3. GPC showed a M_n of 23972 g mol^{-1}, and a PDI of 1.46, so resulting in a relatively uniform distribution but at a molar mass that is not high enough to allow the polymer to form coherent, flexible films. This sample was washed through with water (in an attempt to remove any K_2CO_3 that may not have been washed away by the transfer of the reaction solution into water), vacuum dried and then reprecipitated, but with no improvement in the performance of the film.

Figure 4.3 - PIM-1 (3) film

Immediately following this, another batch, PIM-1 (4), was attempted. Again, a bright yellow powder that dissolved readily in chloroform was made, although this polymer did now form coherent films upon solvent casting. 6.23 g of PIM-1 (4) was synthesised at a yield of 93.8 %. GPC showed a M_n of 99037, a very similar value to that quoted in the original report of Budd et al. [180, 187]. The PDI of PIM-1 (4) was 1.52, compared to Budd et al.'s 2.8, so it is apparent that this synthesis hadn't achieved the same success in forming long chains, but had formed more consistent chains than Budd et al.'s original.

However, the films formed from PIM-1 (4) were not flat and clear as the PIM-1 (2) films had been; these were translucent and angled upwards at the edges, as illustrated in Figure 4.4. This was not necessarily a problem at first glance; these were films from a plentiful batch and formed readily. However, as discussed in section 4.8.3 below, these films showed no porosity. Clearly this was not expected; there is a large body of evidence in the literature that demonstrates that PIM-1 films show intrinsic microporosity, as discussed in section 2.5.2.8, and as shown in section 4.8.1, the powder had shown relatively normal nitrogen adsorption behaviour. Poor kinetics in adsorption behaviour has previously been seen in PIM-1 [318], and it was hypothesised that the film may have developed a non-porous skin, possibly due to quick evaporation of the chloroform. In order to test this, part of the film was ground up with a pestle and mortar, in order to break up the outer layer of the film. A nitrogen isotherm was then performed on this 'roughened' film, and it did show similar uptake to previous PIM-1 films. This evidence was enough to deduce that it was an issue with the film formation, rather than the polymer batch, that was causing the non-porosity.

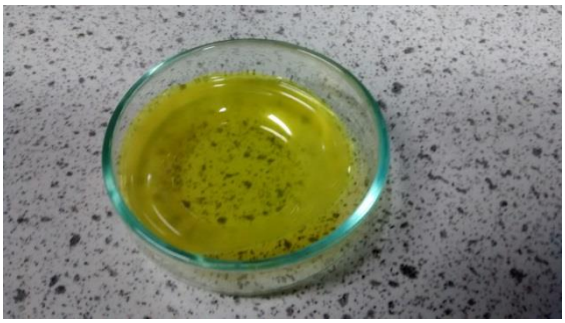

Figure 4.4 - PIM-1 (4) film with raised edges

In light of this, films were then cast in petri dishes that were placed in an evaporating dish and covered with a watch glass, in an effort to slow down the rate of chloroform evaporation. This technique produced flat, translucent films. These films showed the expected porous behaviour, as detailed in section 4.8.3 below.

The final batch of PIM-1 made for this project, PIM-1 (5) was synthesised with the aid of Dr. Sébastien Rochat. 6.86 g of the polymer was recovered at a yield of 99%. GPC demonstrated the M_n of this batch to be 43,374 g mol^{-1}, and a PDI of 1.98. This was a slightly disappointing result, given the high molecular weight of the previous batch. However, when this batch was cast into films, it did not crack, but instead formed very similar films to the early PIM-1 (4), with raised edges. This is likely due to the relatively high M_w of 86,037 g mol^{-1}; the presence of these large chains helps to bind the smaller chains together and stop the film from cracking. Later attempts at PIM-1 (5) films using the larger evaporating dish and watch glass produced flat, smooth films that showed good porosity when tested.

4.1.2. MIL-101

MIL-101 was a much simpler synthesis than PIM-1, in that it was a one pot synthetic method. The major challenge with this synthesis was scaling up, as the synthesis was limited by the 15 mL PTFE liners. Because there were as many as three hydrothermal reactors available to perform this synthesis, it was attempted to perform three concurrent reactions wherever possible, to give a reasonable 'batch' size. Five batches were made during the course of the project; the amounts produced and yields achieved are listed in Table 4.1 below. The yield is calculated based on the number of chromium atoms; the chemical formula of MIL-101 was assumed to be $[Cr_3O(bdc)_3(OH)(H_2O)_2]$ for the fully activated MOF.

Table 4.1 - Amounts synthesised and yields for each of the batches of MIL-101 made for this project.

Batch	Number of concurrent liners	Amount Synthesised (g)	Yield (%)
MIL-101 (1)	3	0.3337	23.3
MIL-101 (2)	1	0.0250	5.22
MIL-101 (3)	3	0.3692	25.7
MIL-101 (4)	3	0.1838	12.8
MIL-101 (5)	2	0.2141	22.4

In all cases, the synthesis produced light green crystals that were easily crumbled when pressure is applied either in the fingers or with a spatula within the vial. Confirmation that this powder is actually MIL-101 was done via PXRD, FTIR and adsorption studies; these are presented in sections 4.2, 4.3 and 4.8.5 respectively.

4.1.3. PIM-MOF Composites

Following successful PIM film synthesis, the next step was to attempt a synthesis of the composite. The first attempt at composite formation was a combination of PIM-1 with MOF-5. This combination was desirable as MOF-5 is a well-known MOF that is beginning to gather the attention of industrial researchers, in particular a consortium between Ford, General Motors, BASF and the University of Michigan within the U.S. DOE's HSECOE [238]. Because there is evidence of the scale up of MOF-5 synthesis [150], it is very likely that the material will become relatively low cost in the near future, and would be an economically advantageous high porosity filler for the composites. Because it is known to be hydrolytically unstable, it may also lead to studies on the effectiveness of PIM-1 as a means of protecting MOF-5 from water vapour. The result of PIM-1/MOF-5 composite synthesis is shown in Figure 4.5.

(a)  **(b)** 

Figure 4.5 - PIM-1/MOF-5 composite film viewed from the (a) top and (b) bottom

As a large amount of PIM-1 had to be used to attain a 10 wt% MOF composite, the film is very thick, and appears to have surface cracks, but is ultimately still cohesive. The transparency of the film has been lost, likely due to this greater thickness. Looking closely at the film, there is no evidence of MOF crystals within the structure. Looking at the other side of the film, the colour is much lighter. This appears as if the MOF has settled during the solvent evaporation process, which would explain the lack of crystals on the upper surface. Clearly, this is not the desired effect, as a homogeneous dispersion of MOF within the PIM would better allow the merging of properties.

One way of avoiding this issue with the thickness of the film would be to use less of both materials. However, this would require splitting a single batch of MOF-5 into a smaller amount, which would present a number of practical issues. Because the MOF is kept under diethylformamide (DEF), it would be very difficult to dry out the MOF completely to be able to accurately weigh the powder for film formation without exposing it to atmospheric conditions for a number of minutes, which may be long enough to degrade the structure. In addition, casting a PIM-1/MOF-5 composite is difficult as an entirely dry atmosphere is required to be able to successfully evaporate the chloroform without exposing the MOF-5 to air, as would be ideal for moisture protection studies. The composite in this study was made by attempting to continuously flow nitrogen over the film for the 48 h in which it was casting, but this will accelerate the evaporation rate of chloroform, which may have resulted in the cracking on the surface, and does not secure the film from airborne water vapour. This may be resolved using a Schlenk line within a fume hood, but securing this facility is difficult, particularly given that many fume hoods users actively discourage exposure of the facility to high concentrations of vapours such as chloroform, fearing potential corrosion of the gas-tight seals.

As a result of this failed experiment, it was decided that using a hydrolytically stable MOF would greatly reduce the difficulty of the synthesis, and more easily allow for consistent testing. The

MOF picked was MIL-101, as this is an easy-to-make MOF material that both the Mays and Burrows groups have significant experience in using [92, 138, 275, 319].

The first attempt at creating a PIM-1 (4)/MIL-101 composite is shown in Figure 4.6. The figure clearly shows three fully consolidated films that don't show the clear two-sided behaviour seen in the PIM-1/MOF-5 film. Whilst these films don't show the same flexibility as a pure PIM-1 film, there is some flexural strength within the films, although they do get noticeably more brittle as the MIL-101 content increases.

Whilst this was a reasonable attempt, the films are clearly heterogeneous. The 20 wt% film was the most homogeneous of the films, as there is no clear colour distinction in the film. The primary issue with these films is agglomeration of the MOF crystals in the middle of the film. As a result of this agglomeration, the films are not flat, with a raised area in the middle. The edges of these films are also very rough; this is largely due to the films sticking to the glass petri dishes in which they were cast. The films were difficult to remove from the petri dishes, despite the use of small amounts of water to lift the films (a technique commonly used to liberate pure PIM-1 films from glass petri dishes). As such, the films required the use of a pair of tweezers with a very sharp point, which was used to 'dig' in underneath the film to attempt to lift the film from the dish – this caused some physical damage to the film edges. There was also an issue with the films with the 30 wt% film beginning to laminate at the edges. This may have been due to relatively fast evaporation causing the film to solidify at different rates; because the lower part adhered to the glass and the upper part of the film is placed under tension both due to the fast evaporation and the agglomerated MOF, there is a shearing force placed on the upper film which has caused it to come away at the edges.

As these films were less homogeneous than desired, another set of composites was synthesised. This attempt changed two parts of the synthetic method, as detailed in section 3.1.5; PTFE petri dishes were used instead of glass; and a final sonication step was performed on the mixed solution before casting. The results of this synthesis are shown in Figure 4.7 below.

The second attempt at film formation produced very homogeneous and smooth films. Clearly, the second sonication step produced a much more homogeneous solution from which the film was cast, and the use of a PTFE dish greatly reduced the adhesion between the film and the dish, so allowing the maintenance of clean edges as the film shrinks with evaporation. The 20 wt% film has showed some warping, potentially due to a weaker seal between the evaporating dish and the watch glass increasing the chloroform evaporation rate. There is very minor warping in the 30 wt% film also, but this is barely noticeable.

One noticeable difference is that there is a very slight difference in the reflectivity of the surface; the upper side of all the films are shiny, whilst the undersides are matted. This effect is not seen in the films produced in glass petri dishes, but is relatively common for those cast in PTFE dishes. This is possibly due to the film not adhering to the petri dish and so allowing evaporation of chloroform from underneath the film, which may have caused small openings in the film that result in surface roughness. Alternatively, it is likely that the PTFE dish is physically rougher than the glass, and the roughness of the underside of these films is due to simple conformation to the surface on which they rested.

Nevertheless, these films are exactly what were expected, and it was therefore decided that this second batch of films would be used for all further testing.

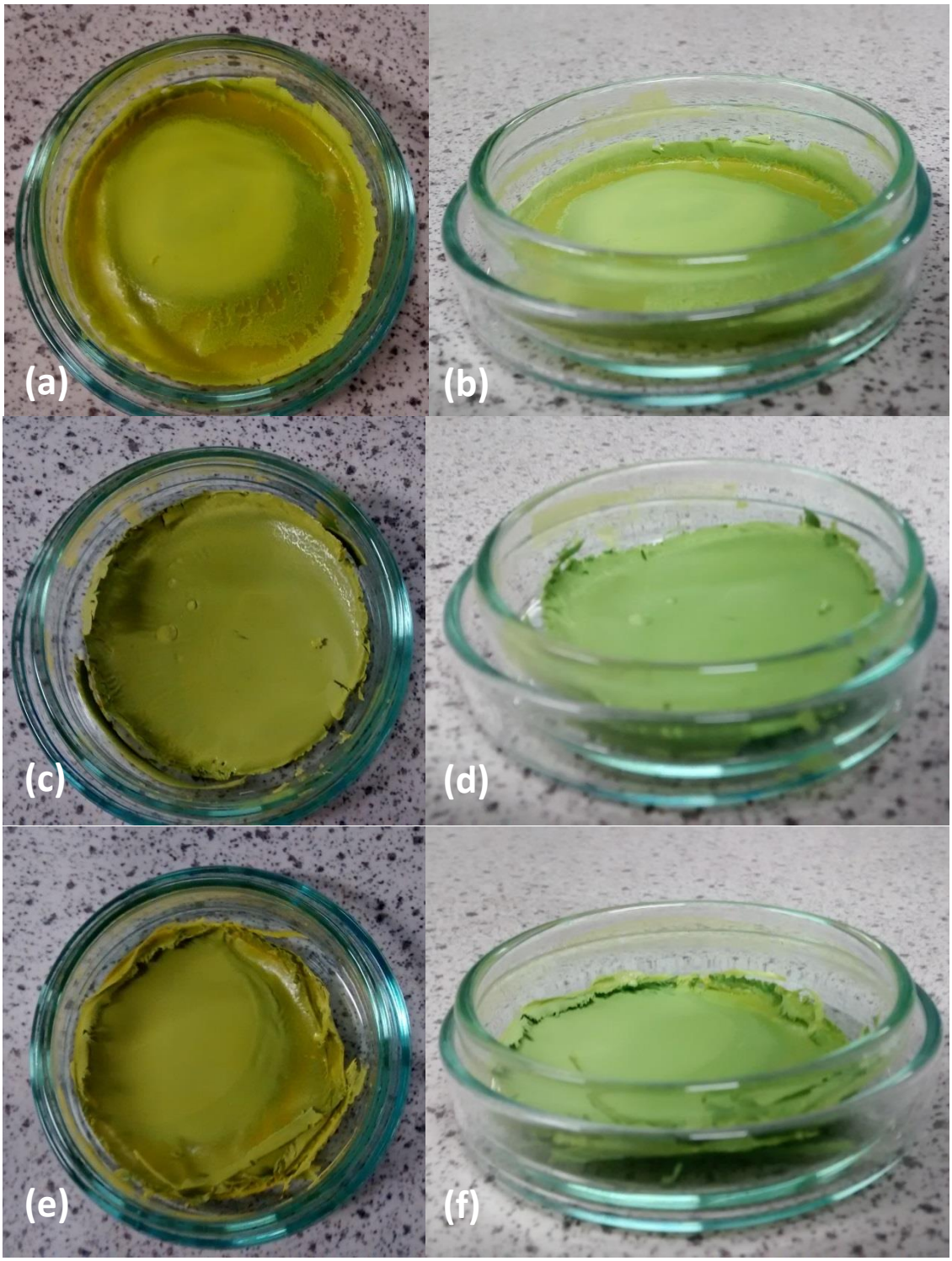

Figure 4.6 - First attempt at PIM-1/MIL-101 films, featuring the birds eye and side on views of films containing (a),(b) 10 wt%, (c),(d) 20 wt% and (e)(f) 30 wt% MIL-101

Figure 4.7 - Second attempt at PIM-1/MIL-101 films, featuring the birds eye and side on views of films containing (a),(b) 10 wt%, (c),(d) 20 wt% and (e)(f) 30 wt% MIL-101.

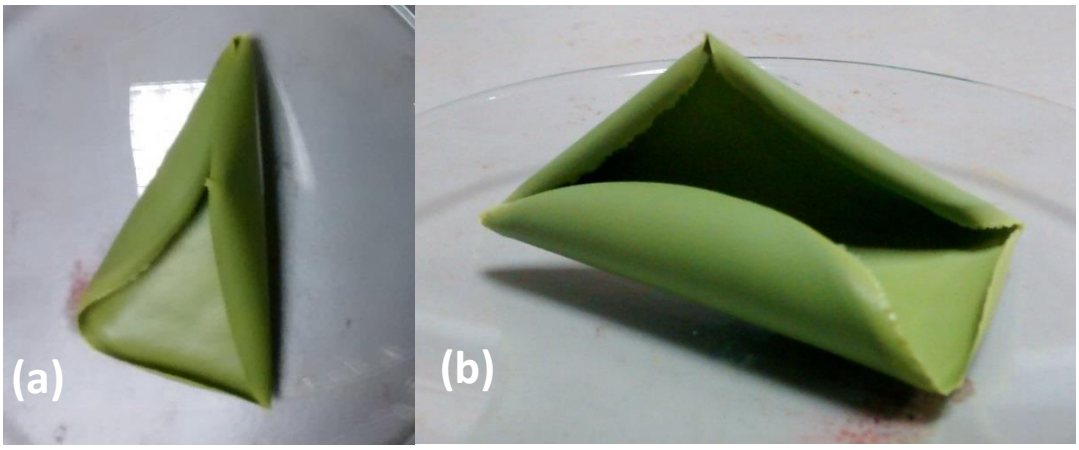

Figure 4.8 - 40 wt% composite as viewed from (a) birds eye and (b) side on views

The attempt at a composite containing 40 wt% composite is shown in Figure 4.8. This composite did form a cohesive film; a pleasant surprise given that other experiments within the group had not always produced such a result. However, it is evident that the film formation process was not flawless – upon visual inspection, the film showed the same heterogeneity the second batch of composites did, although to a much greater extent, with a much smoother and shinier side on the (concave) top side. This composite is also relatively brittle.

The film also exhibits striking curvature. Although these curls can be straightened out when force is exerted normal to the face of the film, it immediately snaps back into the curled shape upon release. This indicates that there is a strong tensile force inherent within the film, which is likely due to a strong PIM-only layer on the top surface of the material. This could be caused by faster than expected evaporation from the surface of the solution causing the quick formation of a PIM layer, which then proceeds to contract as further chloroform is lost. As the rest of the film cures more slowly (and therefore likely better retains its shape), this causes tension in the top part of the film that causes the curvature seen.

Despite the differences in shape, the 40 wt% composite underwent the same characterisation as the other composites in the hope that more information about this composite system could be extracted.

4.2. Powder X-Ray Diffraction

Powder x-ray diffraction was performed on all batches of the MIL-101 in order to ensure its viability. The typical PXRD trace of this material, compared to the traces published by Férey et al. [131] in the initial reporting of MIL-101, and Jiang et al. [138], whose synthetic method was used for this project, is shown in Figure 4.9.

The intensity distribution of MIL-101 (3) shown in Figure 4.9 compares very well to previous studies of this material, so indicating that the material synthesised is indeed MIL-101. Although the maximum intensities of some peaks are different, particularly at 2θ = 2.8° and 16.7°, in general the trace maps very well to these other studies. Indeed, when compared to trace (d), the MOF shows a very strong correlation with the theoretically ideal crystal, albeit with slightly broader peaks. The breadth of these peaks may be due to the nanoparticulate nature of the MOF made by the method of Jiang et al. [138].

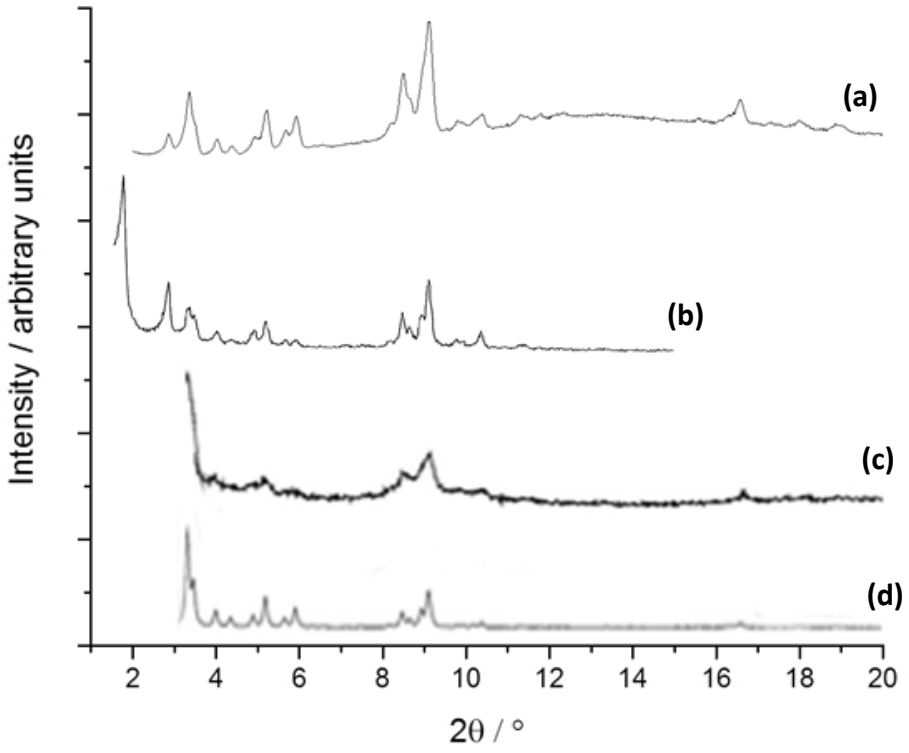

Figure 4.9 - Comparison of XRD traces of MIL-101 from (a) this project (MIL-101 (3)), (b) Férey et al. [131] **, (c) Jiang et al.** [138] **with no crystallising additive, and (d) the simulated XRD trace of Hong et al. cited by Jiang et al. (b) is reproduced from** [131] **with kind permission from the American Association for the Advancement of Science, and (c) and (d) are reproduced from** [138] **with kind permission from The Royal Society of Chemistry.**

One major difference between the PXRD trace for the MIL-101 synthesised in this project and others from the literature is the non-flat baseline of the trace, particularly above 2θ = 6°. Large, gradual changes like this are often an indication of amorphous material present in the sample. Given the MOF is highly crystalline, this non-flat baseline should not be present, and therefore there is evidence of another substance in the tested samples. This idea is also confirmed by visually inspecting the samples that went into the Bruker D8 Advance; these can be seen in Figure 4.10. The MIL-101, once it had been placed into the groove in the sample holder and sheared across the top to provide a level surface into which the X-ray beam is targeted, became noticeably lighter in colour compared to the unmodified MOF. It is likely that both the colour change and the amorphous signal in the XRD are due to the presence of terephthalic acid in the MIL-101 that had not been washed away in the post-synthetic processing. Because the MOF was only activated by heating under vacuum and not subjected to the harsher chemical activation treatments commonly used [137], it is likely that this material may still contain sizeable amounts of terephthalic acid adsorbed to the bare metal sites within the MOF, which would not have been removed by the pre-PXRD degas. This may have produced the whiter colour (pure terephthalic acid is a white solid under standard conditions) of the sheared MIL-101 seen in Figure 4.10.

Figure 4.10 - Comparison of the native and PXRD-loaded MIL-101 samples

Aside from confirmation of successful MOF synthesis, PXRD was also used to investigate the crystallinity of the PIM-1/MIL-101 composites and to ensure that MIL-101 maintained its integrity within the films. The PXRD traces for all of these films, compared with the bare traces for MIL-101 (3) and a PIM-1 (4) film are shown in Figure 4.11.

As expected, the PIM-1 film shows a highly amorphous trace, with no sharp peaks present. However, because the intrinsic microporosity in PIM-1 is caused by the way the polymer chains cannot align, the material contains a series of voids of very similar sizes; Bragg's law applies to any regularly spaced centres of electron density (as it is the electrons with which the x-rays interact), and therefore the regular voidages in PIM-1 should be detectable [281]. The PIM-1 trace in Figure 4.11 shows exactly this phenomenon – the regular drops at 2ϑ = 14, 18 and 23 ° are indicative of d-spacing values of 0.65 nm (loose inter-chain spacing), 0.49 nm (efficient inter-chain spacing) and 0.38 nm (aromatic rings) respectively [320, 321]. The intense peak at 29 ° is from the material on which the sample was placed for testing, and can be ignored for all the samples present.

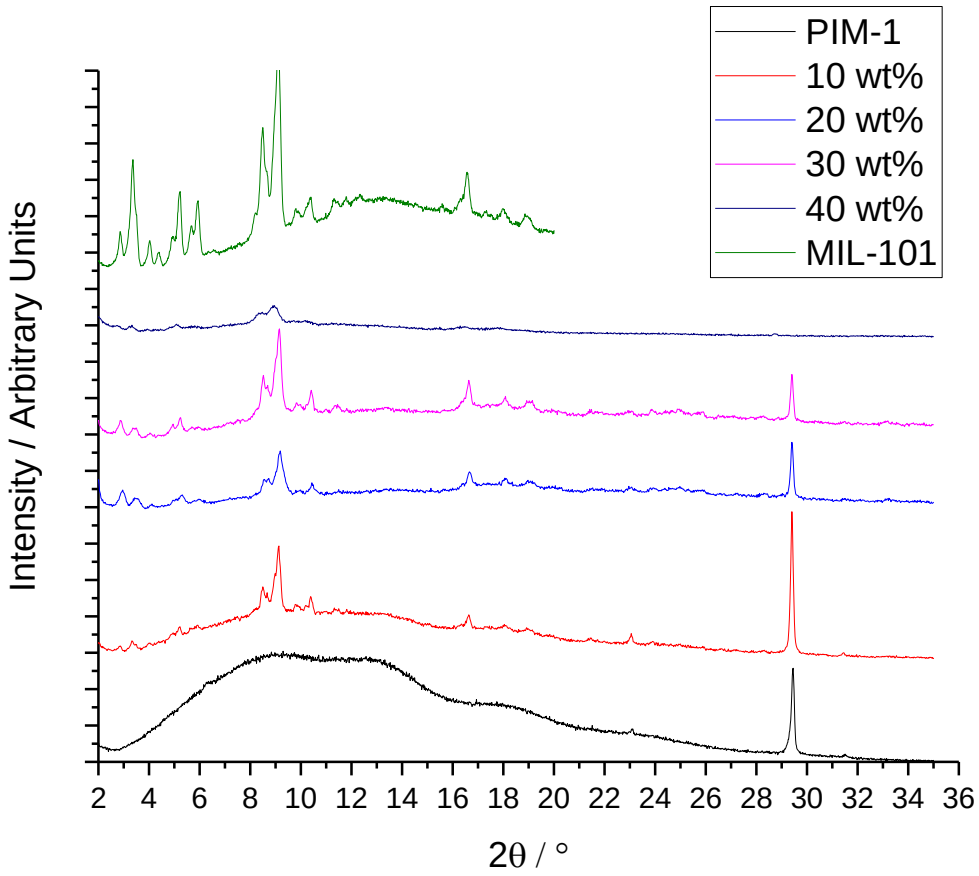

Figure 4.11 - PXRD traces for PIM-1 film, MIL-101 and composites thereof.

The composites, as expected, show a mixture of the behaviours of PIM-1 and MIL-101. All three clearly show the strongest MIL-101 peak (an asymmetrical twin peak in the 8 - 10° range), as well as smaller peaks at 2.8, 3.4, 5.2, 10.4 and 16.6 °, which indicate that MIL-101 successfully survived the film casting process and has retained crystallinity within the consolidated material. The intensities of these MIL-101 responses tends to increase with increasing MIL-101 content, with the 30 wt% film generally showing strong MIL-101 peaks, and the 10 wt% film showing a mostly amorphous response outside of the strong twin peak.

The outlier is the 40 wt% composite. This material shows a comparatively flat XRD spectrum, showing a broad double peak in the 8 - 10° range, as well as a number of very small, near insignificant peaks that appear to correspond to the peaks of the MIL-101 spectrum. This therefore appears to show that MIL-101 is present in the film, but it cannot be said with any certainty that MIL-101 has maintained its structure, or whether the thick PIM top layer is acting as a large amorphous barrier and preventing the strong Bragg response from the MOF from coming through.

The amorphous behaviour of PIM-1 is largely lost in the composite films, although the 10 wt% film does show a significant upward baseline in the $2\theta = 6 – 16$ ° range that appears to echo a similar rise in the PIM-1 response. Such a response is not so clearly visible in either the 20 or 30 wt% films, which not only contain less PIM-1 by ratio, but the high intensity signal from the increased presence of MIL-101 serves to suppress the PIM-1 behaviour into the baseline, which is corrected for during processing of the signal.

4.3. Fourier Transform Infrared Spectroscopy (FTIR)

Fourier Transform Infrared Spectroscopy (FTIR) was performed on PIM-1 (4) film, MIL-101 (4) and all of the composite samples. The spectra for each are presented in Figure 4.12 below.

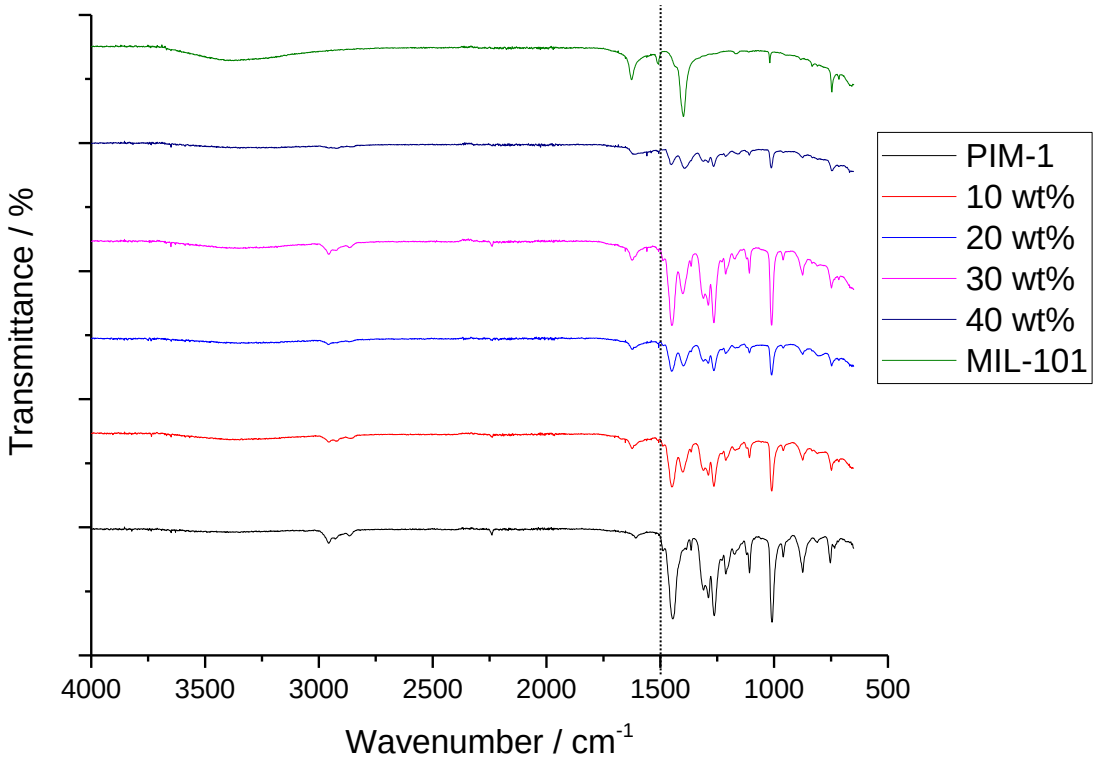

Figure 4.12 - FTIR spectra for PIM-1 film, MIL-101 powder and composite films thereof. The dotted line at 1500 cm^{-1} is provided to guide the eye.

Looking at the IR spectrum for PIM-1, it is possible to identify a number of the characteristic groups within the polymer structure. Much of the identification of these bonds has already been performed by Alentiev et al. [209] – it is possible to directly match the peaks present in the PIM-1 spectrum in Figure 4.12 to those that that study identified. This is done in Table 4.2 below. Clearly, this spectrum is a very good match to previous IR studies of PIM-1, and clearly identifies this material. This is further confirmed by other studies showing very similar spectra for this material [322].

The spectrum for MIL-101 is noticeably less busy, with fewer bond types within the material that could respond to infrared radiation. Nevertheless, this spectrum still compares well to literature [209, 323]. The major peaks seen in this spectrum are due to the Cr – O bond (661 cm^{-1}), in-plane bending of the C-C-H link (717, 748, 1018 cm^{-1}), delocalised carboxylate (O=C-O^-, 1401 cm^{-1}) and C=C stretching (1510, 1631 cm^{-1}) [209]. The very broad peak centred around 3377 is likely due to the O-H bonds both in the hydroxyl groups bonded to the Cr itself, and potentially in some water that is adsorbed in the material.

Changing attention to the spectra of the composites, it is clear to see that the spectra carry large peaks that can be attributed both to the PIM and the MOF. In particular, the very strong peaks at 2956, 1448, 1309-1266 and 1015 cm^{-1} from the PIM and 1625, 1401 and 665 cm^{-1} from the MIL-101 are clearly replicated in all of the spectra, if somewhat less evidently and more broadly in the 40 wt% composite, which is general showed a more muted response. The intensities are less for all of these peaks in all of the composites, a result perhaps expected by the lower amount of each material (as a fraction of the total) present in the composites. There doesn't appear to be much

broadening of the peaks however, despite Alentiev et al.'s finding to the contrary [209]. This may suggest that there is less chemical manipulation between the two components in these composites.

Table 4.2 - Peaks in the FTIR spectrum for PIM-1 as determined by Alentiev et al. [209] **compared to those in the spectrum presented in Figure 4.12**

Alentiev et al. peaks	Group identified	Peaks from Figure 4.12
3055	Aromatic rings (bending and stretching)	3058
3006		-
1607		1612
1490		1488
754		753
2929	C-H (stretching of saturated bonds)	2928
2957		2956
2866		2865
2242	C---N (stretching)	2243
1455	Spiropyran rings (C-H bending)	1448
1370	CH_3 (bending)	1367
1312	C-O-C (stretching)	1309
1291		1289
1269		1266
1013		1015
876	Spiropyran rings (skeletal vibration)	873

4.4. Scanning Electron Microscopy

Scanning Electron Microscopy was performed on PIM-1 in the powder and film morphologies, MIL-101 powder and each of the PIM-1/MIL-101 composites. Secondary electron imaging was used in all cases as it was felt that the image quality was much clearer using this mode, and SEM was performed primarily to visually inspect the materials for this project. The greater topological detail available from backscattered electron imaging was not required. Images for PIM-1 powder are shown in Figure 4.13 below.

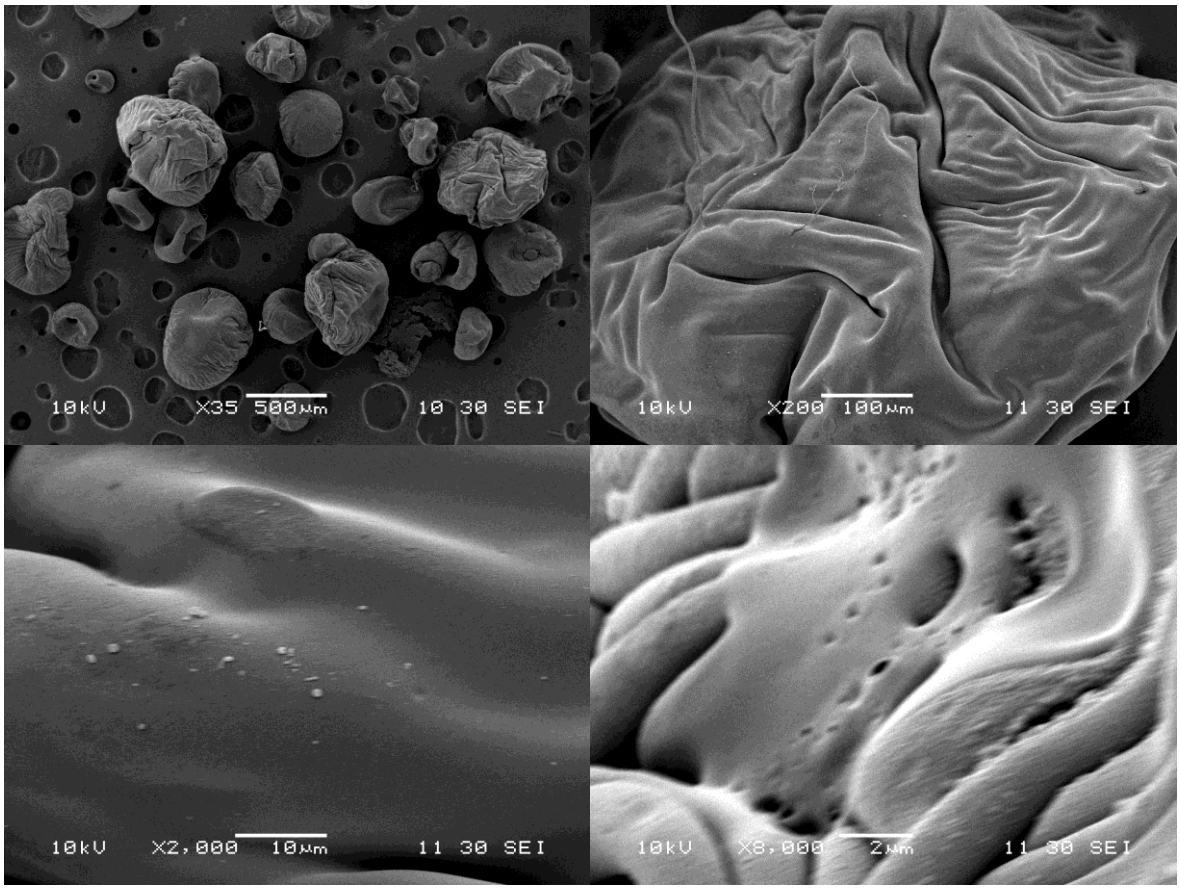

Figure 4.13 - Scanning Electron Microscopy images of PIM-1 powder at (a) x35, (b) x200, (c) x2000 and (d) x8000 magnifications

Part (a) appears to be able to show particles consistently within the 100 – 500 µm range, potentially hinting at a relatively uniform particle size distribution. However, the particles actually featured in the SEM are some of the very smallest present in the sample, as far larger particles that were much more typically sized for the batch were deemed too large to be adequately imaged by the electron beam.

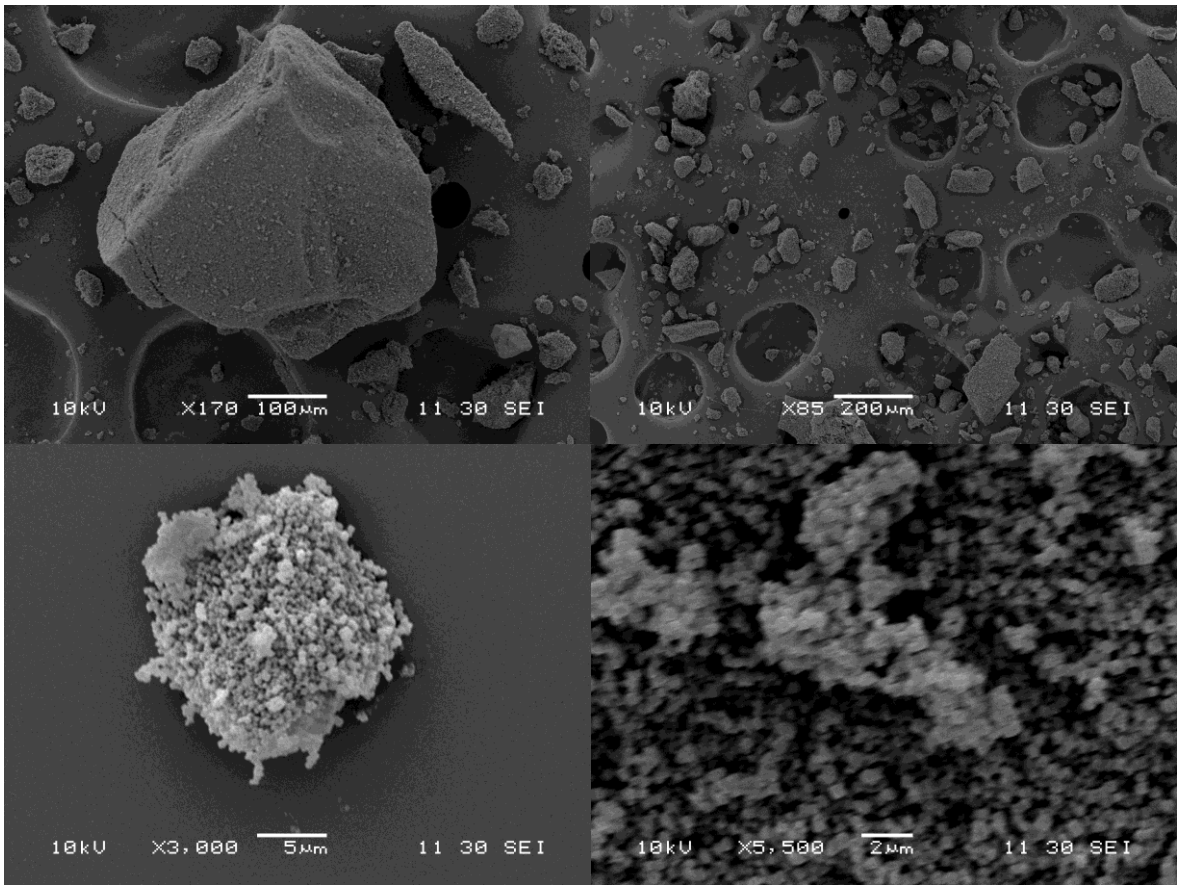

Figure 4.14 - Scanning Electron Microscopy images of MIL-101 powder at (a) x85, (b) x170, (c) x3000 and (d) x5,5000 magnifications

Figure 4.14 shows MIL-101 at a number of different scales. The key finding from these images is the size of the crystals of MOF-5; in particular part (d) shows a closer view of the larger particle shown in part (c). The small nodules visible are the individual crystals of MIL-101, and although the image is slightly blurry, it can be seen that the nodules present have diameters of the order of ~ 500 µm. This particle size is much larger than the typical particle size of Jiang et al [138], who reported an average particle size of 50 nm for their acid-free synthesis, having calculated the distribution from transmission electron microscopy (TEM) images. However, this particle size is consistent with the particle size distribution published by Bromberg et al. [139], who also synthesised MIL-101 hydrothermally without a crystallising agent, and observed particles of ~500 nm in TEM images, although the weight-averaged hydrodynamic diameter of the particles, as measured in suspension in methanol, was 396 nm. This illustrates that the slight changes from the method of Jiang et al. proposed by Sharpe et al. [275] resulted in a larger particle of MIL-101, but with the benefit of a much shorter reaction time.

The other point of interest from Figure 4.14 is the wide variety of particle clusters present within the powder. Although the crystals themselves are ~ 500 nm in diameter, they cluster together in particles as small as a few microns (part (c)) all the way up to particle that are hundreds of µm (part (a)) or even mm in size (visual observation). The very large crystals are formed during the centrifugation and drying process, and are likely caused by the compressive forces generated in the centrifugation. The larger particles easily crumble when exposed to mechanical stress, suggesting these particles are only loosely bound, behaviour typical of powders that have been lightly compressed into larger solid particles.

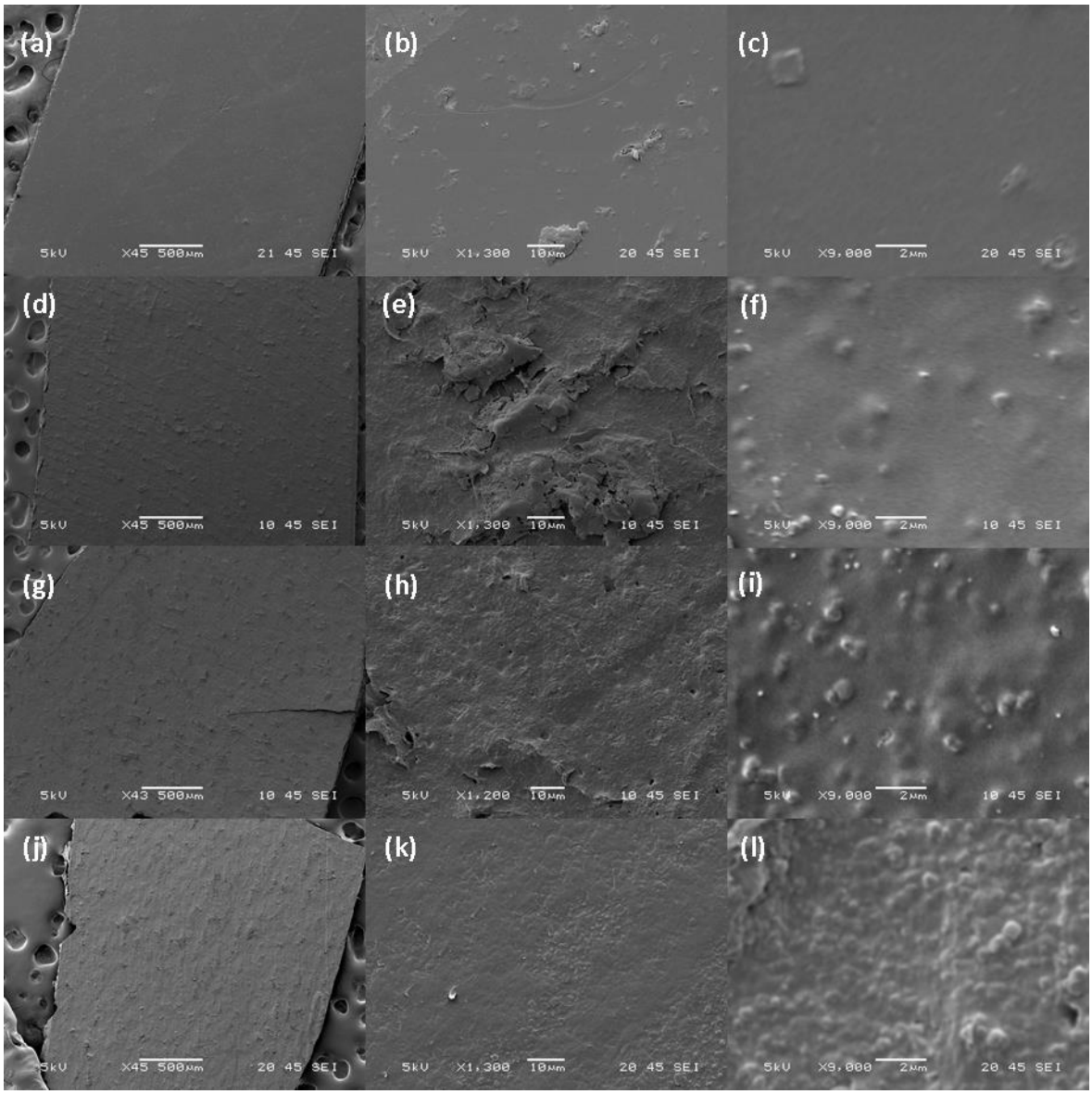

Figure 4.15 – Scanning Electron Microscopy images of the flat faces of (a – c) PIM-1 film, (d – f) 10 wt% composite, (g – i) 20 wt% composite and (j – l) 30 wt% composite at x 45 (left), x 1300 (middle) and x 9000 (right) magnifications

Figure 4.15 shows the faces of the PIM-1 film and all of the composites at a variety of magnifications. It is clear to see that the PIM film is by far the smoothest of the surfaces, which is to be expected given the presence of the particulate MOF in the composites, which serve to distort the surface. Whilst the PIM film with no additive looks very smooth in the lower magnifications, the x1300 and x9000 magnifications in parts (b) and (c) show that the film has a number of small nodules and deposits similar to those seen on the PIM-1 powder in Figure 4.13 above, albeit rather larger and in most cases flatter than those seen on the particle. These are relatively few and far between however, as shown in part (c).

The composites all seem to have a number of ridges along their faces, which are most regular in the 10 wt% film and become less regular with increasing MIL-101 content. The high regularity on this film is possibly due to the use of the PTFE liners, potentially due to the shrinkage of the film as the solvent evaporated. The more random spacing and length of the raised lines on the 20 and 30 wt% composites seem to suggest that these are a function of the MIL-101 content, rather than do to with the casting process.

Aside from these ridges on the surface, each of the composites is scarred with a number of raised bumps in the surface. These are clearly caused by the presence of the MIL-101 crystals in the film pushing the smooth PIM surface upward. From the x43 images in Figure 4.15, it is difficult to see a distinct trend in the roughness, although there appears to be a very slight increase in the number of bumps as the MIL-101 content increases. This trend becomes far clearer in the x9000 images however, as there is a clear progression in the number of bumps in the surface as the MOF content increases. What is also noticeable is that not only do the number of raised parts in the surface increase, but also the size begins to vary more; the 30 wt% film shows a large number of small bumps in the surface alongside the large raises that are present in the 10 and 20 wt% films. As discussed by Smith et al [249] in the analysis of the SEM images of their PIM-1/UiO-66 composites, the crystalline particles on the surface are MOF particles that are not embedded within the polymer, but simply adhered to the film surface. However, the number of these crystalline particles on the surface does not appear to correlate to the MIL-101 content of the film, as the 20 wt% composite seems to show more of these surface particles than the 30 wt%, although the 10 % film does show fewer.

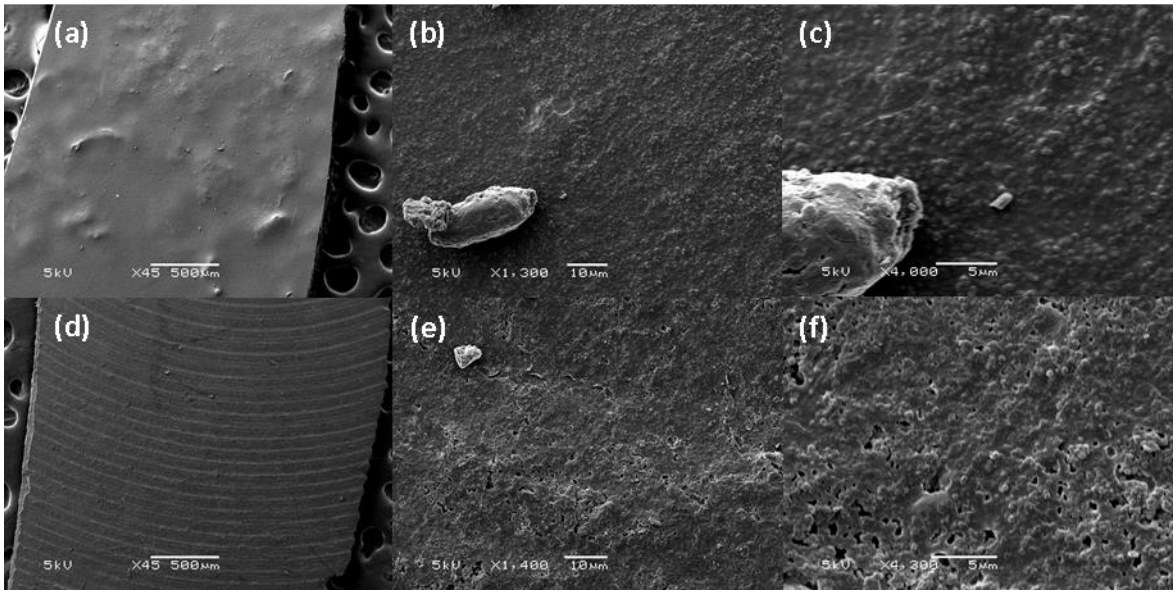

Figure 4.16 - Scanning Electron microscopy images of the top (a - c) and bottom (d - f) faces of the 40 wt% composite at x45 (left) x1300 (middle) and x4000 (right) magnifications respectively.

Both faces of the 40 wt% composite are shown in Figure 4.16. The top side, shown in parts (a) – (c), show strong similarity with the lower MOF content composites, namely the consistent bumps on the surface that are indicative of MIL-101 crystals underneath. This figure also shows the occasional 'lump' of PIM that stud the surface of the films. Interestingly, the bottom of the film looks quite different. At the x45 magnification, clear striations are visible across the surface of the film. These may have been caused during the film formation process, as the evaporating chloroform can much more easily escape the underside of the film at the edges, which may have cause the film in contact with the petri dish to solidify in concentric rings, as the previous stage detaches from the dish surface to expose the next ring inward to the atmosphere.

Looking closer at parts (e) and (f), at higher magnifications the underside of the film shows similarities to the other film face images, as there are MIL-based bumps in the surface and PIM-1 lumps on the surface. The major difference on this side is that there is a large number of visible holes in the surface that are not apparent on any of the SEM images previously viewed in this project. As they are visible to an SEM, these holes are far larger than the nanoporosity for which

these materials were selected, and so must have been created during the film synthesis. They are likely due to evaporating chloroform pockets within the film creating high pressure voids that create open channels through the material in order to escape. These will be larger in this film rather than the lower MOF content materials because of the very thick top layer of PIM, which will be far less permeable to evaporating chloroform and will assist in the formation of the higher pressure voids.

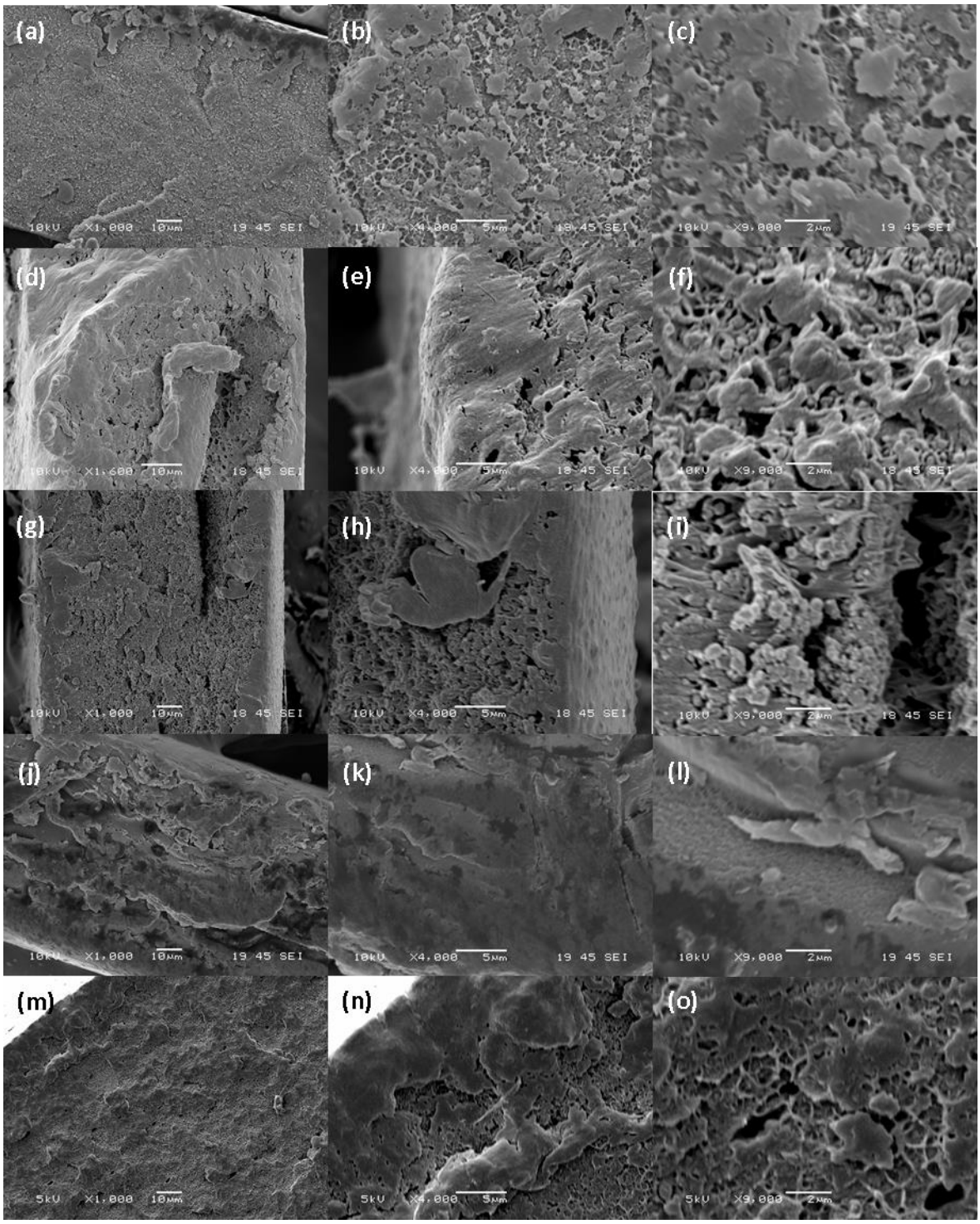

Figure 4.17 - Scanning Electron Microscopy images of the cross-sections of (a – c) PIM-1 film, (d – f) 10 wt% composite, (g – i) 20 wt% composite and (j – l) 30 wt% composite at x 45 (left), x 1300 (middle) and x 9000 (right) magnifications

Figure 4.17 shows SEM images for the cross-sections of the films. These images raise a number of points of interest with regards to morphology of the films. Firstly, it is quite apparent that the

PIM-1 film is highly consolidated, with no evidence of major voids in the films – the surface roughness is all provided by smaller particles that extrude out from the surface. The composites, however, appear to show much greater voidage in the centre of the films, particularly in the 10 and 20 wt% films. This voidage creation is clearly partially to do with the presence of the MOF displacing the PIM, but this does not appear to be the sole case, given the much closer structures of the 30 and 40 wt% films. The rest of this voidage is likely cause by evaporating chloroform escaping from the film as it cured.

It is also apparent from these images that all of the films have a dense layer at the edges of the cross sections, implying a solid outer layer on each of the films. As the PIM-1 and 10 wt% composite samples were cut with scissors in order to prepare the sample, this smooth edge folded in from the faces may have been partly induced by the sample preparation method, but this is not the case for the 20, 30 and 40 wt% composites, which were snapped (due to their high brittleness) in order to prepare the sample. The presence of a thick solid layer on the film faces is highlighted particularly by parts (e), (h) and (n), which show a higher magnification image not only of the solid edge region but also of the open structures underneath.

One other technique that can be applied to the cross-sectional images is to measure the thickness of the films. This was performed manually on the images, as the exact point where the film and the carbon tape meet can be relatively difficult to determine, and the greater precision provided using computational tools is not required for this study. Each image (items (a),(d),(g),and (j) from Figure 4.17 above, and a less magnified image for the 40 wt% composite) were printed out in A4 size, and a number of lines drawn and measured across the film, attempting to remain perpendicular to the edge at all times. These measurements were then averaged, compared to the scale bar on the image, and the following film thicknesses calculated:

Table 4.3 - Thicknesses of the PIM-1 and composite films determined by measurement on cross-sectional SEM images

Composite MIL-101 Content (wt%)	Thickness (µm)
0	109 ± 1
10	70.0 ± 2.0
20	97.2 ± 1.8
30	100 ± 0
40	143 ± 1

Clearly, all of the films had thicknesses of around 100 µm, which would be expected, given that they all contained 0.2 g of PIM-1. The increasing concentration of the MOF, which maintained its own significant free volume when embedded in the film, increased the overall volume of the material and therefore the thickness, given that the composites were all manufactured in the same Teflon petri dishes.

The pure PIM-1 film appears to be thicker than even the 30 wt% composite, even though this film contained as much PIM-1 as the composites, without any of the MOF. This thickness arises from the glass petri dish (in which this film was cast) having a smaller internal diameter than the Teflon dishes; simple geometry determines that this reduced surface area means that the film becomes thicker to compensate for the volume of the solid material in the film. As the reduction in surface area of the glass dish is greater than the reduction in volume from the missing MOF, the PIM film emerges as a thicker membrane. The same effect would explain why the 40 wt% film is so much thicker than the other composites, although decrease in the radial surface area in this case was reduced by the shrinkage of the film.

4.5. Thermogravimetric Analysis

Thermogravimetric analysis for MIL-101 under nitrogen flow is shown in Figure 4.18 below. The spikes visible in run 3 were due to an experimental issue, and can be reasonably ignored.

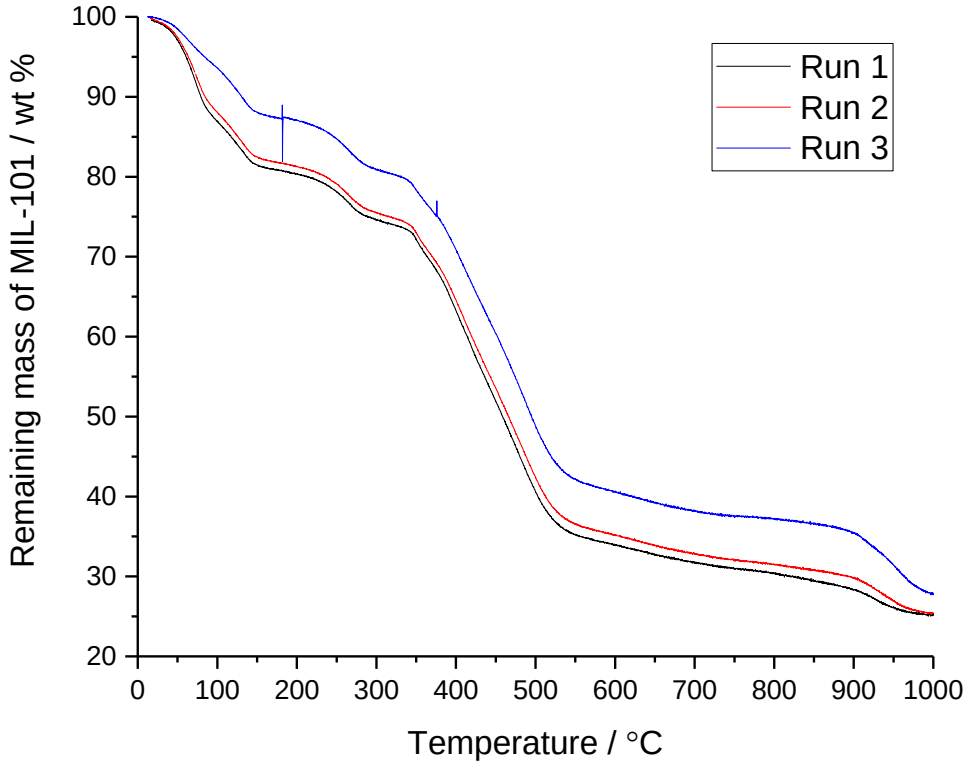

Figure 4.18 - TGA analysis of MIL-101 under 1.8 L h^{-1} N_2 at 5 °C min^{-1}

The anoxic thermal decomposition of MIL-101 appears to occur in a number of stages. The first stage (20 - ~130 °C) can be attributed to the loss of atmospheric adsorbents, particularly water. There is then a plateau between 130 – 200 °C, before a multistep thermal decomposition of the material. This plateau appears to be the last region of stability in the mass before the material starts to break down, so it appears to be that MIL-101 is stable in anoxic conditions up to ~ 200 °C.

The TGA run on a dry weight basis (i.e. with the mass of adsorbents removed) is presented in Figure 4.19, and allows for a closer investigation of these processes. This figure illustrates that the majority of the variation in the runs in Figure 4.18 were due to the varying weights of adsorbent in the samples, and there is good repeatability in these data.

The main thermal decomposition appears to be broken up into three stages: a small drop from 200 – 300 °C; a large drop between 300 – 550 °C; and a relative plateau above 550 °C, albeit with a small drop at the very end of the run. The very large drop is very clearly where the bulk of the organic fraction of the MOF thermally decomposes. In particular, terephthalic acid (the fully protonated form of the bdc linker that constitutes MIL-101) is known to thermally decompose at 300 – 330 °C, therefore is a simple connection to suggest that the breakdown of bdc causes this large mass loss. As there will also be terephthalic acid adsorbed in the pores that may not have been driven off in the early heating; these molecules will also be thermolysing at this point. This multiple step decomposition has been reported for MIL-101 before [324, 325], although there is little available information as to why these multiple drops exist, as it is very common to ignore these smaller drops and solely acknowledge the large decomposition step caused by bdc thermolysis.

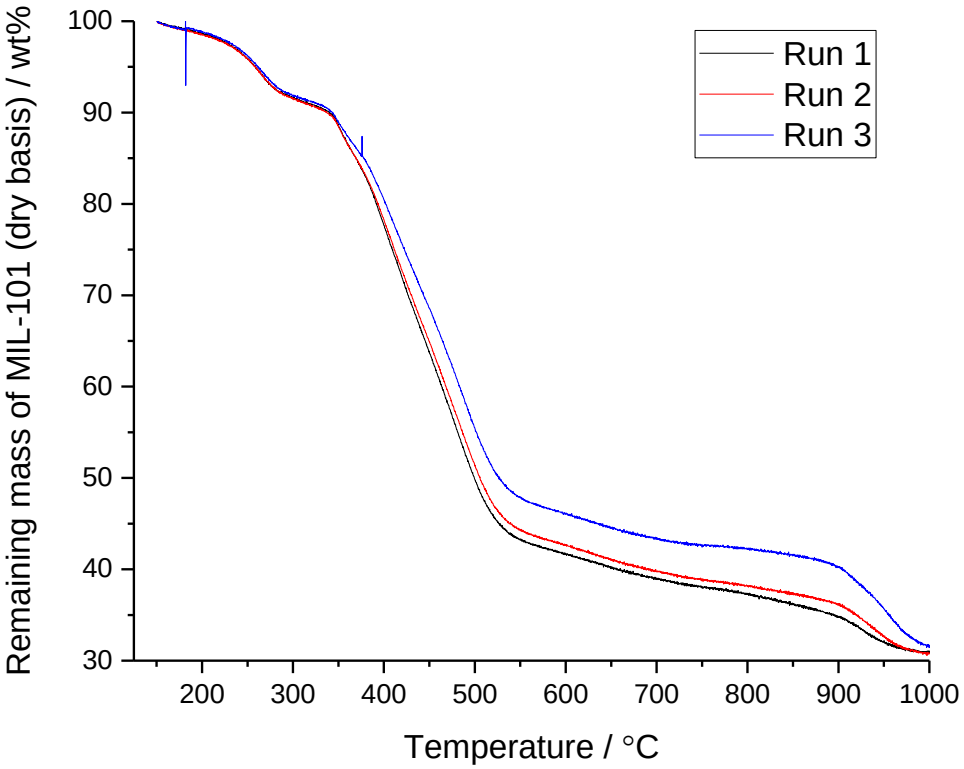

Figure 4.19 - TGA analysis of MIL-101 (dry weight basis) under 1.8 L h^{-1} N_2 at 5 °C min^{-1}

The differential thermogravimetric analysis (DTG) curve presented in Figure 4.20 allows a more detailed examination of the mass losses present. This differentiation was performed with respect to time by the SetSoft 2000 software, but for the purposes of examining mass against temperature, the d(mass)/d(time) curve can be divided by the heating rate (5 °C min^{-1}, a constant) to give the DTG curve with temperature as the independent axis.

Figure 4.20 clearly presents the three separate regions of thermal decomposition identified above. However, it also appears to show that the region of major mass loss is not a single drop but instead three distinct regions of mass loss, potentially indicating that different mechanisms of bdc breakdown are working. However, identifying these separate mechanisms is difficult to do from the analyses present (even the TG-MS data in Figure 4.21 does not show significantly different products between the peaks in this region), and thus for the purposes of this study it is accepted that this entire region is that in which the bdc linkers within the MIL-101 structure thermolyse.

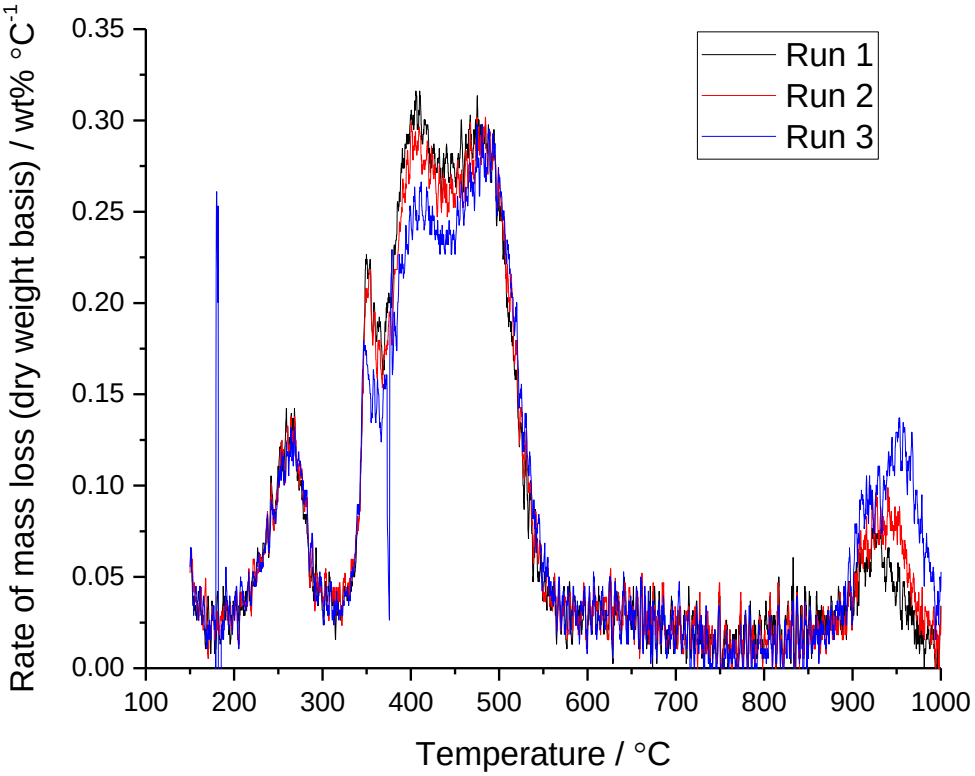

Figure 4.20 - DTG curve against temperature for MIL-101 TGA analyses (dry weight basis)

In order to gain further insight into the decomposition of MIL-101, TG-MS (TGA in which the outgasses are passed into a mass spectrometer) was run on MIL-101, the results of which are seen in Figure 4.21. The TGA curve under argon is identical to that under nitrogen, illustrating in both cases that the sample is thermolysing and not reacting with the carrier gas. For the majority of this run, the mass spectrometry signals confirm the degradation mechanisms: in the 0 – 150 °C region loss of mass is confirmed to be the loss of adsorbents, with a very strong response in m/z = 18 (H_2O) in this region; between 300 – 550 °C, there are strong responses from CO_2 (m/z = 44), H_2O and from higher m/z products indicative of fragments of the bdc linker, such as aromatic rings (m/z ~ 76) and fragments thereof in the 49 -54 and 62 -65 ranges. In the 'plateau' there is a strong response from m/z = 2 (H_2), 18 (H_2O) and 26 (CO), suggesting there is carbonisation of the carbonaceous products that survive the linker breakdown. Finally, the drop at the very end of the run is marked by spikes in CO_2, H_2O and CO, which suggests a further breakdown stage of the carbonaceous products.

However, the first major mass loss step on a dry basis, between 200 – 300 °C, is very curious, as there does not appear to be a clear reason for its cause – although there is a slight spike in CO_2 at this point, there is very little activity in most other signals. The one exception to this rule is m/z = 30, which shows a very clear spike in this region, although this does not correspond to a product that would be obviously present in the MIL-101 structure. The best estimates for this value are either COH_2, which might correspond to a fragment from the edges of the terephthalate in the sample, but the presence of 2 H atoms is unlikely as no part of either MIL-101 nor terephthalic acid has 2 hydrogens bonded (in any combination) to a carbon-oxygen bond. The other option is that m/z = 30 could correspond to NO, which would suggest that there is unwashed nitrate from the MOF precursor. However, there is very little evidence of any of the more oxidised nitrates (NO_2 at M/Z/ = 46 or NO_3 at m/z = 62) emerging at this temperature, which makes this an unlikely explanation, particularly given the multiple washing steps the MOF underwent to remove this reagent.

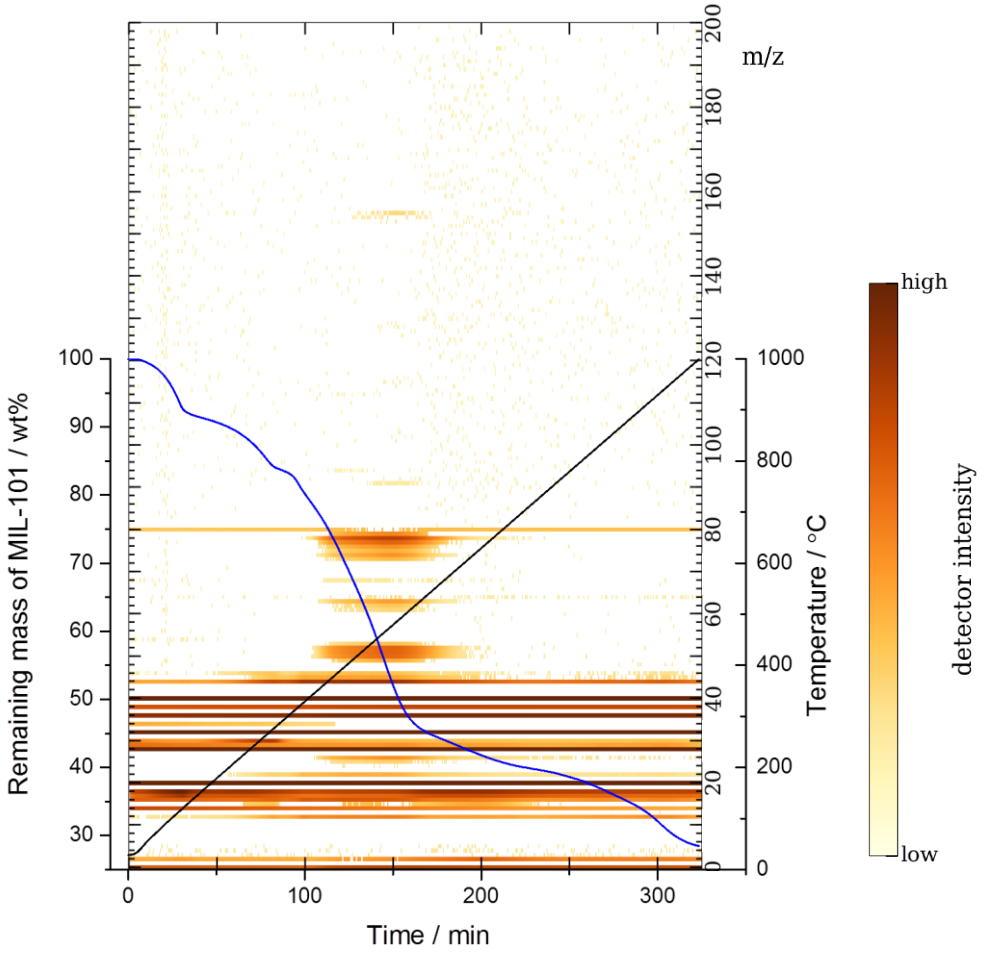

Figure 4.21 – TG-MS analysis of MIL-101 under 1.8 L h^{-1} Ar at 3 °C min^{-1}.

As well as studying the anoxic decomposition of MIL-101 for the purposes of degas temperature determination, knowledge of the response of the material to oxidative conditions is also useful, particularly when considering this material in the case of a tank fire. The TGA runs on MIL-101 in air are presented in Figure 4.22.

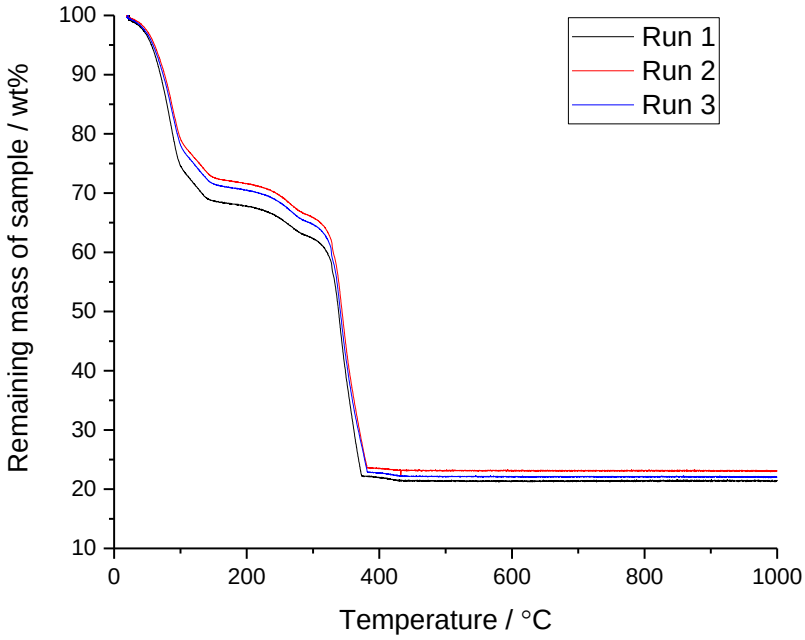

Figure 4.22 - TGA analysis of MIL-101 under 1.8 L h^{-1} air at 5 °C min^{-1}

The TGA runs in air appear to match those in nitrogen relatively closely in the early temperature range – there is an early loss in the 20 – 130 °C region due to adsorptive loss (albeit in this case there appears to be far greater amounts of adsorptive in the material; this is likely a function of the length of time the material has been left exposed to atmospheric conditions), and there is another loss in the 200 – 300 °C range, likely due to the same unidentified mechanism as in the nitrogen runs. However, above 300 °C, the organic linkers no longer thermolyse but instead combust, resulting in a very sudden loss of all of the organic material. This has all occurred by 400 °C, leaving only the chromium trimers which are not lost to the carrier gas flow. These latter two steps are clearly illustrated by the dry basis TGA curve and DTG curves presented in Figure 4.23 below.

As seen in in Figure 4.23 (a), the average remaining mass is 31.2 %, which is slightly higher than the 24.0 wt% that the Cr_3O trimers are estimated to contribute to the mass of MIL-101 based on stoichiometry. The difference is due to further oxidation of the chromium during the combustion of the organic linker. PXRD studies of the remains of MIL-101 after a TGA in air experiment were performed by Liu et al. [326], who demonstrated a very similar PXRD trace to that of Cr_2O_3, and subsequently stated they believed this was the final product of such a run. Assuming none of the chromium in MIL-101 escapes, then on a molar mass basis the end product should be 31.8% of the mass of the product that was started with – a very close value to the average seen in Figure 4.23 (a), and it is therefore likely that this end product is also chromium (III) oxide.

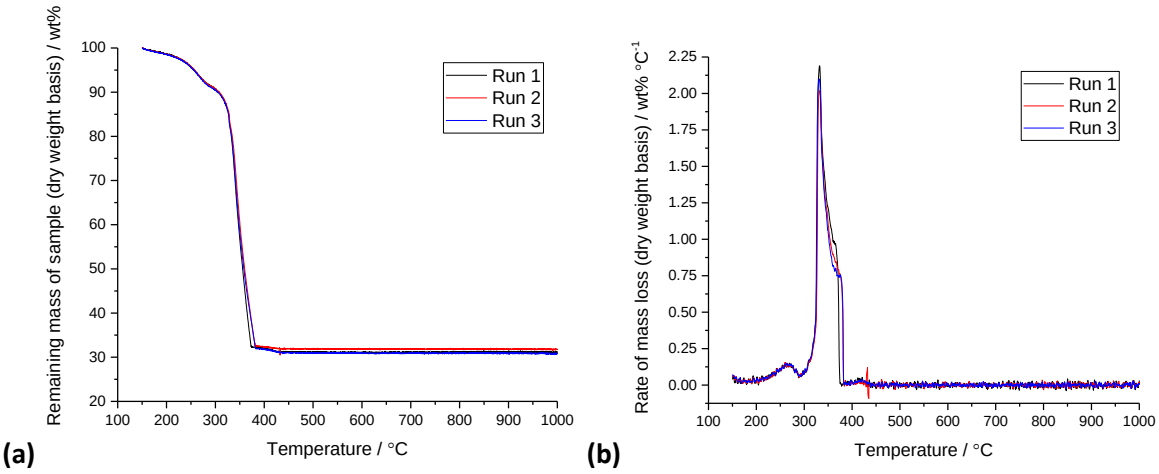

Figure 4.23 – TGA (a) and DTG (b) curves of MIL-101 under 1.8 L min^{-1} air at 5 °C min^{-1} (dry weight basis).

TGA runs on the PIM-1/MIL-101 composites were also performed under anoxic conditions. The results of these studies compared to those of the pure components is presented in Figure 4.24. These have been plotted on a dry weight basis to allow for a more accurate comparison of the decomposition of the materials.

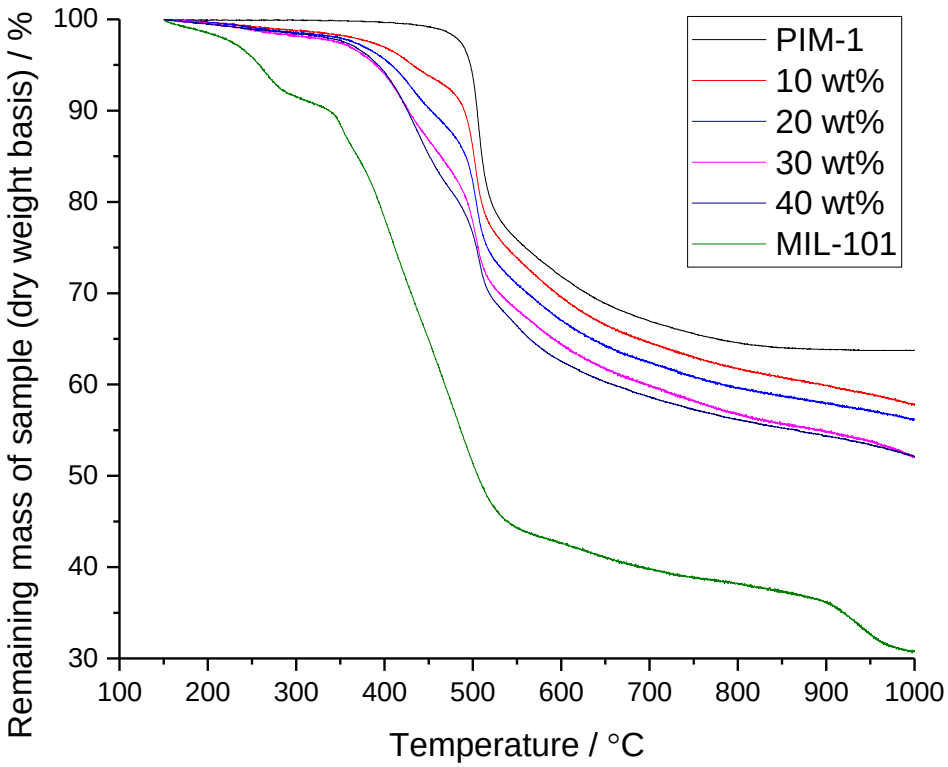

Figure 4.24 - TGA analysis of the PIM-1/MIL-101 composites under 1.8 L h^{-1} N_2 at 5 °C min^{-1} (dry weight basis), compared with TGA runs for pure PIM-1 and MIL-101 under the same atmospheric conditions.

Evaluating Figure 4.24, it is clear to see that there is a linear progression between PIM-1 and MIL-101 in the composites, based on the amount of each material contained. All of the materials showed good stability up to 200 °C, and then showed elements of the bdc linker decay at ~ 350 °C, then stabilising before a large drop due to the decomposition of the PIM at ~ 500 °C (TGA runs on PIM-1 are discussed extensively in section 5.1).

In order to see how closely the composites thermolysed compared to what might be expected if the two components therein acted completely independently, it is possible to compare these experimental values with a predicted curve, calculated by performing a rule of mixtures calculation on the dry basis weight remaining from the PIM-1 and MIL-101 runs for each temperature point. These comparative curves are presented for each composite in Figure 4.25.

Looking at Figure 4.25, there is clearly a very close match between the experimental and predicted TGA curves. This is evidence that in response to high temperature, the components in the composites behave independently, and do not appear to have a mutualistic effect. The biggest exception to this is the 40 wt% composite, which appears to show behaviour more like the PIM than would be expected for its MOF content. This may again show the dominance of the PIM top layer in this material.

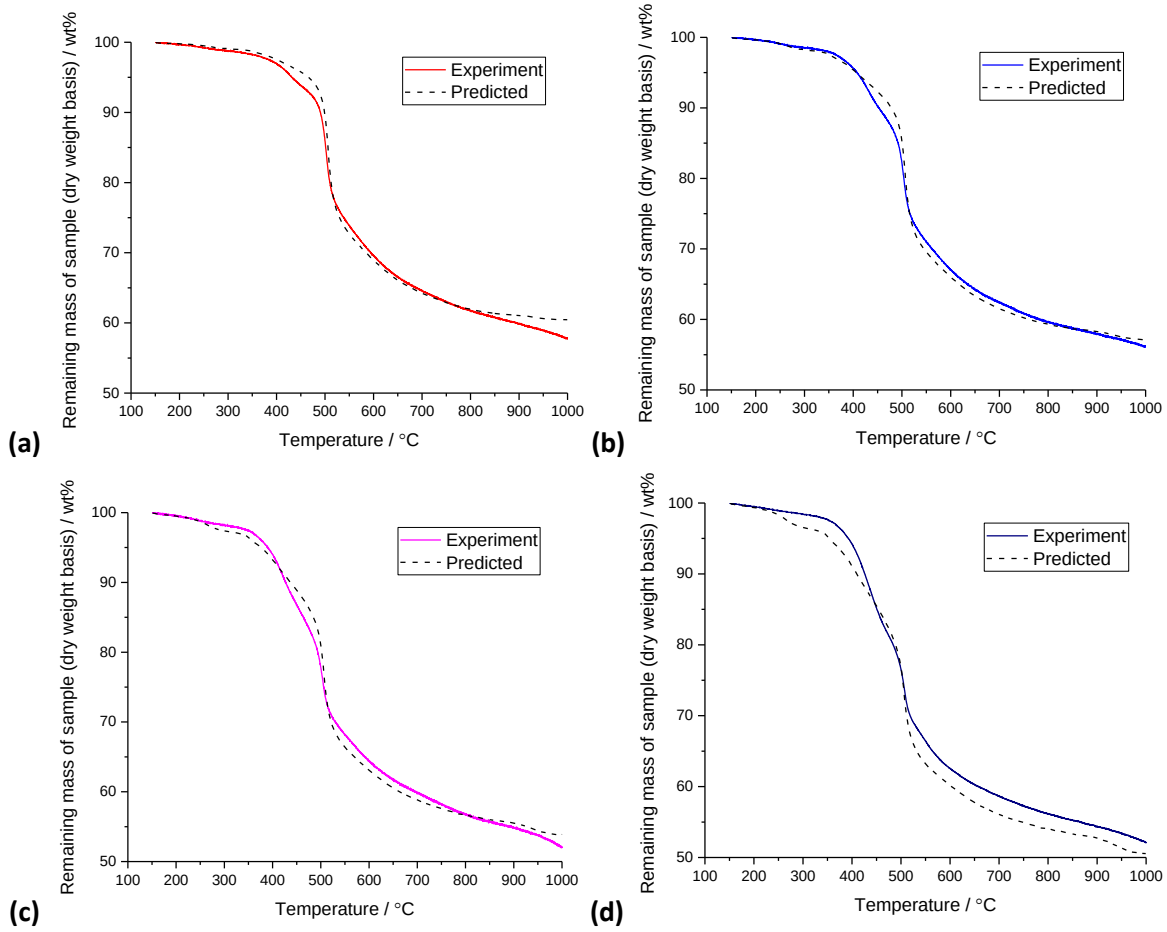

Figure 4.25 – Comparison between the experimentally determined TGA curve (N_2, dry weight basis) and the expected decomposition (calculated by rule of mixtures) for the (a) 10 wt% (b) 20 wt% (c) 30 wt% and (d) 40 wt% composite films.

4.6. Differential Scanning Calorimetry

The reversible heat capacities for PIM-1 film, MIL-101 and the composites were all calculated by TA Instruments' Universal Analysis software following the DSC runs, and are shown in Figure 4.26 below. The heat capacities presented are the reversible heat capacities as calculated by the software, as this value is equivalent to the true specific heat capacity of the materials, and removes factors such as phase changes and reactions (i.e. desorption).

The absolute value of the heat capacity for PIM-1 varies from 1.29 – 1.85 J g^{-1} K^{-1} for this temperature range, with a value of 1.36 J g^{-1} K^{-1} at 0 °C. These values seem reasonable for a polymeric material, given the values for other aromatic polymers, such as poly(ethylene terephthalate) (1.03 J g^{-1} K^{-1} at 0 °C) and polystyrene (1.11 J g^{-1} K^{-1} at 0 °C) [327]. There appears to be some slightly oscillatory behaviour in the low temperature region, although this appears to be an experimental issue, given that it occurs for all the samples shown in Figure 4.26. Taking longer between temperature transitions for equilibration may be one way to eradicate this error.

It is clear to see that the specific heat capacity appears to decrease significantly as the MIL content of the composites increases. Given that the specific heat capacity of a material depends on the ability of the material to convert the inputted heat energy into energy forms other than kinetic energy of the molecule (hence raising the temperature), this would imply that there the PIM-1 film has a greater ability to do this without the MOF particles present. This makes intuitive sense, as the presence of the MIL-101 particles may make it more difficult for the polymer chains

to elongate and bend as the particles provide a steric boundary into which the polymer cannot move and must go around. Limiting the chain behaviour like this would mean more incoming heat becoming kinetic energy of the chains, and therefore lowering the heat capacity. Increasing the concentration of MOF particles would further restrict polymer chain movement, and therefore exacerbate the drop in heat capacity.

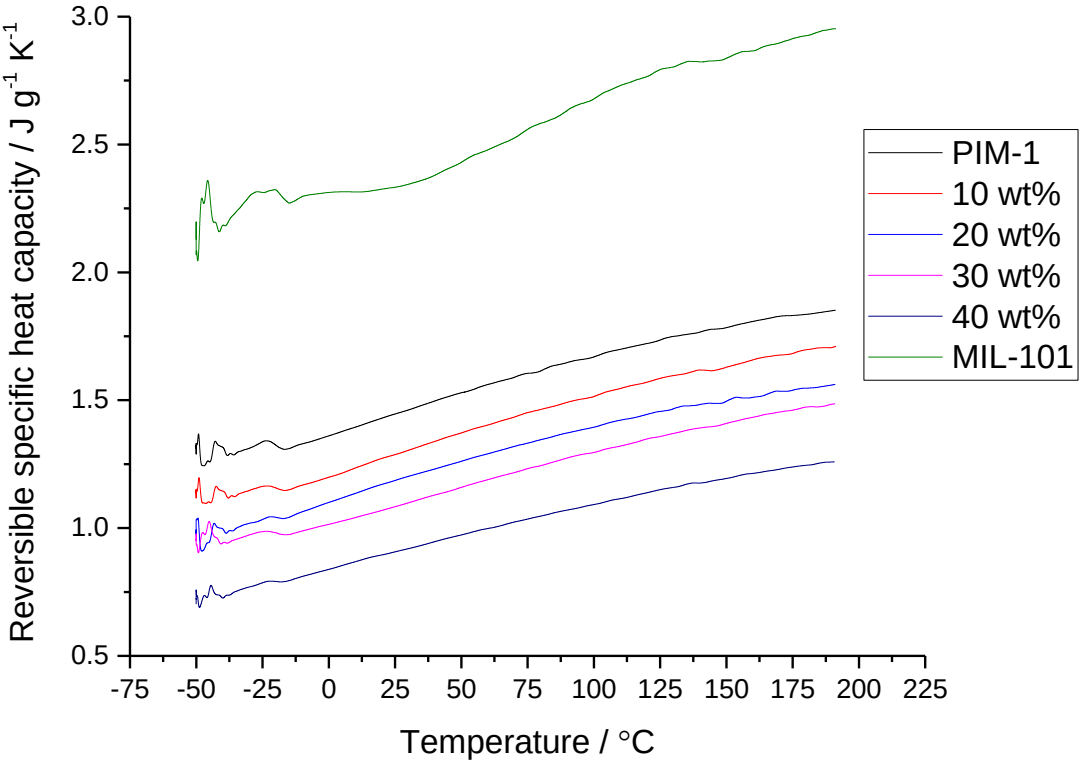

Figure 4.26 - Reversible specific heat capacities calculated for PIM-1 film, MIL-101 powder and composites thereof as calculated by TA Universal Analysis software from MDSC runs

Secondly, the specific heat capacity of MIL-101 powder alone is very high, compared to the rest of the materials tested. This is a rather unexpected result, given the very fixed structure of the material, which would allow for very small molecular bond stretching and vibration within the molecular lattice, but otherwise would simply gain kinetic energy and therefore raise the temperature very quickly. There is also empirical evidence is support this idea; Liu et al. [326] published a detailed MDSC study calculating the heat capacity of MIL-101 between -20 and 140 °C, estimating the value of the heat capacity to be between 0.336 – 0.967 J g^{-1} K^{-1} (241.90 – 695.75 J mol^{-1} K^{-1}) in this range. This lower heat capacity makes more theoretical sense, and also follows the trend seen in Figure 4.26.

Reflecting on the experimental protocol, there are two main reasons the value of the specific heat capacity of MIL-101 may be so different in this study. Firstly, the samples were not degassed prior to being sealed in the aluminium pans used for DSC analysis. The presence of any adsorbed water will have a great effect on the amount of heat entering the sample, and it was desired to remove this wherever possible, so a small hole was poked into the top of each sample pan, and a heating step in the DSC was introduced (the start of each run began with heating to 180 °C, holding at that temperature for 30 minutes, and then cooling down to the start temperature for the recorded experiment). It is possible that this degas step was insufficient for the MIL-101, and that some residual water in the sample had artificially raised the heat capacity.

The second potential reason for the overestimation is uncertainty in the mass measurement of the samples. Although great care was taken to weigh the pans before and after being loaded with sample, and before and after the degassed runs, the weight of the sample is cause for concern, particularly in the MIL-101 sample. This sample appeared to show a mass decrease of ~ 65% between the before and after measurement, which is far more than the TGA (in both air and nitrogen) suggested would be lost. If the mass of dry MIL-101 in the sample is assumed to be the calculated wet mass in the pan multiplied by the fraction of the mass suggested to be dry by the TGA, the heat capacity is calculated to rise from 0.6 to 1.1 J g^{-1} K^{-1} in the temperature range suggested, which is far closer to the values reported by Liu et al. [326]. Clearly, repeating these analyses would give a good indication as to the accuracy of the values presented in Figure 4.26.

4.7. Helium Pycnometry

The results of the helium pycnometry study on PIM-1 (2) are presented in Figure 4.27 below.

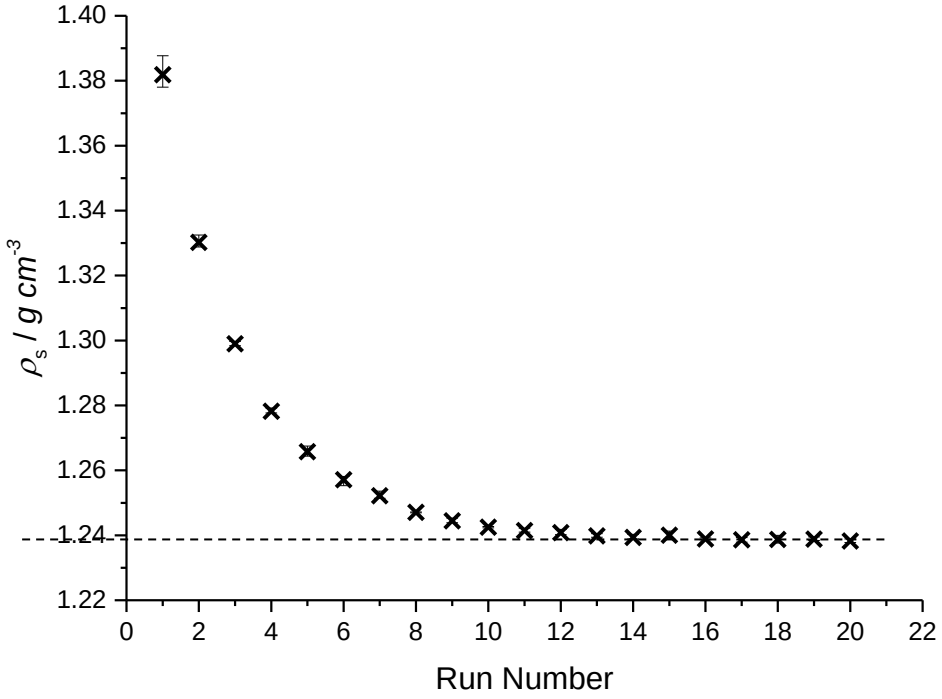

Figure 4.27 - Skeletal density of PIM-1 (2) powder as determined in each run of the helium pycnometer. Error bars show the range of values seen for a particular run. The dashed line shows the apparent settled value.

As expected, the skeletal density (ρ_s) determined by the pycnometer at each run decreases, as helium drives off any adsorbents/solvent left in the pores of the polymer, and thus more volume is accessible to the helium. The value of ρ_s determined in the later runs plateaus, and the true density is reached – in this case, the settled value appears to be 1.24 g cm^{-3}. This value is lower than the skeletal density of 1.4 g cm^{-3} proposed by the groups of Budd and McKeown [192, 193]. This could potentially be because of the low molar mass (the PIM-1 from method 1 was used for this study), or potentially because of unusually high inaccessible volume within the polymer, although the exact cause is as yet unknown.

One point of note from this study is that the value for run 1 of this experiment was 1.38 g cm^{-3}, which is very close to the value of skeletal density quoted by Budd and McKeown [192, 193]. It is unknown whether this value from literature is from a single measurement or from a series of runs of pycnometry, as very little detail on pycnometry measurements is discussed when reporting the value of the skeletal density; this is true of much of the porous materials literature. If the reported

value is indeed generated by a single measurement (i.e. by free volume determination in adsorption measurement equipment), then this material is highly comparable to that previously reported, and there is certainly more discussion to be had regarding the actual skeletal density of this material.

The results of pycnometry studies on PIM-1 (4) are presented in Figure 4.28 below. This trace is very similar to that seen in Figure 4.27, as would be expected given that this is fundamentally the same material. The initial skeletal density for PIM-1 (4) is lower than that of PIM-1 (2) (1.33 and 1.38 g cm^{-3} respectively), but both samples equilibrate at approximately 1.24 g cm^{-3}. This appears to reinforce the idea that the skeletal density is determined not by a single determination with helium, but through a number of runs; it would be very interesting to see studies like this on samples of PIM-1 from other sources to verify this finding.

The main difference between the two samples is the uncertainty in the PIM-1 (4) measurements, although the reason for this is unclear, given that this was performed on the same sample. However, it must be noted that PIM-1 (2) generally came out in harder, darker coloured chunks which may have been less compliant in the pressure of the pycnometer. The measurement of PIM-1 (4) also happened at a much later point than that of PIM-1 (2), so it is possible that the pycnometer may have developed a minor fault, or a component such as the greased o-ring may have degraded slightly, which would result in a more widely differing equilibrium pressure on the same run number for the same batch of material.

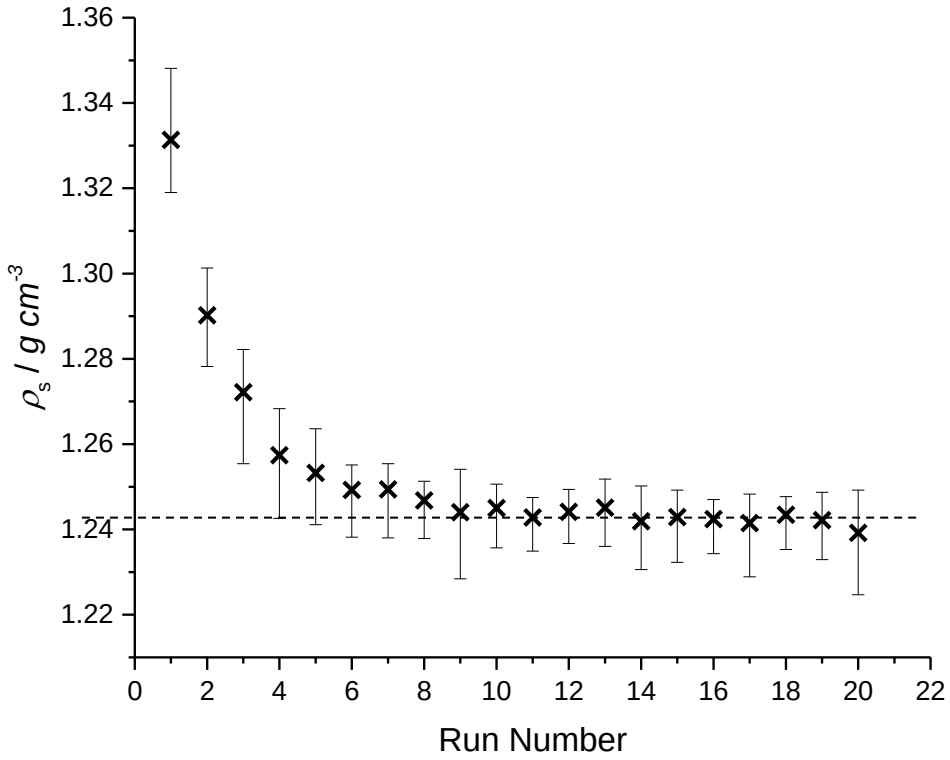

Figure 4.28 - Skeletal density of PIM-1 (4) powder as determined in each run of the helium pycnometer. Error bars show the range of values seen for a particular run. The dashed line indicates the apparent settled value.

The skeletal density determined by 20 pycnometry runs on MIL-101 is shown in Figure 4.29. The density varies with run number much like the behaviour seen in PIM-1, although given that this is a drying effect, it is to be expected. The value for ρ_s generated by run 1 is 1.59 g cm^{-3}, which is at the low end of values previously given for the skeletal density of MIL-101; previous studies in the Mays group have determined the skeletal density to be 1.67 g cm^{-3} [92], and the most complete study of MIL-101 density, performed by Ardelean et al. [143] quoted a helium pycnometry result

of 1.9 g cm^{-3} for the loose powder, decreasing to 1.61 g cm^{-3} for a pellet compressed to three times the density of the bulk powder. The low value found in this project may be due to a number of factors, such as the orientation of terephthalic acid in the pore blocking access pathways for the helium molecules in the pores, so resulting in an apparent volume that is greater than the true value. This being acknowledged, much as the pore volume within these materials can vary greatly (see section 2.5.2.4 for discussion on this point) based on the use of volumetric measurement, the helium pycnometry result can also vary greatly, and therefore a result that is within 6 % of previous studies can be seen as a reasonably corroborated result.

The value of ρ_s for MIL-101 decreases with consecutive runs, and the value appears to equilibrate at approximately 1.32 g cm^{-3}, which appears to be significantly lower than the values determined elsewhere, although this again may be a function of the approach to pycnometry taken – the lack of detail into the method of pycnometry used makes attempting a comparison on this value difficult.

The error present in this study is quite significant, which could either be due to faults within the pycnometer as discussed for PIM-1 (4) above, or due to the sample. Sample-induced error includes potential changes in the presence of terephthalic acid in the pore, which would open/close the availability of porosity depending on sterics; and on the low sample size used for this study. The AccuPyc 1330 is calibrated with a 6.372217 cm^3 standard, and the intention is to fill the sample chamber with as much sample as possible to reach a similar volume displacement. Unfortunately, because the individual samples of MIL-101 were to be kept separate in attempt to retain consistency of sample within the composites, single batch samples of total displaced volume approximately equal to 0.1 cm^3 were used, meaning a systematic error was induced, and a lack of precision in the experimentally determined volumes was induced.

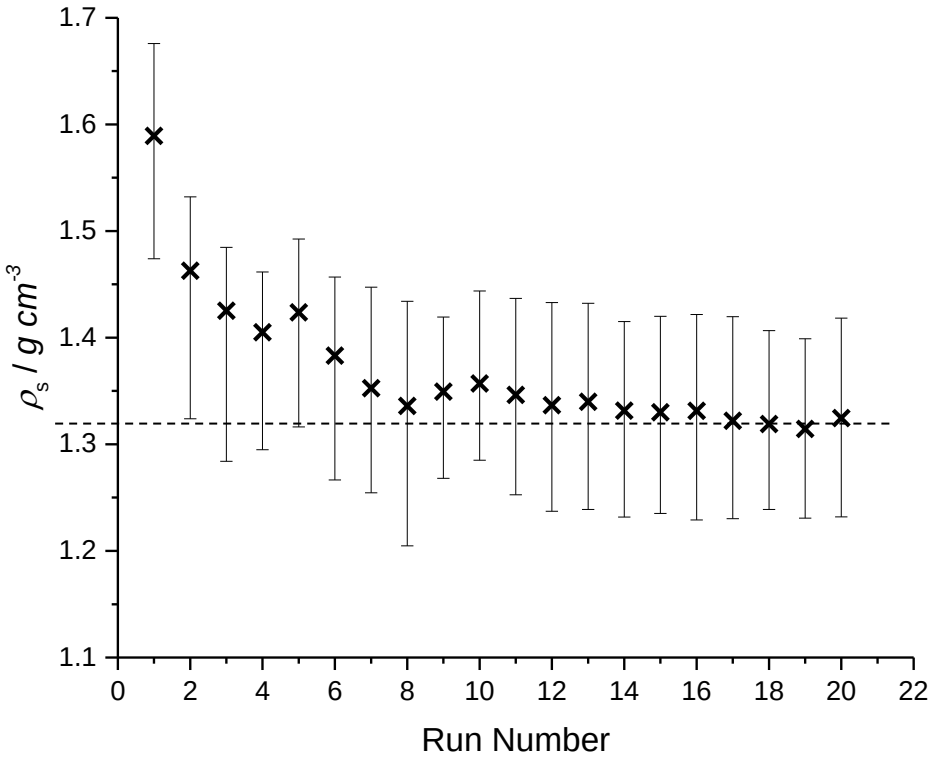

Figure 4.29 - Skeletal density of MIL-101 as determined in each run of the helium pycnometer. Error bars show the range of values seen for a particular run. The dashed line shows the apparent settled value.

Determining the skeletal density of PIM-1 films and the composites is more difficult, largely because it is difficult to gather together enough sample to get an accurate volume determination

in the AccuPyc 1330. One other method that can be used is the skeletal volume determination function in the HTP-1, which is a low-volume helium pycnometry measurement that must be performed before the high pressure hydrogen isotherms in order to correctly determine the gas adsorption. As both the mass of the sample and the skeletal volume of the sample is determined as part of the experimental setup, it is trivial to divide the mass by the skeletal volume to calculate the skeletal density. The skeletal densities for films of PIM-1 (2), PIM-1 (4), MIL-101 and the MIL-101 composites are detailed in Table 4.4 below:

Table 4.4 - Skeletal densities for all the PIM-1, MIL-101 and composite samples tested in the HTP-1 as determined by the machine's helium pycnometry function

Sample	Mass (g)	Skeletal volume (cm^3)	Skeletal Density (g cm^{-3})	Average Density (g cm^{-3})	Standard deviation of density (g cm^{-3})
PIM-1 (2)	0.0662	0.06994	0.947	0.9465	-
PIM-1 (2) film	0.0613	0.06918	0.886	0.8861	-
PIM-1 (4)	0.1175	0.09372	1.254	1.254	-
PIM-1 (4) film	0.1078	0.08472	1.272	1.321	0.057
	0.1271	0.09963	1.276		
	0.1285	0.09944	1.292		
	0.1063	0.07656	1.388		
	0.1018	0.07397	1.376		
MIL-101 (3)	0.0848	0.03595	2.359	2.384	0.036
	0.0665	0.0276	2.409		
10wt%	0.1034	0.0785	1.317	1.295	0.032
	0.1072	0.08426	1.272		
20wt%	0.0977	0.07387	1.323	1.323	-
30wt%	0.1003	0.07629	1.315	1.315	-
40 wt%	0.1094	0.07324	1.494	1.494	-

The values produced by the HTP's freespace functionality appear to estimate a range of values. It is very close to the pycnometer-determined value of 1.24 g cm^{-3} for PIM-1 (4), but shows strong disparity with the pycnometer generated values for PIM-1 (2) powder (0.947 vs. 1.24 g cm^{-3}) and MIL-101 (2.38 vs. 1.32 g cm^{-3}). As every effort was made to measure the correct, dry weight of the sample before loading into the HTP (samples were degassed in the vacuum oven for 2 hours and weighed immediately after before cooling), it is assumed that most of the observed difference is due to skeletal volume determination. There is a number of reasons why there may be a disparity in the measured skeletal volume:

- Sample size - only ~0.1 g of sample is used in the HTP. Compared to the several grams used in the AccuPyc, this has the potential to introduce sample bias, and it would be worth investigating multiple samples using this technique to ensure sample homogeneity.

- Pressure - The HTP commonly doses helium to 50 bar for its pycnometry experiments, rather than the 19.5 psi (1.34 bar) that the accupyc uses – this higher pressure will encourage greater penetration of helium atoms into the pore structure, and so should determine a smaller skeletal volume – as was the case for the MIL-101 sample. Whilst a higher pressure could also increase the risk of adsorption, the pycnometry is performed at room temperature, at which the risk of adsorption of helium is negligible, even at these elevated pressures.
- Lack of runs – In determining the skeletal volume, the HTP performs the pycnometry cycle 3 times and takes an average in order to determine the final volume. This may produce a discrepancy from the AccuPyc as in this system 20 runs are performed, with the volume determined for each run individually outputted, such that an analysis can be performed. It may also appear as though the sample in the HTP does not get the drying effect of being dosed with helium 30 times, but these samples are fully degassed in the HTP system before pycnometry measurement, so the presence of other adsorptives is not an issue.

Turning attention to the values of skeletal density for the composite films, there is a small increase in the skeletal density as the MOF content increases. This would be expected, given the presence of heavier elements in the MOF. The very small increases are expected given the values of ρ_s determined for PIM-1 and MIL-101 above.

4.8. Low Pressure Adsorption (≤ 0.1 MPa)

4.8.1. PIM-1 (2)

The nitrogen isotherm performed on PIM-1 (2) is shown in Figure 4.30 below. The isotherm presented here follows the trend of previous data very closely [185, 187]. There is clear evidence of both the type I(a) and type IV(a) behaviours in the low and medium pressure ranges respectively. There is also a strong hysteresis present, as expected in PIM-1; this is largely due to narrow channels that constrict mass transfer into the larger micropores [185, 192, 202].

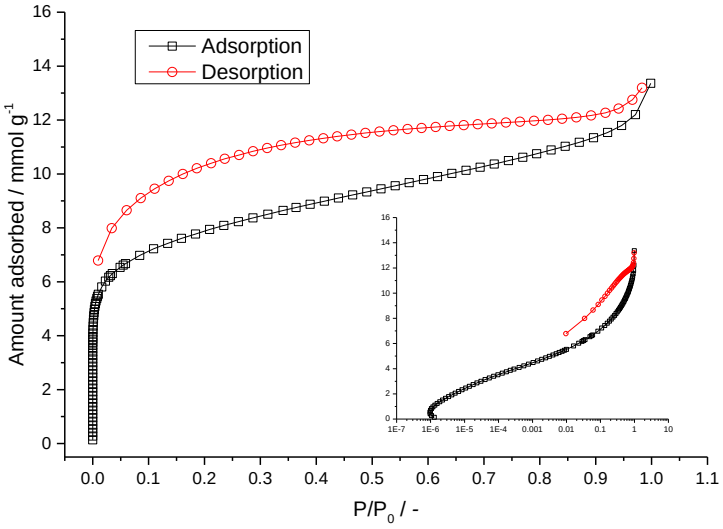

Figure 4.30 - N_2 isotherm for PIM-1 (2) at 77 K. Inset graph is the data plotted on a logarithmic abscissa. Lines are for the purpose of guiding the eye only.

The main differences between this isotherm and those reported in literature are the absolute value of adsorbed nitrogen, which is lower in this case (PIM-1 can adsorb as much as 20 mmol g^{-1}

at P/P_0 = 1 [185]), and the desorption loop is missing a sudden drop in the adsorbed amount at P/P_0 ≈ 0.5. Such sharp drops in the isotherm are often caused by the emptying of pores in which capillary condensation has taken place [71].

When this process is performed on the nitrogen isotherm in Figure 4.30, a value of 592.5 ± 16.5 $m^2 g^{-1}$ is achieved. This is a reasonable value, although it is short of the 750 – 860 $m^2 g^{-1}$ that has been reported for PIM-1 in the past [185, 187]. This drop in surface area is potentially caused by the lower molar mass achieved in this synthesis than those reported in literature (76261 g mol^{-1} vs. > 100000 g mol^{-1} [187, 190]), as longer chains will feel greater steric frustration due to the larger number of kinks in the chain, and the smaller number of chain ends that can fall into free volumes within the material.

However, this value is obtained using the standard P/P_0 = 0.05 – 0.3 range for surface area determination, a methodology that has been proved to be highly inaccurate in samples with large proportions of micropores [74, 307]. When the Rouquerol criteria are applied the PIM-1 sample tested, it fails on both counts: above P/P_0 = 0.111, the value of $n_A(1-P/P_0)$ begins to decrease, and the value of C generated from the BET calculation is -210.97. In order to correct the BET surface area for the PIM-1 sample tested, these criteria were applied to the N_2 adsorption data using the Microactive software. A region of P/P_0 = 0 – 0.111 was selected, in which $n_A(1-P/P_0)$ continually rises. These data, along with the corresponding BET plot, is shown in the supplementary information. This BET plot gives a micropore adjusted BET surface area (henceforth known as a 'Rouquerol BET' value) = 621.2 ± 3.0 $m^2 g^{-1}$. This value is an improvement on the old BET value, as it is closer to the values for PIM-1 surface area reported in literature (although still showing noticeable discrepancy), and meets more of the consistency criteria for a true BET value, with a linear BET plot and a value for C of 2866.

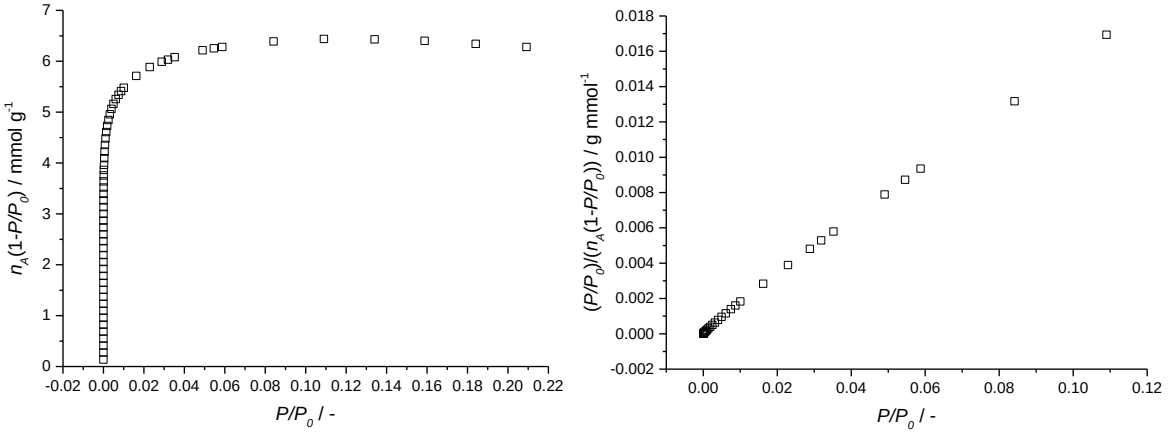

Figure 4.31 - Proof of fulfilment of the Rouquerol BET criteria for PIM-1 (2): (left) plot of $n_A(1-P/P_0)$ vs. P/P_0; (right) BET plot

PSDs calculated using most of these models are presented in Figure 4.32.

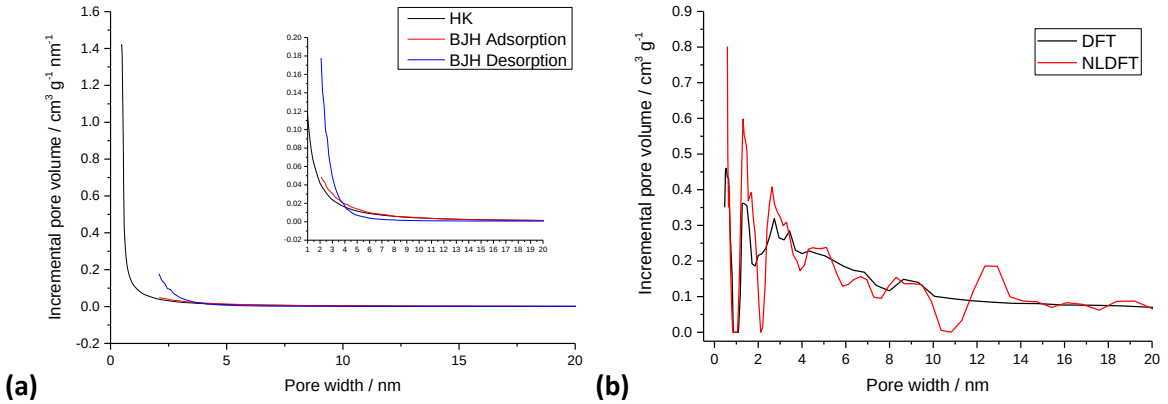

Figure 4.32 - Pore size distributions for PIM-1 (2) from the 77 K N_2 adsorption studies, as determined by the (a) HK and BJH, and (b) DFT models.

There is clearly a number of differences between the models. The HK and BJH distributions show unusually simplistic curves, peaking at the lower limit of each range (0.45 nm for HK, 2 nm for BJH), but both show a hyperbolic decay in the distribution as the pore size increases. This appears to closely match the pore size distributions presented by the groups and collaborators of Neil McKeown and Peter Budd, who on multiple occasions have demonstrated PSDs over the micropore range that closely resemble the data presented in this study [193, 203, 204].

It is also interesting to note from the inset graph in Figure 4.32(a) how close the HK and BJH adsorption curves are; despite HK's perceived weakness in the mesoporous region, it seems to closely trace the BJH curve in this instance. The BJH desorption curve also appears to show a much greater intensity of mesoporosity than the adsorption curve, as previously reported by Chaukura [205], albeit for a small range of pore widths (1.6 – 3.0 nm). Evidently, this is due to the large hysteresis seen in Figure 4.30, but may be an indicator of sorbent-induced swelling in the PIM, as larger pores are seen in the desorption curve than the adsorption. Alternatively, Jeromenok and Weber [202] theorise that data generated in the desorption curve of isotherms that show low P/P_0 hysteresis behaviour may be more representative of the available porosity, as the mass transfer limitations that stop larger micropores from filling effectively in the adsorption curve are not a factor in the desorption step.

The DFT results are very different. As well as appearing to show a different scale of intensity to the HK/BJH results, there is a much steadier decline in the pore size distribution over the nanopore range. DFT shows a large artefact in the distribution at ~ 1 nm. The NLDFT PSD uses a slit pore, carbon surface kernel for the calculation, and requires a regularization value of 0.0316; this value produces a slightly larger error in the goodness of fit, but at the benefit of a smoother distribution with a greatly reduced number of artefacts. The NLDFT appears to illustrate the same pore sizes that the standard DFT PSD does, only in sharper focus – in both PSDs there is a strong peak at 0.5 nm; a broad peak at 1.3 nm, and then the distribution begins to decline slowly, albeit with visible peaks at both 2.6 and 4.5 nm in the NLDFT trace. There is also a small plateau at 12.3 – 12.9 nm. Although there is little evidence in the research literature to corroborate a PSD calculated in this fashion, the free volume analysis performed by Staiger et al. [195] using PALS showed peaks at 0.49 and 0.93 nm for PIM-1 powder, which do align reasonable well with the DFT PSD data in Figure 4.32.

For this sample of PIM-1, the total pore volume is calculated as 0.463 $cm^3\ g^{-1}$ at P/P_0 = 0.998. This value can be corroborated by integrating the PSDs in Figure 4.32. Performing this calculation for the HK and DFT models (which cover the entire range of pore sizes) result in values of 0.463 and

0.412 cm^3 g^{-1} respectively, both of which show reasonable agreement with the single point value. However, these values fall short of the value of 0.68 cm^3 g^{-1} (at P/P_0 = 0.98) reported by Budd et al. [187], most likely due to the lower molecular weight and the greater ease with which the polymer chains will line up with one another. Given that all of the mesoporosity in these materials is 'locked in' at the point of reprecipitation, it is also possible that slight differences in polymer solution concentration, volume of methanol used and stirring speed may have contributed to fixing a different porosity into the PIM-1 powder, although it would be expected that any porosity change induced as a result of these factors would be lost when the films are solution cast.

For calculating the micropore volume of PIM-1 (2) using the DA method, an *n* value of 1 is chosen, and the micropore volume is determined to be 0.300 ± 0.001 cm^3 g^{-1}. Setting *n* to 2 (so applying the DR equation), this value is reduced to 0.230 ± 0.002 cm^3 g^{-1}. These values appear to be very high, given that the total pore volume of the material is 0.436 cm^3 g^{-1}, indicating the high proportion of micropores within the material. Looking at the nitrogen isotherm in Figure 4.30, this appears to be consistent, as approximately half of all the nitrogen uptake occurs before P/P_0 = 0.1. This is also in agreement with Budd et al. [187], who state that their analysis by the HK method indicate "a significant proportion of micropores in the 0.4-0.8 nm range." These values also fall within the 0.194 – 0.3495 cm^3 g^{-1} range given by computational calculations of free volume in PIM-1, which do not acknowledge the mesoporosity created by the reprecipitation [194, 212]. The micropore volume determined by the DA and DR methods can be further checked by integrating the PSDs above in the micropore range. Doing so for the HK and DFT models result in volumes of 0.257 and 0.179 cm^3 g^{-1}. These values show reasonable agreement with DR, although the statistical approaches give much lower values than either the DA or DR approximations. HK shows good agreement with these approaches, with a micropore volume between the two values given.

Following characterisation of the PIM powder, the next logical step was to try and perform the same on the PIM film. Whilst this was attempted with N_2 at 77 K, these isotherms took a very long time to complete in the micropore range (1 point every 12 hours), and the runs failed on multiple occasions due to equilibration errors after refilling the LN_2 Dewars. The length of equilibration for this material may be down to a combination of two factors: the restrictive pathways to the free volume in the material, which may be difficult for the gas molecules to access, given that the mesoporosity should have been removed from the material during the film casting process; and the temperature, as operating at 77 K results in slow diffusion and therefore further mass transfer limitations [328]. The narrow micropores in this material kinetically restrict the entry of N_2 molecules into the pore, which when combined with the slow diffusion kinetics of gases at low temperatures, results in a low rate of diffusion of nitrogen into the pores, so hindering the adsorption process and potentially providing under-equilibrated results, if any [329].

One well documented solution to this problem is to perform CO_2 isotherms as 273 K, as CO_2 has a very similar molecular diameter to N_2, but has a much higher condensation temperature, so avoiding the mass transfer limitations [328]. The CO_2 isotherm performed is shown in Figure 4.33.

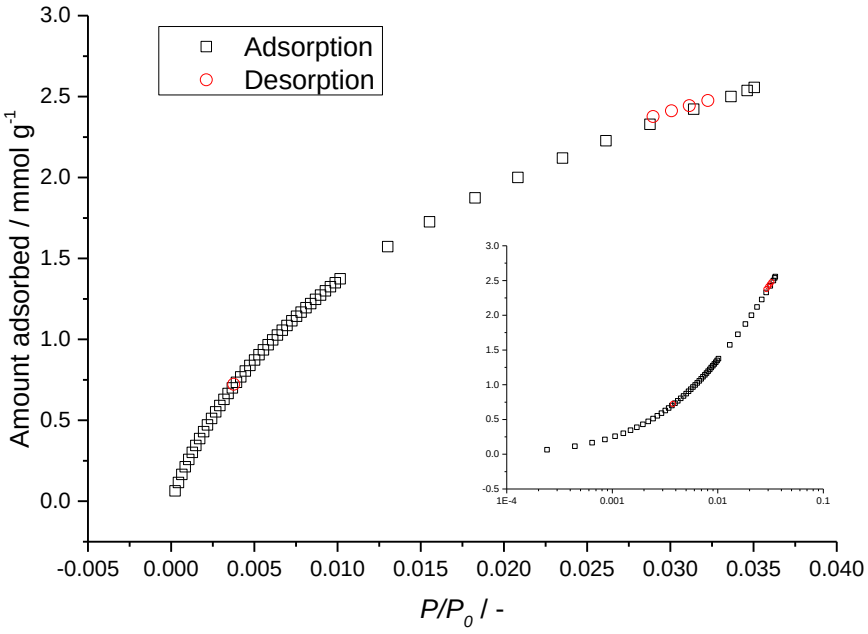

Figure 4.33 - CO_2 isotherm for PIM-1 (2) film at 273 K (P_0 = 0.1 MPa)

The isotherm shows a good uptake over a short range of low pressures, showing the presence of porosity in the film. These data also allows the calculation of a BET surface area, which if every point in the adsorption isotherm is used, is deemed to be 276.4 ± 4.4 $m^2 g^{-1}$. If a lower limit of P/P_0 = 0.01 is used (below which the BET graph is highly non-linear), this value increases to 310.9 ± 7.4 $m^2 g^{-1}$. This value is a rather large drop off from the PIM-1 powder, and is also much smaller than the film BET surface areas reported by Budd et al. [187]. However, this is another positive confirmation that porosity has been maintained through the morphology change, and that a PIM matrix would still act as an adsorbent.

It should also be noted that there is less general agreement on the cross sectional area of adsorbed carbon dioxide molecules than for nitrogen, for which the area used is that based on a close packed liquid-state layer on the surface (0.162 nm^2) [305, 306]. Although 0.21 nm^2 is the reference surface area for CO_2 molecules as set by BS ISO 9277-2010 [305], the value used for these surface areas is 0.142 nm^2, which has been calculated as the average area occupied by CO_2 in a solid-like adsorbed phase, and which has been corroborated with studies on activated carbons [330]. Therefore making direct comparisons between BET surface areas calculated with different gases is a difficult prospect, as the variations in these values can result in a wide variety of values that can skew comparisons.

The 1 bar pressure limit of the ASAP also causes many issues with these data. Because the vapour pressure of CO_2 at 273 K is 34.85 bar, the P/P_0 range that can be covered is very small (the maximum P/P_0 achieved in Figure 4.33 is 0.035), and therefore the adsorption behaviour of any pores larger than micropores will be ignored by these data. In addition, applying the validity criterion to the BET surface area achieved from these data results in a $\left(\frac{P}{P_0}\right)_{n_m}$ = 0.104, well outside the range of pressures used for this experiment. Therefore, whilst using CO_2 at 273 K has been a success in being able to generate an adsorption isotherm for the PIM film, the pressure limit of the ASAP 2020 has severely restricted the utility of the data produced, and a different approach must be considered.

Adsorbent characterisation of the PIM-1/MOF-5 film was not attempted. This is due to the fact that that material was a very thick and hetereogeneous material that would likely have suffered

equivalent, if not worse mass transfer issues for N_2 (at 77 K) experiments, and CO_2 (at 293 K) was not likely to provide a wide enough scope for adequate comparison of the composite with the films. In addition, the MOF-5 composite was manufactured a significant time before these experiments were produced, and it was unlikely that any adsorption characterisation performed on this material would be a true reflection of the composite's performance, given the possible hydrolysis of the MOF-5 in the intervening time.

4.8.2. PIM-1 (4)

The nitrogen isotherm for PIM-1 (4) powder at 77 K is shown in Figure 4.34.

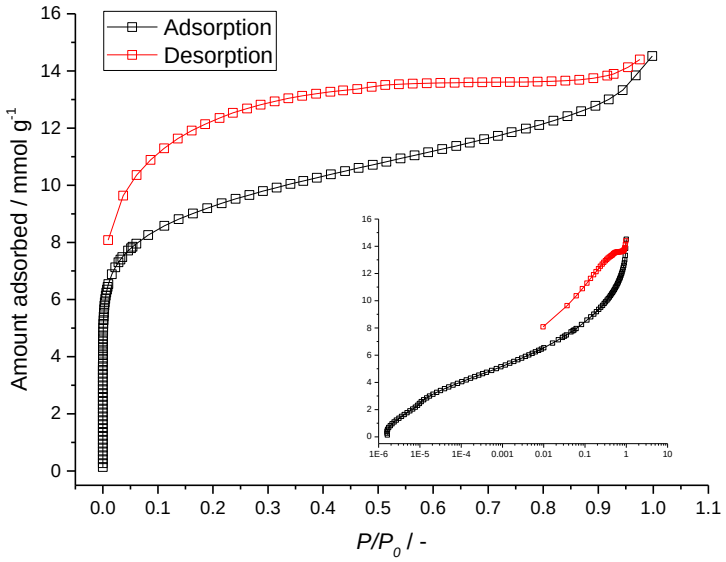

Figure 4.34 - N_2 isotherm for PIM-1 (4) at 77 K. Inset graph is the data plotted on a logarithmic abscissa. Lines are for the purpose of guiding the eye only.

Figure 4.34 shows an isotherm very similar to both Figure 4.30 above and previous isotherms on PIM-1 powder reported in the literature [185, 187], as expected. This batch does however have a higher uptake than the previous sample, particularly in the microporous range (8.6 mmol g^{-1} at P/P_0 = 0.01 and 14.5 mmol g^{-1} at P/P_0 = 1 vs. 7.2 mmol g^{-1} and 13.3 mmol g^{-1} respectively for PIM-1 (2)). This results in a standard BET value of 688 ± 23 m^2 g^{-1} (although this also fails the Rouquerol criteria), and a Rouquerol BET value of 736 ± 3 m^2 g^{-1} over the range P/P_0 = 0 – 0.11. Proof of Rouqerol criteria fulfilment is provided in the supplementary information. These BET values are more typical of a PIM-1 powder, which may well be aided by the greater number averaged molecular mass (M_n) of this batch. Similarly characteristic large hysteresis loops are also demonstrated.

The pore size distributions for PIM-1(4) powder are shown in Figure 4.35 below. Generally, these PSDs are highly reminiscent of those presented in Figure 4.32, which is again logical given that these two samples are fundamentally the same material. The only differences of note are a small peak at 0.53 nm in the HK distribution when the range is focussed on the microporous range, and a similar small peak in the desorptive BJH calculation in Figure 4.35 (b), at 4.0 nm. The peak in part (a) has precedent, as a number of the previously reported PIM-1 micropore distributions [204, 206, 331] shows a shoulder peak in the HK calculation that otherwise interrupts a smooth hyperbolic decay in the available pore volume with increasing pore diameter. However, the mesoporous peak has no correspondence in the literature, so it is unknown whether this is an

undiscovered property of PIM-1 in the as-precipitated state, or simply a function of this particular batch.

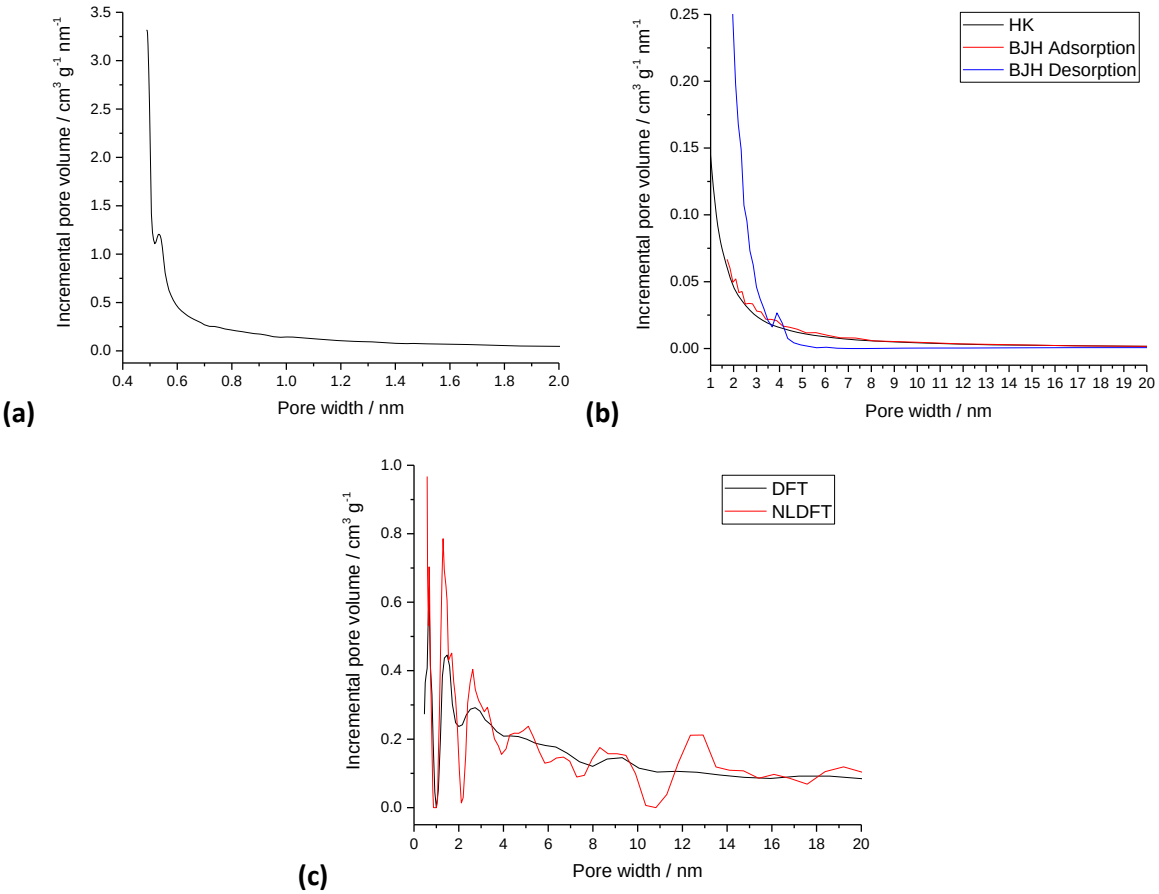

Figure 4.35 - Pore size distributions for PIM-1 (4) from the 77 K N_2 adsorption studies, as determined by the (a) HK, (b) HK and BJH, and (c) DFT and NLDFT models.

The density functional theory-based pore size distributions for PIM-1 (4) are nearly identical to those reported for PIM-1 (2), illustrating consistency in the material. The intensity of response in the microporous range is slightly higher, owing to the greater uptake by PIM-1 (4) in the low P/P_0 range, but the common pores identified are identical to that in PIM-1 (2).

The Gurvich pore volume for PIM-1 (4) is determined to be 0.503 $cm^3\ g^{-1}$ at P/P_0 = 0.998, and the total cumulative pore volumes determined by the HK and DFT models are 0.503 and 0.444 $cm^3\ g^{-1}$ respectively. This again falls short of the Budd et al. [187] quoted value for total pore volume, despite the fact that the GPC-determined M_n of this material was higher than that previously reported. However, the PDI of PIM-1 (4) was a smaller 1.52 than the 2.8 of Budd et al.'s sample, and it is possible that the presence of these much longer chains (and a more uneven chain length distribution) in the Budd et al. sample perhaps has more of a profound effect on the porosity of the material.

The micropore volume of PIM-1 (4) is determined to be 0.273 ± 0.002 or 0.360 ± 0.001 by the DR and DA (n = 1.0279) methods respectively. Integrating the HK and DFT PSDs up to 2 nm gives micropore volumes of 0.306 and 0.218 $cm^3\ g^{-1}$ respectively, again showing that HK provides a moderate value between those provided by the DA and DR methods, whilst the statistical thermodynamic approach proves a significantly lower value. Having established this, these values are higher than for PIM-1 (2) given PIM-1 (4)'s higher uptake in the very low P/P_0 range, but are

still mostly within the micropore volume ranges established by Budd et al. [187] and Larsen et al. [194, 212]. The DA value is higher than Larsen et al.'s upper bound, although this is relatively close, and adjusting the data over which the DA analysis is performed very quickly alters this value to within the range provided.

In addition to the sensitivity of the models to the data selected, it is also worth considering that the material is flexible, and any pore volume calculations performed could quickly become incorrect given the uncertainty over the action of solvation pressure on the porous structure, and the mass transfer limitations created by the tortuous porosity in the material [202]. In this case, the range of values given for both the total and microporous pore volumes in the material can be seen as a general guide, but calculating an accurate, fixed value, as is possible for more rigid and open porous materials such as MOFs, is unlikely.

4.8.3. PIM-1 (4) film

PIM-1 (4) films, whilst easy to cast, proved to be equally as difficult to characterise via N_2 adsorption as PIM-1 (2) had been, namely that any attempt to perform a full isotherm on the material with a view to extracting the pore size distribution and total pore volume data was made difficult by the impractically long equilibration times required for points in the very low P/P_0 range. However, it was still possible to perform short, higher pressure isotherms that provided enough information to calculate the BET surface area in the traditional manner, henceforth known as 'BET isotherms'. Although this method has large flaws as discussed in section 3.11.3, it was decided that some information for comparison was better than none at all, so the short N_2 isotherms were performed.

As discussed in section 4.1.1 above, early attempts at the manufacture of PIM-1 (4) films produced hard, translucent films with raised edges. When BET isotherms were performed on this material, the calculated surface area was 2.61 ± 0.12 $m^2 g^{-1}$, well below the resolution of the ASAP 2020, and a result that implied that the sample had shown no porosity at all. This was highly unexpected, given the large porosity shown by the powder morphology, and it seemed evident that something about the solution casting process had created this issue. It has previously been suggested that PIM-1 forms a thick outer layer upon solution casting that limits molecular transfer through the material [318], and to test whether this was the case, a section of film was cut up and then ground down in a pestle and mortar in order to remove any outer layer and provide open access into the middle of the material for gas molecules; an image of the ground-up film can be seen in Figure 4.36 below.

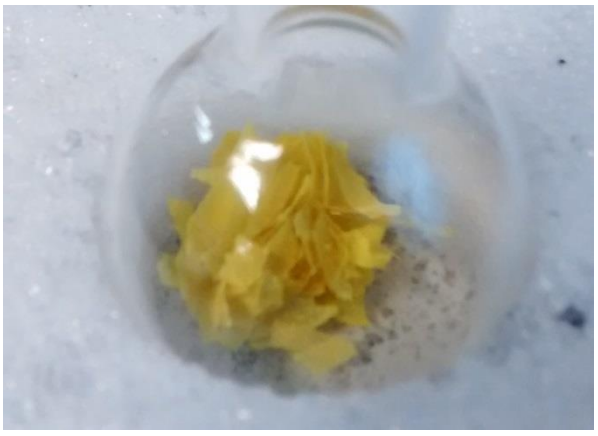

Figure 4.36 - Image of a ground down PIM-1 (4) film held in the glass container for isotherm analysis

A quick BET isotherm on the ground material resulted in a BET surface area of 590 ± 24 m^2 g^{-1}, a much more reasonable surface area given the surface area of the powder material. This was a clear demonstration that the solvent casting process had induced the issue, and a change to this process needed to be made. Thus, for other attempts, the glass petri dish containing the PIM-1 solution was not left solely with a lid on, but the covered dish was left in a glass evaporating dish which was further covered with a watch glass in an attempt to slow the rate of chloroform evaporation further.

Films produced using this slower evaporation method produced a film with a surface area of 540.7 ± 16.0 m^2 g^{-1} without any extra further processing, and all others produced after it, using this same method, all show reasonable uptake. It is therefore imperative that PIM-1 films (and the composites for this study) must be produced slowly to guarantee a minimal impermeable thickness on top of the film, although this may present challenges when moving up to vehicle-scale tanks, as producing large amounts of polymer without the dense outer layer will require a large time investment.

As a guide to the microporosity in the material, CO_2 (273 K) isotherms were performed on this material. This is shown in Figure 4.37 below. The uptake by the PIM-1 (4) film is nearly identical to that shown in PIM-1 (2), although there is slightly lower uptake in the higher pressures. This could either be due to a lower micropore surface area or volume, although this would be counterintuitive given that PIM-1 (4) powder has been shown to have the greater nitrogen uptake and therefore a greater volume of micropores, which should be carried through to the film.

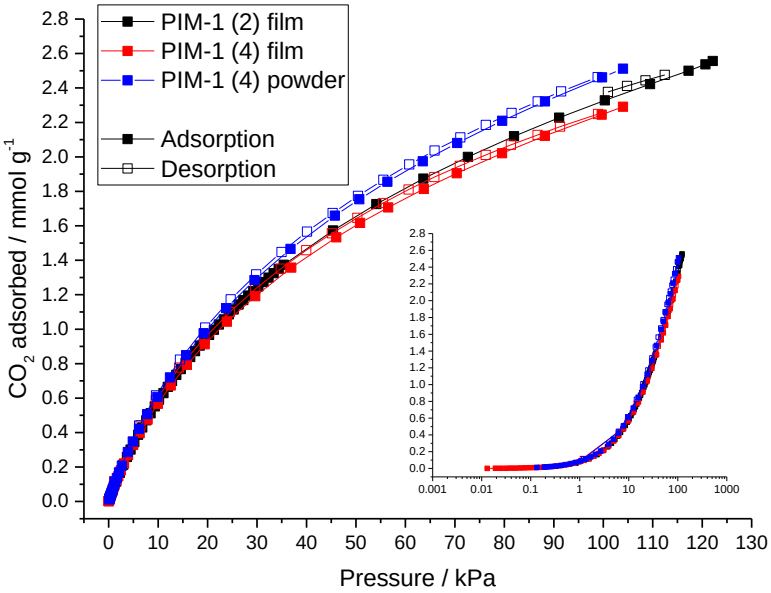

Figure 4.37 - CO_2 isotherms at 273 K for PIM-1(2) film (black) , PIM-1 (4) film (red) and PIM-1 (4) powder (blue). Lines are provided for guiding the eye only.

Alternatively, it could be an issue of mass transport; either the impermeable film formed on PIM-1 (4) films is not entirely lost with the slower evaporation method, or the porosity in the PIM-1 (4) film is more tortuous than that in PIM-1 (2), and so demonstrates a pseudo-equilibrium of lower uptake. However, given that both isotherms are fully reversible, there is no evidence for trapping of CO_2 in larger pores that may be blocked by smaller ones; in this P/P_0 range, it is expected that it is those narrow channels that will be filled, but with little or no interaction with larger pores.

The film morphologies of both PIM-1 batches show inferior CO_2 uptake to the powder form of PIM-1 (4). This is likely due to the loss of 'locked in' porosity when the polymer is solution cast,

both in terms of a small number of micropores that are lost, and primarily in terms of meso-/macroporosity present that facilitated mass transfer into the material.

Although the BET surface area is of limited use in terms of absolute material characterisation on these limited P/P_0 range, it is still useful as a tool for comparison of the uptake of the different materials. The calculated surface areas for the PIM-1 (4) powder and film materials were 327.4 ± 3.9 and 293.7 ± 3.5 $m^2 g^{-1}$ respectively. These values compare reasonably well to the 310.9 $m^2 g^{-1}$ value calculated for the PIM-1 (2) film, and the same trend as the isotherms themselves; namely, that the available area in the PIM-1 (2) film is slightly greater than that of the PIM-1 (4), but the powder material has more available micropore surface area than the films.

Low pressure hydrogen adsorption studies for PIM-1 films proved to be more difficult that both the nitrogen and carbon dioxide studies reported above, largely due to inconsistencies in the isotherms produced by the material. All of the isotherms performed on PIM-1 (4) films on the 3-flex are shown in Figure 4.38 below. It is immediately apparent when inspecting these isotherms that there is a wide spread of uptakes apparent from the 8 runs presented, which given that these were all performed on the same material, highlights some significant issues.

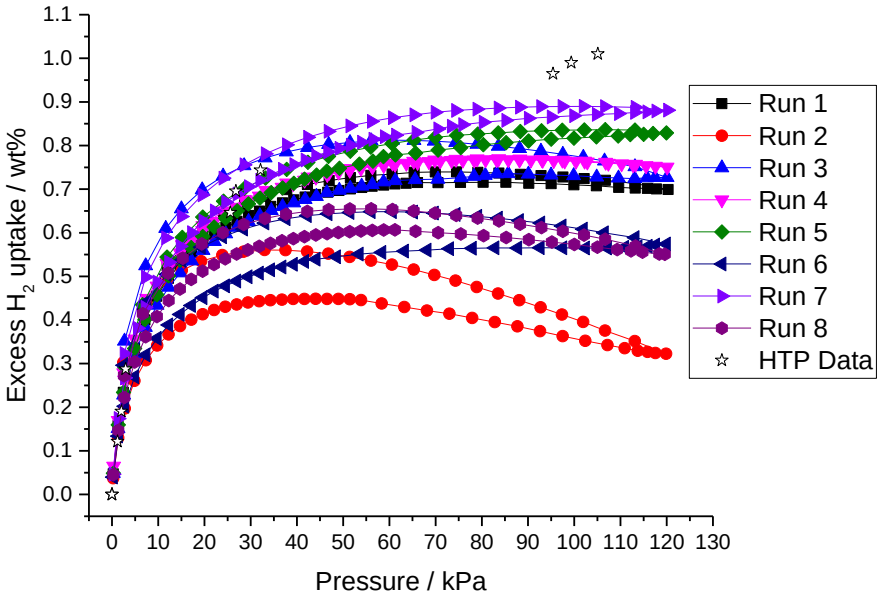

Figure 4.38 - Low pressure (0.1 MPa) H_2 isotherms on a number of PIM-1 (4) films at 77 K. Lines are provided to guide the eye only.

The first unexpected feature of many of these isotherms is the downward slope of some of the adsorption isotherms near 100 kPa. This is a very unexpected result given the very low density of bulk hydrogen at this pressure, and therefore the Gibbs excess adsorption should be nearly equal to the absolute amount adsorbed, which should proceed as a Type I isotherm. This unexpected shape is very likely due to issues with freespace determination. In the same manner that nitrogen diffusion into the pores is heavily impeded by the pore structure of PIM-1, helium at 77 K may suffer similar issues. Further discussion on this issue can be found in section 4.8.4 below.

This inconsistency potentially highlights inconsistencies in the material, likely due to small variances within the film manufacturing process – the low uptake runs present in Figure 4.38 also usually showed much slower nitrogen uptake, even in the early points of BET isotherms, which may suggest that thick layers on the film are at least hindering the adsorption process, if not actively diminishing the amount adsorbed due to volume exclusion. As it is very difficult to 'split' the material into porous and non-porous sections, it would be difficult to verify this hypothesis.

Another interesting feature of these isotherms is that a number (most prominently runs 2,3, and 6) feature very large hysteresis loops. This is entirely unexpected for hydrogen adsorption under these conditions as hysteresis loops of this nature tend to indicate issues with mass transfer into and out of the pores. It would be expected that hydrogen very quickly permeates this material and therefore mass transfer should not be a major issue, but this remains the case. It is interesting to note that these desorption loops show greater uptake than the adsorption, and the point at which each of these desorptions then begins to lose hydrogen again as the pressure decreases is highly comparable to the uptake in the reversible isotherms. This may indicate that the issue in these film samples is not with the overall porosity and adsorptive capacity, but instead highlights an issue of access for the adsorptive molecules to get into the pores.

The low pressure hydrogen uptakes for PIM-1 (4) in both powder and film morphologies are presented in Figure 4.39. The isotherm for the film in this figure is Run 4 from Figure 4.38; it was determined that this run is representative of the most common output from the 3-flex for this material.

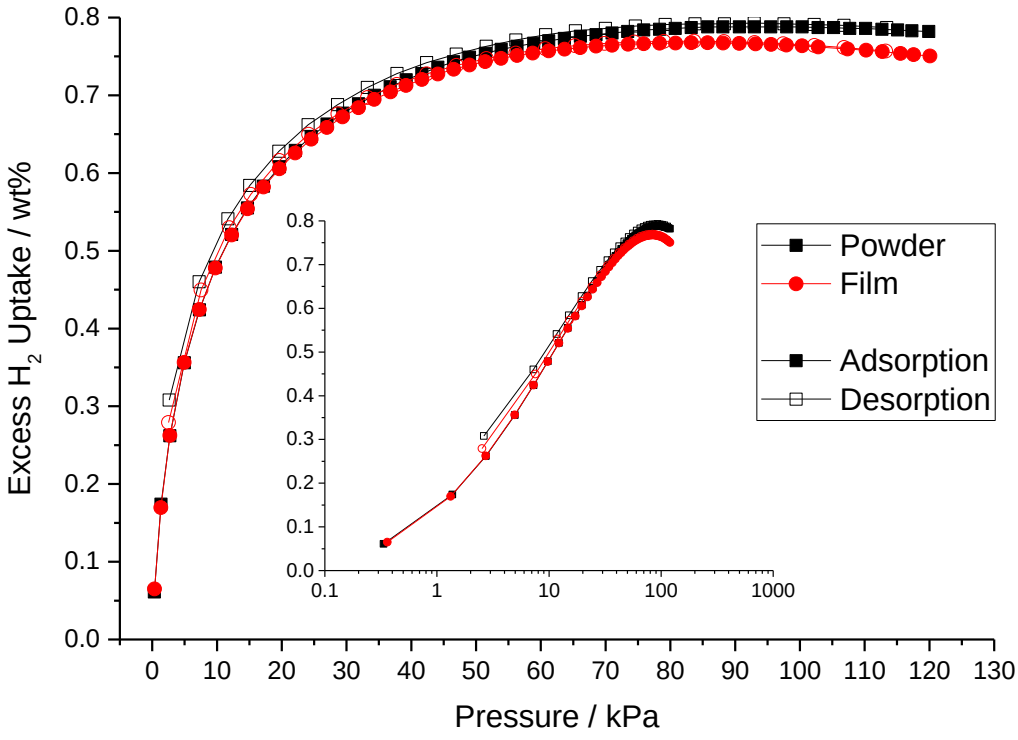

Figure 4.39 - Low pressure (0.1 MPa) H_2 isotherms at 77 K for PIM-1 (4) in powder (black) and film (red) morphologies. Lines are provided to guide the eye only.

From this study, we can see that PIM-1 shows very similar uptake between the powder and film morphologies. This clearly illustrates the maintenance of microporosity within the PIM-1, and potentially suggests that the film could be as potent a hydrogen storage adsorbent as the powder. Certainly, the difference in uptake for hydrogen between the two morphologies appears to be far less than for both nitrogen and carbon dioxide. However, this result must be taken with some scepticism, given the wide array of isotherms that was generated for the film. The powder on the other hand showed much more consistent isotherms between runs; these are shown in the supplementary information (SI-2).

4.8.4. Freespace Determination

A closer inspection of the determined free space values for the isotherms with downward slopes in Figure 4.38 appear to show a greater cold free space for these isotherms than those which have higher uptake without the decrease. This is the opposite of what would be expected if the issue was the exclusion of He from the pores, as such a limitation would result in a higher equilibrium pressure than expected and therefore a smaller free space value. The fact that the freespace is larger for these isotherms suggests that the equilibrium pressure is lower than otherwise would have been expected: this rules out both slow mass transfer (which would produce an artificially high equilibrium pressure) and gas leaking as causes. One possibility is that under these conditions the helium is partially adsorbing to the material, so causing the 'illusion' that there is more helium present by artificially reducing the pressure in the cold region.

In order to further test this issue of free space determination in the 3-flex, three PIM-1 samples were tested by first running a free space analysis on the empty tube, then loading a sample and performing two separate analyses: one in which the freespace is performed immediately after the degas, and a normal analysis in which the hydrogen adsorption isotherm is measured and then the free space is determined. The warm and cold freespaces determined by each experiment are given in Table 4.5 below.

Table 4.5 - Warm and cold freespace analyses from the 3-flex on three PIM-1 samples, comparing the blank, freespace first and normal isotherm values.

Experiment		Tube 1 (powder)	Tube 2 (film)	Tube 3 (film)
Blank tubes	Warm free space (cm^3)	22.4407	21.7558	22.2603
	Cold free space (cm^3)	71.2454	69.2013	70.4455
Freespace first	Warm (cm^3)	22.4759	21.7807	22.2638
	Cold (cm^3)	73.3553	70.1277	71.6676
Normal isotherm	Warm (cm^3)	22.7463	22.0560	22.4756
	Cold (cm^3)	73.2658	70.5902	71.7585

It is very noticeable from Table 4.5 that the blank tubes consistently report a lower cold freespace value than those with the sample in. Given that the exact same tubes were used in exactly the same manner for each experiment, this finding is remarkable, and appears to show clear evidence that the freespace measurement in this system is unreliable. However, in defence of Micromeritics, the company states in the 3-flex help guide that the best way to accurately determine the freespace is to create a blank tube file for each tube, and to use that file for each sample run in that tube. Based on the findings in Table 4.5, it would be prudent to follow this advice in future studies. This approach was attempted for the PIM-1 powder (tube 1); the results are in the isotherm shown in Figure 4.40 below. The isotherms produced with the measured freespace values and the uptake values produced by the HTP (see section 4.9.3) are also provided for comparison.

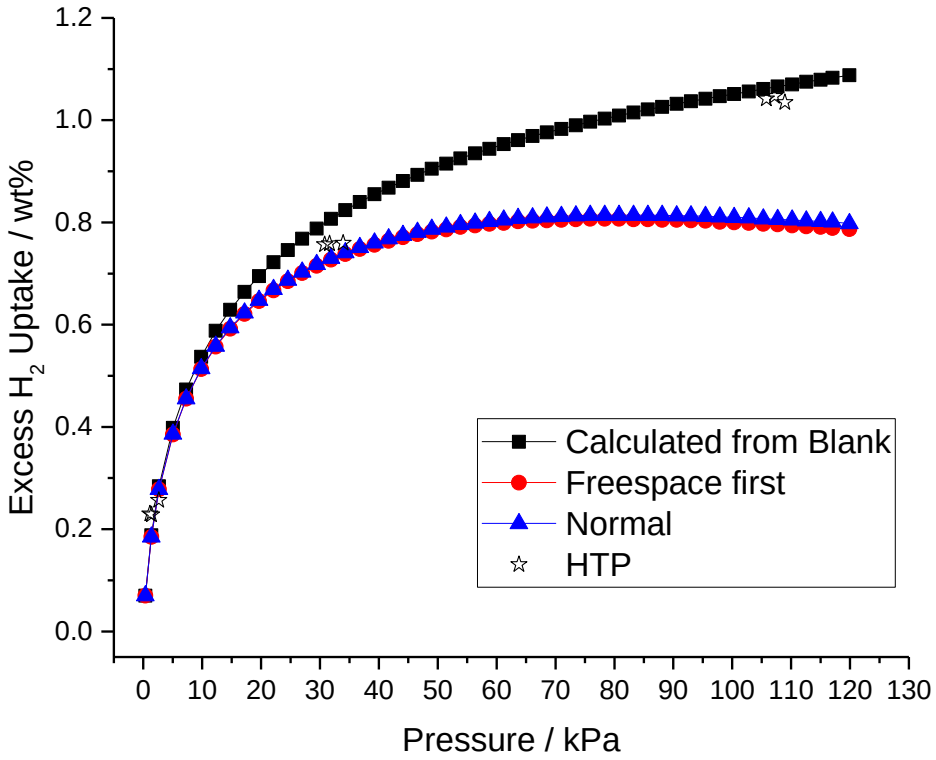

Figure 4.40 - PIM-1 (4) powder isotherms using different freespace determination methods: calculated from the blank tube; freespace measurement before an isotherm; and the normal isotherm sequence. HTP data on the same material are provided for reference. Lines are provided to guide the eye only.

It is very clear from this figure that using the freespace calculated from a blank tube clearly produces the best fit to the same data from another machine, which lends credence to the idea that this is the most accurate determination of the available free space in the tube. However, on a practical level, this is difficult to accomplish, as having a sample file for each tube requires knowing exactly which file corresponds to which tube (which is difficult on a departmental system when tubes are frequently swapped, borrowed and broken) and a new tube file is required for each new tube.

Perhaps the bigger downside to using this system is that in order to calculate the available freespace from a tube file, the sample file requests the skeletal density of the material. In the case of a sample such as PIM-1 powder, in which sufficient quantities have been synthesised to be able to determine this value using a dedicated pycnometer, this is not a problem. However, for samples like the PIM-1 film, this presents a serious issue, as there is no good way of determining the skeletal volume reliably (whilst the HTP could be used for this, again experimental realities prevail, and the demand for that machine is too high for it to be used as a small-scale helium pycnometer). As such, the 'in-house' freespace measurement is the best available tool for isotherm correction, and isotherms produced in this manner are still very useful for comparative studies, such as for the composite materials (see section 4.8.6).

4.8.5. MIL-101

The N_2 adsorption isotherm for MIL-101 is shown in Figure 4.41. This isotherm shape is expected for MIL-101, in that it generally follows a type I isotherm shape, but with the exception of two sharp rises at $P/P_0 = 0.1$ and 0.2; these are due to filling of the two large window types within the MOF structure [131]. The isotherm is fully reversible, as would be expected for a microporous material, indicating structural rigidity. The surface area of this material is calculated to be 2874 m^2

g^{-1}, although BET isotherms on some of the batches indicated a BET surface area as high as 3170 $m^2 g^{-1}$. These values align very well with previously reported values of MIL-101 [132].

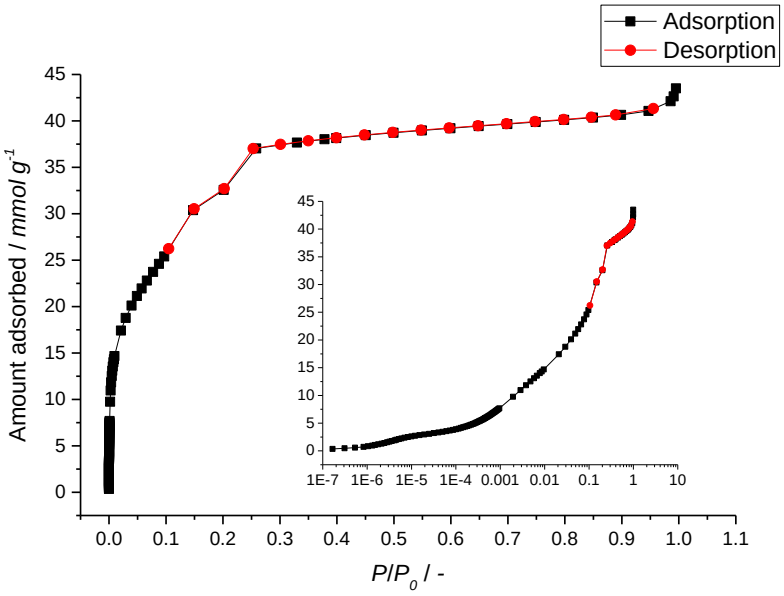

Figure 4.41 - Nitrogen isotherm for MIL-101 at 77 K. Lines are provided to guide the eye only.

The pore size distributions for this material are shown in Figure 4.42 below. In general, all of these PSDs appear to display the trimodal pore sizes that are expected from MIL-101 (at 0.7, 2.9 and 3.4 nm), albeit the varying models appear to show slightly different pore widths at which these responses occur. The HK distribution (a) shows a sharp response at 0.38 nm, and a very strong, reasonably broad peak at 0.58 nm. There is also a small peak at 1.28 nm. Whilst these values are slightly off what would be expected for MIL-101, the strong peak certainly gives evidence of the 0.7 nm cages in the chromium octahedra that were missed at first by the original study of Férey et al. [131]. Both the adsorption and desorption curves of BJH show two strong responses at 1.68 and 2.18 nm, which are likely the two mesoporous cages (2.9 and 3.4 nm) identified by Férey et al. There is also a small upturn at the very start of the BJH adsorption curve, which may be indicative of the microporous voids within the tetrahedra.

The density functional theory distributions show a similar response. The DFT curve shows three major peaks at 0.4, 1.34 and 2.16 nm, whilst the NLDFT curve has three peaks at 1.36, 1.69 and 2.40 nm. Whilst these two theories do not align particularly well with each other, they both show trimodal pore size distributions with much of the porosity technically in the microporous region (< 2 nm). It is worth considering that the kernels used for these DFT calculations were for nitrogen adsorbing to a pure carbon surface, and therefore there is likely to be significant error in these distributions arising from the very different surface chemistry and geometry of the actual adsorbent.

One point to note about all of the peak locations in these distributions is that they are generally smaller than the commonly quoted 0.7, 2.9 and 3.4 nm pores in MIL-101. In this case, this smaller size is likely due to partial pore blocking by terephthalic acid that is strongly adsorbed to the chromium sites in the MOF, and may be reducing the available volume in the cages, so reducing the apparent pore size. It is also worth considering that these quoted values are Van der Waals' radii of the interior of the respective cages in the material, and therefore represent the largest possible available pore size [131, 133].

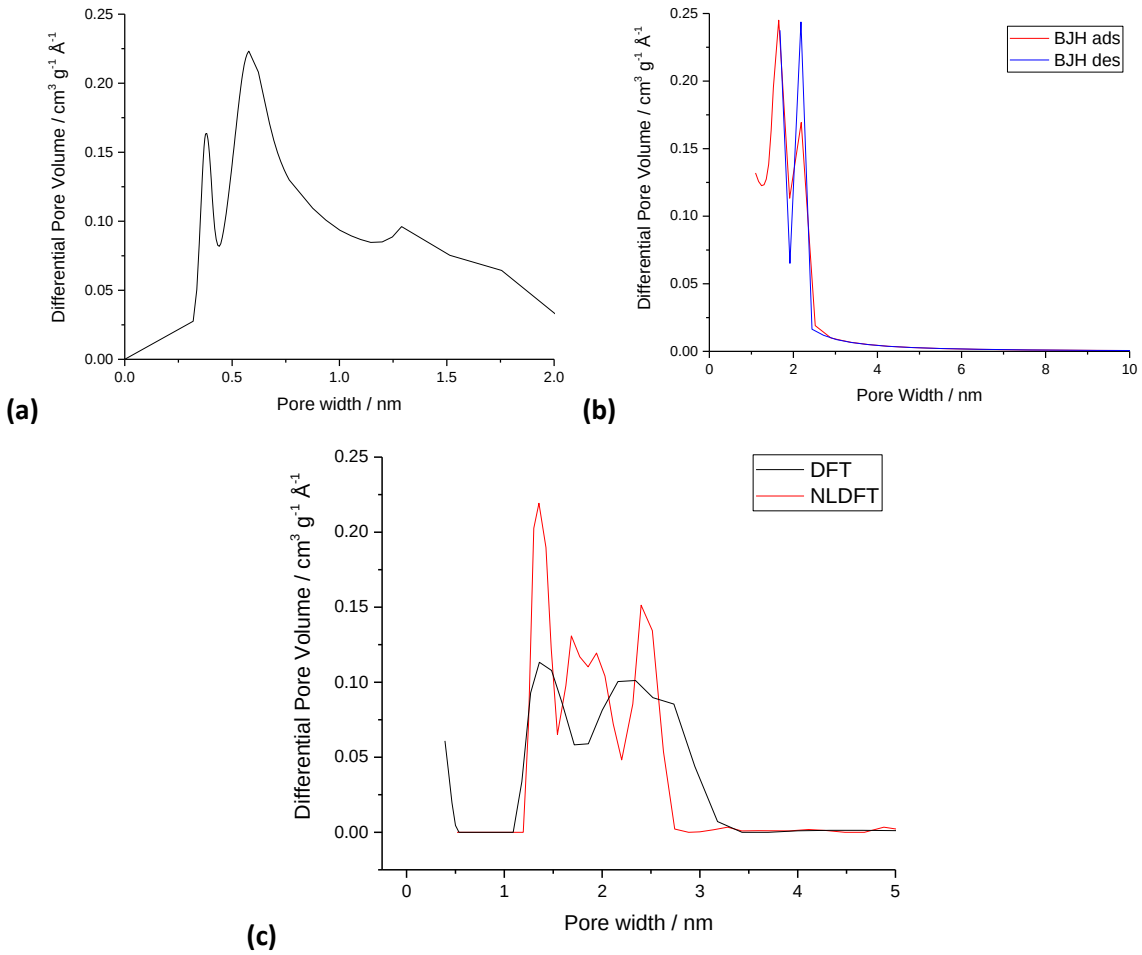

Figure 4.42 - Pore size distributions for MIL-101 calculated from the isotherm presented in Figure 4.41, using the (a) HK, (b) BJH and (c) DFT and NLDFT models

4.8.6. Composites

Once the PIM-1/MIL-101 composites had been synthesised, the first property to test was the nitrogen adsorption for surface area and pore volume calculations. Unfortunately, the presence of the MOF within the PIM did not sufficiently raise the rate of mass transfer into the film such that successful full nitrogen isotherms could be performed, and as such shorter BET isotherms had to be performed to be able to compare the surface areas of the materials. The calculated BET surface areas for both sets of composites, as well as the PIM-1 film and MIL-101 powder that compose these materials, is shown in Figure 4.43.

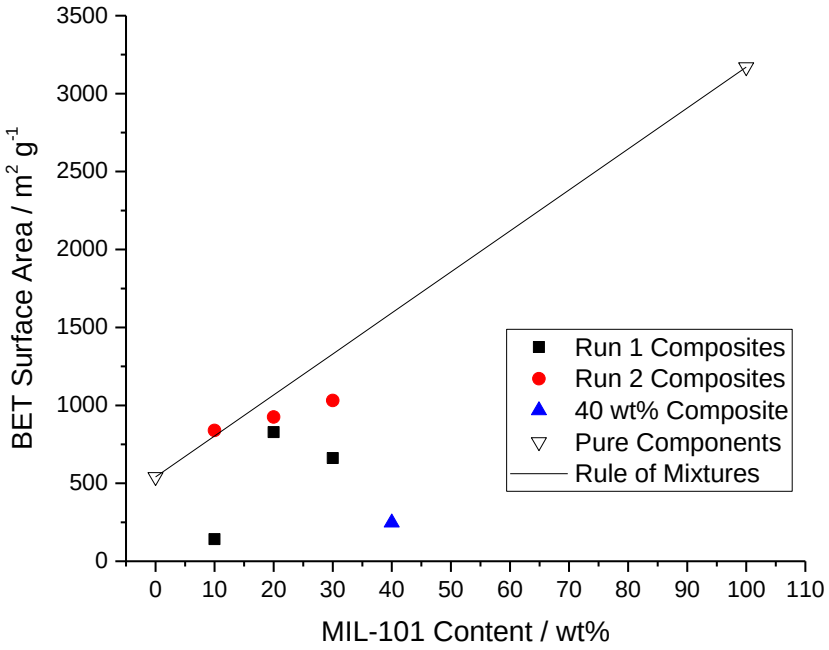

Figure 4.43 - Rule of mixtures analysis for the BET surface areas of the PIM/MIL composites.

Figure 4.43 clearly shows two distinct patterns. The second batch of composites appear to show a clear linear trend, which actually starts with a surface area above what would be expected by a simple rule of mixtures comparison, before trending below this line. The rate of distancing from the rule of mixtures for the higher MOF content composites appears to imply that the full porosity of the MIL-101 is not being accessed, seemingly because access to those pores is being blocked by the PIM-1 matrix, possibly due to the mass transfer issues discussed earlier.

For the first batch of composites (illustrated in Figure 4.6), the available surface areas for these materials are sporadic, and seem to show little correlation between the MOF content of the film and the nitrogen uptake. As these materials were visually heterogeneous and did not seem to show any behaviour in this test that could be labelled as characteristic, all further testing with these materials was abandoned, and the focus for the rest of this study was focussed on the composites made in run 2.

The BET surface area for the 40 wt% composite is far lower than would have been expected given the trend in the Run 2 composites, and this sample clearly has similar issues of gas transport that the Run 1 composites had, albeit perhaps for a different reason, given the clear differences between these material upon visual inspection. It seems likely that in this case the thick layer of PIM-1 that has built up on the surface is severely impeding the flow of adsorptive to the MIL-101 within the material. Despite this poor initial test, further characterisation was performed on this film in an attempt to gain insight into what the extra MOF content may do to the composite performance, and also what effect the layer on the film would have.

The available microporosity of the composites was evaluated using both CO_2 (273 K) and H_2 (77 K) isotherms. The isotherms, and the rule of mixtures analyses for their uptakes, are given in Figure 4.44 and Figure 4.45 respectively.

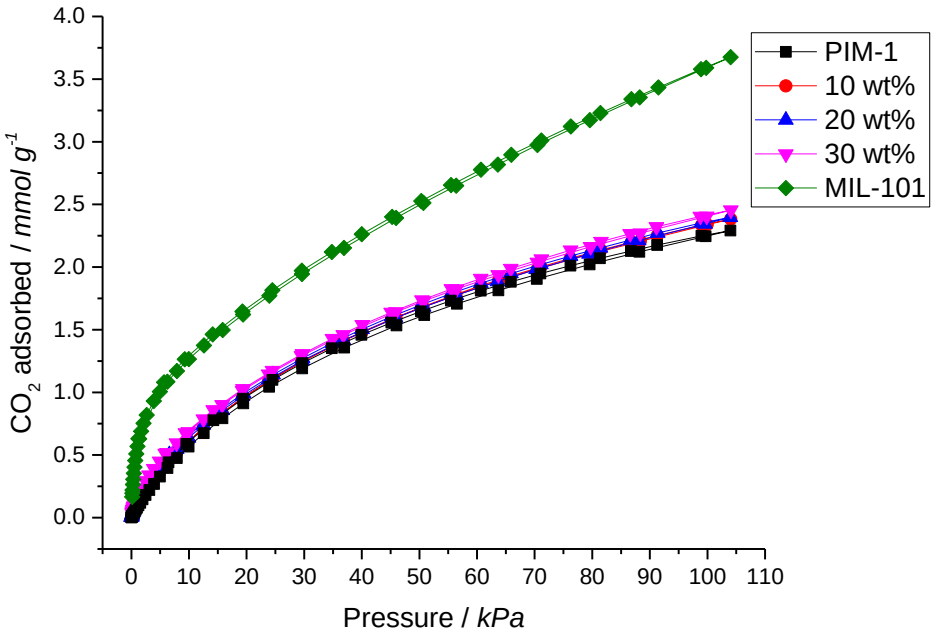

Figure 4.44 – Carbon dioxide isotherms for PIM-1 film, MIL-101 and the composites thereof at 273 K. Lines are provided to guide the eye only.

CO_2 isotherms appear to show very little difference in the microporous uptake between the PIM-1 film and the composite materials, whilst MIL-101 uptakes a relatively large amount of adsorptive. This is also clearly indicated in the rule of mixtures analysis in Figure 4.45, which plots the CO_2 uptakes at 100 kPa for each of the materials. There is a clear linear trend in the relationship between MOF content and uptake, which is positive, but the interaction is clearly PIM dominated, with the amount of increased uptake far less than would be expected if the materials had no interaction. It seems likely that with CO_2, as with N_2, that the high tortuosity of the pore structure limits access to the highly receptive pores of the MIL-101. There also appears to be no percolation effect at these concentrations facilitating the movement of the adsorptive through the material. The BET surface areas calculated from the CO_2 isotherms also show this trend.

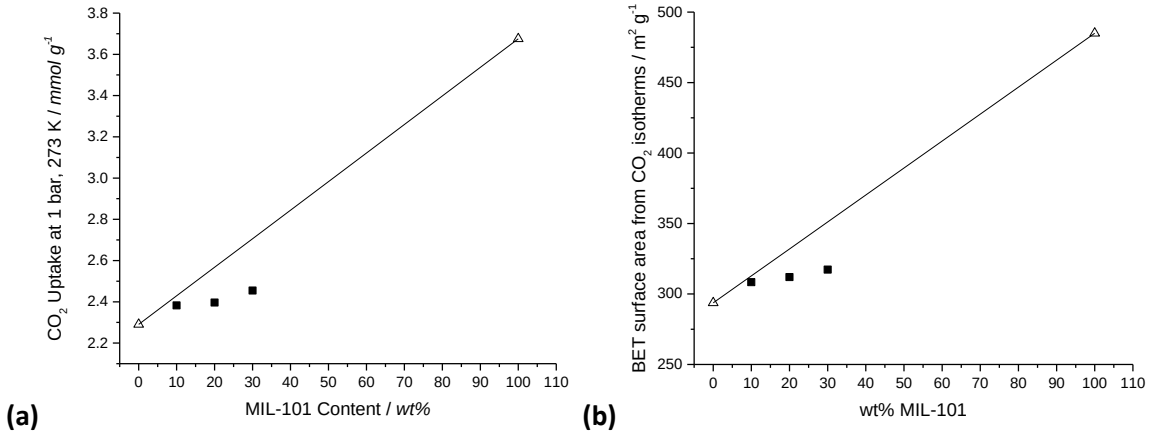

Figure 4.45 - Rule of mixtures analysis for (a) the CO_2 uptakes of the PIM/MIL composites at 1 bar and 273 K and (b) the BET surface areas calculated from these isotherms.

The low pressure hydrogen isotherms at 77 K for the PIM-1 film, MIL-101 and the composites are shown in Figure 4.46. Again, there is a clear progressive trend in the hydrogen uptake, namely that the uptake increases as the MOF content increases, albeit the 20 wt% film showing slightly lower uptake than expected given the relative uptakes of the 10 and 30 wt% films. This slightly lower uptake for the 20 wt% film is also seen in the surface area and CO_2 studies, although it is

less pronounced using these techniques, which implies that it is not likely to be an issue of mass transport into the material, but instead something to do with the total adsorptive capacity. This is possibly due to MIL-101 breakdown in the sonication process, an issue highlighted by the FTIR studies of Alentiev et al [209] discussed in section 4.3 above.

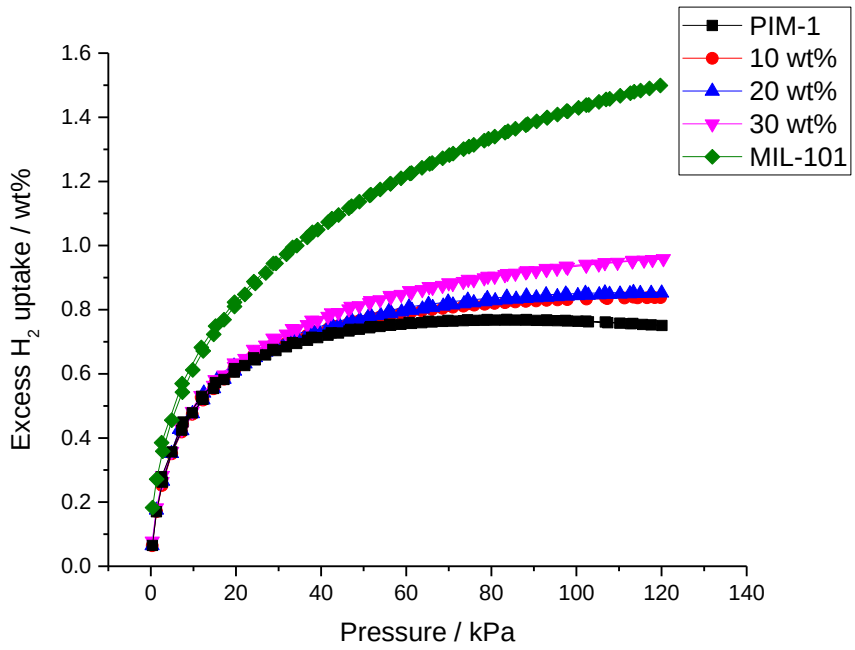

Figure 4.46 - Low pressure (0.1 MPa) H_2 isotherms for PIM-1 film, MIL-101 and the composites thereof at 77 K. Lines are provided to guide the eye only.

One interesting feature of the isotherms in Figure 4.46 is that the composites appear to follow the PIM-1 isotherm quite closely in the low pressures, before separating and increasing their uptake at a greater rate as the pressure increases. Looking at the rule of mixtures analyses at two points (20 and 100 kPa), as shown in Figure 4.47, appears to clearly illustrate this.

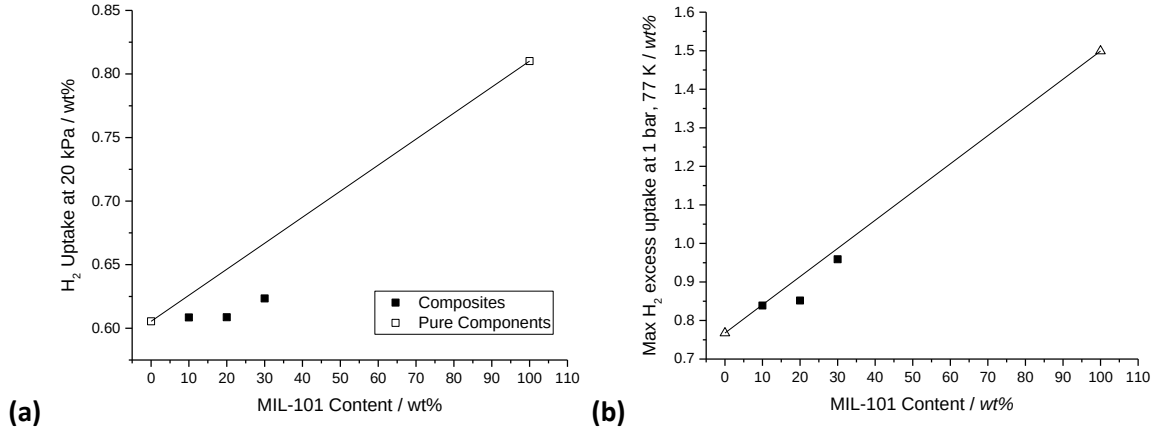

Figure 4.47 - Rule of mixtures analyses of the low pressure H_2 isotherms for the PIM-MIL composites, showing uptake at (a) 20 kPa and (b) 100 kPa.

At 20 kPa, the H_2 uptake is PIM dominated, much like the interaction with CO_2. This demonstrates that even hydrogen appears to have issues accessing the porosity in the pores under conditions that are unfavourable for mass transport. These conditions are a combination of the 77 K temperature, which reduces the diffusivity of the adsorptive, and the very low pressures, which result in a low concentration driving force between the pore and the bulk space. However, as the pressure increases to 100 kPa, the uptake in the composites generally follows the rule of mixtures. The much higher concentrations at these pressures overcomes the mass transfer

resistance and the hydrogen is able to access the full porosity in the MOF, so raising the apparent capacity.

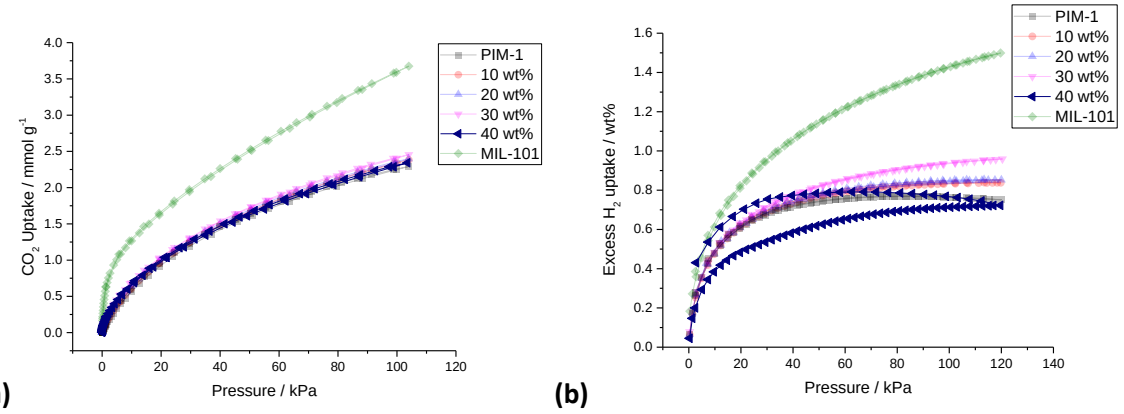

Figure 4.48 - Isotherms up to 0.1 MPa for the 40 wt% composite using (a) CO_2 at 273 K and (b) H_2 at 77 K as adsorptives. The isotherms in Figure 4.44 and Figure 4.46 are provided for comparison. Lines are provided to guide the eye only.

The same isotherm analyses were also performed for the 40 wt% composite – these analyses are presented in Figure 4.48. It is evident from this figure that the adsorptive capacity of the 40 wt% composite are greatly affected by its suboptimal synthesis – the CO_2 uptake, although in the same region as the other composites is actually most comparable to the 10 wt% composite in terms of CO_2 uptake (and therefore microporous capacity).

The hydrogen isotherm in Figure 4.48 (b) is greatly affected by the thick, inaccessible layer on this film – the uptake is shown to be less than the PIM-1 film (although it does show higher uptake than the similarly shaped isotherms on PIM-1, namely runs 2, 6 and 8 in Figure 4.38). The isotherm shows a very large desorption loop that could be indicative of the true adsorption potential of this system – the uptake continues to increase through the desorption loop until~ 40 kPa. At this point, the uptake in the 40 wt% film is greater than that of the 30 wt%, and potentially suggests that a 40 wt% film that emerges from the synthesis process as flat and homogenous may well continue the trends seen in the other composites.

4.9. High Pressure (≤ 20 MPa)

4.9.1. PIM-1 (2)

High pressure hydrogen isotherms were performed a number of times on both PIM-1 samples, in both powder and film morphologies. The isotherms produced by PIM-1 (2) are shown in Figure 4.49 below. Multiple runs were performed for both these materials, showing reasonable repeatability. These graphs are in the supplementary information (SI-3).

Figure 4.49 provides a number of interesting points. Firstly, the adsorption curve appears to follow a typical type I pattern, as is expected with hydrogen due to its supercritical state at 77 K. The uptake for the powder reaches 1.49 wt% at 1 MPa, a very similar (but slightly higher) uptake than the 1.45 wt% reported by McKeown et al. [185]. This is an interesting observation given the lower nitrogen uptake seen in Figure 4.30, which appeared to show lower BET surface area than previously reported. This perhaps suggests that the excess surface area seen in Budd et al. may be in either the mesopore or macropore range, which does not contribute heavily to hydrogen

adsorption, given its tendency to only form monolayers. The isotherm continues to increase, reaching a maximum excess uptake of 1.66 wt% at 3.2 MPa.

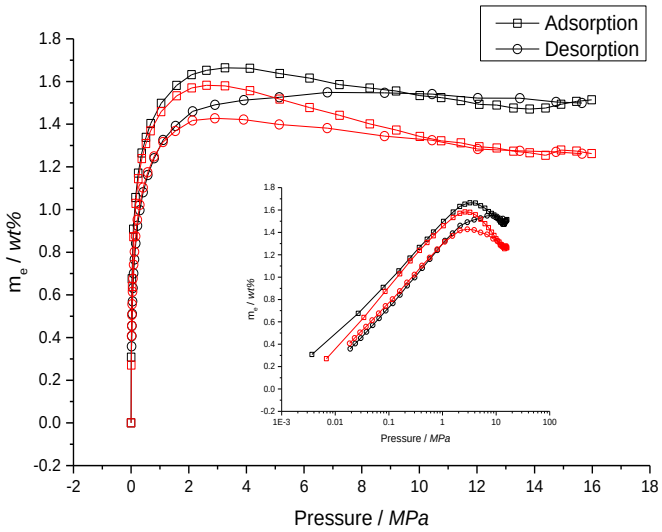

Figure 4.49 – High pressure (16 MPa) H_2 isotherms for PIM-1 (2) powder (black) and film (red) at 77 K. Lines are provided to guide the eye only.

For the film, a maximum of 1.58 wt% is seen at 2.8 MPa, a value which, whilst lower than the powder uptake, is surprisingly close to the powder performance given the loss of surface area as determined by nitrogen analysis. This is further evidence of the maintenance of microporosity when the polymer is cast into the film morphology.

As the pressure increases above the maximum value, the curve begins to decline, as is expected for graphs of the excess adsorption, as the density of the bulk phase gas is increasing, whilst the amount adsorbed is increasingly only very slightly, therefore reducing the difference between what has been taken up and what would be present were no adsorption occurring. There is an upward kink in both curves at ~14 MPa, which is likely caused by a machine fault – at this pressure, the HTP switches pressure transducers to a transducer that is more accurate in the upper pressure range. It is this change in measuring transducer that causes the measured uptake to be higher in this range.

The desorption curves in Figure 4.49 are very unusual. Typically, the desorption curve can be expected to follow the adsorption curve closely, so demonstrating reversibility. However, there is a strong hysteresis loop seen, in which the desorption uptake is initially higher than the adsorption, before dropping quickly and showing much lower uptake than the adsorption. Typically, desorption hysteresis results in an uptake higher than the adsorption curve (as seen in types IV(a) and V in Figure 2.3), due to the slow evacuation of macropores caused by the constrictions present in the pore network delaying the emptying of larger pore volumes [74]. The reason for this unusual hysteresis loop is unknown. However, the multiple run isotherms in the supplementary information (SI-3) appear to show that any changes to the material appear to be completely reversible, as supplementary runs following a degassing period show unchanged uptake and near identical response to pressure.

One theory on this could involve the pressure within the flexible pores of PIM-1. As high pressure hydrogen is dosed in, the pores within the material are subject to very high normal force, particularly when the adsorptive adsorbs and a solvation pressure begins to build in the material [202]. Given that the porosity in PIM-1 is not chemically bonded, as in most porous materials, but is instead the result of a poor relaxation process leaving free volume within the material, there is

little to suggest that these pores could not be pushed wider, particularly in the microporous channels that lead to the larger mesopores. With an expanded pore structure, it is then likely that the equilibrium pressure in the pores is lowered, and more adsorptive desorbs than would have adsorbed at the same dosing pressure, so resulting in the negative hysteresis loop. This expanded structure would only affect the bulk volume of the material, and not the skeletal volume on which the HTP performs its determination of the excess uptake. It has been previously reported that porous materials with flexible pore structures can lead to unusual adsorption isotherms [332], and it is certainly possible that a similar effect is occurring here.

4.9.2. PIM-1 (4) powder

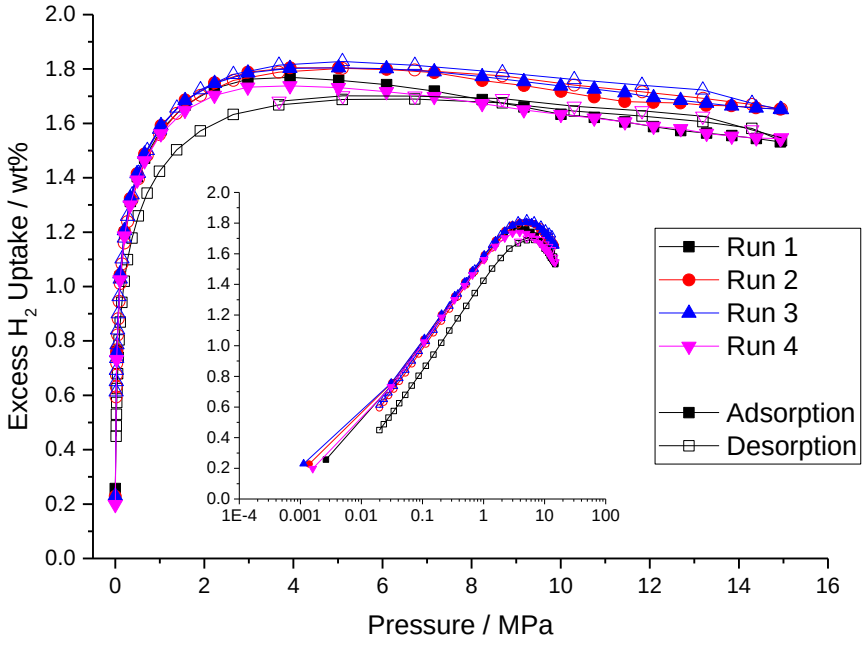

Figure 4.50 - High pressure (15 MPa) H_2 isotherms for PIM-1 (4) powder at 77 K. Lines are provided to guide the eye only.

The high pressure H_2 isotherms for PIM-1 (4) powder are shown in Figure 4.50 above. This material reaches an uptake of 1.59 wt% at 1 MPa, and reaches a maximum excess of 1.80 wt% at 3.92 MPa. This sample appears to have a slightly higher uptake than PIM-1 (2), although the differences are reasonable small and are likely well within the margin of error given the relative certainty of accurately determining the skeletal density of this material. This also matches the trend seen in the nitrogen isotherms, in which uptake both at P/P_0 = 0.1 and P/P_0 = 1 were higher in this sample.

The sample shows reasonable repeatability over the four runs shown in Figure 4.50, albeit there appear to be two main uptake 'paths' that the material follows – which one it takes may be a function of local pressure and temperature conditions, and of the history of the material. Curiously however, there is more divergence in the desorption isotherms of this material. Runs 1 and 4 appear to show the same negative desorption trend seen in PIM-1 (2), but runs 2 and 3 do not; these runs are far more reversible and appear to be showing this material behaving much more like a standard, fixed porosity microporous material. As these runs were all performed on the same sample, this difference cannot be due to heterogeneities in a single film or between different film samples, but something must be occurring in the material itself. This would appear

to back the idea that the high pressure is modifying the pore structure within the material, and it will respond in different ways under different conditions.

In order to further test this idea, a series of runs were done without degassing in between each run, but instead simply cycling the pressure to see how the isotherm might change over time. The results of this experiment can be seen in Figure 4.51. Cycle 1 in this figure is the same run as Run 4 in Figure 4.50.

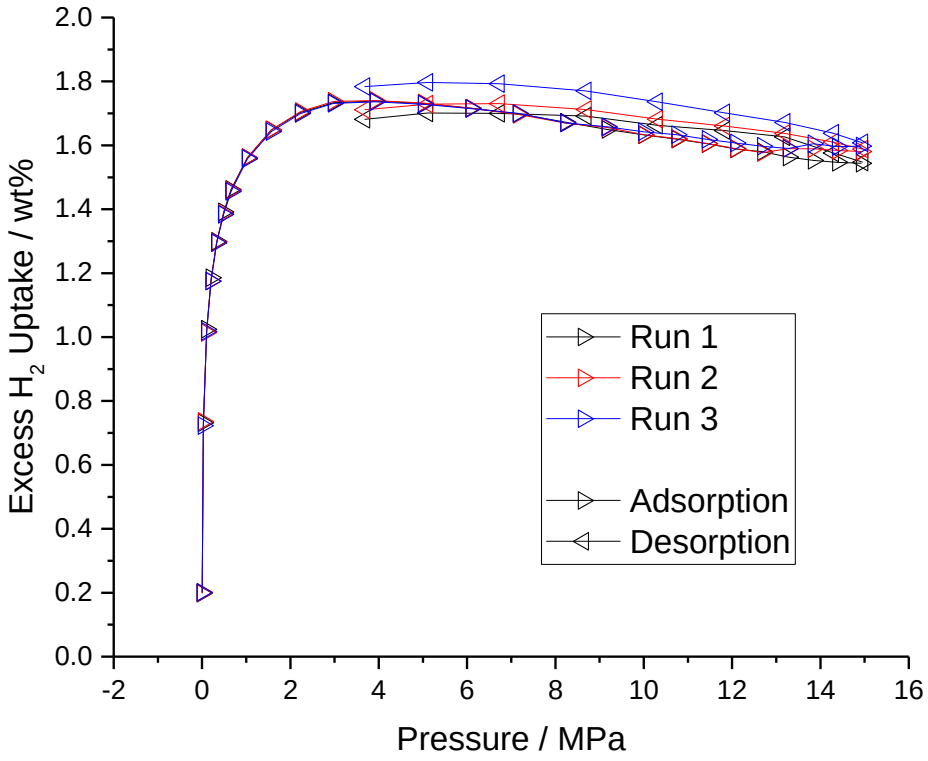

Figure 4.51 - Cycled high pressure H_2 isotherms at 77 K for PIM-1 (4) powder with no degas between runs. Lines are provided to guide the eye only.

Looking at Figure 4.51, there is a very apparent trend. The adsorption curves for each of these runs are highly repeatable, showing very little difference except a very minor increase in the excess adsorption at this higher pressure. However, the desorption curves are clearly different, with each successive run showing a greater uptake at a given pressure the longer the experiment went on. This is apparent evidence that the pore structure is certainly changing over the length of the experiment. However, the rising desorption curves suggest that microporosity is being maintained more over time, and that somehow the constant exposure to adsorbed hydrogen is causing the rigidity of the material to increase. Unfortunately, this was the only experiment that could be run within the timeframe (and limitations of the machine), and further experiments to test this idea could not be performed.

As well as the isotherms at 77 K, which are common due to the abundance and relative inexpense of liquid nitrogen dewars as a temperature control medium, the HTP also has the integral reactor, featuring an active cryocooling system. Using this functionality, isotherms for a number of different temperatures was performed on PIM-1 (4). The isotherms produced are given in Figure 4.52.

In general, the isotherms look reasonable in the < 10 MPa range: there is a steady increase in adsorption as the temperature decreases; and each isotherm starts with a rapid increase before

starting to drop the excess adsorbed. This trend discontinues at 150 K and higher, likely due to the lower density of bulk H_2 at these temperatures resulting in a lower mass displacement.

The obvious striking feature of this figure is how erratic many of the isotherms (and particularly the 90 and 100 K isotherms) are in the higher pressure ranges. Unfortunately, this appears to be a machine fault, as it is inconceivable that such erratic points can be the result of a sample phenomenon. It is striking that the largest of these errors occurs in the runs with the active temperature control set to the lowest values – it would appear that the harder the system has to work to maintain the temperature, the less success it has in producing a smooth, reliable isotherm. However, the erratic data are not caused by inaccuracies in the temperature control; all of the isotherms saw excellent temperature control within ± 1 °C over the course of the run. Nevertheless, these isotherms remain interesting as there are enough reliable data to be able to calculate the isosteric enthalpy of hydrogen adsorption onto PIM-1 using these isotherms; this analysis can be found in chapter 6.

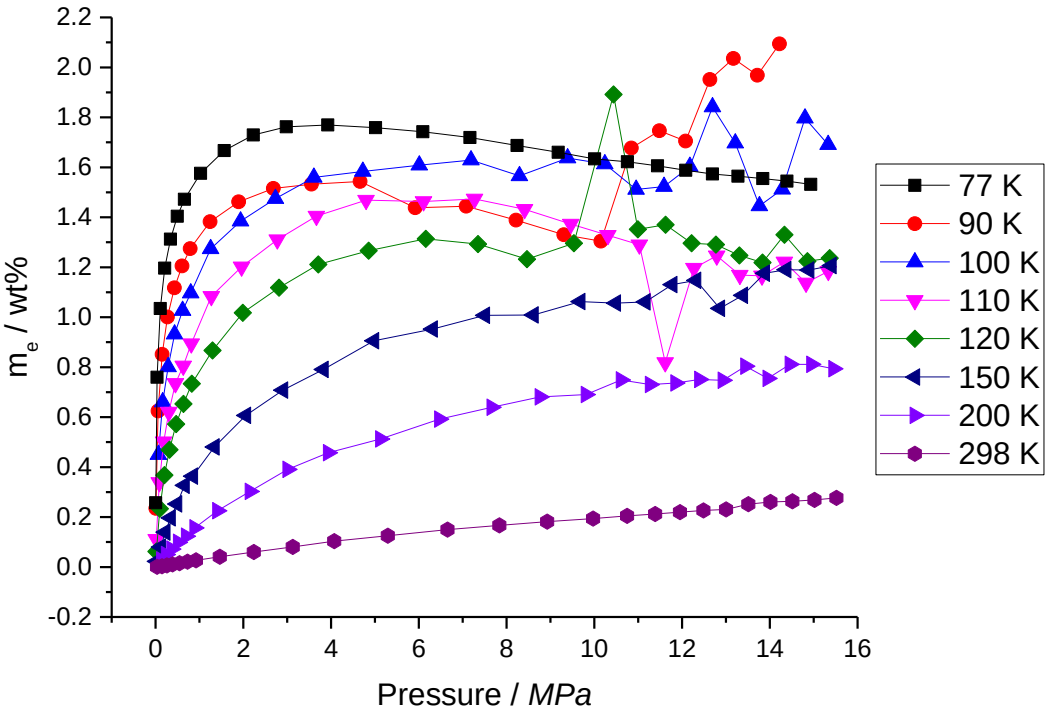

Figure 4.52 - High pressure (16 MPa) isotherms for PIM-1 (4) powder at a variety of temperatures. The 77 K isotherm featured is Run 1 in Figure 4.50. Lines are provided to guide the eye only.

4.9.3. PIM-1 (4) film

The high pressure hydrogen isotherms performed on three separate PIM-1 (4) film samples at 77 K is shown in Figure 4.53. Averaged between the runs, this material uptakes 1.45 wt% at 1 MPa and shows a maximum uptake of 1.55 wt% in the pressure range 2.2 – 3.89 MPa. Both of these values are highly comparable to previous studies on PIM-1, not only in this study (section 4.9.1 above) but in others in the literature [185]. The PIM-1 (2) film isotherm is provided in Figure 4.49 for comparison, and it is clear that the values found for PIM-1 (4) do appear to correlate well with this isotherm in the lower pressure ranges.

However, a clear feature of Figure 4.53 is the lack of repeatability of these isotherms. Despite multiple attempts, there appears to be little correlation between runs, even those performed on the same film sample. There are a couple of reasons why this may be the case. The first of these is

shifting access of the gas to the adsorption sites. If the pores in PIM-1 are flexible and will expand (or potentially contract) under certain pressure conditions, then it is not unfeasible that some pores may be partially or completely closed, which would limit gaseous access to the adsorption sites. It seems very unlikely that mass transfer is an issue given that hydrogen permeates most materials very quickly, and that the isotherm points equilibrate reasonably quickly (every 10-15 minutes or so).

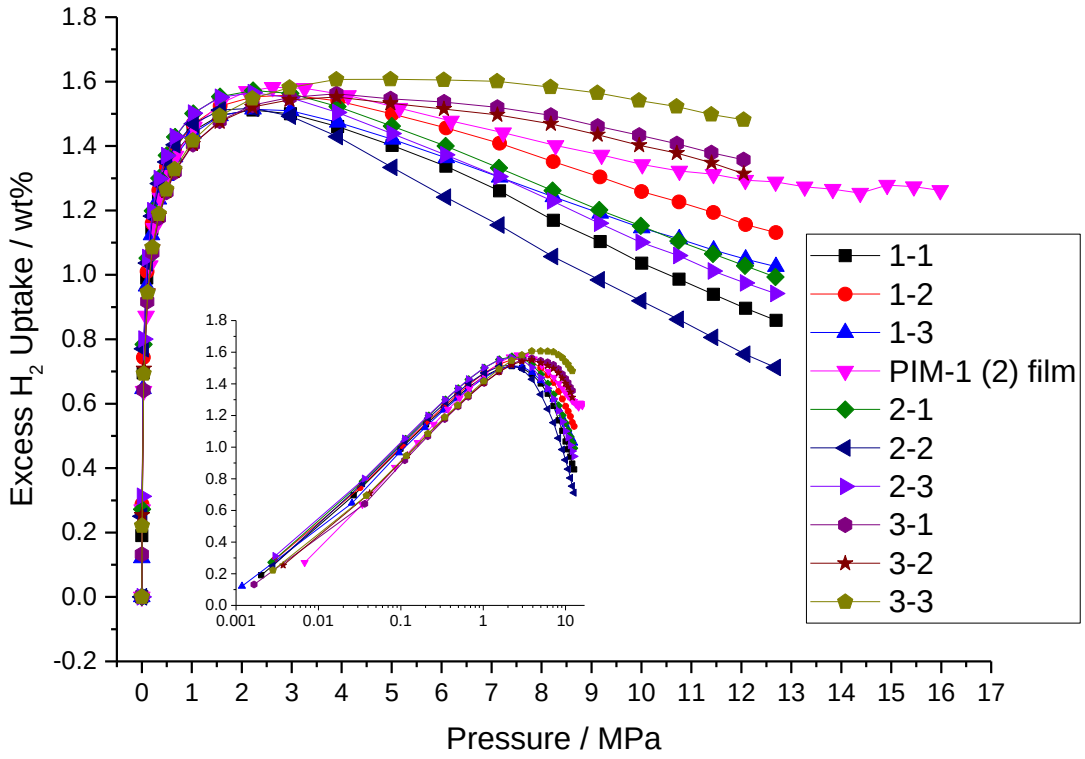

Figure 4.53 - High pressure (13 MPa) H_2 isotherms for PIM-1 (4) film samples at 77 K. The x-y notation in the legend refers to the y^{th} run performed on the x^{th} sample. Lines are provided to guide the eye only.

An alternative for the spread of results between samples may be differences in skeletal density. As a volumetric adsorption device, the HTP requires accurate determination of the available volume the gas has to occupy, and knowing the skeletal volume of the sample is an important part of that. As seen in sections 4.7 and 4.8.4 above, it has been difficult to get a reliable, repeatable skeletal density for PIM-1 films, and thus this adds much uncertainty to the measurement. To get an idea of which isotherms might be closest to the true value, the skeletal density of the films was calculated from the determined dry weight and measured skeletal volume. The calculated skeletal densities are shown in Table 4.6 below.

Table 4.6 - Calculated skeletal densities of PIM-1 (4) films that underwent high pressure H_2 isotherm analysis

Sample	Skeletal Density / g cm^{-3}
1	1.276
2	1.272
3	1.376
PIM-1 (2)	0.886

Table 4.6 presents two interesting points. Firstly, the skeletal densities for samples 1 and 2 are very similar, so it is unsurprising that these isotherms on these two samples all show similar isotherms – runs 1-3, 2-1 and 2-3 come the closest to forming a repeatable isotherm for this material. Secondly, the higher skeletal density of sample 3 appears to have resulted in a slightly

different shape in which the uptake does not rise as quickly but then declines more slowly after the maximum excess point. This behaviour is much more like that seen in the PIM-1 (2) film, although their densities are very different.

Ultimately, it appears to make sense to take the six runs from samples 1 and 2 and use those as the basis for a definitive PIM-1 (4) film isotherm, as their skeletal density most closely matches that determined for PIM-1 powder (1.24 g cm^{-3}), and show the best repeatability. One way of determining what is statistically closest to the 'true' isotherm is to average the isotherms at each point; this can be done easily given that the same number of points was run for each isotherm, and the dosing pressure the same in each case, resulting in a set of pressures for each isotherm that are very similar. On this basis, the uptake at each pressure is then averaged, resulting in an average isotherm for this material, this is shown in Figure 4.54 below.

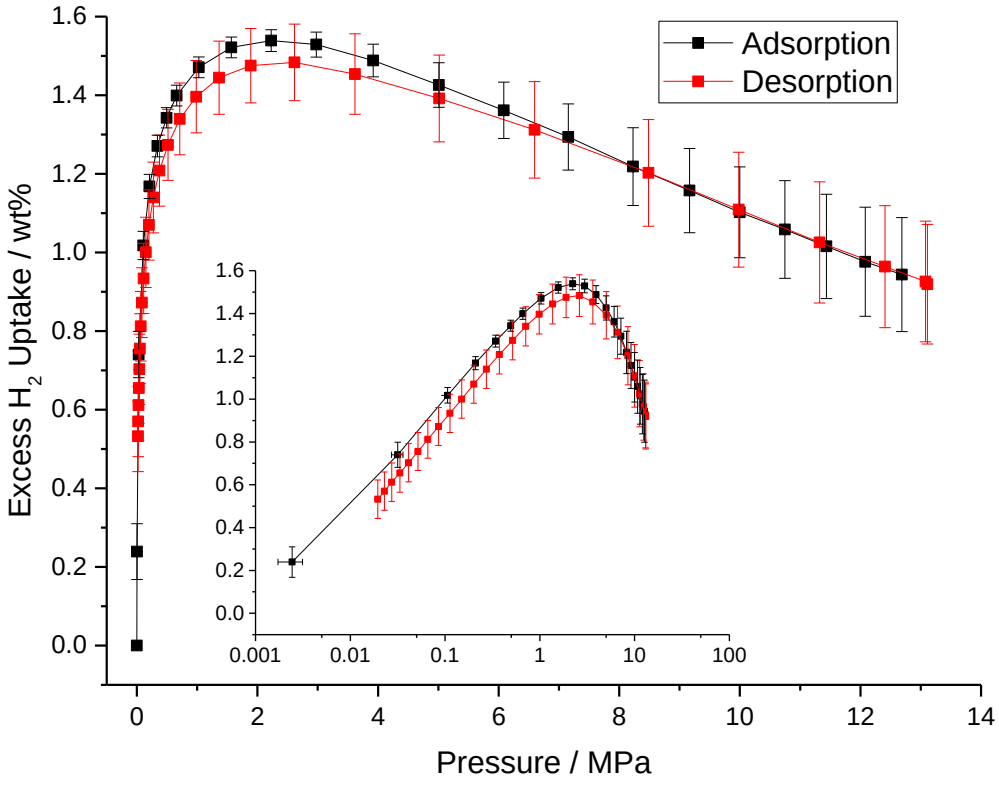

Figure 4.54 - High pressure H_2 isotherm for PIM-1 (4) film calculated from each of the runs performed on samples 1 and 2. Error bars donate the standard deviation, and lines are provided to guide the eye only.

This isotherm shows a clear, smooth trend, with an uptake of 1.47 wt% at 1 MPa and a maximum uptake of 1.54wt% at 2.23 MPa. Again, these figures compare reasonably well with those already discussed; the main difference being the rate at which the excess uptake then declines as the pressure increases. The values at each pressure in this isotherm closely resemble that of sample 2-3, which was one of the three isotherms identified above as most closely resembling a repeated isotherm, which lends credence to the idea that this is a representative isotherm of the sample. The average isotherm overlaid on the isotherms from which it was averaged can be found in the supplemental information.

Although taking an average of isotherms in this way is a highly unusual method of analysis and there remains great uncertainty in what the true uptake of hydrogen by PIM-1 films are, this seems a reasonable starting point from which to compare the adsorption capacity of the composites.

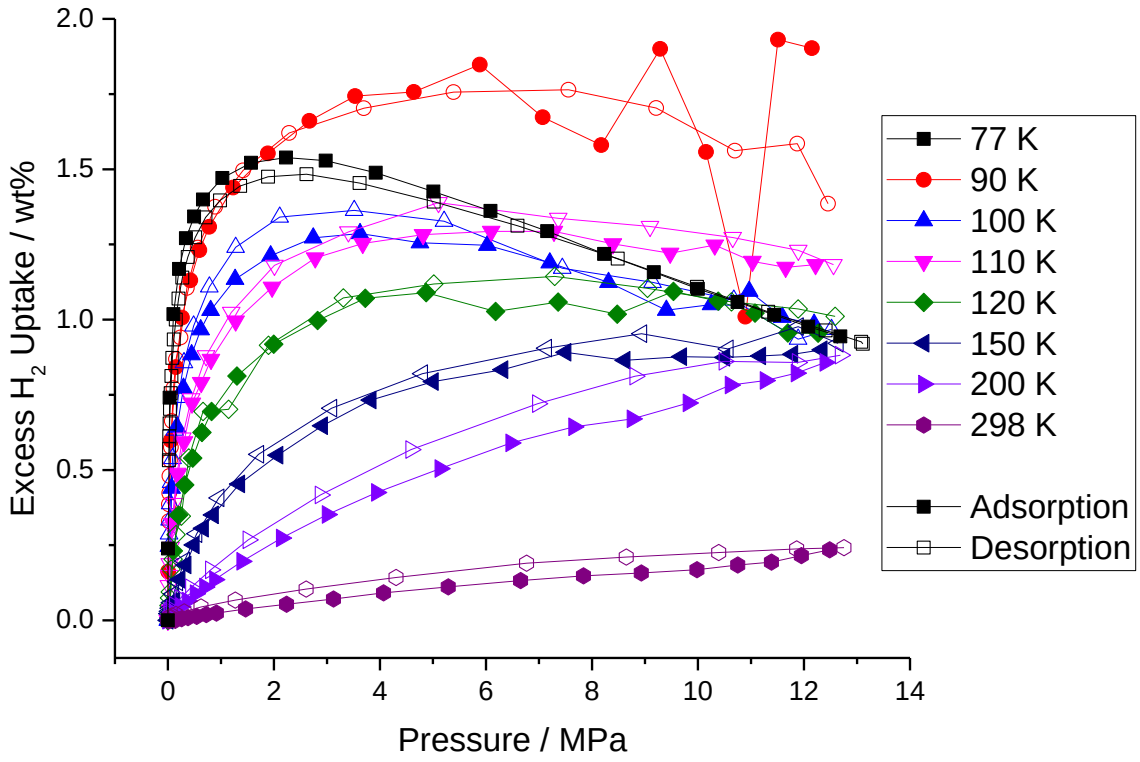

Figure 4.55 - High pressure (16 MPa) isotherms for PIM-1 (4) film at a variety of temperatures. The 77 K isotherm featured is that shown in Figure 4.54. Lines are provided to guide the eye only.

Multiple temperature isotherms for PIM-1 (4) are presented in Figure 4.55 above. Much like for the powder sample, many of the isotherms in this figure are erratic, particularly in the higher pressures and at the lower temperatures. However, unlike the powder sample, the issues with this set of isotherms do not end there: there is frequent overlapping of the amount adsorbed by isotherms of lower temperatures, and the entire run set does not compare well to the isotherm for 77 K (the average isotherm just discussed). Whilst differences in skeletal density may account for some of the difference between the 77 K run and the others, the errors between isotherms are due to system fault, and therefore these data come with great uncertainty. Whilst this question could be clarified with repeated runs, there was not enough time in this project available to dedicate to this question.

4.9.4. MIL-101

The high pressure isotherm for MIL-101 is presented in Figure 4.56 below. As expected, the MOF shows a fully reversible isotherm with high uptake – the maximum excess adsorbed reached 5.3 wt% at 4.9 MPa. This is slightly higher than other studies have reported, particularly for a MIL-101 sample that did not undergo further activation than heating under vacuum, but the difference is minor, and well within the range of total values reported (see section 2.5.2.4 above). The isotherm was also very repeatable, with three runs all closely repeating the same trend.

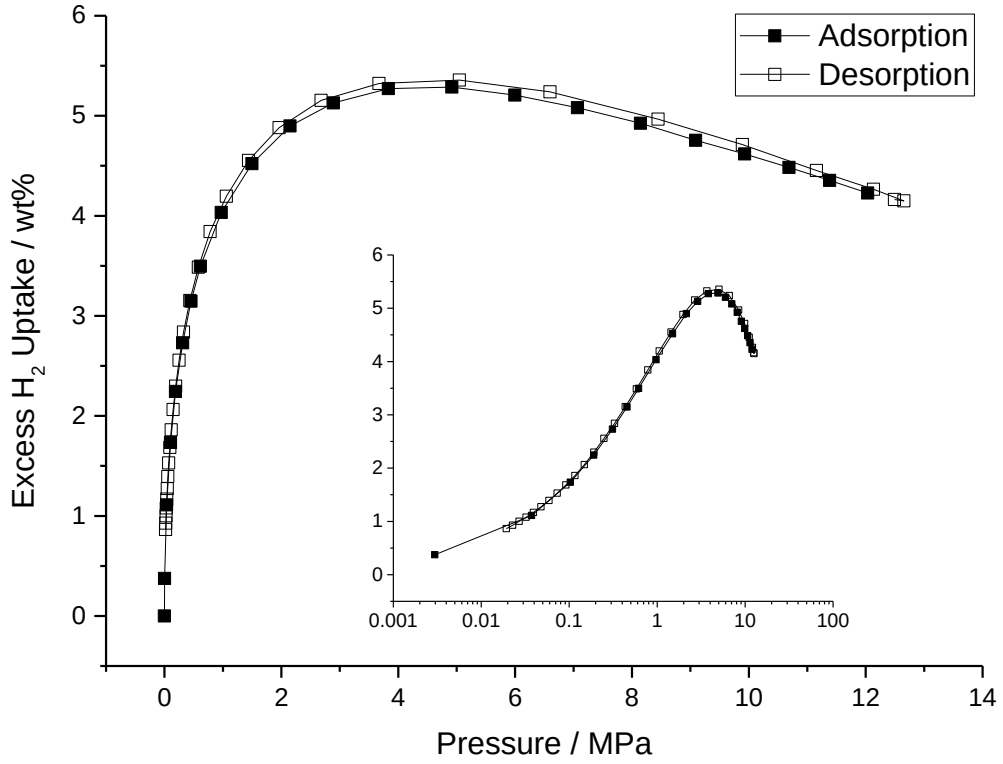

Figure 4.56 - High pressure (13 MPa) H_2 isotherm for MIL-101 at 77 K

4.9.5. Composites

The high pressure hydrogen isotherms for the PIM-MIL composites, along with the pure components, are given in Figure 4.57. The rule of mixtures analyses from these isotherms are given in Figure 4.58.

There is a clear increase in uptake with increasing MIL-101 content, although upon visual inspection of Figure 4.57, it can be seen that it is not a strictly linear increase. Interestingly, the 10wt% composite seems to follow the shape of the PIM-1 isotherm closely, whilst the excess uptake decline in the 20 and 30 wt% films is not so sharp. Analysing this more closely using the rule of mixtures, it becomes clear that although the maximum uptakes do increase with MOF content, the increase does not keep up with rule of mixtures, so implying that the PIM-1 matrix is blocking access to the MIL-101 in order to fully utilise its adsorptive capacity. The pressures at which these are reached do not show a trend at this pressure resolution. These pressures show that the maximum uptake occurs at pressures much higher than the 0.1 MPa tested in the 3-flex, which determined that resistance to H_2 adsorption had been overcome by 0.1 MPa, so there appears to be a discrepancy between the two machines on this subject.

Interestingly, when comparing the excess uptake at the end of the isotherm (12 MPa, Figure 4.58 (c)), the trend then follows the rule of mixtures exactly. This appears to replicate the trend seen in the rule of mixtures analysis for the low pressure hydrogen isotherms, namely that hydrogen adsorption is hindered at lower pressures by the presence of the PIM, but as the main driver of mass transport (pressure) increases, the adsorption uptake begins to reflect the mixture of the two components much more directly.

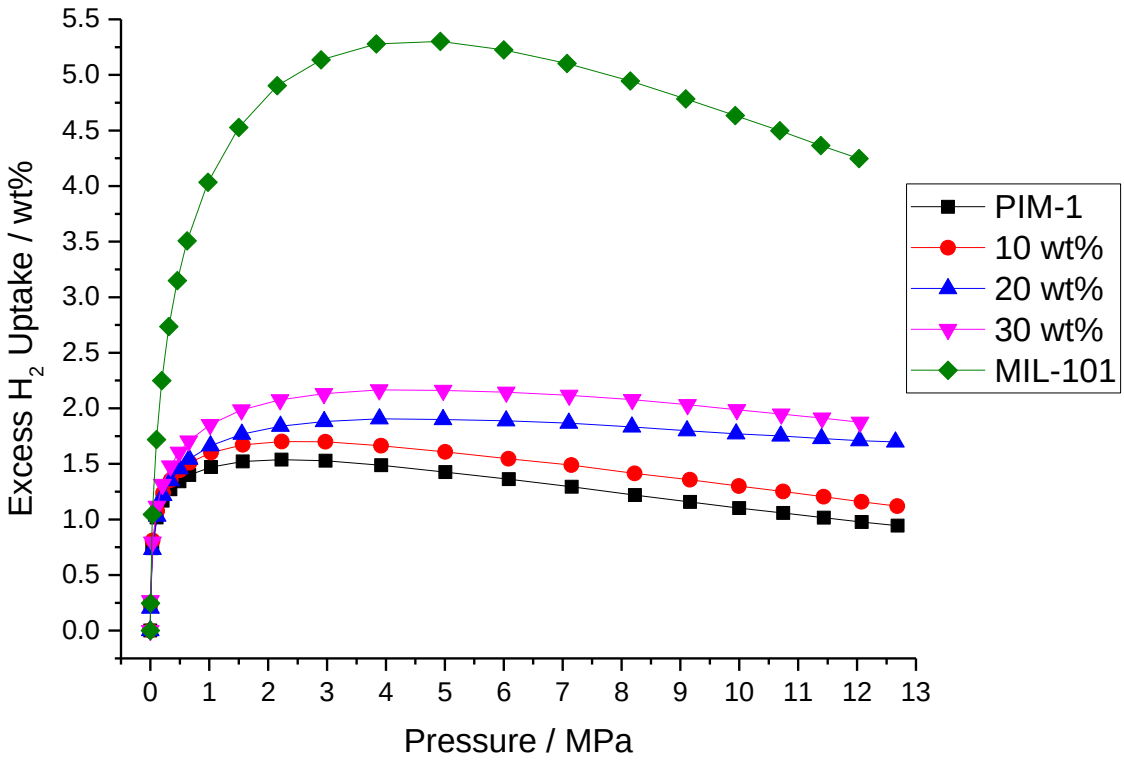

Figure 4.57 - High pressure (13 MPa) H_2 isotherms at 77 K for PIM-1 film, MIL-101 and the composites thereof. Lines are provided to guide the eye only.

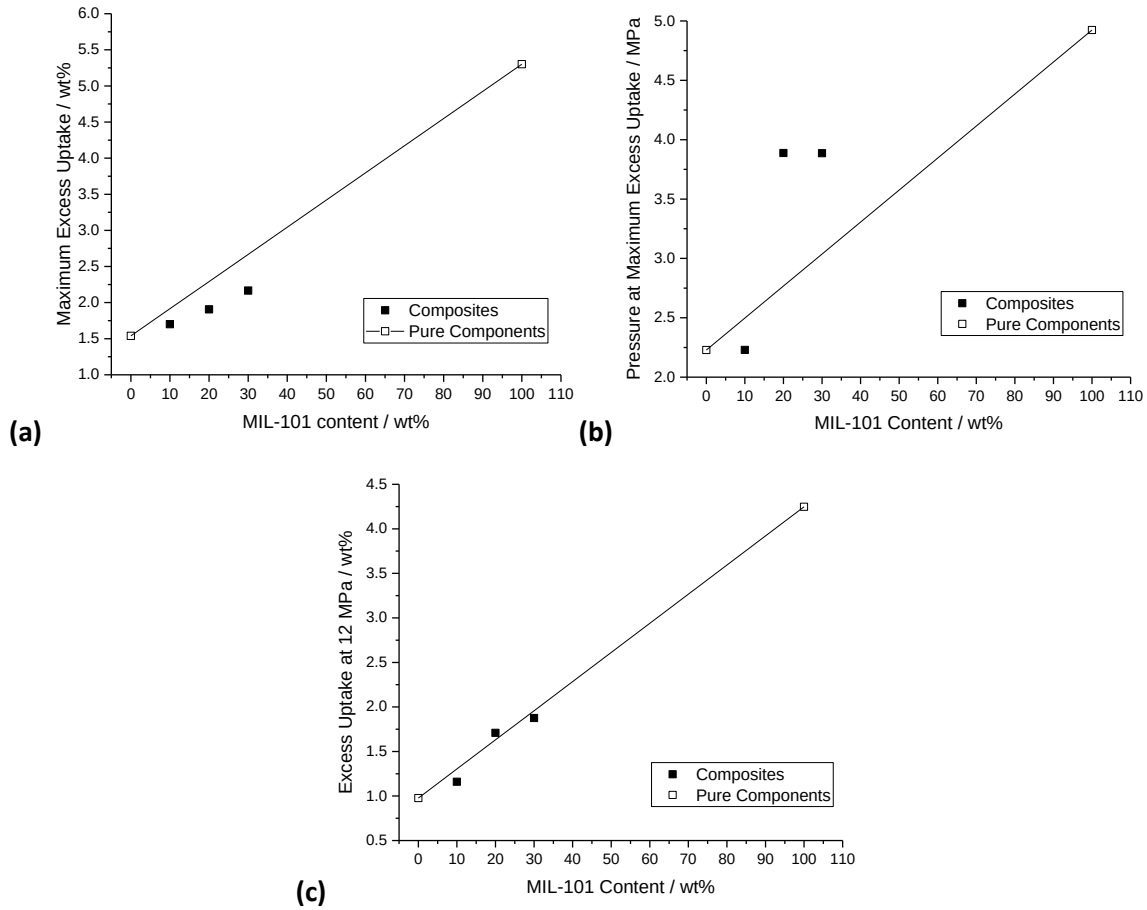

Figure 4.58 - Rule of mixtures analyses for the high pressure H_2 isotherms on the PIM-MIL composites, examining (a) maximum excess uptake, (b) pressure at which the maximum uptake is achieved and (c) the excess uptake at 12 MPa.

It is also curious that the one film that registers above the rule of mixtures line in Figure 4.58 (c) is the 20 wt% film, which had shown reduced performance in all of the other adsorptive tests. This result suggests that there is not any problem with the MIL-101 inside the film, and that it is issues with accessibility of the adsorptive sites that caused the reduced uptake seen in the 3-flex.

The individual runs for these isotherms can be seen in the supplemental information (SI-4). It is interesting to note that the 10 wt% film showed fairly inconsistent repeats, much like the PIM-1 film alone. As the MIL-101 content increased, so did the repeatability of the isotherms, so much so that the 30 wt% film showed three near identical runs. Both the 10 and 20 wt% films also showed large positive desorption curves, suggesting that these adsorption isotherms aren't truly representative of the adsorption capacity of the materials at these pressures, and with further exposure a greater equilibrium amount adsorbed is achievable. This is very likely due to the flexible pore structure in the MOF; this effect is likely born out of a swelling of the PIM pore structure that improves access to the MIL-101, and so increases the uptake. There is no sign of the negative adsorption effect seen in the PIM-1 alone.

The high pressure hydrogen isotherm for the 40 wt% composite is shown in Figure 4.59. Again, it is evident to see that the uptake within this film does not meet expectations as the uptake is lower than that of the 30 wt% composite. However, the performance is closer to expectation in this experiment than for the 3-flex based measurements, which showed performance equivalent to the 10 wt% composite. This is further evidence that the MIL-101 within the composite is 'locked-in' by the thick PIM covering, but with sufficient conditions, the adsorptive can reach through to the MIL-101 in the sample and improve the overall uptake.

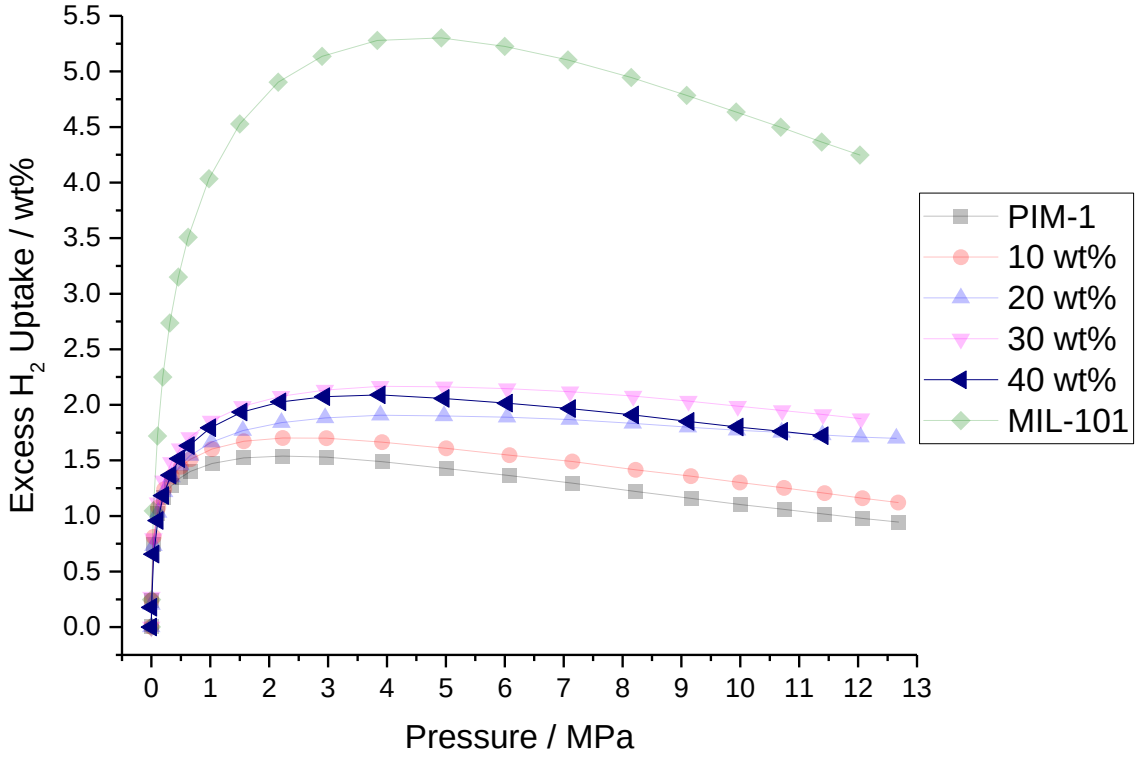

Figure 4.59 - High pressure (12 MPa) H_2 isotherm for the 40 wt% composite at 77 K. The equivalent isotherms for PIM-1 film, MIL-101 and the other composites are shown for comparison. Lines are provided to guide the eye only.

In an attempt to understand how the isosteric enthalpy of the material is affected by the presence of the MIL-101, a series of multiple temperature isotherms were performed on the 30 wt%

composite, given that this material showed excellent uptake and good repeatability and reversibility. This set of isotherms is shown in Figure 4.60 below.

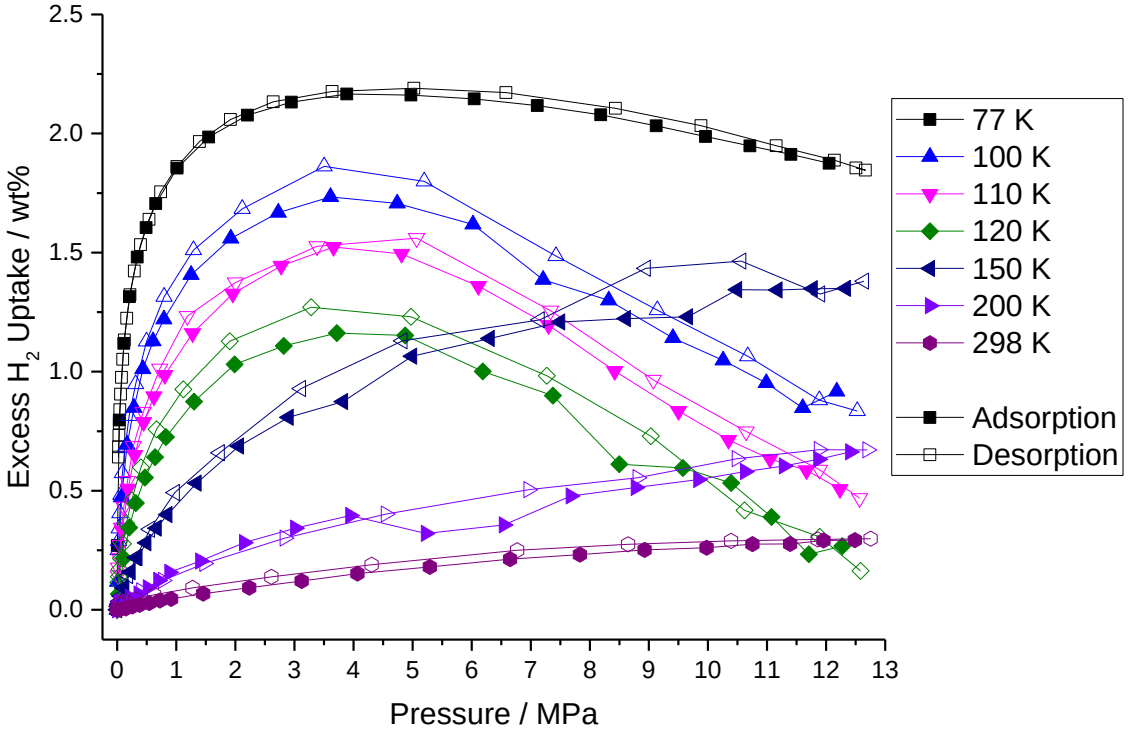

Figure 4.60 - High pressure (13 MPa) isotherms for 30 wt% composite at a variety of temperatures. Lines are provided to guide the eye only.

This is an interesting, if unexpected, set of isotherms. Firstly, the lower temperature isotherms run in the integral reactor show a very different isotherm shape than the higher temperature ones, despite the fact that these were all performed on the same material and have the same skeletal density assigned. This difference can only be assigned to the system, given the consistency of conditions elsewhere. It is interesting to note that below the maximum uptake point (~4 MPa for all the isotherms at 120 K and lower), the isotherms show a reasonable spread, which may indicate that despite the inconsistency of these isotherms, that an analysis of the adsorption enthalpy may yield an enlightening result. As with the PIM-1 (4) multi-temperature isotherms, the validity of this result could be confirmed or otherwise with further testing, but there was insufficient time available within the scope of this project to repeat such results.

4.9.6. Freespace Sensitivity

In light of the difficulty determining accurate skeletal density values for these materials, it is useful to investigate how much a change in the value of the density used will affect the isotherms that are produced. The HTP has a function that easily allows for the changing of the skeletal volume of the sample, so this was altered in a number of samples, and the change is outputted isotherm recorded. Four of the isotherms tested are displayed in Figure 4.61, and uptake values at 1 MPa, 12 MPa and the maximum uptakes for all the isotherms tested, along with the calculated difference from the original HTP-determined skeletal density, are shown in Table 4.7.

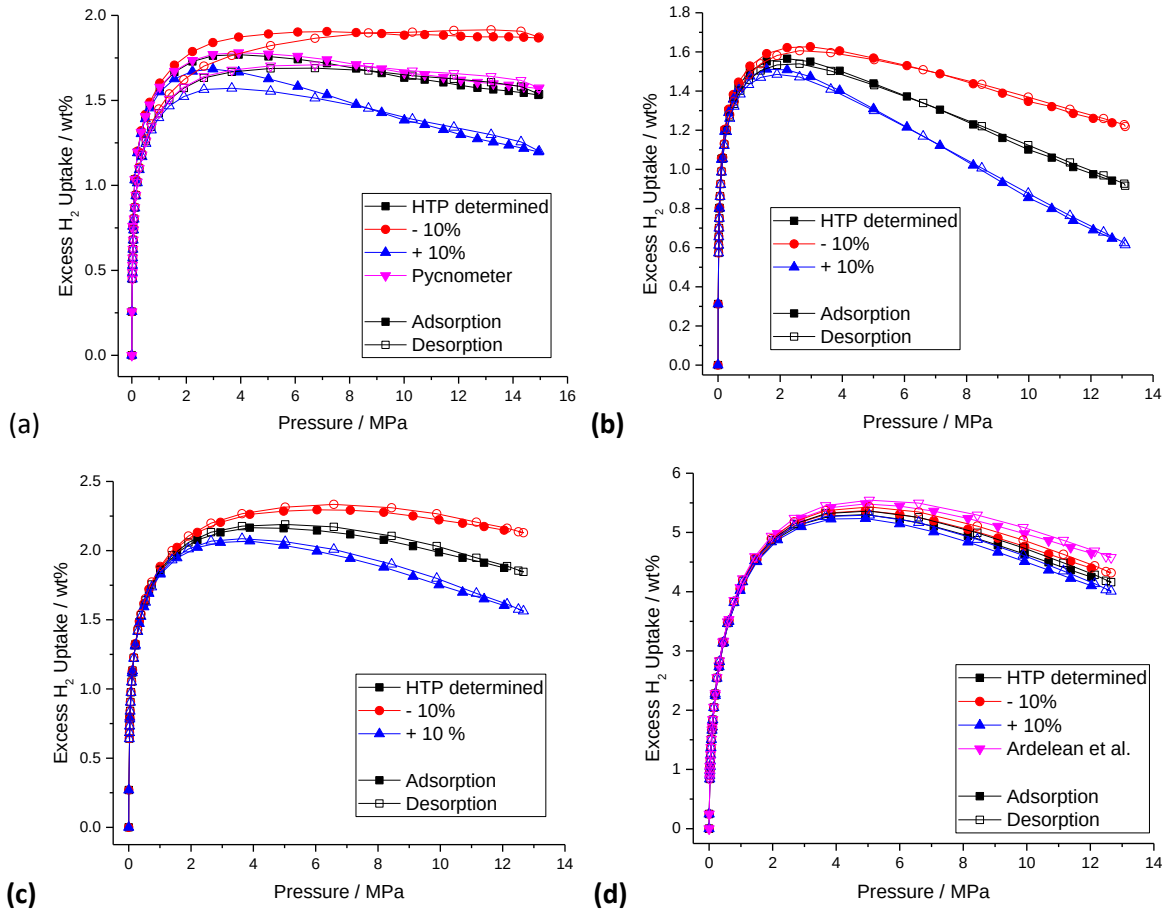

Figure 4.61 -High pressure H_2 isotherms showing the sensitivity of the reported isotherm to the skeletal density used to calculate it. Sensitivities of ± 10% are shown for (a) PIM-1 (4) film, (b) PIM-1 (4) powder, (c) 30 wt% composite and (d) MIL-101, with the pycnometer calculated density for (a) and the Ardelean et al. [143] **reported density for (d) also featured for comparison. Lines are provided to guide the eye only.**

The effect that changing the skeletal density of the material has appears to vary widely by the sample tested. In the PIM-1 (4) samples in particular, changing the available volume appears to have a large effect on the excess uptake, particularly in the higher pressure regions. The MIL-101 sample however appears to be largely unaffected by the change in skeletal density, showing very little response to the change. For the PIM-1 and MIL-101 samples, the isotherms produced by calculating the skeletal density from a pre-known value appear to be relatively close in value, and therefore there is good confidence that the originally reported isotherms are close to accurately representing what is occurring when the material is dosed with adsorptive.

Looking at Table 4.7, it appears that as the MIL-101 content of a material increases, the sensitivity to a changing skeletal density decreases. One effect that may be enhancing this is the raw calculated volume of sample in the system – as it is generally targeted that 100 mg of sample is put into the system for testing, more dense materials will be displacing relatively less volume for the same mass. Therefore a percentage change in skeletal volume will, relative to the size of the sample chamber, be relatively smaller than the less dense materials, which will result in the preceived change in uptake being smaller. This is not the entire reason however, as more of the 30wt% composite was placed into the sample by volume than the 20wt% composite, yet the trend continues.

Table 4.7 - Results of skeletal density sensitivity analysis on key isotherms in this study. Results for uptake at 1 MPa and 12 MPa, and maximum excess uptake are shown.

Sample	Skeletal Density value	Uptake at 1 MPa / wt%	Change from original / %	Maximum Uptake / wt%	Change from original / %	Uptake at 12 MPa / wt%	Change from original / %
PIM-1 Powder	HTP	1.575	-	1.769	-	1.588	-
	- 10%	1.601	1.67	1.905	7.68	1.877	18.2
	+ 10%	1.549	-1.67	1.684	-4.80	1.298	-18.2
	Pycnometer	1.578	0.20	1.780	0.65	1.620	2.02
PIM-1 film	HTP	1.501	-	1.565	-	0.975	-
	- 10%	1.527	1.72	1.626	3.91	1.260	29.22
	+ 10%	1.476	-1.72	1.511	-3.43	0.690	-29.22
10 wt%	HTP	1.601	-	1.700	-	1.159	-
	- 10%	1.627	1.62	1.757	3.34	1.444	24.51
	+ 10%	1.575	-1.62	1.643	-3.34	0.875	-24.51
20 wt%	HTP	1.662	-	1.906	-	1.709	-
	- 10%	1.687	1.48	2.041	7.11	1.982	15.96
	+ 10%	1.638	-1.48	1.809	-5.06	1.436	-15.96
30 wt%	HTP	1.854	-	2.165	-	1.875	-
	- 10%	1.878	1.32	2.295	5.98	2.148	14.56
	+ 10%	1.829	-1.32	2.069	-4.45	1.602	-14.55
MIL-101	HTP	4.034	-	5.301	-	4.247	-
	- 10%	4.047	0.32	5.369	1.28	4.398	3.56
	+ 10%	4.021	-0.31	5.235	-1.24	4.100	-3.46
	Ardelean et al. [143]	4.068	0.86	5.481	3.40	4.648	9.46

The rest of the is difference comes from the ability of the material to uptake adsorbate, and the relatively low post-quilbration pressure that such an uptake generates. For a volumetric adsorption measurement system, the amount of adsorptive present at any one time is determined by the manifold pressure and volume, the sample chamber pressure and volume, and the sample volume. What the system knows about the interaction is the pressures in the manifold and sample chambers both before and after the valve between them is opened, and the volumes of both the chambers (these are calibrated before experiments are performed). Assuming ideal gas behaviour, the equilibration can be represented by the following equation:

$$P_1 V_m + P_2(V_c - V_s) = P_3(V_m + V_c - V_s) + n_A RT \qquad (\mathbf{5.1})$$

where V_m, V_c, and V_s are the manifold, sample chamber and sample skeletal volumes respectively, P_1 and P_2 are the pressures in the manifold and sample chambers pre-experimental point, P_3 is the post-equilibration pressure, and n_A is the amount adsorbed. A change in the sample skeletal density changes the amount of gas held in the sample chamber before the point, the amount in the chamber post-equilibration, and the amount of adsorptive adsorbed.

Consider equation 5.1 with P_1, P_2, P_3, V_m and V_c as known constants. If the amount adsorbed by a material is large, then P_3 will be relatively small. If this is the case, then the amount of gas

calculated to remain in the entire equilibration volume (i.e. the $P_3(V_m + V_c + V_s)$ term) after the equilibration will be reasonably small. Therefore, if there is a shift in the skeletal density of the material, the change in the amount of gas expected in the equilibrated volume will also be small, meaning that the calculated value of uptake will not change much. However, for material that uptakes less adsorptive, P_3 will be larger, meaning the amount of gas expected to be in the bulk phase will also be larger. Therefore the perceived change in the amount of gas expected post-equilibration will be larger when the skeletal density is changed by the same proportion.

Unfortunately, PIM-1 appears to be the most sensitive material in this study to the sensitivity alterations, given both its low density and its relatively low uptakes. It would therefore make accurate skeletal density determination an absolute imperative in order to achieve high accuracy high pressure adsorption measurements. However, given the nature of the film material to make thick layers that are difficult for adsorptives to penetrate into if the synthesis conditions are not controlled carefully, this quickly results in a material whose adsorption performance is difficult to quantify accurately. Careful control of the synthesis conditions, and an accurate method for the skeletal density determination, would go a long way to improving the quality and accuracy of the measurements shown above.

5. Thermal Decomposition of PIM-1 and Activated Carbon Production

5.1. Thermogravimetric Analysis (TGA)

5.1.1. Anoxic decomposition

Figure 5.1 shows four TGA runs on PIM-1: Run 1 is an initial run; runs 2-4 are a full 3 run analysis performed at a later date.

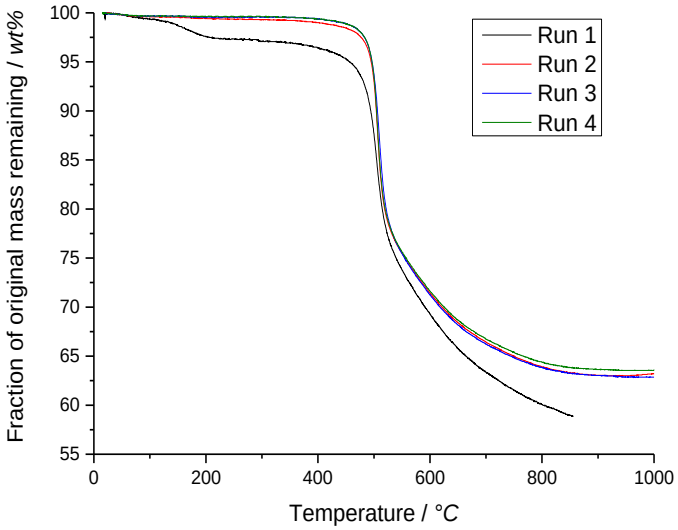

Figure 5.1 - TGA analysis of PIM-1 under 1.8 L h^{-1} N_2 at 10 °C min^{-1}

Run 1 clearly shows three distinct decay regions: an early decay between 0 – 200 °C, a sharp drop between 470 – 520 °C, and then a steadier decay between 520 - 850 °C. This early drop is associated with the loss of solvent remaining in the pores from the synthesis (in this case either chloroform or methanol) and adsorbents gained during air exposure (most likely water and N_2), suggesting that 3 % of the wet weight of the PIM is foreign molecules.

Runs 2 - 4 show the same large decays at high temperature, but not the early drop. The reason the set of three TGA runs show an early loss of ≤ 1% is because this set of TGA was run on PIM-1 powder than had been through helium pycnometry. He pycnometry is a non-destructive test, meaning the sample can be used again, but the helium purges the sample clean and drives off any of the solvent/adsorbent that would be lost in the early temperature range of the TGA scan. There is the possibility that the small loss seen is either due to adsorbents that have been picked up from the air between the two experiments, or that residual helium that has adsorbed in the sample during pycnometry is being lost. Based on this lack of solvent, it is possible to consider runs 2 - 4 the TGA analysis on a dry basis.

After 200 °C, all four runs are largely in agreement. There is a plateau between 200 – 470 °C, which is indicative of thermal stability, and this result matches that found in the literature which

states that PIM-1 is thermally stable up to 350 °C [180, 187]. The drop after 470 °C appears to show a two-step thermal decomposition. This is unusual, as typically once the carbonisation temperature of a polymer is reached, there is a single sharp drop in the mass as other elements in the polymer are driven off. However, the initial drop followed by a more gradual decay seems to be indicative of two separate mechanisms of thermal degradation occurring in the polymer.

To investigate the large decreases in mass more thoroughly, the dry TGA runs in Figure 5.1 were differentiated to produce a DTG curve. This curve is shown in Figure 5.2.

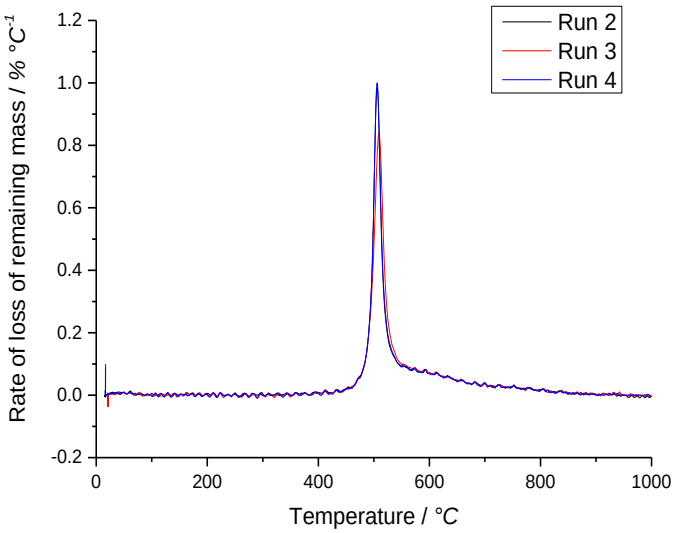

Figure 5.2 - DTG curve against temperature for the dry N_2 TGA runs

Typically, DTG curves of carbonaceous materials in N_2 are Gaussian distributions with three specific points to pick out: the onset temperature, at which the material begins to lose mass at an increasing rate; the peak temperature, where the material is losing mass most quickly; and the finish temperature, at which the rate of decay stops declining at reaches a steady level. Looking at Figure 5.2, there is a clear onset temperature at 470 °C, and a clear peak temperature of 505 °C. This peak temperature very neatly matches the weight loss temperature seen by Staiger et al. [195]. At 550 °C, the trend of the Gaussian peak thus far seen is broken, and the rate of decay begins to drop much less slowly, linearly dropping before slowly tailing off in the 800 – 1000 °C range. This makes identifying a finish temperature very difficult, as the rate does not appear to plateau fully.

Looking in the 500 – 800 °C range of Figure 5.2, the slowed decay almost seems to resemble a second Gaussian curve that is much flatter and broader than the curve driving the main decay. To investigate this possibility, the DTG curve for Run 1 was put through a deconvolution process, in which a Gaussian curve was fitted to the DTG data in Figure 5.2, and a Gaussian fit was then done on the residual remaining from the first fit. The results of these fits, along with the original data, are presented in Figure 5.3(a). The summation of the two Gaussian fits is presented in Figure 5.3(b), and the residuals are presented in the supplementary information (SI-5).

It is clear to see in Figure 5.3(b) that the summation of the two Gaussian curves provides a reasonably good fit to the original data, with the one major error in the approximation appearing on the right shoulder of the data (T = 520 – 580 °C). Certainly, these two curves show good fit to the main peak in the DTG curve, and the long tail in the high temperature region. How the separate curves in Figure 5.3(a) can assist in deducing the mechanism for thermal decomposition depends on their properties; for this, we can use the parameters that OriginPro used to generate the curves.

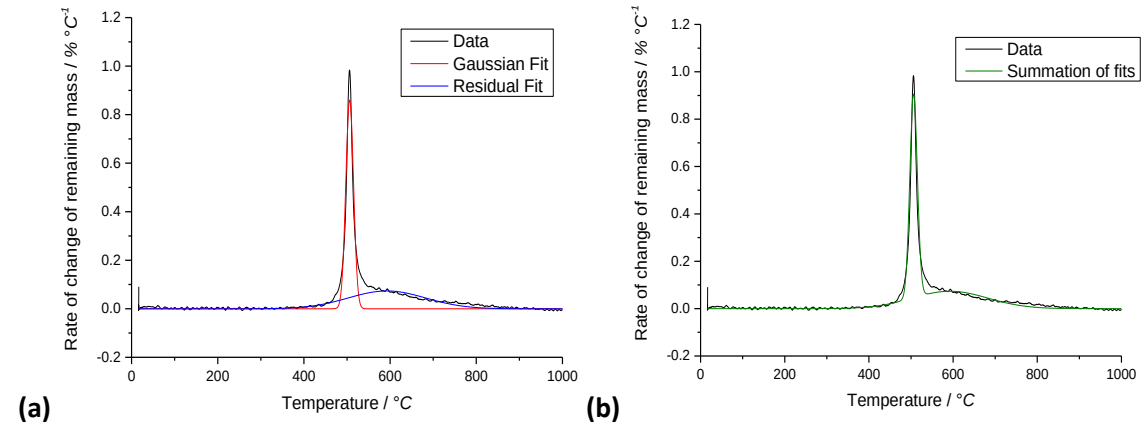

Figure 5.3 - Deconvoluted Gaussian fits for the DTG curve of dry run 1, showing (a) the separated main and residual fits and (b) the summation of the fits against the original data

OriginPro 9.1 uses a modified Gaussian distribution equation for fitting:

$$y = y_0 + \frac{A}{w\sqrt{\pi/2}} e^{-\frac{2(x-x_c)^2}{w^2}} \qquad (5.1)$$

where x and y are the independent and dependent variable (in this case temperature and rate of mass loss) respectively, y_0 is a translating variable to change the baseline of the Gaussian function to match that of the fitted data, A is the area under the curve, x_c is the centre point of the function (the point at which the function is at a maximum, equal to the mean in a standard normal distribution) and w is a measure of the width of the curve (equal to the twice the standard deviation of x). A, x_c and w are useful tools with which to compare the curves, and to gain extra information about the thermal decomposition process; y_0 was fixed to zero for these fits, to ensure that the baseline of the fits went through the flat baseline in the low temperature region of the DTG data, before the onset point. Further data can also be gained from looking more closely at the graphs; the onset and finish temperature (which will be given the symbols T_o and T_f respectively) can clearly be identified from the graph. The values of all five parameters discussed in this paragraph are given in Table 5.1 below.

Table 5.1 - Parameters supplied by OriginPro for the main and residual DTG Gaussian fits shown in Figure 5.1

Parameter	Main Gaussian Fit	Residual Gaussian Fit
A (%)	19.32 ± 0.12	16.55 ± 0.22
x_c (°C)	506.2 ± 0.1	592.6 ± 1.4
w (°C)	17.91 ± 0.14	179.9 ± 2.8
T_o (°C)	475	340
T_f (°C)	540	850

The table raises a number of interesting points. Firstly, w shows that the residual fit is much wider than the main Gaussian fit, which is evident from looking at Figure 5.3. Secondly, x_c, which we can consider the peak rate temperature for either decomposition, is less that 100 °C apart for the two curves. Evidently the peak temperature for the main curve matches that of the DTG data, but to see the peak for the residual curve so close clearly shows that both of these processes are occurring concurrently.

The T_o and T_f values also reflect this. The T_o of the residual fit, which as the earliest initiation point is the onset temperature of the entire process, is much earlier than the 470 °C that was quoted earlier. Interestingly, this onset temperature is very close to the temperature that Budd et al.

[180, 187] gave as the point at which PIM-1 begins to fail. However, because this form of decomposition starts off very slowly (due to the large width of the residual fit), it is not until the main peak initiates at 475 °C that any significant increase in the overall decomposition rate is seen – hence the earlier prediction of 470 °C. The finishing temperature of the main peak is 540 °C – right in the middle of the shoulder of the curve that is not covered by the summation of the fits. The residual fit is rising towards its peak at this point, so it is possible that the curve seen in the data is a simple trending of the rate towards being dominated by the residual curve, rather than the main peak, which is rapidly declining. Following this, the residual peak follows the data relatively closely, until its T_f value of 850 °C

Perhaps the most interesting parameter in Table 5.1 is *A*, which is equivalent to the area under the curve. A has a unit of %, due to the units present in the variables of the DTG curve, and therefore these areas can be directly relatable to how much of the weight loss experienced by the PIM is due to each of these degradation mechanisms. This is directly shown by adding together the two *A* values; this gives a result of 35.87 %, which when taken from 100 % leaves 63.13 %, which is very close the mass remaining in Figure 5.1. Interestingly, whilst the main peak dominates the curve, it only accounts for 2.77 % more of the decomposition than the broad residual peak.

Ultimately, however, these data need to cumulate in a proposed mechanism for the thermal degradation of PIM-1 in anoxic conditions. Ultimately, thermal degradation is the breakage of bonds within the polymer chain, which results in loss of atoms (and therefore mass) to the gas stream where bonds on the surface of the chain are broken. To try and better understand what could be occurring, Table 5.2 below shows the breakdown of mass of the PIM-1 repeat unit by mass

Table 5.2 - Breakdown of PIM-1 unit mass by element

Element	Number in PIM-1 unit	Molar mass (g mol^{-1})	Contribution to PIM-1 unit mass (wt%)
C	29	12.0	76
H	20	1.01	4
N	2	14.0	6
O	4	16.0	14

These data seem to present little match to the data generated from the Gaussian fits. Oxygen appears to be the most likely candidate to explain one of the curves, as it contributes a similar wt% to the polymer chains as was identified by the curves. However, the oxygen present in PIM-1 is solely present in the form of the dioxane linkers, and therefore a loss of this oxygen would result in the polymeric chains of PIM-1 collapsing – this certainly would not result in the black powder that retained a very similar structure to the powder that went into the TGA, and it is therefore unlikely that either of the curves is attributable to this. Whilst nitrogen would be a likely candidate to be kicked off the chains, given their heterogeneity to the rest of the chain and their vulnerable position as an appendage to the terephthalonitrile ring, there is too little of it to account for an entire degradation curve, and the C-N triple bond is very strong. It seems possible that the entire cyanide groups may have been split off, although this still only accounts for 11.3% of the repeat unit's molar mass. Whilst it would be expected that the majority of the carbon in the chain should remain, given the visible black, charred material that remained after the experiment, the amount of carbon present in the unit appears to be greater than the dry weight of polymer left after the TGA run, so some must have been driven off during the process.

5.1.2. TG-MS

In order to further determine what the breakdown mechanism of PIM-1 in anoxic and high temperature conditions, TG-MS experiments were performed on the material. A typical TG curve for the material in an argon atmosphere, and the mass spectrometer response to the outlet gas, is shown in Figure 5.4

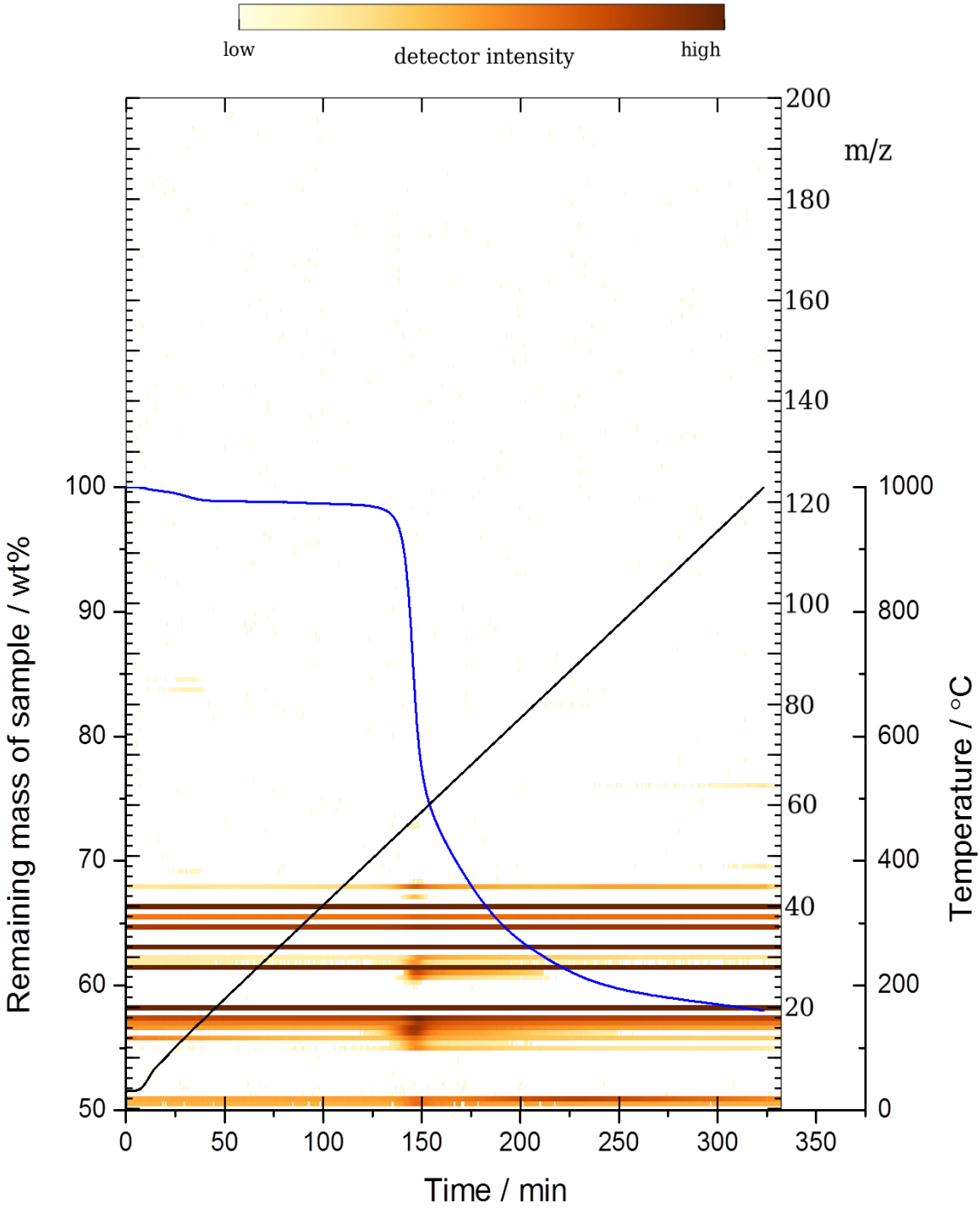

Figure 5.4 - TG-MS analysis for PIM-1 heated at 3 °C min^{-1} under 20 mL min^{-1} Ar

The TGA curve under argon at 3 °C min^{-1} is very similar to the nitrogen runs at 10 °C min^{-1} shown in Figure 5.1, indicating the repeatability of the thermal decomposition of this material under different anoxic environments. This sample again loses ~ 2% of its wet mass as lost adsorbents in the early temperature range, and then holds steady until ~ 450 °C, at which point the same two-

step mechanism appears to occur. However, more detailed analyses are required to see the minor differences between the runs in Figure 5.4 and Figure 5.1; the dry weight basis DTG curve and the Gaussian fits to it for the argon TGA run are shown in Figure 5.5 below, and the parameter values from the fits are given in Table 5.3.

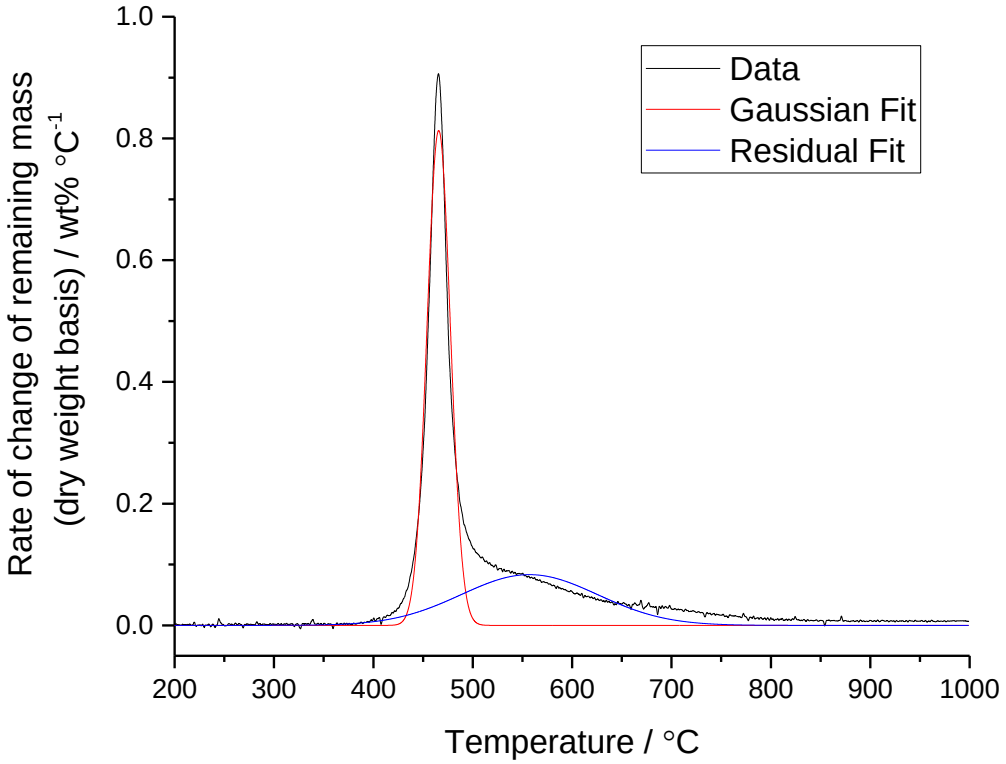

Figure 5.5 - Deconvoluted Gaussian fits for the DTG curve (dry weight basis) calculated from Figure 5.4 , showing the separated main and residual fits

Table 5.3 - Parameters supplied by OriginPro for the main and residual DTG Gaussian fits shown in Figure 5.5

Parameter	Main Gaussian Fit	Residual Gaussian Fit
A (%)	23.88 ± 0.08	14.34 ± 0.10
x_c (°C)	465.7 ± 0.1	557.0 ± 0.57
w (°C)	23.44 ± 0.14	137.2 ± 1.1
T_o (°C)	420	320
T_f (°C)	515	800

It is clear to see that the deconvoluted DTG fits for this TGA run again neatly splits into two separate Gaussian curves, with a similar issue with the combined fit occurring on the right shoulder of the main DTG peak. The calculated parameter values for these curves begin to determine differences between the nitrogen and argon runs. Firstly, the onset, peak and final temperatures for all the curves are slightly lower for the TG-MS run than the run in nitrogen. This is likely due to the slower heating rate in the TG-MS experiment, which was used in order to allow greater resolution in the mass spectroscopy data. The slower heating rate allows for the kinetics of the decomposition reaction associated with a particular temperature to complete more fully before the heat increases to the temperature at which the next reaction occurs. This means that for the slower heating rate, the mass loss associated with a reaction that is triggered at a particular temperature is experienced relatively faster, and is therefore seen to occur at a lower temperature. Whilst the peak temperature (x_c) is slightly lower for this sample than for others reported, this is not too far from the values reported previously, and is not considered erroneous.

In addition, these lower recorded temperatures may in part be due to the lower flow rate of carrier gas in the Evolution TGA versus the TG-92. As the flow of argon was only 20 mL min^{-1} but the nitrogen experiment were performed at 1.8 L h^{-1} (30 mL min^{-1}), the lower recorded temperatures for the onset, peak and final temperatures may be due to a lack of heat dissipation into the carrier gas – if more of the heat that is put into the system by the heating plates is carried away by the carrier gas, then the enthalpy change required to initiate the decomposition will occur later, meaning the loss of mass for that reaction is observed by the balance at a later time, which would therefore associate that reaction with a higher temperature. This effect would be relatively minor, however, given that both machines are specifically designed with their respective carrier gas flows in mind, and so the heating plates would output a heat rate sufficient to heat the carrier gas.

Looking at the values of A generated in Table 5.3, there is a much bigger difference in the area under the two peaks in this run than there was at the faster rate nitrogen studies. This perhaps suggests that the drivers of these different regions are not characteristic to the material, but are perhaps experiment dependent. If this is the case, it does suggest that this two-stage decrease in the mass perhaps is not two separate degradation reactions, but instead one reaction losing mass in a manner dependent on the environment in which it occurs.

The advantage of running TG-MS is that one can use the mass spectroscopy data in an attempt to reinforce the theories already postulated. Looking at Figure 5.4, it is clear to see that a large number of different species were identified, although only a small number of these will correspond to major products emerging from the decomposition. The very strong signals from m/z = 20, 32 and 40 will all be due to the argon carrier gas, and these values can be ignored as the very large amount of argon entering the mass spectrometer in relation to the degradation products means that very little else will be seen in these spectra. There is a presence of air in the chamber: both *m/z* = 14 and 28 are due to atmospheric nitrogen and m/z = 32 is at least partially due to diatomic oxygen. Although a 30 minute purging period is used in the experimental protocol to minimise the presence of air within the chamber, some remains, as detailed by the result, although this declines over the course of the experiment, and in particular the presence of oxygen does not appear to have affected the result greatly. These results can also be ignored.

In the breakdown of an organic product like this, the common groups to look for are those produced by simple breakdown of hydrocarbon materials, particularly CO_2 (m/z = 44), H_2O (m/z = 18) and H_2 (m/z = 2). The intensities of these traces with respect to sample temperature are plotted in Figure 5.6. Clearly, both water and CO_2 show very large peaks in response to the large degradation at ~470 °C, indicating the breakdown of the PIM-1 chains in this temperature range. It is also interesting to note the difference in signal intensity between H_2O and CO_2; the response for water is far higher, suggesting that the material being lost during the thermolysis is far more from hydrogen than from carbon. This finding makes sense given the large amount of carbonaceous material remaining after the anoxic TGA experiments.

One other interesting emerging product is at m/z = 26. This corresponds to the cyanide ion (CN^-), which will be present due to the detachment of cyano- groups from the terethphalonitrile rings. This could present a serious health hazard when considering the breakdown of this material on an industrial level, as cyanide is well known for being toxic to humans. If the production of carbons from PIM-1 (as a result of dedicated manufacturing, or a recycling process), then the emergence of this ion would have to be very carefully planned for to avoid the health implications that exposure to cyanide can bring.

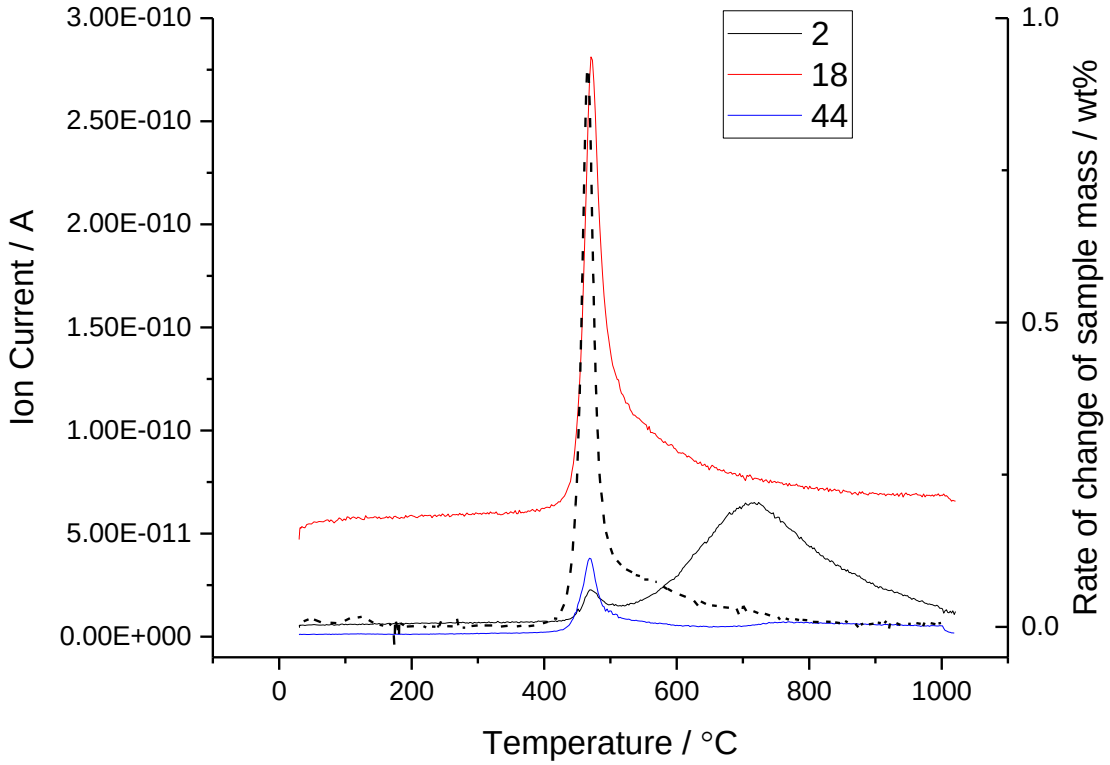

Figure 5.6 - Mass spectrometry responses for H_2 (m/z = 2), H_2O (18) and CO_2 (44) with respect to time elapsed during the TG-MS experiment. The (wet basis) DTG is shown for comparison (black dashed line).

In terms of confirming the two-stage theory for the main decline (or otherwise), there are 2 main pieces of evidence from the TG-MS that appear to prove that this is not the case. The first is that both the m/z = 18 and 44 peaks show a very similar post-peak decline to that seen in the DTG analysis, in that the rate of decline of H_2O/CO_2 emission does not match the rise, but instead reduces much more slowly. This appears to indicate that this slowing down of the rate is not due to the initiation of a new breakdown mechanism, but instead is the continuation of the mechanism driving the main breakdown, but occurring more slowly.

The second piece of evidence is provided by the hydrogen curve in Figure 5.6. The hydrogen peak is the only major signal to increase in the later stages of the experiment; m/z = 48 and 64 also become greater at this time, although these signal are much weaker and later than the peak of the H_2 curve. The peak of the H_2 curve is seen at 712 °C, which is significantly later than any of the peaks found by the residual Gaussian fitting presented in Tables 5.1 and 5.3. This suggests that this mass loss does not coincide with this fitted curve, but instead represents another decomposition mechanism that has far less overall effect on the mass of the solid sample but is significantly different chemistry, a response that it ultimately not shown in the 550 – 650 °C range.

Looking at the by-products of the thermolysis in the mass spectrometer alone can be a difficult method of determining the breakdown mechanism of this material. However, this has been attempted before by Salinas et al. [197], who ran TG-MS on their PIM-1 samples. The results they show match reasonably well to the traces shown in Figure 5.6, particularly the H_2 run, which shows little activity until a large, broad peak centred at 750 °C. The CO_2 peak lines up with the large drop in TGA mass at 510 °C, and then slowly decays as the temperature rises. The relative intensity of the CO_2 peak reported by Salinas et al. is much greater than that seen in Figure 5.6, but given that the mass spectrometer used in this study was not calibrated for quantitative studies, it is possible that similar amounts of the gas are emerging in both cases.

It is the water peak that shows the greatest difference; that shown in Salinas et al. is very broad, with a rise in the signal peaking at the same temperature as the CO_2, but not showing the same sharpness. The signal then falls in a slow, linear manner as the temperature rises. This is quite different to the water response in this study, which shows a much sharper increase in the H_2O response during the region of high mass loss. This could potentially be due to a higher concentration of residual oxygen in the sample chamber reacting with the hydrogen species as they dissociate from the polymer chain, or that as the PIM-1 structure opens up due to decomposition, atmospheric water that is trapped in closed pores or pores with highly restricted access are allowed to escape.

Based on their TG-MS results, Salinas et al. [197] proposed a three-stage decomposition mechanism for PIM-1 in an anoxic, thermolysing environment. They propose that up to 400 °C, there is partial degradation of the dioxane linkages which leads to CO_2 evolution, albeit a very small amount. This creation of polar carbonyl bonds however leads to the formation of cross-linking within the polymer. As the temperature increases through 500°C, the cross-linked polymer then fully degrades, driving off most of the non-carbonaceous appendages and leaving an amorphous black material. The final step, which starts at approximately 675 °C, is a dehydrogenation that results in the large spike in H_2 seen in the MS, but generally has little effect on the weight. This step creates the fully graphitic sheets that the group report through Raman spectroscopy and XRD analysis.

Evaluating the TG-MS data seen from this study, there is little evidence to make changes to the theory postulated by Salinas et al. [197]. Although the DTG curves in Figures 5.2, 5.3 and 5.5 do appear to show a two-step decomposition during the high mass loss step in the TG curve, there is no evidence within the TG-MS traces to suggest that something chemically different is occurring – every m/z value that is present for the sustained decline in the 510 – 625 °C range is also present (and in higher intensity) in the 450-510 °C range, when the DTG curve shows the highest intensity peak. As a result, the decompositions seen in Figures 5.3 and 5.5 are likely to be a function of sample geometry and heat/mass transfer, rather than new chemistry occurring. The TG-MS study in this section also upholds the theories postulated by Salinas et al., as qualitatively similar TG-MS traces are seen, and corroborate with the reactions that the group postulate as the mechanisms for thermolytic decomposition. However, there some differences are seen in the main breakdown products, and the report of Salinas et al. does not report the significant array of other products that come off (and could have serious consequences for ignoring on an industrial scale). Nevertheless, the agreement between the two studies is reasonably good, and there is little need to investigate this matter further (within this study).

5.1.3. TGA in Air

The TGA and DTG curves for PIM-1 heated from 20 – 1000 °C at 10 °C min^{-1} under 1.8 L h^{-1} air are shown in Figure 5.7 below.

Figure 5.7(a) shows very interesting result, in that it doesn't seem to match the nitrogen data at all. There is a similar very small drop in the 0 -200 °C range that is indicative of foreign substances in the material, although the ≤ 1 % drop is again a result of the helium pycnometry run before this experiment. After 350 °C, the pattern is very different. There appears to be one large decrease, but declining at a steady, linear rate rather than showing a sharp drop, as might be expected for a sudden combustion. This slower rate indicates a slow combustion of the polymer that may be dependent on time, more than on temperature. This may be because of the oxygen requirement

of combustion; much sharper drops are often seen in N_2 TGA runs because only heat needs to penetrate the material, and thus bond breaking can occur throughout the material simultaneously. In the case of air, the large drop in mass is due to combustion, as the atoms within the polymer chain react with oxygen from the air, and are lost as the gaseous products of combustion, such as CO_2 and water. However, this breakdown mechanism is dependent on oxygen being present, and it is possible that a restriction on the mass transfer of oxygen into the material stops anything but the surface atoms undergoing the reaction, so slowing the rate of mass loss and resulting in a slower decrease in mass.

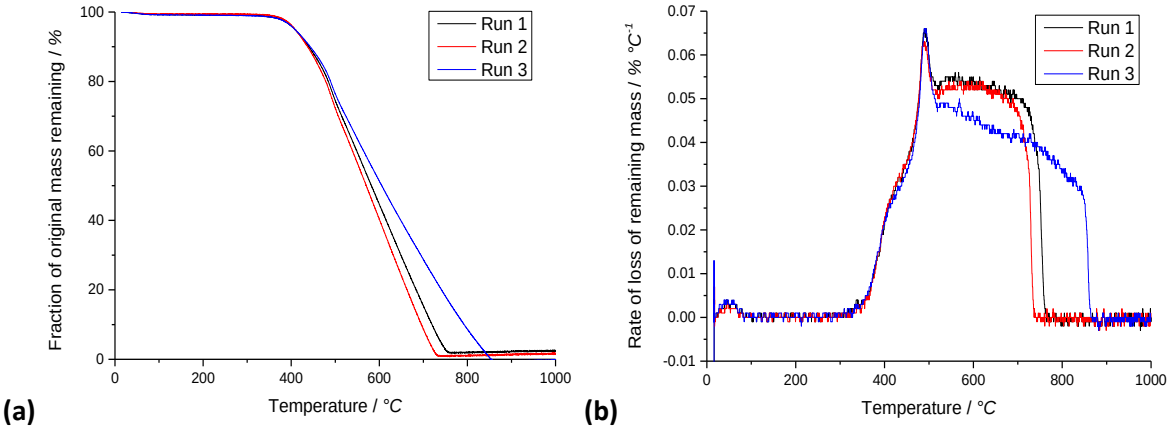

Figure 5.7 - 3 run set of (a) TGA and (b) DTG analyses of PIM-1 under 1.8 L h^{-1} air at 10 °C min^{-1}

The mass decreases all the way to zero, as would be expected given that this is an organic polymer with no metallic content. The non-zero values of mass seen in Figure 5.7(a) are due to inconsistencies between the PIM-1 data and buoyancy correction curves, and should be at zero; following every run, the experimental crucible was completely empty.

This TGA curve in air is not without precedent. Hao, Liao and Chung [201] reported a PIM-1 decomposition in air as part of the characterisation of their PIM-1/ZIF-71 film, and that isotherm charts a decomposition that begins at 350 °C, but does not reach 0 until 650 °C, a very similar rate to that seen in runs 1 and 2 in Figure 5.7. The only major difference is a slight stop in the decrease of Hao, Liao and Chung's run at ~530 °C which is not in the air runs in this study.

The DTG curve in Figure 5.7(b) gives similar insight to the TGA curve. It can be seen in the 0 – 100 °C range that there is a small peak, which is the adsorbates being driven off. The decay in mass initiates at approximately 320 °C and then rises sharply, showing the combustion process initiating. Interestingly, the DTC curve then shows a peak at ~ 490 °C before declining sharply (quite possibly due to the same thermolytic effect seen in the anoxic TGA cases). In the cases of runs 1 and 2, the decay then rises again, plateauing for ~200 °C (reflecting the linear decrease in sample mass in Figure 5.7(a) before declining sharply and abruptly stopping at 0, showing the end point of the decay. Run 3 shows a steady, almost linear decline in its DTG curve after 500 °C, implying a non-linear decay in the mass of the sample which is not immediately obvious looking at Figure 5.7(b). This decay lasts longer than the first two runs, with the sharp drop to 0 coming at 860 °C. Each of these decays after 500 °C shows the material being burnt in the available oxygen; the difference in run 3 is very likely simply due to experimental variation.

5.1.4. TGA Holds

Given the highly carbonaceous nature of the TG product (and reports from various studies that the porosity of PIM-1 increases when carbonised), it was decided that attempting to make porous activated carbons from the PIM-1 material already acquired would be an interesting line of research. The first step towards these materials is to characterise how the material behaves under carbonisation conditions; this can be done by performing TGA runs in which the carbonisation temperature is held constant, and seeing how the mass of the material responds. For PIM-1 carbonisation, it was decided to use the method of Salinas et al. [197] as a guide.

The first experiment performed was a TGA run on PIM-1 (5) powder, ramping up to 800 °C at 5 °C min^{-1}, and then holding at that temperature for 4 hours. The results of all three runs performed this way can be found (plotted on a dry weight basis) in Figure 5.8. The spike in run 2 at 11400 s is an erroneous point due to extenuating circumstances within the experiment, and can be ignored.

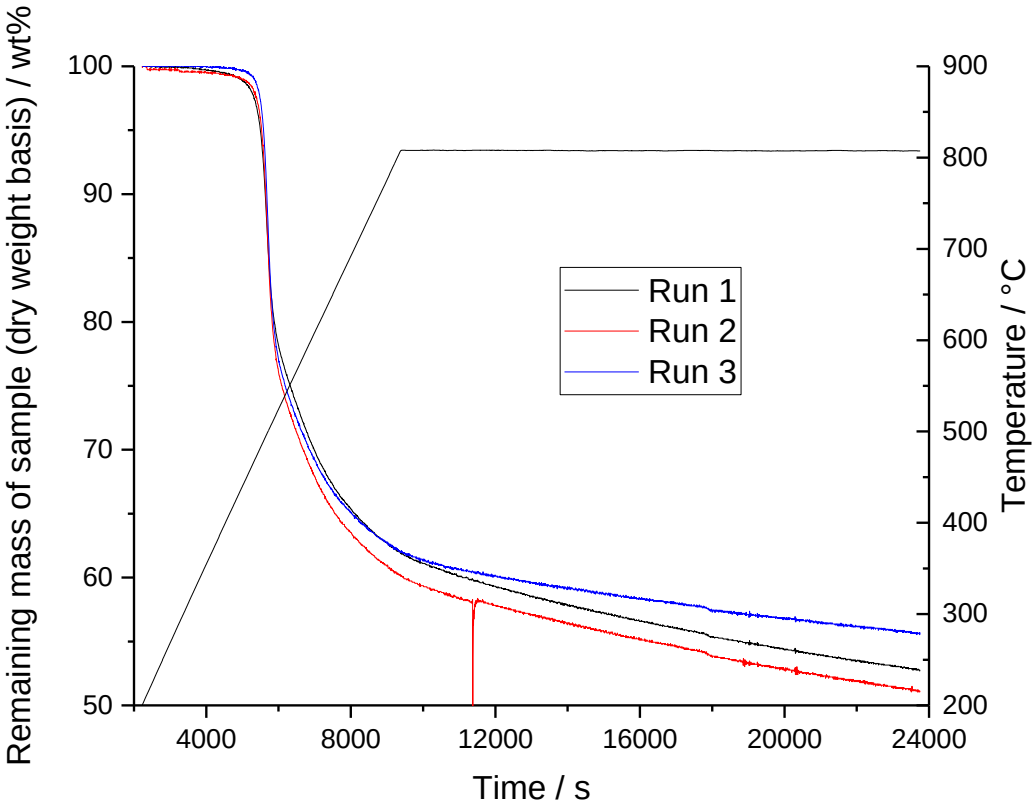

Figure 5.8 - TGA analysis (dry weight basis) of PIM-1 under 1.8 L h^{-1} N_2, featuring a ramp at 5 °C min^{-1}, followed by a 4 h hold at 800 °C.

During the ramp up in temperature, PIM-1 behaves exactly as it does in Figure 5.1, namely there is a large drop off at 480 °C, and the ramp slows down as the temperature increases. What is interesting about this study is that the mass continues to decrease as the temperature is held, and it does not plateau (which would indicate that all but the carbonaceous backbone has been driven off). In order to check when this effect might occur, this experiment was repeated, but instead the temperature hold was performed for 8 hours. The results of this experiment are shown in Figure 5.9.

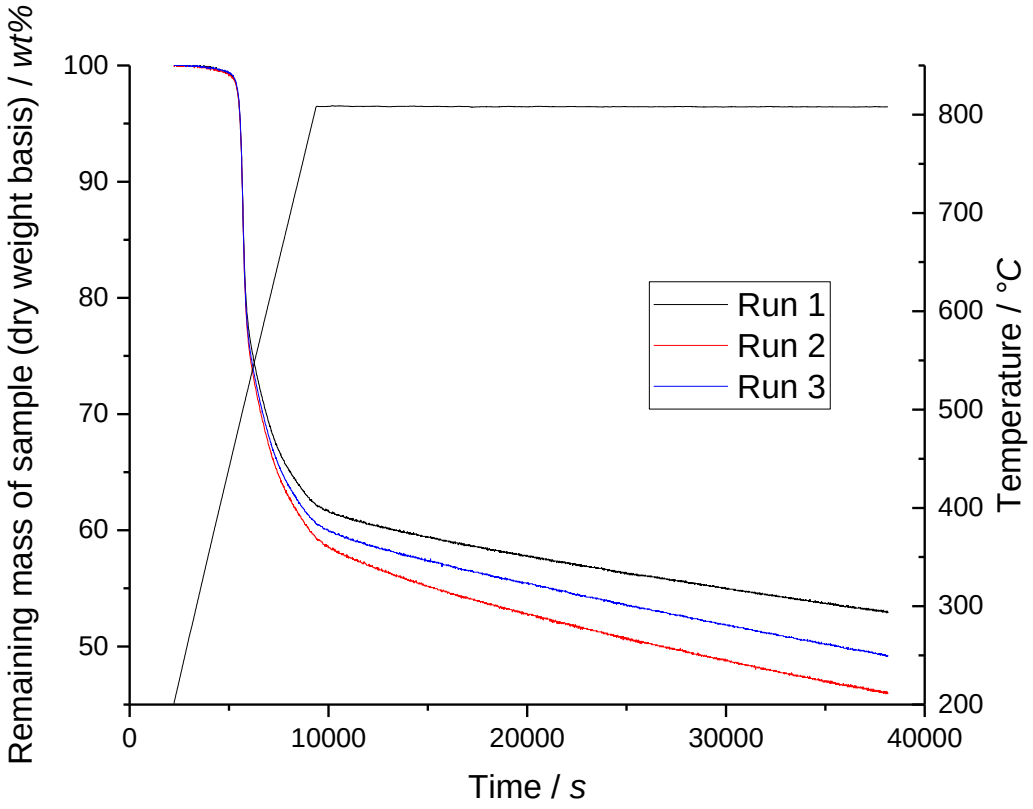

Figure 5.9 - TGA analysis (dry weight basis) of PIM-1 under 1.8 L h^{-1} N_2, featuring a ramp at 5 °C min^{-1}, followed by an 8 h hold at 800 °C.

Curiously, even when held at 800 °C for 8 hours, the mass of the PIM-1 sample does not plateau, instead continuing to decline to as low as 46 % of its original mass (run 2). This either suggests that 8 hours is not long enough for full carbonisation at 800 °C, that 800 °C is not a high enough temperature to strip PIM-1 of its non-carbonaceous appendages, or that something else is occurring within the experiment that is allowing the carbon present to be slowly stripped away.

This final reason could potentially be due to residual oxygen in the reaction chamber: although every effort is made to remove oxygen from the system (pre-flowing before the experiment, continuous flowing of high purity nitrogen throughout the experiment), it could potentially be that what little is present is slowly oxidising the carbonised material. The presence of oxygen is this system must be very low though, given the fast decrease in mass under oxidative conditions seen in Figure 5.7.

Alternatively, this may be due to the morphology of the material itself. Although the powder form of PIM-1 was used for these tests, this material still contains a number of highly tortuous pores, and it is possible that some of the gases evolving from decomposition from deep within the pores cannot escape quickly, and thus these are only lost given sufficient time to escape.

Either way, these experiments are an interesting beginning to working out how to synthesise an activated carbon from PIM-1. Given that there is little sign of the mass decrease stopping any time within an 8 hour window (which is already very long for a typical carbonisation process), it appears that picking any time within the 8 hour window will result in a carbonaceous material (the solid material remaining after all of the experiments detailed here was black in colour) that could be further activated to produce a porous carbon material. As the activated PIM-1 fibres made by Bonso et al. [199] had been both carbonised and activated for an hour each, it was decided for large scale synthesis that carbonisation should occur at 800 °C for 1 hour in inert

conditions, before activation under CO_2 flow (a mild oxidative environment), also for 1 hour at 800 °C.

5.2. Carbonisation and Activation

5.2.1. Carbon Synthesis

PIM-1 samples were carbonised and activated in order to test the adsorptive performance of this class of materials. For the first experiment, two films were made from PIM-1 (5) following the method detailed in section 3.1.2. Each of these films was put through the carbonisation process, and one of the carbonised films was then further activated.

The carbonisation and activation experiments were performed by Jemma Rowlandson at the University of Bristol. Films were placed onto a 6 x 4 cm ceramic dish and placed inside a cylindrical tube furnace. Carbonisation was performed flowing 500 ml min^{-1} of argon over the sample, and the temperature was ramped to 800 °C at 5 °C min^{-1}, before a temperature hold at 800 °C for 1 hour. The furnace was then left to cool overnight with the gas still flowing. Activation was performed the same way, although carbon dioxide was used as the carrier gas.

Images of the carbonised and activated films produced by this process, and the mass losses measured, are shown in Figure 5.10. The mass losses experienced were consistent with multiple runs of the carbonisation showing near identical burn off.

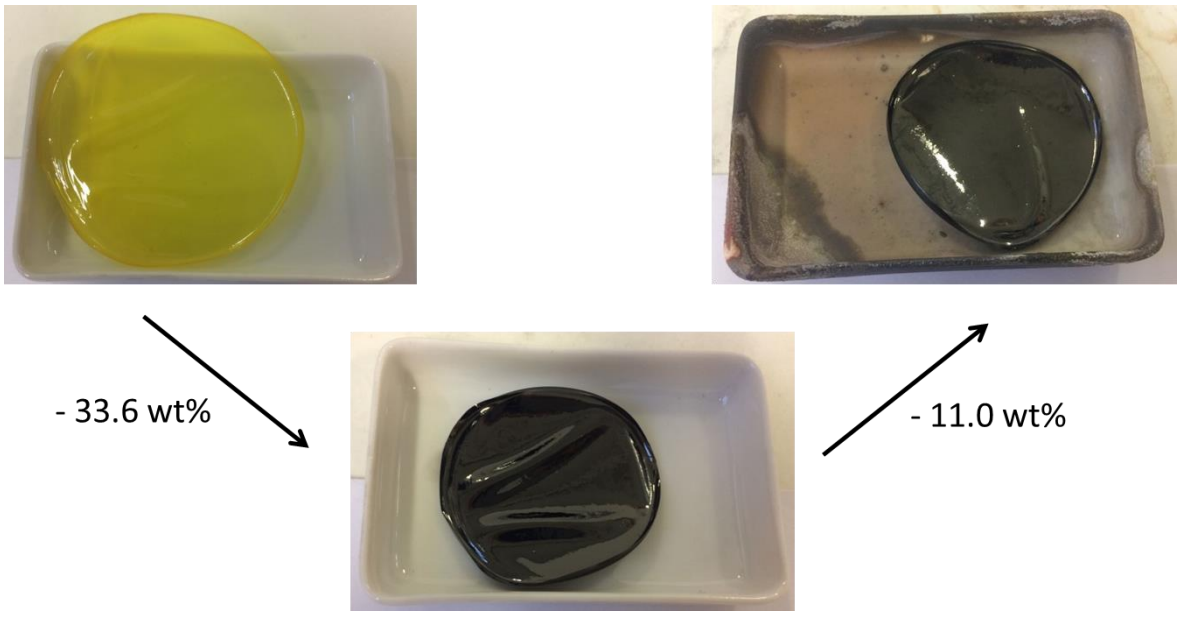

Figure 5.10 - Schematic illustrating the carbonisation and activation processes performed on a PIM-1 (5) film. The carbonised film is shown in the middle, and the carbonised film is in the upper right. wt% values quoted are the fraction of mass lost during the synthesis.

Looking at Figure 5.10, it is clear to see that the PIM films maintain their structural integrity during the carbonisation and activation processes, which is a benefit when considering final application; this maintenance of cohesion may allow the material to be formed into a particular shape (such as a hydrogen tank liner) before carbonisation. The carbon films are much more brittle than the PIM, meaning the creation of alternative shapes must be done before carbonisation. However, this still has the potential to be much more useful than forcing carbon powders into fixed shapes via

binding and extrusion or compression, as the PIM could be pre-formed into the desired shape and then carbonised to produce a high-value end product.

Both the carbonised and activated films have shrunk during the course of the experiment, although this is to be expected when considering that the samples are losing significant amounts of mass. The warping evident in the carbon films is also caused by the carbonisation, likely caused by the shrinking of the material whilst maintaining a cohesive, thicker top layer. No cracks were seen in either the carbonised or activated films.

The films have a very clear two-tone appearance: the top side is very smooth and shiny, and is jet black in colour; whilst the underside is more matted, and has a silvery-grey appearance. Whilst this is likely a reflection of the PIM films that went into the furnace (the shiny side is likely due to the thicker layer on the top of the film, as discussed in section 4.1.3 above). However, the silver-grey appearance is a potential clue that there is graphitic material within the material, as it is common in carbons produced in this way for carbons containing graphitic sheets to show this silver-grey colour with a slight sheen. Testing for this graphitic phase was done via Raman spectroscopy and PXRD, which are detailed in sections 5.2.3 and 5.2.4 below.

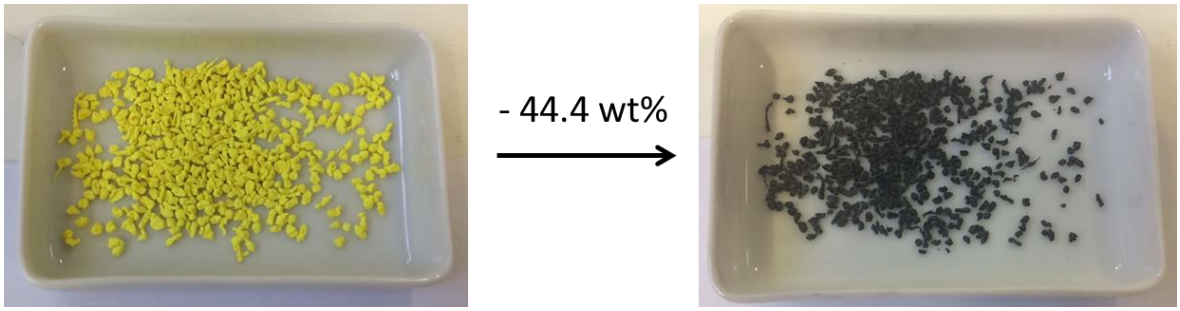

Figure 5.11 - Schematic illustrating the carbonisation performed on a PIM-1 (5) powder sample. The wt% value quoted is the fraction of mass lost during the synthesis.

In addition to making carbonised PIM films, it was decided to try carbonising a PIM powder also. The 'before and after' images for this process are shown in Figure 5.11. Much like the films, the powder turns a black colour with a slight silver-grey sheen on the surface, again potentially illustrative of graphitic material within the sample. The particles retain most of the size of the original, although upon close visual inspection it is apparent that the particles have shrunk a little.

The burn off of the PIM-1 powder was 44.4 wt%, which is very close to the values seen in the TGA with temperature hold experiments shown in Figure 5.8 and Figure 5.9. The average mass loss after 1 hour of the hold (on a wet weight basis, given the powder entered into the furnace was not pre-degassed) was 42.04 %, so the 44.4 % seen on the large scale replicates these results very well.

5.2.2. CHN Analysis

One simple analysis that can illuminate what occurred during the carbonisation process is CHN analysis, which gives the relative composition of carbon, hydrogen and nitrogen in the materials. Each of the 5 samples detailed in section 5.2.1 were tested (by Stephen Boyer of London Metropolitan University), the results of which can be seen in Figure 5.12 below.

The PIM-1 samples in the CHN analyser show very good correlation with the expected proportions of C, H and N as calculated from stoichiometry, shown in Table 5.2 above. Any discrepancy (particularly for the carbon content, which is ~ 2 % below that expected for both samples) is likely

due to the presence of adsorbates within the material, as the sample was not degassed before running, and any adsorbates driven off by the heating in the CHN analyser will have been caught in the traps and registered. Otherwise, this is a strong result, and proves that this technique can give an accurate overview of the composition of the other materials.

As expected, the carbonised materials show a material composition that is more heavily skewed towards carbon, with the carbon contents in the film and powder morphologies registering at 83.64 and 84.28 % respectively. It is interesting to note that neither the hydrogen nor the nitrogen present within the polymer have been driven off completely by the carbonisation – the CN groups in particular appear to have resisted thermolysis, although this finding does correlate the long TGA experiments in section 5.1.4 – the fact the mass did not plateau after 8 hours suggested that there was more material to lose, and it is very plausible that the CN appendages were not driven off fully by a 1 hour hold.

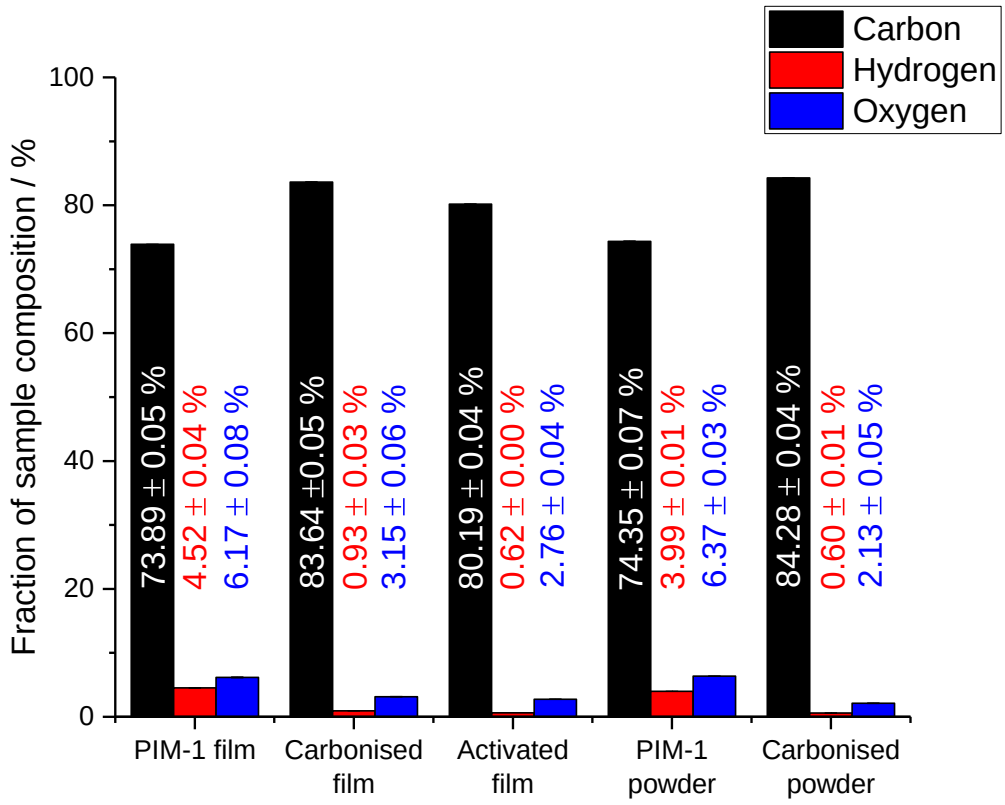

Figure 5.12 - Elemental composition of PIM-1 samples and the carbonised and activated products therefrom, as determined by the CHN Elemental Analyser. The error quoted is the standard deviation.

In all of the cases in Figure 5.12, there is a sizeable proportion of mass not accounted for by either C, H or N – this is mostly attributable to oxygen. The presence of adsorbates, such as water and minor traces of chloroform remaining from the film formation may also be depressing the reported mass fractions.

Oxygen plays a big role in the molecular structure of PIM-1 because of the dioxane linkages that hold the spirobisindane and terephthalonitrile units together; as such, oxygen constitutes 14 wt% of PIM-1. This oxygen must largely be preserved during the carbonisation process, as it is critical to the structure of the remaining material – if all of the oxygen was to be driven off, the remaining material would be mostly the original reagents for the material without the reactive -OH and –F groups, and the material would collapse into a powder. The fact that these materials do not do this, and the hinting that graphitic material may be present in the material, suggests that the dioxane linkers have been maintained.

The dioxane linkers are also likely the main reason why the carbon content appears to decrease during the activation process. During activation, CO_2 oxidises some of the carbon within the material, which is then lost to the gas flow (primarily as CO). However, the oxidising conditions will not affect the dioxane linkers holding the material together, and this mass is nearly totally preserved. This decrease in carbon present but maintenance of total oxygen results in a relative fall in carbon mass fraction in the activated material.

Hydrogen and nitrogen both decrease during the activation process also – these will have been caused either by a continuation of the thermolytic effect of the temperature, or may also have been oxidised by the flowing CO_2.

5.2.3. Raman Spectroscopy

Raman Spectroscopy was performed by Dr. Mi Tian (University of Bath) on each of the five samples to get a chemical fingerprint for the materials, and to investigate the potential of a graphitic phase in the carbonised materials. The Raman spectra for the PIM-1 samples are shown in Figure 5.13, and for the carbonised samples are in Figure 5.14.

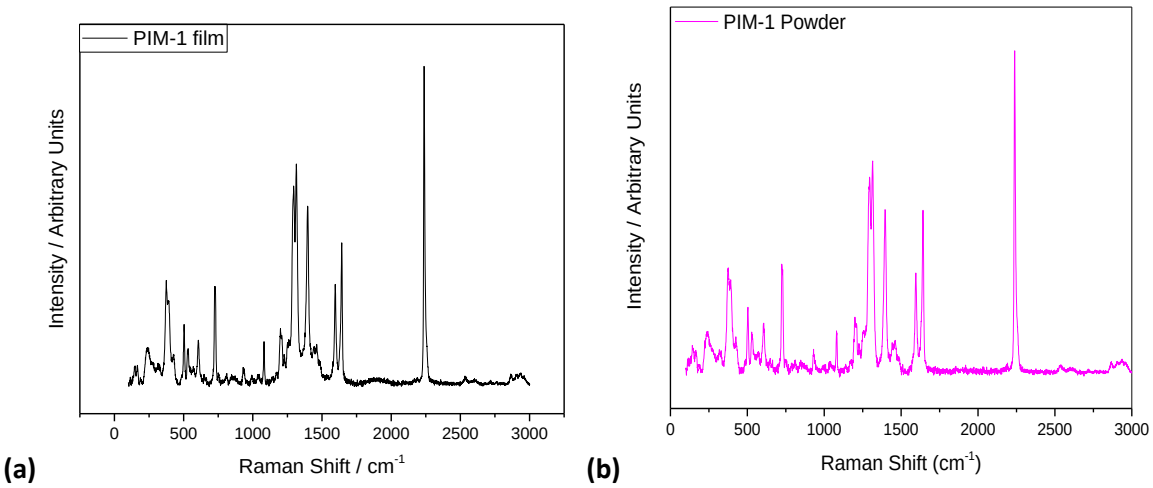

Figure 5.13 - Raman spectra for PIM-1 film (a) and powder (b) samples.

The Raman spectra for the PIM-1 films appear highly complex, which is to be expected given the large number of functional groups that make up the material. Curiously, all previous reporting of the Raman spectra discovered by the authors does not report the full spectrum, but instead tends to show smaller regions of it, particularly when comparing to carbonaceous products manufactured from the material [198, 242]. Comparing the above spectra to these smaller, previously reported spectra, the peak locations and relative intensities show a good match, and this information provides further confirmation that the synthesised material is PIM-1.

Using Raman spectra tables [333–335], it is possible to estimate the identities of particular peaks. Although some peaks are easily identifiable (e.g. the nitrile group at 2250 cm^{-1}), the majority of the peaks do not easily fit into an identifiable bracket that would allow for the bond and vibrational mechanism from which the peak arises. It is possible to use more detailed theory and/or resonance calculation software could more accurately identify the bonds and vibration modes causing the Raman shifts seen [333]. However, because the structure of PIM-1 is well known and these spectra have been generated purely for comparative purposes, it was deemed beyond the scope of this study to investigate this in detail.

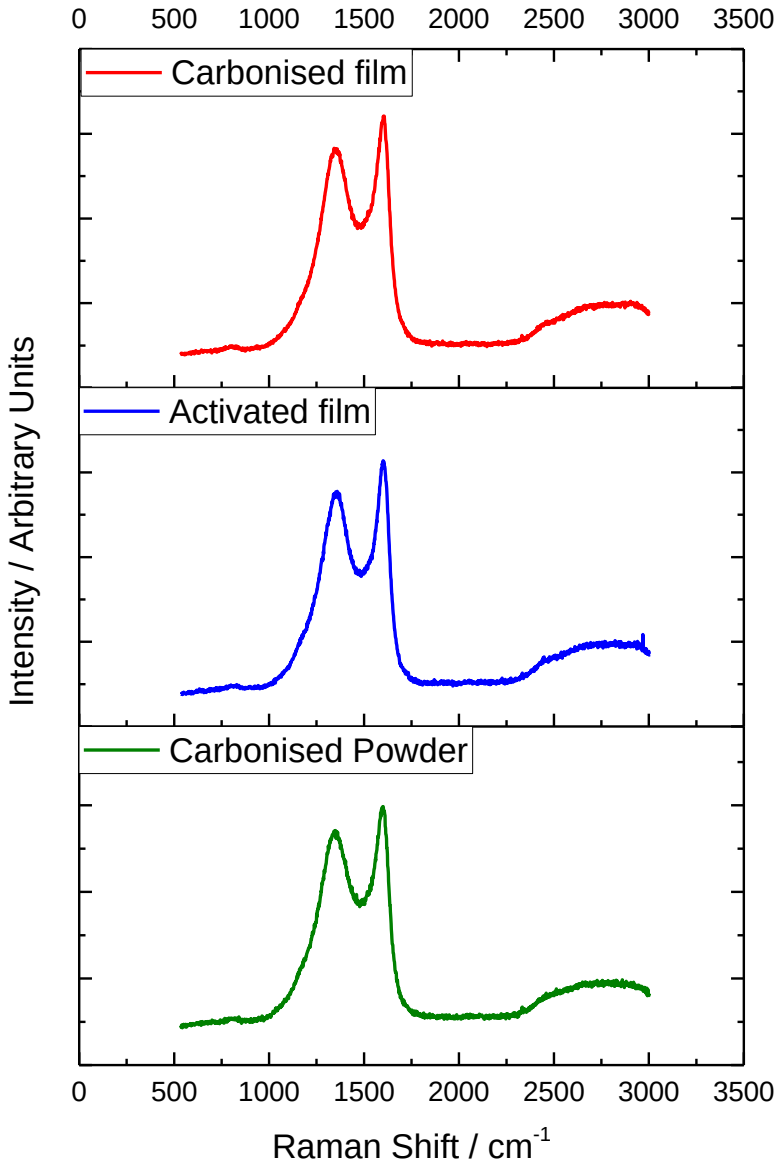

Figure 5.14 - Raman spectra for the carbonised and activated PIM-1 films, and the carbonised PIM-1 powder.

Looking at the Raman spectra of the carbonised materials, it is immediately obvious that they are highly different from the PIM-1 spectra, primarily in that the multitude of peaks from the various functional groups have been removed, and what remains is a simple spectra that is highly characteristic of carbonaceous materials, as identified by multiple previous studies [183, 197–199]. The primary peaks seen can be attributed as the D (1300 cm^{-1}) and G peaks (1600 cm^{-1}), which are representative of amorphous and graphitic phases respectively [199, 336]. This is clear evidence of the presence of a graphitic phase within the material, which is indeed likely causing the silver-grey colour of the underside of the films. The large bump from 2400 – 3000 cm^{-1} is likely the D* peak, which is an overtone of the D. It is highly common in samples containing disordered carbon material [337].

Although it appears as though there are only 2 peaks of significance in these spectra, the range over which they cover suggest that there may be multiple signals causing the output spectra. One common way to tease apart these phenomena is to deconvolute the spectrum between 1000 – 2000 cm^{-1}. A first attempt at a two peak convolution (SI-6, Figure 1) using the multipeak fitting function in OriginPro (Lorentzian peaks) on the carbonised film spectrum produced a reasonable fit, but left a large gap in the ~1500 cm^{-1} range, and there is a small bump at ~ 1200 cm^{-1} that is

unaccounted for. As both of these sites have been recognised both theoretically and empirically as potential sites of activity in carbons that are a mix of graphitic and disordered [198, 199, 336], it became apparent that deconvoluting these peaks also could produce a result with scientific grounding. Reattempting this deconvolution but with a focus on four peaks produces the convolution seen in Figure 5.15 below. The deconvolutions for the other carbons in Figure 5.14 can be found in the supplementary information (SI-6).

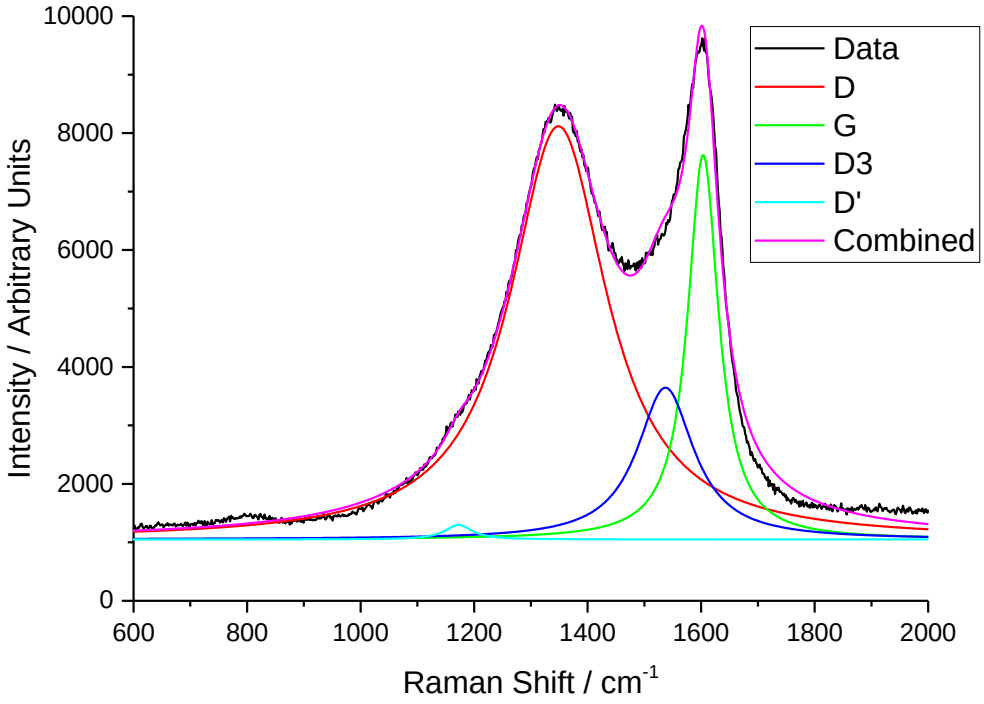

Figure 5.15 - Deconvoluted Raman spectrum for the carbonised PIM-1 film

These four peaks are the previously identified D and G peaks, and the newly identified contributors are the D3 (at 1500 cm^{-1}, caused by amorphous phases at the interstitial sites in a disturbed graphitic lattice) and D' (sp^2-sp^3 bonds) peaks [199]. The ratios between them appear consistent with previously reported Raman spectra for PIM-1-sourced carbons [198, 199].

A further study can that be easily performed is the determination of the degree of crystallinity. This is simply performed by taking the ratio of the integrals of the D and G peaks (*I(D)/I(G)*); the results of this analysis are shown in Table 5.4. In general, all of the values seen for these samples are relatively high (Bonso et al. [199] reported a value of 2.32 for their carbon fibres; Kim et al. [198] report 1.84 for their carbonaceous films). This high value suggests that there is a relatively low content of graphitic material within the PIM-1 carbons made for this study. This is perhaps due to a relatively gentle carbonisation process; the temperatures used for both the Bonso et al and Kim et al. studies were 1000 °C, and Bonso et al used H_2O rather than CO_2 as their activation agent, which is well known to be a harsher activation agent [88]. The laser wavelength also affects the I(D)/I(G) ratio [338], and both of the studies cited above used longer wavelength radiation of the carbons than the 532 nm laser used in this study.

Table 5.4 – Degree of crystallinity and average crystallite sizes calculated for each of the carbonised PIM-1 samples from the Raman deconvolutions

Parameter	Carbonised film	Activated film	Carbonised powder
I(D)/I(G)	3.385	3.071	3.585
L_a	5.680	6.259	5.363

The *I(D)/I(G)* ratio can also be used to estimate the average size of the crystalline phases within a material (L_a). The relationship between crystallite size and intensity band ratio was first demonstrated by the systematic studies of Tuinstra and Koenig, who demonstrated that L_a was inversely proportional to *I(D)/I(G),* and has been developed by a number of groups over the years to more precisely determine the constant of proportionality [338]. The best attempt to date is the modified Tuinstra-Koenig equation proposed by Cançado et al. [338], who determined a general equation allowing lasers of any wavelength to be factored into the calculation. The values of L_a for the carbons demonstrated in this study were determined using this equation, and the results can be found in Table 5.4.

As expected, the high values of *I(D)/I(G)* have resulted in a low crystallite size. These low sizes suggest that the carbons made in this study are not the full sheets of graphitic carbon that typically make up an activated carbon, but instead a mostly amorphous polymer of carbon with small isolated regions of crystalline graphite between them. This value appears to further indicate that there is further scope for carbonisation of this material, particularly when comparing the carbonised and activated films; there is a clear progression in terms of reduced *I(D)/I(G)* and increased crystallite size with the extra processing afforded to the activated film, which certainly indicates that more intensive processing may result in a purer, more graphitic activated carbon.

One last point of note from Figure 5.14 is the relatively broad nature of the peaks seen in all of the spectra. Although in the main two peaks this can at least partially be put down to multiple different Raman scatterings interacting, it is also known that broad peaks in spectra can be caused by fine crystallite size [337]. The low L_a values calculated for these materials support this idea, particularly for the very broad and low intensity peak seen in the 2400 – 3000 cm^{-1} range.

5.2.4. PXRD

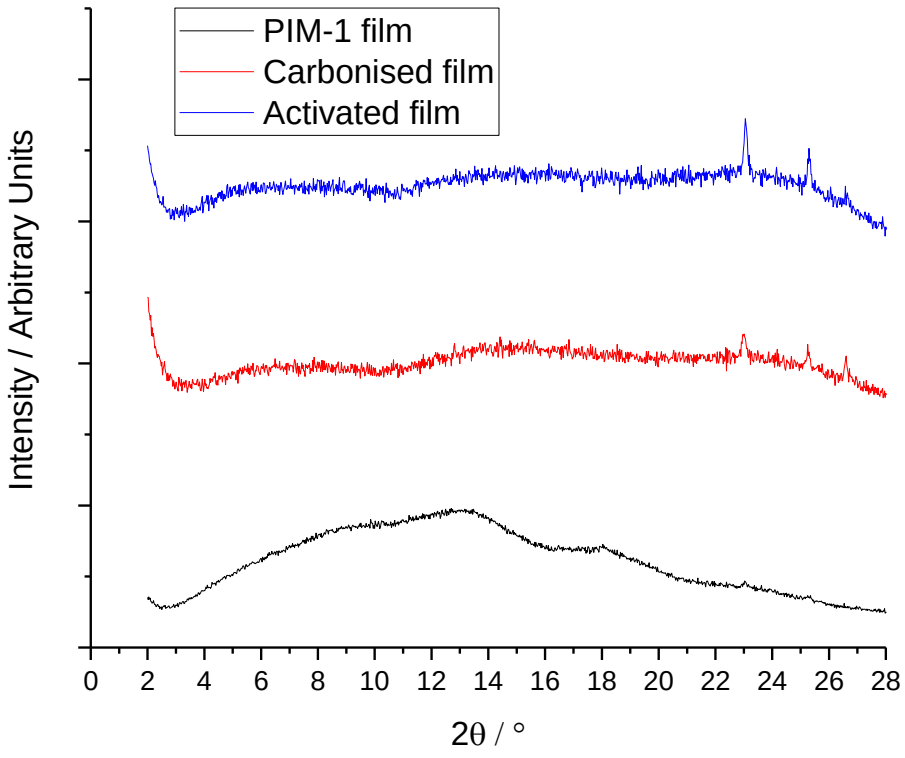

Figure 5.16 - PXRD traces for the PIM-1 (5) film and the carbonised and activated films. The carbon films have been magnified x4.5 to give a clearer view of the trace.

PXRD was performed on all of the film samples only; the results can be seen in Figure 5.16. The traces for both the carbonised and activated films have been multiplied by x4.5 in order to better see the traces.

The trace for PIM-1 (5) is, as expected, exactly the same as PIM-1 (4), showing peaks at 2ϑ = 13, 18 and 23 °. However, it cannot be said that this behaviour is replicated in the carbon materials. Although there are very broad rises in the traces centred on 2ϑ = 6, 13 and 23 °, these are too shallow and too broad to accurately designate to any particular Bragg distance or chemical feature of the material. These materials also do not match the carbonised PIM-1 sample of Salinas et al. [197], which showed a large, very broad peak around 24°, which would strongly indicate the presence of graphitic material.

The only features of interest in the PXRD traces for the carbons are three small, relatively sharp peaks at 2ϑ = 23.1, 25.3 and 26.6 °. These are an interesting feature as sharp peaks in this region of the spectrum on carbon materials often indicate graphitic material – the PXRD spectrum for graphite produces a very strong peak at 2ϑ = 26 ° (the 002 plane between graphitic layers), even when incorporated into a majority of amorphous material [339]. However, the carbons from PIM-1 in this study do not show this single, strong peak, but instead shows much smaller peaks that are slightly misaligned in the spectra from the ideal for graphite.

Multiple peaks in the 23 – 26 ° degree range have been reported before for activated carbon samples; Girgis et al. [340] attributed these peaks to fragmented crystallite phases. This correlates with the graphitic crystallite sizes calculated from the Raman spectra; the ~ 5 – 6 nm crystalline phases are very small and are surrounded by large domains of amorphous material; these could then be acting to suppress the strong response of the graphitic material. These techniques together appear to determine the nature of the carbon within these materials, primarily that there are small and relatively insignificant regions of graphitic crystallinity surrounded by large swathes of amorphous carbon material.

5.2.5. SEM

Scanning electron microscopy images were taken of all the carbon samples. These are presented in Figure 5.17 - Figure 5.20 below.

The faces of the carbonised film are shown in Figure 5.17. The top side (parts (a) – (c)) show a very flat surface, much like the PIM-1 surface seen in Figure 4.15. This is a product of the smooth, shiny nature of the surface. However, there is a clear rise in the density of features on the surface, particularly holes. Parts (b) and (c) clearly illustrate a number of holes of various sizes in the top surface, which would have been formed as the gases produced by the pyrolysis force their way out of the material through areas on the surface weakened by thermolysis occurring on the external surface.

The bottom side of the material (the silver-grey, matted side) is shown in parts ((d) – (f)). This side is much rougher at all scales, which explains the difference in shininess, and is likely caused by the same stepwise curing effect seen in the PIM-1/MIL-101 composites discussed in section 4.1.3. The higher magnifications also show a higher density of holes from which gases escaped the film, which will have been due to the softer, less set polymer on the underside of the film providing a path of least resistance for the escaping gases. There is also a large number of divots in the surface, again likely caused by thermolysis in a defect in the surface causing the defect to hollow out.

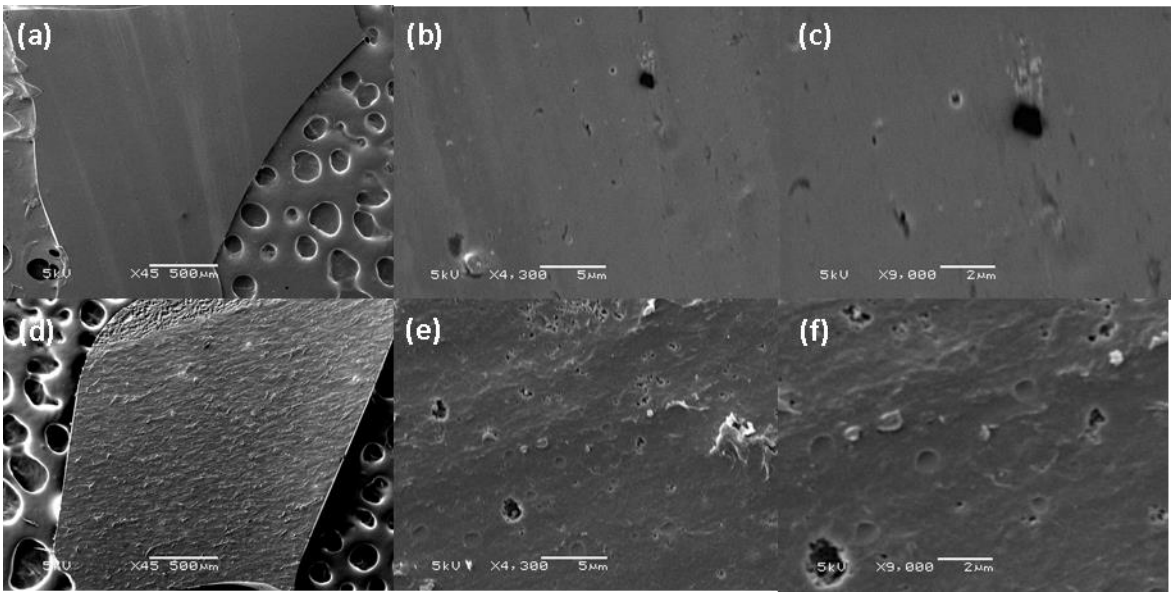

Figure 5.17 - Scanning Electron microscopy images of the top (a - c) and bottom (d - f) faces of the carbonised PIM-1 film at x45 (left) x4300 (middle) and x9000 (right) magnifications respectively.

Figure 5.18 shows the faces of the activated carbon film. Much like the carbonised film, there is a clear difference in the surface roughness of the top and the bottom of the films, with the shiny top surface appearing much smoother than the matted underside. It is apparent from parts (a) – (c) that this top surface shows more defects and holes than the carbonised equivalent. The large divots seen in part (a) are likely caused by pressing down on the sample with sharp tweezers, which would cause the broad depressions. Parts (b) and (c) illustrate that the top surface of the activated film is more porous than for the carbon films, which is a product of the greater time and reactivity of the activation conditions increasing the rate of gas production, and the susceptibility of the surface to developing divots, which could then act as weak points for the gases to burst through the surface. The underside of the activated film is also visibly rougher than the carbonised film. The divots and holes are larger and more frequent, and there is a large 'crater' in part (e), which shows a very rough surface on the interior featuring a large number of smaller divots where the thermolysis reaction has taken hold.

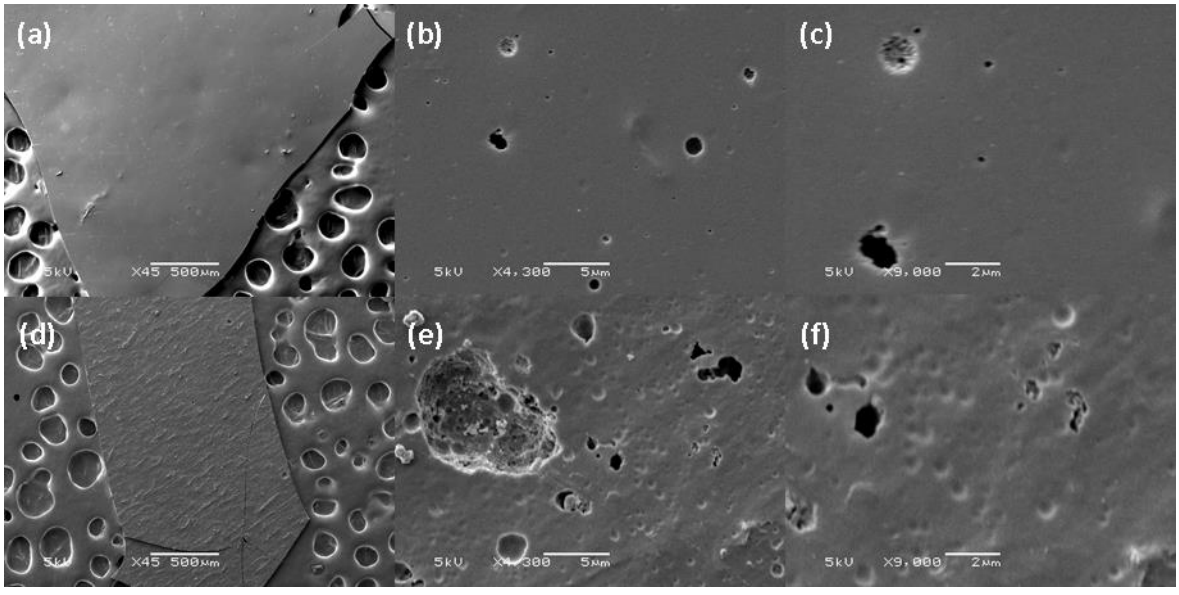

Figure 5.18 - Scanning Electron microscopy images of the top (a - c) and bottom (d - f) faces of the activated PIM-1 film at x45 (left) x4300 (middle) and x9000 (right) magnifications respectively.

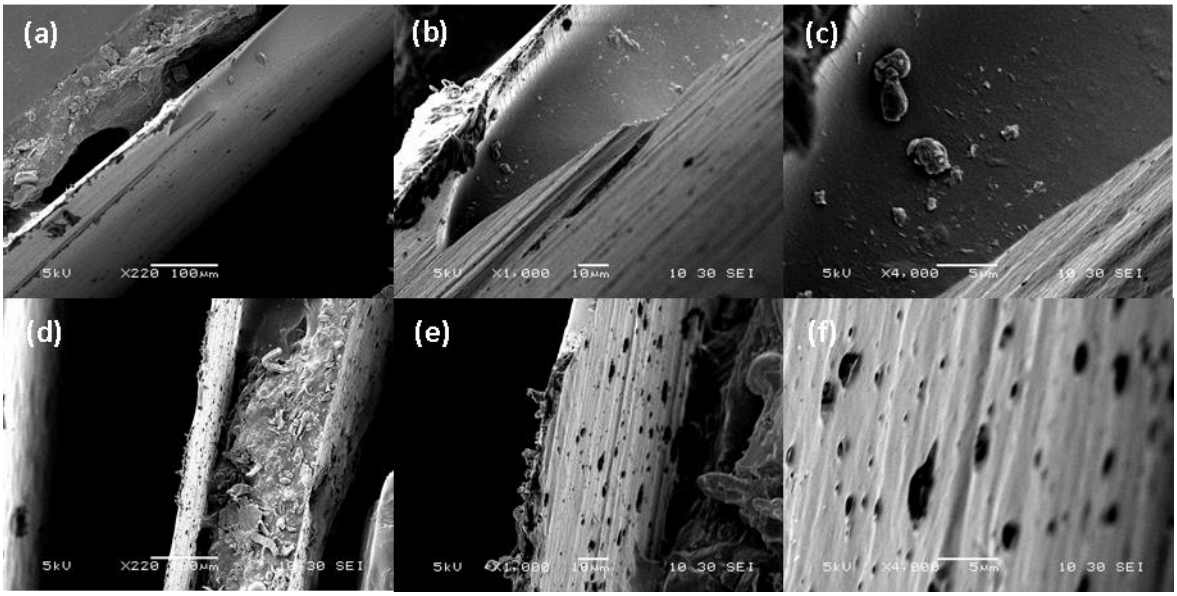

Figure 5.19 - Scanning Electron microscopy images of the cross sections of the carbonised (a - c) and activated (d - f) PIM-1 films at x220 (left) x1000 (middle) and x4000 (right) magnifications respectively.

The cross-sectional images of the film edges are presented in Figure 5.19. The carbonised film (parts (a) – (c)) shows a film with clear striations through it, which given the very solid nature of the PIM-1 from which it came, is either a function of the carbonisation process, or is a remnant of the sample preparation method.

There is a very large open section in the part of the film pictured, which is an unexpected feature. It is curious to see that within this gap there is a number of small nodules, the largest being ~ 3 µm in size, that are reminiscent of those found on the surface of PIM-1. This, combined with the surface within this open section being very smooth, suggests that this void was already present in the film before the carbonisation process, as these nodules would not be created by the carbonisation, and the surface of this cavity looks a lot like the surface of the film illustrated in Figure 5.17.

The other feature of note from these images is the number of holes in the surface. On the left of Figure 5.19 (a), there are 2 large dark regions, which appear to be large cavities in the film, likely caused by the thermolysis. However, if these dark regions are believed to be holes, then the large number of large dark regions on the top side of the film, attached to the bright white part of the film, must also be free volume. This illuminated part of the film is very likely the shiny top layer of the film, which appears to indicate that there is a large number of cavities just below this thicker top part of the film, and that the top layer is beginning to delaminate from the rest of the film.

A closer look at the solid region to the left of the image in Figure 5.19 (a) (shown in the supplementary information, SI-7) also shows a number of sub-micron holes in the cross-section, which indicates the emergence of small void volumes and channels within the material. These will have been caused both by the breakdown of the material and the emergence of the gases creating local high pressure regions that form the channels seen.

The cross-sectional view of the activated film can be seen in Figure 5.19 parts (d – f). This film also shows similar striations through the material parallel to the top and bottom surfaces, although if this is a phenomenon caused by the carbonisation process then it would be expected to be maintained, if not amplified, by the activation process.

The main feature of the edge of the activated film is the large number of holes that appear to have been 'punched' through the material. These appear to be of a similar density as those seen in the carbonised film, but these holes are generally larger, and all appear to have slightly raised edges around them, suggesting that they were created through the application of blunt force, rather than chemically reacted, which would leave a smoother edge of the pore (as seen on the faces of these films in Figure 5.17 and Figure 5.18 above). It is also interesting to note that the density of these large holes is much greater in the lower part of the film (the right hand side from the view provided in Figure 5.19), as though much more activity was occurring in this region of the film during the carbonisation and activation processes.

There is also evidence of thick top layer lamination in these images. The shiny top layer is on the left of the film as it is viewed in parts (d - f), and there are clearly regions where the material appears to be coming loose. This phenomenon is particularly well illustrated in part (e), where the top layer stops overlapping the rest of the film as it does at the very top of the image, and begins to peel away, revealing a number of large voids within the film just beneath this layer.

All of these findings appear to show a material that has undergone chemical change within the body of the material, but has done so heterogeneously, with a very dense top layer that has undergone relatively little change. Furthermore, the top layer is beginning to delaminate from the rest of the material, which appears to be more porous as a result of gas ejection from the material.

As with the composite images in Figure 4.17, the images in Figure 5.19 can be measured to uncover a rough estimate for the thicknesses of the composite films. The thicknesses are measured to be 59.83 ± 3.55 µm for the carbonised film, and 33.24 ± 3.66 µm for the activated film. These values make sense, as mass is lost from the films during both the carbonisation and activation processes, and this can happen from the surfaces as well as internally, so resulting in external layers of the material being removed and the thickness decreased. Curiously, in both cases the thickness reduction is greater (in percentage terms) than the mass loss, which suggests that not much volume is being maintained inside the material, but is primarily being lost from the outside. The adsorption testing presented in section 5.3 will determine whether this is the case.

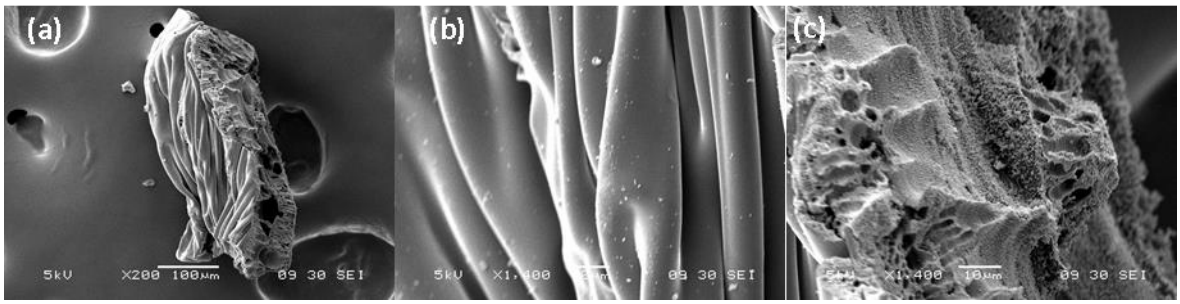

Figure 5.20 - Scanning Electron microscopy images of carbonised PIM-1 powder at x200 (a) and x1400 (b, c) magnifications respectively.

SEM images of the carbonised PIM-1 powder are shown in Figure 5.20 above. These images are interesting as they appear to show both similarity and great difference from the original PIM-1 powder images in Figure 4.13. Parts (a) and (b) show a very smooth, folded surface that has been maintained from the original material, as well as the small nodules of polymer on the surface that appear to have not been affected by the carbonisation process. From these views, this material is clearly derived from PIM-1 powder. However, the right side of the particle in part (a) (shown in greater magnification in part (c)) appears to show a much more open surface structure, with both regular large holes and a highly roughened surface (likely caused by the creation of smaller pores

in the surface material, as well as further burn off therefrom). This heterogeneity in the particle perhaps suggests a similar top surface effect as seen in the films, although due to the lack of evidence for a mass transfer-limiting portion of the surface of the particle, this two-sided nature is likely due to the emergence of the gas-channelling pores on one side of the particle effectively serving all of the thermolysis reaction that occurs within.

5.3. Adsorption Characterisation

5.3.1. Low Pressure (≤ 0.1 MPa)

The low pressure nitrogen isotherms performed on all 5 samples are shown in Figure 5.21 below. As with the PIM-1 films and composites reported in section 4.8, the adsorption equilibration for the PIM-1 films and the carbonised films took a very long time in the low pressure region, such that the experiments would expire (all of the LN_2 in the dewar would boil off and cause the saturation tube to overpressure, triggering the system to end the experiment prematurely). As such, reduced BET isotherms had to be performed in order to compare the uptakes between the materials. As discussed in section 4.8.3, the BET surface areas from these isotherms will not be fully representative of the available surface areas of the materials, but instead have utility as a metric for comparison.

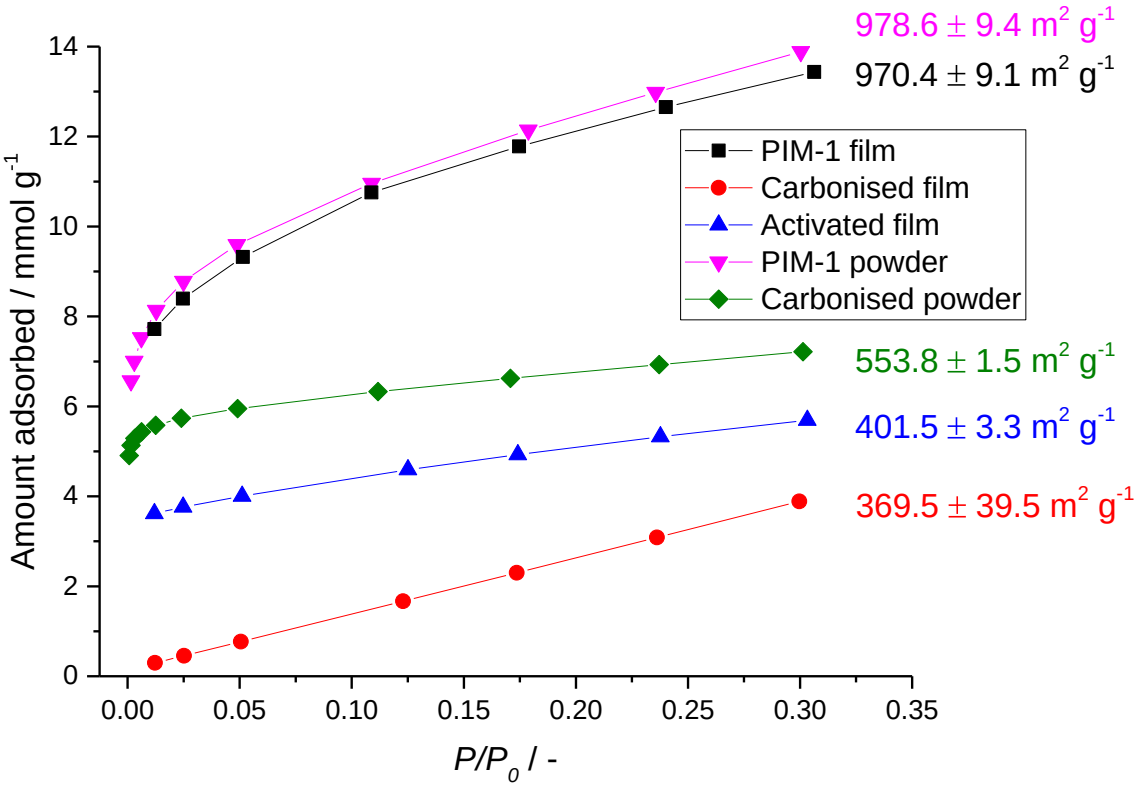

Figure 5.21 - N_2 BET isotherms at 77 K for the PIM-1 (5) samples and the carbonised and activated products made therefrom. Lines are provided to guide the eye only.

There is a number of points raised by this set of isotherms and surface areas. Firstly, it is interesting to see the performance of both the PIM-1 powder and film morphologies perform very similarly, suggesting that any 'locked-in' mesoporosity in this sample of PIM-1 powder is relatively insignificant.

Secondly, in both the film and powder morphologies, there is a large drop off in the nitrogen uptake after the material is carbonised. This is a feature that is commonly seen in carbon materials from PIMs and other porous polymers, largely due to thermal cross linking, which collapses any mesoporosity in the material but increases the number of micropores [183, 198, 199]. This results in the much sharper knee in the isotherm for the carbonised powder. This reduced mesoporosity in the carbonised material is seen in the much flatter isotherm profiles through the P/P_0 = 0.05 – 0.3 range. The exception to this is the carbonised film, which appears to show very little uptake in the microporous region, but a much greater rate of increase through the pressure range in which the mesopores begin to fill. This is likely due to heavy mass transfer limitation into this film, which is corroborated by the H_2 adsorption studies below (Figure 5.23).

The other point of note is that the activated film shows a clear increase in uptake over the carbonised film from which it was made, but it compares poorly to the original PIM film. The improvement from the carbonised film is expected, as it is by design that the CO_2 oxidising environment burns away some of the material, forming porosity (in particular micropores) in the process. However, it would be expected that the nitrogen uptake in the activated film would be greater than the PIM from which it was synthesised, and this result perhaps suggest that the activating conditions chosen were too mild to sufficiently replace the mesoporosity that had been lost due to crosslinking during carbonisation. Part of the high uptake for the PIM film shown is also due to the use of a freshly synthesised film for this study, rather than one from the exact same batch as the carbon films. Measuring the porosity of a PIM film straight after it is made will result in greater uptake than if left for a number of days due to thermodynamic aging (see section 2.5.2.8), and due to the logistics of the carbonisation process in this study, the films were left for a number of weeks before they were carbonised, so likely giving a less porous starting material. The new film was likely a better synthesis also, as towards the end of the study the quality of the synthesised films was higher due to experimental practice.

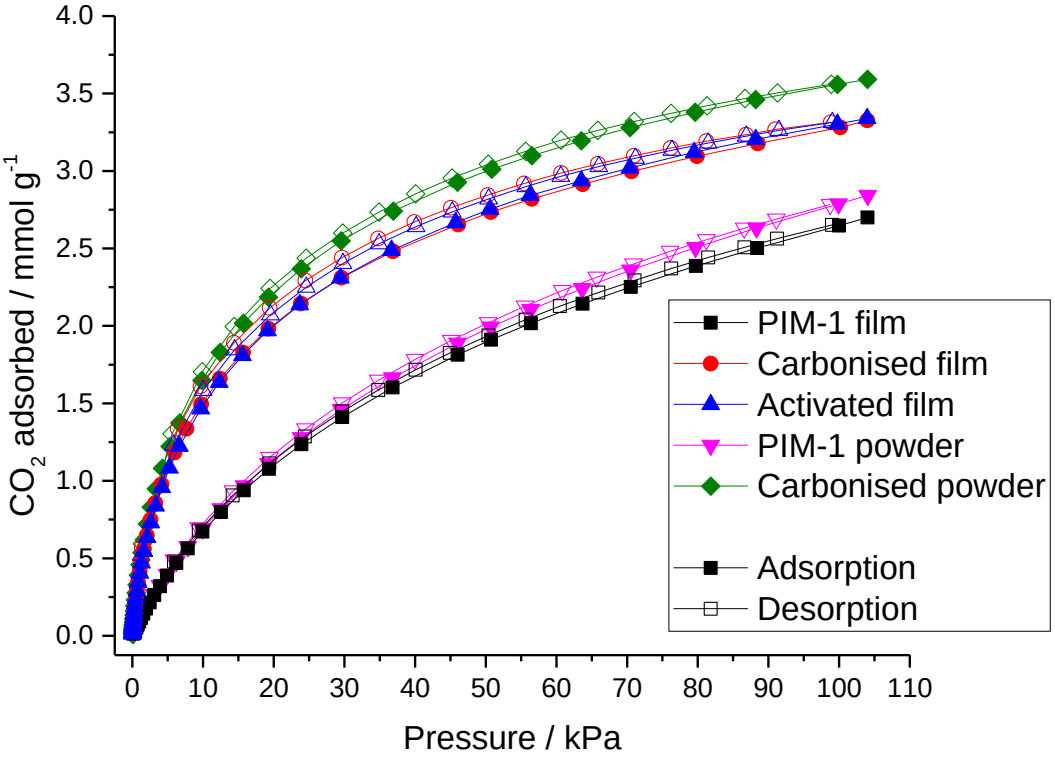

Figure 5.22 - CO_2 isotherms at 273 K for the PIM-1 (5) samples and the carbonised and activated products made therefrom. Lines are provided to guide the eye only.

Carbon dioxide isotherms at 0 °C were performed for all of the samples, and the result are shown in Figure 5.22. This result is far more aligned with what would be expected for these materials, namely that the carbonised materials show much higher activity in the microporous region than the original PIM materials. The difference in uptake between powder and film is also maintained through carbonisation, suggesting that the microporosity in the PIM is not being eliminated by the cross-linking during carbonisation, but that it is only being added by the elimination of mesoporosity – this would also explain why there is a slightly bigger increase in uptake in the carbonised materials (from film to powder) than in the originals. The CO_2 uptake for the carbonised film also demonstrates that the low uptake seen in the low pressure regions of the nitrogen isotherm at far more to do with mass transfer than with lack of adsorption capacity, given the ample extra uptake of CO_2 demonstrated here.

Another interesting point of note is that the uptake for the activated film is essentially identical to that for the carbonised film. This is surprising as it would be expected that more microporosity would be generated within the material during the activation process, which should have shown a greater CO_2 uptake in the range possible in the 3-flex. Based on this evidence, it is apparent that the activation has cleared out the pathways within the material to the micropores within the material, but has not actually increased the microporosity itself. However, this can be demonstrated further by testing for hydrogen adsorption.

Low pressure hydrogen isotherms for PIM-1 and its carbonisation products are shown in Figure 5.23 below. As with the PIM-1/MIL-101 composites, there is a downward inflexion in the high pressure region of the isotherms. This erroneous result is again due to issues with freespace analysis of these materials, particularly in the film materials, which have already displayed erroneous results consistent with difficulties in mass transfer of the adsorptive. Although the shapes of these isotherms may not be consistent with the true excess uptake experienced within the pores, the apparent uptakes shown here can unveil some information on the relative utilities of these materials for adsorptive hydrogen storage. The only exception to this is the PIM-1 powder, which only shows a very small inflection at the end of the isotherm, and therefore is unlikely to have experienced the issues with freespace determination to the same extent as the other materials.

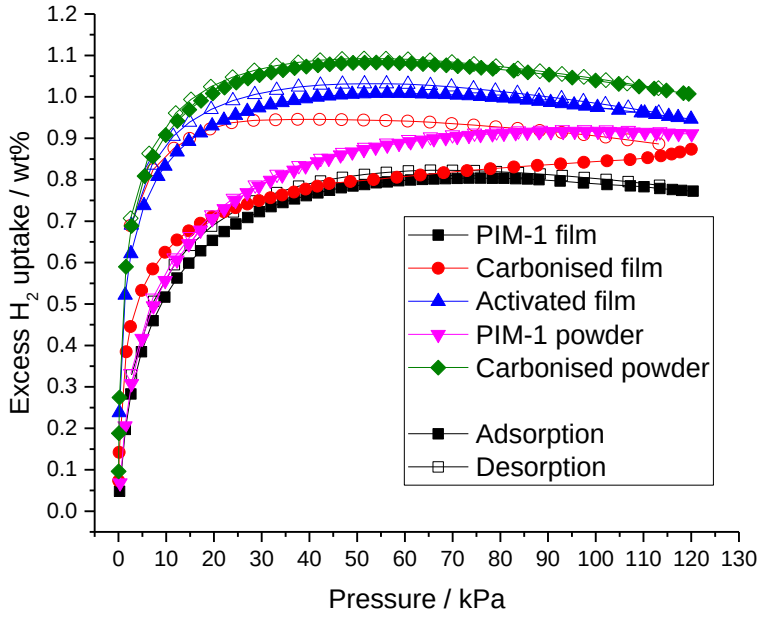

Figure 5.23 - Low pressure (0.1 MPa) H_2 isotherms at 77 K for the PIM-1 (5) samples and the carbonised and activated products made therefrom. Lines are provided to guide the eye only.

It is immediately obvious looking at Figure 5.23 that carbonising the materials improves the hydrogen uptake, particularly in the low pressure region of the isotherm. This is true for both the powder and film morphologies, and is corroboration of the effect seen for the CO_2 uptake, namely that the carbonised materials appear to show much higher microporous activity. The difference in H_2 uptake between the carbonised powder and activated film are close but the powder still has a consistently higher uptake, which mirrors behaviour from the CO_2 isotherms.

The isotherm for the carbonised film is unusual, as it shows an uptake very similar to that of the PIM-1 film, but with a large desorption loop. As suggested in section 4.8.3, this is due to issues with adsorption site accessibility, despite the fact that hydrogen is a very good penetrator of these materials. It is interesting to note that the desorption curve keeps rising as the pressure decreases until it matches the desorption curve of the activated film; this again suggests that the number of adsorption sites within micropores is near identical for the two materials, and that the activation conditions used have served only to clear out the diffusion pathways rather than to add extra capacity.

5.3.2. High Pressure (≤ 20 MPa)

High pressure hydrogen isotherms were only run on the carbonised and activated films due to time constraints. The runs for the carbonised and activated films are presented below in Figure 5.24 and Figure 5.25 respectively, and a comparison of the two with a representative PIM-1 (4) isotherm can be found in Figure 5.26.

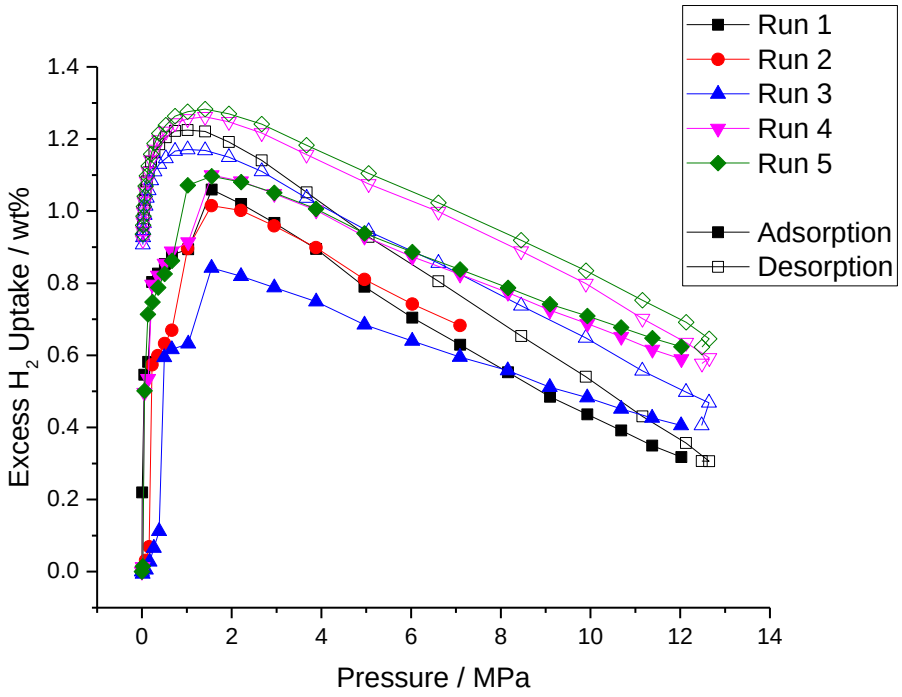

Figure 5.24 - High pressure (13 MPa) H_2 isotherms for the carbonised PIM-1 film at 77 K. Lines are provided to guide the eye only.

The isotherm appears to show a maximum excess uptake of 1.10 wt% at 1.56 MPa, albeit after a series of large steps in the upwards isotherm. There is a large desorption loop seen in every run in this series; the maximum uptake during desorption is 1.28 wt% at 1.41 MPa. The uptakes are disappointing, given the 1.55 wt% uptake seen in the PIM-1 films. It is particularly curious that this happens in a material that appeared to show much higher uptake of hydrogen in the low pressure isotherms (Figure 5.23). This seems likely to be due to a much greater abundance of

ultramicropores, which readily adsorb hydrogen in the very low pressure range, but a relative lack of larger micropores, which continue the increase in the amount of hydrogen stored as they fill at relatively higher pressures. The shape of these isotherms may also reveal information about the material and its interaction as an adsorbent.

The most striking aspect of these isotherms is the large steps in the adsorption curve between 0 – 1.5 MPa. This is highly unexpected behaviour, and has never been seen before within the group for this machine. It is also very interesting that this happened repeatedly, suggesting that this is not a function of random machine error, but instead suggests it is a function of material structure. One potential explanation of this behaviour is the restrictive system of throats and cavities within the original PIM-1 material that has been made inflexible by the carbonisation process. The small 'throats' fill up with hydrogen at low pressures, and restrict access to larger cavities. As the pressure rises, the pressure drop across the throat increases until the point at which the throat is opened, either by hydrogen being physically displaced into the cavity by molecular impact from the high pressure side, or the throat showing some flexibility and opening enough to allow passage through to the larger cavity. This would explain the large, sudden and consistent rises that appear to occur with rising pressure.

Another interesting feature of these isotherms is the sharp downward trajectory of the adsorption curves following the maximum excess uptake. This is a function of the bulk hydrogen density increasing at a much higher rate than the density of the adsorbed phase hydrogen, and suggests that after a relatively low pressure, the density of hydrogen in the adsorbed phase is not increasing very much, whilst the bulk density increases. By logical extension, this suggests that the pores fill with adsorbent very quickly, either suggesting that the isosteric enthalpy of adsorption is very high (it is known to be reasonably high for some activated carbons [92, 145, 257, 341], but it is unlikely that this material experiences an interaction strength with hydrogen beyond that previously reported for other carbonaceous materials), the surface is highly homogenous, or that the porosity is highly microporous in this material, resulting in the filling of ultramicropores in the low pressure ranges, and there being no larger pores in which hydrogen can fill and densify effectively in the higher pressure regions.

The last major point of note is the very large hysteresis loops. Typically, hydrogen desorbs solely in a reversible type I fashion due to its high permeability, so consistent desorption looping suggests mass transfer limitation. As with the low pressure hydrogen isotherms, it appears that the desorption curve approaches the true adsorption capacity of the material as the pressure decreases, due to the extra time at pressures higher than the maximum excess pressure. This idea is supported by the very repeatable nature of the desorption curve in the 0 – 2 MPa range, despite very varied adsorption curves beforehand. Hydrogen at high pressures should be extremely permeable to any sort of porous material, so the idea that there are mass transfer limitations here seem fanciful, but the repeatability of these desorption curves seen to indicate that some phenomenon within the material is limiting the access of hydrogen into some of the porous voids within the material. This hypothesis is therefore also consistent with the idea of narrow inflexible restrictions within the material that greatly restrict the access of hydrogen into larger pores.

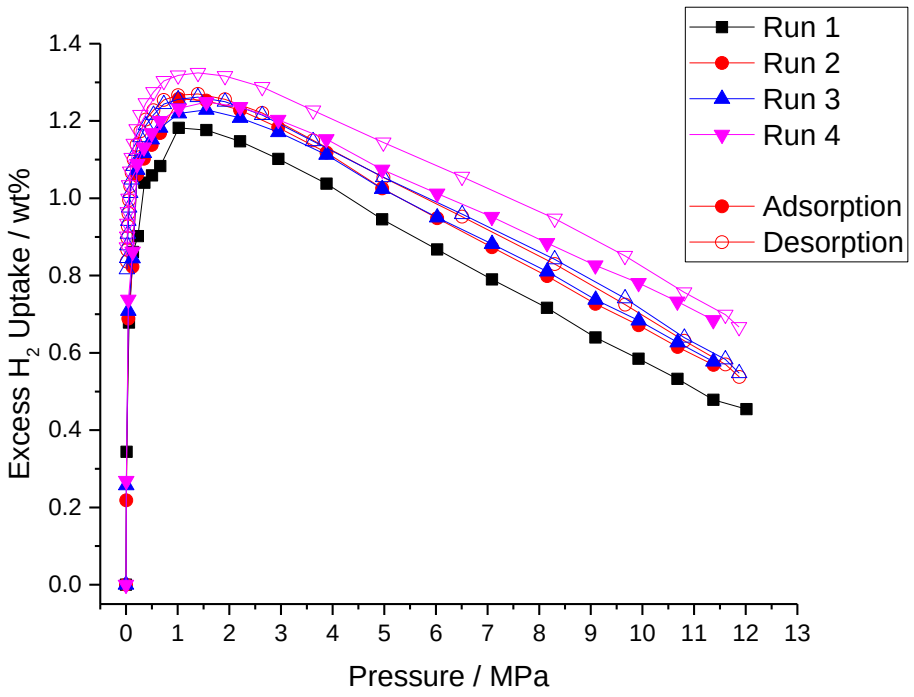

Figure 5.25 - High pressure (13 MPa) H_2 isotherms for the activated carbon PIM-1 film at 77 K. Lines are provided to guide the eye only.

The high pressure H_2 isotherms for the activated film are shown in Figure 5.25. These runs show smooth, largely reversible isotherms that show a maximum excess uptake of 1.25 wt% at 1.55 MPa. Although the improved repeatability and reversibility are welcome, the overall uptake performance is disappointing, as there seems to be little difference between this film and the carbonised film from which it was made. This performance appears to corroborate with the hypothesis that the activation on this film helped to open up some of the finer microporous channels that were causing severe mass transfer limitations within the carbonised film, but there is little evidence that the activation conditions used created more pore volume that is suitable for the adsorption of hydrogen.

It is interesting to note that despite the large steps seen in the adsorption curves in Figure 5.24 largely being eradicated, there is still a clear step in the 0.4 – 0.5 MPa range for adsorption in the activated film. This clearly demonstrates that the narrow throats that caused the erratic behaviour in the carbonised film have not been removed entirely in this material, and lends further weight to the idea that harsher activation conditions would be welcomed in this material, as there is certainly scope for more material removal in order to create further useful free volume.

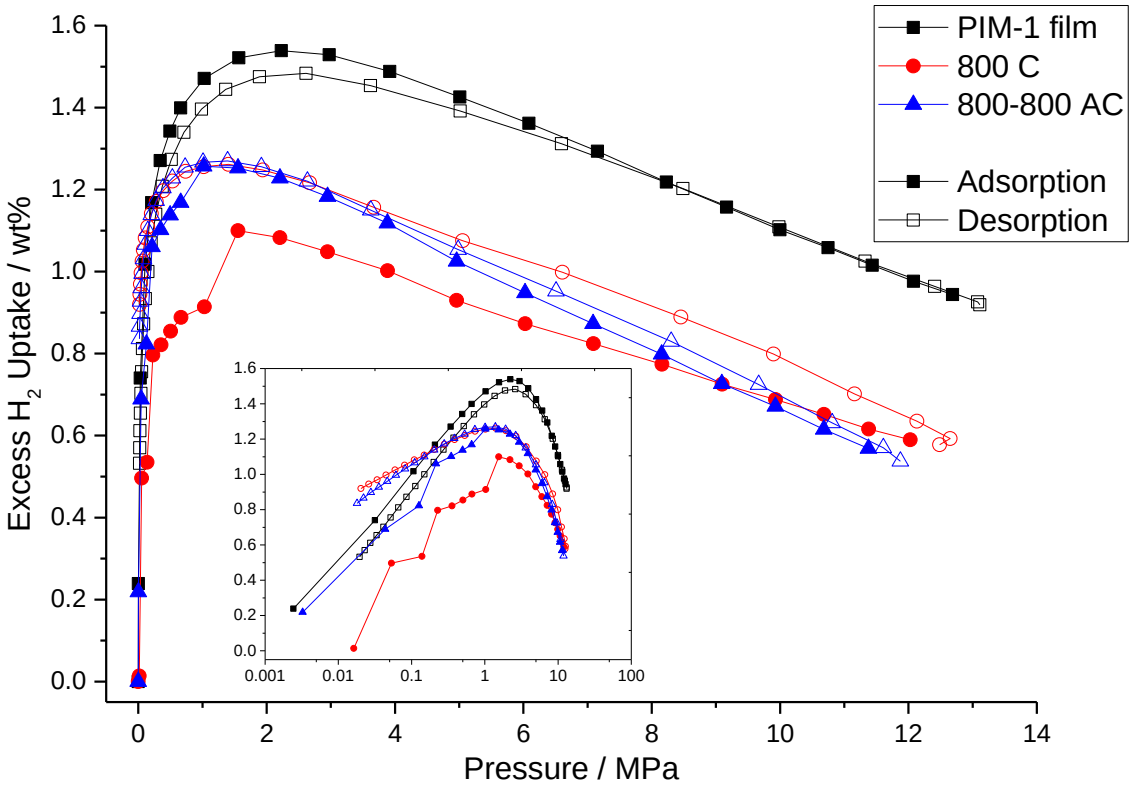

Figure 5.26 - Comparison of the high pressure isotherms for the carbonised and activated PIM-1 films and PIM-1 (4) film at 77 K. The inset contains the same isotherms plotted on a logarithmic ordinate axis. Lines are provided to guide the eye only.

Finally, representative isotherms of both the carbonised and activated films are plotted against the average PIM-1 (4) film isotherm (from Figure 4.54) in Figure 5.26. This figure clearly illustrates the similarity in the uptake seen in both materials, particularly in the desorption curves. It also illustrates the highly disappointing uptake seen in these materials compared to the precursor material from which it came, with the PIM-1 (4) film (which itself showed reasonably disappointing performance compared to other forms of PIM-1 tested in this study) vastly outperforming these films.

This is a clear indication that the free volume within the material is not being maintained as it goes through carbonisation, and although the shape and repeatability improve following activation, there is no improvement in the available free volume for hydrogen adsorption at higher pressures. It is very possible that this is in part due to mild activating conditions, as carbonisations of PIM-1 have undergone longer, higher temperature and more chemically aggressive processes to produce high porosity materials [198, 199]. If this material were to undergo a more aggressive activation, then it would be very likely that the hydrogen uptake would be higher, and could potentially match some of the very high surface areas and uptakes that have previously been seen for activated carbon materials [70, 257, 275, 342], whilst maintaining some of the practical benefits seen in these films, namely the ability to pre-mould the PIM-1 film before the carbonisation process. Sadly, there was insufficient resource to be able to perform such an optimisation of the carbonisation/activation conditions in this study, but would make for a very interesting line of future work.

6. Modelling and Hydrogen Storage Capacity Calculations

6.1. Theory

In order to be able to demonstrate how the porous materials tested in previous chapters will perform in larger scale scenarios, it is desirable to model these materials in order to find parameters that can accurately simulate the behaviour within the pressure range tested, and then to apply this behaviour to a model that will accurately determine how much hydrogen will be contained in systems containing the materials. The theory behind such models (as previously proposed by the Mays group) is detailed in this section, and the rest of the chapter will detail their application to the materials tested in this study.

6.1.1. Parameter Fitting

The modelling is performed using a relatively simple two phase model [275, 343], which is illustrated in Figure 6.1.

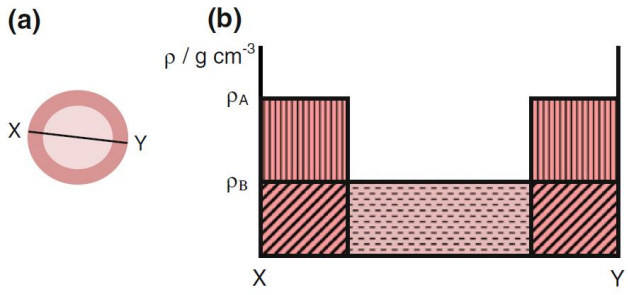

Figure 6.1 - Visualisation of two-phase model of hydrogen storage in an adsorbent pore, viewed as (a) the cross section of a circular pore and (b) the density profile in the pore as viewed perpendicular to the cross section XY. Reproduced from [275] **with kind permission from Springer Nature.**

Consider a pore volume (v_p) that is filled with a particular amount of gas, namely the total mass of adsorptive occupying that pore (m_T). In a pore where adsorption is occurring, the gas in the pore can be assumed to occupy one of two states, either in the densified adsorbate phase or as the bulk gas that infiltrates into the pore. The masses of these are represented by m_A and m_B respectively. A simple mass balance gives:

$$m_T = m_A + m_B \tag{6.1}$$

It is assumed that these two phases each occupy a particular volume within the pore (i.e. they are two distinct phases occupying volumes v_A and v_B respectively), but between them occupy the entire available volume, such that:

$$v_P = v_A + v_B \tag{6.2}$$

In addition, the phases are assumed to have uniform densities (designated ρ_A and ρ_B respectively). In this case, the mass balance can be expanded to:

$$m_T = \rho_A v_A + \rho_B v_B \tag{6.3}$$

It is at this point that the Gibbs definitions of adsorption phases must be considered. As stated in section 2.5.1, the excess amount adsorbed (m_E) is formally defined as the amount of adsorptive

present in the pore above what would be there if there were no interaction with the pore wall. If this were the case, the amount of gas in the pore would solely be equal to the pore volume multiplied by the bulk gas density, and thus the excess uptake can be expressed as:

$$m_E = m_T - \rho_B v_p \tag{6.4}$$

Substituting the expanded mass balance (equation 6.3) into the definition of excess adsorption (6.4) gives:

$$m_E = \rho_A v_A - \rho_B v_A \tag{6.5}$$

Experimentally, v_A is a very difficult parameter to determine, given the currently available methods. One method around this difficulty is to utilise the fractional filling volume Θ, which is defined as the ratio of the volume occupied by the adsorbent to the total available pore volume:

$$\Theta = \frac{v_A}{v_P} \tag{6.6}$$

This allows for the excess adsorption to be expressed in terms of the total pore volume as:

$$m_E = (\rho_A - \rho_B)\Theta v_p \tag{6.7}$$

Fundamentally, equation 6.7 is the core equation around which the modelling of the high pressure isotherms will occur. However, the fractional filling volume must be assigned a numerical value in order for this to be possible. As the total amount of hydrogen adsorbed in a system very frequently takes the shape of a type I isotherm (see Figure 2.3), it is assumed that the filling fraction expands in line with type I behaviour. As such, a type I isotherm equation is required to model this behaviour. There is a large number of candidates for this function; the Langmuir equation was the first one proposed in 1918 to describe adsorption site filling on a homogeneous surface [275]:

$$\Theta = \frac{bP}{1 + bP} \tag{6.8}$$

where P is the gas pressure above the surface, and b is the Langmuir affinity constant, which is a measure of the strength of the interaction between the adsorptive molecules and the surface, and can be used to gain insight on the adsorption enthalpy. However, this equation is very simple, and the single parameter available can make consistent high accuracy fitting difficult. A number of alternative type I isotherms have been tried directly within this model [275] and similar models [206], and one fitting equation that emerges as being both relatively simple and consistently providing good quality of fit is the Tóth equation, which was first derived in 1962 by József Tóth to adapt the Langmuir equation for energetically heterogeneous surfaces [275]:

$$\Theta = \frac{bP}{(1 + (bP)^c)^{\frac{1}{c}}} \tag{6.9}$$

In this equation, c is the Tóth parameter, which is a measure of the homogeneity of the surface. The value is limited to between 0 (completely heterogeneous surface) and 1 (completely homogeneous surface – in this case the Tóth equation reverts back into the Langmuir). Taking equation 6.9 and substituting into equation 6.7 derives:

$$m_E = (\rho_A - \rho_B)\left(\frac{bP}{(1 + (bP)^c)^{\frac{1}{c}}}\right)v_p \tag{6.10}$$

This equation contains all of the parameters that will be fitted to the empirical isotherms. The values of P and m_E are provided by the data, and the parameters ρ_A (the density of the adsorbate), b (the affinity parameter), c (the heterogeneity parameter) and v_p (the specific pore volume) can all be adjusted to improve the quality of fit of the curve to the data.

The bulk density of hydrogen (ρ_B) is gathered from the thermophysical properties site of the National Institute of Standards and Technology (NIST) Chemistry Webbook, which uses the highly accurate Leachman equation of state to calculate the densities [34]. The data is recalled by using a modified form of the ideal gas law:

$$\rho_B = \frac{1}{Z}\frac{PM_r}{RT} \tag{6.11}$$

Where M_r is the molar mass of hydrogen, and Z is the compressibility. The compressibility is a factor used to correct for non-ideality of the gas, particularly at higher pressures. Z is calculated using equation 6.11:

$$Z = \frac{P\dot{V}}{RT} \tag{6.12}$$

where $\dot{V}$ is the molar volume. As P, T and $\dot{V}$ are all given by the NIST database, the compressibility can be calculated as a function of the pressure. To transform these discrete data into a continuous function for parameter fitting, the Z vs. P curve is fitted to a rational function [343]:

$$Z = \frac{1 + qP + rP^2}{1 + sP + tP^2} \tag{6.13}$$

Values for the parameters q, r, s and t are determined from parameter fitting, and are given in the supplementary information (SI-8). Equation 6.13 can be substituted into 6.11, which in turn can be substituted into 6.10, which gives:

$$m_E = \left(\rho_A - \left(\frac{1 + sP + tP^2}{1 + qP + rP^2}\right)\left(\frac{PM_r}{RT}\right)\right)\left(\frac{bP}{(1 + (bP)^c)^{\frac{1}{c}}}\right)v_p \tag{6.14}$$

Equation 6.14 is an equation relating m_E solely as a function of P and the four parameters that are to be determined by the parameter fitting. This is the equation fed directly into the OriginPro software for modelling purposes.

It is important to note that up to now, all values of m and v_p have been treated as extensive properties (i.e. as absolute masses and volumes with base units kg and m^3). However, in the context of porous materials, it is much more convenient to treat these values as intensive, for three primary reasons: because the absolute masses and volumes in question are very small; the outputs of the measurement equipment are delivered in intensive amounts; and comparing materials can only be done comparing intensive properties. In order to apply this to the masses and volumes discussed in this chapter, the values are divided by the (post-degassing) dry mass of the adsorbent present in the system, such that m_A, m_B and m_T take on units of [wt%] ([g g^{-1}] · [100 %]) and v_p becomes specific pore volume, with a unit of [cm^3 g^{-1}].

6.1.2. Isosteric Enthalpy of Adsorption

In order to better understand the energy requirements of charging and discharging a tank full of adsorbent, knowledge of the isosteric enthalpy of adsorption for hydrogen on the material in

question is desired. This value is generated from multiple temperature isotherms using the Clausius-Clapeyron equation:

$$\left.\frac{\partial P}{\partial T}\right|_{n_A} = \frac{\Delta h P}{RT^2} \tag{6.15}$$

Where Δh is the change in molar enthalpy as a result of the adsorption. This expression is the result of the application of the exact thermodynamic Clapeyron equation, but altered for the calculation of molar enthalpies, and with two major assumptions applied: the molar volume of the bulk adsorbent is far greater than that of the adsorbate phase; and the bulk adsorptive behaves as an ideal gas [92]. Integrating equation 6.15 yields the following equation:

$$\ln P = \frac{Q}{R}\left(\frac{1}{T_i} - \frac{1}{T_f}\right) \tag{6.16}$$

where Q is the differential isosteric enthalpy of adsorption, and T_i and T_f are the initial and final temperatures of the system. This equation yields a simple linear approach to determining the isosteric enthalpy of adsorption, in that the gradient of a plot of ln P against the inverse temperature for a given uptake (otherwise known as an isostere) will yield the differential enthalpy of adsorption at that uptake. It must be noted that the uptake values used for the calculation of enthalpies is the absolute amount adsorbed, as the excess adsorbed is a thermodynamic partition and is not a separate phase, which this approach requires [71, 92]. The absolute adsorbed does define a separate thermodynamic phase [92], and is simply calculated from the parameters determined in the fitting using the following equation:

$$m_A = \rho_A \theta_A v_p \tag{6.17}$$

It must also be noted that the Clausius-Clapeyron equation, whilst relatively simple to use, does show some inaccuracies, particularly at the higher mass uptakes. This is very likely due to the assumptions made in the formation of the equations, namely that at conditions under which higher uptakes occur, the molar volume of the adsorbate phase becomes non-negligible, and the bulk adsorptive behaviour becomes increasingly non-ideal [92]. While the use of the full Clapeyron equation is recommended for finding the isosteric enthalpy, given it is desirable to have as accurate a figure as possible whenever modelling of such a system will be performed [257], it was decided not to use this approach in this study given that the isotherms generated for this solution have large errors associated with them (so losing any accuracy that may be gained from this more accurate method) and that the isosteres necessary for the solution of the Clapeyron equation (with the software available to the author) require the use of the Q values generated by the Clausius-Clapeyron, which will likely compound any errors generated within this method.

One quick and reasonably rough approach that can be used to check the values generated by the Clausius-Clapeyron approach is to use the temperature dependence of the affinity parameter b, by calculating its dependence on temperature using a Van't-Hoff style relationship [343]:

$$b = b_0\left(\frac{Q_b}{RT}\right) \tag{6.18}$$

where b_0 is an entropic factor and Q_b is the characteristic adsorption enthalpy. This equation is easily linearised by taking logarithms of both sides, and therefore a plot of ln b against $1/RT$ yields a gradient equal to the enthalpy of adsorption, and a y-intercept equal to the entropic factor. Whilst this approach is not as thermodynamically rigorous as even the Clausius-Clapeyron, it does

produce 'ballpark' values for the isosteric enthalpy, and can prove useful in this case as a means against which to check the calculated *Q* values without relying on the same isosteres.

6.1.3. Tank Mass Balance

Following accurate replication of the empirical data using the non-linear parameter fitting process described above, these data then have to be entered into a mass balance to evaluate the material's performance on the tank scale. The model used for this calculation was proposed by Sharpe et al. [344]. Consider a tank of internal volume V_C containing a particular amount of adsorbent, illustrated as particulate matter in Figure 6.2:

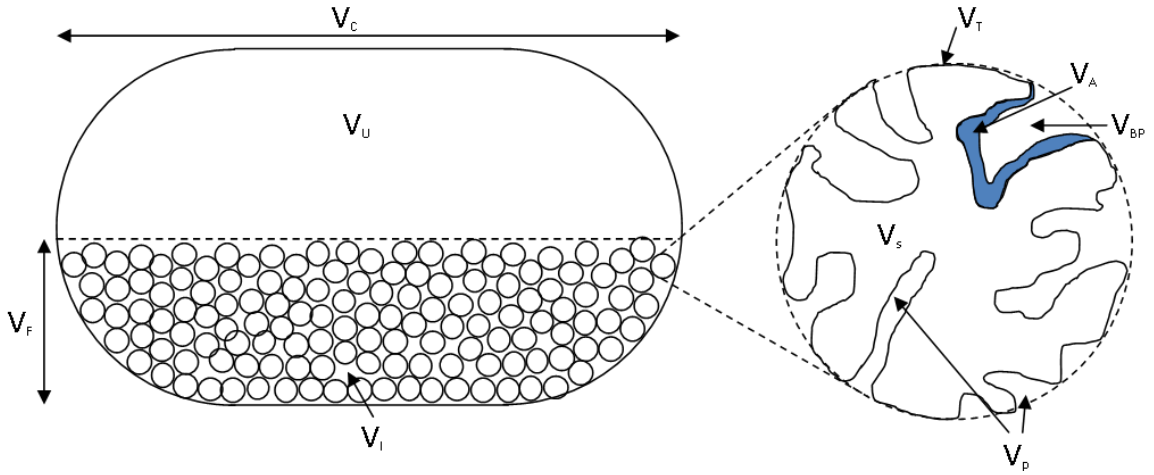

Figure 6.2 - Illustration of the various volumes defined by the mass balance model

This internal tank volume can immediately be broken down into two main volumes: the volume of the tank in which the adsorbent is contained (V_F) and the empty ullage volume (V_U):

$$V_C = V_U + V_F \tag{6.19}$$

One way to quickly define how full of adsorbent the tank is is to define the fill factor (*f*) as the ratio of volume occupied by adsorbent to the total internal tank volume:

$$f = \frac{V_F}{V_C} \tag{6.20}$$

However, solid materials do not always occupy all of the volume that the body generally fills, and as such V_F can be broken down into two further volumes: the empty interstitial volume between particles of adsorbent (V_I) and the total volume occupied by the particles (V_T), such that:

$$V_F = V_I + V_T \tag{6.21}$$

Like the fill ratio, the amount of volume the adsorbent actually takes up can be altered, for example by compressing a powder. As such, the packing factor (*x*) can be defined to quickly identify how densely packed the solid material is. It is defined as:

$$x = \frac{V_T}{V_F} \tag{6.22}$$

Considering the adsorbate itself, the total volume occupied by the adsorbate is made up primarily of three phases: the solid adsorbent itself, the densified adsorbate phase, and the bulk phase gas within the pores. However, depending on how one wishes to categorise these phases, V_T can be expressed two different ways: it can either be expressed as the sum of the skeletal volume of the adsorbent (V_S) and the pore volume (V_p), which is made up of both the adsorbate (V_A) and bulk

gas (V_{BP}) volumes; alternatively it can be seen as the sum of the skeletal and adsorbate phases (i.e. the displaced volume of gas in the system V_D) and the bulk gas phase within the pores alone:

$$V_T = V_s + V_p = V_D + V_{BP} \tag{6.23}$$

$$V_D = V_A + V_s \tag{6.24}$$

$$V_p = V_A + V_{BP} \tag{6.25}$$

In order to determine the total mass of hydrogen (M_H) contained within the tank, consider equation 6.3, but on an extensive basis:

$$M_H = \rho_A V_A + \rho_B V_B \tag{6.26}$$

In this application, V_B is known to be the total volume available to the bulk gas, namely the ullage, interstitial and porous bulk gas volumes. This transforms equation 6.22 into:

$$M_H = \rho_A V_A + \rho_B V_U + \rho_B V_I + \rho_B V_{BP} \tag{6.27}$$

Applying equations 6.19, 6.21 and 6.25 to this gives:

$$M_H = \rho_A V_A + \rho_B (V_C - V_F) + \rho_B (V_F - V_T) + \rho_B \left(V_p - V_A\right) \tag{6.28}$$

This can then be simplified by introducing the fill and packing ratios introduced in equations 6.20 and 6.22:

$$M_H = \rho_A V_A + \rho_B V_C (1 - f) + \rho_B (f V_C - x f V_C) + \rho_B \left(V_p - V_A\right) \tag{6.29}$$

The $\rho_A V_A$ and $\rho_B(V_p - V_A)$ terms in this equation can now be rewritten in terms of parameters ρ_A and v_p from the parameter fitting. The total pore volume in the tank (V_p) can be calculated by multiplying the specific pore volume by the total skeletal mass of adsorbent (M_s):

$$V_p = M_S v_p \tag{6.30}$$

Which, when substituted along with equation 6.6 into 6.29 yield:

$$M_H = \rho_B V_C (1 - fx) + \rho_B M_S v_p (1 - \Theta_A) + \rho_A M_s v_p \Theta_A \tag{6.31}$$

The skeletal mass is a product of the skeletal density (ρ_s) of the adsorbate and the total skeletal volume:

$$M_s = \rho_s V_s \tag{6.32}$$

M_s can be rearranged to be expressed in terms of known parameters by applying equations 6.23 and 6.30 and rearranging, which gives

$$M_s = \frac{\rho_s V_T}{1 + \rho_s v_P} \tag{6.33}$$

Replacing the M_s term in equation 6.31 with the expression in 6.33 and simplifying with the fill factor and packing ratios yields:

$$M_H = \rho_B V_C (1 - fx) + \frac{fx\rho_s V_C}{1 + \rho_s v_p} v_p [\rho_B (1 - \Theta_A) + \rho_A \Theta_A] \tag{6.34}$$

This can then be further simplified by substituting equations 6.4 and 6.7, which leaves:

$$M_H = \rho_B V_C (1 - fx) + \frac{fx\rho_s V_C}{1 + \rho_s v_P} m_T \tag{6.35}$$

This can then be further generalised by dividing the total mass of hydrogen in the tank by the total tank volume, which provides a mass density value for hydrogen in the entire interior volume of the tank:

$$\frac{M_H}{V_C} = \rho_B(1 - fx) + \frac{fx\rho_s}{1 + \rho_s v_P} m_T \quad (\mathbf{6.36})$$

This is a highly elegant solution, as it allows for multiple-scale analysis of a material (due to the generalised format). In order to do this, the only inherent information of the material that is required is the total mass of hydrogen stored in the material, which is easily calculable from the derived parameters, the pore volume, which is calculated either through the parameter fitting or directly from N_2 isotherms, and the skeletal density, which was measured as part of the empirical testing. The fill and packing ratios allow for design variations, as these can be specified for a given system (the system can be voluntarily filled to a particular ratio, and powders can be left loose at an inherent packing factor, or compressed in an attempt to raise the hydrogen stored in the available volume).

This solution can also be used to estimate the energy stored within the tank. This is simply calculated by multiplying the mass density of hydrogen by its lower heating value. This value is a volumetric energy density that can quickly be compared to other energy vector materials, such as gasoline or electric battery materials, although true comparison of the storage systems require further knowledge of the containing materials and the balance of plant equipment required [344].

The other point of note is that due to the need for a delivery pressure to be maintained within a vehicle, the amount stored by a system, and the amount delivered, are different. In order to calculate how much hydrogen is delivered by a system, a minimum absolute delivery pressure of 0.15 MPa (0.5 barg, as suggested by Bhatia and Myers [257]) is assumed, and the amount of hydrogen present in the system at that pressure is subtracted from the entire storage curve. This presents a more realistic analysis of what will actually be available to the system recovering this hydrogen.

This model does have flaws however: it assumes that the behaviour of a ~ 100 mg sample of adsorbent will behave exactly the same as potentially tens of kilograms, ignoring any potential issues with heat and/or mass transfer, and hydrogen uptake is assumed to be the same no matter the packing ratio (which has been proven to be false for some MOF powders [143, 156]). Nevertheless, given the difficulty of establishing high capacity hydrogen storage systems, this model is a useful method for estimating the behaviour of materials in a large scale scenario.

6.2. Software

Experimental data are fitted to determine model parameters using OriginPro 2016 software (OriginLab, Northampton, MA, USA). This is done using the non-linear fitting function in Origin, which uses the Levenberg-Marquart algorithm [345]. Fundamentally, the algorithm seeks to minimise the reduced chi-squared parameter (χ^2) which is defined in a least squares problem as follows [343]:

$$\chi^2 = \frac{1}{n_{ex} - n_{para}} \sum_{i=1}^{m} w_i [Y_i - E(Y_i)]^2 \quad (\mathbf{6.37})$$

Where n_{ex} is the number of experimental data points, n_{para} is the number of parameters being fitted to the data, w_i is the weighting parameter (which can be used to account for experimental

error), Y_i is the inputted dependent values, and $E(Y_i)$ is the calculated set of the same dependent value.

Levenberg-Marquant attempts to solve this using a method that combines the already well understood step-gradient method (in which the solution takes a step of arbitrary size in the directon of greatest descent towards the local minimum solution) and the Gauss-Newton method (which uses second derivative information on the curvature of the function, as well as the gradient, to step towards the minimum). Also known as the damped Gauss-Newton method, Levenrburg-Marquart has the advantage of being able to take large steps using step-gradient-like behaviour when a long way from the final solution, but can converge on the final solution quickly with smaller steps using the Gauss-Newton behaviour [346].

Origin aims to reduce the chi-square tolerance (the difference between the current and previous iteration of χ^2, divided by their summation) to $\leq 10^{-9}$ within 400 iterations. This was performed primarily for parameter fitting to the empirical hydrogen isotherms discussed in this chapter, but was also used for the deconvolution of the DTG curves and Raman spectra for PIM-1, as discussed in sections 5.1.1 and 5.2.3 respectively.

The output of the parameter fitting in Origin issues not only a value, but an error in the form of the standard error. The standard error is defined as the standard deviation of the sample, divided by the square root of the number of data points across which the calculation was performed. It is commonly quoted as the standard deviation of the sampling population, but is commonly understood as a measure of how well the sample mean represents the population mean [345]. All error bars presented in this chapter are the standard error of the fit as determined by OriginPro.

Origin also publishes a number of quality of fit parameters with each fitting performed. As well as publishing both the χ^2 and reduced χ^2 values, origin issues an R^2 value, otherwise known as the coefficient of determination (COD). It is a measure of the variation in the response variable that is caused by the independent variable (i.e. how much of that variance that the model is responsible for). It can take values between 0 and 1, with 1 indicating the highest dependency, and therefore the highest quality of fit [347]. An adjusted R^2 value, that eliminates the ability of excessive numbers of parameters to artificially inflate the standard R^2 value, is also provided.

6.3. Parameter Fitting

The fits to many of the high pressure hydrogen isotherms are discussed in this section. The regular residual of the fits, an important consideration of the modelling to show that the model is not showing large biases in certain regions of the data, can be found for all of the fits discussed in the supplementary information (SI-9).

6.3.1. PIM-1 (2)

The fits of equation 6.14 to the PIM-1 (2) data (shown in Figure 4.49) are shown in Figure 6.3 and Table 6.1 below.

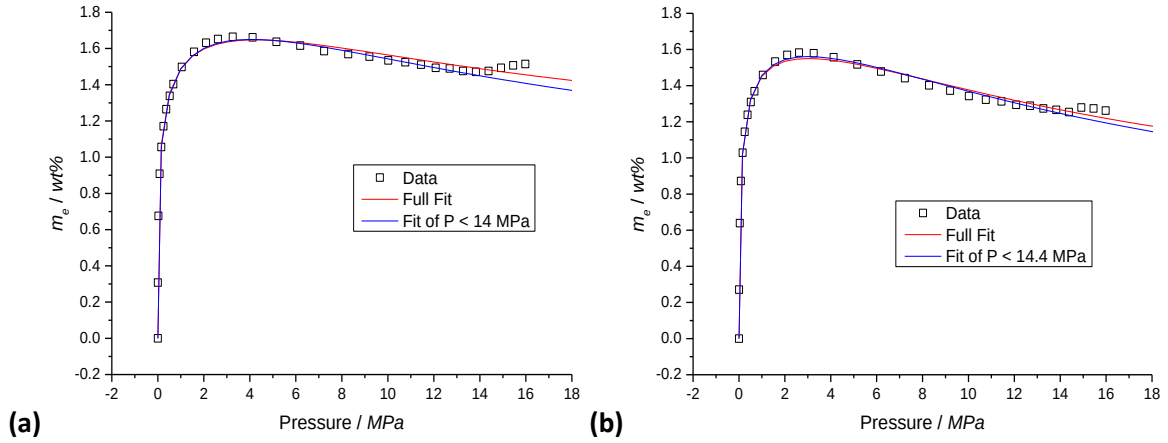

Figure 6.3 - PIM-1 (a) powder and (b) film H_2 isotherms, with the full and restricted fits shown

Figure 6.3 shows that Origin is capable of producing very good fits to the data, a finding confirmed by the error calculations of the software itself, as the COD R^2 value is never lower than 0.996. However, it is interesting to note that the rise in hydrogen uptake in the region P > 14 MPa for the powder, and P > 14.4 MPa for the film, has a significant effect on the fit, slowing the decay of the fitted curve, an effect which could have a significant influence on the model of stored hydrogen at a later point. Therefore, fits in which this rising uptake data were not included were performed, to see what effect this would have on both the fits in general, and the parameters the model outputs. The blue lines in Figure 6.3 are these restricted data set fits, and they clearly better adhere to the decreasing data. The difference between the full and restricted data fits is more pronounced in the powder sample, largely due to the greater increase seen in the high pressure region.

Table 6.1 - Values for the parameters ρ_A, b, c and v_p from Origin fitting of the PIM-1 powder and film H_2 isotherms. All parameters are given to three significant figures, and the uncertainties to the same number of decimal places as the parameter.

Parameter	Powder		Film	
Fit range	Full	P < 14 MPa	Full	P < 14.4 MPa
ρ_a (g cm^{-3})	0.155 ± 0.009	0.133 ± 0.004	0.125 ± 0.005	0.115 ± 0.003
b (MPa^{-1})	420 ± 195	684 ± 200	63.6 ± 14.8	74.7 ± 13.2
c (-)	0.294 ± 0.029	0.260 ± 0.014	0.443 ± 0.032	0.413 ± 0.022
v_p (cm^3 g^{-1})	0.167 ± 0.021	0.219 ± 0.016	0.166 ± 0.012	0.190 ± 0.011

Table 6.1 reveals a number of interesting trends. Firstly, the adsorbate density in all four cases is greater than 0.1 g cm^{-3}, which puts the density of the adsorbed hydrogen within the region of solid-like hydrogen (the mass density of solid molecular hydrogen has been estimated at 0.086 g cm^{-3} [348]). This finding in itself is not without precedent, as previous modelling studies have estimated solid-like densities of adsorbed hydrogen in micropores [275], which in turn have been supported by direct observation via in-situ inelastic neutron scattering [349]. Remarkably, the densities shown here are substantially higher than the 0.086 g cm^{-3} value, indicating densities equivalent to compressed solid H_2. The density is consistently higher for the powder than for the film, a finding likely explained by the minor differences in pore structure within the two materials.

In addition, v_p is reasonably consistent across all four fits, and the values appear to be of similar value to the microporous pore volume calculated by the DR model and from the PSD integrations. On reflection, this makes sense as the vast majority of hydrogen adsorption is performed by micropores, due to the pore filling mechanism by which they are filled, rather than the creation of

a monolayer on the surface area in larger pores. Therefore these data can be seen to be a validation of the micropore calculations performed earlier.

The affinity and heterogeneity parameters appear to be quite inconsistent, however. The values for *b* in the powder appear to be very high, whilst those in the film are rather low. As this is fundamentally the same material, it would be expected that the affinity of hydrogen to the surface (a characteristic that *b* represents) would be very similar in both materials, so the reason for this disparity requires further investigation. It is worth noting that the values of *b* in this fit show large associated errors. Conversely, c is much lower for the powder than for the film. As *c* is a measure of the surface heterogeneity, it would again be expected that the surface (namely, the polymer chains) would be very similar for both morphologies of PIM-1, yet the modelling produces very different values. It is possible that although the pore volumes for these materials are similar, the distribution with regard to pore diameter is different, and that potentially smaller pores within the powder form cause artificially high uptake in the low pressure regions, a factor that would serve to both raise *b* and lower *c*. It is worth noting that the values of *b* and *c* are somewhat dependent upon one another in equation 6.3, and that there may be some overcompensation by one variable to compensate for the other.

6.3.2. PIM-1 (4)

The first issue that requires attention when considering fitting to the PIM-1 (4) samples is which of the multitude of disparate isotherms measured at 77 K to use as the representative behaviour of this material under these conditions. Considering the isotherms discussed in section 4.9.3, it is possible to fit the six equations (Both 3 run sets of samples 1 and 2), and likewise to fit the average equation plotted in Figure 4.54. The fits can be seen in Figure 6.4, and the parameters found can be seen in Table 6.2.

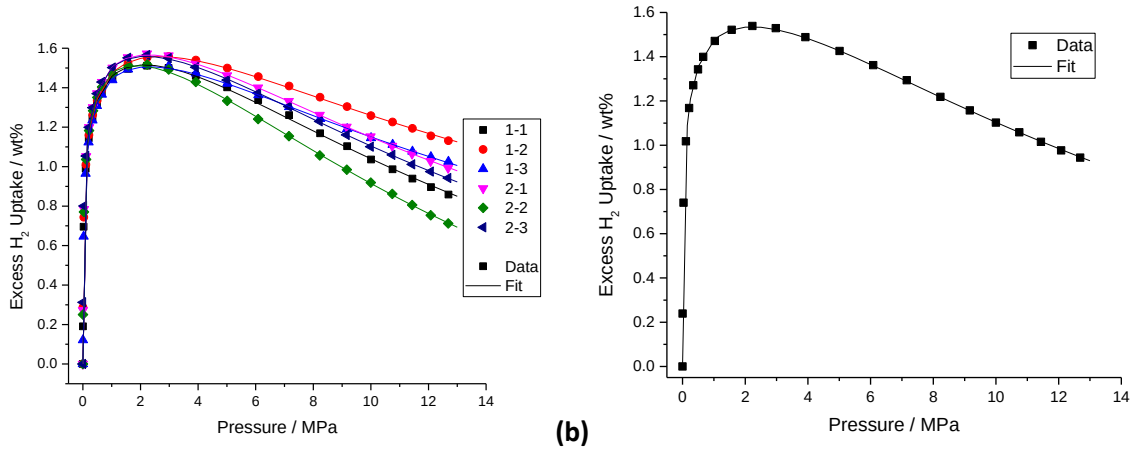

Figure 6.4 - Plots of the high pressure H_2 (77 K) isotherms for the PIM-1 (4) film samples, with their fitting curves for (a) the six raw data curves and (b) the averaged curve.

Figure 6.4 illustrates a series of very good fits to each of the isotherms, and the very low χ^2 and very high R^2 values seen in Table 6.2 confirm this. Looking at the individual parameters in Table 6.2, it is clear that there is sizeable difference between the values for each of the parameters, with the largest value being 49 %, 276 %, 15 % and 53 % higher than the lowest value for ρ_A, *b*, *c* and v_p respectively. Nevertheless, each value appears to be reasonable within the physical context associated with each parameter. It is encouraging to note that when the parameters of each of the six separate runs are averaged, the values they produce are generally within 1-2% of those independently determined for the 'average' isotherm, which further lends credence that the

average isotherm, whilst not actually produced by any single isotherm of this material, is representative of the range of behaviours produced.

Table 6.2 - Parameter fits for the high pressure hydrogen isotherms for PIM-1 films (runs 1 – 6 and the average in Figure 4.53 and Figure 4.54). All values are given to 3 significant figures except the R^2 values, which are quoted to 4.

Run	ρ_A	b	c	v_p	$m_{A,max}$	χ^2	R^2
	g cm^{-3}	MPa^{-1}	-	cm^3 g^{-1}	wt%	$(wt\%)^2$	-
2-1	0.0659	439	0.290	0.401	2.65	2.22E-4	.9988
2-2	0.0865	773	0.268	0.315	2.73	5.31E-5	.9997
2-3	0.0805	211	0.346	0.285	2.29	7.62E-5	.9996
3-1	0.0731	543	0.287	0.364	2.66	4.53E-5	.9997
3-2	0.0581	369	0.308	0.436	2.53	1.08E-5	.9994
3-3	0.0692	795	0.272	0.396	2.74	2.80E-5	.9998
Mean	0.0722	522	0.295	0.366	2.60	-	-
Averaged	0.0710	437	0.297	0.362	2.57	6.11E-5	.9997
% diff	-1.66	-1.63	0.712	-1.02	-0.981	-	-

The values of the parameters found for the average isotherm are generally encouraging: the adsorbate density is slightly lower than that of solid-like hydrogen, but still show a sizeable increase over the bulk phase density (it is the equivalent of supercritical H_2 at 77 K and 33 MPa); the value of *b* is very similar to that reported for the PIM-1 (2) powder above, so indicating a similar affinity to this material; the low value of *c* is reasonable given the high chemical heterogeneity of the surface of PIM-1 and the low temperature; and the pore volume is very similar to the micropore volumes reported for PIM-1 (4) powder by the DR, DA and integrated PSD methods (section 4.8.2).

The other major point of note with these values is how they compare to the data previously seen for PIM-1 (2). Looking at both Table 6.1 and Table 6.2, it is clear to see that the values reported for PIM-1 (4) vary significantly from those reported for the PIM-1 (2) films, but instead show much closer values to those reported for the PIM-1 (4) powder, differing significantly only in the reported adsorbate density. The reasons for this occurring are unclear, although PIM-1 is an amorphous material and the films are created through an uncontrolled bulk technique, potentially resulting in materials with quite different properties despite their chemical equality. Alternatively, the powder sample has a more open pore structure and shows less experimental error, so may produce more accurate values from smaller data sets.

Now that the representative isotherm for PIM-1 (4) film at 77 K has been determined, a full comparison of the powder and film morphologies of PIM-1 (4) can be done across multiple temperatures. Each of the four parameters is compared for the temperatures and morphologies in Table 6.3 and Figure 6.5 - Figure 6.7, and the quality of fit parameters are provided in Table 6.4. All of the isotherms and their fitting curves are shown in the supplementary information (SI-10).

Table 6.3 – Adsorbate density (ρ_A) parameter for the PIM-1 (4) powder and film samples at multiple temperatures (77 - 298 K). All density and error values are quoted in g cm^{-3}. All values quoted to 3 significant figures.

	Powder		Film	
Temperature	ρ_A	error	ρ_A	error
77	0.131	0.003	0.0710	0.0005
90	0.0710	0.0031	0.0724	0.0062
100	0.193	0.151	0.0703	0.0087
110	0.0559	0.0089	0.0819	0.0135
120	0.0563	0.0163	0.0691	0.0124
150	0.0647	0.0151	0.0641	0.0145
200	0.131	0.204	2.11	101.05
298	3.64	673.69	9.86	12576

Looking at Table 6.3, it is clear to see that there is a significant difference between the powder and film morphologies, both in the absolute value of the adsorbate density and in the consistency of the value between temperatures, something that would be expected to be temperature independent. Looking at the 77 K values, the values of PIM-1 (4) show good agreement with those of PIM-1 (2). However, as the temperature rises, it is evident that the PIM-1 powder changes erratically, whilst the film keeps a reasonably stable value throughout the isotherms. This is in immediate contrast to the visual appearance of the isotherms (Figure 4.52 and Figure 4.55). Interestingly, aside from the 77 and 100 K isotherms, the reported densities in the PIM-1 powder are similar to, if not slightly lower than those reported for the film, so indicating that it may be the film, rather than the powder, which gives the more representative density value in the PIM-1 (2) samples above. These densities are all those of highly compressed liquid hydrogen, although only the high values reported for the powder at 77 and 100 K reported solid-like densities that have been seen for other materials. There also appears to be no discernible trend in the density as the temperature changes, which is expected given that the model assumes constant density across temperatures.

The densities reported for the powder at 298 K and the film at both 200 and 298 K are extraordinarily large, and are a by-product of the lack of progression in the isotherm from which they came. As the isotherm only rises in the < 16 MPa range for higher temperatures, there is no maximum excess or downward curve to which the curve can fit, and without this information the ρ_A and v_p parameters become mathematically inseparable. These isotherms, despite showing reasonable quality of fit numbers, do not complete the fitting to Origin's own requirements, and the results are parameters that when combined produce reasonable isotherms, but individually lose all effective meaning.

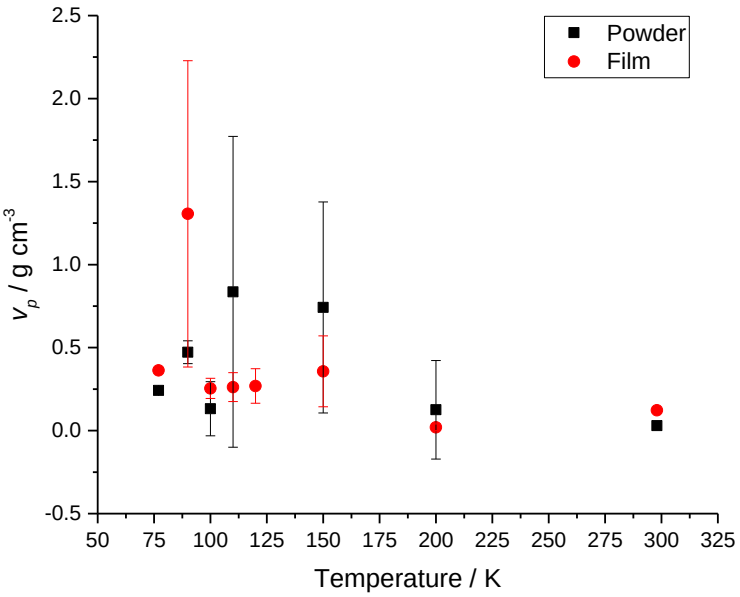

Figure 6.5 - Pore volume (v_p) parameter for the PIM-1 (4) powder and film samples at multiple temperatures (77 - 298 K). The standard error has not been included for the 298 K data due to very large values.

Much like the adsorbate densities, the pore volumes shown in Figure 6.5 appear to show much larger inconsistency across the temperatures for the PIM-1 (4) powder than the film. Aside from a large outlier at 90 K (due to the erratic isotherm), the pore volume reported for the film stays relatively consistently around 0.3 g cm^{-3}, which compares well to the microporous volume of PIM-1 previously reported both in the literature and in this study. The two studies for which this is not true, at 200 and 298 K, are products of the non-completed fits and can be neglected. For the powder sample, the values are highly erratic and do not point to a single trend, although the points that trend furthest from the expected 0.3 – 0.6 cm^3 g^{-1} value also show the largest standard error, perhaps indicating that a more consistent value does exist for this material but is greatly affected by errant isotherms. This is particularly acute for the 120 K point, which reported a pore volume of 11.3 cm^3 g^{-1}, a clearly nonsensical value produced by the highly errant point at 10.4 MPa, and the inconsistent uptake above this pressure.

Despite the erroneous behaviour noted for both the adsorbate density and pore volume parameters above, the calculated values for the Langmuir affinity parameter, seen in Figure 6.6, appear to behave more closely to what is theoretically expected. The 90 K isotherm for the film aside, both sets of data show large values of *b* in the low temperature range, and exponentially decline as the temperature increases. It is interesting to note that the *b* value for the powder is significantly higher than for the film at 77 K, which given that *b* is a measure of the strength of interaction between the surface and the adsorptive, should be the same for both morphologies. At the higher temperatures however, the values are far more closely aligned.

It is interesting to note that in the inset graph in Figure 6.6, the points do not decrease linearly on a logarithmic scale, but instead decrease in a hyperbolic-like manner, which is encouraging to be able to fit these data to a Van't Hoff plot to calculate the characteristic energy of these materials. This data set is encouraging that despite the low quality isotherms from which these parameters are derived, the energetic parameters appear to behave as expected, and that determination of the isosteric enthalpy of PIM-1 can still be performed with any level of confidence.

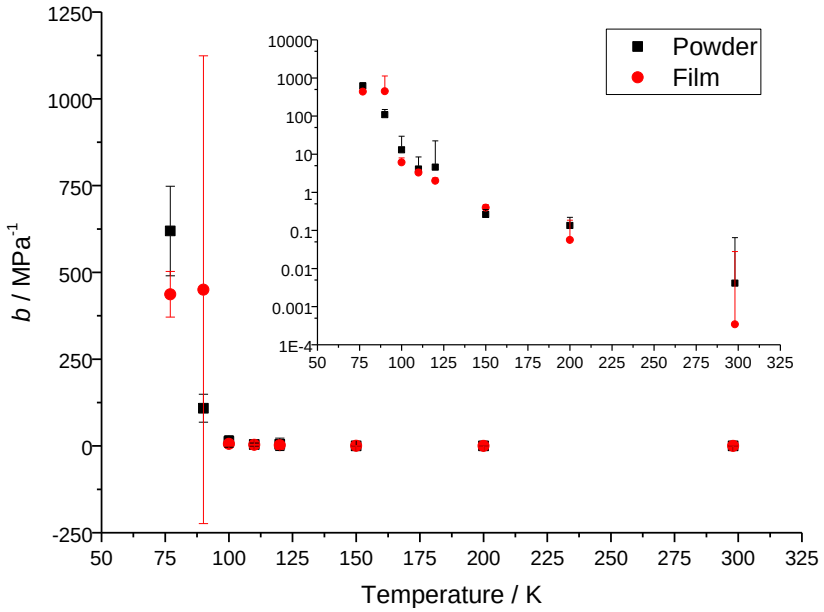

Figure 6.6 - Langmuir affinity parameters (*b*) determined for the PIM-1 (4) powder and film samples at multiple temperatures (77 – 298 K). The inset plots the same data on a logarithmic ordinate. Standard errors have not been plotted in the negative direction in the inset due to negative values.

The values for the Tóth heterogeneity parameter can be seen in Figure 6.7. Generally, it is expected that the value of *c* increases as the temperature increases, as the greater kinetic energy of the adsorptive molecules means they approach the surface more randomly, and the surface therefore appears more homogeneous to the surface. In these data sets, there is slight evidence of such a trend in the very low temperatures (77 – 100 K), although this is largely abandoned in the medium temperatures (100 - 150 K). Attempting to infer a trend within these data is difficult however, as the standard errors reported for nearly all of the values quoted are significant (likely due to the low quality of the isotherms that went into the fitting).

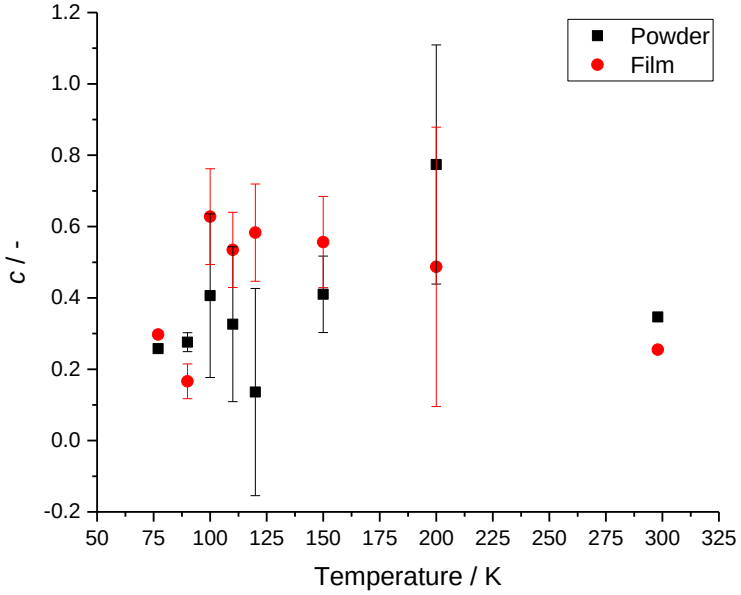

Figure 6.7 - Tóth heterogeneity parameter (*c*) for the PIM-1 (4) powder and film samples at multiple temperatures (77 - 298 K). The standard error has not been included for the 298 K data due to very large values.

Table 6.4 shows the measures of quality of fit provided by Origin. It is evident that much of the error induced in the parameters above comes from Origin's lack of ability to provide high quality fits in the middling temperatures, particularly for the powder sample, in which χ^2 rises to as high

as 0.0151 for the 120 K isotherm, which shows great inconsistency in the high pressure region. For the film sample, the quality of fit is more consistently high, so indicating that Origin was better able to match the data provided, and producing parameter values with more confidence. It is worth noting that quality of fit only indicates Origin's ability to fit the theoretical equation to the data it is provided, but cannot recognise the relative quality of the isotherms entered, and as such it is prudent to show caution with regard to the values generated by the parameter fitting to the film isotherms, as the isotherms (shown in Figure 4.55) do not match what would be expected of such a multi-temperature run.

Table 6.4 - χ^2 and R^2 values for each of the fittings to the PIM-1 (4) data

	Powder		Film	
Temperature	χ^2	R^2	χ^2	R^2
77	8.59E-05	0.9994	6.11E-05	1.0000
90	2.58E-04	0.9983	0.00182	0.9941
100	0.00804	0.9479	0.00230	0.9861
110	0.0105	0.9315	0.00105	0.9949
120	0.0151	0.9262	9.48E-04	0.9938
150	1.14E-04	0.9994	1.70E-04	0.9987
200	1.97E-04	0.9979	8.25E-05	0.9993
298	1.95E-05	0.9983	4.50E-05	0.9941

6.3.3. MIL-101

As a point of comparison, parameter fitting was performed on the MIL-101 isotherm. The isotherm, along with two curves fitted to it, is presented in Figure 6.8 below.

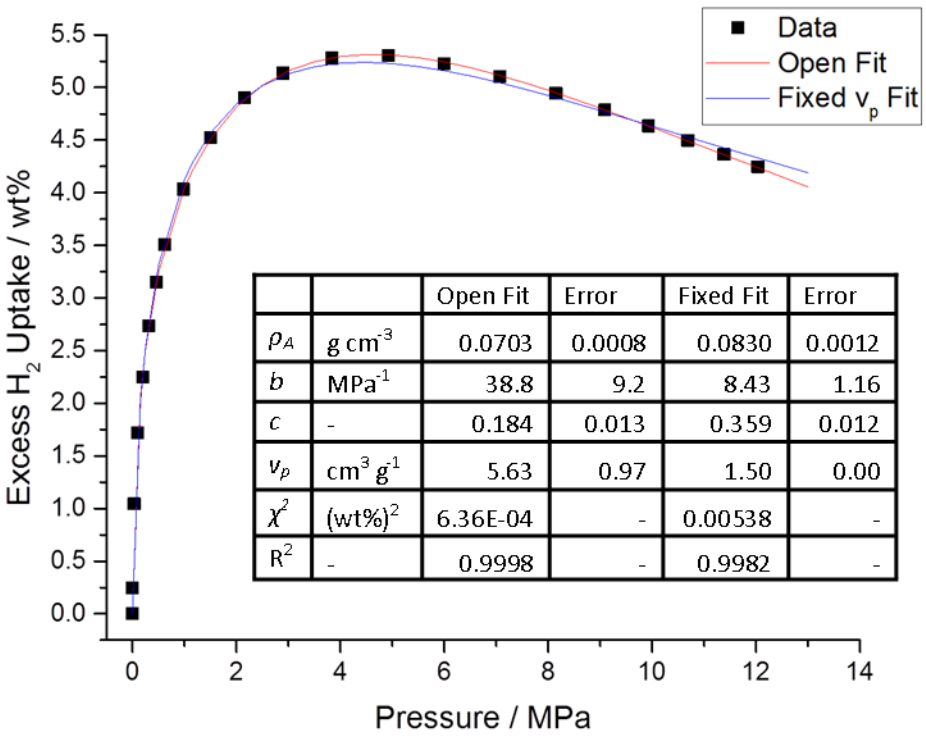

		Open Fit	Error	Fixed Fit	Error
ρ_A	g cm^{-3}	0.0703	0.0008	0.0830	0.0012
b	MPa^{-1}	38.8	9.2	8.43	1.16
c	-	0.184	0.013	0.359	0.012
v_p	cm^3 g^{-1}	5.63	0.97	1.50	0.00
χ^2	(wt%)^2	6.36E-04	-	0.00538	-
R^2	-	0.9998	-	0.9982	-

Figure 6.8 - High pressure H_2 isotherm (77 K) for MIL-101 plotted with the fitting curves, generated by both unrestricted fitting (red line) and fixing the pore volume to 1.5 cm^3 g^{-1} (blue). The parameters generated by the fit are given in the table. All values are given to 3 significant figures, with the exception of R^2, which is quoted to 4.

Originally, the parameter fit to the MIL-101 isotherm was performed with no restrictions, as it was for most of the other fits shown in this chapter. Whilst this produced a high quality fit with very little error from the empirical data (the red line in Figure 6.8), the parameters themselves showed an erroneous result, as the pore volume quoted for this fit was 5.63 $cm^3\ g^{-1}$, a value that is 4 – 5 times higher than the pore volumes determined by the traditional porosity models (HK, DFT etc.) on N_2 isotherms. As such, the fit was performed again, this time fixing the value of the pore volume to 1.5 $cm^3\ g^{-1}$, a value very close to that determined for this MIL-101 sample previously in this study (see section 4.8.5). This resulted in a fit that, whilst not as close to the empirical data as the open fit, showed excellent approximation of the data (the blue line in the above figure) whilst retaining reasonable values for the other parameters. This latter fit was therefore accepted as the required fit moving forward, as the very large pore volume in the open fit would cause a highly erroneous result if these values were used in the tank scale mass balance (see section 6.5.3 below).

Looking at the parameters produced by the fixed fit, some interesting values are produced. The adsorbate density of 0.0830 g cm^{-3} near perfectly matches the density of solid hydrogen, and this material is therefore assumed to densify hydrogen to solid-like levels in its pores. The value of *b* is rather low for an isotherm at 77 K, given the values in the 10^2 – 10^3 range consistently reported at 77 K for PIM-1, but this is reasonable, as MOFs have tended to show lower isosteric enthalpies of adsorption than carbonaceous adsorbents. This phenomenon likely explains the lower rate at which the excess uptake increases, and the higher pressure that MIL-101 shows its maximum excess uptake. The *c* parameter for this fit is 0.359, which is curiously high for an inherently heterogeneous material, given the presence of the Cr nodes and the bdc linkers. However, if some residual terephthalic acid is still adsorbed to the open Cr sites, then these acid molecules would behave chemically very similarly to the bdc linkers, which would increase the homogeneity of the material and therefore artificially increase the *c* value.

6.3.4. PIM-1/MIL-101 Composites

The PIM-1/MIL-101 composites are the materials of greatest interest in this study, given their desired combination of material properties, and uncovering the nature of H_2 adsorption within these materials was a desired objective of this study. H_2 isotherms of the 10, 20 and 30 wt% composites are found in Figure 6.9, and the rule of mixtures plots of the parameters can be found in Figure 6.10.

Figure 6.9 illustrates that the parameter fitting produced high quality fits to all three isotherms, with R^2 values no lower than 0.9998 for any. The parameters produced by these fits produced some wide ranging and at times unexpected behaviour, as shown by the rule of mixtures plots.

The adsorbate density in the composites varied greatly, with only the 10 wt% composite showing a density comparable to those found either in the PIM-1 film or the MIL-101. Both the 20 and 30 wt% films showed ρ_A values well into the solid-like density region, although given that these materials are combinatorial, there is little evidence to explain why such an increase would be seen. It is possible that the interaction between PIM-1 and MIL-101 theorised by Alentiev et al. [209] may have produced ultramicropores within the films that allow for efficient hydrogen densification that neither pure material can do on its own.

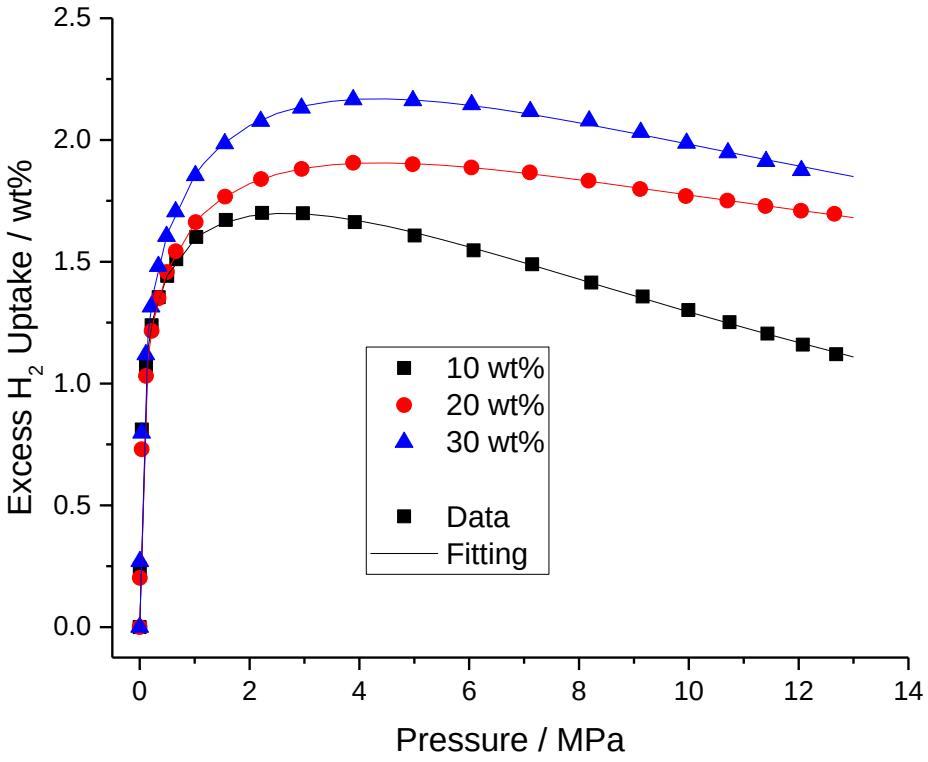

Figure 6.9 - Plots of the high pressure H_2 (77 K) isotherms for the PIM-1/MIL-101 composites with their fitting curves.

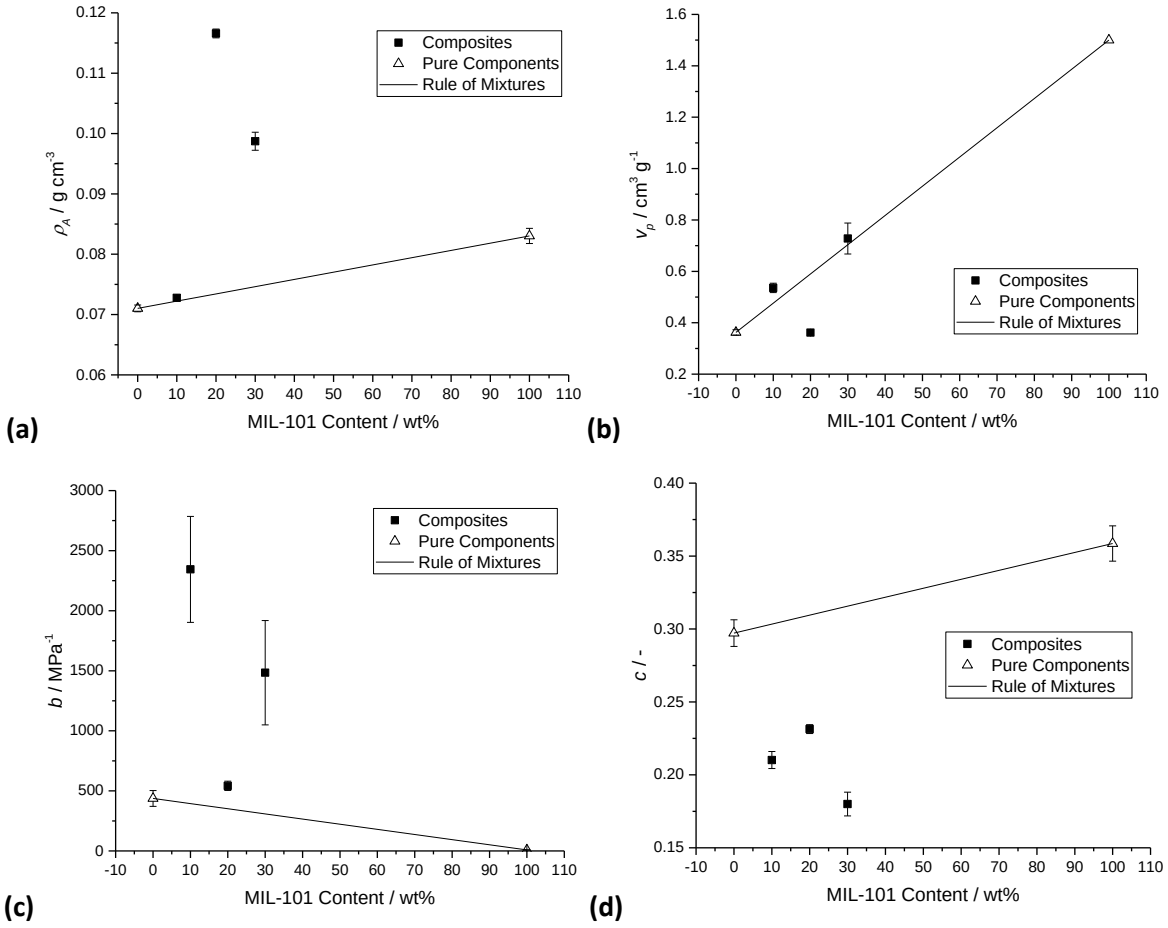

Figure 6.10 - Rule of Mixtures analysis for the fitting parameters across the PIM-1/MIL-101 composites tested (all at 77 K).

The only parameter that appears to a rule of mixtures-type behaviour is the apparent pore volume. Both the v_p for the 10 and 30wt% films have values slightly above the rule of mixtures line, and 20 wt% appears below it, mirroring the trend seen for low pressure hydrogen uptake seen in Figure 4.47(b). These data therefore appear to show the porosity in the material increasing as a result of the MIL-101 dosing.

The *b* and *c* parameters from these fits are best considered together, as they appear to be complete opposites in terms of the parameter values produced and their relationship to the rule of mixtures. The *c* values are all much lower than the rule of mixtures, particularly the 10 and 30 wt%. This makes sense however, as the composites are a combination of two chemically different materials that themselves show heterogeneity along their surfaces, meaning the overall heterogeneity of the surface is further reduced. As a result, the Tóth parameter is reduced.

As a result of this heterogeneity, the affinity of hydrogen to the surface can be affected, particularly as highly attractive parts of the surface (such as the cyano group in the PIM-1, or exposed chromium in the MOF) contribute to a decreased homogeneity. Therefore, it is unsurprising that the Langmuir parameters for the 10 and 30 wt% composite films are higher than that of the 20 wt% film, and that all of them are greater than the *b* values for the pure components, as although it is the same elements that are present within these materials as the pure components, the arrangement of these elements may be resulting in overlapping potentials that result in a greater affinity for the gas molecules. Alternatively, this increase could be purely mathematical, based on the close interconnectedness of the *b* and *c* parameters in equation 6.14. Rigorous determination of the isosteric enthalpy of adsorption performed on the 30 wt% composite (section 6.4.3) will provide a better insight into the strength of interaction between adsorbent and adsorbate in this case.

In order to calculate the isosteric enthalpy, a number of isotherms on 30 wt% composite at a range of temperatures were performed (Figure 4.60). The parameter fits to these isotherms are plotted with respect to temperature in Figure 6.11 - Figure 6.14 below, and the fitted curves to the isotherms can be seen in the supplementary information (SI-10).

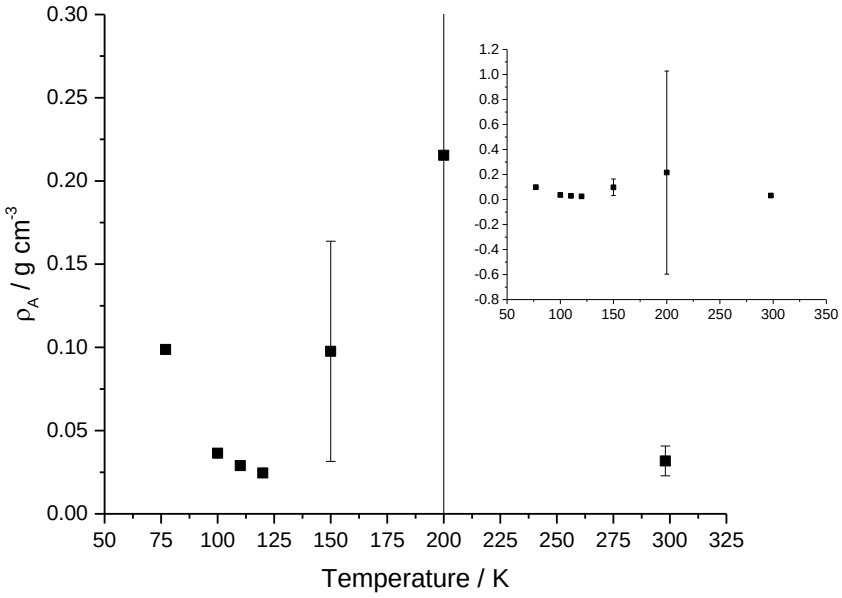

Figure 6.11 - Adsorbate density (ρ_A) parameter for the 30 wt% composite at multiple temperatures (77 - 298 K). The inset is the same plot on a larger scale ordinate in order to fully illustrate the error at 200 K.

The adsorbate density in the composite appears to vary greatly with temperature. Although the 77 K value shows a reasonable density of 0.0987 g cm^{-3}, which is matched by the 150 K point (at 0.976 cm^3 g^{-1}, albeit with a large degree of error), the points between 100 – 120 K are all very low, and decrease with increasing temperature. Given that the adsorbate density should be should be temperature independent (and therefore uniform across the temperatures), there is a large variety of values produced in this fitting. The low values in the middle temperatures are likely due to the low (and early) maximum uptake and rapid excess decreases in the higher pressures, which were noted as unusual features of these isotherms in section 4.9.5. Neither of the fits on 200 or 298 K converged, resulting in the highly unusual value at 200 K in this figure.

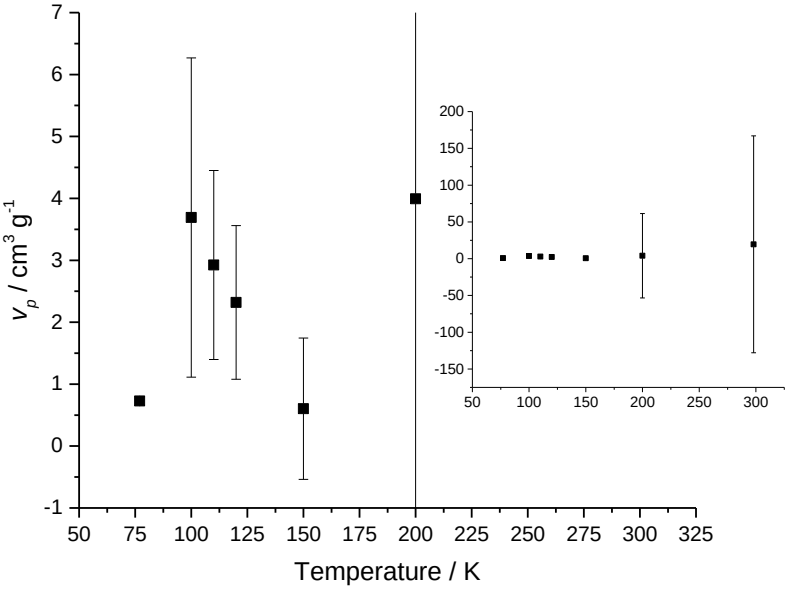

Figure 6.12 - Pore volume (v_p) parameter for the 30 wt% composite at multiple temperatures (77 - 298 K). The inset is the same plot on a larger scale ordinate in order to fully illustrate the errors at 200 and 298 K.

The pore volume for this material suffers from the same issues at the adsorbate density, namely that the unusual shapes of the isotherms in the low-to-middle temperatures results in a highly scattered series of values for a parameter that, by definition, is constant no matter the temperature. The only two values that come close to matching are those of 77 and 150 K, matching the trend seen in Figure 6.11. The lack of convergence for the 200 and 298 K isotherms is highly evident in Figure 6.12, as both the values are very high for a pore volume in this material, and the error produced is orders of magnitude larger than the values themselves, therefore losing all substantive meaning.

Despite the huge array of inconsistent values and large errors seen in the adsorbate density and pore volume parameters, the Langmuir affinity parameters appear to match expected behaviour. There is a large jump from 77 K to the other values, which is expected, and when these data are plotted on a logarithmic ordinate, the resulting curve appears to be hyperbolic, which matches the Van't-Hoff profile desired for calculating the characteristic energy of adsorption. Based on these data, it was decided that the isotherms, although highly unusual in profile, could provide a useful insight into the isosteric enthalpy of this material, although such a value would have to take into account the quality of the data used to calculate the value.

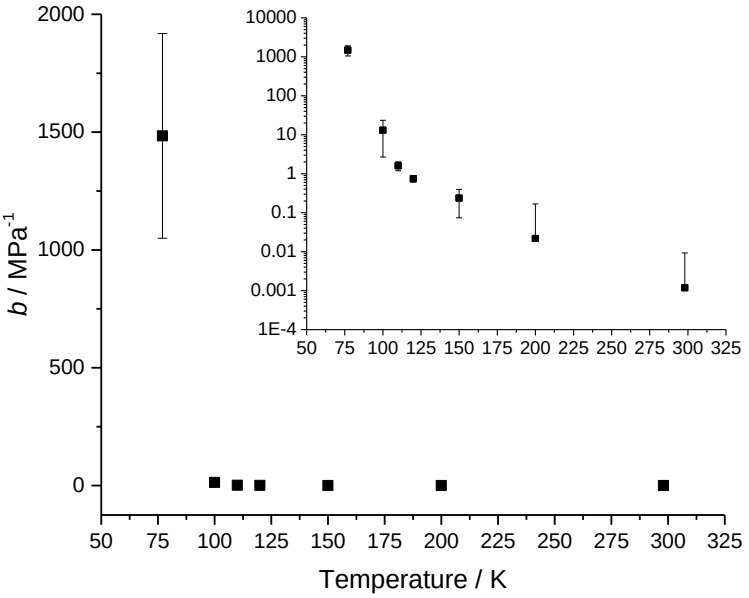

Figure 6.13 - Langmuir affinity parameters (*b*) determined for the 30 wt% composite at multiple temperatures (77 – 298 K). The inset plots the same data on a logarithmic ordinate. Standard errors have not been plotted in the negative direction in the inset for the 200 and 298 K points due to negative values.

Like the Langmuir parameter, the Tóth parameter in Figure 6.14 appears to trend as expected in the lower temperatures. The value rises continuously from 77 – 120 K, as would be expected, although it flattens out at 150 K, and then reduces afterwards (albeit these last two values have little meaning given the lack of convergence in the fit). The error associated with each value also appears to increase as the temperature increases, although the reason for this is unknown.

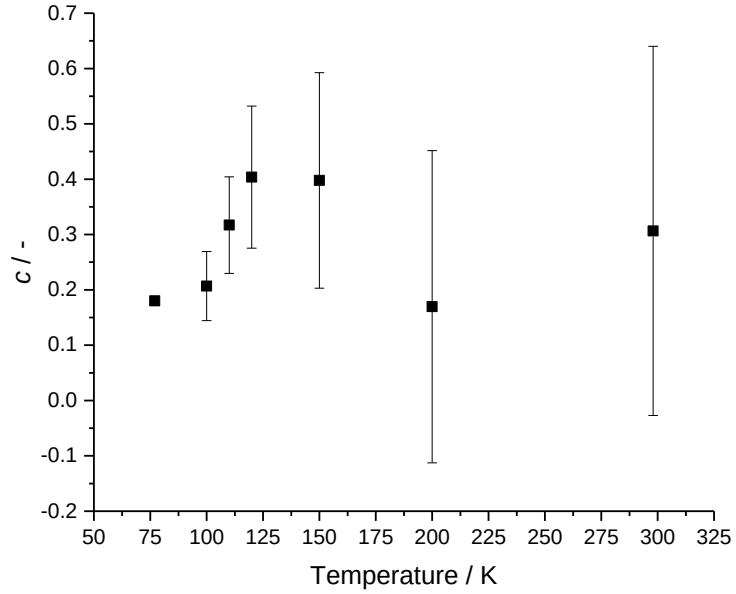

Figure 6.14 - Tóth heterogeneity parameter (*c*) for the 30 wt% composite at multiple temperatures (77 - 298 K).

6.3.5. Carbon Films

When evaluating the high pressure H_2 isotherms on the carbonised and activated PIM-1 films, it is evident to see that the carbonised film does not show a type I isotherm in the lower pressure range, due to the 'steps' seen in the isotherm. Although a fit was attempted on the desorption curve of this isotherm, which is much smoother, the lack of data in the very low pressure range means that Origin cannot start a fit, let alone fail to converge one, as has been seen in the high

temperatures for the sample above. As a result, a parameter fit was not performed for the carbonised sample.

Although a moderate step exists as the top of the carbonised film isotherm, the behaviour is close enough to type I behaviour that a reasonable fit can be performed. The fit produced, and the parameters determined, can be seen in Figure 6.15.

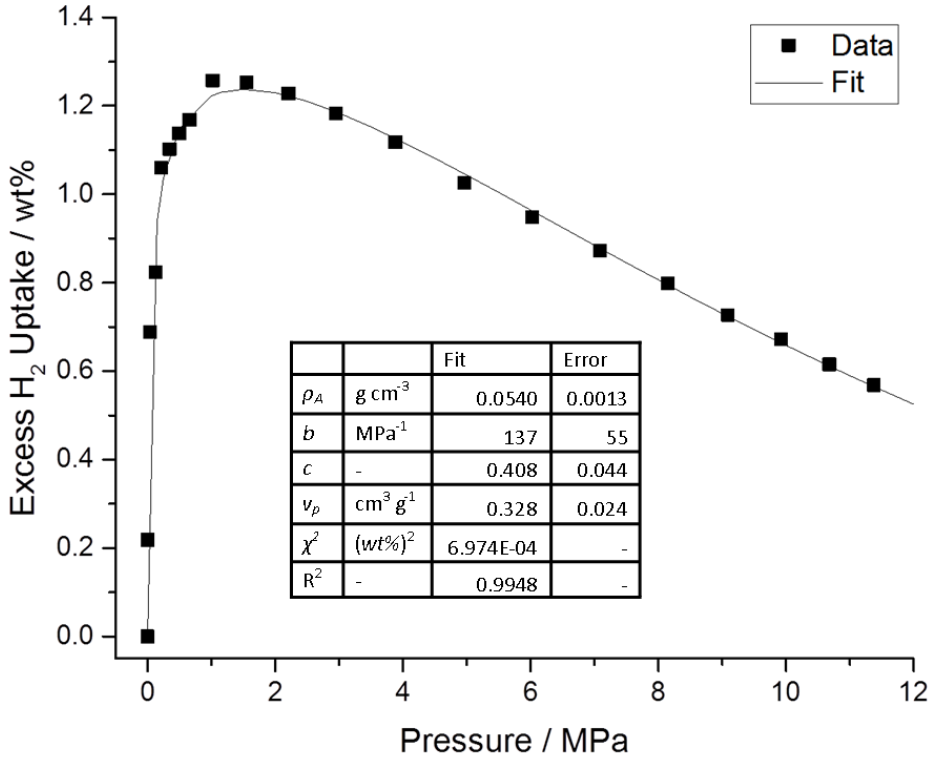

		Fit	Error
ρ_A	g cm^{-3}	0.0540	0.0013
b	MPa^{-1}	137	55
c	-	0.408	0.044
v_p	cm^3 g^{-1}	0.328	0.024
χ^2	$(wt\%)^2$	6.974E-04	-
R^2	-	0.9948	-

Figure 6.15 - High pressure H_2 isotherm (77 K) for PIM-1 activated carbon plotted with the fitting curve. The parameters generated by the fit are given in the table. All values are given to 3 significant figures, with the exception of χ^2 and R^2, which are quoted to 4.

Looking at the fit, it is clear to see that the fit is very good in the very low (< 0.5 MPa) and high (> 2 MPa) pressure ranges, but in the region around the maximum excess uptake, the fit is strongly deviated by the 'step' in the isotherm. Although Origin produces a high quality fit to these data (R^2 = 0.9948), it is evident that the parameters will be slightly affected by the presence of this step, which lowers the maximum excess uptake (compared to the uptake shown in the desorption step in Figure 5.26. It is therefore worth acknowledging that the parameters produced may contain a level of error not seen in the standard error, but instead induced by the isotherm from which the fit was taken.

Looking at the parameters produced, the majority of values appear to be reasonable. The Langmuir affinity parameter of 137 MPa^{-1} is higher than that deduced for the MIL-101, but lower than for PIM-1, which suggests an isosteric enthalpy somewhere between that of the aforementioned materials. The Tóth parameter of 0.408 suggests a more homogeneous surface than the native PIM-1, which is reasonable given that the carbonisation process should remove most of the non-carbon atoms from the chain (bar the dioxane linkers holding the polymer together), and the pore volume of 0.328 cm^3 g^{-1} suggests a pore volume slightly higher than that of the microporous volume in PIM-1, which again would be expected given the expected effect of the activation is to create further porosity in the material by combusting some of the carbon

present. The slight rise in this value correlates with the slight increase in low pressure CO_2 and H_2 uptake in this material seen in Figure 5.22 and Figure 5.23.

The value that is perhaps the most unexpected is the adsorbate density, which at 0.054 g cm^{-3} is far lower than the solid-like densities previously seen in carbonaceous adsorbents [349]. This low value is very likely due to the low uptake seen in the material, as well as the sharp descent in excess adsorption with rising pressure. It may also have been artificially deflated by the trend of the fit to follow the step in the isotherm.

6.3.6. Effect of skeletal volume sensitivity

The uncertainty in the skeletal volume determined by the HTP-1 not only causes issues in the isotherms that the instrument produces, but that uncertainty is inherently carried through to the parameter fitting that is performed on those isotherms. As a result, it is prudent to investigate how the parameters produced from these isotherms are affected by changes in the isotherm, and to determine whether the parameters determined for the samples above are reliable. This testing was done by performing fitting to all of the isotherms presented in Table 4.7; the results of this analysis can be seen in Table 6.5 below.

A number of points arise from this analysis. Firstly, it is apparent that increasing the skeletal density value always reduces the adsorbate density and Langmuir parameters, whilst raising the pore volume and Tóth parameters. This is to do with the change in isotherm shape, as it is evident from Figure 4.61 that higher skeletal density isotherms have lower maximum uptakes and sharper decreases in excess with rising pressure, which primarily serve to suppress the calculated adsorbate density. Conversely, this sharper drop also makes the pore volume appear larger.

Looking across the columns, it is clear that the change in skeletal density affects ρ_A and v_p far more than both *b* and *c*. 10% changes in the skeletal density almost always produce much larger changes in these parameters (apart for MIL-101, which has already been seen to be largely stable in the face of skeletal density alterations), indicating that these parameters are the least trustworthy in the case of uncertain skeletal density determination. The most stable parameter is *c*, which does not alter more than 4% in any of the cases listed in Table 4.7. However, because this value is limited to between 0 and 1 by definition, it would be very difficult to induce very large changes in this parameter.

The Langmuir parameter is an interesting case in this regard. Table 4.7 shows that the change in *b* with skeletal density is slightly more than the induced change, although the largest change in *b* is 1.63 times the induced change in the density. This does mean that the Langmuir parameter is sensitive to the skeletal density, and therefore any uncertainty in ρ_s cannot simply be dismissed, but it does not change greatly like the values of ρ_A and v_p far. Therefore, it can generally be seen as varying proportionally with the skeletal density, and values of the characteristic energy calculated from these values can maintain about the same level of certainty as the isotherms themselves.

Interestingly, the magnitude of the changes in parameter values is not homogeneous in both directions; in every case, the magnitude of the parameter change is greater when the skeletal density is reduced than when it is increased. The standard errors for these changes are generally similar, indicating no discernible issue with the certainty of the fitting. This statement was only true of the maximum uptake in the isotherm metrics (the equivalent pressure for which also changes heterogeneously), which suggests that the parameters directly follow the change in the

isotherm shape, rather than absolute values at given pressures. This statement presents a conclusion in which an overestimation of the skeletal density will result in a more accurate parameter fit than an equivalent underestimation.

Table 6.5 – Parameter values for fits to the isotherms generated by skeletal density sensitivity analysis. All values are quoted to 3 significant figures.

Sample	Skeletal Density value	ρ_A	$\Delta(\rho_A)$	b	$\Delta(b)$	c	$\Delta(c)$	v_p	$\Delta(v_p)$
		g cm^{-3}	%	MPa^{-1}	%	-	%	cm^3 g^{-1}	%
PIM-1 Powder	HTP	0.131	-	619	-	0.258	-	0.242	-
	-10%	0.230	74.7	696	12.4	0.249	-3.4	0.146	-40.0
	+10%	0.091	-30.8	557	-10.1	0.266	3.3	0.336	38.4
	Pycno.	0.138	5.1	627	1.2	0.257	-0.4	0.232	-4.4
PIM-1 film	HTP	0.069	-	795	-	0.272	-	0.396	-
	-10%	0.093	34.0	860	8.2	0.265	-2.3	0.304	-23.1
	+10%	0.055	-20.6	739	-7.0	0.278	2.3	0.486	22.6
10 wt%	HTP	0.073	-	2344	-	0.210	-	0.536	-
	-10%	0.095	29.9	2693	14.9	0.204	-3.1	0.435	-18.9
	+10%	0.059	-19.2	2064	-12.0	0.217	3.1	0.632	18.0
20 wt%	HTP	0.117	-	542	-	0.231	-	0.362	-
	-10%	0.170	46.2	600	10.6	0.224	-3.1	0.261	-27.8
	+10%	0.088	-24.7	494	-8.9	0.238	3.0	0.457	26.4
30 wt%	HTP	0.099	-	1484	-	0.180	-	0.728	-
	-10%	0.126	28.1	1725	16.3	0.174	-3.6	0.617	-15.3
	+10%	0.080	-18.6	1294	-12.8	0.186	3.5	0.830	14.1
MIL-101	HTP	0.070	-	38.8	-	0.184	-	5.63	-
	-10%	0.072	2.9	39.5	1.8	0.182	-1.2	5.69	1.1
	+10%	0.068	-2.7	38.1	-1.7	0.187	1.2	5.57	-1.0
	Ardelean et al. [136]	0.076	8.0	40.8	5.1	0.178	-3.3	5.81	3.2

It was discussed in section 4.9.6 that the changes in key metrics of the isotherms became generally less sensitive to skeletal density changes with increasing MIL-101 concentration. Looking down the columns of Table 4.7, there is no evidence of the same trend, with the difference in parameters varying with no discernible pattern. Although PIM-1 still shows the greatest sensitivity and MIL-101 the least, the films do not follow this trend, with the 20 wt% composite in particular bucking any trend that might otherwise have developed. It is also curious to note that the parameters for the PIM-1 powder isotherms are more sensitive than the film parameters, despite the opposite being true for the isotherms themselves. These findings appear to reaffirm the idea that the parameters are far more sensitive to isotherm shape than to absolute values for a given pressure, as how the shape changes for a given change in density varies depending on the original isotherm shape.

6.4. Isosteric Enthalpies of Adsorption

6.4.1. PIM-1(4) powder

As detailed in section 6.1.2, if multiple temperature isotherms have been performed on a sample, then the isosteric enthalpy of adsorption can be calculated by determining the absolute amount adsorbed on the sample at each point (which is easily performed using the parameters found using the Origin fitting), to then rearrange these data into the form of isosteres (to match the linearised form of the Clausius-Clapeyron equation). The isosteres calculated in this manner for the PIM-1 (4) powder runs are presented in Figure 6.16. The isosteres produced for PIM-1 (4) powder generally show good linearity, which is encouraging for the determination of the enthalpy. However, the data set at 1000/*RT* = 1.0 (which corresponds to the 120 K isotherm) is highly offset, likely due to the fit to this isotherm showing a much more rounded shape with a much later maximum uptake, which will have affected the parameters generated by the fit and therefore the absolute adsorption calculations. This is despite the individual parameters for this isotherm not standing out significantly when reviewing Table 6.3 and Figure 6.5 - Figure 6.7. The data at 1000/*RT* = 0.6 and 1.2 are also both more spread out than the other sets, which will further contribute to the error in the final value.

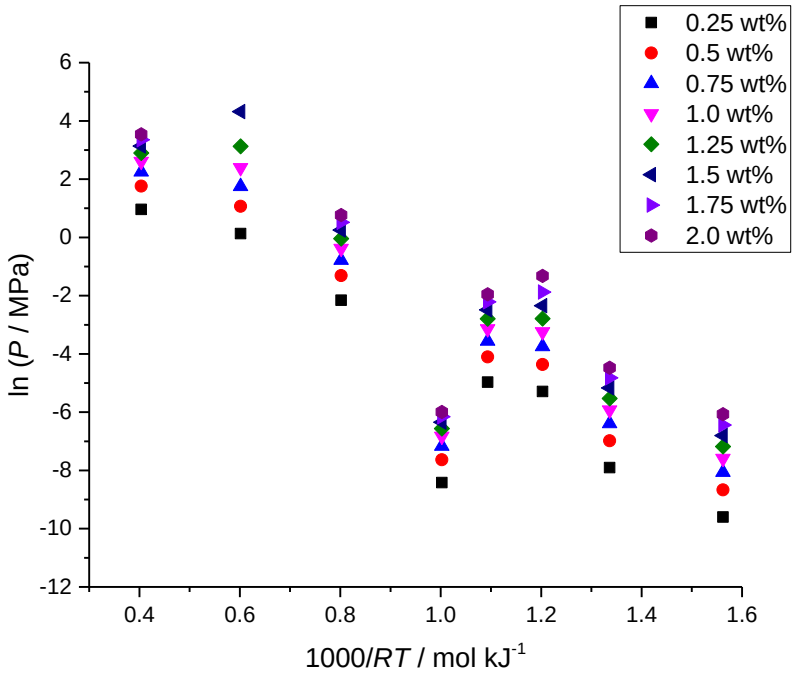

Figure 6.16 – Isosteres calculated for H_2 uptake on PIM-1 (4) powder at absolute uptakes between 0.25 and 2 wt% in intervals of 0.25 wt%.

With these data, the gradients of the linear fits to each isostere are calculated, and this value is the isosteric enthalpy of adsorption for that uptake. The relationship between isosteric enthalpy and uptake for PIM-1 (4) powder is presented in Figure 6.17.

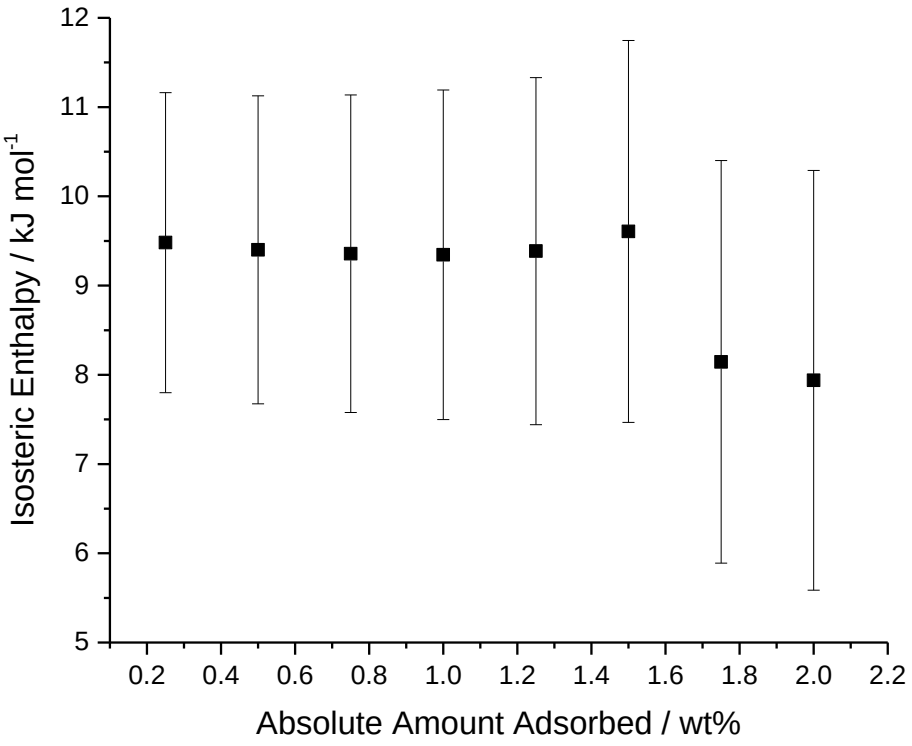

Figure 6.17 – Isosteric enthalpy of adsorption for H_2 adsorbing onto PIM-1 (4) powder at absolute uptakes between 0.25 – 2.0 wt%. All enthalpies are exothermic. The error bars presented are standard errors of the fits to the linearised isosteres.

The result of this calculation is remarkably consistent with what would be expected from such an analysis; namely, that the enthalpy is high at low coverage and steadily reduces as the uptake increases. The value of this enthalpy also appears to be as expected, as the enthalpy calculated by Tedds [206] declined from - 9.7 kJ mol^{-1} at minimal coverage to – 6.7 kJ mol^{-1} at 0.8 wt%; the value of the enthalpy recorded in this case appears to hold much more steadily as the uptake increases, declining from -9.5 kJ mol^{-1} at 0.2 wt% to -7.9 kJ mol^{-1} at 2 wt%. It is known that the Clausius-Clapeyron becomes less accurate at higher uptakes however, as the assumptions used in simplifying the Clapeyron equation become invalid, so these higher uptake values do have greater uncertainty associated with them, a fact illustrated by the R^2 values of the linear fits consistently decrease with increasing uptakes.

An alternative method of enthalpy determination is taking a Van't-Hoff plot of the Langmuir affinity parameters. The plot for this data set is presented in Figure 6.18. As detailed in section 6.1.2, finding the gradient of the plot of ln *b* against 1/*RT* produces the characteristic adsorption enthalpy, an adsorptive-adsorbent dependent value which is not strictly defined as the enthalpy of adsorption, but is related to it [275, 343]. Finding its value in this manner provides a good way to check the calculated isosteric enthalpy value via a different method that is easily implemented.

The Van't-Hoff plot shows the data in a reasonable linear fit, with no evident deviation from the expected Van't-Hoff behaviour. Interestingly, the value for the characteristic energy produced by this fit is -9.86 kJ mol^{-1}, which is a very good fit to the isosteric enthalpy calculated by the Clausius-Clapeyron approach, and well within the standard error shown in Figure 6.17. Although the isosteric enthalpy and the characteristic energy are not the exact same measurement, and should not be treated as such, they are related, and observing very similar values for these parameters is encouraging.

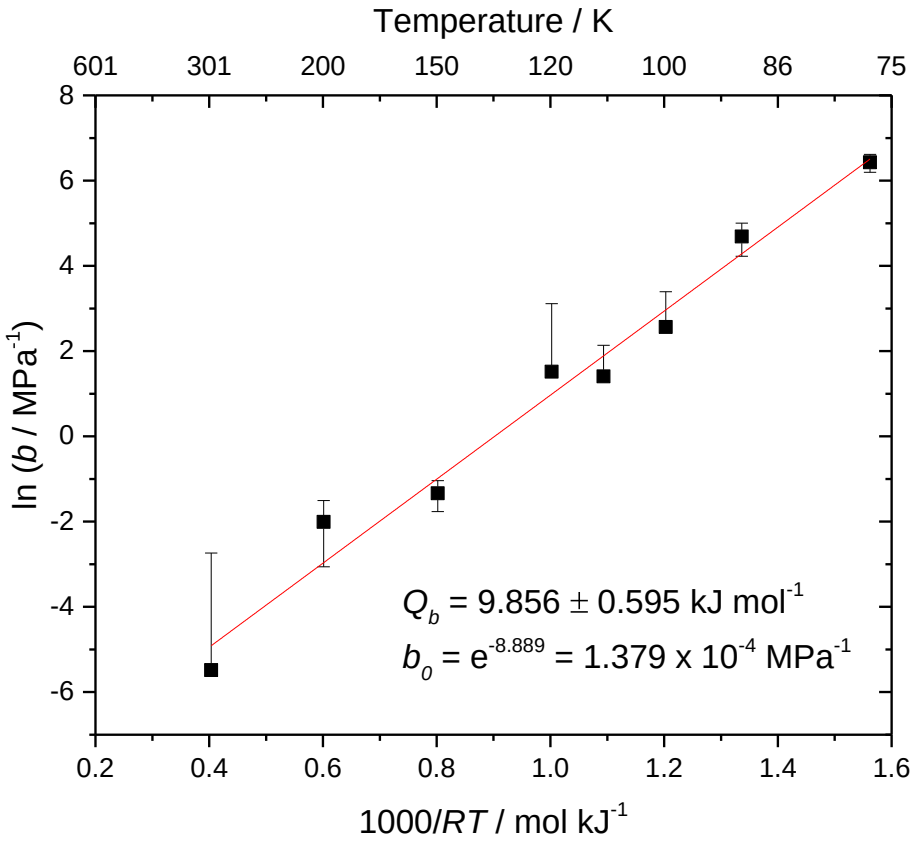

Figure 6.18 –Van't-Hoff plot of the Langmuir affinity parameters (*b*) against inverse temperature for the multiple temperature PIM-1 (4) H_2 isotherms. Negative errors for the values at 0.4, 1.0, 1.1 and 1.2 mol kJ^{-1} are not illustrated due to negative values before the logarithm is applied. The red line is a line of best fit to the data.

It is interesting that the isosteric enthalpy of adsorption is much higher for PIM-1 than is typically reported for other, higher uptake materials, such as activated carbons [92, 257] or MOFs [92, 145]. Although the chemical heterogeneity of the PIM surface, and particularly the presence of the highly electrophilic –CN groups on the chains would increase the affinity of the hydrogen to the surface, it is unlikely that this is the sole driver of the increase in enthalpy, given that MOF materials, which often feature bare metal sites that have very high affinities for adsorptives, tend to feature much lower enthalpies of adsorption. It is likely that the pore size within the material has an effect on the isosteric enthalpy, particularly in the very fine microchannels, where the bonding potentials can overlap and encourage greater affinity towards the surface. Ultimately, it is these very fine micropores that give PIM-1 its high enthalpy of adsorption, but ultimately limit its utility as a storage medium, as these channels are likely too fine to give easy access to the larger voids further within the material.

6.4.2. PIM-1(4) film

The isosteres calculated from the PIM-1 film multiple temperature isotherms are presented in Figure 6.19. Much like the isosteres calculated for the powder sample, the film isosteres generally show good linearity, although there is a major exception at 1000/*RT* = 1.3, which is derived from the 90 K isotherm for this material that, upon reviewing Figure 4.55, is highly erratic. As a result, this data set was omitted from the isosteric enthalpy calculations. The other isosteres are generally well aligned, although some occur over a broader range of pressures than others. The isosteric enthalpies calculated from the gradients of these isosteres are presented in Figure 6.20.

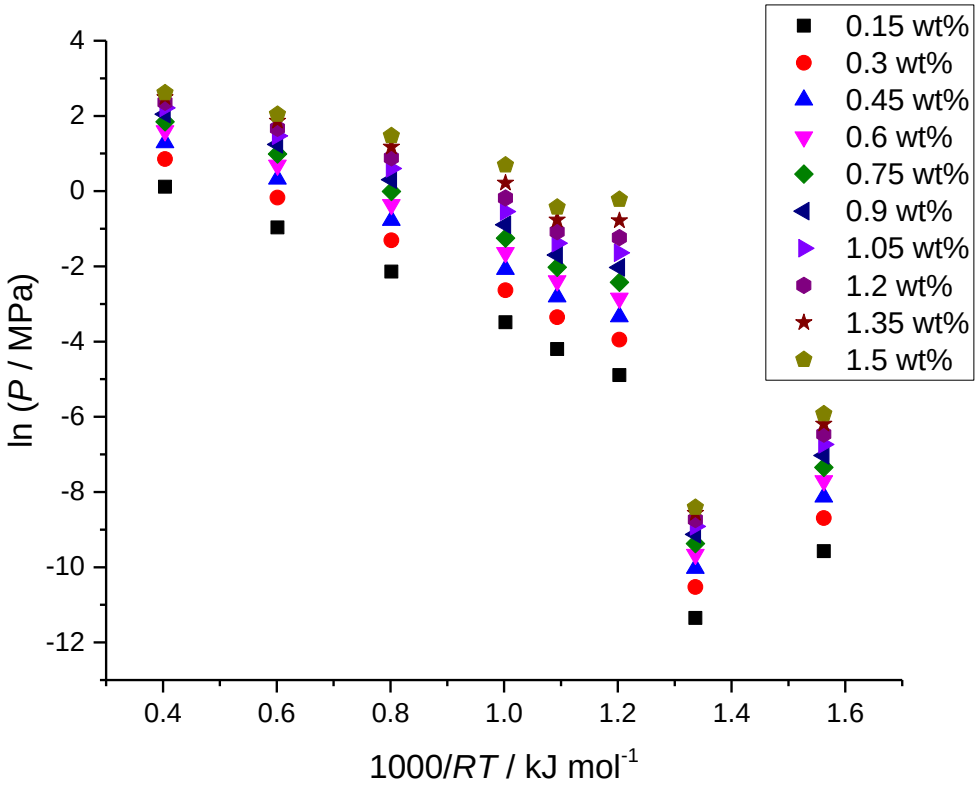

Figure 6.19 - Isosteres calculated for H_2 uptake on PIM-1 (4) film at absolute uptakes between 0.15 and 1.5 wt% in intervals of 0.15 wt%.

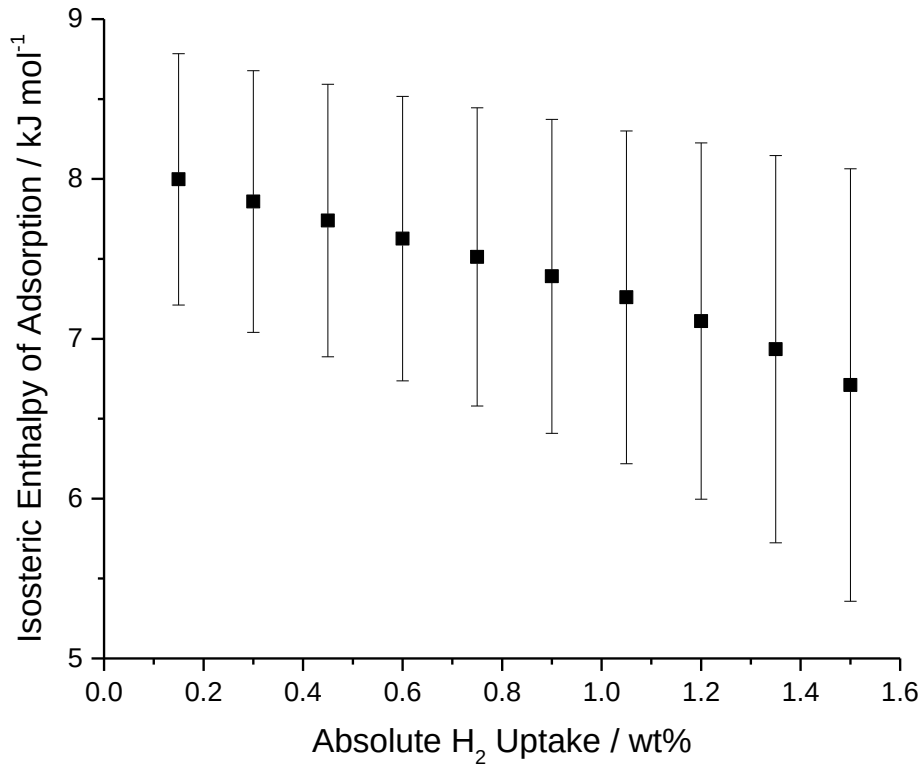

Figure 6.20 - Isosteric enthalpy of adsorption for H_2 adsorbing onto PIM-1 (4) film at absolute uptakes between 0.15 – 1.5 wt%. All enthalpies are exothermic. The error bars presented are standard errors of the fits to the linearised isosteres.

There are two main points of interest when observing Figure 6.20 and comparing it to Figure 6.17. Firstly, the enthalpy at the lowest coverage investigated (0.15 wt% for the film, 0.25% for the powder) is much lower for the film than for the powder. This is despite the fact that the materials

are chemically identical, and therefore the affinity of hydrogen molecules to the surface should, at least in theory, be identical. However, the value of -8.0 kJ mol^{-1} determined for the film morphology is 16 % lower than the value for the powder. Although this is not an enormous difference, small changes in isosteric enthalpy can result in large changes in the tank scale energy balance: a 0.5 kJ mol^{-1} difference in the enthalpy results in a 1 MJ difference in a 4 kg hydrogen tank [92].

This is a clear demonstration that the pore morphology can have a strong effect on the isosteric enthalpy, although in this case it appears that there are fewer fine microchannels in the film morphology than in the powder, given the relative magnitudes of the values. This corroborates the higher uptakes of both CO_2 and H_2 in the 0 – 0.1 MPa range seen in the powder (see Figure 4.37 and Figure 4.39). This difference may have been affected by the relative age of the materials, as the PIM-1 films were very recently formed before testing, whilst the powder sample had been reprecipitated months before, so allowing time for the porosity in the material to close up.

The second point of interest is the more rapid decline in the enthalpy with increasing uptake. This is typically associated with a greater surface heterogeneity, as the high affinity sites are quickly filled in the low uptake regions, leaving only the surfaces with lower affinity, so decreasing the overall attraction at higher coverages [92]. It would therefore be expected that the enthalpy would decrease at the same rate for both morphologies, although this is clearly not the case. It may therefore be the case that the enthalpy for the film is more dependent on the heterogeneity of the surface than for the powder, in which the enthalpy is dominated by the lower micropore size.

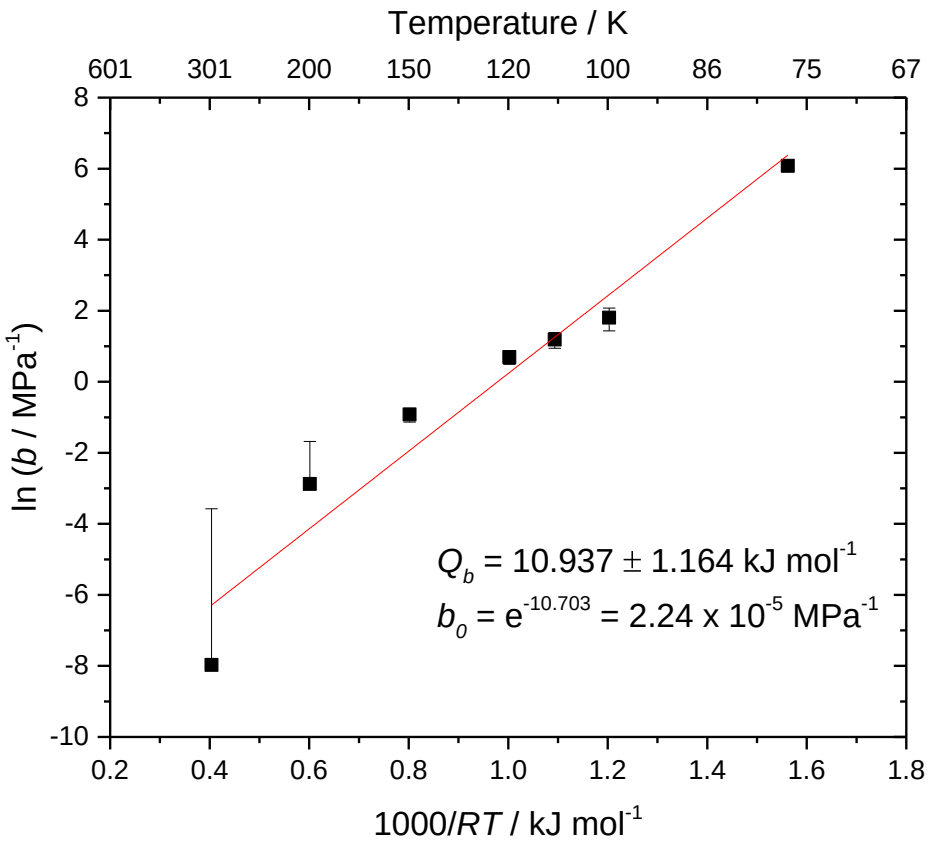

Figure 6.21 – Van't-Hoff plot of the Langmuir affinity parameters (*b*) against inverse temperature for the multiple temperature PIM-1 (4) film H_2 isotherms. Negative errors for the values at 0.4, and 0.6 mol kJ^{-1} are not illustrated due to negative values before the logarithm is applied. The red line is a line of best fit to the data.

The characteristic energy of PIM-1 (4) film is shown in Figure 6.21. Curiously, the value of Q_b in this case is -10.9 kJ mol^{-1}, which is far higher than the isosteric enthalpies for both powder and film morphologies, and also the Q_b value found for the powder. This misaligned value is likely due to the low quality of both the isotherms fed into this calculation, which would produce parameter values that diverge the energy values produced through different methods. The large characteristic enthalpy value is also not affected by the apparent difference between the 77 K data point and those generated in the HTP's integral reactor, as reperforming this analysis without the point at 1000/RT = 1.6 actually increases the characteristic energy slightly (to -11.4 kJ mol^{-1}).

Ultimately, this analysis reveals the flaws in the analysis performed here, and the values of the enthalpy calculated must be viewed highly sceptically. A repeat of this experiment with properly working and calibrated equipment, and controlling for aging in the polymer, could reveal yet more information about this material. However, this was not possible in the assigned time for this project, and must be consigned to future work.

6.4.3. 30wt% Composite

The isosteres calculated for the 30 wt% composite multi-temperature runs are presented in Figure 6.22. As with those calculated for the PIM-1 samples, the isosteres generally show reasonable linearity, although the 200 K isotherm set (1000/RT = 0.6) is strikingly low in value compared to the other data sets. Nevertheless, the full data range was used to calculate the isosteric enthalpy, which can be seen in Figure 6.23.

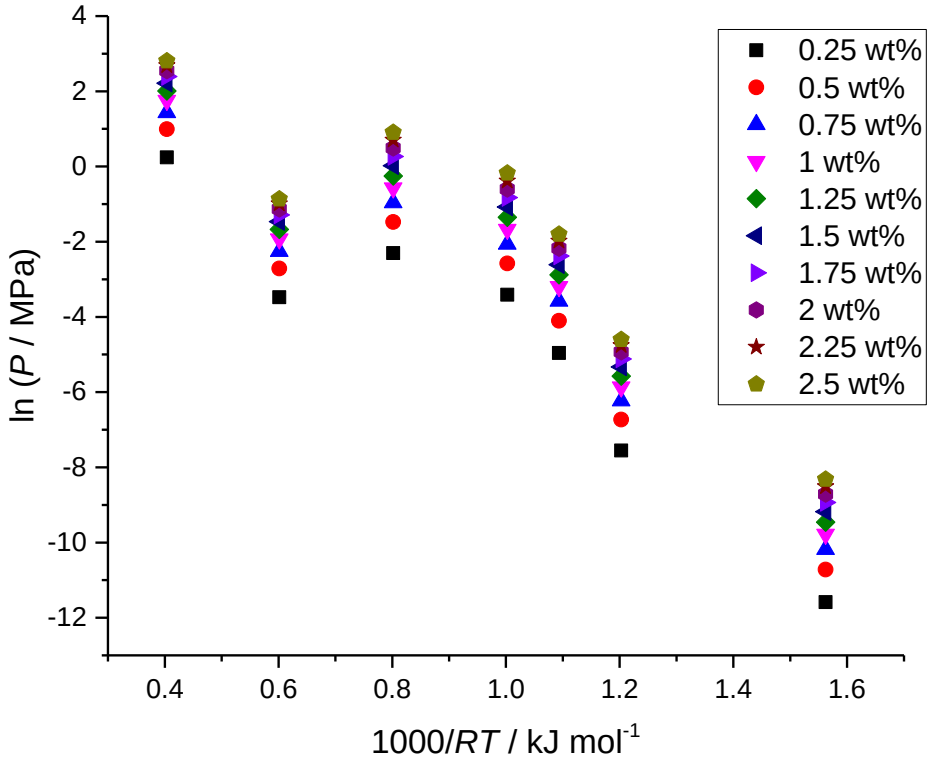

Figure 6.22 - Isosteres calculated for H_2 uptake on the 30 wt% composite at absolute uptakes between 0.25 and 2.5 wt% in intervals of 0.25 wt%.

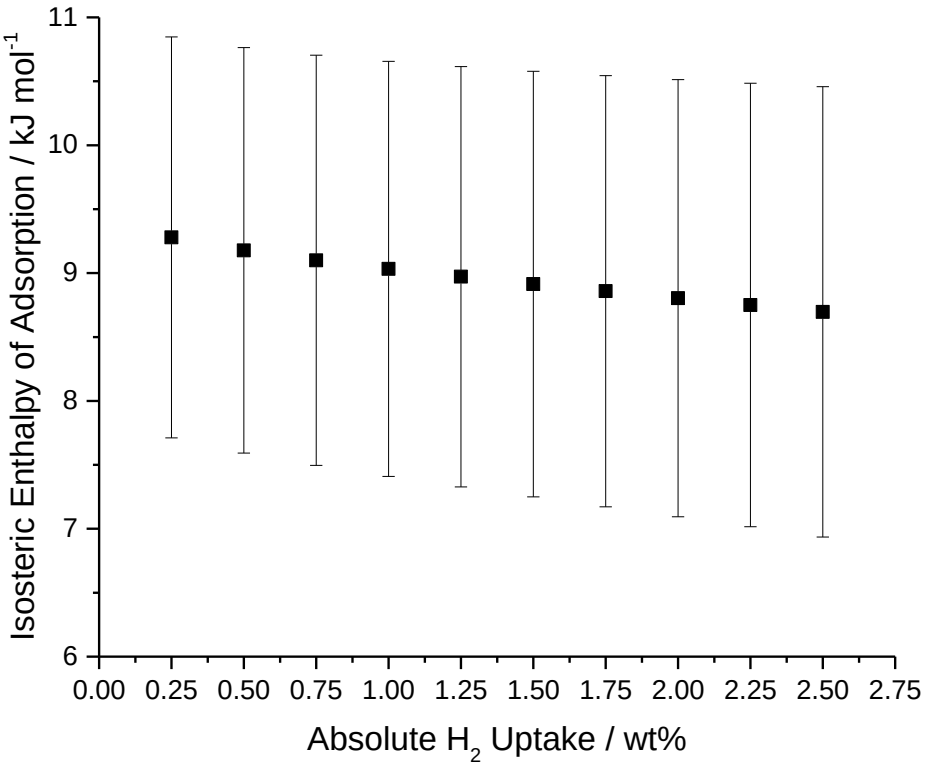

Figure 6.23 - Isosteric enthalpy of adsorption for H_2 adsorbing onto 30 wt% composite at absolute uptakes between 0.25 – 2.5 wt%. All enthalpies are exothermic. The error bars presented are standard errors of the fits to the linearised isosteres.

The enthalpy presented here is striking in its similarity to the enthalpies presented for the PIM-1 morphologies above. The starting value is at -9.3 kJ mol^{-1}, and steadily declines to – 8.7 kJ mol^{-1} at 2.5 wt%. Both of these are particularly similar to the PIM-1 powder enthalpy presented in Figure 6.16, although with a lower starting value, and the decline as the uptake increases is actually shallower than the powder. Both of these statements are in sharp contrast to the enthalpy calculated for MIL-101 by Bimbo et al. [92], which started at – 6.0 kJ mol^{-1} at zero coverage and declined to 2.5 kJ mol^{-1}. There is very little evidence of this behaviour in the enthalpy seen in the composites, instead showing much stronger PIM-like behaviour, and reaffirming that the interactions of hydrogen molecules within the composites are dominated by the PIM.

The Van't-Hoff plot for the 30 wt% composite is shown in Figure 6.24. The value produced for the characteristic energy is - 11.5 kJ mol^{-1}, a very high value that is significantly different from the values produced by the isosteric enthalpy. This value is even larger than that found for the PIM-1 film, and therefore shows little evidence of the presence of the MOF (which shows a much lower enthalpy). Again, one can only hypothesise that the significant difference in the values is due to the low quality of the series of isotherms used to produce these data, and that a higher quality data set would produce a series of calculations that more closely align.

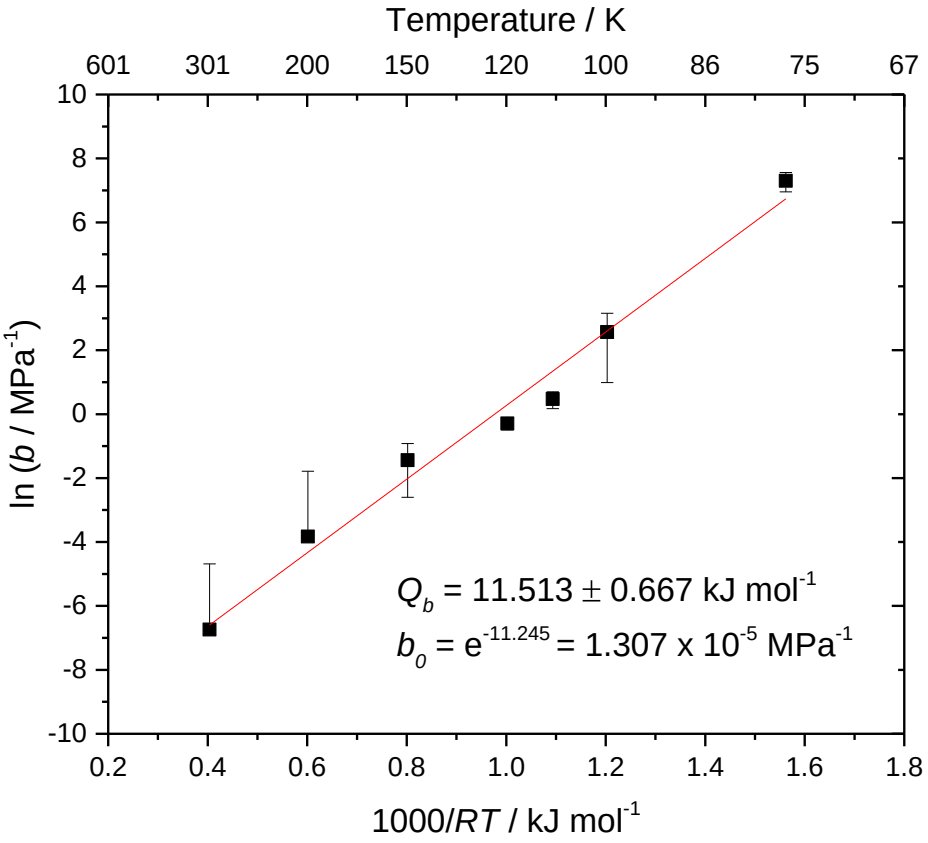

Figure 6.24 - Van't-Hoff plot of the Langmuir affinity parameters (*b*) against inverse temperature for the multiple temperature 30 wt% composite H_2 isotherms. Negative errors for the values at 0.4, and 0.6 mol kJ^{-1} are not illustrated due to negative values before the logarithm is applied. The red line is a line of best fit to the data.

6.5. Mass Balances

Aside from investigations into the isosteric enthalpy of adsorption for these systems, the parameter fitting performed in section 6.3 allows for the determination of how much hydrogen a system containing these materials could store, using the mass balance equation derived in section 6.1.3. The analyses for PIM-1, MIL-101 and their composites are presented in this section.

6.5.1. PIM-1 powder

For this analysis, the total uptake of PIM-1 should be relatively constant despite the slight variations in parameter values seen between the PIM-1 (2) and PIM-1 (4) samples. Therefore, the analysis presented here is based on the data for PIM-1 (4) powder, as this provides the most direct comparison between the original materials and the MMM composites. The amount of hydrogen stored in tank volumes containing PIM-1 powder at various fill ratios is presented in Figure 6.25.

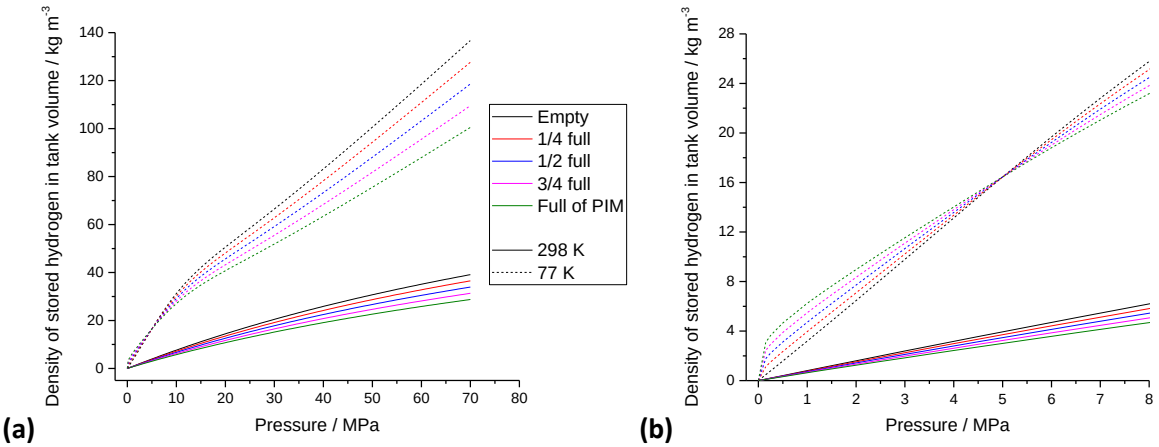

Figure 6.25 – The amount of hydrogen stored by PIM-1 powder in a tank volume filled to fill ratio values of 0, 0.25, 0.5, 0.75 and 1 at 77 K (dashed lines) and 298 K (solid lines). Part (b) illustrates the same plot, but rescaled to better illustrate the break even point. Both plots use the same legend.

The stored hydrogen densities presented in this figure unveil a number of interesting points. Firstly, it is clear to see that under atmospheric temperature conditions, there is no benefit to using this adsorbent, as the amount of hydrogen adsorbed by PIM-1 at 298 K does not offset the lost volume for the bulk gas to occupy, and therefore the amount stored by this system at this temperature is less for any system containing PIM-1, and the performance decays with increasing presence of the solid.

At 77 K, the conclusion is different. In the low pressures, there is a clear benefit to including the adsorbent, as the PIM rapidly adsorbs hydrogen. However, at the pressure rises, the benefit reduces, as bulk gas density increases at a greater rate than the rate of adsorption in the higher pressures. As such, the stored amounts at the various fill fractions converge until they reach the break-even point, at which there is no benefit to having the adsorbent present, and going to a higher pressure would make the presence of the adsorbent detrimental to the storage performance of the system. For the PIM-1 powder, the break even pressure is relatively low at 5.0 MPa. This is due to the relatively high affinity of hydrogen to PIM-1, which means that most of the adsorption occurs in the low pressures, and the low uptake of the material, which when divided through by the displaced volume (V_D) creates a relatively low density that is quickly overwhelmed by the rapidly rising bulk gas density at 77 K.

Although there is only a small pressure range in which this material outperforms cryocompressed systems, the true comparison is against standard compressed tanks. In order to achieve the same 16.5 kg m^{-3} density found at PIM-1 powder's break even point, compressed tanks must be pressurised to 23.2 MPa. Whilst this is not an insignificant pressure, it is a long way short of the current pressures used in commercial hydrogen storage. Ultimately, this discrepancy highlights the main issue with PIM-1 as an adsorbent and one of the largest motivators for this study; that PIM-1, despite its beneficial workability and thermal and mechanical properties, is not a sufficient adsorbent for gas storage, and the challenge is therefore to enhance the material such that a competitive adsorbent can be produced.

However, evaluating storage is not where this discussion can end. In any engineered hydrogen system, the gas must be moved from where it is stored to the unit in which it is utilised, be that a fuel cell or a combustion engine. In any case, a positive gas pressure must be maintained in order to deliver the hydrogen, and therefore the tank volume cannot be emptied to zero pressure, as this would require extra energy in order to create a vacuum within the tank. Instead, a minimum delivery pressure must be defined, and the hydrogen available above this pressure classified as

'deliverable' hydrogen. For this study, a minimum pressure of 0.15 MPa is used, as this ensures a 0.5 bar delivery pressure, as used by Bhatia and Myers [257]. The deliverable hydrogen available from tanks containing PIM-1 powder is detailed in Figure 6.26 below.

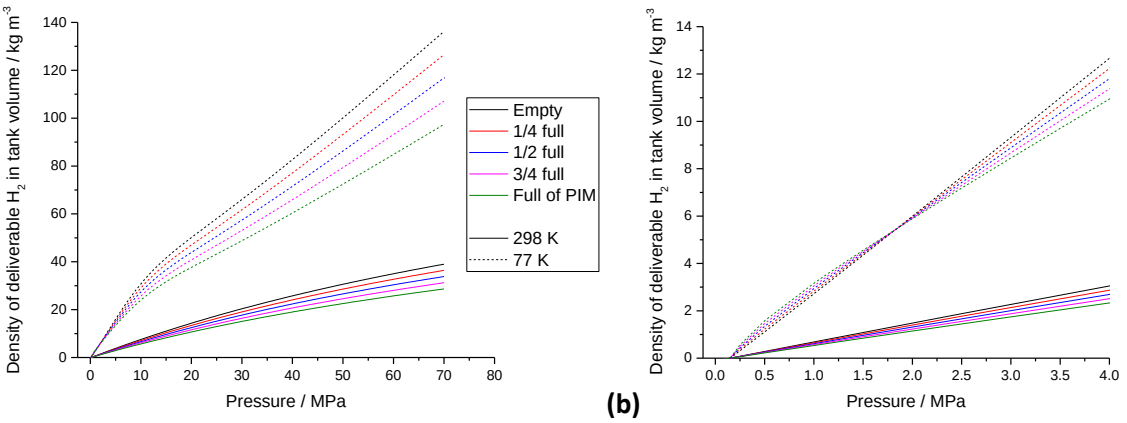

Figure 6.26 - The amount of hydrogen delivered by PIM-1 powder in a tank volume filled to fill ratio values of 0, 0.25, 0.5, 0.75 and 1 at 77 K (dashed lines) and 298 K (solid lines). Part (b) illustrates the same plot, but rescaled to better illustrate the break even point. Both plots use the same legend.

Figure 6.26 paints a bleaker picture than Figure 6.25 does. Because of the high affinity of PIM-1, much of the adsorbent performance occurs in the very low pressure range, and as such when the hydrogen adsorbed in the first 0.15 MPa is removed from the calculation, the deliverable hydrogen from this system suffers disproportionately compared to the compression-reliant systems, in which very little gas is present in the low pressures.

The result of this for PIM-1 powder is that the break even pressure is reduced from 5.0 MPa to 1.8 MPa, which gives a very narrow pressure operating window in which the use of PIM powder as an adsorbent is effective. However, the density of deliverable hydrogen at this pressure is a lowly 5.4 kg m^{-3}, which would require 920 L of volume to store the 5 kg of hydrogen requisite for a 500 km range. This is a volume comparable to the entire interior of a light duty vehicle, and is therefore entirely infeasible for this purpose.

6.5.2. PIM-1 film

The amount of hydrogen stored in a tank containing PIM-1 film is shown in Figure 6.27 below.

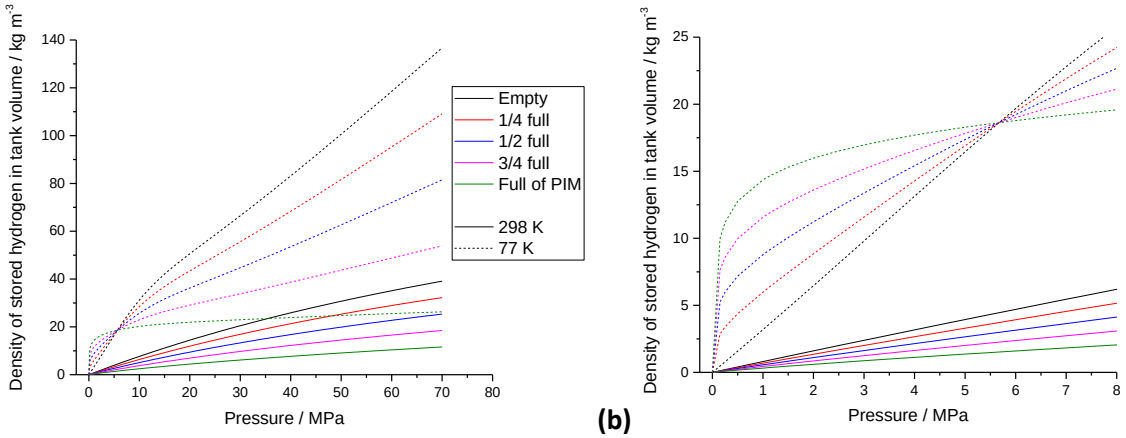

Figure 6.27 - The amount of hydrogen stored by PIM-1 film in a tank volume filled to fill ratio values of 0, 0.25, 0.5, 0.75 and 1 at 77 K (dashed lines) and 298 K (solid lines). Part (b) illustrates the same plot, but rescaled to better illustrate the break even point. Both plots use the same legend.

Although the excess uptake of the film morphology of PIM is lower than that of the powder, the amount stored within these materials is remarkably similar. In the storage case illustrated in Figure 6.27(b), there are very clear delineations between the respective fill ratios for the 77 K case, and the break even point is at 5.7 MPa, and contains a hydrogen density of 18.6 kg m^{-3}.

Both of these values are higher than for the powder, which is an interesting finding, but is explained by the fact that the film is assumed to be laminated into the tank as an ever-thicker liner, and therefore the packing ratio of this material is 1; the powder is assumed only to be loosely tapped into the volume, and the packing ratio is calculated from the bulk density of the powder, which is much lower. However, in a real world scenario, such a thick 'block' of PIM film would experience high heat and mass transfer resistances, and other measures would have to be taken to alleviate these, such as leaving intercalating voids to enhance mass transfer into the middle of the material, and using a heat exchanging material (such as the HexCell and MATI designs proposed by the HSECOE [271, 272]). Any necessary provisions like these would serve to occupy volume and therefore reduce the volumetric density of the hydrogen stored.

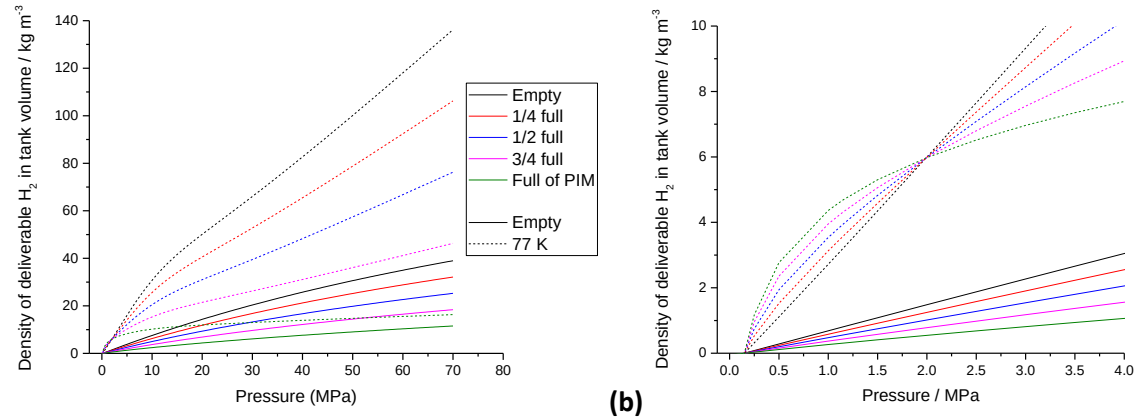

Figure 6.28 - The amount of hydrogen delivered by PIM-1 film in a tank volume filled to fill ratio values of 0, 0.25, 0.5, 0.75 and 1 at 77 K (dashed lines) and 298 K (solid lines). Part (b) illustrates the same plot, but rescaled to better illustrate the break even point. Both plots use the same legend.

Much like for the powder, the deliverable hydrogen from the PIM-1 film (illustrated in Figure 6.28) declines significantly as a result of the high enthalpy of the material. In this case, the break even point is at 2.0 MPa, at which the density of deliverable hydrogen is 6.0 kg m^{-3}. Again, this is a long way short of the 39.0 kg m^{-3} deliverable hydrogen from a standard compression tank, and further serves to illustrate the shortfalls of PIM-1 as an adsorbate.

6.5.3. MIL-101

The stored and deliverable hydrogen available from tank volumes filled with MIL-101 are available in Figure 6.29 and Figure 6.30 below. The 298 K data used for this analysis had been generated for previous studies within the Mays research group [275, 344].

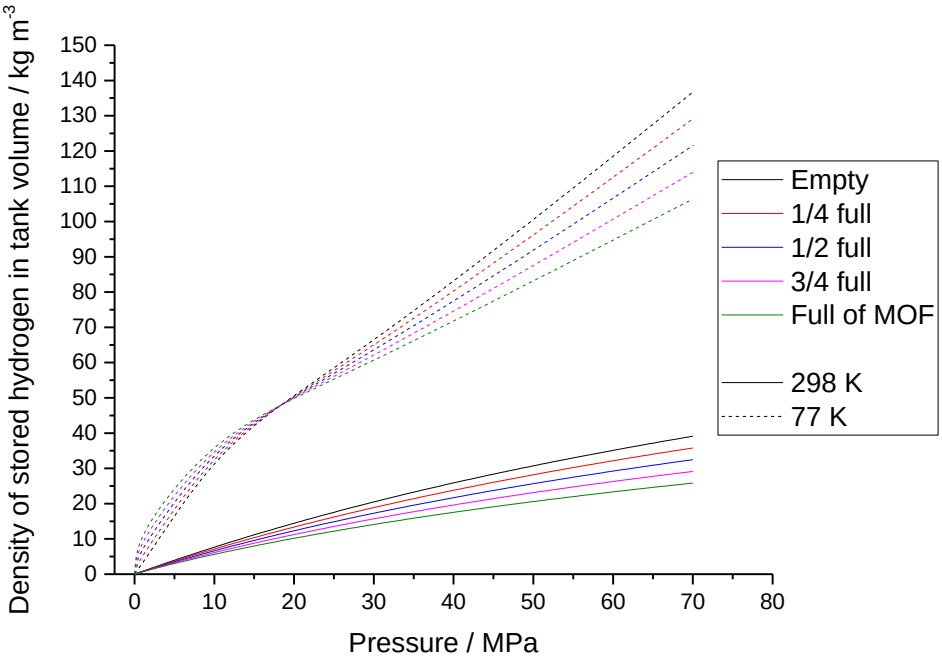

Figure 6.29 - The amount of hydrogen stored by MIL-101 powder in a tank volume filled to fill ratio values of 0, 0.25, 0.5, 0.75 and 1 at 77 K (dashed lines) and 298 K (solid lines). Part (b) illustrates the same plot, but rescaled to better illustrate the break even point. Both plots use the same legend.

The results for MIL-101 are much more encouraging. Although at the scale used in Figure 6.29 there does not appear to be much difference between the full and empty cases at 77 K, there is still very much a benefit at these pressures, and the break even pressure is not reached until 18.4 MPa. The stored density of hydrogen at this pressure is 48.0 kg m^{-3}, which, as is evident from the figure, is higher than the density of 298 K hydrogen at 70 MPa. However, like PIM-1, this material gives no benefit at room temperature, as the uptake under these conditions is simply too low.

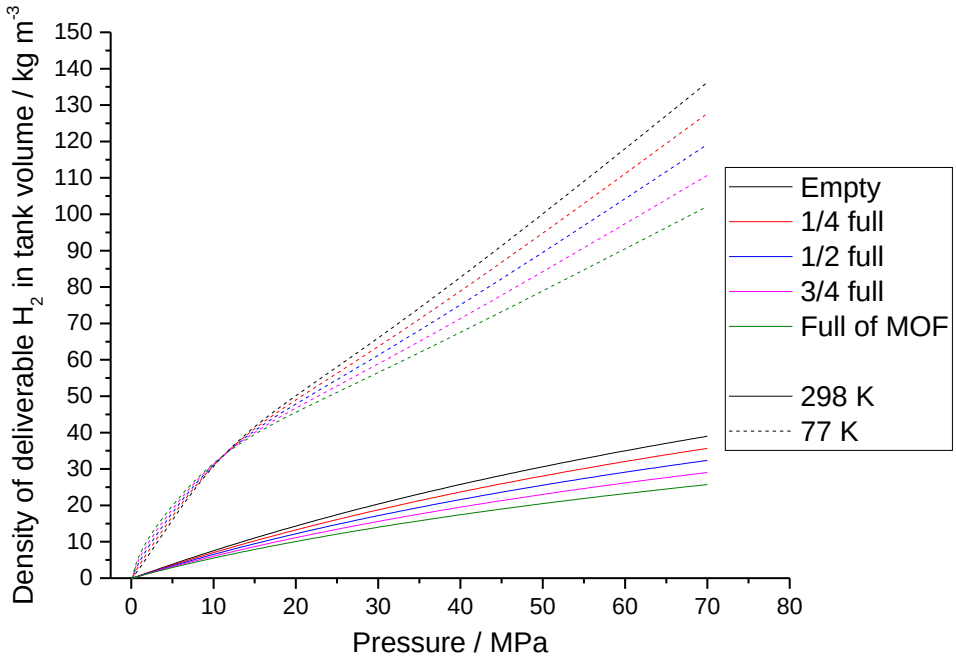

Figure 6.30 - The amount of hydrogen delivered by MIL-101 powder in a tank volume filled to fill ratio values of 0, 0.25, 0.5, 0.75 and 1 at 77 K (dashed lines) and 298 K (solid lines). Part (b) illustrates the same plot, but rescaled to better illustrate the break even point. Both plots use the same legend.

The deliverable hydrogen from MIL-101-based systems shown in Figure 6.30 above is very interesting. The break even pressure of MIL-101 under these conditions is 11.3 MPa, at which the density of deliverable hydrogen is 33.9 kg m^{-3}. This value is 13% lower than the deliverable density of 298 K compression at 70 MPa (the equivalent pressure for standard compression is 57.1 MPa), and so ultimately the MIL-101 system is not capable of matching the amount of hydrogen output from a compressive tank whilst still outperforming a cryocompressed system. However, the pressure at which this storage density is achieved is significantly reduced, and operating at this pressure could open a wider discussion on the gravimetric and volumetric efficacy of this system, particularly given that either much less carbon fibre could be used to maintain such a pressure (therefore saving on weight, volume and cost), or even switching over to a glass-fibre reinforced polymer shell, which would significantly reduce cost.

This result also illustrates the requirement for very high uptake materials to compete in this field. Although the MIL-101 showed reasonable excess uptake (5.3 wt%), it still comes up short when compared on a bulk volume basis to current technologies. Whilst densifying the MOF may offer a way to increase the stored density, this approach often suffers from diminishing returns, as compressed MOFs commonly show lower uptakes on a gravimetric basis. Ultimately, materials that uptake much more hydrogen straight after synthesis are required, as these are the materials that could store hydrogen at such a density that the current technologies could be challenged for ultimate performance, whilst offering the convenience of lower pressures, albeit at the cost of requiring a cryogenic system.

6.5.4. PIM-1/MIL-101 Composites

The stored and deliverable hydrogen available from tanks containing the 10, 20 and 30 wt% composites can be seen in Figure 6.31. This analysis provides some interesting conclusions, particularly regarding the shapes of the curves.

Looking down the left column of Figure 6.31, it is immediately apparent that the 20 wt% composite shows a much larger difference between the full volumes and the emptier ones, namely that the amount stored in the full tank rises very quickly in the low pressures, but then flattens out, whilst the emptier volumes rise steadily. This is in contrast to the stored curves for the 10 and 30 wt% composites, which also see an early rise due to adsorption, but see the increase in uptake decline more slowly, meaning that there is a less obvious difference between the various fill ratios. This difference in behaviour is due to the parameters used to derive these curves: the parameters for the 20 wt% composite resulted in a much higher adsorbate density than the other two, but also a lower pore volume. Such a result translates to highly effective adsorption in the lower pressures, so resulting in a very quick rise in uptake in the lower pressures, but there is relatively little room for the increasing bulk gas density to have an effect, so the increase in the higher pressures (which are driven by bulk gas density increases) are less pronounced, resulting in a sharper ‘knee’ in the curve.

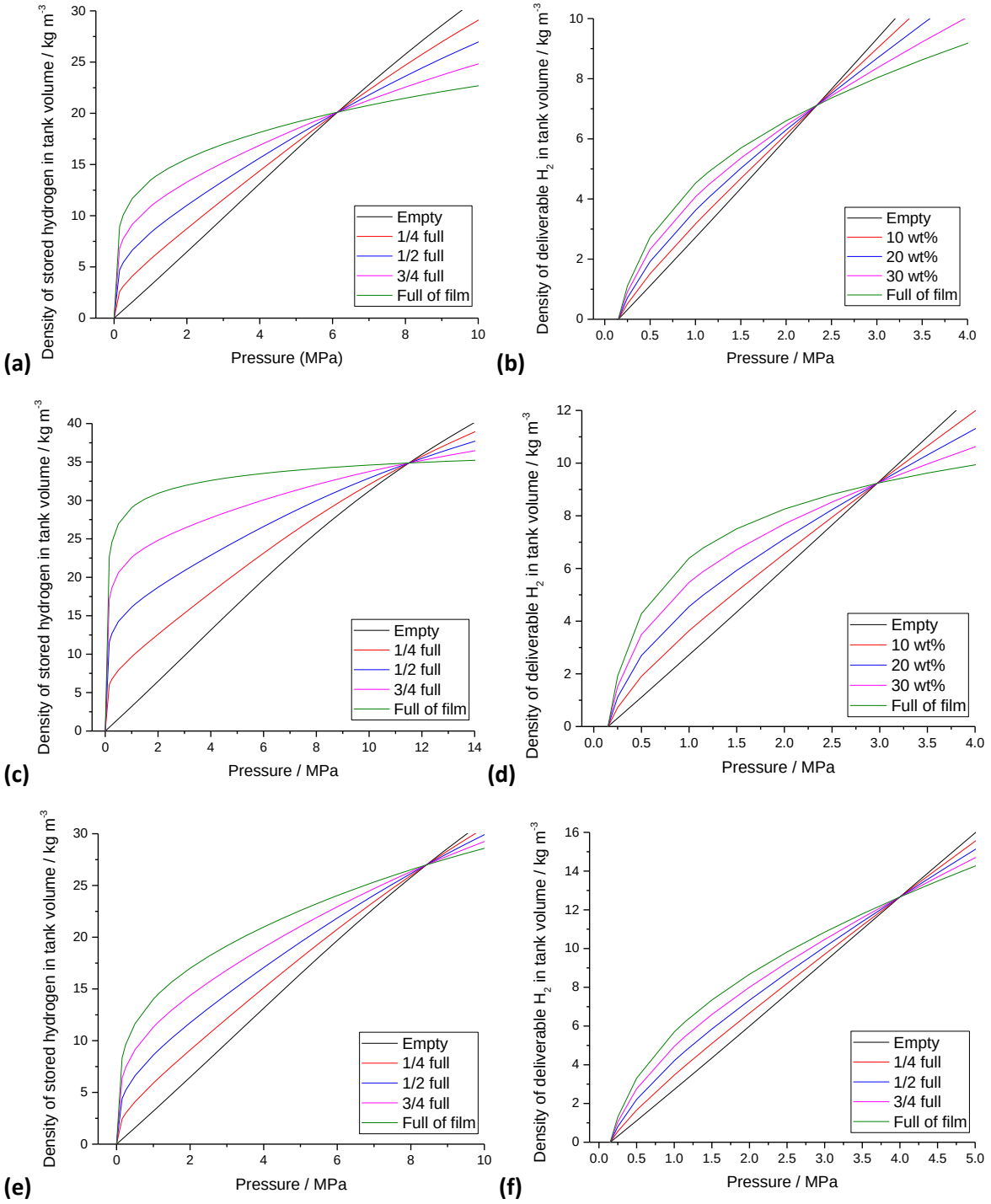

Figure 6.31 - The amount of hydrogen stored (a, c, e) and delivered (b, d, f) by the PIM-1/MIL-101 composites in a tank volume filled to fill ratio values of 0, 0.25, 0.5, 0.75 and 1 at 77 K. Parts (a) and (b) are for the 10 wt% composite, (c) and (d) represent the 20 wt% and (e) and (f) the 30 wt%.

For the deliverable hydrogen, the curves are all much more compressed than their storage equivalents. This is due to the high uptakes in the low pressure regions due to the adsorption, although it is clear that this affects the 20 wt% result more than the others. The break even pressures for the delivered hydrogen, as for the samples previously seen, are greatly depressed due to this large amount of 'lost' hydrogen that adsorption systems capture. Numerical analysis of the break even pressures is conveniently done using rule of mixtures analysis; the ROM plots of both storage and delivery break even pressures, and the hydrogen densities at these pressures, are presented in Figure 6.32.

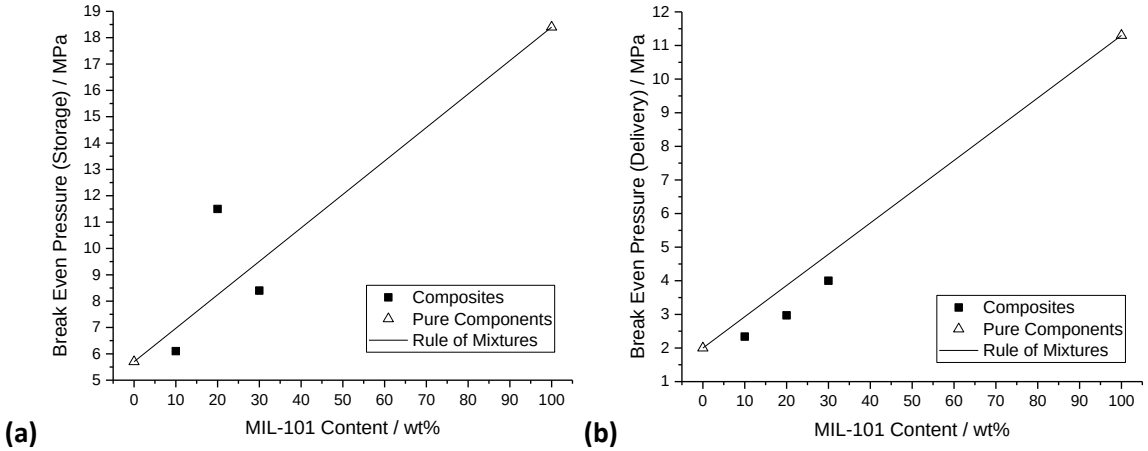

	Break Even H_2 Density / kg m^{-3}	
MIL-101 Content	Stored	Delivered
0	18.6	6.0
10	20.1	7.1
20	34.9	9.2
30	27.0	12.7
100	48.0	33.9
Compression (298 K)	39.1	39.0

Figure 6.32 – Direct comparison of the (a) stored and (b) deliverable hydrogen available from a volume containing PIM-1 film, MIL-101 and the composites thereof. Both analyses are for full tanks at 77 K, apart from the dashed lines, which represent 77 K cryocompressed hydrogen. The table details the stored and deliverable densities at the respective break even points.

Looking at Figure 6.32, it appears that for both storage and delivery, the general trend in break even pressure is to rise with increasing MIL-101 content. The general trend does point towards the presence of the MOF, and in particular the greater pore volume afforded to the composites with greater MOF content, having a beneficial impact in terms of the hydrogen storage performance of the material. However, this increase is less than would be expected if perfect mixing of the properties was enforced, which again highlights the dominance of the PIM in this system.

The only major aberration to this trend is the unusually high values for storage in the 20 wt% composite. This was due to the unexpectedly slow decline in excess uptake for the 20 wt% composite in Figure 4.57 – as the excess declines, less extra adsorptive is uptaken, whilst for the same pressure increase, the amount of hydrogen gained through increasing density of the bulk phase continues to rise. For adsorbents in which the excess decreases quickly in the high pressure range, a low break even pressure is seen as the amount of hydrogen that would be present in bulk gas in the volume occupied by both adsorbent and adsorbate quickly rises above that stored in the adsorbate. For slower excess decreases, the adsorbate continues to uptake adsorptive in higher pressures, so delaying the pressure at which the bulk gas outperforms the adsorbate. The 20 wt% composite represents this latter case, hence the higher break even pressure.

6.6. System Scale Analysis

Ultimately, the best way to judge the efficacy of these materials is to calculate their gravimetric and volumetric storage densities on a system scale; this allows for direct comparison with the DOE targets, and can give an indication of where this technology stands in relation to the other competitors. Traditionally, this has been quite difficult to do for adsorptive systems, particularly for those in academic research, as determining the system weight and volume requires knowledge of not only the material that contains the hydrogen-carrying substance (and its thickness), but also requires a design that allows for the determination of the necessary balance of plant equipment.

However, some designs for adsorbent based systems have recently emerged. One of the most readily available of these designs is the work of the HSECOE, who have presented their research of the development of a MOF-5 based storage tank (see section 2.7 for more details). One very interesting piece of information is given in the presentation of Anton and Motyka [271], who gave details as to the mass and volume breakdown of their model of a large scale tank featuring both loose MOF-5 powder and their HexCell heat exchanger. This breakdown is given in Table 6.6 below. These details are convenient, as following the application of some assumptions, these values can be applied to the materials presented in Figure 6.32.

Table 6.6 – Masses and volumes of the adsorptive hydrogen storage system components for the HexCell tank design proposed by Anton and Motyka [271]

Item	Mass / kg	Volume / L
Tank	107.0	109.0
Heat Exchanger	9.8	3.6
Adsorbent	35.1	166.4
Balance of Plant Equipment	16.7	16.5
Total	174.5	295.8

In order to use this design in order to calculate the system densities for the materials tested in this study, the following assumptions have been made:

- The volume of the tank available to the adsorbate has not changed.
- The powder materials occupy this volume at their loose bulk densities (i.e. not compacted)
- The film materials completely occupy the volume, i.e. the packing ratio is 1.
- All adsorptive behaviour within the tank behaves identically as in the HTP.
- The volume of the composite is additive.
- The contact between the PIM film and the MOF particles is excellent, such that there are no voids within the composite induced by the MOF beyond the pore volume of the MOF itself.

With these assumptions in place, the amount of adsorbate within the tank is determined by calculating the bulk densities of the composites, and multiplying the bulk densities of all the materials by the volume available to the adsorbate. The amount of hydrogen available from this system is calculated by multiplying the deliverable hydrogen density by the volume of adsorbate. The system gravimetric density is then calculated by summation of the hydrogen stored, the adsorbate mass and the other masses detailed in Table 6.6, and dividing this into the mass of deliverable hydrogen. The volumetric density is calculated by dividing the deliverable hydrogen by the total volume of the system (295.8 L). The results of these calculations can be seen in Table 6.7 below.

Table 6.7 is highly enlightening. It is quickly apparent when evaluating this that the PIM-1-based systems show disappointing densities, particularly in reference to the 2017 DOE targets, which set the 2020 targets for gravimetric energy density at 4.5 wt%, and the volumetric target at 30 g L^{-1}. The only one of these materials that comes close to meeting the DOE targets is the loose MIL-101, although this is to be expected given the relative performance seen throughout this study. The MIL performs well against the MOF-5 proposed by Anton and Motyka [271], as the 3.26 wt% and 19.07 g L^{-1} compare to 3.1 wt% and 21.0 g L^{-1} estimated for the MOF-5, but without the issues of hydrolytic instability presented by MOF-5. This does however come with the caveat that the MIL-101 was tested loose, compared to a MOF-5 sample that has been compressed, a processing step that has already been shown to reduce the gravimetric capacity of MIL-101 [143].

Table 6.7 – Masses of adsorbent, stored and deliverable hydrogen and the total system, as well as system gravimetric and volumetric H_2 storage densities for the PIM-1 film, MIL-101 and composites thereof inserted into the HSECOE's HexCell tank design.

MIL-101 Content	Mass of adsorbent	Stored H_2	Deliverable H_2	Total System Mass	Gravimetric Energy Density	Volumetric Energy Density
wt%	kg	kg	kg	kg	wt%	g L^{-1}
0	178.9	3.10	1.00	315.5	0.32	3.38
10	160.0	3.34	1.18	296.9	0.40	4.00
20	142.1	5.81	1.54	281.4	0.55	5.19
30	127.8	4.49	2.11	265.8	0.79	7.14
100	31.6	7.99	5.64	173.1	3.26	19.07

When analysing the composites, it can clearly be seen that adding the MOF does improve the performance of the film, as the reduced bulk density and higher uptake compound to produce better than linear improvement in both gravimetric and volumetric densities. However, the dominance of the PIM in these materials, and the relatively modest performance of MIL-101 limit the capacity of the composites. Anton and Motyka [271] report that 298 K compression shows 2.6 wt% and 20.1 g L^{-1}, which puts the performance of the film materials into contrast, and ultimately it is clear that these materials will not be suitable for hydrogen storage in vehicles. Whilst PIM-based composites could show potential with a sufficiently potent filler, these materials are not suitable for vehicular hydrogen storage in their current guise.

7. Concluding Remarks

7.1. Conclusions

The aim of this study was to determine how effective PIM-1 is as a hydrogen storage material, and whether its capacity could be sufficiently improved through physical adaptation that a competitive hydrogen storage system could be produced using the adapted PIM as a base. In light of this aim and the objectives detailed in section 0, the following conclusions can be drawn:

1. PIM-1 synthesis is well reported in the literature and, once understood, is a relatively easy process to undertake. However, synthesis of high molecular weight polymers capable of film formation requires solid understanding of anhydrous polymer chemistry, and can be difficult to newly establish within a research group. MIL-101, on the other hand, is very simply synthesised through a one pot hydrothermal process, and requires relatively little attention. These findings fulfil objective 1.

2. PIM-1 film formation is a deceptively difficult process, as careful control of the environmental conditions is required in order to ensure a good result. The literature on this formation is relatively light, but it is imperative to develop a standard within a research for the time and environmental conditions required to produce flat, coherent films that are homogenous in all dimensions and show the expected porosity when tested. This is perhaps even truer for composite films, as these are even more difficult to synthesise as required. However, with careful control of the formation process, PIM/MOF composites that show behaviours reflecting both of the constituent components, via a multitude of techniques, can be synthesised. The completion of these tasks fulfils objective 2.

3. PIM-1 shows excellent thermal resistance for a polymeric material. TGA analysis shows that the material is resistant to ~500 °C in anoxic conditions, and up to 400 °C in air. The polymer has also been confirmed, via TG-MS, to decompose in a three-step mechanism as proposed by Salinas et al. [197]. MIL-101 decomposes in line with previous studies. The composites thermally decompose near-perfectly in line with linear combinations of the decomposition curves of their components. Heat capacities have been determined for PIM-1 and composites thereof for the first time, and appear reasonable when compared with other glassy polymers, although the heat capacity of the composites is adversely affected by the presence of the particulate. In completing these studies, objective 4.c is met.

4. Difficulties in synthesising the quantity of MIL-101 required to make composite samples for studies such as static tensile strength analysis have meant that testing the mechanical properties of the composite materials has not been possible. As a consequence, objective 4.b has not been met. The tensile strength of PIM-1 has been tested within the Mays research group, but outside the scope of this study; the results of this testing can be found in Polak-Kraśna et al. [196].

5. The adsorptive behaviour of PIM-1 has been extensively tested. PIM-1 powder shows both BET surface areas and pore volumes comparable with those previously found in the literature (730 $m^2 g^{-1}$ and 0.5 $cm^3 g^{-1}$ respectively). Microporosity is shown to contribute a large portion of this porosity, as indicated by both the pore size distribution (a broad

distribution that declines in intensity as the pore size grows) and by pore size analysis (~0.3 cm^3 g^{-1} is present in the form of micropores). PIM-1 film shows a reduced uptake thanks to the more settled polymer chain structure, but still shows 540 m^2 g^{-1} and 0.3 m^2 g^{-1}, virtually all of which is present in the form of micropores. Mass transfer limitations prevented the determination of the material's pore size distribution, but 0.1 MPa CO_2 and H_2 analysis show near identical microporous performance to the powder samples. MIL-101, at 2874 – 3170 m^2 g^{-1} and a trimodal PSD, matches previously reported samples.

6. High pressure hydrogen is adsorbed at a peak excess of 1.8 wt% in PIM-1 powder (at 3.92 MPa and 77 K), and 1.6 wt% in the film morphology (at 2.2 MPa and 77 K). These materials appeared to show low repeatability of isotherm, caused mainly by flexibility of the porosity in the polymer. This is a particular issue in the films, which can give very different results depending on the age and chemical, thermal and pressure histories of the material. MIL-101, as a fixed pore material, showed much greater repeatability. Its optimal pore size for hydrogen storage and open cage structure facilitate a much higher excess storage capacity (5.3 wt% at 4.9 MPa and 77 K).

7. Porous performance in the PIM-MIL composites is generally improved by the presence of the MOF, as BET surface area and low pressure adsorption performance all improve with increasing MIL-101 content. However, this improvement is not perfectly along the trend predicted by the rule of mixtures, and demonstrates that adsorption is dominated by the PIM matrix, largely due to the mass transfer limitations of adsorptives diffusing through the polymer. The high pressure H_2 uptakes for these materials also follow this trend.

8. Carbonising PIM-1 in the manner performed in this project showed curious behaviour, in that the BET surface areas and high pressure H_2 take ups were both lowered by the carbonisation, but the CO_2 and low pressure H_2 performances were both increased. This performance is likely due to mass transfer issues into the material. The lack of performance increase suggests that there is no gain from carbonising PIM-1 for hydrogen storage purposes with this set of synthesis conditions.

9. In all cases, the determination of skeletal density is critical to the quality of the data obtained. PIM-1 is a flexible porous material whose porosity can be affected by its age and chemical history, and accurately determining its skeletal density is difficult; this is an issue that has largely been ignored by the scientific community studying this material. Such issues with the determination of ρ_s has a great effect on the determined uptake of adsorptive in the material, and the confidence with which values for BET surface area and maximum uptake must be viewed highly sceptically without a confident grasp of the skeletal density of the material. This conclusion, along with conclusions 5 – 8, show that objective 4.a has been met comprehensively.

10. Parameter fitting to the isotherms above confirm previously found results that the hydrogen adsorbate density is either that of highly compressed liquid or solid hydrogen, and pore volumes in PIM-1 match the microporous volume within the material. The Tóth parameter indicates relatively high heterogeneity, as expected. MIL-101 produced a series of parameters that, whilst accurate to the isotherm, showed an abnormally high pore volume; fixing the pore volume in the fitting produced a good isotherm fit and more realistic parameters. Trends within the same material at different temperatures showed some expected behaviour, although the low quality of the isotherms undermined this

study. There was limited matching of the composite parameters (at 77 K) to the rule of mixtures. These findings satisfy objective 5.

11. Isosteric enthalpy calculations for PIM-1 using the Clausius-Clapeyron isostere method produced a value of the enthalpy (-9.5 kJ mol^{-1}) relative to uptake that closely matched previously generated data, whilst extending this study to much higher pressures than ever previously seen. The same study on PIM-1 film produced a lower value (~ -8.0 kJ mol^{-1}), although the uncertainty within this sample is much greater. The 30 wt% composite produced a very similar enthalpy profile to PIM powder, although the characteristic energy for this sample was much higher.
12. It has been comprehensively demonstrated that the composite materials made for this study do not meet the required standard of hydrogen storage required for the light duty vehicle application. Unmodified PIM-1, in both powder and film morphologies, does not match the required storage density, and although an improvement is seen with the MIL-101 composites, the window of benefit over standard cryocompression is small. Although a unique design for a tank containing this material was not possible with the available time (thus not meeting the requirement of objective 6), using the system parameters provided by Anton & Motyka [271], it was demonstrated that only MIL-101 comes close to matching the 2020 DOE targets, with the closest composite (30 wt%) showing 0.79 wt% and 7.14 g L^{-1} on a system scale. For this kind of material to work for this application, a filler material capable of much larger hydrogen uptake is required, and/or chemical modification to the polymer matrix may be required to enhance the storage capacity of the material.

7.2. Future Work

Following this study, a number of lines of further study are possible. Some of the possible follow up studies to the work presented are discussed below.

1. Many of the isotherms attempted in this study, and the parameter fitting performed using these isotherms, are uncertain due to the relative uncertainty around the skeletal density of PIM-1 (particularly in the film morphology). Close attention should be paid to the skeletal density of PIM-1, and attempting to determine how the measured density changes with age would be a valid line of study (despite the fact that the skeletal density should be a constant property of the material). Reattempting these studies, paying close attention to both the age and chemical history of the materials, would greatly reduce the uncertainty of these measurement and be able to provide a near-definitive representation of the gas storage capacity of the material.
2. There is a large number of available filler materials (in powder morphologies) that could be used to enhance the hydrogen storage of PIM-1 in this MMM format. Any porous powder that can be suspended in the solvents of PIM-1 (such as activated carbons, MOFs and other porous polymers) can easily be inserted into a PIM-1 membrane, and may have a further beneficial effect than that seen with the MIL-101 in this study. Such studies are ongoing (such as Rochat et al. [350], and an article currently in preparation within the Mays group led by Dr. Tian), although further study with much higher uptake MOFs, such as NU-100, are required to determine whether this approach may be feasible to meet the DOE targets.

3. PIM-1 is a porous hydrophobic material, which may have benefits in terms of shielding hydrolytic MOFs from humidity whilst allowing access to other adsorptives. One of the serious challenges of using these high uptake MOF materials is their high sensitivity to moisture, and PIM-1 could be used as a coating material, using techniques similar to those seen in this project. A formal study investigating the susceptibility of a hydrolytically unstable MOF to humidity with and without PIM-coating could open a new avenue of studies based around these granular composite gas storage materials.

4. There are a number of properties that a large-scale PIM-1 composite would require to be a useful engineering material for hydrogen storage. A wide variety of studies could be performed to better understand these materials and to project their dynamic performance in a tank. TEM imaging of the film cross sections could provide greater understanding of the MOF distribution in the composite, and therefore how the synthesis may be improved. Studies performed to determine the thermal conductivity of PIM-1 and all the materials made therefrom would provide a useful follow up to the specific heat capacity values determined in this project. Quantifying the mass transfer of hydrogen through both thin films and larger thicknesses of PIM-1-based materials would also provide further insight into the potential utility of this material for adsorptive hydrogen storage.

5. The model used to analyse these materials, whilst well established and previously demonstrated to correspond well to empirical results, assumes a rigid, inflexible porous material (in which the pore size distribution does not change). This ultimately does not hold for PIM-1, which is known to be a highly flexible porous material. Development of this model that could account for flexibility within the pores given particular conditions could provide a more accurate account of the conditions within the material by providing more accurate values for the parameters. Fitting to isotherms performed with high confidence will also improve the accuracy of the parameter fits.

6. It is evident purveying the literature around PIM-1 that it is a highly popular material for gas separation membranes, and its use as an adsorbent is diminishing. There is no evidence of a PIM-1/MIL-101 composite being used as a gas separation membrane, and therefore these materials may still have value in this application. Testing this membrane material for various gas pairs, such as CO_2/CH_4 or N_2/O_2 could provide a number of industrial applications in which this material could provide useful.

7. The carbonisation of PIM-1 performed in this study proved disappointing, as the carbon material were shown to have lower adsorptive uptakes as the PIM. This generally does not match experience with the process, and it is expected that by altering the conditions used to carbonise the material. A study in which the carbonisation conditions are optimised to produce an adsorbent may well be different to carbonising for use as a separation membrane or an electrolytic material, and would therefore be a valuable study in its own right, and may also produce a highly valuable material for hydrogen storage.

8. Most of the designs for adsorbent-based hydrogen tanks have followed a conventional tank design, largely due to the stability of the shape to resistive forces. As adsorbents provide the greatest benefit (excess uptake) at relatively low pressures, the potential for tanks of any shape is much greater. An investigation into conformable tanks containing adsorbents could therefore be performed. For the PIM-1 composites in particular, investigating how to utilise the mechanical strength of the film whilst overcoming the

mass transfer limitations through the material may provide a very different set of mass and volume bases upon which to determine the system gravimetric and volumetric energy densities, which may improve the uptake performance of adsorbent film-based systems. Conformable tanks are also far more likely to be adopted by vehicle engineers, as they can adjust the shape of the tank to fit their overall vehicle design, rather than designing the vehicle around the tanks.

8. References

1. United Nations Department of Economic and Social Affairs. World Population Prospects: Key findings & advance tables. New York City; 2017.

2. Federal Reserve Bank of Boston. How do we measure Standard of Living? [Internet]. The Ledger. 2003 [cited 2015 Sep 28]. Available from: https://tinyurl.com/y8uj4lzj

3. U.S. Energy Information Administration. International Energy Outlook 2017. Washington DC; 2017.

4. International Energy Agency. Energy Efficiency 2017. 2017.

5. International Energy Agency. Key world energy statistics 2017. 2017.

6. International Energy Agency. Key World Energy Statistics 2014. 2014.

7. British Petroleum. BP Statistical Review of World Energy June 2014. 2014.

8. REN21. Advancing the Global Renewable Energy Transition: Highlights of the REN21 Renewables 2017 Global Status Report in perspective. 2017.

9. nuclearinfo.net. Waste from Nuclear Power [Internet]. 2010. Available from: http://nuclearinfo.net/Nuclearpower/WebHomeWasteFromNuclearPower

10. Jewell J. Ready for nuclear energy?: An assessment of capacities and motivations for launching new national nuclear power programs. Energy Policy. 2011;39:1041–55.

11. REN21. Renewables 2014 Global Status Report. 2014.

12. Orecchini F, Santiangeli A. Beyond smart grids – The need of intelligent energy networks for a higher global efficiency through energy vectors integration. Int J Hydrogen Energy. 2011;36:8126–33.

13. Kousksou T, Bruel P, Jamil A, El Rhafiki T, Zeraouli Y. Energy storage: Applications and challenges. Sol Energy Mater Sol Cells. 2014;120:59–80.

14. Wilson IAG, Rennie AJR, Hall PJ. Great Britain's Energy Vectors and Transmission Level Energy Storage. Energy Procedia. 2014;62:619–28.

15. Winter C-J. Hydrogen energy — Abundant, efficient, clean: A debate over the energy-system-of-change. Int J Hydrogen Energy. 2009;34:S1–52.

16. Ramachandran R, Menon RK. An overview of industrial uses of hydrogen. Int J Hydrogen Energy. 1998;23:593–8.

17. Balat M. Potential importance of hydrogen as a future solution to environmental and transportation problems. Int J Hydrogen Energy. 2008;33:4013–29.

18. Kalamaras CM, Efstathiou AM. Hydrogen Production Technologies: Current State and Future Developments. Conf Pap Energy. 2013;690627.

19. Harrison K, Levene J. Electrolysis of Water. In: Rajeshwar K, McConnell R, Licht S, editors. Sol Hydrog Gener. Springer New York; 2008. p. 41–63.

20. Symes D, Taylor-Cox C, Holyfield L, Al-Duri B, Dhir A. Feasibility of an oxygen-getter with nickel electrodes in alkaline electrolysers. Mater Renew Sustain Energy. Springer Berlin Heidelberg; 2014;3:27.

21. Godula-Jopek A. Hydrogen Production by Electrolysis. WILEY-VCH Verlag; 2015.

22. Soltani R, Rosen MA, Dincer I. Assessment of CO2 capture options from various points in steam methane reforming for hydrogen production. Int J Hydrogen Energy. Pergamon; 2014;39:20266–75.

23. Sigma-Aldrich. Hydrogen Material Safety Data Sheet [Internet]. MSDS. 2015 [cited 2015 Jul 14]. Available from: https://tinyurl.com/lvzotuy

24. Wallner T, Lohse-Busch H, Gurski S, Duoba M, Thiel W, Martin D, et al. Fuel economy and emissions evaluation of BMW Hydrogen 7 Mono-Fuel demonstration vehicles. Int J Hydrogen Energy. 2008;33:7607–18.

25. Stone R. Introduction to Internal Combustion Engines. Basingstoke: Palgrave Macmillan; 2009.

26. Kirubakaran A, Jain S, Nema RK. A review on fuel cell technologies and power electronic interface. Renew Sustain Energy Rev. 2009;13:2430–40.

27. Toyota Motor Corporation. 2016 Toyota Mirai Fuel Cell Sedan Production Information [Internet]. Press Release. 2014 [cited 2016 Jul 28]. Available from: http://pressroom.toyota.com/releases/2016+toyota+mirai+fuel+cell+product.htm

28. Hyundai Motor Co. Drive the World's First Mass-Produced Fuel Cell CUV [Internet]. 2015 [cited 2015 Jul 15]. Available from: https://www.hyundaiusa.com/tucsonfuelcell/

29. Honda Motor Co. Honda FCX Clarity - Vehicle Specifications [Internet]. Off. Website. 2016 [cited 2016 Jul 27]. Available from: http://world.honda.com/FCXClarity/specifications/

30. US Department of Energy. Target Explanation Document: Onboard Hydrogen Storage for Light-Duty Fuel Cell Vehicles. Washington DC; 2017.

31. NEDO. FCH 2009-2010: Development of Fuel Cell and Hydrogen Technologies. 2009.

32. NEDO. NEDO Revises and Pre-releases Fuel Cell Section of NEDO's Technology Development Roadmap for Fuel Cells and Hydrogen. NEDO; 2017.

33. Durbin DJ, Malardier-Jugroot C. Review of hydrogen storage techniques for on board vehicle applications. Int J Hydrogen Energy. 2013;38:14595–617.

34. National Institute of Standards and Technology. NIST Chemistry WebBook [Internet]. NIST Webb. 2014 [cited 2015 Sep 28]. Available from: http://webbook.nist.gov/chemistry/

35. Jensen JO, Vestbø AP, Li Q, Bjerrum NJ. The energy efficiency of onboard hydrogen storage. J Alloys Compd. Elsevier; 2007;446–447:723–8.

36. Mori D, Hirose K. Recent challenges of hydrogen storage technologies for fuel cell vehicles. Int J Hydrogen Energy. 2009;34:4569–74.

37. Hua TQ, Ahluwahlia RK, Peng J-K, Kromer M, Lasher S, McKenney K, et al. Technical assessment of compressed hydrogen storage tank systems for automotive applications. Int J Hydrogen Energy. Pergamon; 2011;36:3037–49.

38. Toyota Motor Corporation. Toyota Mirai Fuel Cell Saloon [Internet]. Press Release. 2015 [cited 2016 Jul 28]. Available from: http://media.toyota.co.uk/2015/03/toyota-mirai-fuel-cell-saloon/

39. Yamashita A, Kondo M, Goto S, Ogami N. Development of High-Pressure Hydrogen Storage System for the Toyota "Mirai." SAE International ; 2015.

40. Ube Industries Ltd. UBE Nylon Resin Used in High-Pressure Hydrogen Tank of Toyota Mirai Fuel Cell Sedan [Internet]. Press Release. 2014 [cited 2016 Jul 28]. Available from: http://www.ube-ind.co.jp/english/news/2014/20141208_01.htm

41. Akiba E. Hydrogen energy R & D: The Roadmap and State-of-Art of Japan, and Activities of Kyushu University. 8th World Renew Technol Congr. New Delhi; 2017.

42. O'Malley K, Ordaz G, Adams J, Randolph K, Ahn CC, Stetson NT. Applied hydrogen storage research and development: A perspective from the U.S. Department of Energy. J Alloys Compd. 2015;645:S419–22.

43. Gardiner M. Energy requirement for hydrogen gas compression and liquefaction as related to vehicle storage needs. 2009.

44. Jorgensen SW. Hydrogen storage tanks for vehicles: Recent progress and current status. Curr Opin Solid State Mater Sci. 2011;15:39–43.

45. Zhou L. Progress and problems in hydrogen storage methods. Renew Sustain Energy Rev. 2005;9:395–408.

46. Fuster B, Houssin-Agbomson D, Jallais S, Vyazmina E, Dang-Nhu G, Bernard-Michel G, et al. Guidelines and recommendations for indoor use of fuel cells and hydrogen systems. Int J Hydrogen Energy. Pergamon; 2017;42:7600–7.

47. Zhevago NK, Denisov EI, Glebov VI. Experimental investigation of hydrogen storage in capillary arrays. Int J Hydrogen Energy. Pergamon; 2010;35:169–75.

48. Chabak A. Tank and Material for Storage of Hydrogen Gas. USPTO; 2008.

49. Chabak A. Apparatus and Cartridge for Storage of Compressed Hydrogen Gas. USPTO; 2010.

50. Stern M. Hydrogen gas high pressure storage system. WIPO; 2014.

51. C.EN Ltd. Prototypes [Internet]. cenh2.com. [cited 2017 Oct 11]. Available from: http://www.cenh2.com/prototypes

52. Ahluwalia RK, Peng JK. Dynamics of cryogenic hydrogen storage in insulated pressure vessels for automotive applications. Int J Hydrogen Energy. 2008;33:4622–33.

53. Petitpas G, Bénard P, Klebanoff LE, Xiao J, Aceves S. A comparative analysis of the cryo-compression and cryo-adsorption hydrogen storage methods. Int J Hydrogen Energy. 2014;39:10564–84.

54. Aceves SM, Berry GD, Martinez-Frias J, Espinosa-Loza F. Vehicular storage of hydrogen in insulated pressure vessels. Int J Hydrogen Energy. Pergamon; 2006;31:2274–83.

55. Brunner T. Cryo-compressed Hydrogen Storage - Motivation and Infrastructure Implications [Internet]. STORHY Final Event. Paris; 2008 [cited 2016 Jul 28]. Available from: http://www.storhy.net/finalevent/pdf/WS3_CcH2_BMW-Brunner.pdf

56. Boeriu H. BMW Prototype with Hydrogen Fuel Cell - First Drive [Internet]. BMW Blog. 2015 [cited 2016 Jul 28]. Available from: http://www.bmwblog.com/2015/07/02/bmw-prototype-with-hydrogen-fuel-cell-first-drive/

57. BMW Group. BMW Group Innovation Days 2015: Drive technologies of the future. [Internet]. Press Release. 2015 [cited 2016 Jul 28]. Available from: https://tinyurl.com/ybp68thn

58. Kunze K, Kircher O. Cryo-Compressed Hydrogen Storage. Oxford; 2012.

59. Aceves SM, Espinosa-Loza F, Ledesma-Orozco E, Ross TO, Weisberg AH, Brunner TC, et al. High-density automotive hydrogen storage with cryogenic capable pressure vessels. Int J Hydrogen Energy. Pergamon; 2010;35:1219–26.

60. Brunner T, Kampitsch M, Kircher O. Cryo-Compressed Hydrogen Storage. In: Stolten D, Samsun RC, Garland N, editors. Fuel Cells Data, Facts, Fig. 1st ed. John Wiley & Sons; 2016. p. 162–76.

61. BMW Group. First hydrogen station with two types of refuelling technology. Latest move by the BMW Group and TOTAL will take forward the development of hydrogen fuel cell vehicles. [Internet]. Press Release. 2015 [cited 2016 Jul 28]. Available from: https://tinyurl.com/yd7ye3mr

62. Hwang HT, Varma A. Hydrogen storage for fuel cell vehicles. Curr Opin Chem Eng. 2014;5:42–8.

63. Broom DP. Potential Storage Materials. In: Broom DP, editor. Hydrog Storage Mater. Springer, London; 2011. p. 19–59.

64. Müller K, Arlt W. Status and Development in Hydrogen Transport and Storage for Energy Applications. Energy Technol. 2013;1:501–11.

65. Hanlon JM, Reardon H, Tapia-Ruiz N, Gregory DH. The Challenge of Storage in the Hydrogen

Energy Cycle: Nanostructured Hydrides as a Potential Solution. Aust J Chem. CSIRO Publishing; 2012;65:656.

66. Mosher DA, Tang X, Brown RJ, Arsenault S, Saitta S, Laube BL, et al. High Density Hydrogen Storage System Demonstration Using NaAlH4 Based Complex Compound Hydrides. 2007.

67. Headen T. Hydrogen Storage - Without the High Pressure. H2FC Hann 2013. 2013.

68. Jehan M, Fruchart D. McPhy-Energy's proposal for solid state hydrogen storage materials and systems. J Alloys Compd. 2013;

69. Walker GS. Solid state hydrogen for stationary energy systems. I-SEE Semin. Bath: University of Bath; 2016.

70. Masika E, Mokaya R. Hydrogen Storage in High Surface Area Carbons with Identical Surface Areas but Different Pore Sizes: Direct Demonstration of the Effects of Pore Size. J Phys Chem C. American Chemical Society; 2012;116:25734–40.

71. Rouquerol F, Rouquerol J, Sing K. Adsorption by Powders & Porous Solids: Principles, Methodology and Applications. 1st ed. London: Academic Press; 1999.

72. Richard M-A, Cossement D, Chandonia P-A, Chahine R, Mori D, Hirose K. Preliminary evaluation of the performance of an adsorption-based hydrogen storage system. AIChE J. Wiley Subscription Services, Inc., A Wiley Company; 2009;55:2985–96.

73. Eberle U, Felderhoff M, Schüth F. Chemical and Physical Solutions for Hydrogen Storage. Angew Chemie Int Ed. 2009;48:6608–30.

74. Thommes M, Kaneko K, Neimark A V., Olivier JP, Rodriguez-Reinoso F, Rouquerol J, et al. Physisorption of gases, with special reference to the evaluation of surface area and pore size distribution (IUPAC Technical Report). Pure Appl Chem. 2015;87:1051–69.

75. Yushin G, Dash R, Jagiello J, Fischer JE, Gogotsi Y. Carbide-Derived Carbons: Effect of Pore Size on Hydrogen Uptake and Heat of Adsorption. Adv Funct Mater. 2006;16:2288–93.

76. Rouquerol F, Rouquerol J, Sing KSW. Thermodynamics of Adsorption at the Gas/Solid Interface. In: Rouquerol F, Rouquerol J, Sing KSW, Llewellyn PL, Maurin G, editors. Adsorpt by Powders Porous Solids Princ Methodol Appl. 2nd ed. Academic Press; 2014. p. 25–56.

77. Dailly A, Poirier E. Evaluation of an industrial pilot scale densified MOF-177 adsorbent as an on-board hydrogen storage medium. Energy Environ Sci. The Royal Society of Chemistry; 2011;4:3527.

78. Schlichtenmayer M, Streppel B, Hirscher M. Hydrogen physisorption in high SSA microporous materials – A comparison between AX-21_33 and MOF-177 at cryogenic conditions. Int J Hydrogen Energy. 2011;36:586–91.

79. Sing KSW. Adsorption by Active Carbons. In: Rouquerol F, Rouquerol J, Sing KSW, Llewellyn PL, Maurin G, editors. Adsorpt by Powders Porous Solids Princ Methodol Appl. 2nd ed. Oxford: Academic Press; 2014. p. 321–92.

80. Sing KS. Overview of Physical Adsorption by Carbons. In: Bottani EJ, Tascón JMD, editors. Adsorpt by Carbons. Elsevier; 2008. p. 3–12.

81. McKeown NB, Budd PM. Polymers of intrinsic microporosity (PIMs): organic materials for membrane separations, heterogeneous catalysis and hydrogen storage. Chem Soc Rev. The Royal Society of Chemistry; 2006;35:675–83.

82. Marsh H, Rodríguez-Reinoso F. Activated Carbon. Elsevier; 2006.

83. Sevilla M, Fuertes AB, Mokaya R. High density hydrogen storage in superactivated carbons from hydrothermally carbonized renewable organic materials. Energy Environ Sci. The Royal Society of Chemistry; 2011;4:1400.

84. Suhas, Carrott PJM, Ribeiro Carrott MML. Lignin--from natural adsorbent to activated carbon: a review. Bioresour Technol. 2007;98:2301–12.

85. Aygün A, Yenisoy-Karakaş S, Duman I. Production of granular activated carbon from fruit stones and nutshells and evaluation of their physical, chemical and adsorption properties. Microporous Mesoporous Mater. 2003;66:189–95.

86. Martínez de Yuso A, Rubio B, Izquierdo MT. Influence of activation atmosphere used in the chemical activation of almond shell on the characteristics and adsorption performance of activated carbons. Fuel Process Technol. 2014;119:74–80.

87. Cechinel MAP, Ulson de Souza SMAG, Ulson de Souza AA. Study of lead (II) adsorption onto activated carbon originating from cow bone. J Clean Prod. 2014;65:342–9.

88. Sevilla M, Mokaya R. Energy storage applications of activated carbons: supercapacitors and hydrogen storage. Energy Environ Sci. The Royal Society of Chemistry; 2014;7:1250–80.

89. Marsh H, Crawford D, O'Grady T., Wennerberg A. Carbons of high surface area. A study by adsorption and high resolution electron microscopy. Carbon N Y. 1982;20:419–26.

90. Zhou L, Sun Y, Zhou Y. Storage of Hydrogen on Carbon Materials: Experiments and Analyses. Chem Eng Commun. Taylor & Francis; 2006;193:564–79.

91. Xu W-C, Takahashi K, Matsuo Y, Hattori Y, Kumagaia M, Ishiyama S, et al. Investigation of hydrogen storage capacity of various carbon materials. Int J Hydrogen Energy. Pergamon; 2007;32:2504–12.

92. Bimbo N, Sharpe JE, Ting VP, Noguera-Díaz A, Mays TJ. Isosteric enthalpies for hydrogen adsorbed on nanoporous materials at high pressures. Adsorption. 2014;20:373–84.

93. Jordá-Beneyto M, Suárez-García F, Lozano-Castelló D, Cazorla-Amorós D, Linares-Solano A. Hydrogen storage on chemically activated carbons and carbon nanomaterials at high pressures. Carbon N Y. Pergamon; 2007;45:293–303.

94. Cheng F, Liang J, Zhao J, Tao Z, Chen J. Biomass Waste-Derived Microporous Carbons with Controlled Texture and Enhanced Hydrogen Uptake. Chem Mater. American Chemical Society; 2008;20:1889–95.

95. Akasaka H, Takahata T, Toda I, Ono H, Ohshio S, Himeno S, et al. Hydrogen storage ability of porous carbon material fabricated from coffee bean wastes. Int J Hydrogen Energy. Pergamon; 2011;36:580–5.

96. Yang R, Liu G, Li M, Zhang J, Hao X. Preparation and N2, CO2 and H2 adsorption of super activated carbon derived from biomass source hemp (Cannabis sativa L.) stem. Microporous Mesoporous Mater. Elsevier; 2012;158:108–16.

97. Bader N, Ouederni A. Optimization of biomass-based carbon materials for hydrogen storage. J Energy Storage. Elsevier; 2016;5:77–84.

98. Geim AK, Novoselov KS. The rise of graphene. Nat Mater. Nature Publishing Group; 2007;6:183–91.

99. Gadipelli S, Guo ZX. Graphene-based materials: Synthesis and gas sorption, storage and separation. Prog Mater Sci. Pergamon; 2015;69:1–60.

100. Yuan W, Li B, Li L. A green synthetic approach to graphene nanosheets for hydrogen adsorption. Appl Surf Sci. North-Holland; 2011;257:10183–7.

101. Guo CX, Wang Y, Li CM. Hierarchical Graphene-Based Material for Over 4.0 Wt % Physisorption Hydrogen Storage Capacity. ACS Sustain Chem Eng. American Chemical Society; 2012;120928163241005.

102. Dillon AC, Jones KM, Bekkedahl TA, Kiang CH, Bethune DS, Heben MJ. Storage of hydrogen in single-walled carbon nanotubes. Nature. 1997;386:377–9.

103. Züttel A, Sudan P, Mauron P, Kiyobayashi T, Emmenegger C, Schlapbach L. Hydrogen storage in carbon nanostructures. Int J Hydrogen Energy. 2002;27:203–12.

104. Froudakis GE. Hydrogen storage in nanotubes & nanostructures. Mater Today. Elsevier; 2011;14:324–8.

105. Maesen T. The Zeolite Scene - An Overview. In: Čejka J, van Bekkum H, Corma A, Schüth, editors. Introd to Zeolite Sci Pract Vol 168. 3rd ed. Elsevier; 2007.

106. Dong J, Wang X, Xu H, Zhao Q, Li J. Hydrogen storage in several microporous zeolites. Int J Hydrogen Energy. 2007;32:4998–5004.

107. Masika E, Mokaya R. Preparation of ultrahigh surface area porous carbons templated using zeolite 13X for enhanced hydrogen storage. Prog Nat Sci Mater Int. 2013;23:308–16.

108. Fujiwara M, Fujio Y, Sakurai H, Senoh H, Kiyobayashi T. Storage of molecular hydrogen into ZSM-5 zeolite in the ambient atmosphere by the sealing of the micropore outlet. Chem Eng Process Process Intensif. 2014;

109. James SL. Metal-organic frameworks. Chem Soc Rev. 2003;32:276–88.

110. Gangu KK, Maddila S, Mukkamala SB, Jonnalagadda SB. A review on contemporary Metal–Organic Framework materials. Inorganica Chim Acta. Elsevier; 2016;446:61–74.

111. Alhamami M, Doan H, Cheng C-H. A Review on Breathing Behaviors of Metal-Organic-Frameworks (MOFs) for Gas Adsorption. Mater (Basel, Switzerland). Multidisciplinary Digital Publishing Institute (MDPI); 2014;7:3198–250.

112. Horike S, Shimomura S, Kitagawa S. Soft porous crystals. Nat Chem. Nature Publishing Group; 2009;1:695–704.

113. Kaskel S. Appendix B: Datasheets. In: Kaskel S, editor. Chem Met Fram Synth Charact Appl. Weinheim, Germany: Wiley-VCH Verlag GmbH & Co. KGaA; 2016. p. 825–32.

114. Kaye SS, Dailly A, Yaghi OM, Long JR. Impact of preparation and handling on the hydrogen storage properties of Zn4O(1,4-benzenedicarboxylate)3 (MOF-5). J Am Chem Soc. American Chemical Society; 2007;129:14176–7.

115. Farha OK, Eryazici I, Jeong NC, Hauser BG, Wilmer CE, Sarjeant AA, et al. Metal-organic framework materials with ultrahigh surface areas: is the sky the limit? J Am Chem Soc. American Chemical Society; 2012;134:15016–21.

116. Wang TC, Bury W, Gómez-Gualdrón DA, Vermeulen NA, Mondloch JE, Deria P, et al. Ultrahigh surface area zirconium MOFs and insights into the applicability of the BET theory. J Am Chem Soc. American Chemical Society; 2015;137:3585–91.

117. Frost H, Düren T, Snurr RQ. Effects of surface area, free volume, and heat of adsorption on hydrogen uptake in metal-organic frameworks. J Phys Chem B. American Chemical Society; 2006;110:9565–70.

118. Farha OK, Özgür Yazaydın A, Eryazici I, Malliakas CD, Hauser BG, Kanatzidis MG, et al. De novo synthesis of a metal–organic framework material featuring ultrahigh surface area and gas storage capacities. Nat Chem. Nature Research; 2010;2:944–8.

119. Goldsmith J, Wong-Foy AG, Cafarella MJ, Siegel DJ. Theoretical Limits of Hydrogen Storage in Metal–Organic Frameworks: Opportunities and Trade-Offs. Chem Mater. American Chemical Society; 2013;25:3373–82.

120. Ren J, Langmi HW, North BC, Mathe M. Review on processing of metal-organic framework (MOF) materials towards system integration for hydrogen storage. Int J Energy Res. 2015;39:607–20.

121. Mason JA, Veenstra M, Long JR. Evaluating metal–organic frameworks for natural gas storage. Chem Sci. The Royal Society of Chemistry; 2014;5:32.

122. Wales DJ, Grand J, Ting VP, Burke RD, Edler KJ, Bowen CR, et al. Gas sensing using porous materials for automotive applications. Chem Soc Rev. The Royal Society of Chemistry; 2015;44:4290–321.

123. Noguera-Díaz A. Structure Property Relationships in Nanoporous Materials for Hydrogen Storage. University of Bath; 2016.

124. Noguera-Díaz A, Bimbo N, Holyfield LT, Ahmet IY, Ting VP, Mays TJ. Structure–property relationships in metal-organic frameworks for hydrogen storage. Colloids Surfaces A Physicochem Eng Asp. Elsevier; 2016;496:77–85.

125. Rowsell JLC, Yaghi OM. Strategies for hydrogen storage in metal--organic frameworks. Angew Chem Int Ed Engl. 2005;44:4670–9.

126. Song L, Zhang J, Sun L, Xu F, Li F, Zhang H, et al. Mesoporous metal–organic frameworks: design and applications. Energy Environ Sci. The Royal Society of Chemistry; 2012;5:7508.

127. Silva P, Vilela SMF, Tomé JPC, Almeida Paz FA. Multifunctional metal–organic frameworks: from academia to industrial applications. Chem Soc Rev. The Royal Society of Chemistry; 2015;44:6774–803.

128. Julien PA, Mottillo C, Friščić T. Metal–organic frameworks meet scalable and sustainable synthesis. Green Chem. The Royal Society of Chemistry; 2017;19:2729–47.

129. Kaskel S. Appendix A: MOF Suppliers. In: Kaskel S, editor. Chem Met Fram Synth Charact Appl. Weinheim, Germany: Wiley-VCH Verlag GmbH & Co. KGaA; 2016. p. 823.

130. Sigma-Aldrich. Search Results > Basolite [Internet]. sigmaaldrich.com. 2017 [cited 2017 Oct 1]. Available from: https://tinyurl.com/ydyyqq2z

131. Férey G, Mellot-Draznieks C, Serre C, Millange F, Dutour J, Surblé S, et al. A chromium terephthalate-based solid with unusually large pore volumes and surface area. Science. American Association for the Advancement of Science; 2005;309:2040–2.

132. Bhattacharjee S, Chen C, Ahn W-S. Chromium terephthalate metal-organic framework MIL-101: synthesis, functionalization, and applications for adsorption and catalysis. RSC Adv. The Royal Society of Chemistry; 2014;4:52500–25.

133. Streppel B, Hirscher M. BET specific surface area and pore structure of MOFs determined by hydrogen adsorption at 20 K. Phys Chem Chem Phys. The Royal Society of Chemistry; 2011;13:3220–2.

134. Lebedev OI, Millange F, Serre C, Van Tendeloo G, Férey G. First Direct Imaging of Giant Pores of the Metal−Organic Framework MIL-101. Chem Mater. 2005;17:6525–7.

135. Rallapalli PBS, Raj MC, Senthilkumar S, Somani RS, Bajaj HC. HF-free synthesis of MIL-101(Cr) and its hydrogen adsorption studies. Environ Prog Sustain Energy. 2016;35:461–8.

136. Hong D-Y, Hwang YK, Serre C, Férey G, Chang J-S. Porous Chromium Terephthalate MIL-101 with Coordinatively Unsaturated Sites: Surface Functionalization, Encapsulation, Sorption and Catalysis. Adv Funct Mater. WILEY-VCH Verlag; 2009;19:1537–52.

137. Llewellyn PL, Bourrelly S, Serre C, Vimont A, Daturi M, Hamon L, et al. High Uptakes of CO2 and CH4 in Mesoporous Metal—Organic Frameworks MIL-100 and MIL-101. Langmuir. American Chemical Society; 2008;24:7245–50.

138. Jiang D, Burrows AD, Edler KJ. Size-controlled synthesis of MIL-101(Cr) nanoparticles with enhanced selectivity for CO2 over N2. CrystEngComm. The Royal Society of Chemistry; 2011;13:6916.

139. Bromberg L, Diao Y, Wu H, Speakman SA, Hatton TA. Chromium(III) Terephthalate Metal Organic Framework (MIL-101): HF-Free Synthesis, Structure, Polyoxometalate Composites, and Catalytic Properties. Chem Mater. American Chemical Society; 2012;24:1664–75.

140. Ming Y, Chi H, Blaser R, Xu C, Yang J, Veenstra M, et al. Anisotropic thermal transport in MOF-5 composites. Int J Heat Mass Transf. 2015;82:250–8.

141. Huang BL, Ni Z, Millward A, McGaughey AJH, Uher C, Kaviany M, et al. Thermal conductivity of a metal-organic framework (MOF-5): Part II. Measurement. Int J Heat Mass Transf. 2007;50:405–11.

142. Latroche M, Surblé S, Serre C, Mellot-Draznieks C, Llewellyn PL, Lee J-H, et al. Hydrogen storage in the giant-pore metal-organic frameworks MIL-100 and MIL-101. Angew Chem Int Ed Engl. 2006;45:8227–31.

143. Ardelean O, Blanita G, Borodi G, Lazar MD, Misan I, Coldea I, et al. Volumetric hydrogen adsorption capacity of densified MIL-101 monoliths. Int J Hydrogen Energy. 2013;38:7046–55.

144. Rowsell JLC, Spencer EC, Eckert J, Howard JAK, Yaghi OM. Gas Adsorption Sites in a Large-Pore Metal-Organic Framework. Science (80-). 2005;309:1350 LP-1354.

145. Schmitz B, Müller U, Trukhan N, Schubert M, Férey G, Hirscher M. Heat of Adsorption for Hydrogen in Microporous High-Surface-Area Materials. ChemPhysChem. WILEY-VCH Verlag; 2008;9:2181–4.

146. Oh H, Lupu D, Blanita G, Hirscher M. Experimental assessment of physical upper limit for hydrogen storage capacity at 20 K in densified MIL-101 monoliths. RSC Adv. The Royal Society of Chemistry; 2014;4:2648–51.

147. Klyamkin SN, Berdonosova EA, Kogan E V, Kovalenko KA, Dybtsev DN, Fedin VP. Influence of MIL-101 Doping by Ionic Clusters on Hydrogen Storage Performance up to 1900 Bar. Chem – An Asian J. WILEY-VCH Verlag; 2011;6:1854–9.

148. Eddaoudi M, Eubank JF. Insight into the Development of Metal-Organic Materials (MOMs): At Zeolite-Like Metal-Organic Frameworks. In: MacGillivray LR, editor. Met Fram Des Appl. Hoboken, NJ: John Wiley & Sons; 2010. p. 37–89.

149. Rosi NL, Eckert J, Eddaoudi M, Vodak DT, Kim J, O'Keeffe M, et al. Hydrogen storage in microporous metal-organic frameworks. Science. 2003;300:1127–9.

150. Ming Y, Purewal J, Liu D, Sudik A, Xu C, Yang J, et al. Thermophysical properties of MOF-5 powders. Microporous Mesoporous Mater. 2014;185:235–44.

151. Li H, Eddaoudi M, O'Keeffe M, Yaghi OM. Design and synthesis of an exceptionally stable and highly porous metal-organic framework. Nature. Macmillian Magazines Ltd.; 1999;402:276–9.

152. Greathouse JA, Allendorf MD. The interaction of water with MOF-5 simulated by molecular dynamics. J Am Chem Soc. American Chemical Society; 2006;128:10678–9.

153. Hausdorf S, Wagler J, Mossig R, Mertens FORL. Proton and water activity-controlled structure formation in zinc carboxylate-based metal organic frameworks. J Phys Chem A. American Chemical Society; 2008;112:7567–76.

154. Huang L. Synthesis, morphology control, and properties of porous metal–organic coordination polymers. Microporous Mesoporous Mater. 2003;58:105–14.

155. Ming Y, Purewal J, Yang J, Xu C, Soltis R, Warner J, et al. Kinetic Stability of MOF-5 in Humid Environments: Impact of Powder Densification, Humidity Level, and Exposure Time. Langmuir. American Chemical Society; 2015;31:4988–95.

156. Veenstra M, Yang J, Xu C, Gaab M, Arnold L, Mueller U, et al. Ford/BASF-SE/UM Activities in Support of the Hydrogen Storage Engineering Center of Excellence. DOE 2014 Annu Merit Rev Proc. Washington DC; 2014.

157. Wu D, Xu F, Sun B, Fu R, He H, Matyjaszewski K. Design and Preparation of Porous Polymers. Chem Rev. American Chemical Society; 2012;112:3959–4015.

158. Tsyurupa MP, Maslova LA, Andreeva AI, Mrachkovskaya VA, Davankov VA. Sorption of

organic compounds from aqueous media by hypercrosslinked polystyrene sorbents 'Styrosorbrs. React Polym. Elsevier; 1995;25:69–78.

159. Dawson R, Cooper AI, Adams DJ. Nanoporous organic polymer networks. Prog Polym Sci. Pergamon; 2012;37:530–63.

160. Spoto G, Vitillo JG, Cocina D, Damin A, Bonino F, Zecchina A, et al. FTIR spectroscopy and thermodynamics of hydrogen adsorbed in a cross-linked polymer. Phys Chem Chem Phys. The Royal Society of Chemistry; 2007;9:4992.

161. Ahn J-H, Jang J-E, Oh C-G, Ihm S-K, Cortez J, Sherrington DC. Rapid Generation and Control of Microporosity, Bimodal Pore Size Distribution, and Surface Area in Davankov-Type Hyper-Cross-Linked Resins. Macromolecules. American Chemical Society; 2005;39:627–32.

162. Jiang J-X, Su F, Trewin A, Wood CD, Campbell NL, Niu H, et al. Conjugated Microporous Poly(aryleneethynylene) Networks. Angew Chemie Int Ed. WILEY-VCH Verlag; 2007;46:8574–8.

163. Chaoui N, Trunk M, Dawson R, Schmidt J, Thomas A. Trends and challenges for microporous polymers. Chem Soc Rev. The Royal Society of Chemistry; 2017;46:3302–21.

164. Palma-Cando A, Brunklaus G, Scherf U. Thiophene-Based Microporous Polymer Networks via Chemical or Electrochemical Oxidative Coupling. Macromolecules. American Chemical Society; 2015;48:6816–24.

165. Yuan S, Kirklin S, Dorney B, Liu D-J, Yu L. Nanoporous Polymers Containing Stereocontorted Cores for Hydrogen Storage. Macromolecules. American Chemical Society; 2009;42:1554–9.

166. Li A, Lu R-F, Wang Y, Wang X, Han K-L, Deng W-Q. Lithium-Doped Conjugated Microporous Polymers for Reversible Hydrogen Storage. Angew Chemie Int Ed. WILEY-VCH Verlag; 2010;49:3330–3.

167. Ben T, Ren H, Ma S, Cao D, Lan J, Jing X, et al. Targeted Synthesis of a Porous Aromatic Framework with High Stability and Exceptionally High Surface Area. Angew Chemie Int Ed. WILEY-VCH Verlag; 2009;48:9457–60.

168. Ben T, Pei C, Zhang D, Xu J, Deng F, Jing X, et al. Gas storage in porous aromatic frameworks (PAFs). Energy Environ Sci. The Royal Society of Chemistry; 2011;4:3991.

169. Lu W, Yuan D, Zhao D, Schilling CI, Plietzsch O, Muller T, et al. Porous Polymer Networks: Synthesis, Porosity, and Applications in Gas Storage/Separation. Chem Mater. American Chemical Society; 2010;22:5964–72.

170. Yuan D, Lu W, Zhao D, Zhou H-C. Highly Stable Porous Polymer Networks with Exceptionally High Gas-Uptake Capacities. Adv Mater. WILEY-VCH Verlag; 2011;23:3723–5.

171. Côté AP, Benin AI, Ockwig NW, O'Keeffe M, Matzger AJ, Yaghi OM. Porous, crystalline, covalent organic frameworks. Science. American Association for the Advancement of Science; 2005;310:1166–70.

172. Furukawa H, Yaghi OM. Storage of Hydrogen, Methane, and Carbon Dioxide in Highly Porous Covalent Organic Frameworks for Clean Energy Applications. J Am Chem Soc. American Chemical Society; 2009;131:8875–83.

173. Ramimoghadam D, Gray EM, Webb CJ. Review of polymers of intrinsic microporosity for hydrogen storage applications. Int J Hydrogen Energy. 2016;41:16944–65.

174. Alahakoon SB, Thompson CM, Occhialini G, Smaldone RA. Design Principles for Covalent Organic Frameworks in Energy Storage Applications. ChemSusChem. 2017;10:2116–29.

175. Cao D, Lan J, Wang W, Smit B. Lithium-Doped 3D Covalent Organic Frameworks: High-Capacity Hydrogen Storage Materials. Angew Chemie Int Ed. WILEY-VCH Verlag; 2009;48:4730–3.

176. Klontzas E, Tylianakis E, Froudakis GE. Designing 3D COFs with Enhanced Hydrogen Storage Capacity. Nano Lett. American Chemical Society; 2010;10:452–4.

177. Holst JR, Trewin A, Cooper AI. Porous organic molecules. Nat Chem. Nature Publishing Group, a division of Macmillan Publishers Limited. All Rights Reserved.; 2010;2:915–20.

178. James SL. The Dam Bursts for Porous Liquids. Adv Mater. 2016;28:5712–6.

179. Giri N, Del Pópolo MG, Melaugh G, Greenaway RL, Rätzke K, Koschine T, et al. Liquids with permanent porosity. Nature. Nature Research; 2015;527:216–20.

180. Budd PM, Ghanem BS, Makhseed S, McKeown NB, Msayib KJ, Tattershall CE. Polymers of intrinsic microporosity (PIMs): robust, solution-processable, organic nanoporous materials. Chem Commun (Camb). The Royal Society of Chemistry; 2004;230–1.

181. Budd PM, McKeown NB, Fritsch D. Polymers of Intrinsic Microporosity (PIMs): High Free Volume Polymers for Membrane Applications. Macromol Symp. 2006;245–246:403–5.

182. McKeown NB. Polymers of Intrinsic Microporosity. ISRN Mater Sci. 2012;2012.

183. Rong Y, He D, Sanchez-Fernandez A, Evans C, Edler KJ, Malpass-Evans R, et al. Intrinsically Microporous Polymer Retains Porosity in Vacuum Thermolysis to Electroactive Heterocarbon. Langmuir. American Chemical Society; 2015;31:12300–6.

184. McKeown NB. The synthesis of polymers of intrinsic microporosity (PIMs). Sci China Chem. Science China Press; 2017;60:1023–32.

185. McKeown NB, Budd PM, Book D. Microporous Polymers as Potential Hydrogen Storage Materials. Macromol Rapid Commun. 2007;28:995–1002.

186. Rakow NA, Wendland MS, Trend JE, Poirier RJ, Paolucci DM, Maki SP, et al. Visual Indicator for Trace Organic Volatiles. Langmuir. American Chemical Society; 2010;26:3767–70.

187. Budd PM, Elabas ES, Ghanem BS, Makhseed S, McKeown NB, Msayib KJ, et al. Solution-Processed, Organophilic Membrane Derived from a Polymer of Intrinsic Microporosity. Adv Mater. 2004;16:456–9.

188. Kricheldorf HR, Lomadze N, Fritsch D, Schwarz G. Cyclic and telechelic ladder polymers derived from tetrahydroxytetramethylspirobisindane and 1,4-dicyanotetrafluorobenzene. J Polym Sci Part A Polym Chem. Wiley Subscription Services, Inc., A Wiley Company; 2006;44:5344–52.

189. Du N, Song J, Robertson GP, Pinnau I, Guiver MD. Linear High Molecular Weight Ladder Polymer via Fast Polycondensation of 5,5′,6,6′-Tetrahydroxy-3,3,3′,3′-tetramethylspirobisindane with 1,4-Dicyanotetrafluorobenzene. Macromol Rapid Commun. WILEY-VCH Verlag; 2008;29:783–8.

190. Song J, Du N, Dai Y, Robertson GP, Guiver MD, Thomas S, et al. Linear High Molecular Weight Ladder Polymers by Optimized Polycondensation of Tetrahydroxytetramethylspirobisindane and 1,4-Dicyanotetrafluorobenzene †. Macromolecules. American Chemical Society; 2008;41:7411–7.

191. Zhang P, Jiang X, Wan S, Dai S. Advancing polymers of intrinsic microporosity by mechanochemistry. J Mater Chem A. The Royal Society of Chemistry; 2015;3:6739–41.

192. Budd PM, Butler A, Selbie J, Mahmood K, McKeown NB, Ghanem B, et al. The potential of organic polymer-based hydrogen storage materials. Phys Chem Chem Phys. The Royal Society of Chemistry; 2007;9:1802–8.

193. Heuchel M, Fritsch D, Budd PM, McKeown NB, Hofmann D. Atomistic packing model and free volume distribution of a polymer with intrinsic microporosity (PIM-1). J Memb Sci. 2008;318:84–99.

194. Larsen GS, Lin P, Siperstein FR, Colina CM. Methane adsorption in PIM-1. Adsorption. 2010;17:21–6.

195. Staiger CL, Pas SJ, Hill AJ, Cornelius CJ. Gas Separation, Free Volume Distribution, and Physical Aging of a Highly Microporous Spirobisindane Polymer. Chem Mater. American Chemical Society; 2008;20:2606–8.

196. Polak-Kraśna K, Dawson R, Holyfield LT, Bowen CR, Burrows AD, Mays TJ. Mechanical characterisation of polymer of intrinsic microporosity PIM-1 for hydrogen storage applications. J Mater Sci. Springer US; 2017;52:3862–75.

197. Salinas O, Ma X, Litwiller E, Pinnau I. Ethylene/ethane permeation, diffusion and gas sorption properties of carbon molecular sieve membranes derived from the prototype ladder polymer of intrinsic microporosity (PIM-1). J Memb Sci. 2016;504:133–40.

198. Kim HJ, Kim D-G, Lee K, Baek Y, Yoo Y, Kim YS, et al. A Carbonaceous Membrane based on a Polymer of Intrinsic Microporosity (PIM-1) for Water Treatment. Sci Rep. Nature Publishing Group; 2016;6:36078.

199. Bonso JS, Kalaw GD, Ferraris JP, Burke AF, Conway BE, Conway BE, et al. High surface area carbon nanofibers derived from electrospun PIM-1 for energy storage applications. J Mater Chem A. The Royal Society of Chemistry; 2014;2:418–24.

200. Al Kutubi H, Rassaei L, Olthuis W, Nelson GW, Foord JS, Holdway P, et al. Polymers of intrinsic microporosity as high temperature templates for the formation of nanofibrous oxides. RSC Adv. Royal Society of Chemistry; 2015;5:73323–6.

201. Hao L, Liao K-S, Chung T-S. Photo-oxidative PIM-1 based mixed matrix membranes with superior gas separation performance. J Mater Chem A. The Royal Society of Chemistry; 2015;3:17273–81.

202. Jeromenok J, Weber J. Restricted Access: On the Nature of Adsorption/Desorption Hysteresis in Amorphous, Microporous Polymeric Materials. Langmuir. American Chemical Society; 2013;29:12982–9.

203. Budd P, Msayib K, Tattershall C, Ghanem B, Reynolds K, McKeown N, et al. Gas separation membranes from polymers of intrinsic microporosity. J Memb Sci. 2005;251:263–9.

204. McKeown NB, Gahnem B, Msayib KJ, Budd PM, Tattershall CE, Mahmood K, et al. Towards polymer-based hydrogen storage materials: engineering ultramicroporous cavities within polymers of intrinsic microporosity. Angew Chem Int Ed Engl. 2006;45:1804–7.

205. Chaukura N. Sorption of Gases and Liquids by Polymers of Intrinsic Microporosity (PIMs). University of Manchester; 2011.

206. Tedds SP. Microporous Materials for Hydrogen Storage. University of Birmingham; 2011.

207. Zhang R, Phalen RN, Cataquis A, Desta M, Kloesel M. Study of highly porous polymers for H2 fuel storage using positron annihilation lifetime spectroscopy. Int J Hydrogen Energy. Pergamon; 2015;40:8732–41.

208. Lima de Miranda R, Kruse J, Rätzke K, Faupel F, Fritsch D, Abetz V, et al. Unusual temperature dependence of the positron lifetime in a polymer of intrinsic microporosity. Phys status solidi – Rapid Res Lett. WILEY-VCH Verlag; 2007;1:190–2.

209. Alentiev AY, Bondarenko GN, Kostina Y V., Shantarovich VP, Klyamkin SN, Fedin VP, et al. PIM-1/MIL-101 hybrid composite membrane material: Transport properties and free volume. Pet Chem. 2014;54:477–81.

210. Swaidan R, Ghanem BS, Litwiller E, Pinnau I. Pure- and mixed-gas CO2/CH4 separation properties of PIM-1 and an amidoxime-functionalized PIM-1. J Memb Sci. Elsevier; 2014;457:95–102.

211. Patel HA, Yavuz CT. Noninvasive functionalization of polymers of intrinsic microporosity for enhanced CO2 capture. Chem Commun. The Royal Society of Chemistry; 2012;48:9989.

212. Larsen GS, Lin P, Hart KE, Colina CM. Molecular Simulations of PIM-1-like Polymers of Intrinsic Microporosity. Macromolecules. American Chemical Society; 2011;44:6944–51.

213. Jue ML, McKay CS, McCool BA, Finn MG, Lively RP. Effect of Nonsolvent Treatments on the

Microstructure of PIM-1. Macromolecules. American Chemical Society; 2015;48:5780–90.

214. Budd P, McKeown N, Ghanem B, Msayib K, Fritsch D, Starannikova L, et al. Gas permeation parameters and other physicochemical properties of a polymer of intrinsic microporosity: Polybenzodioxane PIM-1. J Memb Sci. 2008;325:851–60.

215. Kurchan J. In and out of equilibrium. Nature. Nature Publishing Group; 2005;433:222–5.

216. Lau CH, Konstas K, Thornton AW, Liu ACY, Mudie S, Kennedy DF, et al. Gas-Separation Membranes Loaded with Porous Aromatic Frameworks that Improve with Age. Angew Chemie Int Ed. WILEY-VCH Verlag; 2015;54:2669–73.

217. Lau CH, Nguyen PT, Hill MR, Thornton AW, Konstas K, Doherty CM, et al. Ending Aging in Super Glassy Polymer Membranes. Angew Chemie Int Ed. WILEY-VCH Verlag; 2014;53:5322–6.

218. Du N, Cin MMD-, Pinnau I, Nicalek A, Robertson GP, Guiver MD. Azide-based Cross-Linking of Polymers of Intrinsic Microporosity (PIMs) for Condensable Gas Separation. Macromol Rapid Commun. WILEY-VCH Verlag; 2011;32:631–6.

219. Bernardo P, Bazzarelli F, Tasselli F, Clarizia G, Mason CR, Maynard-Atem L, et al. Effect of physical aging on the gas transport and sorption in PIM-1 membranes. Polymer (Guildf). 2017;113:283–94.

220. Tiwari RR, Smith ZP, Lin H, Freeman BD, Paul DR. Gas permeation in thin films of “high free-volume” glassy perfluoropolymers: Part I. Physical aging. Polymer (Guildf). Elsevier; 2014;55:5788–800.

221. Swaidan R, Ghanem B, Litwiller E, Pinnau I. Physical Aging, Plasticization and Their Effects on Gas Permeation in “Rigid” Polymers of Intrinsic Microporosity. Macromolecules. American Chemical Society; 2015;48:6553–61.

222. Lloyd M. Robeson. Correlation of separation factor versus permeability for polymeric membranes. J Memb Sci. Elsevier; 1991;62:165–85.

223. Lloyd M. Robeson. The upper bound revisited. J Memb Sci. Elsevier; 2008;320:390–400.

224. Li FY, Xiao Y, Chung T-S, Kawi S. High-Performance Thermally Self-Cross-Linked Polymer of Intrinsic Microporosity (PIM-1) Membranes for Energy Development. Macromolecules. American Chemical Society; 2012;45:1427–37.

225. Song Q, Cao S, Pritchard RH, Ghalei B, Al-Muhtaseb SA, Terentjev EM, et al. Controlled thermal oxidative crosslinking of polymers of intrinsic microporosity towards tunable molecular sieve membranes. Nat Commun. 2014;5:4813.

226. Son S-Y, Noh Y-J, Bok C, Lee S, Kim BG, Na S-I, et al. One-step synthesis of carbon nanosheets converted from a polycyclic compound and their direct use as transparent electrodes of ITO-free organic solar cells. Nanoscale. The Royal Society of Chemistry; 2014;6:678–82.

227. Liu C, Wilson ST, Lesch DA. UV-cross-linked membranes from polymers of intrinsic microporosity for liquid separations. Google Patents; 2010.

228. Li FY, Xiao Y, Ong YK, Chung T-S. UV-Rearranged PIM-1 Polymeric Membranes for Advanced Hydrogen Purification and Production. Adv Energy Mater. 2012;2:1456–66.

229. Du N, Robertson GP, Song J, Pinnau I, Guiver MD. High-Performance Carboxylated Polymers of Intrinsic Microporosity (PIMs) with Tunable Gas Transport Properties. Macromolecules. American Chemical Society; 2009;42:6038–43.

230. Weber J, Du N, Guiver MD. Influence of Intermolecular Interactions on the Observable Porosity in Intrinsically Microporous Polymers. Macromolecules. 2011;44:1763–7.

231. Liao K-S, Lai J-Y, Chung T-S. Metal ion modified PIM-1 and its application for propylene/propane separation. J Memb Sci. 2016;515:36–44.

232. Liao K-S, Japip S, Lai J-Y, Chung T-S. Boron-embedded hydrolyzed PIM-1 carbon membranes for synergistic ethylene/ethane purification. J Memb Sci. 2017;534:92–9.

233. Larsen GS, Hart KE, Colina CM. Predictive simulations of the structural and adsorptive properties for PIM-1 variations. Mol Simul. Taylor & Francis; 2014;40:599–609.

234. Zhang J, Kang H, Martin J, Zhang S, Thomas S, Merkel TC, et al. The enhancement of chain rigidity and gas transport performance of polymers of intrinsic microporosity via intramolecular locking of the spiro-carbon. Chem Commun. The Royal Society of Chemistry; 2016;52:6553–6.

235. Du N, Robertson GP, Pinnau I, Guiver MD. Polymers of Intrinsic Microporosity with Dinaphthyl and Thianthrene Segments †. Macromolecules. American Chemical Society; 2010;43:8580–7.

236. Biloe S, Goetz V, Mauran S. Characterization of adsorbent composite blocks for methane storage. Carbon N Y. 2001;39:1653–62.

237. Liu D, Purewal JJ, Yang J, Sudik A, Maurer S, Mueller U, et al. MOF-5 composites exhibiting improved thermal conductivity. Int J Hydrogen Energy. 2012;37:6109–17.

238. Veenstra M, Yang J, Xu C, Purewal J, Gaab M, Arnold L, et al. Ford/BASF-SE/UM Activities in Support of the Hydrogen Storage Engineering Center of Excellence [Internet]. 2015 DOE Annu. Merit Rev. Washington DC; 2015 [cited 2015 Aug 20]. Available from: http://www.hydrogen.energy.gov/pdfs/review15/st010_veenstra_2015_o.pdf

239. Ahn J, Chung W-J, Pinnau I, Song J, Du N, Robertson GP, et al. Gas transport behavior of mixed-matrix membranes composed of silica nanoparticles in a polymer of intrinsic microporosity (PIM-1). J Memb Sci. 2010;346:280–7.

240. Castro-Muñoz R, Fíla V, Dung CT. Mixed Matrix Membranes Based on PIMs for Gas Permeation: Principles, Synthesis, and Current Status. Chem Eng Commun. Taylor & Francis; 2017;204:295–309.

241. Gonciaruk A, Althumayri K, Harrison WJ, Budd PM, Siperstein FR. PIM-1/graphene composite: A combined experimental and molecular simulation study. Microporous Mesoporous Mater. 2015;209:126–34.

242. Shin Y, Prestat E, Zhou K-G, Gorgojo P, Althumayri K, Harrison W, et al. Synthesis and characterization of composite membranes made of graphene and polymers of intrinsic microporosity. Carbon N Y. 2016;102:357–66.

243. Koschine T, Rätzke K, Faupel F, Khan MM, Emmler T, Filiz V, et al. Correlation of gas permeation and free volume in new and used high free volume thin film composite membranes. J Polym Sci Part B Polym Phys. 2015;53:213–7.

244. Mason CR, Buonomenna MG, Golemme G, Budd PM, Galiano F, Figoli A, et al. New organophilic mixed matrix membranes derived from a polymer of intrinsic microporosity and silicalite-1. Polymer (Guildf). Elsevier; 2013;54:2222–30.

245. Bushell AF, Budd PM, Attfield MP, Jones JTA, Hasell T, Cooper AI, et al. Nanoporous organic polymer/cage composite membranes. Angew Chem Int Ed Engl. 2013;52:1253–6.

246. Wu X, Tian Z, Wang S, Peng D, Yang L, Wu Y, et al. Mixed matrix membranes comprising polymers of intrinsic microporosity and covalent organic framework for gas separation. J Memb Sci. 2017;528:273–83.

247. Bushell AF, Attfield MP, Mason CR, Budd PM, Yampolskii Y, Starannikova L, et al. Gas permeation parameters of mixed matrix membranes based on the polymer of intrinsic microporosity PIM-1 and the zeolitic imidazolate framework ZIF-8. J Memb Sci. 2013;427:48–62.

248. Semino R, Ramsahye NA, Ghoufi A, Maurin G. Microscopic Model of the Metal-Organic Framework/Polymer Interface: A First Step toward Understanding the Compatibility in Mixed Matrix Membranes. ACS Appl Mater Interfaces. American Chemical Society; 2016;8:809–19.

249. Smith SJD, Ladewig BP, Hill AJ, Lau CH, Hill MR. Post-synthetic Ti Exchanged UiO-66 Metal-Organic Frameworks that Deliver Exceptional Gas Permeability in Mixed Matrix Membranes. Sci Rep. 2015;5:7823.

250. Khdhayyer MR, Esposito E, Fuoco A, Monteleone M, Giorno L, Jansen JC, et al. Mixed matrix membranes based on UiO-66 MOFs in the polymer of intrinsic microporosity PIM-1. Sep Purif Technol. 2017;173:304–13.

251. Naseri M, Mousavi SF, Mohammadi T, Bakhtiari O. Synthesis and gas transport performance of MIL-101/Matrimid mixed matrix membranes. J Ind Eng Chem. Elsevier; 2015;29:249–56.

252. Ma J, Ying Y, Guo X, Huang H, Liu D, Zhong C, et al. Fabrication of mixed-matrix membrane containing metal–organic framework composite with task-specific ionic liquid for efficient CO_2 separation. J Mater Chem A. The Royal Society of Chemistry; 2016;4:7281–8.

253. Liu Y-Y, Zeng J-L, Zhang J, Xu F, Sun L-X. Improved hydrogen storage in the modified metal-organic frameworks by hydrogen spillover effect. Int J Hydrogen Energy. Pergamon; 2007;32:4005–10.

254. Lin K-S, Adhikari AK, Su Y-H, Shu C-W, Chan H-Y. Synthesis, characterization, and hydrogen storage study by hydrogen spillover of MIL-101 metal organic frameworks. Adsorption. Springer US; 2012;18:483–91.

255. Xiang Z, Hu Z, Yang W, Cao D. Lithium doping on metal-organic frameworks for enhancing H2 Storage. Int J Hydrogen Energy. Pergamon; 2012;37:946–50.

256. Rallapalli PBS, Raj MC, Patil D V., Prasanth KP, Somani RS, Bajaj HC. Activated carbon @ MIL-101(Cr): a potential metal-organic framework composite material for hydrogen storage. Int J Energy Res. 2013;37:746–53.

257. Bhatia SK, Myers AL. Optimum conditions for adsorptive storage. Langmuir. American Chemical Society; 2006;22:1688–700.

258. Xiao J, Wang J, Cossement D, Bénard P, Chahine R. Finite element model for charge and discharge cycle of activated carbon hydrogen storage. Int J Hydrogen Energy. 2012;37:802–10.

259. Xiao J, Hu M, Bénard P, Chahine R. Simulation of hydrogen storage tank packed with metal-organic framework. Int J Hydrogen Energy. 2013;38:13000–10.

260. Xiao J, Zhou T, Cossement D, Bénard P, Chahine R. Coupled thermal simulation of hydrogen storage tank-Dewar flask system. Int J Hydrogen Energy. 2013;38:10880–8.

261. Xiao J, Peng R, Cossement D, Bénard P, Chahine R. Heat and mass transfer and fluid flow in cryo-adsorptive hydrogen storage system. Int J Hydrogen Energy. 2013;38:10871–9.

262. Ubaid S, Zacharia R, Xiao J, Chahine R, Bénard P, Tessier P. Effect of flowthrough cooling heat removal on the performances of MOF-5 cryo-adsorptive hydrogen reservoir for bulk storage applications. Int J Hydrogen Energy. Pergamon; 2015;40:9314–25.

263. Ubaid S, Zacharia R, Xiao J, Chahine R, Bénard P. Effect of para–ortho conversion on hydrogen storage system performance. Int J Hydrogen Energy. Pergamon; 2014;39:11651–60.

264. Ubaid S, Zacharia R, Xiao J, Chahine R, Bénard P, Tessier P. Charge–discharge cycling, flowthrough cooling and para-ortho conversion for cooling bulk hydrogen storage tank filled with MOF-5. Int J Hydrogen Energy. Pergamon; 2016;41:1044–52.

265. Kumar S, Raju M, Senthil Kumar V. System simulation models for on-board hydrogen storage systems. Int J Hydrogen Energy. 2012;37:2862–73.

266. Senthil Kumar V, Raghunathan K, Kumar S. A lumped-parameter model for cryo-adsorber hydrogen storage tank. Int J Hydrogen Energy. 2009;34:5466–75.

267. Siegel D, Tamburello D. Development of an Adavnced Hydrogen Storage System Based on Adsorbent Media. World Hydrog Energy Conf. Toronto, ON; 2012.

268. Paggiaro R, Michl F, Bénard P, Polifke W. Cryo-adsorptive hydrogen storage on activated carbon. II: Investigation of the thermal effects during filling at cryogenic temperatures. Int J Hydrogen Energy. 2010;35:648–59.

269. Schlemminger C, Næss E, Bünger U. Cryogenic adsorption hydrogen storage with enhanced heat distribution – An in-depth investigation. Int J Hydrogen Energy. Pergamon; 2016;41:8900–16.

270. Schlemminger C, Næss E, Bünger U. Adsorption hydrogen storage at cryogenic temperature – Material properties and hydrogen ortho-para conversion matters. Int J Hydrogen Energy. Pergamon; 2015;40:6606–25.

271. Anton DL, Motyka T. Hydrogen Storage Engineering Center of Excellence [Internet]. 2016 Annu. Merit Rev. Proc. Washington DC; 2016 [cited 2017 Oct 13]. Available from: https://www.hydrogen.energy.gov/pdfs/review16/st004_anton_2016_o.pdf

272. Anton DL, Hardy BJ, Tamburello DA, Corgnale C, Sulic M. Hydrogen Storage Engineering Center of Excellence [Internet]. FY 2016 Annu. Prog. Rep. Washington DC; 2016 [cited 2017 Oct 13]. Available from: https://www.hydrogen.energy.gov/pdfs/progress16/iv_b_1_anton_2016.pdf

273. Bakker S, van Lente H, Meeus MTH. Dominance in the prototyping phase—The case of hydrogen passenger cars. Res Policy. 2012;41:871–83.

274. Hirose K. Hydrogen Storage Technologies – View of Current and Future from Car Manufacture . World Hydrog Energy Conf 2012. Toronto, ON, Canada; 2012.

275. Sharpe JE, Bimbo N, Ting VP, Burrows AD, Jiang D, Mays TJ. Supercritical hydrogen adsorption in nanostructured solids with hydrogen density variation in pores. Adsorption. 2013;19:643–52.

276. Yaghi OM, Eddaoudi M, Li H, Kim J, Rosi N. Isoreticular metal-organic frameworks, process for forming the same, and systematic design of pore size and functionality therein, with application for gas storage. United States: USPTO; 2003.

277. Organisation for Economic Co-Operation & Development. Test No. 119: Determination of the Low Molecular Weight Content of a Polymer Using Gel Permeation Chromatography. OECD Guidel Test Chem Sect I Phys Prop. OECD Publishing; 1996.

278. Higson S. Analytical Chemistry. Oxford University Press; 2004. p. 235–6.

279. International Standards Organization. BS ISO 16014-1:2012 Plastics. Determination of average molecular mass and molecular mass distribution of polymers using size-exclusion chromatography. General principles. British Standards Institute; 2012.

280. BSI Group. BS EN 13925-1:2003 Non-destructive testing. X-ray diffraction from polycrystalline and amorphous materials. General principles. 2003.

281. Manning B, Ichimura A. Bruker D8 ADVANCE Powder XRD Instrument Manual and Standard Operating Procedure (SOP). San Francisco, CA; 2006.

282. Tavernier S. Detectors Based on Scintillation. Exp Tech Nucl Part Phys. Berlin, Heidelberg: Springer Berlin Heidelberg; 2009. p. 167–208.

283. Bates J. Fourier transform infrared spectroscopy. Science (80-). 1976;191.

284. Michael S. Bradley. FT-IR: How and Why? ThermoFisher Scientific;

285. Block Engineering. FTIR and Michelson Interferometer Technology Overview [Internet]. 2017 [cited 2017 Jul 18]. Available from: http://blockeng.com/technology/ftirtechnology.html

286. Cantafio C. How the SEM Works [Internet]. 1998 [cited 2017 Jan 16]. Available from: http://antoine.frostburg.edu/engin/sem/workings.html

287. Wells OC. Scanning Electron Microscopy. McGraw-Hill; 1974.

288. Jeol Ltd. SEM Q&A.

289. Fultz B, Howe J. Inelastic Electron Scattering and Spectroscopy. In: Fultz B, Howe J, editors.

Trasm Electron Microsc Diffractometry Mater. Berlin: Springer Berlin Heidelberg; 2013. p. 181–236.

290. RSC Instrumental Criteria Sub-Commitee. CHNS Elemental Analysers. 2008.

291. Horiba Scientific Ltd. The Theory of Raman Spectroscopy [Internet]. Raman Acad. 2017 [cited 2017 Jul 20]. Available from: https://tinyurl.com/yc7ss282

292. Ferraro JR, Nakamoto K, Brown CW. Instrumentation and Experimental Techniques. In: Ferraro JR, Nakamoto K, Brown CW, editors. Introd Raman Spectrosc. 2nd ed. Academic Press; 2003. p. 95–146.

293. Horiba Scientific Ltd. What laser wavelengths are used for Raman spectroscopy? [Internet]. Raman Acad. 2017 [cited 2017 Jul 20]. Available from: https://tinyurl.com/y7kz4eb5

294. Horiba Scientific Ltd. What types of laser (Rayleight) filtering are used? [Internet]. Raman Acad. 2017 [cited 2017 Jul 20]. Available from: https://tinyurl.com/y9agspcj

295. Setaram. Evolution DTA, DSC, TGA, TGA-DTA/DSC, TGA-EGA, TMA: The top of the range in thermal analyzers. 2016.

296. Gross JH. Mass Spectrometry. Berlin, Heidelberg: Springer Berlin Heidelberg; 2011.

297. Reusch W. Mass Spectrometry [Internet]. chemistry.msu.edu. 2013 [cited 2017 Jan 18]. Available from: https://tinyurl.com/z3xeq4q

298. International Standards Organization. BS EN ISO 11357-1:2016 Plastics. Differential Scanning Calorimetry (DSC). General Principles. British Standards Institute; 2016.

299. TA Instruments. DSC Differential Scanning Calorimeter Q SeriesTM Getting Started Guide. 2007.

300. International Standards Organization. BS EN ISO 11357-4:2013 Plastics. Differential scanning calorimetry (DSC). Determination of specific heat capacity. British Standards; 2013.

301. Thomas LC. Modulated DSC ® Paper #1 Why Modulated DSC ® ? ; An Overview and Summary of Advantages and Disadvantages Relative to Traditional DSC.

302. Lacey AA, Price DM, Reading M. Theory and Practice of Modulated Temperature Differential Scanning Calorimetry. Modul Temp Differ Scanning Calorim. Springer Netherlands; 2006. p. 1–81.

303. Malbrunot P, Vidal D, Vermesse J, Chahine R, Bose TK. Adsorbent Helium Density Measurement and Its Effect on Adsorption Isotherms at High Pressure. Langmuir. American Chemical Society; 1997;13:539–44.

304. Sing KSW, Rouquerol F, Rouquerol J. Classical Interpretation of Physisorption Isotherms at the Gas-Solid Interface. In: Rouquerol J, Rouquerol F, Llewellyn P, Maurin G, Sing KSW, editors. Adsorpt by Powders Porous Solids Princ Methodol Appl. 2nd ed. Academic Press; 2014.

305. International Organization of Standardization. ISO 9277:2010 - Determination of the specific surface area of solids by gas adsorption — BET method. 2008.

306. Sing KSW. Assessment of Surface Area by Gas Adsorption. In: Rouquerol J, Rouquerol F, Llewellyn P, Maurin G, Sing KSW, editors. Adsorpt by Powders Porous Solids Princ Methodol Appl. 2nd ed. Academic Press; 2014.

307. Rouquerol J, Llewellyn P, Rouquerol F. Is the BET equation applicable to microporous adsorbents? Stud Surf Sci Catal. Elsevier; 2007;160:49–56.

308. Sing KSW, Rouquerol F, Rouquerol J, Llewellyn PL. Assessment of Mesoporosity. In: Rouquerol F, Rouquerol J, Sing KSW, Llewellyn PL, Maurin G, editors. Adsorpt by Powders Porous Solids Princ Methodol Appl. 2nd ed. Academic Press; 2014. p. 307–12.

309. Ghosal R, Smith DM. Micropore characterization using the Dubinin-Astakhov equation to analyze high pressure CO2 (273 K) adsorption data. J Porous Mater. 1996;3:247–55.

310. McEnaney B. Adsorption and Structure in Microporous Carbons. Carbon N Y. 1988;26:267–74.

311. Micromeritics. Appendix C: Calculations. ASAP 2020 Author's Man. Norcross, GA: Micromeritics; 2006.

312. Groen JC, Peffer LA., Pérez-Ramírez J. Pore size determination in modified micro- and mesoporous materials. Pitfalls and limitations in gas adsorption data analysis. Microporous Mesoporous Mater. 2003;60:1–17.

313. Barrett EP, Joyner LG, Halenda PP. The Determination of Pore Volume and Area Distributions in Porous Substances. I. Computations from Nitrogen Isotherms. J Am Chem Soc. American Chemical Society; 1951;73:373–80.

314. Horváth G, Kawazoe K. Method for the calculation of effective pore size distribution in molecular sieve carbon. J Chem Eng Japan. 1983;16:470–5.

315. Thommes M, Cychosz KA. Physical adsorption characterization of nanoporous materials: progress and challenges. Adsorption. Springer US; 2014;20:233–50.

316. Sing KSW, Rouquerol F, Llewellyn PL, Rouquerol J. Assessment of Microporosity. In: Rouquerol F, Rouquerol J, Sing KSW, Llewellyn PL, Maurin G, editors. Adsorpt by Powders Porous Solids Princ Methodol Appl. 2nd ed. Academic Press; 2014. p. 303–20.

317. Landers J, Gor GY, Neimark A V. Density functional theory methods for characterization of porous materials. Colloids Surfaces A Physicochem Eng Asp. 2013;437:3–32.

318. Jeffs C. Removal of toxic industrial chemicals using novel adsorbent hollow fibres. University of Bath; 2015.

319. Bimbo N, Xu W, Sharpe JE, Ting VP, Mays TJ. High-pressure adsorptive storage of hydrogen in MIL-101 (Cr) and AX-21 for mobile applications: Cryocharging and cryokinetics. Mater Des. 2015;89:1086–94.

320. Hao L, Li P, Chung T-S. PIM-1 as an organic filler to enhance the gas separation performance of Ultem polyetherimide. J Memb Sci. 2014;453:614–23.

321. Yong WF, Li FY, Chung T-S, Tong YW, Ito Y, Claridge JB, et al. Highly permeable chemically modified PIM-1/Matrimid membranes for green hydrogen purification. J Mater Chem A. The Royal Society of Chemistry; 2013;1:13914.

322. Chaukura N, Maynard-Atem L. Interaction of a Polymer of Intrinsic Microporosity (PIM-1) with Penetrants. Am J Appl Chem. Science Publishing Group; 2015;3:139.

323. Zhou X, Huang W, Shi J, Zhao Z, Xia Q, Li Y, et al. A novel MOF/graphene oxide composite GrO@MIL-101 with high adsorption capacity for acetone. J Mater Chem A. The Royal Society of Chemistry; 2014;2:4722–30.

324. Zhang Z, Wang H, Chen X, Zhu C, Wei W, Sun Y. Chromium-based metal–organic framework/mesoporous carbon composite: synthesis, characterization and CO2 adsorption. Adsorption. Springer US; 2015;21:77–86.

325. Su L, Xiong Y, Yang H, Zhang P, Ye F, Wu Q, et al. Prussian blue nanoparticles encapsulated inside a metal–organic framework via in situ growth as promising peroxidase mimetics for enzyme inhibitor screening. J Mater Chem B. The Royal Society of Chemistry; 2016;4:128–34.

326. Liu S, Xu F, Liu L-T, Zhou Y-L, Zhao W. Heat capacities and thermodynamic properties of Cr-MIL-101. J Therm Anal Calorim. Springer Netherlands; 2017;129:509–14.

327. The Engineering Toolbox. Polymers - Specific Heats [Internet]. Eng. Toolbox. 2017 [cited 2017 Aug 1]. Available from: http://www.engineeringtoolbox.com/specific-heat-polymers-d_1862.html

328. Jagiello J, Thommes M. Comparison of DFT characterization methods based on N2, Ar, CO2, and H2 adsorption applied to carbons with various pore size distributions. Carbon N Y.

2004;42:1227–32.

329. Garrido J, Linares-Solano A, Martin-Martinez JM, Molina-Sabio M, Rodriguez-Reinoso F, Torregrosa R. Use of nitrogen vs. carbon dioxide in the characterization of activated carbons. Langmuir. American Chemical Society; 1987;3:76–81.

330. Cascarini de Torre LE, Bottani EJ, Steele* WA. Amorphous Carbons: Surface Structure and Adsorptive Properties. Langmuir. American Chemical Society; 1996;12:5399–406.

331. Chakura N. Sorption of Gases and Liquids by Polymers of Intrinsic Porosity. University of Manchester; 2011.

332. Krause S, Bon V, Senkovska I, Stoeck U, Wallacher D, Többens DM, et al. A pressure-amplifying framework material with negative gas adsorption transitions. Nature. Nature Publishing Group, a division of Macmillan Publishers Limited. All Rights Reserved.; 2016;532:348–52.

333. Adar F. Introduction to Interpretation of Raman Spectra Using Database Searching and Functional Group Detection and Identification. Spectroscopy. 2016;31:16–23.

334. Horiba Jobin Yvon Ltd. Raman Spectroscopy for Analysis and Monitoring [Internet]. Raman Appl. Note. [cited 2017 Aug 25]. Available from: https://tinyurl.com/y92e9z4v

335. University of Toronto Scarborough TRACES Lab. RAMAN Band Correlation Table [Internet]. [cited 2017 Aug 25]. Available from: http://www.utsc.utoronto.ca/~traceslab/raman correlation table.pdf

336. Pimenta MA, Dresselhaus G, Dresselhaus MS, Cançado LG, Jorio A, Saito R, et al. Studying disorder in graphite-based systems by Raman spectroscopy. Phys Chem Chem Phys. The Royal Society of Chemistry; 2007;9:1276–90.

337. Jawhari T, Roid A, Casado J. Raman spectroscopic characterization of some commercially available carbon black materials. Carbon N Y. 1995;33:1561–5.

338. Cançado LG, Takai K, Enoki T, Endo M, Kim YA, Mizusaki H, et al. General equation for the determination of the crystallite size La of nanographite by Raman spectroscopy. Appl Phys Lett. 2006;88:163106.

339. Walker PL., Rakszawski JF., Amington AF. Determination of Graphitic and Amorphous Carbons. ASTM Bull. 1955;52–4.

340. Girgis BS, Temerk YM, Gadelrab MM, Abdullah ID. X-ray Diffraction Patterns of Activated Carbons Prepared under Various Conditions. Carbon Lett. 2007;8:95–100.

341. Bénard P, Chahine R. Determination of the Adsorption Isotherms of Hydrogen on Activated Carbons above the Critical Temperature of the Adsorbate over Wide Temperature and Pressure Ranges. Langmuir. American Chemical Society; 2001;17:1950–5.

342. Gundiah G, Govindaraj A, Rajalakshmi N, Dhathathreyan KS, Rao CNR. Hydrogen storage in carbon nanotubes and related materials. J Mater Chem. The Royal Society of Chemistry; 2003;13:209–13.

343. Bimbo N, Ting VP, Hruzewicz-Kołodziejczyk A, Mays TJ. Analysis of hydrogen storage in nanoporous materials for low carbon energy applications. Faraday Discuss. The Royal Society of Chemistry; 2011;151:59.

344. Sharpe JE, Bimbo N, Ting VP, Rechain B, Joubert E, Mays TJ. Modelling the potential of adsorbed hydrogen for use in aviation. Microporous Mesoporous Mater. 2015;209:135–40.

345. Marquardt DW. An Algorithm for Least-Squares Estimation of Nonlinear Parameters. J Soc Ind Appl Math. Society for Industrial and Applied Mathematics; 1963;11:431–41.

346. Ranganathan A. The Levenberg-Marquardt Algorithm. 2004;

347. OriginLab. Interpreting Regression Results [Internet]. Orig. Help. [cited 2017 Oct 22]. Available from: https://tinyurl.com/y9smq58l

348. Silvera I. The solid molecular hydrogens in the condensed phase: Fundamentals and static properties. Rev Mod Phys. 1980;52:393–452.

349. Ting VP, Ramirez-Cuesta AJ, Bimbo N, Sharpe JE, Noguera-Diaz A, Presser V, et al. Direct Evidence for Solid-like Hydrogen in a Nanoporous Carbon Hydrogen Storage Material at Supercritical Temperatures. ACS Nano. American Chemical Society; 2015;9:8249–54.

350. Rochat S, Polak-Kraśna K, Tian M, Holyfield LT, Mays TJ, Bowen CR, et al. Hydrogen storage in polymer-based processable microporous composites. J Mater Chem A. The Royal Society of Chemistry; 2017;5:18752–61.

9. Electronic Supplementary Information

Contents: